

THIS WEEK

EDITORIALS

WORLD VIEW Authors' lists should give way to online databases **p.475**

POOR COPIES Man-made salt marshes lack biodiversity **p.476**



A LEG UP How salamanders regrow amputated limbs **p.477**

A second wind for the president

A lack of leadership has hampered progress against global warming. If Barack Obama earns a second term as US president, will he have the energy to tackle climate?

Barack Obama entered the White House on a wave of hope that was every bit as real for scientists as for voters. Early optimism gave way before often-nasty political realities, but Obama mostly made good on his promises by appointing top-flight researchers to his administration, elevating science within federal agencies and making research and development the foundation of a broader vision of innovation. As he makes his pitch for another four years, there can be little doubt that he intends to continue supporting science. But the vision that he laid out four years ago remains a work in progress.

Nowhere is this clearer than with energy and climate. As discussed on page 488, the president has increased investments in research and development that may one day help to reduce the cost of clean energy technologies and hasten progress on fighting global warming. Regulations that aim to clean up the atmosphere and protect public health are already encouraging a transition towards cleaner energy. Obama also deserves credit for staking out a centrist position on energy issues, leaving room for both renewables and the smart development of domestic fossil-fuel resources. But as the political discussion about climate has degenerated to a frightening degree during the past four years, he has offered too little leadership on these issues.

The polarization has its roots in both the politics of the economic crisis and the dearth of quick, cheap solutions. Curbing emissions on the scale required to avert dangerous warming is a daunting challenge, but it is feasible and will be cost-effective in the long term. Shifting to cleaner energy would bring benefits not just to climate, but also to air quality, infrastructure and public health. But the cleanest sources of power cost more up front, and politicians are loath to increase energy prices when the economy is struggling. And although the number of green-energy jobs is increasing, shutting down old coal-fired power plants means job losses — and political protests — on a local scale. This has fuelled angry opposition to the modest pollution regulations that Obama's administration has rolled out during his first term.

Given the toxic political atmosphere surrounding the November elections, it is perhaps understandable that the administration, Democrats and even some environmentalists are saying little about global warming. But by failing to speak out, they have often ceded the airwaves to deniers. Although polling shows that almost two-thirds of US citizens support some kind of action on global warming, law-makers in Washington DC are back to debating the validity of climate science. The United States needs leadership that is willing and able to uphold and act on the science.

If Obama wins a second term, he will need to take on the political opposition and bring apparently disparate interests together. This means laying out a clear vision for the future, and making the immediate steps clear. Fortunately, Obama might find it easier to do this during a second term, when he would be free

to think about his legacy instead of about re-election.

His opponent, Mitt Romney, has a record on global warming that is spotty at best. As governor of Massachusetts from 2003 to 2007, Romney initially supported, then backed out of, the Regional Greenhouse Gas Initiative, a cap-and-trade programme to reduce emissions from electricity generation across New England. Last year, he broke with Republican ranks and declared global warming a threat, but more recently he has questioned its severity. He is now proposing to roll back the government's regulatory powers. If he wins the election, scientists will have to work with the new administration and hope that the president will muster the courage to take on his own party and govern as the centrist he was in Massachusetts, where he introduced a state health-care initiative that was the model for Obama's national effort.

The next round of greenhouse-gas policies is likely to consist of targeted measures, unlike the economy-wide cap-and-trade approach that failed in 2010. The Obama administration has regulated emissions from vehicles and required sharp increases in fuel economy; the next big target is electricity generation. Like the car industry, utility companies want economic certainty. Environmentalists want emissions reductions. Is there a way to ensure both without over-burdening consumers? Or could a carbon tax make a comeback as a way to increase revenues and lower income taxes?

Whatever the next steps, they will require bringing the business community together with scientists, environmentalists, workers and others. A clever leader might yet be able to build support for viable political solutions where seemingly narrow interests converge. ■

Therapy deficit

Studies to enhance psychological treatments are scandalously under-supported.

Depression takes many forms, and it is not always easy to diagnose. There is no doubt, however, that it represents a colossal health burden. According to the World Health Organization, it is one of the leading illnesses when ranked by impact on productivity, and directly affects 121 million people worldwide.

As has been discussed in *Nature's* pages, the standard research-based model of therapy development for psychiatric disorders — target identification, drug discovery and clinical investigation — is imploding as biologists grapple with the complexities and drug companies see too



US ELECTION
Science and Politics in America
nature.com/election2012

few prospects to keep investing. Most psychologists agree that the drugs already in use are efficacious to a point, but with plenty of room for improving their effectiveness and reducing side effects.

Psychological treatments are the other arm of therapy for depression and many psychiatric disorders. The literature is full of trials indicating that they are in some contexts more effective and better at preventing relapse than pharmaceutical interventions. There are no physical side effects, but some of the best-validated treatments depend on therapists with training. Unlike drug therapies, there are no multibillion-dollar suppliers of these treatments with the motivation to market them and make them easily obtainable.

The money being spent on researching psychological therapies is tiny by comparison with budgets for fundamental neuroscience and for translation and drug discovery. And yet such therapies have the potential to make a substantive difference to new categories of patients. What is more, treatments could doubtless be improved in their existing applications by deeper investigation of their outcomes.

This fundamental funding imbalance is compounded by the fact that the sources of research funding disfavour studies of psychological treatments that focus only on efficacy. *Nature* would be the last to question the importance of research for causal or mechanistic insights. But the brain's complexity and relative inaccessibility leaves a gulf between the current basic understanding and the observed pathologies of human minds. Taking existing psychological therapies and improving and extending their psychological models and applications, and developing new ones, regardless of the underlying neural processes in the brain, is also a justifiable endeavour for funding agencies. Given the immediate benefits this research could bring, the deficit of interest in funding it is a scandal.

Take one prominent example. Since 2006, UK governments have increasingly committed to a programme called Improving Access to Psychological Therapies. This massive, enlightened initiative in psychotherapeutic capacity-building has increased the number of practising cognitive behavioural therapists by several thousand, providing more than 600,000 people with access to these services, particularly patients with depression and anxiety disorders.

“Psychological therapies have the potential to make a substantive difference to patients.”

Inspect the databases of this programme and you find large variations in outcomes between UK regions. A deeper look would allow one to examine many factors relating to the effectiveness of such treatments, thereby opening the prospect of improvements in the United Kingdom and elsewhere.

As psychologists outside Britain will confirm, despite the variability in outcomes, this programme represents a world-beating standard thanks to the scale of its implementation and the validation of its treatments by the UK National Institute for Health and Clinical Excellence. And yet since its inception, the UK government has prevented any of the funds from being used for scientific research on the factors underlying its measured impacts.

This is an extreme example. Many funding agencies around the world are too keen solely to support mechanistic investigations with potential long-term payoffs, and too unwilling to appreciate that part of their portfolio should be oriented towards identifying immediately effective psychological interventions. Success in this area would further encourage policy-makers to enhance much-needed access to treatment for psychiatrically ill individuals. After all, many of these people are taxpayers who ultimately fund research into brains and minds. ■

Poison postures

Researchers working on controversial topics must take care how they promote their results.

“**Y**es, GMOs are poisons,” screamed the front cover of last week's issue of the respectable French news weekly, *Le Nouvel Observateur*. The blatantly fallacious headline was the opening salvo in a blitz of media coverage about research published online in the journal *Food and Chemical Toxicology*. The paper, from a research group led by Gilles-Eric Seralini, a molecular biologist at the University of Caen in France, claimed to show that consumption of a genetically modified (GM) maize (corn) that had already been approved for animal and human consumption and of the herbicide Roundup greatly elevates rates of cancer and other illnesses, and causes premature deaths, in rats.

With such strong claims and the predictably large effect they will have on public opinion, researchers should take care how they present their findings to the public and the media. They should spell out their results clearly; emphasize the limitations and caveats; and make it clear that the data still need to be assessed, and replicated, by the scientific community.

That didn't happen. The paper was promoted in a public-relations offensive, with a related book and film set for release this week. Furthermore, journalists wishing to report the research had to sign confidentiality agreements that prevented them from contacting other scientists for comment on the paper until after the embargo had expired. Some, to their credit, refused, or accepted and then revisited the story critically once their hands were no longer tied by these outrageous restrictions.

The result was the exclusion of critical comment in many of the breaking stories — the ones that most people will remember. But much criticism has followed (see page 484). In hindsight, journalists who agreed to the conditions should have contacted the journal publisher

— in this case, Elsevier — which no doubt would have done its best to have made the paper available under embargo without such constraints.

The embargo system gives journalists advance access to papers on the premise that it will give them time to research the story fully before presenting it to the public. The system also benefits journals and authors because it helps to maximize press coverage, but at its heart, it is about helping to improve the quality of science reporting. Crucially, the embargo system allows journalists to consult scientists not involved in the work before interpreting it for the public.

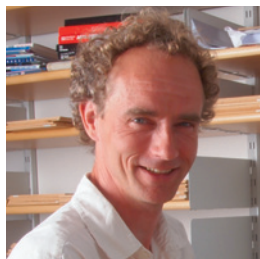
The criticisms that followed questioned both the study's methodology and findings. Given its exceptional claims, the authors of the paper now need to make their raw data available so that they can be carefully assessed by scientists with appropriate expertise, and the work replicated or refuted — thus will the study stand or fall. The European Food Safety Agency, and other advisory and regulatory bodies, are planning to assess the research, and these assessments should be as transparent as possible, so that the public can be confident about whatever they conclude.

The events of last week also illustrate a long-standing flaw in the debate over the safety of GM crops. Many have used last week's publication to claim that GM foods are a health risk. But even if one GM crop were to be shown to have serious adverse health effects, that would say little about others: the safety of any genetic modification depends on the crop and on the particular changes introduced. Scientists who support transgenic crops fall into the same trap when they claim that the many GM crops that have passed safety tests somehow show that ‘GMOs are safe’. They should instead be giving the message that GM foods must be assessed on a case-by-case basis.

Too often in the GM-food debate, generalizations and extremism lead to sterile public and political discourse that obscures key issues: what sorts of GM crops might bring true benefits to agriculture and consumers; how to avoid monopolization of farming choices; and what types of sustainable agriculture we want in the future. Polarized debates, not GMOs, are the poison to be avoided. ■

➤ NATURE.COM
To comment online,
click on Editorials at:
go.nature.com/xhunq

A. MEER



It is time for full disclosure of author contributions

Online databases could increase fairness and transparency by fully documenting the role of each contributor to a paper, says **Sebastian Frische**.

When it comes to apportioning credit, science could learn from the movies. Since 1934, the Academy of Motion Picture Arts and Sciences, which awards the Oscars, has maintained an index to film credits, now called the Motion Picture Credits Database. For every film being considered for an award, the contribution of each person who worked on it, from hair stylists to the lead actress, is documented. Science, for all its focus on assessing and quantifying, has nothing like this.

The main currency in the world of science is authorship. Authorships enable scientists to accumulate citations, which seem to be established as the 'true' measure of successful and important science. Authorships are key to getting grants and winning promotions, and are also the foundation for a recently proposed algorithm for predicting scientists' success — their future *h*-index (D. E. Acuna *et al.* *Nature* **489**, 201–202; 2012).

Yet authorship is a dubious indicator. Sophisticated readers know that decoding an author list in terms of actual contribution to the scientific paper is close to impossible, unless you are involved yourself. Students find that they have to contribute much more to be listed as an author than more senior researchers do. Initially, students can feel exploited, but they may get used to the system. Eventually, if they choose an academic career, they may (more or less willingly) adopt the behaviour themselves. Political and personal relations also determine whether a contributor appears in the list of authors or under 'Acknowledgements'.

Some disciplines follow conventions in which list order reflects the relative importance or type of contribution. However, only experienced readers understand the conventions, which differ between disciplines and can be difficult to apply to papers with many authors.

For example, a six-page paper on the discovery of the Higgs boson at the Large Hadron Collider at CERN, Europe's particle-physics laboratory near Geneva, Switzerland, was followed by seven pages of author names, but readers without a deep understanding of the experiment's organization have no way of deducing the roles of the authors. They could not all have written the manuscript, and skilled people not listed probably also contributed to the experiments. Simplifying each person's contribution to a co-authorship results in an incomplete picture of their role in the work.

Scientific publishers are aware of the problems of authorship, and many journals (such as *Nature*) publish descriptions — often in broad terms — of the contributions of each author. However, these accounts are mainly intended to keep author lists free of people who have made no real contribution to the work.

DECODING AN
AUTHOR LIST
IN TERMS OF ACTUAL
CONTRIBUTION
TO THE SCIENTIFIC
PAPER IS CLOSE TO
IMPOSSIBLE.

➔ **NATURE.COM**
Discuss this article
online at:
go.nature.com/qtpehz

They provide little detail on what each author did. And they leave out people whose activities — fund-raising or data acquisition, for example — are not enough to qualify for authorship, but are still pivotal.

A better system could soon emerge. Already, databases of scientific authors such as ResearcherID.com, BioMedExperts.com and ResearchGate.net allow authors to interact, form interest groups and rate each others' publications. ResearchGate has even introduced a new metric based on a scientist's contributions and activity in the network.

As a natural next step, these online networks could give the authors of a paper an opportunity to publish detailed accounts of each person's contribution. With a mouse click, each contributor could verify what others contributed, resulting in merit lists validated by all participants. A similar, but paper-based, system has existed for decades in Denmark, where co-author declarations document what work PhD

students contributed to the papers included in their theses. The rigorous rules for authorship, requiring substantial contributions to the design of the work, data gathering and writing, would no longer be relevant, because each contribution could be described and valued. Everyone who made the science possible would be properly acknowledged, and the word 'author' could regain its true meaning.

In the highly competitive film industry, credit lists are the basis for the CVs of the diverse professionals needed to produce a blockbuster. A full contribution database would offer similar benefits to scientists. Contributors could generate updated, verified and detailed accounts of their scientific merits using a few clicks. Journals, funding agencies and employers would all come to rely on the system. Journals might replace the authors and acknowledgments sections in papers with online credit lists, funding agencies could use the system to generate validated CVs for the review process and employers could find the person with just the right skills and experience for the job.

The technical platform for such a database could emerge from the world of music, software development, film, journalism or any other creative industry. With the right technology, writing and approving entries in these networks could become everyday routine, just as 'liking' something on Facebook is today. Validated web-based information networks will allow documented skills — not just numbers of papers or citation-based indices — to count towards advancement in academic life. The transparency and distributed nature of such networks would create a strong incentive for honesty, and fundamentally improve the morale and culture of science. ■ **SEE CAREERS P.591**

Sebastian Frische is associate professor of biomedicine at the University of Aarhus, Denmark.
e-mail: sfri@ana.au.dk

DISEASE

Cells turn back clock in diabetes

In type 2 diabetes, the pancreas's β cells stop making insulin because they revert to progenitor cells, rather than because they die, as has been thought.

A team led by Domenico Accili at Columbia University in New York studied mice lacking the *Foxo1* gene, which is involved in cell specialization or differentiation, in their β cells. The animals produced fewer β cells and developed high blood-sugar levels. Moreover, the authors found that the β cells reverted back to endocrine progenitor cells, which are unable to make insulin. Mice in two other models of diabetes also produced such de-differentiated β cells.

Turning these stem cells back into β cells could be a way to treat type 2 diabetes, the authors suggest.

Cell 150, 1223–1234 (2012)

DRUG DEVELOPMENT

Fragile-X drug in humans and mice

A drug called arbaclofen has shown potential for relieving symptoms of fragile X syndrome — a genetic disease that causes intellectual disability and autism — according to a clinical and an animal study published back-to-back.

Fragile X syndrome is caused by a faulty gene, which leads to excessive protein synthesis at neuronal connections, or synapses, in the brain, and to exaggerated excitatory neurotransmission. Two teams led by scientists from Seaside Therapeutics in Cambridge, Massachusetts, investigated whether

arbaclofen — which promotes inhibitory neurotransmission by activating GABA_A receptors — could mitigate symptoms.

Paul Wang and his colleagues ran a placebo-controlled clinical trial in 63 people with fragile X. They found no effect on irritability, but social function improved in 27 people who had severe social impairment.

In a study of mice with the condition, Aileen Healy and her colleagues found

that the drug corrected the excessive protein synthesis and associated synaptic abnormalities.

Sci. Transl. Med. 4, 152ra127; 152ra128 (2012)

NANOTECHNOLOGY

Pulsating tubes act as pumps

Nanometre-scale tubules made of self-assembled molecules have been designed to expand

and contract with changing temperature, pumping molecules out of their interior.

Nanotubes are normally too rigid to allow major structural changes, thanks to the bonds that hold their shape. Myongsoo Lee at Seoul National University and his colleagues created pulsating nanotubules from bent carbon-based chains that stack together in water. The 'arms' of the chains overlap to form staggered



ECOLOGY

Artificial marshes fall short

Man-made salt marshes have less biodiversity than similar naturally occurring habitats, and so are failing to meet European regulations.

Natural salt marshes lost to coastal development or erosion must be replaced with biologically equivalent replicas under European Union law. Hannah Mossman at the University of East Anglia in Norwich, UK, and her team compared the vegetation at 35 salt marshes that had been man-made or created by storm surges with that at 34 naturally occurring marshes across the United

Kingdom. The researchers found that the natural habitats were home to many plants, including sea lavender (*Limonium vulgare*, pictured left), thrift (*Armenia maritima*) and sea plantain (*Plantago maritima*), that were often absent in replica habitats (pictured right).

The authors suggest that management of artificial marshes should be improved using measures such as planting extra species.

J. Appl. Ecol. <http://dx.doi.org/10.1111/j.1365-2664.2012.02198.x> (2012)

hexagonal rings that then assemble into a tube. When the temperature rises or falls, the segments slide against each other and the tubule expands or contracts, undergoing extensive structural changes but maintaining its hollow arrangement.

Science 337, 1521–1526 (2012)

MICROBIAL ECOLOGY

Symbiosis may fertilize seas

An unusual partnership between single-celled algae and cyanobacteria may provide a key source of nitrogen for marine life, and could shed light on how plants evolved to have photosynthetic organelles.

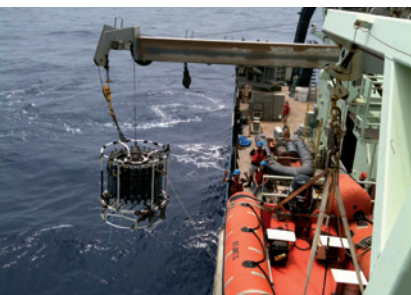
Jonathan Zehr at the University of California, Santa Cruz, and his colleagues investigated a widespread cyanobacterium that lacks certain genes involved in photosynthesis and metabolism but can convert atmospheric nitrogen into forms that other organisms can use. Zehr and his team sampled sea water (pictured) to look for symbiotic partners of the bacterium, and found a kind of unicellular alga. The bacterium attaches to the cell wall of the alga, and provides it with nitrogen in exchange for carbon.

The symbiosis is probably crucial to global carbon and nitrogen cycles, and is analogous to the early stages of an evolutionary process in which plants acquired microbes that would eventually become chloroplasts, the organelles that perform photosynthesis.

Science 337, 1546–1550 (2012)

J. BURTON/NATUREPL.COM

K. TURK-KUBO/SCIENCE/AAAS



CLIMATE CHANGE

Arctic snow lost faster than ice

The rate of loss of Arctic snow cover during spring is outpacing even the rapid decline of sea ice.

Chris Derksen in Toronto and Ross Brown in Montreal, both of Environment Canada, looked at satellite data on high-latitude snow cover between April and June since 1979, and compared it with observed changes in the extent of Arctic sea ice in the same period. In most Arctic land areas, snow cover remaining in June had decreased by almost 20% per decade. Arctic sea ice, which this summer melted to a new record low, has declined by about 10% per decade since 1979.

State-of-the-art climate models have considerably underestimated the accelerating downward trend in both snow cover and sea-ice extent since 2005, the authors note.

Geophys. Res. Lett. <http://dx.doi.org/10.1029/2012GL053387> (2012)

DEVELOPMENTAL BIOLOGY

Salamanders heal like embryos grow

The Mexican axolotl salamander, known for its ability to regrow lost limbs, may heal by reprogramming cells in the stumps of the amputated limbs to mimic developing embryonic cells.

Tony Hunter at the Salk Institute for Biological Studies in La Jolla, California, and his colleagues found that limb amputation in the axolotl (*Ambystoma mexicanum*, pictured) triggered expression of two genes, *PL1* and *PL2* — which are active in sperm and egg cells and in developing embryos — in the new outgrowth. The same genes were not stimulated near superficial wounds. Suppressing production of the *PL1* and *PL2* proteins



increased cell death in the developing limb and slowed its growth. Lower levels of the proteins were also linked to decreased levels of FGF8, a molecule important in normal limb development.

The findings could inform strategies for regenerating tissue in humans, the authors say.

Dev. Biol. 370, 42–51 (2012)

BIOCHEMISTRY

Enzyme design inspired by cancer

Mutations found in human cancer cells have been used to make enzymes that catalyse a reaction important in nylon production.

COMMUNITY CHOICE

The most viewed papers in science

CELL IMAGING

A peek at organelles in live cells

HIGHLY READ
on www.pnas.org
in August

Small molecules can be used for high-resolution fluorescence imaging of membrane-bound organelles in living cells.

A team led by Guo-Qiang Bi at the University of Science and Technology of China in Hefei and Xiaowei Zhuang at Harvard University in Cambridge, Massachusetts, developed a fluorescence-imaging method that uses common membrane probes. The researchers showed that the fluorescence of eight such probes can be switched on and off in living cells in normal culture medium, enabling high-resolution imaging. Using the probes, the researchers were able to obtain images of key organelles, including the power-generating mitochondria, with a spatial resolution of 30–60 nanometres and a temporal resolution of 1–2 seconds. This allowed them to capture previously unseen details about the dynamic membranes of the organelles, such as structures involved in the fusing of mitochondria.

Proc. Natl Acad. Sci. USA 109, 13978–13983 (2012)

Hai Yan and his colleagues at Duke University in Durham, North Carolina, identified stretches of amino acids from oxidoreductase enzymes with cancer-associated mutations. These mutations change the chemical reaction that the enzymes carry out on their substrates, molecules with a backbone of five carbon atoms. The researchers introduced these amino-acid residues into the active sites of related enzymes that act on substrates containing six carbon atoms. The resulting enzyme performed the desired cancer-associated reaction on six-carbon molecules, and could catalyse a reaction in the synthesis of adipic acid, a precursor of nylon.

The authors suggest that data from sequenced cancer genomes could be used to increase functional diversity in enzymes.

Nature Chem. Biol. <http://dx.doi.org/10.1038/nchembio.1065> (2012)

NATURE.COM

For the latest research published by Nature visit:

www.nature.com/latestresearch

SEVEN DAYS

The news in brief

BUSINESS

Database case

The American Chemical Society (ACS), the world's largest scientific society, is likely to have to pay US\$11.5 million in compensation to a small start-up company after a ruling by the Ohio Supreme Court on 18 September. The court ruled that the ACS, based in Washington DC, filed a lawsuit to unfairly suppress chemical-informatics firm Leadscope of Columbus, Ohio. See page 482 for more.

Drug-makers unite

Ten giant pharmaceutical companies have formed a non-profit organization called TransCelerate BioPharma, with the goal of making clinical trials more efficient. By setting universal standards in trial design and data collection, the group could shave time and expense off the drug-development process, says Garry Neil, head of TransCelerate and a former vice-president of science and technology at Johnson & Johnson. Smaller companies are invited to join the team. See go.nature.com/jj2sky for more.

POLICY

Stem-cell funds

The European Parliament's legal committee has recommended that research involving human embryonic stem cells should not be funded in the European Union's upcoming Horizon 2020 research programme. The committee refers to a decision by the European Court of Justice, which ruled on ethical grounds last October that treatments based on such cells were not patentable (see *Nature* **480**, 310–312; 2011). Horizon 2020 is intended to

promote Europe's economic competitiveness, and the parliamentary committee argues that research that cannot be patented should not be supported under the programme.

Ethics hub

A US\$1.5-million online resource for scientists teaching responsible conduct of research (RCR) was officially launched on 20 September. The Ethics CORE website (www.nationalethicscenter.org) is funded by the US National Science Foundation (NSF) and directed by C. K. Gunsalus, an expert on research integrity at the University of Illinois at Urbana-Champaign. The America COMPETES Act of 2007 made RCR training mandatory for all NSF grant

recipients; the foundation implemented the requirement in 2010. See go.nature.com/m38bnp for more.

Rainforest threat

Deforestation is on the rise again in the Brazilian Amazon. The amount of clear-cut land hit 522 square kilometres in August 2012, up from 163 km² in the same month last year, according to satellite measurements made by Brazil's National Institute for Space Research (INPE), based in São José dos Campos. Deforestation had been on the wane since April 2011. See go.nature.com/b7ej2p for more.

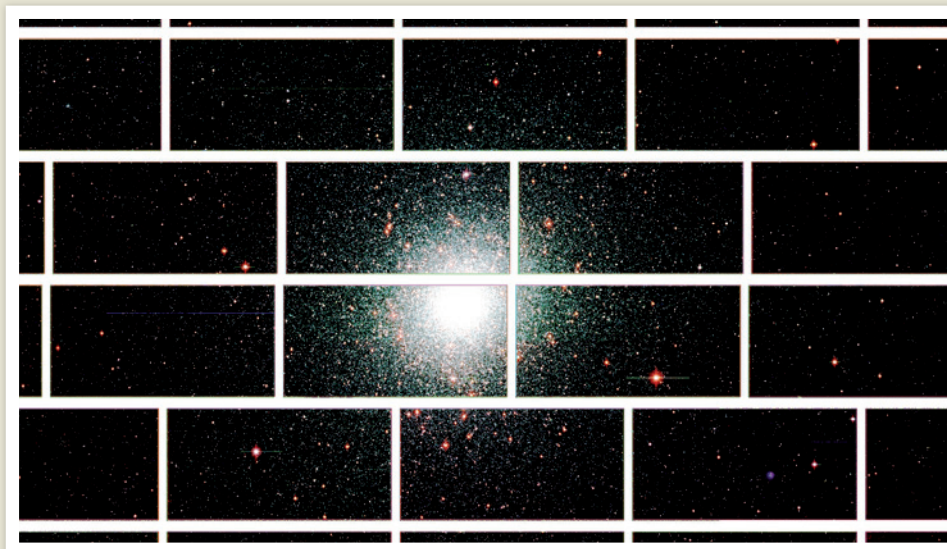
Immigration bill

The US House of Representatives rejected a bill on 20 September that would

have granted permanent residency — commonly referred to as 'green card' status — to 55,000 foreign scientists and engineers with advanced degrees from US universities each year. Both presidential candidates have expressed support for admitting more workers in these disciplines, but the bill failed to garner the two-thirds majority needed to pass. See go.nature.com/hatvjq for more.

Arsenic in rice

Two US reports have reignited worries about arsenic poisoning from rice and prompted politicians to introduce legislation on 21 September that would limit the toxic substance. On 19 September, the consumer protection group Consumers Union, based in Yonkers, New



DARK ENERGY SURVEY COLLABORATION/FERMI LAB

First light for dark-energy lens

A camera designed to hunt for signs of dark energy, a force thought to be responsible for the Universe's rapid expansion, snapped its first images on 12 September. The images from the Dark Energy Survey camera (*Nature* **489**, 190–191; 2012), which is mounted on

the 4-metre Blanco telescope in Chile, were generated as part of a testing phase that is set to end in December. This stitched-together image of sections of sky shows the globular star cluster 47 Tucanae, which is around 5,000 parsecs from Earth. See go.nature.com/ya5y2p for more.

York, and the US Food and Drug Administration released reports that found inorganic arsenic in rice products. The presence of the substance is probably the result of the use of arsenic-based pesticides in cotton fields that were later used for rice farming. See go.nature.com/puezou for more.

PEOPLE

Development boost

Chinese President Hu Jintao announced a US\$1.5-million donation to TWAS, the academy of sciences of the developing world, on the opening day of the organization's 23rd general meeting in Tianjin, China, on 18 September. The donation means that China overtakes Brazil as the largest contributor to the organization, which is based in Trieste, Italy. Chemist Bai Chunli, current president of the Chinese Academy of Sciences, was also elected as the organization's president.

AZT-maker dies

Jerome Horwitz, the chemist who inadvertently created the first antiretroviral drug for AIDS, azidothymidine (AZT), died on 6 September, aged 93. News of his death emerged last week. Horwitz (**pictured**) created AZT in the 1960s to combat cancer, but he shelved



the drug after it showed little efficacy against the disease. A company that later became part of GlaxoSmithKline patented AZT in the 1980s when it was found to be effective against AIDS. Horwitz received no money for his discovery because he no longer owned the compound, but he did go on to produce treatments for diseases such as cancer at the Wayne State University School of Medicine in Detroit, Michigan, until he retired in 2005.

Fraud inquiry

Cardiff University is launching an investigation into allegations of scientific misconduct in the laboratory of its dean of medicine, Paul Morgan, a spokeswoman for the UK institution confirmed on 17 September. The allegations — that images have been manipulated in at least six of the laboratory's research papers — appeared on the website science-fraud.org

in July, and the university launched an initial screening panel on 6 August. The panel recommended the formal investigation.

RESEARCH

Chimp research cut

The US National Institutes of Health (NIH) is ending its funding for chimpanzee work at the largest centre for such research that it supports. The agency will retire 110 chimpanzees from the New Iberia Research Center, part of the University of Louisiana at Lafayette, it said on 21 September. There are still 308 chimpanzees available for invasive experiments at two other NIH-supported centres; the agency says that these animals are sufficient for dwindling research needs. See go.nature.com/8mkgnf for more.

Cancer ambitions

A leading US cancer centre said last week that it will spend up to US\$3 billion over the next ten years on a programme to significantly increase the odds of surviving eight cancers. Under the Moon Shots initiative, research teams at the MD Anderson Cancer Center in Houston, Texas, will focus on cancer of the prostate, lung and ovary, and on a type of breast cancer as well as melanoma, two leukaemias

and a related blood syndrome. See go.nature.com/levbl for more.

XMRV ruled out

The retrovirus XMRV is not linked to chronic fatigue syndrome (CFS), a definitive study that cost US\$2.3 million concluded on 18 September. A 2009 paper found signs of XMRV infection in people with CFS (V. C. Lombardi *et al. Science* 326, 585–589; 2009), but was retracted in 2011 because of concerns that the results were caused by contamination. The latest study (H. J. Alter *et al. mBio* 3, e00266-12; 2012) is co-authored by members of two teams that reported associations between XMRV and related viruses and CFS. See go.nature.com/vadrb7 for more.

EVENTS

Arctic drilling stops

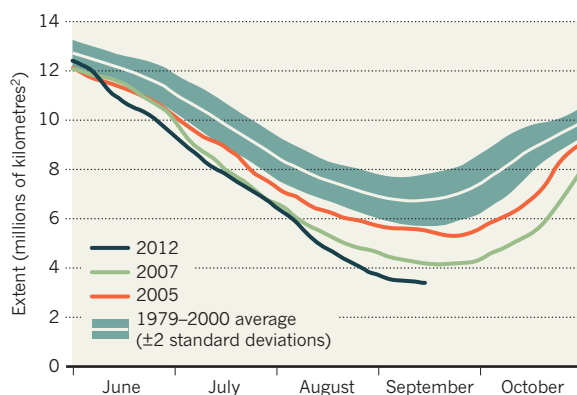
Plans to drill for oil and gas resources off the coast of Alaska have been abandoned following damage to oil containers on the spill-clean-up barge *Arctic Challenger*, oil company Shell announced on 17 September. The setback means that the mission no longer meets the safety requirements for a permit to drill specific wells. Shell will continue to bore exploratory 'top holes' in the Chukchi Sea in preparation for further drilling, which has now been delayed until 2013. See go.nature.com/zynxtq for more.

TREND WATCH

Arctic sea-ice coverage reached the lowest point of this year's summer melt on 16 September, the US National Snow and Ice Data Center in Boulder, Colorado, has declared. On that date, around 3.41 million square kilometres of sea in the Arctic were at least 15% covered in ice, under the measurement system used by the data centre. The new low is by far the smallest figure seen in 33 years of satellite measurements — and possibly the lowest late-summer ice extent in more than 5,000 years.

SHRINKING ARCTIC SEA ICE

Sea-ice coverage in the Arctic bottomed out this week at the lowest extent ever measured by satellites.



CORRECTIONS

The story 'Yellow river turns red' (*Nature* 489, 182; 2012) should have termed the Yangtze the golden river. And the story 'Murder plea' (*Nature* 489, 341; 2012) wrongly located the Madison County circuit court. It should have been in Huntsville, Alabama.

NATURE.COM

For daily news updates see:
www.nature.com/news

NEWS IN FOCUS

CHEMISTRY US society thwarted in attempt to block competitor **p.482**

AGRICULTURE Cancerous rats rouse opponents of GM crops **p.484**

GENOMICS Sequencing powerhouses make an East-West marriage **p.485**



POLITICS Grading Barack Obama's science performance **p.488**

A. STENIN/RIA NOVOSTI



Olga Zelenina, seen in the dock at a hearing, is being held in prison in Moscow on a charge of abetting drug trafficking.

HUMAN RIGHTS

Researchers campaign to free jailed Russian chemist

Narcotics expert Olga Zelenina recognized as a political prisoner.

BY QUIRIN SCHIERMEIER

Russian scientists have reacted with alarm to the jailing of a colleague, narcotics expert Olga Nikolaevna Zelenina, on charges of aiding drug trafficking. Researchers believe that Zelenina has been falsely accused, and fear that the free pursuit of science in Russia is in jeopardy. "With state repression being a recurring issue in this country, the outcome of this case is very important for us all," says Mikhail Gelfand, a biologist at the Institute for Information Transmission Problems in Moscow.

As *Nature* reported last week (*Nature* <http://doi.org/jd5>; 2012), Zelenina, an analytical chemist at the Penza Agricultural Institute in Russia, was arrested at her home on 15 August by officials from the Russian Federal Drug Control Service (FDCS), who were accompanied by masked and armed members of a special police unit. Five days later, a judge at Moscow's Zyuzino District Court ruled that Zelenina would be detained until 15 October, pending a trial.

Zelenina seems to have been targeted because of a scientific report that she prepared in September 2011 for the defence attorneys of

Sergey Shilov, a Russian businessman under investigation by the FDCS. As an expert on narcotic compounds in hemp and poppy, Zelenina was asked to assess the concentration of opiates in a 42-tonne shipment of food poppy seeds that Shilov had imported from Spain in 2010. Russia banned cultivation of the opium poppy (*Papaver somniferum*) in 1987, but the seeds can still be imported for use in foods including bread or cake, as long as they are free of alkaloids such as morphine and codeine. The seeds themselves do not contain these compounds, but other parts of the plant do, and can contaminate shipments. ►

► In her analysis, Zelenina found that the concentration of opium alkaloids in Shilov's seed shipment was negligible, and that there was no scientific evidence that the seeds had been imported for the purpose of extracting illegal drugs. Her report also stated that it is technically impossible to completely eliminate these alkaloids from batches of poppy seeds.

Her findings apparently did not please the FDCS. Although a Moscow court ruling on 24 September raised hopes that Zelenina's case could be heard sooner than October, she remained in custody as *Nature* went to press. For now, Zelenina shares a cell with activist Nadezhda Tolokonnikova, one of three members of the Russian punk band Pussy Riot who were last month sentenced to two years in jail on charges of hooliganism. Their crime was singing a song critical of Russian president Vladimir Putin in Moscow's Cathedral of Christ the Saviour.

Zelenina's "is the most outrageous case I've heard of so far", says Ivan Gololobov, a

sociologist at the University of Warwick in Coventry, UK, who has read the Russian-language report that was used to make the case against the chemist. Gololobov notes that Russia often restricts speech and art that are critical of the government. "But the case of Zelenina, an expert who expressed independent opinions and arrived at scientific conclusions different from those of the prosecutors, is a step further," he says. "She stands accused not for oppositional activity or for her political opinions, but simply because of her independent professional expertise. If proven guilty, she is facing a severe sentence." A conviction could carry a sentence of several years in prison.

Natalia Andreeva, Zelenina's Moscow-based lawyer, says that the case is reminiscent of that of botanist and geneticist Nikolai Vavilov. He was jailed in 1940 and died in prison three years later, having challenged the non-Mendelian doctrines of heredity propagated at the time by Trofim Lysenko and backed by Joseph Stalin.

Last month, the Russian government's human-rights commissioner, Vladimir Lukin, appealed against Zelenina's detention without success. Zelenina is now recognized as a political prisoner by the Union of Solidarity, a Russian human-rights watchdog. And last week, Russian scientists launched an online petition campaigning for her immediate release (go.nature.com/ihxmxu).

The case reveals the inferior status of professional science in modern Russia, says Mikhail Feigel'man, a physicist at the Landau Institute for Theoretical Physics in Moscow. "There is a lot of talk going on here these days that the absence of a functioning system of technological innovation and professional scientific expertise is one of the big problems in this country," he says. "These qualities have indeed all but vanished — and Olga's case makes me fear that they will not come back any time soon. Scientists in Russia will understand that what they are doing is more likely to get them in trouble than do anything good for society." ■

INTELLECTUAL PROPERTY

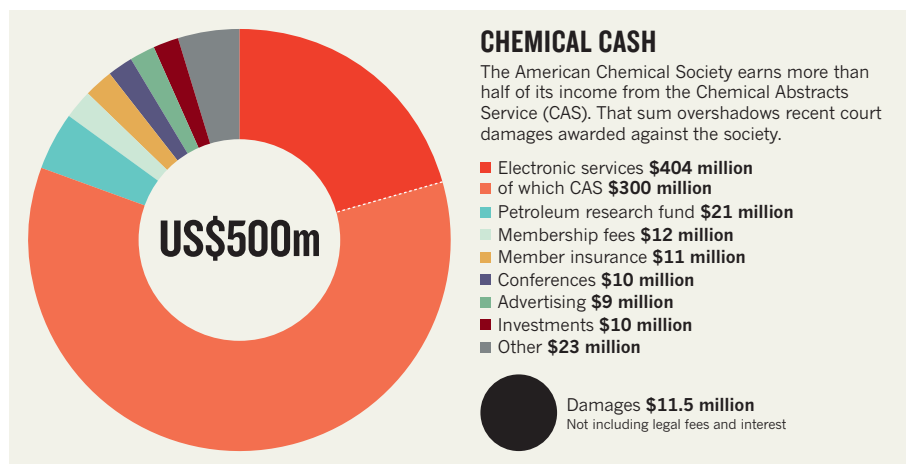
Chemical society tried to block business competitor

Court ruling raises concerns among some American Chemical Society members.

BY EUGENIE SAMUEL REICH

The world's largest scientific society tried to unfairly obstruct a tiny entrepreneurial start-up from competing with its most lucrative scientific information product. That is the main conclusion of a ten-year legal battle that leaves the American Chemical Society (ACS) facing millions of dollars in penalties and sharp questions from some of its members about whether its business practices conflict with its mission to advance the chemical sciences.

The 18 September ruling by the Ohio Supreme Court focuses on the society's cash cow: the Chemical Abstracts Service (CAS), which offers access to a database of 68 million chemical compounds, indispensable to many chemists the world over. By typing in the name of a chemical or submitting a drawing of its structure, researchers can access reams of data about the molecule's properties, or a list of academic papers referring to it. According to court documents in the case, CAS makes up about 60% of the society's gross revenue, amounting to some US\$300 million a year. By contrast, membership payments raise only about \$12 million



SOURCE: ACS

(see 'Chemical cash'). The society, a non-profit organization based in Washington DC, ploughs the cash back into programmes for chemistry education, academic meetings and improvements in chemical-information resources.

In 2002, the ACS sued Leadscape, a chemical-informatics firm in Columbus, Ohio. The society alleged that the company had infringed ACS intellectual property when

the firm obtained a patent on software to display correlations between structural features of chemical compounds and their biological and physical properties.

The ACS argued that Leadscape's product was based on an aborted project called PathFinder, which two of three Leadscape co-founders had worked on in the 1990s when they were employed by CAS, also based

R. GABALDA/AFR/GETTY

in Columbus. A trial court and an appeals court in Ohio both ruled against the ACS, but the society requested that the case be reviewed by the Ohio Supreme Court. That court has now refuted the society's allegations, and has instead upheld counterclaims by Leadscope that the ACS filed an "objectively baseless" lawsuit to unfairly quash a competitor.

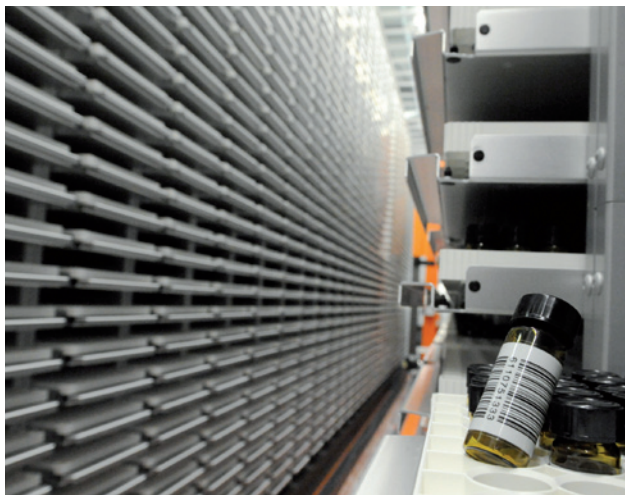
The ruling means that the ACS will probably have to pay Leadscope \$11.5 million in compensation — the amount awarded by the trial court in 2008 and upheld by the appeals court in 2010. However, the ruling clears the ACS of defaming Leadscope, a charge that lower courts had upheld, letting the society off the hook for a further \$15 million in damages.

The Supreme Court found that, although the ACS did make false public statements about Leadscope infringing its intellectual property, those statements were an accurate summary of allegations already mentioned in court documents and which the public had a legitimate interest in knowing about.

Both the ACS and a lawyer for Leadscope declined to give interviews because the Supreme Court ruling must still be implemented by the original trial court in Franklin County, Ohio. The society has previously said that part or all of the court's award may be covered by its legal insurance. In a statement responding to the Supreme Court's verdict, the ACS said that the ruling "will not impact ACS member dues; ACS products, programs or services; ACS staffing levels; or the ability of ACS to achieve its mission".

But some of the society's 164,000 or so members, who include chemists from academia, industry and government, are not convinced. "I believe that this lawsuit has brought damage to the society, not only financially, but also reputationally," says Steven Bachrach, a chemist at Trinity University in San Antonio, Texas, an ACS member who has followed the case. "I'm concerned about the standing of the society in pursuing this aggressively after losing twice."

Richard Apodaca, an ACS member who is founder of Metamolecular, a chemical-software company in La Jolla, California, says that as a software entrepreneur, he sympathizes



A virtual analogue to the molecule libraries in industrial labs (pictured), the Chemical Abstracts Service contains data on millions of compounds.

with Leadscope. "I was shocked the ACS was being predatory," he comments. "I felt kind of ashamed to be an ACS member and for the ACS to be doing this." Court documents state that in 2002, Leadscope lost an important venture-capital deal because the ACS lawsuit scared off the investor, and that a financing deal the company later obtained was on less-favourable terms.

Apodaca says that, like any organization, the ACS has the right to defend its intellectual property, and that it is increasingly common for large software companies to pursue competitors who they believe may have stolen their products. But in this case, the court found that the ACS had no evidence of Leadscope copying source code from any software developed at CAS. Experts from Leadscope and the ACS, who had compared the source codes for Leadscope's product and PathFinder line-by-line, both testified in court that the products were completely different. The Supreme Court ruling says that although PathFinder and the Leadscope product perform similar functions, the idea of developing such tools could not be considered a trade secret of the ACS.

The court rulings in favour of Leadscope emphasized the actions of Robert Massie, a lawyer and businessman who has been president of CAS since 1992. The court referred to evidence suggesting that before the ACS filed its lawsuit, Massie had been monitoring Leadscope closely and was aware that it was running out of money. Further evidence showed

that he had e-mailed the governor of Ohio's office to try to dissuade him from visiting Leadscope; and that the then-director of information technology for CAS had told Massie that he simply did not know whether Leadscope's product infringed the ACS's intellectual property. Massie did not respond to an e-mail from *Nature* drawing his attention to the court's remarks and asking for comment.

ACS v. Leadscope is the most recent example of the society's efforts to protect its intellectual property. In 2005, the ACS accused the US National Institutes of Health of unfair competition in pioneering PubChem, a database linking chemical compounds with their biological activity, although that dispute has never reached court

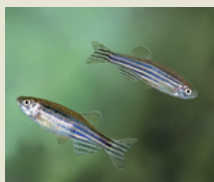
(see *Nature* 435, 718–719; 2005). In 2004, the society sued Google, claiming that the name (but not the content) of its free Google Scholar service infringed on the ACS's trademarked SciFinder Scholar software. That case was settled out-of-court in 2006 on confidential terms.

Donald Lewis, a patent lawyer based in San Diego, California, who is a member of the ACS Division of Chemistry and the Law, thinks that the society's pursuit of Leadscope runs counter to its goal to advance chemistry — something on which the society's status as a non-profit, non-tax-paying organization depends. By developing a chemical-information product that is useful to researchers, Leadscope was arguably doing its bit to improve chemistry too, Lewis suggests. "In my opinion, the Leadscope case illustrates an instance where the ACS's business interests were pursued by its professional management to the detriment of the advancement of chemical sciences," he says. "I'm interested in the soul of the ACS."

"In my view, this is not a fair representation of our members' opinions," Madeleine Jacobs, chief executive of the ACS, wrote in an e-mail to *Nature*. She declined to comment on the recent court ruling, but emphasized that the society spends its revenues on fulfilling its mission through programmes to improve chemists' qualifications and the scientific literacy of the public, and by providing "the most accurate, most trusted, and most in-depth chemical information in the world". ■


**MORE
ONLINE**

TOP STORY

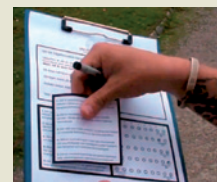


Custom gene editing rewrites zebrafish DNA
go.nature.com/nmhspe

MORE NEWS

- African neighbours divided by their genes go.nature.com/pswdjb
- Amazon fire analysis hits new heights go.nature.com/siw3jn
- Bacteria replicate close to the physical limit of efficiency go.nature.com/tqyd6k

VIDEO



How to push a moral compass off course
go.nature.com/zallnf

B. BEWAN/ARDEACOM

PLOS ONE

Rat study sparks GM furore

Cancer claims put herbicide-resistant transgenic maize in the spotlight.

BY DECLAN BUTLER

Europe has never been particularly fond of genetically modified (GM) foods, but a startling research paper published last week looks set to harden public and political opposition even further, despite a torrent of scepticism from scientists about the work.

The study¹, published in the peer-reviewed journal *Food and Chemical Toxicology*, looked for adverse health effects in rats fed NK603 maize (corn), developed by biotech company Monsanto to resist the herbicide glyphosate and approved for animal and human consumption in the European Union, United States and other countries. It reported that the rats developed higher levels of cancers, had larger cancerous tumours and died earlier than controls. The researchers have not conclusively identified a mechanism for the effect.

The rats were monitored for two years (almost their whole lifespan), making this the first long-term study of maize containing these specific genes. About a dozen long-term studies of different GM crops have failed to find such stark health effects². An earlier test of NK603 maize in rats in a 90-day feeding trial — the current regulatory norm — sponsored by Monsanto showed no adverse effects³.

The explosion of media coverage about the findings has energized opponents of GM food, especially in Europe. French Prime Minister Jean-Marc Ayrault said that, if the results are confirmed, the government will press for a Europe-wide ban on the maize. The European Commission has instructed the independent European Food Safety Agency (EFSA) in Parma, Italy, to assess the study.

Many scientists, however, have already questioned the study's methodology and findings. They assert that the data presented in the paper do not readily allow the claims to be independently assessed, and they question the study's experimental design and its statistical analysis of any differences between the treated groups and controls. Other scientists point out that the Sprague-Dawley strain of rats used in the experiments has been shown to be susceptible to developing tumours spontaneously, particularly as they grow older, making it difficult to interpret the results. Monsanto itself said that

the study “does not meet minimum acceptable standards for this type of scientific research”.

The €3.2-million (US\$4.1-million) study was led by Gilles-Eric Seralini, a molecular biologist at the University of Caen, France, in collaboration with the Paris-based Committee for Research and Independent Information on Genetic Engineering (CRIIGEN), whose scientific board he heads. CRIIGEN bills itself as



Tumours developed more readily in rats fed genetically modified maize than in controls, recent research reports.

an “independent non-profit organization of scientific counter-expertise to study GMOs, pesticides and impacts of pollutants on health and environment, and to develop non polluting alternatives”. The article's publication coincides with the launch this week of a book by Seralini, *Tous Cobayes? (All of Us Guinea-Pigs Now?)*, which tells the story of the research project and is accompanied by a film and a television documentary.

In a written response to *Nature's* questions, Seralini and Joël Spiroux de Vendômois, president of CRIIGEN and a co-author of the paper, say that they have been surprised by the “violence” and immediacy of scientists' criticisms. They argue that most of the critics are not toxicologists, and suggest that some may have competing interests, including working to develop transgenic crops. They also point out some errors by critics, such as claims that graphs in the paper showing rat survival over time do not include data for the controls.

The authors concede that Sprague-Dawley rats may not be the best model for such long-term studies, but argue that the difference between the NK603-fed rats and controls is

marked, and that many fewer control rats developed tumours in middle age. The 90-day trial of Monsanto's NK603 maize used in its authorization also used Sprague-Dawley rats, they add.

José Domingo, a toxicologist at Rovira i Virgili University in Reus, Spain, and a managing editor of *Food and Chemical Toxicology*, says that the study raised no red flags during peer review. Domingo, who last year authored a

critical review of safety assessments of GM plants⁴, has previously complained about the lack of independent feeding studies of GM foods.

The controversy over the findings is likely to be settled only after detailed analysis of the paper and its data, and replication of the experiments. But Seralini says he won't release his data until the raw data underpinning the authorization of NK603 in Europe are also made public. And he wants all the data to be assessed by an independent international committee, arguing that experts involved in the authorization of the maize should not be involved. EFSA chief Catherine Geslain-Lanéelle disagreed, and said that her agency is well placed to assemble a multidisciplinary group to give an impartial assessment.

Some scientists, however, have long questioned whether such feeding studies are appropriate for testing the safety of whole foods, says Peter Kearns, head of food safety, nanosafety and chemical accidents for the Organisation for Economic Co-operation and Development in Paris. They were designed for testing chemicals where precise doses of purified and well-characterized compounds can be administered, whereas compounds in foods are heterogeneous, and doses are difficult to control. Regulators rely mainly on more robust tests that compare the toxicological and nutritional profiles of GM foods with their non-GM counterparts to screen for potential concerns.

Resolution of the debate over the safety of GM foods can come only from rigorous science clarifying the issues, Kearns adds. ■

SEE EDITORIAL P.474

1. Seralini, G.-E. *et al. Food Chem. Toxicol.* <http://dx.doi.org/10.1016/j.fct.2012.08.005> (2012).
2. Snell, C. *et al. Food Chem. Toxicol.* **50**, 1134–1148 (2012).
3. Hammond, B., Dudek, R., Lemen, J. & Nemeth, M. *Food Chem. Toxicol.* **42**, 1003–1014 (2004).
4. Domingo, J. L. & Giné Bordonaba, J. *Environ. Int.* **37**, 734–742 (2011).

GENOMICS

China buys US sequencing firm

BGI's rescue of Complete Genomics will keep a valued technology afloat.

BY MONYA BAKER

Since it started sequencing genomes in 2009, the DNA services company Complete Genomics has garnered praise for its technology, but little commercial success. Researchers valued its ability to produce readouts of entire human genomes with minimal errors, but they feared for the future of the company, based in Mountain View, California, which lost US\$72.3 million in 2011 alone. Now BGI, whose sequencing facility in Shenzhen, China, is the largest in the world, has tossed Complete Genomics a lifeline.

On 17 September, BGI announced that it had agreed to merge with the struggling firm and would spend \$117.6 million to buy up its shares. The rescue was welcomed not just by the company's board of directors, but also by those who worry that diminishing choices is a problem for genomics.

"Right now, Illumina would have a monopoly

CAREFUL READING

A 2011 test of DNA-sequencing methods compared technologies from Complete Genomics and Illumina.

	Single nucleotide variants		Insertions and deletions	
	Detected	Validated*	Identified	Validated*
In common	3,295,023	100%	215,382	93%
Illumina only	345,100	13%	390,060	91%
Complete Genomics only	99,578	94%	206,461	100%

* A small, random sample of variants was reanalysed by a more accurate but more expensive method.

if Complete Genomics went under," says Michael Snyder, director of the Stanford Center for Genomics and Personalized Medicine in Palo Alto, California. Instruments made by Illumina of San Diego, California, account for most of the world's sequencing output. Maintaining competition in the industry will keep prices low and technologies improving, Snyder says.

Like Complete Genomics, BGI sells sequencing services rather than equipment or reagents, but it relies chiefly on instruments made by

Illumina. Complete Genomics has its own instrument and software platform, which is specialized for sequencing whole human genomes.

Although comparing ever-changing platforms is never straightforward, a 2011 analysis of the same genome read by Complete Genomics and Illumina technology showed that although the former found fewer variants in the DNA sequence relative to a standard reference, it was more accurate (see 'Careful reading')¹. In July, Complete Genomics ►

SOURCE: REF. 1

► described a technique that reduces error rates in sequenced genomes to 1 in 10 million base pairs and shrinks the amount of DNA required to generate a sequence². The technique also distinguishes between DNA fragments that come from paternal and maternal versions of the same chromosome. This can reveal, for example, whether mutations occur in one or both copies of a gene, and so whether an individual is at risk of developing a certain disease or is merely a carrier.

"That's going to be a game changer in how whole-genome sequences are interpreted and analysed," predicts Thomas Barber, a geneticist at Eli Lilly in Indianapolis, Indiana, who works with both BGI and Complete Genomics. BGI's acquisition means that researchers will continue to benefit from such advances. Having the two companies under the same ownership could combine the strengths of both.

Amanda Murphy, an analyst with equity investment firm William Blair in Chicago, Illinois, says that the market for Complete Genomics' expertise is poised to grow. Most human sequencing has so far focused on exomes, the roughly 1.5% of the genome that codes for protein. But the recent ENCODE project³ and other research is revealing functions of non-protein-coding regions. "I think the world is moving towards whole-genome sequencing," she says. "The demand just wasn't there fast enough" for Complete Genomics to hang in on its own.

Demand for services is increasing as well. Many researchers want to use sequencing data but do not want to invest in the expertise and instruments needed to do the sequencing themselves. Even large academic sequencing centres often have more sequencing projects than capacity.

A major drawback of Complete Genomics' technology is that it takes 2 to 3 months to produce a sequence, which discourages medical uses. But the platform is expected to get faster. Peter van der Spek, head of bio-informatics at Erasmus Medical Center in Rotterdam, the Netherlands, worries that innovation will stall under BGI, although a spokesman for BGI says that Complete Genomics' current scientific staff is expected to stay with the company and that development would continue.

Either way, the community is better off with options, says Richard Gibbs, director of the Human Genome Sequencing Center at Baylor College of Medicine in Houston, Texas. "If we just had one test and one machine and one process, things would happen, but not as fast." ■

1. Lam, H. Y. K. *et al. Nature Biotechnol.* **30**, 78–82 (2011).
2. Peters, B. A. *et al. Nature* **487**, 190–195 (2012).
3. The ENCODE Project Consortium *Nature* **489**, 57–74 (2012).

PUBLISHING

Open-access deal for particle physics

Consortium brokers agreement with 12 journals.

BY RICHARD VAN NOORDEN

The entire field of particle physics is set to switch to open-access publishing, a milestone in the push to make research results freely available to readers.

Particle physics is already a paragon of openness, with most papers posted on the preprint server arXiv. But peer-reviewed versions are still published in subscription journals, and publishers and research consortia at facilities such as the Large Hadron Collider (LHC) have previously had to strike piecemeal deals to free up a few hundred articles.

After six years of negotiation, the Sponsoring Consortium for Open Access Publishing in Particle Physics (SCOAP³) is now close to ensuring that nearly all particle-physics articles — about 7,000 publications last year — are made immediately free on journal websites. Upfront payments from libraries will fund the access.

So that individual research groups do not need to arrange open publication of their work, the consortium has negotiated contracts with 12 journals that would make 90% of high-energy-physics papers published from 2014 onwards free to read, says Salvatore Mele, who leads the project from CERN, Europe's high-energy physics laboratory near Geneva, Switzerland, and home of the LHC. According to details announced on 21 September, six of the journals will switch their business models entirely from subscription to open access. It is "the most systematic attempt to convert all the journals in a given field to open access", says Peter Suber, a philosopher at Earlham College in Richmond, Indiana, and a proponent of open access.

The consortium invited journals to bid for three-year open-access publishing contracts, and ranked them by an undisclosed algorithm that weighed their fees against their impact factors and the licences and delivery formats they offer. Under the deal, the journals will receive an average of €1,200 (US\$1,550) per paper. *Physical Review D*, the journal that publishes most papers in the field, negotiated a fee of US\$1,900 per article "on the principle that we should maintain our revenue", says Joe Serene, treasurer and publisher at the American Physical Society, which owns the journal. But the society's

prestigious *Physical Review Letters* missed out because its bid was too high, says Serene (the journal currently charges authors \$2,700 for individual open-access articles). CERN and SCOAP³ will continue to negotiate individual open-access agreements with journals not included in the deal, and more could join when the contract is renegotiated in 2016.

Mele says that the goal of SCOAP³ is to switch the discipline's journals to open access without researchers noticing any effect on their grant funding or on the way they publish papers. The consortium will pay the contracts from an annual budget of €10 million, which is funded not by authors or research grants, but by pledges from more than a thousand libraries, funding agencies and research consortia across the world.

"It is the most systematic attempt to convert all the journals in a given field to open access."

In effect, existing journal subscription fees are being repurposed to provide the open-access funds.

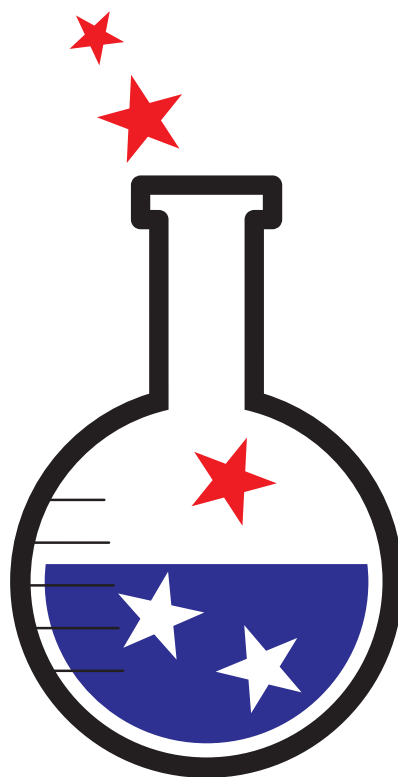
Before any contracts can be signed, however, publishers must reduce the price of their subscription packages to offset the income from SCOAP³ — a complex calculation to ensure that libraries don't pay twice for the same content. Then SCOAP³ must collect its pledges — not a foregone conclusion, as some libraries may be tempted to renege, figuring that their institution won't lose access to the free papers anyway.

Mele hopes that success could trigger a domino effect in fields such as astronomy and astrophysics. "I personally believe that once this is demonstrated to work, some variations, fine-tuning and adaptation of the idea will emerge," he says.

But Serene and others caution that SCOAP³ may be hard to replicate. It has unique advantages in that most high-energy-physics papers are published in just a few journals, and that the field can be driven and coordinated by one central organization, CERN.

Suber notes the stark contrast between the quiet brokering of SCOAP³ and the battles playing out over mandates for open-access publication by research funders such as foundations and government agencies (see *Nature* **486**, 302–303; 2012). "I call it the peaceful revolution," he says. ■

► **NATURE.COM**
For a complete list of participating journals see go.nature.com/3yvpzq



Political science

Science and politics are uneasy bedfellows. The first is built on evidence and objectivity; the second thrives on opinion and persuasion. Nowhere is that relationship more fraught than in the United States, where the need to win votes can trump scientific evidence on issues such as climate change and public health — and where scientists may have little sympathy for political give and take. This week, *Nature* scrutinizes the intersection of politics and science in the run-up to the US election on Tuesday 6 November. With the presidency, all 435 spots in the House of Representatives and 33 of the 100 seats in the Senate at stake, the outcome could change the course of US science for the next four years.

When Barack Obama swept into office, he pledged to make science a guiding tenet of his leadership. A News Feature on page 488 examines how that pledge has fared in the face of hard political realities and crises such as the

Deepwater Horizon oil spill.

A pair of Comment pieces examines the relationship between scientists and Congress. On page 494, Lawrence Goldstein, a stem-cell biologist at the University of California, San Diego, urges researchers to hound their congressional representatives to make the case for funding science. And on page 493, Rush Holt, a physicist and Democratic congressman from New Jersey, says that Congress would function better if more of his colleagues thought like scientists, or sought their advice. Such interactions would leave both politicians and scientists better informed — and the relationship between their fields a little less fraught. ■ [SEE EDITORIAL P.473](#)



US ELECTION

Science and Politics in America
nature.com/election2012



The Obama experiment

BY JEFF TOLLEFSON

Nearly four years after US President Barack Obama pledged to put science in its rightful place, Nature asks if he kept his word.

On 15 December 2008, president-elect Barack Obama made clear to the world that science would have a central seat in his administration. At a press conference in Chicago, Obama introduced Nobel laureate Steven Chu as the next secretary of the energy department and the person who would help to wean the country off its addiction to climate-warming fossil fuels. "His appointment should send a signal to all, that my administration will value science," Obama said.

Within days, he announced other members of his future staff, who would make up a star-studded science team (see 'The science dream team'): marine ecologist Jane Lubchenco

would head the National Oceanographic and Atmospheric Administration in Washington DC and physicist John Holdren would be Obama's science adviser and head the Office of Science and Technology Policy, also in Washington DC. They joined Lisa Jackson, a respected chemical engineer with political experience, who had been named to run the US Environmental Protection Agency (EPA) in Washington DC. After taking office, the

president completed the team by appointing geneticist Francis Collins at the National Institutes of Health (NIH) in Bethesda, Maryland, and geophysicist Marcia McNutt at the US Geological Survey in Reston, Virginia. Never before had a president assembled such a strong crop of researchers to lead his science agencies.

"The truth is that promoting science isn't just about providing resources — it's about protecting free and open inquiry," Obama proclaimed as he made the initial appointments. "It's about listening to what our scientists have to say, even when it's inconvenient — especially when it's inconvenient."

Scientists and environmentalists swooned; they had spent 8 years complaining that the administration of President George W. Bush had overly politicized science. Climate researchers in government had charged that they were being muzzled and that their data were being manipulated. Pollution regulations were blocked or watered down. With Obama's election, scientists would finally have a president who not only said the right things but actually appointed the right people. Even journalists drooled. "Science Born Again in the White House, and Not a Moment Too Soon," read a headline in *Wired* magazine, endorsing Obama's appointments with a swipe at Bush's reputation as a born-again Christian.

The love affair would soon cool, however, as the Obama administration started to hit a number of obstacles while trying to govern a politically fractured nation in the midst of the worst economic crisis in 70 years. The president has not fulfilled some of his top science-related

M. RILEY/POLARIS/EYEVINE



US ELECTION

Science and Politics in America
nature.com/election2012

promises, such as passing climate legislation to reduce the nation's emissions of greenhouse gases. He has paid relatively little attention to NASA and the NIH, and got into bruising budget wars with Congress that sapped support for some science agencies. And his vaunted team stumbled in its response to the Deepwater Horizon oil spill in the Gulf of Mexico, which damaged the administration's credibility with some researchers.

But as Obama and his science team round out their first term in office and make a bid for a second, they can point to substantial achievements, some of them little noticed. Even in fiscally tight times, Obama has invested heavily in science education and research, particularly in energy. His administration has also made headway in tackling pollution, in part by introducing the country's first greenhouse-gas regulations. And by driving the creation of integrity policies that seek to protect scientists from political interference (see 'Integrity test'), his team has sent positive signals to agencies that had become demoralized during the Bush years.

"The president never let up in his consistent support for science, and actually he got a lot done in spite of the Republican resistance," says Neal Lane, who was science adviser to former President Bill Clinton and is now a professor at Rice University in Houston, Texas.

STIMULATING SCIENCE

Within a week of the election in November 2008, and with the economy in free fall, Obama's advisers started working with the scientific community to survey 'shovel-ready' projects for potential inclusion in a stimulus package intended to boost construction and get people back to work. They initially aimed for US\$5 billion in initiatives, but House Democrats doubled that in a draft of the stimulus bill released on 15 January 2009, five days before Obama's inauguration. And the role of science and innovation continued to grow.

On 17 February, exactly 4 weeks into office, Obama signed a \$787-billion stimulus bill that contained at least \$53 billion for science. The bill made good on Obama's promises to advance basic and applied research and development aimed at the major problems of the day, including clean energy and global warming. It boosted research funding by \$2 billion at the National Science Foundation in Arlington, Virginia, and by \$8.2 billion at the NIH. As he signed the bill at the Denver Museum of Nature & Science in Colorado, Obama called it the biggest increase in the history of basic-research funding.

"You would have to go back to the 1940s, when Harry Truman became president, to find an administration that was receptive to doing something really significant on scientific research straight out of the box," says Michael Lubell, who handles government affairs for the American Physical Society in Washington DC and was one of a trio of scientists who helped to compile the initial suggestions for the science

stimulus package. "And I think part of it has to do with Obama himself. This guy likes science."

In those early months, the science agenda continued to ride high. In April, Obama visited the National Academy of Sciences in Washington DC and proposed a long-term expansion of funding for basic and applied research and development. When he submitted his budget for 2010, Obama fulfilled that promise by including full funding for the America COMPETES Act, a stalled 2007 initiative that called for a doubling of the federal budget for physical sciences. He also increased funding for science and mathematics education.

"The president never let up in his consistent support for science, and actually he got a lot done."

Bigger budgets were not the only things that were fuelling optimism. In March, Obama overturned Bush's restrictions on using federal funds to support research into human embryonic stem cells, and other early moves by the administration thrilled energy and climate researchers. On 19 May 2009, the president invited the chief executives of ten of the world's largest car manufacturers to the White House Rose Garden to announce a historic agreement to establish the first greenhouse-gas standards for US vehicles. For two decades, the companies had been fighting against attempts to make cars more efficient, but the economic crisis and new regulatory authority had given Obama some leverage over the industry. Tough regulations in California had also helped to make car makers more receptive to higher standards. Obama's team later brokered a pact with the automobile industry to nearly double the average fuel efficiency of cars by 2025, to around 23 kilometres per litre.

"A lot of the credit goes to the president, who really persevered and insisted that this was going to be part of the package," says Kevin Knobloch, president of the Union of Concerned Scientists, an advocacy group based in Cambridge, Massachusetts. "He believed that technology was the key to saving the industry."

The deal was part of a broader push by the White House to reduce emissions. In 2007, the Supreme Court had given the EPA the power to regulate greenhouse gases, but the Bush administration had declined to do so. When Jackson came in, she immediately went to work building up the regulatory system.

This new-found authority extended beyond vehicles; in theory, the EPA could regulate greenhouse-gas emissions from any source, but neither the president nor Congress preferred that route for cutting emissions. Instead, there were high hopes that Congress would act. In June, the House of Representatives took the first step and passed comprehensive climate

legislation seeking to reduce US greenhouse-gas emissions by roughly 80% below 2005 levels by 2050, leaving the Senate as the next big hurdle.

But then the climate bill had to wait. Obama and his team wanted first to push a health-care overhaul through Congress that would tame rising costs and expand insurance to millions of Americans. The plan was to deal with health care before Congress took its August break and then shepherd climate legislation through the Senate in time for Obama to take something concrete to the United Nations' global-warming summit in Copenhagen in December. But the health-care initiative

proved divisive and time-consuming.

Obama ended up flying into Copenhagen empty-handed. He pledged that the United States would reduce its emissions; but without the backing of law-makers at home, he could make no binding commitments.

On Christmas Eve of 2009, the Senate finally passed the health-care legislation. It was a historic achievement, decades in the making, but it would come at a heavy political price.

AN OILY MESS

If the health-care bill demonstrated the administration's skills with Congress, then the way it handled NASA in early 2010 revealed how easily relations could sour. When the president rolled out his budget request in February, it held a bitter surprise for congressional supporters of the space agency. On the list of projects to be eliminated was Constellation, a programme to develop massive rockets to return humans to the Moon.

"This was a major policy pronouncement but it was revealed in a budget release," says Scott Pace, director of the Space Policy Institute at George Washington University in Washington DC. Normally, an administration prepares Congress for such a change — but Obama's sudden move led to what Pace calls a "bruising, year-long fight" with lawmakers in both parties. Eventually, several parts of the Constellation programme were reinstated. But by then, NASA had become an agency adrift, left to the mercy of parochial interests in Congress.

Human space flight and many other elements of NASA's mission were never priorities of the Obama administration. In the 2013 budget request, the agency's astrophysics and planetary-science programmes lost 8% of their funding compared with 2008. Obama was more interested in fixing problems with his home planet, and boosted funding for NASA's Earth-sciences programmes by 44% over the same period.

The science dream team

Early in his administration, Barack Obama named some stellar scientists to lead the agencies that oversee US civilian research and development activities. Here is how some of the scientific team have fared over the past 4 years.



JOHN HOLDREN

Office of Science and Technology Policy and president's science adviser



STEVEN CHU

Department of Energy



JANE LUBCHENCO

National Oceanographic and Atmospheric Administration



FRANCIS COLLINS

National Institutes of Health



LISA JACKSON

Environmental Protection Agency

2009

👍 • Less than 2 months after taking office, Obama asked him to provide agencies with guidance on developing scientific-integrity policies within 120 days.

👍 • Convinces Congress to provide funding for high-risk energy research programme, ARPA-E, and for small energy hubs for innovative research.

👍 • Helps to resolve management problems in building new weather satellites.

👍 • Approves first new human embryonic-stem-cell lines made available to agency grantees under Obama's liberalized policy.

👍 • Announces agreement with car makers to establish first greenhouse-gas standards for US vehicles.

2010

• After a long delay, he finally issues guidelines at the end of year and agencies begin crafting policies.

👍 • Launches hubs that focus on computer simulation for nuclear reactors; fuels from sunlight; and energy-efficient buildings.

👍 • Helps to lead effort to create national ocean policy that harmonizes management of coastal and marine areas.

👍 • Goes public with plans for a translational-research centre.

👍 • Works with transportation department to finalize greenhouse-gas and fuel-efficiency standards for vehicles.

2011

👎 • Gets into fight with Congress after he met with Chinese officials, despite a congressional ban. Congress slashes budget of his office by one-third.

👎 • Comes under fire from Congress after Solyndra, a solar-energy company that had received more than \$500 million from the energy department, goes bankrupt.

👎 • Alienates scientists over disputes about amount and fate of oil spilled in Deepwater Horizon accident.

👎 • Congress kills plan to create a National Climate Service, one of her main goals.

👎 • Agency's grant application success rates fall to historic low of 18%.

👍 • Issues rule to reduce emissions of mercury and other toxins from power plants, one of multiple regulations that has made coal-fired power plants less competitive compared with natural gas and renewables.

2012

👍 • By September, federal agencies have produced draft or final integrity guidelines.

👍 • Department starts work on two new hubs, focusing on energy storage and critical materials.

👎 • Withdraws plan to appoint chief scientist after losing battle with Congress over administration's response to oil spill; new ocean policy encounters troubles on Capitol Hill.

• Translational-research centre operates for 9 months without a permanent leader. Christopher Austin is named head in September.

👍 • Proposes rule to set greenhouse-gas emissions standards for new power plants.

👎 • Court overturns rule to limit amount of pollution from power plants that crosses into other states.

BOTTOM LINE

Helped to raise profile of science and science integrity but could have done more to push for better policies across the federal government.

Tried to overhaul bureaucracy while invigorating and focusing research and development activities at the energy department.

Despite stumbles during the oil spill, Lubchenco pushed a solid scientific agenda but encountered opposition in Congress to marine policies.

Oversaw massive budget infusion early on, but funding picture turned grim, leading to widespread unhappiness among biomedical researchers.

Tightened pollution controls and laid the groundwork for regulating greenhouse-gas emissions, despite an openly hostile environment on Capitol Hill.

INTEGRITY TEST

A drive to put science above politics has hit some rough patches.

Two months into his new job, President Barack Obama gathered a group of scientists at the White House to sign a memorandum on scientific integrity that declared “Science and the scientific process must inform and guide decisions of my Administration”. The 2009 statement promised that “political officials should not suppress or alter scientific or technological findings and conclusions”. For US researchers, the agreement came as a welcome change from the administration of George W. Bush, which had frequently been accused of infringing on science.

Watchdog groups that track scientific integrity say that Obama’s administration has generally kept those promises — with some notable exceptions. Government scientists are reporting less political interference and more freedom to speak publicly than they experienced under the previous administration. “Agencies change slowly, but if they can change slowly into this culture of transparency, then we can win,” says Francesca Grifo of the Union of Concerned Scientists in Cambridge, Massachusetts, who has spent time working with staff at federal agencies to develop integrity policies.

Even so, the transition has taken much longer than anticipated. Obama’s science adviser, John Holdren, was supposed to issue guidelines for agencies within 120 days of Obama signing the memo, but it took nearly two years. Now, however, all US government agencies have either final or draft policies on scientific integrity, says Rick Weiss, chief of communications for the White House Office of Science and Technology Policy, which Holdren heads. Many of the policies that have been released explicitly forbid agency leadership from tampering with scientific results.

Still, there have been lapses, charge critics. In December 2011, the US Food and Drug Administration (FDA) concluded that the morning-after contraceptive pill, Plan B One Step (levonorgestrel), should be made available to girls under the age of 17 without a prescription. But that decision was overruled by Health and Human Services Secretary Kathleen Sebelius. Obama said that he supported Sebelius’ decision and that “her judgement was that there was not enough evidence” that the youngest adolescents would be able to use the pill properly. Margaret Hamburg, the FDA commissioner, disputed that decision and stood up for agency scientists, who had determined there was sufficient evidence that younger teens were able to use the medication correctly and safely.

Sebelius’s intervention was “deeply disturbing”, said Susan Wood, a health-policy expert at George Washington University in Washington DC and a former assistant commissioner for women’s health at the FDA. “Once again the scientific and medical expertise has been overruled.” The FDA faced controversy again two months ago when agency managers were found to have spied on the e-mails of five staff scientists.

The April 2010 oil spill from BP’s Deepwater Horizon rig in the Gulf of Mexico also raised concerns about integrity. In May 2010, Marcia McNutt, director of the US Geological Survey in Reston, Virginia, wrote in an e-mail to scientists working to estimate the size of the spill that the White House was trying to understate the numbers. That e-mail was obtained and released by the watchdog group Public Employees for Environmental Responsibility, based in Washington DC. McNutt’s comments echoed the concerns of many scientists, who had argued that government estimates of the oil spill were much too low.

Grifo says that a major problem with translating policies on scientific integrity into action has been a lack of commitment by agency leadership. But that is not the case across the board. Wood says, for instance, that Hamburg took a remarkable public stance by backing her agency’s scientists, even though she was overruled. “Her Plan B decision was a clear stand-up for both science and public health in the face of controversy. Good for her. You don’t often see that in senior political appointees,” she says. **E.S.R., J.T., M.W.**

his big ambitions. In December 2011, he and a few dozen colleagues gathered for beers at the Rock Bottom brewery in Bethesda to celebrate one of the biggest changes at the agency in a generation. Collins and his team had succeeded in creating the National Center for Advancing Translational Sciences (NCATS), providing the administration with another victory in applied research.

Collins had proposed NCATS a year earlier, to catalyse the ailing process of drug development by attacking bottlenecks in clinical trials, toxicology research and other areas. Although his plan hit some resistance in the NIH, in industry and on Capitol Hill, Collins managed to convince key members of Congress to support the shifting of funds within the NIH to create the \$575-million

centre, and it opened in the final days of 2011.

Some critics question the centre’s mission. At a congressional hearing in March, Roy Vagelos, former chief executive of drug-maker Merck, asked whether anyone believed that NCATS would be able to solve problems that are stumping the pharmaceutical industry. “If you believe that, you believe in fairies,” he said.

In May, Collins announced the first fruits of the centre. Standing with the research chiefs of three top pharmaceutical companies, he unveiled a \$20-million effort to resurrect drugs that had passed safety trials but had been shelved by industry for business reasons or because they did not work for specific conditions. Under the agreement, the companies gave NIH-funded scientists a stab at repurposing those compounds. “The Obama administration is all about innovation,” says Collins. “And that’s very much what NCATS means to do.”

As the election nears, Obama’s science team is racing to finish up its work. On 28 August, the EPA and the transportation department finalized the changes in vehicle standards that Obama initiated in the rose garden with car makers more than three years ago. In the intervening years, the EPA has moved forward with its Supreme Court authority and begun to lay the groundwork for a broad array of climate regulations. In March, it proposed a rule that would set emissions standards for new power plants and effectively ban coal plants unless they capture and bury carbon dioxide.

Looking back over the past four years, Holdren says that “President Obama has made an unprecedented commitment to science, technology and innovation. ... He promised on inauguration day to ‘restore science to its rightful place’ — a promise he has kept in spades.”

But even his supporters acknowledge that the president did not achieve some of his biggest science-related goals. Carol Browner served as Obama’s climate and energy adviser during the first two years and led the administration’s push to pass climate legislation. “There’s the disappointment of not getting legislation,” she says. “But we didn’t just sit on our hands.”

In his speech to the Democratic Convention on 6 September, Obama laid out some of his energy goals, should the country extend his stay in the White House. He talked about further reducing oil imports and advancing natural-gas production. He discussed improving energy efficiency and advancing clean, renewable energies. “And yes, my plan will continue to reduce the carbon pollution that is heating our planet because climate change is not a hoax,” he said. But in sharp contrast to the soaring rhetoric and bold plans of 2008, he didn’t make any big promises. ■ **SEE EDITORIAL P.473**

Jeff Tollefson covers energy and environment for *Nature* in New York. Additional reporting by *Eric Hand, Meredith Wadman and Eugenie Samuel Reich.*

COMMENT

POLITICS Scientists can improve government by wooing their lawmakers **p.494**

PRODUCTIVITY Evidence that helpful colleagues improve others' output **p.496**

HISTORY Richard Holmes celebrates the science-biography revival **p.498**



FORECASTING When Bayesian statistics can help to sort signal from noise **p.501**

POLARIS/EYEVINE



US Representatives Rush Holt and Nancy Pelosi tour a magnetic resonance imaging facility.

Politicians should think like scientists

A more rigorous, analytical and far-sighted approach would improve the US political process, says **Rush Holt**.

Before I was elected to the US Congress in 1998, I taught and researched topics such as solar spectroscopy and plasma physics. This background inspired some of my constituents to make bumper stickers that read: "My congressman IS a rocket scientist!" The residents of central New Jersey seemed to be calling for more science, or at least more scientific thinking, in Congress.

I agree. Scientists, engineers and technologists are not necessarily smarter or wiser than others, but we have many habitual practices of mind that would be valuable in the sluggish legislative process. 'Scientific thinkers' — and



US ELECTION

Science and Politics in America
nature.com/election2012

to be clear, not all such thinkers are professional scientists — have a deep appreciation for evidence. They have a realistic understanding of technology's promises and pitfalls. They work comfortably with estimates and data. They use statistical reasoning. They are more alert to the mental tricks that they, like all humans, play on themselves. Most importantly, they understand that the path towards good solutions is paved with uncertainty, trial and error; that conclusions should be tentative; and that alternative views should be entertained.

Although the legislative branch rarely deals with matters involving, say, stellar chromospheres or the radio-frequency heating of ions, it tackles many issues in which scientific thinking does (or should) come into play. For example, after the vote-counting controversy of the 2000 US presidential election, I saw a difference in approach between scientists and others as Congress moved to update our nation's voting technology.

Lawmakers and election officials around the United States — most of them non-scientists — quickly embraced the idea of electronic voting machines, and Congress provided more than US\$3 billion to help states to convert their voting systems. According to advocates, electronic machines would eliminate incompletely punched ballots ('hanging chads') that could misrepresent voters' intentions; they would prevent people from voting for more than one person in the same race ('over-voting') or neglecting to cast ballots in other races ('under-voting'); and they would produce a quick tally on election night. What could be better?

Computer scientists were alarmed. Software, they pointed out, is prone to subtle errors. In the privacy of the voting booth, how will the voter know that her or his vote has been recorded as intended? And after the voter leaves the booth, how will election watchers ensure that each vote was recorded as the voter intended? A potentially even greater problem is that elections are tempting targets for hackers.

Most legislators, having little training in scientific thinking, either did not recognize these limitations or assumed that such problems could be pre-empted by testing software. The best solution — and one that I have proposed many times in Congress ▶

— is to use a paper ballot marked by the voter or by a machine in view of the voter. Yet, today we still do not have a national standard for voter-verified, auditable ballots.

Scientific thinkers are also more alert to the cognitive biases that can lead to irrational decisions. For example, politicians (like everyone else) are often guilty of 'short-term-ism': the desire to enjoy rewards now rather than invest them for later. Yet government actions — infrastructure projects, say, or education programmes — play out over decades, long past the careers of individual lawmakers. Scientists are generally comfortable thinking about processes on different timescales — of millions or even billions of years. Scientific thinking can thus build strong arguments for investment in roads, bridges, trains and laboratories that will not produce profits tomorrow but will pay off powerfully in the decades to come.

NUMBERS GAME

Many lawmakers are uncomfortable with statistical reasoning. Take surveillance, for example: the New York City Police Department, as part of its counterterrorism programme, has conducted surveillance of suspected Muslims at restaurants and stores and monitored student groups and mosques around the United States. When I spoke in opposition to these surveillance programmes and called them 'profiling', some of my non-scientist colleagues said that such profiling is keeping the United States safe, even if it is ethnically discriminatory.

But my colleagues were disregarding the fact that terrorists are exceedingly rare. Since

2001, Muslims have boarded planes in the United States perhaps 50 million times. If officials had screened each of these travellers using a protocol that could detect terrorists with, say, 99.9% accuracy, about 50,000 people would have been wrongly accused of terrorism. Billions of dollars would have been wasted in profiling and detaining innocent people, creating

"Scientific thinking builds arguments for investments that will pay off powerfully in the decades to come."

profound distrust among targeted communities.

Statistical reasoning would lead one to recognize that this money would be far better devoted to on-the-ground intelligence gathering.

Scientists are just more comfortable with uncertainty than non-scientists. This trait would come in handy for lawmakers, who often must take action despite conflicting evidence. For example, a failure to understand ordinary fluctuations in noisy climate data allows some members of Congress to believe that claims of human-induced climate change are a hoax, or that the data are so chaotic that no policy action can be devised.

A similar discomfort with uncertainty is evident on the first Friday of each month, when politicians react to the labour department's monthly jobs report. Earlier this month, legislators (egged on, it should be said, by the news media) spent countless hours debating the implications of a report that businesses created 29,000 fewer jobs in August than economists expected. Yet few

grasped that the survey's margin of error was 100,000 jobs at the 90% confidence level. Those 29,000 jobs could very well have been a statistical blip rather than a real trend.

How can we increase scientific thinking in Congress? One way, of course, is to elect more scientists — and I strongly encourage scientists to consider seeking political office. But that is an unlikely solution. More non-scientists need to feel comfortable thinking like scientists. This is not without precedent — not all legislators hold law degrees, but all must be comfortable thinking like lawyers when drafting a bill or reading a statute. When I need to think like a lawyer, I turn to legal professionals for help. Congress has a staff of lawyers at the Office of Legislative Counsel, which helps members to turn their ideas into legislative language. Shouldn't legislators who have scientific questions be able to seek similar guidance from scientists and, over time, pick up more scientific ways of thinking?

Until 1995, Congress had a dedicated staff of professional scientists in the Office of Technology Assessment. This office was eliminated in a round of foolish budget cuts. It should be re-established, and in the interim, we scientists should seek to make our voices heard in other ways: through meetings with members of Congress, letters to editors, town halls and other public forums. ■

Rush Holt represents the 12th congressional district of New Jersey, West Windsor, New Jersey 08550, USA.
e-mail: rush.holt@mail.house.gov

Know your representatives

Lawrence Goldstein urges researchers to talk to lawmakers about science.

Twenty years ago, after moving to San Diego, California, I went to visit the US congressman for my new district. I was responding to the American Society for Cell Biology, which had encouraged its members to visit their congressional representatives and tell them why federal funding for the US National Institutes of Health (NIH) was important to the welfare of the United States. I had heard that this congressman was a former fighter pilot and very conservative, but nothing could have prepared me for our first meeting.

As soon as we sat down, he told me that he thought that the NIH should be privatized. I was surprised, but being stubborn, I continued to visit him once or twice a year for the next few years. Each time, I would explain

how biomedical research leads to a better understanding of basic biology and disease, and how this translates to new and successful approaches to disease therapy. Over time, his meetings with me and with other scientists and patient advocates in our community led to a dramatic change in his view on public funding for biomedical research.

This conservative congressman became a member of a key appropriations subcommittee, on which he fought for substantial increases in NIH funding and even voted to loosen restrictions on funding for embryonic

stem-cell research. Personal interactions between scientists and legislators are crucial in today's increasingly technological world, in which science policy and funding become more important with each passing year.

GOOD INFLUENCE

Some of my colleagues prefer not to interact with members of Congress — they think that one scientist's voice doesn't carry much weight amid the cacophony that assails most officials. Yes, the executive branch of the US government receives considerable formal advice on science policy¹. But the president can get very little done without the support of Congress.

Members of Congress determine the amount of money available for science,



US ELECTION
Science and Politics in America
nature.com/election2012

and they often pass major laws affecting science policy. Many of them have never met a working scientist. It is here that individual scientists can have great personal and scientific impact.

This is true at the state level as well. In California, individual scientists have influenced lawmakers in positive and important ways². For example, following the moratorium on the use of human materials in nuclear-transfer experiments after Dolly the sheep was cloned in 1997, California senators requested advice from me and other biomedical scientists about how to proceed with the technology. We travelled to the state capitol several times to speak to policy-makers and give briefings to members of the legislature. We helped them to understand the research issues and ramifications of various legislative approaches to the issue.

Ultimately, the legislators crafted laws that have served as a good model for how to approach stem-cell science in a thoughtful way. The laws created a regulatory system that restricts the few practices that all would agree are inappropriate, namely the implantation of any product of nuclear transfer using human materials. They also established a group to develop additional regulations in California.

In 2003–04, another group of scientists (myself included) and patient advocates worked together to develop and secure voter approval for California's landmark Proposition 71, which provides US\$3 billion for stem-cell research over ten years in a competitive, peer-reviewed funding system. The initiative included requirements for ethics regulations and rigorous review of funding proposals, partly because of the advice my colleagues and I provided during drafting.

BUILD BRIDGES

Developing relationships with potential allies takes surprisingly little time and effort. A couple of visits a year to the capitol or a legislator's local offices, reinforced by the occasional letter, can go a long way towards building a long-lasting rapport. Scientists will not always make an impact on the first try; they must maintain contact and a consistent message over time.

Some non-scientists have frustrating initial opinions based on incomplete data. My colleagues and I often encountered the mistaken belief that embryonic stem cells come from aborted fetuses. But providing accurate information while being respectful of people's values and beliefs can have a large

“Providing accurate information can have a large influence on legislation.”



California's Proposition 71, passed with scientists' help, provides US\$3 billion for stem-cell research.

influence on legislation. Patient advocates, in particular, bring a human touch that reminds legislators (and scientists) of the important consequences of their work.

Scientists should follow a few simple principles when meeting with lawmakers. It is important to be friendly and informative, and to avoid jargon. People will not care about your message if they cannot understand it: for example, say 'blood-forming' instead of 'haematopoietic'. Also, focus on science during meetings; do not stray to other issues. To avoid seeming parochial, keep conversations in the context of what is good for the nation and society at large; do not talk only about what is good for science and scientists. Bring promising statistics — such as estimates that every dollar the NIH spends on research creates \$2.20 in local economic growth, or that gains in average lifespan due to scientific research have added \$3.2 trillion a year to the US economy since 1970 (ref. 3).

Do not focus solely on lawmakers. Interact also with their staff members, who are usually bright and motivated and can be relied on for information and informal communication throughout the year. Finally, remember that you do not have to be a well-known senior scientist to make an impact. An educated and concerned approach to scientific issues is the most important credential you can bring to a meeting⁴.

Lawmakers need to hear about why

research matters. For example, the United States spends more than \$200 billion a year caring for people with Alzheimer's disease, yet the NIH and private foundations spent less than \$500 million during the 2011 fiscal year to fight the disease. This 400:1 ratio is inadequate, even in a time of fiscal crisis. It is comparable to a family spending \$10,000 a year on a problem but only \$25 a year on finding a solution.

As scientists, it is a mistake for us to say we are too busy to reach out to lawmakers. If we do not try, science funding will continue to decrease in the coming years; lawmakers will enact restrictive policies that are not informed by the best scientific information available; and society will be poorer for our absence. ■

Lawrence Goldstein is Distinguished Professor in the Departments of Cellular and Molecular Medicine and Neurosciences at the University of California, San Diego, School of Medicine, La Jolla, California 92093, USA.
e-mail: lgoldstein@ucsd.edu

1. Pielke Jr, R. *Nature* **450**, 347–348 (2007).
2. Goldstein, L. S. B. *Mol. Biol. Cell* **22**, 3943–3944 (2011).
3. US Department of Health and Human Services. *Impact of NIH Research* <http://go.nature.com/yqygzp> (2012).
4. Goldstein, L. S. B. *Mol. Biol. Cell* **23**, 3279–3280 (2012).



Honour the helpful

Alexander Oettl presents evidence that scientists who share advice and expertise enhance their colleagues' productivity.

What kind of scientist does a department want to hire? The investigator who churns out high-impact papers and travels around the world giving seminars? Or someone with an average publication record who is always discussing other people's work with them, attending seminars and providing feedback on colleagues' papers?

Most departments would probably hire the first one and not think twice. I believe the choice is not so straightforward. Traditionally, science has been an individual pursuit, in which people were valued for their personal output and achievements. Discovery increasingly relies on teamwork and yet scientists are still judged only by what they themselves accomplish.

Throughout my career I've had excellent colleagues. Even if they weren't participating directly in a project, they provided crucial advice that shaped an experiment, gave thoughtful criticisms of manuscripts and

shared data and expertise with anyone who asked. Such people are often thanked in the acknowledgments of papers, not listed as co-authors. But this quality — I call it 'helpfulness' — isn't measured in job applications nor is it considered by hiring committees.

It should be. By reviewing the acknowledgements in immunology papers since 1950, I have found that when principal investigators (PIs) who were frequently thanked by others died unexpectedly, the quality of the papers of their collaborators dropped. In contrast, the quality of co-authors' work changed little after the passing away of PIs who were not particularly helpful to others.

To me, this hints that we need to re-evaluate what makes some scientist 'stars'; to make room for those who may have fewer individual achievements but are a major source of support and feedback for the people around them. Especially nowadays, when it can seem harder than ever to spare time to

help someone else, such collegiality should be encouraged. It benefits the entire scientific enterprise.

WITH THANKS

I examined the acknowledgements from the *Journal of Immunology* — the society journal of the American Association of Immunologists (impact factor 5.788) — from 1950 to 2007 (more than 50,000 papers), using software to note who was thanked, and for what (A. Oettl *Manage. Sci.* **58**, 1122–1140; 2012). To find investigators who probably died while still actively working and publishing — and thus can act as a quasi-natural experiment — I extracted obituaries from more than 400,000 immunology articles from Web of Science and the American Association of Immunologists newsletter. I then looked for people who died within 50 years after publishing their first paper, and checked that they and their co-authors were actively publishing up to the PI's death.



ILLUSTRATION BY OLIVER MUNDAY

I found 149 PIs (either first or last authors) who had died in mid-career. Of these, 63 were in the top 20% of people thanked in all acknowledgements for the year in at least one year of their publishing career. I call this group 'helpful'. Thirty-five of the PIs in this group were also highly productive, defined as being in the top 5% for the number of annual citations and high-impact-factor immunology publications. I similarly divided the less helpful PIs into productive and less productive categories.

I found that co-authors of helpful PIs experienced a similar decrease in the number of papers published after the death

of those PIs as did the co-authors of less helpful and less productive PIs (see 'When help fades'). But co-authors of the helpful PIs experienced a distinct decline in the quality of their publications compared with the less helpful groups — as judged on the impact factors of the journals in which they published. Co-authors of the helpful and most productive PIs experienced a 22% decline ($P < 0.01$), whereas those of the helpful but less productive PIs saw a 20% decline. In some cases, the dip lasted for more than five years.

Co-authors of highly productive and helpful PIs received 21% fewer citations, by a 2010 cut-off, for work published after the PI's death. Citations dropped by 28% on average over the same time period for co-authors of helpful but not particularly productive PIs.

In contrast, co-authors of the 17 PIs who were not particularly helpful but had published many papers in high-impact journals, did not experience any statistically significant decline in the quality or number of their publications or in the number of citations received after their colleague's death. This may seem as if working with unhelpful colleagues means that a scientist's subsequent work is saved from being affected. But these results also suggest that had these co-authors worked with a helpful PI over the same period, their productivity might have been even greater.

The impact of a death was particularly profound on co-authors of PIs who were helpful with conceptual feedback, such as advice and criticism. Perhaps this is because such services are harder to replace than technical expertise, reagents and other study materials.

A good question is: if those helpful PIs with average publication records have such a positive impact on their colleagues' experiments, why aren't they more successful themselves? But there are many instances in science where these qualities don't go hand in hand — for example, many referees can

have a substantive, positive effect on the quality of a manuscript even though they may not have been able to produce a work of similar quality themselves.

Of course this study has limitations. It examines acknowledgements in just one journal within a single biomedical field. In

"Collegiality should be encouraged. It benefits the entire scientific enterprise."

addition, the deaths I record are by no means exhaustive, as I must rely on secondary data sources. Ideally, I would examine whether there is an increase in work quality after the formation of a relationship with

a helpful PI, rather than the effects of the loss of that benefit. But this would require an elaborate randomized field experiment involving forced co-authorship — hardly a realistic possibility.

TEAM SPIRIT

My results suggest that scientists who are helpful have a major impact on their colleagues' careers — and have been undervalued by a scientific enterprise that rewards individual achievement above all else.

It is time to look more closely at what qualities we value most in scientists. Researchers who generate numerous high-impact papers may have little time to discuss problems, criticize manuscripts or mentor students. Those who produce a stream of average papers may have a much more positive impact on the careers of the people around them. Researchers looking for collaborators may sometimes opt for a helpful colleague who is not a major force in their field over a rock-star scientist who rarely replies to e-mails.

So hiring committees should look beyond an applicant's publication record. They should read the recommendations of peers and look for signs that the individual might influence departmental dynamics in a positive way.

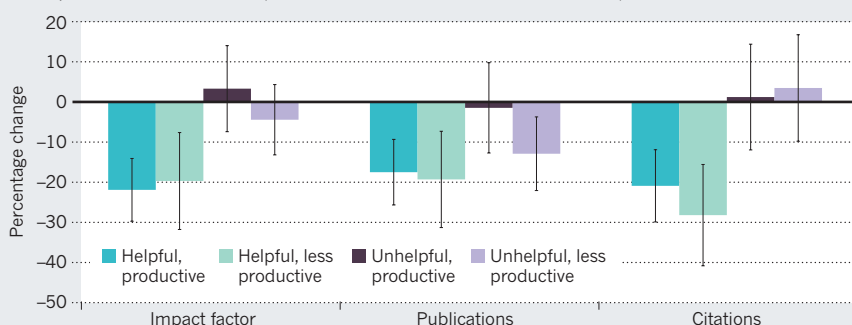
Perhaps we should even develop a metric that measures helpfulness, such as average acknowledgments per year? And funding agencies could give 'helpfulness' awards for generosity that has benefited the field at large, to encourage scientists to help others.

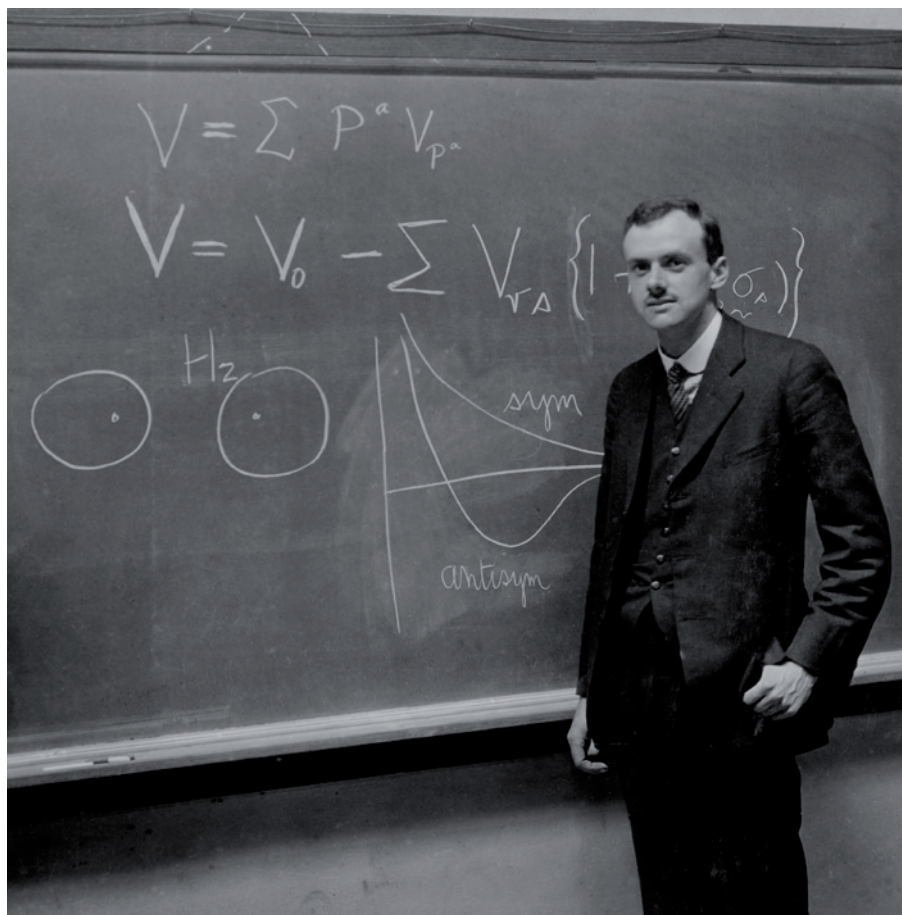
Of course, not every scientist is able to be more helpful. For those who have trouble interacting with others, say, trying to change their natural inclinations and personality will be a losing battle. But science does need to change its reward structure so that researchers who do a lot for others are not penalized. ■

Alexander Oettl is an assistant professor at the Georgia Institute of Technology Scheller College of Business, Atlanta, Georgia 30308, USA.
e-mail: alex.oettl@scheller.gatech.edu

WHEN HELP FADES

After 'helpful' PIs die in mid-career, their co-authors experience a dramatic decline in high-impact publications and citations. In contrast, there is no significant change in these for co-authors of 'unhelpful' PIs after their death (error bars indicate 95% confidence intervals).





The history of science is about people such as Paul Dirac, as well as the discoveries they made.

BIOGRAPHY

The scientist within

Richard Holmes celebrates today's revival of science biography, a tradition spanning 300 years.

Nearly two decades on from the explosion in popular-science publishing, books by luminaries such as Stephen Hawking and Richard Dawkins are still selling in six figures, and authors such as Brian Cox and Rebecca Skloot are drawing a younger generation of readers. But I am struck by a new emphasis — on popular-science biography. As I learned while researching my book *The Age of Wonder* (Harper, 2008), the “life scientific” can be an extraordinarily gripping adventure.

There is a noble tradition of science biography stretching back to the 1600s. Recently, a fresh hunger to understand the making of science through the making of scientists has

emerged. We want to read about scientific work as part of a life story — to know what makes a scientist tick, and what set them ticking. We are intrigued to learn that Dawkins, the eminent biologist and atheist, had “a normal Anglican upbringing”, was inspired by the Dr Doolittle books and taught in 1960s San Francisco, in the time of flower power and demonstrations against the war in Vietnam.

The form is currently undergoing unprecedented transformation. Biographers are tackling highly complex and challenging areas such as X-ray crystallography, general relativity and quantum physics, explaining them as pure adventures of the human spirit.

We see this in spellbinding biographies, from Georgina Ferry's *Dorothy Hodgkin* (Granta; 1998) and Walter Isaacson's *Einstein* (Simon & Schuster, 2007) to Graham Farmelo's award-winning biography of Paul Dirac, *The Strangest Man* (Faber and Faber, 2009) — which drew praise from readers as varied as Michael Frayn, Tom Stoppard and Martin Rees.

THE EVOLUTION OF A THEORY

A whole spectrum of books on Charles Darwin, published to mark the 2009 bicentenary of his birth, illuminated the debate surrounding the emergence and implications of evolutionary theory. Led by Janet Browne, who treated *On The Origin* itself as a biographical subject, and Adrian Desmond and James Moore, who looked at Darwin's work on human origins, this biographic experimentation expanded in original ways. Rebecca Stott's *Darwin's Ghosts* (Bloomsbury, 2012), for example, is a prequel consisting of vivid portraits of early evolutionists, starting with Aristotle doing marine biology on the isle of Lesbos.

Stott's book is part of a growing trend for group biographies of scientists. These use teamwork, competition and personal rivalry to reframe science as a kind of social history. Outstanding examples cover groupings in every century. Arabic trailblazers of the ‘dark’ ages and people of the early medieval period star in Jim Al-Khalili's *Pathfinders* (Allan Lane, 2010). Lisa Jardine's *Ingenious Pursuits* (Little, Brown and Co., 1999) focuses on seventeenth-century European natural philosophers, and Jenny Uglow's *The Lunar Men* (Faber and Faber, 2002) displays the enlightened industrialists of the eighteenth century. We can relish the pioneering efforts of nineteenth-century palaeontologists in Deborah Cadbury's *The Dinosaur Hunters* (Fourth Estate, 2000), and marvel at the groundbreaking work of twentieth-century physicists in Manjit Kumar's *Quantum* (Icon Books, 2008).

Mathematics could be seen as the hardest nut to crack biographically because of its abstract language. Yet Simon Singh rendered it thrilling in his treasure-hunt of a group biography over four centuries, *Fermat's Last Theorem* (Fourth Estate, 1997).

PROFILE PIONEERS

But what of that earlier tradition of science biography? The word ‘scientist’ was coined only in 1834, and there is a popular misconception that individual scientific ‘lives’ — such as Henry Mayhew's *Young Humphry Davy* (1855) — are essentially a Victorian creation. In fact, as with literary biography, these go back well over 300 years. In the

NATURE.COM

For an author's take on writing biography, see: go.nature.com/xgb9tg

1680s, John Aubrey wrote *Brief Lives* of William Harvey, Edmund Halley and Robert Boyle, as well as of Shakespeare and Milton.

A surprising pioneer of the form in the eighteenth century was Samuel Johnson. Along with his dictionary and *The Lives of the Most Eminent English Poets* (1781), Johnson also wrote *The Life of Dr Herman Boerhaave* (1739), a vivid short biography of the great Dutch botanist and medical doctor who founded clinical teaching at Leiden, improved diagnostic techniques and isolated urea.

Johnson perceived that Boerhaave's childhood was essential to his adult science. He writes, for instance, of Boerhaave's gruesome teenage leg ulcer: "his own pain taught him to compassionate others, and his experience of the inefficacy of the methods then in use, incited him to attempt the discovery of others more certain."

Similarly, William Stukeley in his *Life of Newton* (1752) is careful to cite "the extraordinary pregnancy of his genius, whilst a boy". Stukeley gives vivid descriptions of Newton's boyish windmills, counter levers and water clocks. Stukeley also relates the first known version of the young Newton's famous vision of "universal gravitation" in the orchard at Woolsthorpe, Lincolnshire, as he contemplates the falling of an apple from a tree: "Why sh^d it not go sideways, or upwards? but constantly to the earth's centre? ... there must be a drawing power in matter. & the sum of the drawing power in the matter of the earth must be in the earth's center, not in any side of the earth." (Stukeley's original manuscript, one of the treasures of the Royal Society, can be read at <http://royalsociety.org/library/moments/newton-apple>).

The growing fascination with scientific biography in the nineteenth century is illustrated by the supplements to the fourth, fifth and sixth editions of the *Encyclopaedia Britannica*, completed in 1824. Of 165 lives selected for individual treatment, 35% were broadly scientific. Another landmark was David Brewster's *The Life of Sir Isaac Newton* (1831), which presented the natural philosopher as a secular saint, "the high-priest of science" and a man of universal genius. Like Stukeley, Brewster emphasized the originality of mind revealed by Newton's boyhood. Brewster also gave the idea of scientific childhood a new, metaphorical dimension.

It was his superb final chapter that called attention to Newton's now celebrated remark about the mysterious, shifting infinity of scientific truth: "...to myself I seem to have been only like a boy playing on the seashore, and diverting myself in now and then finding a smoother pebble or a prettier shell than ordinary, whilst the great Ocean of truth lay all undiscovered before me." Newton may

here have been adapting an image from Book IV of Milton's *Paradise Regained* — the observation that "wise men" may think themselves "deep versed" in research, yet in reality may be "as children gath'ring pebbles on the shore".

SETBACKS AND SERENDIPITIES

In what ways do biographies, whether written last year or in the seventeenth century, throw light on science and scientists? The Royal Society, announcing a historic symposium, Writing Scientific Biography, in 2008, observed that such works "show us the human face of science: the motivations, set-backs, serendipities and moments of enlightenment in the quest for knowledge".

I think they do more. First, they show the crucial shaping power of childhood and youth, where the scientific vocation and vision begin to emerge. Second, they examine the nature of the creative breakthrough. Eureka moments are only one manifestation. Discovery may equally be the product of painful years of research, experiment and thought, as with Darwin or Dirac. Or it may be the result of a short but intense period of competition and rivalry, as with Francis Crick, James Watson, Rosalind Franklin and Linus Pauling, in the race to discover the structure of DNA.

Third, biographies point to the importance of the inner, imaginative and emotional life. They contradict the fallacy that all scientists are icy rationalists. The great US physicist Richard Feynman played the bongos. The famously elusive chemist Henry Cavendish was a secret member of the notorious Cat and Bagpipes Club. Michael Faraday was an elder of the Sandemanian church. James Clerk Maxwell wrote Scottish poetry and accompanied himself on the guitar. Alan Turing was an outstanding marathon runner. All these traits and

characteristics can be linked to the energies that both inspired and occasionally impeded their research.

Fourth, biographies show that error and uncertainty are central to discovery, in a way that is lost in 'the literature', that official record of scientific endeavour. Victorian histories of science tended to propose models of unbroken, cumulative progress, which encouraged the alarming triumphalism of classical science in the early twentieth century. Contemporary 'scientism' has perhaps inherited something of this bias. By contrast, individual biography reveals doubt, scepticism and the historically shifting

boundaries of interpretation and truth. The forthcoming life of the nuclear physicist J. Robert Oppenheimer by Ray Monk (the inspired biographer of Ludwig Wittgenstein and Bertrand Russell)

reveals just such a powerful field of political, financial and ethical ambiguities surrounding US science during the cold war.

Biographies can also probe originality and disputed cases of priority, as in the "discovery" of oxygen by Antoine Lavoisier, or Joseph Priestley or Carl Scheele; or the theory of evolution by Darwin or Alfred Russel Wallace. They show that at particular times, certain areas of science are intensely active and open to discovery — currently, cosmology, neuroscience and nanotechnology — while others are comparatively dormant. It is in these active areas that the linked forces of teamwork and rivalry are most fiercely alive, and their consequences can be best understood.

In *The Strangest Man*, for instance, Graham Farmelo memorably compares the development of quantum mechanics in the 1920s by a team of 50 physicists to "a group of construction workers" labouring on an enormous building site occupying much of northern Europe. "Virtually all the builders were male, under thirty, intensely competitive and craving the respect of their peers as well as the blessing of posterity."

So science is always a story. A detective story, perhaps; a mystery story; a love story; even, on occasion, a ghost story (the Higgs boson?). But always a story of human lives. And that is what seems to fascinate us — again. ■

Richard Holmes is the author of *The Age of Wonder*, which won the 2009 Royal Society Prize for Science Books. His new book, *Falling Upwards: How the Romantics Took to the Air*, will be published in spring 2013.
e-mail: richard.holmes@osb.me.uk



Samuel Johnson wrote a biography of medic Herman Boerhaave in 1739.



FOOD SCIENCE

Digestive tracts

Barbara Ketcham Wheaton samples a brace of food-related science and technology histories.

Food has long exercised the scientific mind. Now, two books open windows on the dynamic interplay of science, technology and the culinary arts in history. Emma Spary, in *Eating the Enlightenment*, explores concerns about physiology and morality vis-à-vis cuisine at the dawn of modern science. Meanwhile, food historian Bee Wilson's *Consider the Fork* delves into the chewy past of kitchen technology.

Focusing on Paris during the tumultuous years from 1670 through to the mid-eighteenth century, Spary examines questions and controversies surrounding the edible — from food and drink addictions to the dangers of mixing social classes at cafés. She shows how French thinkers, medics, clergymen and café proprietors probed matters digestive from scientific and philosophical standpoints. They asked many questions. What was the correct diet for an intellectual? Were the spirits in liqueurs a good thing? Were cafés suitable venues for the display of literary wit?

Spary shows how scientists of the time debated whether we digest food by dissolving it with acid in the 'chemical laboratory' of the stomach (the iatrochemical theory), or by mechanically grinding it with the teeth and then more finely with the stomach. The chemist Louis Leméry spoke for the iatrochemists in his *Traité des Aliments* (1702) in postulating acid or alkaline fermentation of foodstuffs during digestion. In the 1730s, working separately, Antoine-René Ferchault de Réaumur validated the iatrochemical theory in experiments with living birds.

Even Jacques de Vaucanson, inventor of automata, got in on the act by 'demonstrating' the process of chemical digestion through mechanical trickery. His famous Digesting Duck automaton appeared to eat, digest and excrete grain, although the 'input' and 'output' were purportedly in separate compartments.

Eating the Enlightenment: Food and the Sciences in Paris

E. C. SPARY

University of Chicago Press: 2012. 368 pp. \$45, £29

Consider the Fork: A History of How We Cook and Eat

BEE WILSON

Basic Books: 2012. 352 pp. \$26.99

A particularly heated debate swirled about whether an austere, 'natural' diet supported a clear mind and pure body better than did a luxurious, sophisticated one. Spary cites many of the influential cookbooks from both camps, including Marin's *Les Dons de Comus* (1739) on the sumptuous side and Menon's *La Cuisinière Bourgeoise* (1746) on the natural one.

Philosophers took sides, with Voltaire plumping for luxury; his trout and cream, for instance, was both praised and vilified (for causing indigestion). 'Natural man' Rousseau, by contrast, wrote, "If I am given milk, eggs, salad, cheese, brown bread, and ordinary wine I am sufficiently entertained." In this, Rousseau was backed by medical reformer Philippe Hecquet, who in around 1700 advocated a simple, nearly meat-free diet as morally and hygienically superior.

The Enlightenment's obsession with classes of food and their effects is echoed in *Consider the Fork*. Wilson's take on technologies of cooking and eating mixes material sciences, engineering, anthropology and history. Organized under eight broad topics — including fire, ice, cutting and grinding — the book spans millennia, and covers tools from Neolithic mortars and pestles to modernist cuisine's liquid-nitrogen canisters. The focus is Western, but Wilson is well informed about equipment from elsewhere, especially Asia.

She emphasises how technologies determine what we eat. Electric refrigerators, for instance, elbowed out curing and smoking

as necessary household techniques, and put fresh and cooked-from-frozen food on the daily table. Meanwhile, some odder inventions, such as the mechanical apple parer, have fallen off the counter edge for good in most kitchens.

The chapter on knives is excellent. In 3,000 BC, bronze knives were shaped like modern ones, but dulled so quickly that flints were often used in preference. Iron knives came into use around 700 BC, and within a few centuries carbon-steel knives were being made both in China and the West.

In modern times the French have used many specialized knives, from the mushroom-fluting bird-billed knife to the flexible fish knife that slips fillets of sole off the bone. Such elaborate differentiation is part of French history; at European tables of the fifteenth century, carvers conducted knife-work theatrics, wielding a variety of blades to dismember and serve all sorts of flesh, fish and fowl. However, in the Chinese kitchen a single rectangular cleaver, the tou, is used for the most robust butchering tasks, as well as the finest dicing and shredding. Originating towards the end of the Chou dynasty (1045–256 BC), when steel technology came to China, skills with this single blade became ever more refined and the language of cutting and shredding ever more specialized. Beautifully cut ingredients remain at the heart of Chinese gastronomy.

In the past 60 years, two waves of game-changing equipment have entered the kitchen. The food processor and microwave arrived in the mid-twentieth century. More recently, the 'lab' apparatus and ingredients as yet unfamiliar to the home cook — such as the gelling agents iota carrageenan and konjac gum — have begun to appear as essentials for whipping up the confections of molecular gastronomy. Once again, hard-won skills become redundant, and the increasing use of instruments has diminished our sensory involvement with the act of cooking.

Even skills such as whisking have gone the way of the medieval boar spit in many kitchens. Today, swathes of people in the Northern Hemisphere need scarcely touch their dinner until they sit down to eat it. Wilson is clearly ambivalent about these technological tides.

Meanwhile, home videos of meals cooked from the monumental *Modernist Cuisine* (Cooking Lab, 2011) by Nathan Myhrvold, Chris Young and Maxime Bilet can be found on YouTube. A new cycle of debate begins. ■

Barbara Ketcham Wheaton is honorary curator of the Culinary Collection at the Schlesinger Library, Radcliffe Institute for Advanced Study, Harvard University, Cambridge, Massachusetts, and the author of *Savouring the Past: the French Kitchen and Table from 1300 to 1789*. e-mail: bkwheaton@verizon.net

STATISTICS

Forecasting with finesse

Paul Ormerod assesses a Bayesian take on predicting everything from poker games to climate change.

Nate Silver is an intriguing man. A statistician by training, he developed a system for forecasting baseball performance that has had real influence on how the top teams evaluate potential players. His blog made accurate predictions about the 2008 US Presidential election. He has a regular slot in the *New York Times*. And now, in his thoughtful, engaging *The Signal and the Noise*, he offers an array of fascinating examples of forecasting, from baseball and elections to poker, chess, stock markets, terrorist attacks, earthquakes and climate change.

The 'signal' in the title refers to genuine information, which can be used for prediction. 'Noise' is the purely random component of data, which cannot. A serious problem with many forecasting models is that they try to explain too much, and end up 'explaining' the noise. Silver documents this little-known but fundamental problem of 'overfitting' in clear terms.

Silver has a serious scientific purpose. He is highly critical of the dominant, frequentist approach in statistics, which relies on the frequency of one possibility coming up over a number of trials to determine the true probability. For example, if heads come up more frequently than tails when a coin is tossed, your confidence that the coin is biased will increase the more tosses you observe. Silver is a fervent advocate of the rival approach: Bayesian statistics. This is just as mathematically rigorous, but is a more heuristic approach, in which you form a view about the chances of an event happening and revise this estimate as new information comes to light. So, your prior estimate that a coin is biased will depend on whether the person flipping is a seedy man in a bar or the Archbishop of Canterbury. If the former, you may conclude it is

biased after, say, only three heads come up in succession.

Most of Silver's examples come from the social sciences,

which encompass the really difficult problems, such as forecasting the economy. In the natural sciences, a theory that explains the past will also, in general, be usable for making predictions about the future. Not so the social sciences, in which a clear distinction usually needs to be made between explanation and prediction. For example, there are models that describe well why price changes in stock markets in the past exhibit the features they do; these are based on how traders behave. Forecasting is much harder; and 'predictive' models are essentially pure extrapolations, over very short time periods, of past data, with no behavioural content.

In the natural sciences, theories can be developed and verified — or, to be more accurate, not falsified — by the evidence obtained from replicable experiments. In the social sciences, such strong support for a theory is rarely, if ever, possible. For example, there is currently a major debate about whether increases in public spending will boost the economy. Despite a huge amount of theoretical and empirical work, economists are no nearer to a consensus than they were 50 years ago.

The availability of 'big data' — from mobile-phone usage and social-network use, for instance — is currently seen by many as raising the potential for social sciences to approach the predictive power of the natural sciences. Detailed behavioural observation, the reasoning goes, would be a step closer to the

realm of replicable experiments. Silver is profoundly sceptical about this possibility, and argues that a massive increase in data will make predictions more prone to failure, not less. As he puts it, "the number of *meaningful* relationships ... is [tiny]... there isn't any more truth in the world than there was before the Internet".

Silver points out a key critique of Bayesian analysis, which is that it introduces the 'unscientific' concept of personal judgement. But in the social sciences, this is required all the time, even when the frequentist approach is used.

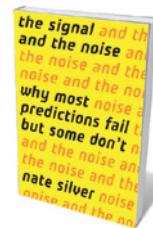
A revealing case emerged in 2007, when the Bank of England produced its 'fan charts', showing the potential range of outcomes for economic growth over the next five years. This indicated that the probability of a UK recession occurring in 2008–12 was essentially zero. But the economists had used data from only 1993–2006 to calibrate the probability distribution of growth rates; they had convinced themselves that their 1990s theories had solved problems of the economy once and for all. Using the frequentist approach, they had judged data from before 1993 as irrelevant — which we now know to be profoundly wrong.

Silver discusses the poor record of economic forecasting at length, and is correct in stressing the importance of understanding the data, rather than just pouring it into a statistical package and pressing the button. He does not, however, make clear how a Bayesian approach could have predicted the financial crisis.

Nor does he discuss the extent to which a given data set contains any signal at all, rather than being completely dominated by noise. In data sets in the social sciences, there are often many factors that can influence outcomes, and behaviour varies over time; so the data produced by a system is often indistinguishable from a random series. In such cases, neither the frequentist nor the Bayesian approach will produce successful forecasts.

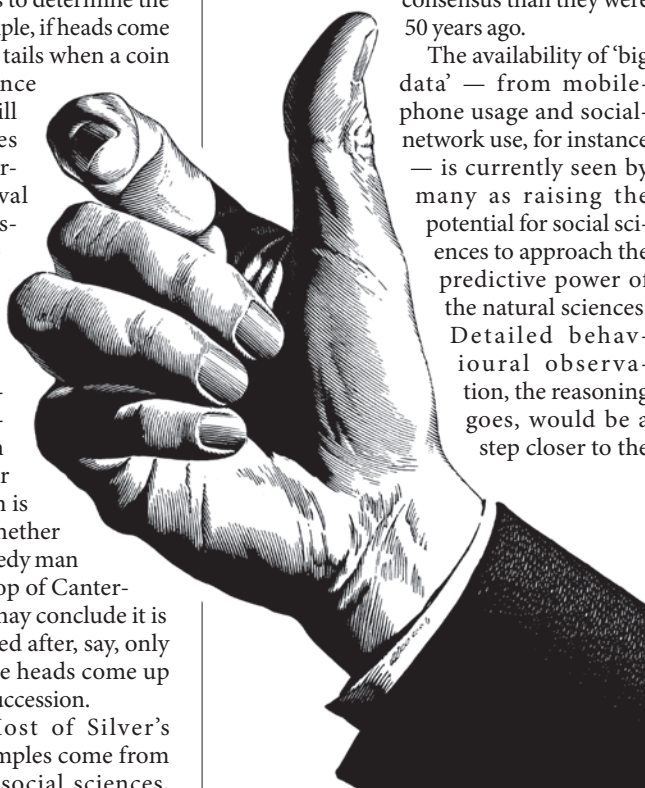
But, overall, Silver does make a good case for a Bayesian approach. His book is a lively, well-argued corrective to the prevailing view that we need large amounts of data before we can make intelligent and accurate forecasts. ■

Paul Ormerod is an economist and complex-systems theorist, and author of *Positive Linking: How Networks Can Revolutionise the World*.
e-mail: pormerod@volterra.co.uk



The Signal and the Noise: Why So Many Predictions Fail — but Some Don't

NATE SILVER
Penguin: 2012.
352 pp. \$27.95



➔ NATURE.COM
For more on
Bayes' theorem of
probability, see:
go.nature.com/2h3ecm

Correspondence

Redirect research to control coffee pest

The coffee-berry borer (*Hypothenemus hampei*) was accidentally introduced into Brazil in 1913 and later invaded coffee plantations throughout South and Central America, Mexico and the Caribbean. The insect still causes worldwide annual losses of some US\$500 million, affecting the incomes of more than 20 million coffee-farming families in roughly 80 nations. We contend that a radical change in research direction is called for if the damage inflicted by this pest is to be contained.

The topic has generated more than 1,600 papers, so far with little practical success. This is partly because the insect spends most of its life concealed inside the coffee berry feeding on the seeds, making its management difficult. But it may also be because the focus on developing biological control agents such as fungal entomopathogens and parasitoids is too narrow. The results have been disappointing, and major practical and economic obstacles have prevented their implementation in the field.

Research should instead be aimed at exploring potential attractants and repellents, and at gaining a better understanding of the microbiota associated with the insect.

Francisco Infante, Jeanneth Pérez *El Colegio de la Frontera Sur, Tapachula, Chiapas, Mexico.*
Fernando E. Vega *USDA, ARS, Beltsville, Maryland, USA.*
fernando.vega@ars.usda.gov

Follow the money on climate controversy

Dan Kahan's analysis of the 'controversy' over climate change is insightful up to a point (*Nature* **488**, 255; 2012). But there is one crucial factor that he does not mention: money.

The climate-change controversy has been created

by a tiny group of people whose livelihoods depend on it. Oil and its derivatives have made these people extremely rich, so they perpetrate the idea that climate change induced by the use of fossil fuels is a myth to ensure that they stay that way.

The public is prey to a systematic campaign to pollute the science-communication environment (as Kahan so aptly puts it), backed by vast wealth. This campaign is being indirectly abetted by the US Supreme Court, which has declared that political groups may spend limitless amounts of money without identifying themselves. **Thomas E. DeCoursey** *Rush University Medical Center, Chicago, Illinois, USA.*
tdcourse@rush.edu

Green issues are catching on in China

Your report on the rise of environmental protest in China (*Nature* **488**, 261–262; 2012) is backed up by findings of the Pew Global Attitudes Project, which indicate that 80% of Chinese people now rate environmental protection as a priority (see go.nature.com/tehbh9).

Landmark cases include spontaneous protests against paraxylene pollution in Xiamen in 2007 and in Dalian in 2011; against garbage incineration at Panyu in 2009; and against waste-water pollution in Qidong earlier this year. So far, people seem more concerned about the impact of local pollutants than about national environmental issues (W. Li, J. Liu and D. Li *J. Environ. Mgmt* **98**, 65–72; 2012).

These protests have raised awareness of environmental pollution among local governments and forced them to address some of the issues.

Environmental protection on a wider scale will demand more concerted action, with strong leadership and organization, and regulations that protect the

rights of individuals. It will mean supporting the winners and compensating those who could lose out economically.

Qiang Wang, Xi Chen *Xinjiang Institute of Ecology and Geography, China.*
qiangwang7@gmail.com
Yi-Chong Xu *Griffith University, Australia.*

Rationality: Evidence must prevail

I strongly disagree with Daniel Sarewitz's suggestion that non-mathematicians must use faith to "believe" in the Higgs boson (*Nature* **488**, 431; 2012). The particle's existence is based on hard evidence, not belief.

Evidence is why most ill people visit doctors, rather than sacrifice chickens or visit priests. If we were to abandon evidence, we would soon be in some post-modernist hell. As for faith, the rational thought that underpins science provides us with a system that works. It fosters questioning and makes risky, falsifiable predictions; religion does neither, as it demands blind acceptance of dogma.

Had science and rationality been abandoned in favour of religion, then the stoning of adulterers would be much more common and there would have been many fewer women participating in the Olympic Games. Let's be grown up, rational, accept evidence and put the fairies to bed.

David J. Hosken *University of Exeter Cornwall Campus, Penryn, UK.*
d.j.hosken@exeter.ac.uk

Rationality: Science is not bad faith

Perhaps Daniel Sarewitz (*Nature* **488**, 431; 2012) should read more Ludwig Wittgenstein. The philosopher opposed the view of religion as a flawed version of science, lacking in evidence, sophistication or predictive

power. Rather, he considered religion a matter of shared practices, observance and ritual that has a special significance to its practitioners. To that extent, there is no meaningful opposition between religion and science: they do not even occupy the same logical space.

Sarewitz's account of what religion can teach science indicates a belief that the two activities are somehow similar and express the same aim. Viewing temples and falling in love can be moving experiences, but they don't reveal a hidden reality whose articulation eludes science.

I am not a believer in the Higgs boson (or related particles) merely because of a cultural artefact. I was born in a country that trusts theoretical physicists more than, say, astrologists (who need no physics for their predictions). That situation has arisen because of the divergent successes of the physical sciences and astrology in understanding the world.

Religion need not be bad science; science is not bad faith. **Andy Greenfield** *Medical Research Council Harwell, UK.*
a.greenfield@har.mrc.ac.uk

Rationality: Religion defies understanding

Daniel Sarewitz suggests that we need ways of "understanding our world beyond the scientifically rational" (*Nature* **488**, 431; 2012). Our species has derived many things from its various religions — some fair and noble, others foul and destructive — but understanding is not one of them. **Andrew Blight** *Acorda Therapeutics, Ardsley, New York, USA.*
arborlight@gmail.com

CONTRIBUTIONS

Author guidelines can be found at go.nature.com/cmchno.

EVOLUTION

How the unicorn got its horn

An experiment studying bacterial populations over thousands of generations shows that a novel trait can evolve through rearrangement and amplification of a few pre-existing genes. [SEE ARTICLE P.513](#)

HEATHER HENDRICKSON & PAUL B. RAINEY

Evolutionary novelties such as flight, flowers and eyes are central to life's diversity, and yet explanations for their origins are anything but straightforward. The difficulty arises because the relevant events happened a long time ago under circumstances that are poorly understood. However, in this issue, Blount *et al.*¹ (page 513) unravel molecular details underpinning a major innovation in a trait (phenotype) that evolved in bacterial populations after 30,000 generations. The capacity to store ancestral types in a state of suspended animation and then sequence their genomes has provided a remarkably complete picture of the main genetic events that gave rise to an instance of evolutionary novelty*.

The 'modern evolutionary synthesis', which provides the accepted account of evolution, unites Charles Darwin's gradualism — the view that evolution proceeds through gradual changes — with Gregor Mendel's concept of genes as discrete units. But some have argued that the resulting notion of incremental mutational change does not provide an adequate framework for explaining how phenotypic innovations arise^{2,3}. What steps precede a major evolutionary advance such as the eye? Far from being a simple philosophical point, the need for mechanistic understanding at this level is paramount, and Blount *et al.* (researchers in Richard Lenski's laboratory) provide direct insight into how innovation happens.

In 1988, Lenski initiated what is now the longest-running project in experimental evolution. He took a clone (a group of genetically identical cells derived from a single cell) of the fast-growing bacterium *Escherichia coli* and founded 12 independent populations, each resident in a flask containing a simple medium, with glucose as the sole source of carbon. Every day for almost 25 years, a sample of each population has been transferred to a fresh flask — which means that these populations have gone through 55,000 generations. In addition to daily transfer, the researchers have been periodically storing samples at -80°C , thereby ensuring

*This article and the paper under discussion¹ were published online on 19 September 2012.

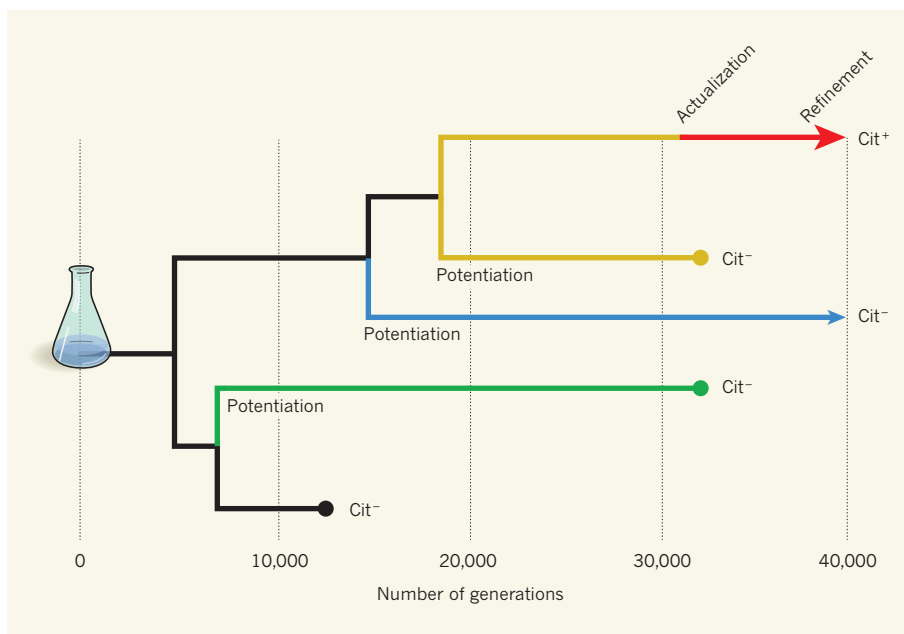


Figure 1 | The evolution of a new trait. In 1988, Richard Lenski took a single clone formed by genetically identical *Escherichia coli* bacteria and propagated it, with daily transfer, in 12 independent flasks. Whereas the original cells could use citrate as a nutrient only in the absence of oxygen (Cit^- cells), bacteria in one of the flasks eventually evolved the ability to use it with oxygen present (Cit^+ cells, indicated in red). After analysing the genomes of the microbes at different stages of the process, Blount *et al.*¹ (researchers in Lenski's laboratory) found that the original clone had diverged into competing lineages — some of which went extinct and some of which prospered. The authors report that, for the new ability to appear, the bacterial populations went through three successive evolutionary steps. 'Potentiating' mutations (of unclear nature) were required for cells to acquire 'actualizing' mutations that consisted of a specific rearrangement of a few genes and that allowed some growth — although poor — on citrate in the presence of oxygen. Further 'refining' mutations, which involved duplications of the rearranged DNA sequence, were needed for robust growth under such conditions.

access to a detailed history of ancestral states. Moreover, unlike fossils, these frozen ancestors are readily brought back to life.

Although Lenski's group reported adaptations that improved the microbes' fitness from the earliest stages of the experiment, something remarkable happened after about 31,000 generations. One of the populations (Ara-3) evolved the capacity to use citrate as a nutrient⁴. Citrate, a chelating agent that facilitates iron uptake, is a component of the growth medium. Although *E. coli* can 'digest' citrate when oxygen is absent, it typically cannot do so under the aerobic conditions of this experiment. The fact that the microbe can use citrate under some circumstances raises an

important point: new genes are not invented *de novo*. Quite the contrary — evolution builds on the raw material at its disposal. The bacterium has the building blocks necessary for the evolution of aerobic citrate utilization, but realization of this capacity requires a rewiring and refinement of regulatory connectivities.

To understand the nature of the genetic changes conferring the ability to use citrate in the presence of oxygen (a trait dubbed the Cit^+ phenotype), Blount *et al.* returned to the freezer and resuscitated ancestral Cit^- populations from earlier time points in the Ara-3 lineage. When the researchers tried to 'replay' the evolution of the trait, they found that

the Cit⁺ phenotype appeared again only in populations derived from the most recent Cit⁻ lineages. This result suggested that genetic changes had occurred in these lineages that made it possible for the Cit⁺ phenotype to evolve. Although the precise nature of such 'potentiating' mutations is unclear, the important fact is that they took place (Fig. 1).

The step that made the cells weakly Cit⁺ — the 'actualization' step — was easier to identify. The authors examined a genomic region that carries the gene *citT*, which encodes a protein (citrate transporter) needed for citrate to enter the cell. In the original bacterial strain, *citT* is located downstream of *citG* (another gene required for citrate utilization) and *rnk*, a functionally unrelated gene that participates in energy metabolism. In each of the derived Cit⁺ cells, Blount *et al.* found a distinctive genomic rearrangement that fused *rnk* to *citG*. As a result, expression of *citG* and *citT* came under the control of the promoter (regulatory sequence) of *rnk*, which allowed their expression in the presence of oxygen. What's more, the authors found that a single copy of the genetic rearrangement was insufficient to generate the Cit⁺ phenotype, and

"New genes are not invented de novo. Quite the contrary: evolution builds on the raw material at its disposal."

that there was a tandem array of between two and nine copies in Cit⁺ cells. Therefore, gene duplications took a very low level of citrate transport and propelled it to life-sustaining levels. All cells that inherited the genetic

fusion (the actualizing mutation), followed by amplification (a 'refining' mutation), were Cit⁺.

The discovery of the Cit⁺ mutants in Lenski's experiment has been a mote in the eye for those suggesting that major phenotypic innovations cannot be explained by micro-evolutionary (gradual) processes. Indeed, for anti-evolutionists, lack of mechanistic detail has even allowed room for divine intervention. After several attempts to politely address the concerns of one critic, Lenski responded publicly in what has proven to be one of the most competent and direct defences of science versus dogma for some time. It includes the memorable phrase⁵, "In other words, it's not that we claim to have glimpsed 'a unicorn in the garden' — we have a whole population of them living in my lab!"

With knowledge of the key events that determine this unicorn's horn, one can next look for lessons of a general nature. The idea that genetic evolution might conform to a set of rules is attractive⁶. Capture and amplification of other genes' promoters have been shown to facilitate adaptation in a variety of situations^{7,8}, but the extent to which these kinds of events can fuel phenotypic innovation depends on prior history, chance and fortuitous factors

such as genome architecture. Blount and colleagues' work shows that evolution, given sufficient time, will take advantage of any opportunity — but opportunity may depend on the most fickle of potentiating events. Unfortunately, predicting the nature of these crucial potentiating mutations may well lie beyond reach. Nevertheless, on a positive note, this work strengthens a central premise of the modern evolutionary synthesis: genetic change is gradual. Phenotypic change, however, can be dramatic. ■

Heather Hendrickson and Paul B. Rainey
are at the New Zealand Institute for Advanced Study, Massey University, Auckland 0745,

New Zealand. **P.B.R.** is also at the Max Planck Institute for Evolutionary Biology, Plön, Germany.

e-mail: p.b.rainey@massey.ac.nz

1. Blount, Z. D., Barrick, J. E., Davidson, C. J. & Lenski, R. E. *Nature* **489**, 513–518 (2012).
2. Pigliucci, M. *Phil. Sci.* **75**, 887–898 (2008).
3. Gould, S. J. *The Structure of Evolutionary Theory* (Belknap, 2002).
4. Blount, Z. D., Borland, C. Z. & Lenski, R. E. *Proc. Natl Acad. Sci. USA* **105**, 7899–7906 (2008).
5. http://rationalwiki.org/wiki/Lenski_affair
6. Stern, D. L. & Orgogozo, V. *Science* **323**, 746–751 (2009).
7. Whoriskey, S. K., Nghiem, V. H., Leong, P. M., Masson, J. M. & Miller, J. H. *Genes Dev.* **1**, 227–237 (1987).
8. Andersson, D. I. *Science* **282**, 1133–1135 (1998).

QUANTUM COMPUTATION

Spinning towards scalable circuits

Silicon devices form the backbone of modern computers. It turns out that they might also be a natural hardware platform for a new era of computing technology that uses the principles of quantum physics. SEE LETTER P.541

LEE C. BASSETT & DAVID D. AWSCHALOM

More than 50 years ago, the invention of integrated circuits based on silicon transistors (tiny electronic switches) revolutionized electrical and computer engineering. It allowed room-sized computers made of vacuum tubes to be replaced with individual semiconductor chips, which have continued to become exponentially smaller and more powerful. Now, a new kind of computing that relies on quantum rather than classical physics has the potential to crack problems inaccessible to even the most powerful classical computers of the foreseeable future. However, we are still searching for the best physical architecture for such quantum machines — even a suitable 'quantum vacuum tube', let alone the transistor equivalent, remains elusive.

Among many candidates for the quantum bits (qubits) of information that form the basis of quantum computing, the spins of single electrons or isolated nuclei in host semiconducting materials offer great potential for incorporation into large-scale devices. Silicon is a particularly attractive host material, in no small part because of its use in the well-developed microchip industry. On page 541 of this issue, Pla *et al.*¹ report the first fully functional electron-spin qubit based on a single phosphorus atom placed in a silicon device*.

*This article and the paper under discussion¹ were published online on 19 September 2012.

In addition to the two allowed states, 0 or 1, of classical bits (for example, the on/off states of transistors in a processor, or the magnetization direction of magnetic domains on a hard disk), a qubit, being quantum mechanical, can also exist in an arbitrary superposition of 0 and 1. Quantum mechanics also allows for non-trivial correlations between the states of multiple qubits, whereby measurement of one qubit alters the states of the others. A reasonably sized quantum machine could leverage the vastly increased number of states offered by superpositions, along with non-classical qubit correlations, to solve certain types of problem much more efficiently than any classical computer.

Many important problems fall into this category, including Peter Shor's famous algorithm² to find a number's prime factors, and the simulation of complex quantum systems. The large-scale implementation of Shor's algorithm would fundamentally alter data encryption, and quantum simulators have the potential to revolutionize physics, chemistry and materials science, and therefore to drive advances in engineering, biology and medicine.

The prototypical qubit is the spin of an elementary particle such as an electron that can point either 'down' (0) or 'up' (1). Even ignoring quantum effects, these two spin states can be used as the logical states for classical information processing — this is the essence of 'spintronics'. But quantum computation also requires full control of superposition

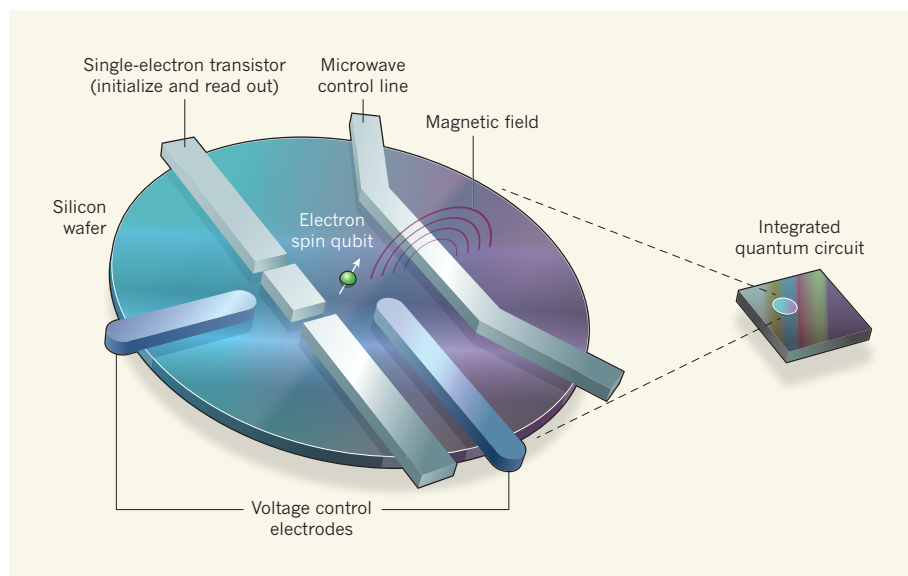


Figure 1 | A spin qubit device. Pla and colleagues have constructed¹ a qubit device that could be incorporated into a future silicon-based integrated quantum circuit. The device's components are all based on standard silicon microfabrication technology. The qubit is the spin of an electron bound to a single phosphorus atom implanted below the surface of a silicon wafer, and is controlled by a set of surface electrodes. A transistor that is sensitive to the charge of a single electron (a 'single-electron transistor') is used to initialize and read out the spin, and a separate microwave control line generates an oscillating magnetic field to coherently control the spin. A set of voltage control electrodes provides electrostatic tuning to turn the readout on or off.

states, including preservation of the relative quantum phase of the up and down spin states. Such 'phase coherence' is extremely fragile, being easily washed away (decohered) by noise from external sources. Qubit implementations therefore seek to balance two inherently contradictory requirements: the ability to engineer strong interactions between qubits and external fields to initialize, manipulate and subsequently read out quantum states; and the ability to switch off those interactions — using 'knobs' such as voltages and currents — so that coherence is preserved during a calculation. Atoms and ions isolated in a vacuum, for example, offer long coherence times but are difficult to scale into large devices, whereas implementations based on semiconductor technology, which seem easier to scale up, typically suffer from higher rates of decoherence.

The qubit constructed by Pla *et al.* effectively combines the advantages of both atomic and solid-state implementations by using the spin of an electron bound to a single phosphorus atom that is implanted in a silicon substrate near a microfabricated transistor (Fig. 1). The architecture, inspired by Bruce Kane's proposal³ more than a decade ago, exploits the remarkable properties of 'shallow donor atoms', such as phosphorus, at low temperatures. Phosphorus is commonly added to silicon to enhance its electrical conductivity for microelectronics, because each phosphorus atom provides an extra electron that is mobile at room temperature. Below liquid-helium temperatures (4.2 kelvin), however, the

electron becomes bound to the atom's nucleus, providing a 'trapped spin' that can be used as a qubit.

Certain intrinsic properties of silicon protect these donor-bound electrons from decoherence, particularly a low density of nuclear spins (95% of natural silicon is the isotope silicon-28, which has no nuclear spin) and weak coupling between the orbital motion of its electrons and their spin. In high-purity silicon samples enriched with the ²⁸Si isotope, electron-spin coherence times of ensembles of phosphorus atoms can exceed 1 second⁴, the longest known of any solid-state electron spin. Most importantly, with modern nanofabrication technology, it is possible to position a single phosphorus atom near control electrodes to form a quantum device.

Initialization and readout of spin states in a system similar to that of Pla and colleagues has already been demonstrated⁵, using a clever technique called spin-to-charge conversion. In this process, the phosphorus atom's electron spin is converted into a difference in the atom's charge state (either ionized or neutral) by arranging that the electron will leave the atom by tunnelling to a nearby nanoscale silicon transistor only if it is in the 'up' state. The same transistor subsequently measures the charge state (and hence also the spin) and resets the qubit in the 'down' state, which serves as the starting point for the next operation. In no small technical feat, Pla *et al.* have now added a microwave control electrode to this single-donor/transistor architecture operating at millikelvin

temperatures. The electrode generates magnetic fields oscillating at a frequency of 30 gigahertz to coherently manipulate the qubit between initialization and readout operations (Fig. 1).

It is encouraging that the coherence time measured in this device, about 200 microseconds, is close to the value of about 300 μ s measured for ensembles of phosphorus donors in silicon samples that have the natural isotopic composition⁶. This suggests that added noise from the electrodes and from the qubit's proximity to impurities on the substrate's surface is not too detrimental. With this device, a typical 'quantum operation' driven by the microwave field lasts about 100 nanoseconds, which means that more than 1,000 operations are possible within the coherence time. With further developments in microwave engineering to increase the strength of the oscillating magnetic field, sub-nanosecond operations are attainable⁷. Moreover, if isotopic purification boosts the coherence time close to the exceptional values of about 1 second measured⁴ for ensembles of isolated phosphorus atoms in ²⁸Si, an unprecedented ratio of about 10⁹ operations per coherence time could be feasible.

By engaging the nuclear spin of phosphorus, even more powerful applications will be possible. Nuclear coherence times can exceed those of electrons by several orders of magnitude, and a fully functional electron-spin qubit should allow quantum control of the coupled nuclear spin, as has been demonstrated for a similar electron–nuclear spin system in diamond⁸. The long-lived nuclear spin could then act as a built-in 'quantum memory node' for each electron-spin qubit.

The crucial next step for silicon-based quantum information technology will be to develop devices that have multiple qubits coupled together, as is required for full-scale quantum computation. The recent demonstration of atomically precise placement of donor atoms⁹ is encouraging, because it would allow two donors to be placed close enough to each other (about 10 nanometres) for exchange interactions to mediate the coherent transfer of quantum information between them. Such precision engineering might also allow the assembly of more elaborate structures, such as chains of donor atoms that could be used as a 'spin bus'¹⁰ to convey quantum information around a large-scale device, perhaps between separated computational devices such as the one demonstrated by Pla and co-workers. If all of these pieces come together, it could be that future 'integrated quantum circuits' do not look so very different — in terms of materials, processing and control electronics — from the classical ones we have been using for the past 50 years. ■

Lee C. Bassett and David D. Awschalom
are at the Center for Spintronics and Quantum

Computation, University of California,
Santa Barbara, Santa Barbara, California
93106, USA.
e-mail: awsch@physics.ucsb.edu

1. Pla, J. J. *et al. Nature* **489**, 541–545 (2012).
2. Shor, P. W. in *Proc. 35th Annu. Symp. Foundations*

- of Computer Science (ed. Goldwasser, S.) 124–134 (IEEE Comput. Soc., 1994).
3. Kane, B. E. *Nature* **393**, 133–137 (1998).
 4. Tyryshkin, A. M. *et al. Nature Mater.* **11**, 143–147 (2012).
 5. Morello, A. *et al. Nature* **467**, 687–691 (2010).
 6. Tyryshkin, A. M. *et al. J. Phys. Condens. Matter* **18**, S783–S794 (2006).

7. Fuchs, G. D., Dobrovitski, V. V., Toyli, D. M., Heremans, F. J. & Awschalom, D. D. *Science* **326**, 1520–1522 (2009).
8. Robledo, L. *et al. Nature* **477**, 574–578 (2011).
9. Fuechsle, M. *et al. Nature Nanotechnol.* **7**, 242–246 (2012).
10. Hollenberg, L. C. L., Greentree, A. D., Fowler, A. G. & Wellard, C. J. *Phys. Rev. B* **74**, 045311 (2006).

NETWORK SCIENCE

Luck or reason

The concept of preferential attachment is behind the hubs and power laws seen in many networks. New results fuel an old debate about its origin, and beg the question of whether it is based on randomness or optimization. **SEE LETTER P.537**

ALBERT-LÁSZLÓ BARABÁSI

Often a field's most profuse concept is also its most mysterious. Think wave-functions in quantum mechanics, dark energy in astrophysics and non-coding DNA in genomics. Network science has its own: preferential attachment, which states that the more connected a network node is, the more links it will acquire in the future. The impact of preferential attachment is hard to miss — the principle is responsible for the omnipresent network hubs, from Facebook and Google on the World Wide Web to protein p53, the 'cancer hub', in human cells. However, its origins remain a source of constant wonder and speculation. The latest attempt to shed light on its roots is presented by Papadopoulos *et al.*¹ on page 537 of this issue*.

Preferential attachment made its first appearance in 1923 in the celebrated urn model of the Hungarian mathematician György Pólya², and it has reappeared repeatedly over the past century, particularly in the social sciences. Although Robert Merton named it the Matthew effect³ in 1968 after the Gospel of Matthew, "For everyone who has will be given more, and he will have an abundance", its current usage emerged only in 1999, with the discovery that it accounts for the power-law distributions observed in several real networks⁴.

A new node joining a network, such as a new web page or a new protein, can in principle connect to any pre-existing node. However, preferential attachment dictates that its choice will not be entirely random, but linearly biased by the degree of the pre-existing nodes — that is, the number of links that the nodes have with other nodes. This induces a rich-get-richer effect, allowing the more-connected nodes to gain more links at the expense of their less-connected counterparts. Hence, the large-degree nodes turn into hubs

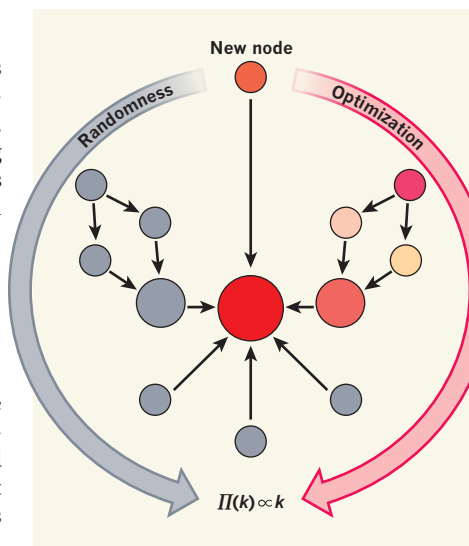


Figure 1 | Randomness or optimization? Two families of models could explain the origin of preferential attachment in networks, according to which the probability $\Pi(k)$ that a new node links to a pre-existing node that has degree k (the number of links that the node has with other nodes) is proportional to k . One family of models, to which the model introduced by Papadopoulos *et al.*¹ belongs, assumes that preferential attachment is rooted in an optimization framework (right side). In these models, a new node will connect to the node that is most similar to it (most similar colour) but also has the largest degree. The central node offers the best balance between these two options. The other family of models relies on randomness (left side). In this case, the new node is colour-blind, so it randomly selects a link and connects to its target. Once again, the central node, which has the most links pointing to it, has the highest chance of being selected.

and the network becomes scale-free — the probability distribution of the degrees over the entire network follows a power law. This is a frail set-up, as any nonlinearity in preferential attachment will either eliminate the hubs or generate super-hubs, leading to the loss of

the scale-free property⁵. However, in every system in which it has been possible to measure preferential attachment, a linear form has been detected^{6,7}.

The centuries-old proverb 'birds of a feather flock together' captures the idea that humans tend to hang out with those who are similar to them. Sociologists call this homophily, and it is perhaps one of the best documented concepts in the social sciences. Papadopoulos *et al.*¹ propose that homophily might also contribute to preferential attachment. They introduce a model in which each node is assigned a randomly chosen position along a circle that serves as a 'homophily space': the closer two nodes are to each other on the circle (that is, the smaller the angle θ spanned by the nodes when measured from the circle's centre), the more similar they are (see Fig. 1 of the paper¹). The network expands through the addition of new nodes, such that a node added at time $t = 1, 2, \dots$ will choose to connect to a pre-existing node added at time s only if node s offers the smallest of all possible products $s\theta_{st}$, where θ_{st} is the angular distance between nodes s and t . Hence the new node optimizes its choice between two often conflicting interests: the node it will link to should be the most connected (the oldest, with the smallest s) and the most similar to it (the smallest θ_{st}).

Interestingly, by placing each node at distance $r_t = \ln t$ from the centre of the homophily circle, the authors find that the network evolves not on the circle but in a hyperbolic space, a geometrical space that is familiar mainly to those well versed in cosmology and general relativity. In this space, strange things can happen, such as parallel lines meeting each other and triangles that have zero-degree angles. Yet the model has its simplest interpretation in this peculiar space, where new nodes simply connect to the nodes closest to them. The authors show that the resulting network is scale-free and that a linear preferential attachment is the model's emerging feature.

The new model fuels a slowly evolving debate — is preferential attachment rooted in pure chance or in some form of optimization? Indeed, the most accepted mechanisms of preferential attachment rely on dumb luck. The simplest one is this: first randomly select a link in a directed network, for example the links of the World Wide Web that point to a document; then connect the new node to the selected link's target⁸. The more connected

*This article and the paper under discussion¹ were published online on 12 September 2012.

nodes have an advantage here, as the chance that a new node connects to them is proportional to their degree. Variants of this simple mechanism lie behind the popular copying model proposed to explain the scale-free nature of the web⁹ and the emergence of hubs in protein-interaction networks through gene duplication^{10,11}. According to these mechanisms, preferential attachment does not require human agency, but is rather a consequence of purely random actions. By contrast, Papadopoulos and colleagues' model calls for clear agency, as each new node seeks to link to the closest and oldest node. In this respect, the model supports earlier mechanisms, developed in the context of the Internet^{12,13}, proposing that preferential attachment is rooted in a wish to balance distance to the target node with some utility, such as access to bandwidth.

Both approaches are tempting. Random models ask little of us, and demonstrate how random actions can result in outcomes that are not so random. Yet we do not think that the choices we make are ever random, fuelling the attractiveness of models that invoke some form of optimization.

This tension between two equally attractive but apparently opposing alternatives is

by no means new. In the 1960s, the economist Herbert Simon and the mathematician Benoît Mandelbrot fought a fierce public dispute, with Simon defending the role of randomness and preferential attachment in explaining the power-law distribution of word frequencies in text, and Mandelbrot arguing for an optimization framework¹⁴. In the past decade, experimental evidence for preferential attachment in the context of networks has tilted the argument in Simon's favour. And now the debate is shifting to a deeper question — whether preferential attachment is the outcome of random actions or optimization (Fig. 1).

This debate helps us to understand how preferential attachment emerges in an identical form in such widely different systems. The fact that the effect is widespread suggests that it probably derives from both agency and random actions. Most complex systems have a bit of both, so we do not need to choose between them. Luck or reason, preferential attachment wins either way. And so do we, gaining a deeper understanding of this puzzling yet ubiquitous force. ■

Albert-László Barabási is at the Center for Complex Network Research, Northeastern

University and in the Department of Medicine, Harvard Medical School, Boston, Massachusetts 02115, USA.
e-mail: barabasi@gmail.com

1. Papadopoulos, F., Kitsak, M., Serrano, M. A., Boguñá, M. & Krioukov, D. *Nature* **489**, 537–540 (2012).
2. Eggenberger, F. & Pólya, G. *J. Appl. Math. Mech. (ZAMM)* **3**, 279–289 (1923).
3. Merton, R. K. *Science* **159**, 56–63 (1968).
4. Barabási, A.-L. & Albert, R. *Science* **286**, 509–512 (1999).
5. Krapivsky, P. L., Redner, S. & Leyvraz, F. *Phys. Rev. Lett.* **85**, 4629–4632 (2000).
6. Jeong, H., Neda, Z. & Barabási, A.-L. *Europhys. Lett.* **61**, 567–572 (2003).
7. Newman, M. E. J. *Phys. Rev. E* **64**, 025102(R) (2001).
8. Dorogovtsev, S. N., Mendes, J. F. F. & Samukhin, A. N. *Phys. Rev. Lett.* **85**, 4633–4636 (2000).
9. Kumar, R. *et al.* in *Proc. 19th Symp. Princ. Database Syst.* (eds Vianu, V. & Gottlob, G.) 1–10 (ACM, 2000).
10. Pastor-Satorras, R., Smith, E. & Solé, R. V. *J. Theor. Biol.* **222**, 199–210 (2003).
11. Vazquez, A., Flammini, A., Maritan, A. & Vespignani, A. *ComplexUs* **1**, 38–44 (2003).
12. D'Souza, R. M., Borgs, C., Chayes, J. T., Berger, N. & Kleinberg, R. D. *Proc. Natl Acad. Sci. USA* **104**, 6112–6117 (2007).
13. Fabrikant, A., Koutsoupias, E. & Papadimitriou, C. in *Proc. 29th Int. Colloq. Automata, Languages and Programming* (eds Widmayer, P. *et al.*) 110–122 (Springer, 2002).
14. Kornai, A. *Mathematical Linguistics* 71 (Springer, 2008).

response. Skin consists of an outer epidermal layer and an inner dermal layer. Seifert *et al.* report that the animals regrew skin with hair within 30 days of damage, and that the epidermis re-formed more rapidly in *Acomys* species than in *M. musculus*. Furthermore, they found that less underlying wound-bed tissue (which is associated with scarring) formed in *Acomys*, and that this tissue was composed predominantly of the extracellular matrix (ECM) molecule collagen III, rather than of aligned fibrils of collagen I, which is characteristic of scar formation in mammals. Finally, the authors observed that the healing epidermal cells of *Acomys* formed new hair follicles, and that the signalling pathways involved in follicle formation resembled those used during embryonic hair development.

In skin healing in other mammals, *de novo* hair-follicle formation is considered difficult to achieve — although not unheard of. Hair-follicle regeneration has been seen in large wounds made in rabbits and in *M. musculus*^{5,6}. In these conditions, epidermal cells 'crawl' over the open wound to form a new epidermal layer that contains many hair follicles. Interestingly, these new hairs remain unpigmented, whereas it can be seen in Seifert and colleagues' paper that the new *Acomys* hairs are the usual colour.

Taken together, these results indicate that the epidermal cells that cover wounded tissue during healing can establish interactions with the underlying cells that promote hair-follicle formation. Cross-talk between the epidermis and underlying mesenchymal cells is known

REGENERATIVE BIOLOGY

Skin, heal thyself

Simply grabbing an African spiny mouse can cause it to lose up to 60% of the skin on its back. Analysis of the mouse's astounding shedding and healing capacity provides insight into the biomechanics of tissue regeneration. SEE LETTER P.561

ELLY M. TANAKA

Most people know that lizards can elude predators by jettisoning their tail, a process called autotomy. The tail musculature and bone organization of these reptiles allow breakage at defined planes when the need arises¹ and, after healing, the tail is restored as an imperfect but functional replica of the original². By contrast, only owners of exotic pets may have witnessed the escapades of the African spiny mouse (genus *Acomys*), which shimmies away by losing its tail skin. On page 561 of this issue, Seifert *et al.*³ reveal that the skin shedding and regeneration observed in the tail extend to other parts of the mouse's body, paving the way for detailed studies of the molecular and structural basis of this fascinating — and potentially therapeutically useful — ability.

Previous analysis⁴ showed that the tail skin of spiny mice is more loosely attached to the underlying muscle and bone than the tail skin of other rodents such as the common house mouse (*Mus musculus*), a feature that

probably facilitates its shedding in *Acomys*. To assess further the skin properties of spiny mice, Seifert and colleagues examined wild-caught specimens of two species, *Acomys kempfi* and *Acomys percivali*. Even as the researchers collected them, they noticed that the animals lost up to 60% of the skin on their back when they were grabbed by hand in a normal manner (see Fig. 1c of the paper³).

When the researchers put *Acomys* skin under defined loads, they found it to be very brittle: it had a 20-fold lower tensile strength than skin from *M. musculus*, and 77-fold less energy was required to elicit skin tearing. The authors observed no predefined breakage-point structures in *Acomys* skin, suggesting that an overall fragility accounts for the ease in shedding. It is not yet clear what molecular or biomechanical properties underlie this fragility, although Seifert *et al.* point out that the hair follicles are larger and take up a greater proportion of the skin's surface in *Acomys* than in *Mus* species, which might have some effect.

Perhaps even more impressive than the shedding ability of *Acomys* is their healing

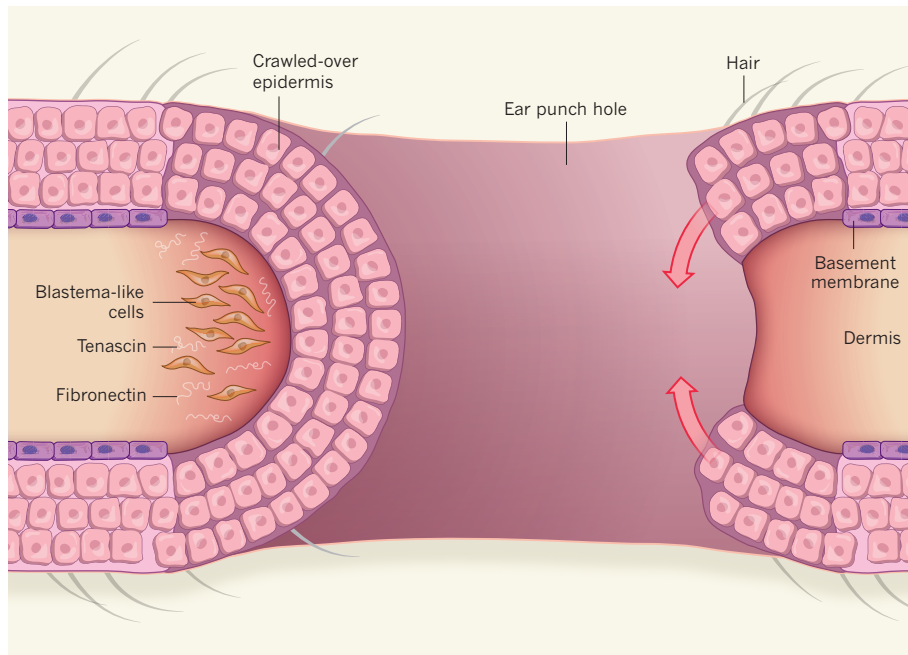


Figure 1 | Wound repair in African spiny mice. Seifert *et al.*³ studied tissue regeneration in *Acomys* mice after a hole 4 millimetres in diameter was punched in the ear. They show that the holes were filled in by regeneration of cartilage, adipose tissue and skin, which included the dermal and epidermal layers and contained hair follicles. The process involved rapid re-formation of the skin's outer layer by crawling epidermal cells. Underneath this layer, proliferation of mesenchymal cells led to the formation of a cell mass (which also contained the proteins fibronectin and tenascin) that looks similar to the blastema formed during limb regeneration in salamanders, which is known to promote regeneration of structures such as bone and nervous tissue⁹. During this process, the basement-membrane layer of the extracellular matrix that usually separates the dermis from the epidermis was absent.

to be crucial for embryonic hair-follicle development (for a review, see ref. 7). It seems that this cross-talk can still occur in adult mammalian skin during wound healing, but that in many mammalian species the initiation of epidermal crawling is slow to occur. By contrast, *Acomys* wound healing seems to be characterized by rapid re-epithelialization (during development and wound healing, the cells that will form the epidermis are called the epithelium) and hair-follicle regeneration. It is worth noting that extremely rapid re-epithelialization is also a hallmark of limb and tail regeneration in amphibians such as frogs and salamanders⁸.

Finally, Seifert and colleagues further tested the regenerative capacity of *Acomys* tissue by assessing the response of the animals' ear tissue to having a hole punched through it. They found that the holes were filled in by cartilage, adipose, dermal and epidermal structures, although not by muscle. In fact, the regeneration process was, in many ways, similar to that of complete limb regeneration in salamanders. In these amphibians, the stump of an amputated limb is rapidly covered by a layer of non-proliferating epidermal cells. Proliferation of mesenchymal progenitor cells in the underlying tissues then produces a cell mass called the blastema⁹. Communication between the epidermal layer and the blastema promotes the regeneration of bones, peripheral nerves and

muscles¹⁰. During this process, the basement-membrane layer of the ECM that normally separates the epidermis from the dermis is absent, and the blastema cells are surrounded by the ECM molecules fibronectin, hyaluronic acid and tenascin^{11–15}.

Seifert *et al.* report that *Acomys* ear-tissue regeneration closely resembles this process: there was rapid formation of a non-proliferative epidermal layer accompanied by mesenchymal cell proliferation; no basement membrane was established between the wound epidermis and the mesenchymal layer; and the mesenchymal tissue was rich in fibronectin, tenascin and collagen III (Fig. 1). By contrast, when the authors assessed the ear-punch response in *M. musculus* (ear holes do not regenerate in these mice), the authors observed only initial, but not persistent, mesenchymal cell proliferation. Furthermore, the *M. musculus* mesenchymal cells expressed the smooth-muscle protein actin, which is characteristic of cells laying down fibrils of collagen I that contribute to scar tissue. The authors observed only weak actin expression in *Acomys*.

Although ear-punch regeneration has been described previously in rabbits, some strains of mice and other mammals^{16–18}, Seifert and colleagues' analysis of this response in spiny mice confirms that rapid re-epithelialization and a distinct profile of ECM deposition correlate with successful tissue regeneration

in mammals. These studies suggest that the pathways leading to regeneration, at least of the skin, that are normally associated with amphibians are also accessible in mammals. Unlocking this cascade in a controlled manner in other wound situations may help to promote scarless healing. However, one aspect that the authors did not address in these studies is whether alteration of the immune response, which has been proposed to contribute to scar-free healing and successful regeneration, is another feature of *Acomys*'s impressive regenerative abilities^{19,20}. How an animal can lose 60% of its back skin and yet survive both microbial attack and tissue desiccation will be another intriguing aspect for future studies. ■

Elly M. Tanaka is at the DFG Center for Regenerative Therapies, Technische Universität Dresden, 01309 Dresden, Germany.

e-mail: elly.tanaka@crt-dresden.de

1. Pratt, C. W. *J. Anat.* **80**, 184–188 (1946).
2. Simpson, S. B. *Jr Am. Zool.* **10**, 157–165 (1970).
3. Seifert, A. W. *et al. Nature* **489**, 561–565 (2012).
4. Shargal, E., Rath-Wolfson, L., Kronfeld, N. & Dayan, T. *J. Zool.* **249**, 187–193 (1999).
5. Breedis, C. *Cancer Res.* **14**, 575–579 (1954).
6. Ito, M. *et al. Nature* **447**, 316–320 (2007).
7. Schneider, M. R., Schmidt-Ullrich, R. & Paus, R. *Curr. Biol.* **19**, R132–R142 (2009).
8. Repesh, L. A. & Oberpriller, J. C. *Am. J. Anat.* **159**, 187–208 (1980).
9. Hay, E. D. & Fischman, D. A. *Dev. Biol.* **3**, 26–59 (1961).

10. Tassava, R. A. & Garling, D. J. *J. Exp. Zool.* **208**, 97–109 (1979).
11. Gulati, A. K., Zalewski, A. A. & Reddi, A. H. *Dev. Biol.* **96**, 355–365 (1983).
12. Christensen, R. N. & Tassava, R. A. *Dev. Dyn.* **217**, 216–224 (2000).
13. Nace, J. D. & Tassava, R. A. *Dev. Dyn.* **202**, 153–164 (1995).
14. Onda, H., Poulin, M. L., Tassava, R. A. & Chiu, I. M. *Dev. Biol.* **148**, 219–232 (1991).
15. Calve, S., Odelberg, S. J. & Simon, H. G. *Dev. Biol.* **344**, 259–271 (2010).
16. Heber-Katz, E. *Semin. Cell Dev. Biol.* **10**, 415–419 (1999).
17. Bedelbaeva, K. *et al. Proc. Natl Acad. Sci. USA* **107**, 5845–5850 (2010).
18. Williams-Boyce, P. K. & Daniel, J. C. *Jr J. Anat.* **149**, 55–63 (1986).
19. Martin, P. *et al. Curr. Biol.* **13**, 1122–1128 (2003).
20. Harty, M., Neff, A. W., King, M. W. & Mescher, A. L. *Dev. Dyn.* **226**, 268–279 (2003).

ELECTRONICS

‘Cut and stick’ ion gels

Ion gels are composites of ionic liquids and polymers. Free-standing forms of ion gels have now been made that can be neatly cut with a razor blade and stuck onto semiconductor materials to make transistors.

MASASHI KAWASAKI & YOSHIHIRO IWASA

Mobile phones cannot function without the battery and the billions of tiny electronic switches (transistors) that they contain. The transistors control the flow of electrons in semiconductors to allow the processing and storage of information, whereas the battery stores electrochemical

energy to power the transistors. The first transistor was invented in 1947 by William Shockley, John Bardeen and Walter Brattain. Interestingly, the initial experiments that led to the realization of the device used a liquid electrolyte — a mixture of a liquid solvent and ions — to control the electron transport in a semiconductor. In other words, the first true transistor was not an all-solid-state

device but an electrochemical one¹.

Because of the enormous success of solid-state electronics, this early history of transistors and the usefulness of liquid electrolytes in electronic devices have been somewhat forgotten. In the past decade, however, transistors based on electrolytes and electrochemical concepts have been receiving renewed attention, because they offer functionalities beyond those of conventional, all-solid-state transistors. Writing in *Advanced Materials*, Lee *et al.*² report a rubber-like material that is made from an ionic liquid (a salt that exists in the liquid state at room temperature) and a polymer and which can be ‘cut and stuck’ onto semiconductors to make a transistor.

Electrolytes are ionically conducting but electronically insulating substances. When an electrolyte is placed on an electronically conducting solid, an electrical double layer (EDL) is formed at the interface, an effect that was first modelled by Helmholtz³ in 1853. Owing to the nanoscale gap between its two charged layers, the EDL has a huge capacitance (ability to store charge) — of the order of 1–10 microfarads per square centimetre ($\mu\text{F cm}^{-2}$). This value is 10–1,000 times greater than that of conventional electrical capacitors, which are based on solid insulators.

By using an EDL in place of a solid insulator, which is typically made of silicon dioxide or aluminium oxide, researchers have made transistors that show surprising and potentially useful effects, including electric-field-induced phase transitions such as insulator-to-metal transitions⁴, superconductivity⁵ and ferromagnetism⁶. In most cases, ionic liquids were used because they have high ionic conductivity and yield a large EDL capacitance. However, for electronic devices, materials that have mechanical and structural integrity are often required.

But in the twenty-first century, we no longer have to rely solely on solid-state materials to attain such integrity. Ion gels — a mixture of ionic liquids and macromolecular components — offer an alternative. They combine

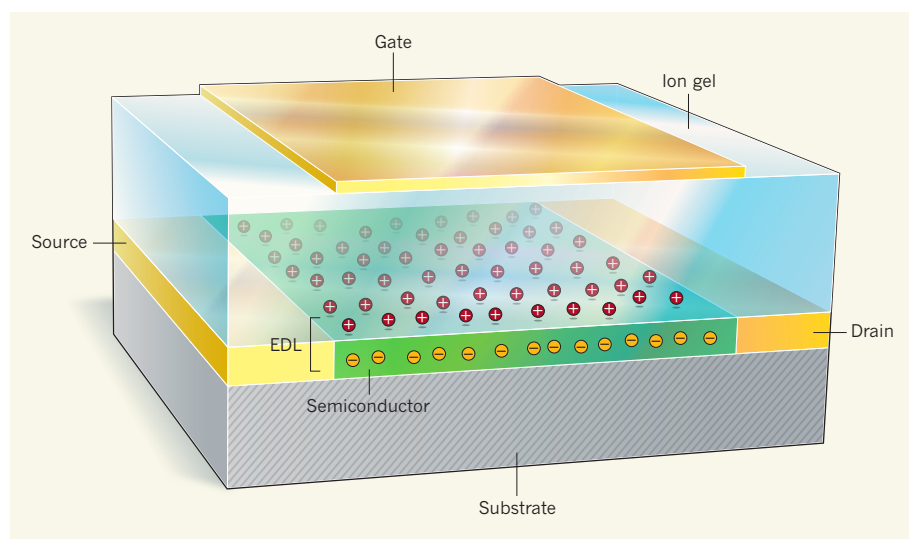


Figure 1 | An ion-gel transistor. Lee and colleagues² have made a free-standing ion gel that can be placed on a semiconductor to make a transistor. The ion gel serves as the device's gate insulator, separating the gate electrode from the semiconductor that forms the channel between the source and drain electrodes and which is laid on a substrate. When the device is switched on, an electrical double layer (EDL) of charges forms at the interface between the ion gel and the semiconductor, giving the device a large electrical capacitance.

the advantages of ionic liquids and solid insulators, including manipulation at room temperature⁷. Lee *et al.*² now demonstrate free-standing, rubber-like ion gels that can be cut with a razor blade and stuck onto several semiconductor materials to produce a transistor. Their approach therefore offers a neat way of making transistors.

The macromolecular components of ion gels are block copolymers — polymers in which two or more chemically distinct monomer units are linked together. In their experiments, Lee *et al.* made free-standing 0.6-millimetre-thick films of ion gels by using a weight ratio of block copolymer to ionic liquid of 1:4. The capacitance of the EDL that formed at the interface between the semiconductor and the ion gel was as high as 10 $\mu\text{F cm}^{-2}$. Similar free-standing ion-gel films have been used as solid electrolytes in lithium-ion batteries. But Lee *et al.* used such films as gate insulators in transistors; gate insulators separate the transistor's semiconducting channel from its gate electrode (Fig. 1). What's more, the authors demonstrated transistors made from both typical organic and inorganic semiconductors; these showed current based on 'holes' (notional particles formed by the absence of electrons) and electrons, respectively. This method can thus be applied to any type of semiconducting material.

Because ion gels can be made in many forms (there are large numbers of ionic liquids and polymers), they could be used to obtain diverse novel device structures and functionalities⁷. For instance, printing of ion gels on substrates has already been demonstrated⁸. Finally, combinations of ion gels and a variety of electronic conductors — not only semiconductors but also metals, superconductors and magnets — will make 'iontronics'⁹, electronics based on ionic functions, a rich field of materials science. ■

Masashi Kawasaki and Yoshihiro Iwasa are at the *Quantum Phase Electronics Research Center and in the Department of Applied Physics, University of Tokyo, Tokyo 113-8656, Japan, and at the RIKEN-Advanced Science Institute, Wako, Japan.*
e-mail: kawasaki@ap.t.u-tokyo.ac.jp

1. Brattain, W. H. & Gibney, R. B. US patent 2,524,034 (1948).
2. Lee, K. H. *et al. Adv. Mater.* **24**, 4457–4462 (2012).
3. von Helmholtz, H. *Pogg. Ann.* **LXXXIX**, 211 (1853).
4. Nakano, M. *et al. Nature* **487**, 459–462 (2012).
5. Ueno, K. *et al. Nature Mater.* **7**, 855–858 (2008).
6. Yamada, Y. *et al. Science* **332**, 1065–1067 (2011).
7. Lodge, T. P. *Science* **321**, 50–51 (2008).
8. Cho, J. H. *et al. Nature Mater.* **7**, 900–906 (2008).
9. Leger, J., Berggren, M. & Carter, S. *Iontronics: Ionic Carriers in Organic Electronic Materials and Devices* (CRC, 2010).

CANCER METABOLISM

When more is less

A tightly regulated enzyme balances energy production and the synthesis of macromolecules from glucose in cancer cells. Upsetting this balance by stimulating the enzyme's activity can suppress tumour growth in mice.

LEI JIANG & RALPH J. DEBERARDINIS

The development of cancer is associated with a suite of metabolic changes that support the energetic and biosynthetic requirements of tumour-cell proliferation. Many of these changes are stimulated by the same genetic mutations that drive tumorigenesis, suggesting that normalizing the tumour cells' metabolism by pharmacological means could suppress cancer progression. An enhancement of glycolysis, a cellular pathway that produces both energy and precursors of macromolecules, is a classic metabolic hallmark of cancer, making the glycolytic pathway an attractive target in which to test this hypothesis. Writing in *Nature Chemical Biology*, Anastasiou *et al.*¹ show that targeting a form of the enzyme pyruvate kinase that is commonly found in tumour cells can redistribute the fate of glucose-derived metabolites away from biosynthetic pathways, and suppress tumour growth in mice.

The ability of the glycolytic pathway to produce ATP — the main cellular energy-transfer molecule — is largely dependent on the activity of pyruvate kinases. There are various mammalian forms of pyruvate kinase, and tumour cells typically express the M2 isoform (PKM2), which shows reduced enzyme activity compared with other pyruvate kinases. This was initially thought to be somewhat paradoxical in cancer cells, in which abundant expression of glucose transporters and glycolytic enzymes conspires to enhance overall glycolysis. But one advantage of a bottleneck at the end of an otherwise active pathway is to force some of the intermediates it produces to accumulate, analogous to a partially closed valve at the bottom of a column of fluid (Fig. 1). It is now thought that the aggregation of metabolites behind this valve may promote their transfer into accessory pathways, including those that generate macromolecular building blocks and other substrates needed for cellular replication².



50 Years Ago

The third annual scientific meeting of the British Academy of Forensic Sciences ... was called to consider "The Hazards of the Road", a subject to which, having regard to the increasing public danger deriving from motor traffic, the sciences appear to have devoted disproportionately little research ... [P]sychological tests on those involved in accidents ... tended to show personality traits such as aggressiveness, carelessness, impulsiveness and the like which are not present to the same degree in those persons who have been free from accidents ... Older people tend to make up for their longer reaction times by driving more slowly ... Although as a man grows older, into middle age or further, his reaction time is slowed, his eyesight is not quite what it used to be and his hearing is impaired, he nevertheless becomes a better driver.

From *Nature* 29 September 1962

100 Years Ago

When nature was fashioning man the forces of natural selection made one hand more apt to perform skilled movements than the other. Why precisely it was the right hand that was chosen in the majority of mankind we do not know ... The fact that a certain proportion of mankind is left-handed, and that such a tendency is transmitted to only some of the descendants of a left-handed person, might perhaps suggest that one half of mankind was originally left-handed and the other right-handed, and that the former condition was recessive in the Mendelian sense ... The superiority of one hand is as old as mankind, and is one of the factors incidental to the evolution of man.

From *Nature* 26 September 1912

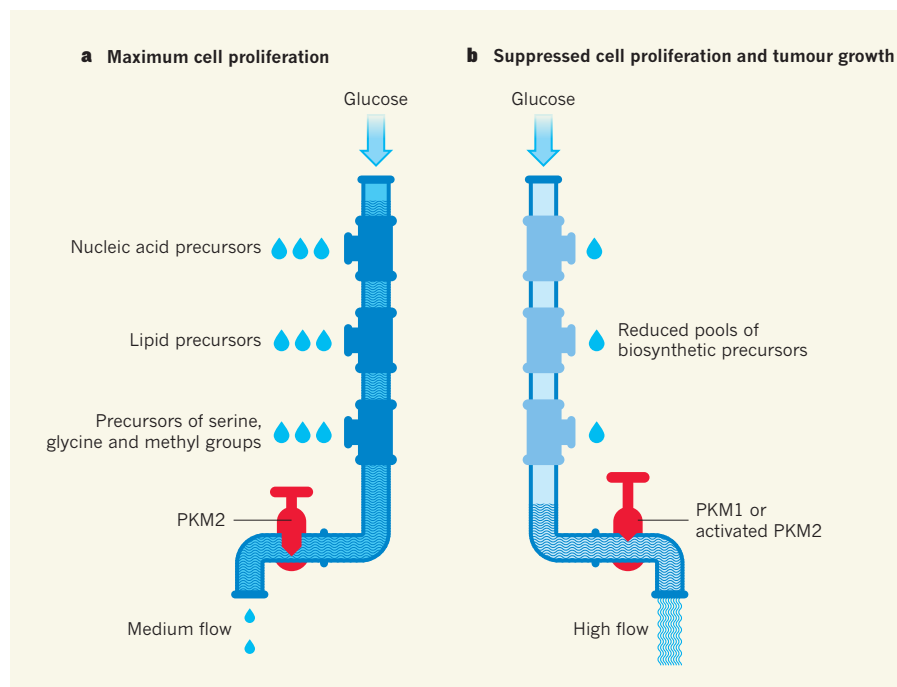


Figure 1 | A metabolic bottleneck. During glucose metabolism (glycolysis), the enzyme pyruvate kinase acts as a 'tap' that regulates the rate of flow out of the pathway. **a**, Cancer cells often express the M2 form of the enzyme (PKM2), which has lower enzymatic activity than other isoforms of pyruvate kinase. This, combined with the robust glycolysis that is also a hallmark of cancer cells, leads to an accumulation of glycolytic intermediates, including precursors of nucleic acids, lipids, serine, glycine and methyl groups. The accumulation in turn stimulates the biosynthetic pathways into which these intermediates feed, thereby contributing to the rapid cell proliferation seen in tumours. **b**, By contrast, enhancing pyruvate kinase activity by replacing PKM2 with the more active PKM1 isoform causes a decline in these pools of biosynthetic precursors and reduced cell proliferation³. Anastasiou *et al.*¹ show that a similar tumour-suppressive effect can be achieved using small molecules that enhance PKM2 activity.

This explanation for the role of PKM2 in cancer gained momentum when it was demonstrated that replacing PKM2 in cancer cells with the more active PKM1 isoform resulted in higher overall activity of pyruvate kinase but reduced macromolecular synthesis and tumour growth in mice³. Further support came from studies showing that many of the processes that regulate PKM2 in cancer cells, such as binding of the enzyme by tyrosine-phosphorylated proteins, act to reduce rather than stimulate its enzymatic activity^{4,5}.

A possible implication of this picture of cancer-cell glycolysis is that stimulating PKM2 activity — in effect, opening the floodgates — might impair tumour growth by reducing the availability of macromolecular precursors. Anastasiou *et al.* tested this idea by using small molecules that clamp the enzyme into a highly active tetramer configuration (a complex containing four subunits of the enzyme), and then analysing tumour-cell glycolysis. They found that cellular pools of glucose-dependent biosynthetic intermediates became depleted, and that flux through the pathways supplied by them was suppressed. Treatment with the PKM2 activator molecules also reduced the proliferation of cancer cells subjected to low oxygen levels, a condition that favours glycolysis. Finally, when the authors treated

tumour-bearing mice by oral administration of PKM2 activators, they found suppressed levels of biosynthetic intermediates in the tumours, and substantially slower tumour growth. Importantly, the small molecules also rendered PKM2 insensitive to blockade by tyrosine-phosphorylated proteins, suggesting that the agents might provide durable metabolic effects even in tumours that are programmed to reduce the activity of pyruvate kinases.

These studies of PKM2 activation provide a foundation for broader investigations of metabolism and cancer biology. Anastasiou and colleagues' results indicate that PKM2 affects biosynthesis in more subtle ways than those shown in Figure 1. For example, they found that activating PKM2 reduces the flux from glucose metabolism to fatty-acid synthesis, a pathway typically thought to involve the formation of pyruvate (a glycolytic intermediate molecule) by pyruvate kinases. Together, these new data imply that submaximal PKM2 activity helps to channel metabolites into biosynthetic pathways through mechanisms that do not simply involve an accumulation of intermediates, but that are not yet fully understood. It will be interesting to test whether modulating glycolysis through PKM2 activation or other mechanisms can be extended to suppress the proliferation

of cells under conditions of normal oxygen levels, because such suppression would also be desirable in fast-growing areas of tumours that are well perfused by oxygen.

The push to understand PKM2 function, and now to manipulate it to suppress tumour growth, emphasizes a shift in focus in cancer metabolism research. Since Otto Warburg's early experiments on tumour glycolysis in the 1920s, work in this field has largely centred on how tumours produce energy. But recent studies have taken a much broader view of the metabolic network in cancer cells, leading to a greater appreciation of the complexities of biosynthesis, reduction-oxidation homeostasis and other facets of metabolism that support cell survival and proliferation. These investigations have uncovered many unexpected roles for metabolism in cell signalling and the regulation of gene expression, extending the reach of metabolic enzymes into essentially every area of cell biology⁶. These newly identified functions are highly relevant to cancer. Consider, for example, that PKM2 also acts as an activator of gene expression, such that it has proliferation-promoting activities that are independent of its enzymatic function⁷.

Finally, Anastasiou *et al.* have illustrated an important concept in the metabolic control of tumorigenesis. They show that activating PKM2 suppresses cell proliferation — but severely inhibiting this enzyme is known to have similar effects, and can induce tumour regression in mice^{8,9}. It is likely that the highest rates of cell proliferation are the result of a metabolic network in which a set of enzymes that, like PKM2, contribute to biosynthesis are precisely controlled, but whose maximal activation is counterproductive. These nodes may be the most easily disrupted control points in the metabolic network, and identifying them should offer the best opportunities for metabolic therapy in cancer. ■

Lei Jiang and Ralph J. DeBerardinis are at the Children's Medical Center Research Institute, University of Texas Southwestern Medical Center, Dallas, Texas 75390-8502, USA.

e-mail: ralph.deberardinis@utsouthwestern.edu

1. Anastasiou, D. *et al.* *Nature Chem. Biol.* **8**, 839–847 (2012).
2. Mazurek, S., Boschek, C. B. & Eigenbrodt, E. *J. Bioenerg. Biomembr.* **29**, 315–330 (1997).
3. Christofk, H. R. *et al.* *Nature* **452**, 230–233 (2008).
4. Christofk, H. R., Vander Heiden, M. G., Wu, N., Asara, J. M. & Cantley, L. C. *Nature* **452**, 181–186 (2008).
5. Hitosugi, T. *et al.* *Sci. Signal.* **2**, ra73 (2009).
6. Lu, C. & Thompson, C. B. *Cell Metab.* **16**, 9–17 (2012).
7. Luo, W. *et al.* *Cell* **145**, 732–744 (2011).
8. Vander Heiden, M. G. *et al.* *Biochem. Pharmacol.* **79**, 1118–1124 (2010).
9. Goldberg, M. S. & Sharp, P. A. *J. Exp. Med.* **209**, 217–224 (2012).

The authors declare competing financial interests.
See go.nature.com/e69jt8 for details.

Genomic analysis of a key innovation in an experimental *Escherichia coli* population

Zachary D. Blount^{1,2}, Jeffrey E. Barrick^{2,3,4}, Carla J. Davidson⁵ & Richard E. Lenski^{1,2}

Evolutionary novelties have been important in the history of life, but their origins are usually difficult to examine in detail. We previously described the evolution of a novel trait, aerobic citrate utilization (Cit⁺), in an experimental population of *Escherichia coli*. Here we analyse genome sequences to investigate the history and genetic basis of this trait. At least three distinct clades coexisted for more than 10,000 generations before its emergence. The Cit⁺ trait originated in one clade by a tandem duplication that captured an aerobically expressed promoter for the expression of a previously silent citrate transporter. The clades varied in their propensity to evolve this novel trait, although genotypes able to do so existed in all three clades, implying that multiple potentiating mutations arose during the population's history. Our findings illustrate the importance of promoter capture and altered gene regulation in mediating the exaptation events that often underlie evolutionary innovations.

Evolutionary novelties are qualitatively new traits that open up ecological opportunities and thereby promote diversification^{1,2}. These traits are thought to arise typically by the exaptation of genes that previously encoded other functions^{2–6} through processes such as domain shuffling⁷, altered regulation⁸ and duplication followed by neo-functionalization^{9,10}. Multiple mutations may be necessary to produce the new function^{9,11}, and thus its potential to evolve may be contingent on subtle differences between species, populations or even genotypes. A complete understanding of the evolution of a novel trait requires explanation of its ecological function, its physiological basis, the underlying mutations and the history of the accumulated changes².

Evolution experiments with microorganisms offer unparalleled opportunities to assess the evolution of novel traits^{12–15}. Microbes have rapid generations and large populations, and new technologies allow discovery of mutations throughout their genomes^{16–19}. Samples can be frozen and revived, allowing phylogenies and mutational histories to be constructed and analysed^{18,19}.

Twelve populations of *Escherichia coli* have been propagated in the long-term evolution experiment (LTEE) for over 40,000 generations in a glucose-limited minimal medium¹³. The medium also contains abundant citrate, which is present as a chelating agent²⁰, but *E. coli* cannot exploit citrate as a carbon and energy source in the well-aerated conditions of the experiment^{21,22}. The inability to grow aerobically on citrate is a long-recognized trait that, in part, defines *E. coli* as a species²³. Spontaneous citrate-using (Cit⁺) mutants are extraordinarily rare²⁴, but a Cit⁺ variant evolved in one population (designated Ara-3) around 31,000 generations²⁰. Cit⁺ cells became dominant after 33,000 generations, although Cit[−] cells persisted. This shift was accompanied by a several-fold increase in total population size owing to the high concentration of citrate relative to glucose in the medium.

The emergence of the Cit⁺ trait was contingent upon one or more earlier mutations in the population's history. When evolution was replayed from clones isolated at various time points, clones from later generations were more likely to produce Cit⁺ mutants than did the ancestor and other early clones²⁰. This finding implied that a genetic background evolved that 'potentiated' the evolution of this trait. In

principle, this effect could involve two distinct mechanisms. One possibility is that the rate of mutation, or certain types of mutation, increased such that the required event was more likely to occur in later generations. The other possibility is an epistatic interaction, such that the expression of a mutation that produced the Cit⁺ trait required one or more preceding mutations. Here we report the results of extensive whole-genome re-sequencing that allowed us to reconstruct the population's history, identify mutations underlying the Cit⁺ phenotype, and elucidate the physiological basis of this novel trait.

Genome sequences and phylogeny

We sequenced 29 clones sampled at various generations from population Ara-3, including nine Cit⁺ and three Cit[−] clones known to be potentiated²⁰ (Supplementary Table 1). Mutations including single-nucleotide polymorphisms (SNPs) as well as deletions, insertions and some chromosomal rearrangements were identified (Supplementary Table 2) by comparing reads to the genome of the ancestral strain, REL606 (ref. 25). Inversions and other rearrangements that involved long sequence repeats would have escaped detection.

We reconstructed the population's phylogenetic history from presence-absence matrices of all mutations identified in the sequenced genomes. Figure 1 shows that the population was polymorphic for most of its history. Several clades, each represented by multiple clones, arose before 20,000 generations. One of them, which we call UC (unsuccessful clade), was not seen after 15,000 generations. Clades C1, C2 and C3 coexisted through the evolution of Cit⁺ and beyond. C1 includes four clones, the earliest from generation 25,000, although a molecular clock (Fig. 1 inset) implies that C1 diverged from the ancestor of C2 and C3 before 15,000 generations. C2 and C3 had diverged by generation 20,000. C3 includes both Cit[−] clones and all the Cit⁺ clones, although the first Cit⁺ cells did not arise until ~31,000 generations. Two mechanisms may explain the prolonged coexistence of the Cit[−] lineages. First, they may all have acquired beneficial mutations without one gaining enough advantage to fix²⁶. Alternatively, they might have filled subtly different niches, such as through the differential use of secreted metabolites^{27,28}.

¹Department of Microbiology and Molecular Genetics, Michigan State University, East Lansing, Michigan 48824, USA. ²BEACON Center for the Study of Evolution in Action, Michigan State University, East Lansing, Michigan 48824, USA. ³Department of Chemistry and Biochemistry, The University of Texas, Austin, Texas 78712, USA. ⁴Institute for Cellular and Molecular Biology, The University of Texas, Austin, Texas 78712, USA. ⁵Department of Microbiology, Immunology, and Infectious Diseases, University of Calgary, Calgary, Alberta T2N 4N1, Canada.

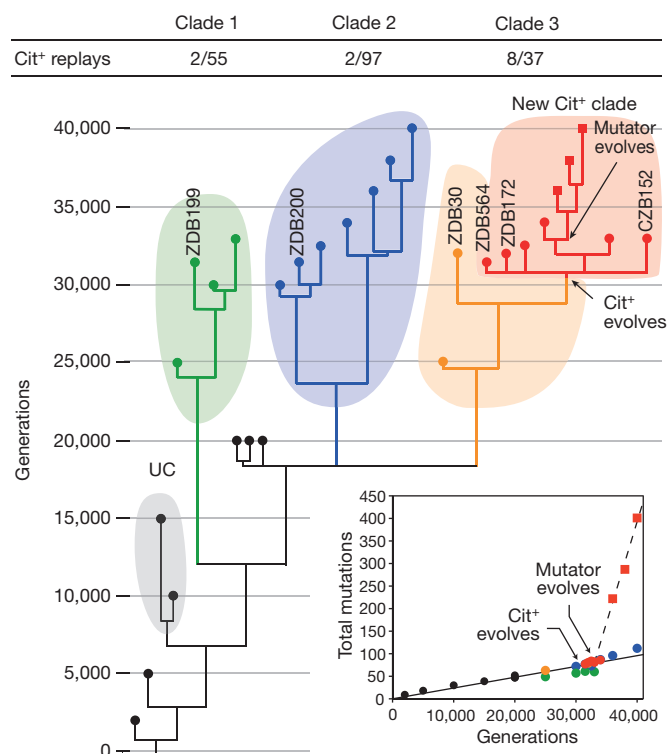


Figure 1 | Phylogeny of Ara-3 population. Symbols at branch tips mark 29 sequenced clones; labels are shown for clones mentioned in main text and figures. Shaded areas and coloured symbols identify major clades. Fractions above the tree show the number of clones belonging to the clade that yielded Cit^+ mutants during replay experiments (numerator) and the corresponding total used in those experiments (denominator). Inset shows number of mutations relative to the ancestor. The solid line is the least-squares linear regression of mutations in non-mutator genomes; the dashed line is the corresponding regression for mutator genomes.

The sequenced Cit^+ clones from generation 36,000 and later have an SNP in the *mutS* gene that produces a premature stop codon and truncates the MutS protein, thereby causing a defect in methyl-directed mismatch DNA repair²⁹. We sequenced *mutS* from three Cit^+ clones from each of generations 33,000, 34,000, 35,000, 36,000, 37,000 and 38,000, and found this SNP in 0, 0, 2, 3 and 3 clones, respectively, indicating that the mutation arose after the origin of the Cit^+ lineage. Also, none of the 20 Cit^- genomes has this mutation. As a consequence, Cit^+ genomes from later generations accumulated SNPs much faster than Cit^- and early Cit^+ genomes (Fig. 1 inset). Mutator phenotypes evolved in several other populations in the LTEE^{18,30}, so this change was not unique to the Cit^+ lineage.

Evolution of the Cit^+ function

The evolution of the Cit^+ trait involved three successive processes: potentiation, actualization and refinement. The ancestor's rate of mutation to Cit^+ was immeasurably low, with an upper bound of 3.6×10^{-13} per cell-generation²⁰. Potentiation refers to the evolution of a genetic background in which this function became accessible by mutation. An extremely weak Cit^+ variant had emerged by 31,500 generations, which represents the actualization step. The new function was then refined, which allowed the efficient exploitation of citrate, the rise of the Cit^+ subpopulation to numerical dominance, and the expansion of the total population size. Of these processes, actualization is the most tractable for study owing to the discrete phenotypic change, and we therefore focused on identifying and characterizing the mutational basis of actualization. With that information in hand, additional analyses then shed new light on the processes of refinement and potentiation.

Actualization of the Cit^+ function

One reason that *E. coli* cannot grow aerobically on citrate is its inability to transport citrate^{24,31,32}. The origin of the Cit^+ phenotype therefore required expression of a citrate transporter. All nine sequenced Cit^+ genomes have two or more tandem copies of a 2,933-base-pair segment that includes part of the citrate fermentation (*cit*) operon (Fig. 2a). The amplified segment contains two genes: *rna*, which encodes RNase I³³, and *citT*, which encodes a broad-spectrum C_4 -di- and tri-carboxylic acid transporter that functions in fermentation as a citrate/succinate antiporter³². The boundary upstream of *citT* is in the 3' end of the *citG* gene, which encodes triphosphoribosyl-diphospho-CoA synthase, whereas the boundary downstream of *rna* is in the 5' end of *rnk*, which encodes a regulator of nucleoside diphosphate kinase³⁴. This amplification is not present in the ancestor or any of the sequenced Cit^- genomes, and it is only found in population samples after the evolution of the Cit^+ lineage (Supplementary Table 3). Polymerase chain reaction (PCR) screens also failed to detect this segment in 27 Cit^- clones from generations 33,000 through 40,000, whereas it was found in all 33 Cit^+ clones from the same generations (Supplementary Table 4).

Amplification mutations can alter the spatial relationship between structural genes and regulatory elements, potentially causing altered regulation and novel traits^{35–38}. The structure of the *cit* amplification led us to propose that the Cit^+ trait arose from an amplification-mediated promoter capture (Fig. 2b and Supplementary Fig. 1). The amplification joined upstream *rnk* and downstream *citG* fragments, producing an *rnk-citG* hybrid gene expressed from the upstream *rnk* promoter. Because the *citT* and *citG* genes are normally monocistronic, the downstream copy of *citT* should therefore be co-transcribed with the hybrid gene. If the *rnk* promoter directs transcription under oxic conditions, then the new *rnk-citT* regulatory module might allow *CitT* expression during aerobic metabolism and thereby confer a Cit^+ phenotype³².

To test this hypothesis, we first examined the capacity of the *rnk-citT* module to support *citT* expression in oxic conditions. We constructed a low-copy (one to two per cell) plasmid, pCDrnk-*citT*lux, with an *rnk-citT* module in which *citT* was replaced by the *luxCDABE* reporter operon. We made two other plasmids, pCDrnklux and pCDcitlux, in which the reporter was under the control of the native upstream regulatory regions of *rnk* and *citT*, respectively. We transformed each plasmid into REL606, the ancestral strain; ZDB30, a potentiated C3 clone from generation 32,000; and ZDB172, a weakly Cit^+ clone from generation 32,000. We measured expression (light production) during growth and stationary phase under oxic conditions (Fig. 3). The native *citT* regulatory region showed no expression (above background) in any strain, indicating that *citT* is normally silent under oxic conditions. The native *rnk* regulatory region was expressed in all three strains, with a peak around the transition into stationary phase. Expression from the evolved *rnk-citT* module was much weaker, but there were small spikes in expression in ZDB30 and ZDB172 coincident with peak expression from the native *rnk* regulatory region. These results indicate that the *rnk-citT* module can support *citT* expression during aerobic metabolism.

This hypothesis also predicts that the introduction of the *rnk-citT* module should confer a Cit^+ phenotype, whereas the loss of the *cit*

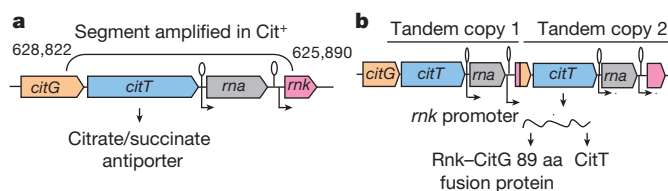


Figure 2 | Tandem amplification in Cit^+ genomes. **a**, Ancestral arrangement of *citG*, *citT*, *rna* and *rnk* genes. **b**, Altered spatial and regulatory relationships generated by the amplification.

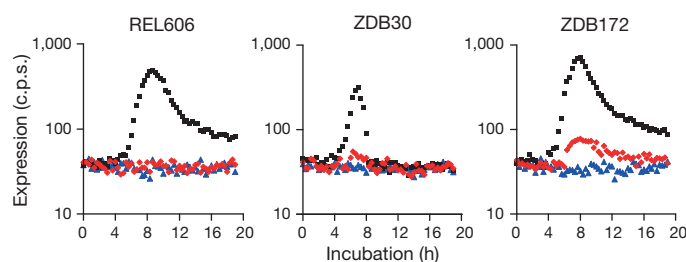


Figure 3 | Expression levels from native *citT*, native *rnk* and evolved *rnk-citT* regulatory regions during aerobic metabolism. Average time course of expression for the ancestral strain REL606 (left) and evolved clones ZDB30 (centre) and ZDB172 (right), each transformed with *lux* reporter plasmids pCDcitTlux (blue), pCDrnklux (black) and pCDrnk-citTlux (red). Expression was measured as counts per second (c.p.s.). Each curve shows the average of four replicates.

amplification should cause reversion to a Cit⁻ state. We tested whether the *rnk-citT* module confers a Cit⁺ phenotype by inserting a single copy of an amplification fragment containing the *rnk* promoter immediately upstream of the chromosomal copy of *citT* (Fig. 4a) in potentiated clone ZDB30. This construct, ZDB595, indeed has a Cit⁺ phenotype, although it is extremely weak, similar to the earliest evolved Cit⁺ variants (Fig. 4b). In the same medium used in the LTEE, ZDB595 experienced a lag of more than 60 h after glucose depletion, followed by a short period of abortive and inconsistent growth on citrate (Fig. 4b, c). These data indicate that the initial Cit⁺ type was too weak to allow exploitation of citrate under the daily-transfer regime of the LTEE. Nonetheless, ZDB595 had a small (1.0%) but significant competitive advantage over ZDB30 in the same environment ($n = 10$, $t = 3.09$, two-tailed $P = 0.0128$). We also isolated 13 Cit⁻ revertants of a 33,000-generation Cit⁺ clone, CZB154. All had lost the *cit* amplification based on both PCR and Southern blot analyses (Supplementary Fig. 2), further supporting the hypothesis that the amplification event had produced the Cit⁺ phenotype.

Refinement of the Cit⁺ function

Given the extremely weak initial Cit⁺ phenotype, additional mutations must have refined the new function. Refinement is an open-ended

process, and we focus only on early refining mutations that led to the rise of Cit⁺ cells to high frequency and the concurrent expansion of the population. These mutations are evidenced by the improvement on citrate of Cit⁺ clones isolated between 31,500 and 33,000 generations (Supplementary Fig. 3). We examined the genomes of the five sequenced Cit⁺ clones from before the population expansion, including one from generations 31,500, 32,000 and 32,500 and two from generation 33,000. We focused on the mutations on the line of descent for the Cit⁺ subpopulation, where that line is defined by the presence of the same mutations in clones from generations 34,000, 36,000 and 38,000 (Supplementary Tables 5–8). Two SNPs and one insertion sequence (IS) element were present in only one of the 33,000-generation genomes. The IS insertion and one SNP seem unrelated to growth on citrate. The remaining SNP is in the regulatory region of *dctA*, which encodes a transporter of succinate and other C₄-di-carboxylic acids³⁹. This mutation may improve recovery of succinate exported in exchange for citrate. However, the other 33,000-generation clone grew better on citrate (Supplementary Fig. 3). Thus, the *dctA* mutation does not seem to be responsible for the population expansion, although it might have been advantageous to its carriers.

These early Cit⁺ genomes also show increases in *cit* copy number. The earliest one had a tandem duplication, whereas later genomes had a three-copy tandem array within a larger tandem duplication, a four-copy tandem array, a tandem duplication in a larger three-copy tandem array and a nine-copy tandem array (Supplementary Table 9). Changes in amplification copy number readily occur by recombination, and they have been implicated in the refinement of other weak functions^{40,41}. These changes increased the number of *rnk-citT* modules relative to the earliest Cit⁺ genome (Fig. 5a) and presumably increased the expression of CitT as well. To test whether an increased number of *rnk-citT* modules could have caused the population expansion, we cloned the module (Fig. 5b) into the high-copy plasmid pUC19 (ref. 42) and moved the resulting plasmid, pZBrnk-citT, into the potentiated clone ZDB30. The resulting strain, ZDB612, is strongly Cit⁺, rapidly transitions from glucose to citrate and grows similarly to the 33,000-generation clone CZB152 (Fig. 5c). The increased number of *rnk-citT* modules can thus explain the refinement of the Cit⁺ phenotype that allowed the population expansion.

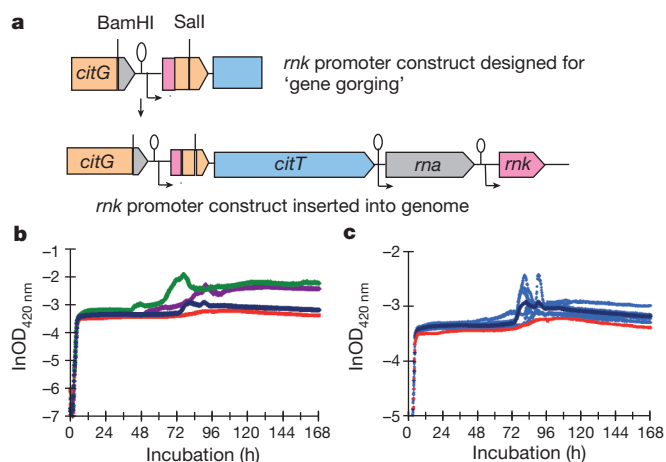


Figure 4 | New *rnk-citT* module confers Cit⁺ phenotype in potentiated background. a, Engineered construct containing the *cit* amplification junction with the *rnk* promoter, and the arrangement following its insertion into the chromosome. b, Average growth trajectories in DM25 of potentiated clone ZDB30 (red), its isogenic construct with chromosomal integration of the *rnk-citT* module ZDB595 (blue), 31,500-generation Cit⁺ clone ZDB564 (purple) and 32,000-generation Cit⁺ clone ZDB172 (green). c, Trajectories of ZDB595 compared to its parent. Light blue trajectories show heterogeneity among replicate cultures of ZDB595; dark blue and red are averages for ZDB595 and its parent, ZDB30, as in panel b (except different scale).

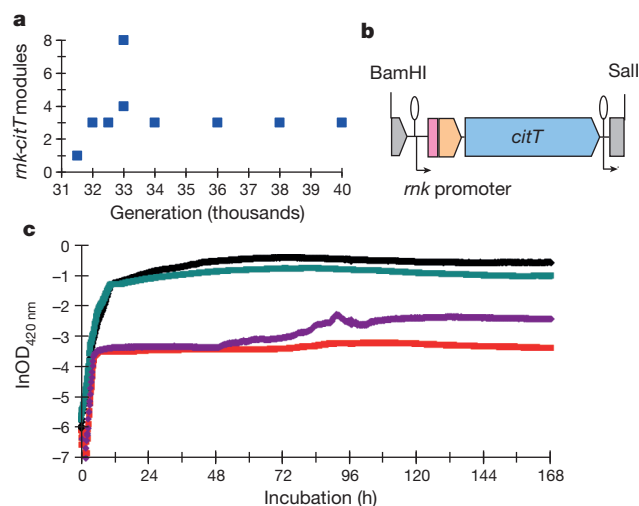


Figure 5 | Refinement of Cit⁺ phenotype by increased number of *rnk-citT* modules. a, Change in *rnk-citT* module copy number in sequenced Cit⁺ clones over time. b, Structure of *rnk-citT* module cloned into high-copy plasmid pUC19 to produce pZBrnk-citT. c, Growth trajectories in DM25 of potentiated Cit⁻ clone ZDB30 (red), 31,500-generation Cit⁺ clone ZDB564 (purple), 33,000-generation Cit⁺ clone CZB152 (black), and ZDB612, a pZBrnk-citT transformant of ZDB30 (green). Each trajectory is the average of six replicates.

In contrast to the early variation in *cit* amplification, later Cit^+ genomes have four-copy tandem arrays (Fig. 5a). Amplifications tend to be unstable^{40,41}, and further refinement may have favoured more stable classes of mutations. The evolution of the mutator phenotype in the Cit^+ lineage complicates efforts to identify these later refining mutations, but some interesting candidates include SNPs in *citT* itself: *gltA*, which encodes citrate synthase; and *aceA*, which encodes isocitrate lyase.

Potential of Cit^+ evolution

Before the Cit^+ trait could evolve, the Ara-3 population had to evolve a genetic background in which that new function was accessible by mutation. Potentiation was demonstrated by 'replay' experiments using 270 clones sampled over the population's history²⁰. The replays produced 17 Cit^+ mutants that derived from 13 clones, all from generation 20,000 or later. Fluctuation tests confirmed that potentiated clones had increased mutation rates to Cit^+ , although such mutations were still extremely rare²⁰.

Phylogeny implies multiple potentiating mutations

The potentiating mutations are not known to confer any phenotype amenable to screening, so there is no simple way to distinguish between potentiated and non-potentiated clones. Instead, we examined the distribution of the 13 potentiated clones identified by the replay experiments using mutations (Supplementary Table 10) that differentiated clades UC, C1, C2 and C3 (Fig. 1). We also determined the distribution of the other 256 evolved clones used in the replays to assess the coverage of the clades in those experiments (Supplementary Fig. 4). Overall, 205 clones were assigned to clades, including 12 potentiated clones (Supplementary Table 11). Sixteen from generations 15,000 and earlier were in clade UC. The others came from generations 20,000 and later including 55 in C1, 97 in C2, and 37 in C3. Potentiated clones occurred in all three with 8 in C3 and 2 each in C1 and C2. Nonetheless, this distribution is highly non-random (two-tailed Fisher's exact test comparing C3 with C1 and C2 combined, $P = 0.0003$; this test shows no difference between C1 and C2, $P = 0.6206$). These data, and the absence of any Cit^+ mutants generated by the ancestor, indicate that potentiation involved at least two mutations, with one arising before these three clades diverged and another in C3 (Fig. 1).

Alternative hypotheses

Two distinct mechanisms might explain the potentiation effect. One is epistasis, whereby an interaction between the potentiating background and the actualizing mutation is needed to express the Cit^+ phenotype. The second is that the background physically promoted the final mutation; for example, a later rearrangement may require some prior genomic rearrangement. If expression of Cit^+ required earlier mutations, then the *rnk-citT* module should confer a weaker Cit^+ phenotype in a non-potentiated background than a potentiated background. Alternatively, if potentiation facilitated the amplification event itself, then that module should produce an equally strong Cit^+ phenotype in both potentiated and non-potentiated backgrounds.

Evidence for epistasis

To test these predictions, we first tried to move the single-copy *rnk-citT* module into the ancestral chromosome, but several attempts were unsuccessful. This outcome is not surprising under the epistasis hypothesis; a key step was screening potential recombinants for citrate use, and the single-copy module conferred an extremely weak Cit^+ phenotype even in a potentiated C3 clone (Fig. 4). Instead, we moved plasmid pZBrnk-*citT* into the ancestor and clones from clades C1, C2 and C3, and examined their growth trajectories (Fig. 6). All four transformants grew on citrate after depleting the glucose. However, transformants of the ancestor and C1 and C2 clones grew poorly on citrate, even with this high-copy plasmid, as shown by long lags while

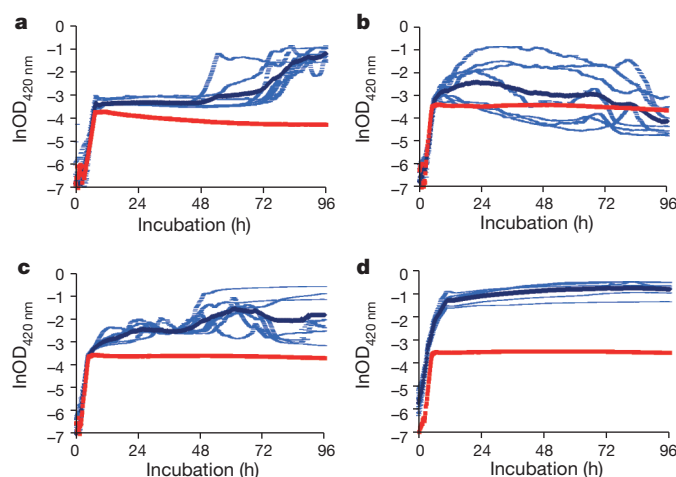


Figure 6 | Evidence for epistatic interactions in potentiation of Cit^+ phenotype. Growth trajectories in DM25 of diverse clones transformed with the pZBrnk-*citT* plasmid. **a**, Ancestral strain REL606 and its transformant ZDB611. **b**, Clade C1 clone ZDB199 and its transformant ZDB614. **c**, C2 clone ZDB200 and its transformant ZDB615. **d**, C3 clone ZDB30 and its transformant ZDB612. Red and dark blue trajectories are averages for the parent clone and its transformant; light blue trajectories show the replicates for the transformant.

transitioning from glucose to citrate, low yields, and inconsistent trajectories across replicates (Fig. 6a–c). By contrast, ZDB612, the transformant of a potentiated C3 clone, grew much faster, more extensively, and consistently across replicates (Fig. 6d). These differences demonstrate epistatic interactions between the *rnk-citT* module and mutations that distinguish the backgrounds.

These data also support the phylogenetic association between clade C3 and the strength of potentiation in the replay experiments. We examined C3 for candidate mutations that may contribute to potentiation. A mutation in *arcB*, which encodes a histidine kinase⁴³, is noteworthy because disabling that gene upregulates the tricarboxylic acid cycle⁴⁴. That mutation might interact with the *rnk-citT* module by allowing efficient use of citrate that enters the cell via the *CitT* transporter. We tried repeatedly to move the evolved and ancestral *arcB* alleles between strains to test this hypothesis, but without success. In any case, the profound differences in growth trajectories on citrate enabled by the high-copy plasmid (Fig. 6) support the hypothesis that potentiation depends, at least partly, on epistasis between the genetic background and the amplification mutation that generated that module.

Evidence against the physical-promotion hypothesis

We examined the Cit^+ mutants from the replay experiments²⁰ for additional evidence on the nature of potentiation. The physical-promotion hypothesis predicts that these mutants should have *cit* amplifications similar or identical to the original one. If epistatic interactions enhanced *citT* expression only from the *rnk* promoter, then the prediction would be the same. However, if epistasis operated at some broader physiological level, then the replays should have diverse mutations that share only the property that they enable expression of the citrate transporter in the oxic environment of the LTEE. We examined 19 re-evolved Cit^+ mutants to identify the relevant mutations; the *citT* region was examined in all of them, and the genomes of six were sequenced. All have mutations affecting *citT*, and most clearly put that gene downstream of a new promoter (Supplementary Table 12). Four sequenced Cit^+ mutants were derived from Cit^- clones that were also sequenced. Besides *citT*-related mutations, these sequenced mutants had one to three other mutations; no gene was mutated in multiple cases, and none seem related to citrate use (Supplementary Table 13), supporting the

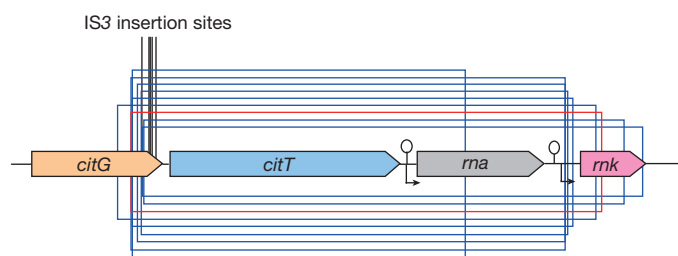


Figure 7 | Mutations that produced Cit^+ phenotype in 14 replay experiments. The red box shows the boundaries of the 2,933-bp amplified segment that actualized the Cit^+ function in the original long-term population. Blue boxes show *citT*-containing regions amplified in eight replays that produced Cit^+ mutants. Vertical black lines mark five locations where IS3 insertions produced Cit^+ mutants in six other replays.

inference that the *citT* mutations were responsible for all of the re-evolved Cit^+ phenotypes.

The Cit^+ mutants arose by diverse mutational processes (Supplementary Table 12). Eight have *citT* duplications similar to the original one, though no two share the same boundaries (Fig. 7). In seven of these, the duplications generated alternative versions of the *rnk-citT* module; in the other, the second *citT* is downstream of the *rna* promoter. Six mutants have an IS3 element inserted in the 3' end of *citG* (Fig. 7). IS3 carries outward-directed promoter elements that can activate adjacent genes^{27,45}. Two mutants have large duplications encompassing all or part of the *cit* operon. One mutant has a large inversion that places most of that operon downstream of the promoter for the fimbria regulatory gene *fimB*, and another has a deletion in *citG* that presumably formed a new promoter. Also, most of these mutants have stronger phenotypes (Supplementary Fig. 5) than the earliest Cit^+ clones in the main experiment (Fig. 4b and Supplementary Fig. 3). In any case, this new function arose in potentiated backgrounds by a variety of mutational processes that recruited several different promoters to allow *CitT* expression during aerobic metabolism. Thus, these data do not support the physical-promotion hypothesis, whereas the strain-specific differences in growth on citrate conferred by the *rnk-citT* module provide clear and compelling evidence for epistasis (Fig. 6). However, these hypotheses are not mutually exclusive, and we cannot reject the possibility that some mutation rendered the genome (or the affected region) more prone to physical rearrangements (including mobile-element insertions) and thereby also contributed to the overall potentiation effect.

Perspective

The evolution of citrate use in an experimental *E. coli* population provided an unusual opportunity to study the multi-step origin of a key innovation. Comparative studies have shown that gene duplications have an important creative role in evolution by generating redundancies that allow neo-functionalization^{5,6,8–10}. Our findings highlight the less-appreciated capacity of duplications to produce new functions by promoter capture events that change gene regulatory networks³⁸. The evolution of citrate use also highlights that such actualizing mutations are only part of the process by which novelties arise. Before a new function can arise, it may be essential for a lineage to evolve a potentiating genetic background that allows the actualizing mutation to occur or the new function to be expressed. Finally, novel functions often emerge in rudimentary forms that must be refined to exploit the ecological opportunities. This three-step process—in which potentiation makes a trait possible, actualization makes the trait manifest, and refinement makes it effective—is probably typical of many new functions.

METHODS SUMMARY

Evolution experiment. Twelve *E. coli* B populations were propagated for over 20 years by daily 100-fold transfers into a minimal medium, DM25, containing

139 μM glucose and 1,700 μM citrate^{13,46}. Population samples were frozen every 500 generations. The focus of this study was population Ara-3, in which the ability to grow on citrate under oxic conditions evolved by 31,500 generations²⁰.

Genome sequencing. Clones were sequenced on Illumina GA, GA II and GA IIX instruments. The reads were deposited in the NCBI SRA database (SRA026813). Mutations were predicted from read alignments to the ancestral genome (REL606)²⁵ using the *breseq* pipeline⁴⁷ and refined by further analyses for specific mutations.

Phylogenetic analysis. The most parsimonious tree was calculated using the irreversible Camin–Sokal model⁴⁸ with presence-absence data in each genome for all mutational events. Branch lengths were calculated by a maximum likelihood procedure with additional parameters for ancestral and mutator rates of Poisson-distributed mutation accumulation. Other clones were put in clades based on Sanger sequencing to screen for 10 phylogenetically informative mutations.

Expression experiments. Promoter regions for *citT*, *rnk* and the *rnk-citT* module were cloned into the *lux* reporter plasmid pCS26-pac⁴⁹, and transformed into strains REL606, ZDB30 and ZDB172. Light emission was measured as a proxy for luciferase expression for 19 h in DM25 in 96-well plates with intermittent shaking. Assays were replicated fourfold for each construct.

Primers and clones. Primer pairs used in genetic analyses and strain constructions are shown in Supplementary Table 14. Supplementary Table 15 describes the clones used in growth-trajectory experiments.

Full Methods and any associated references are available in the online version of the paper.

Received 18 June; accepted 22 August 2012.

Published online 19 September 2012.

- Mayr, E. In *Evolution after Darwin* (ed. Tax, S.) Vol. 1, 349–380 (Univ. Chicago Press, 1960).
- Pigliucci, M. What, if anything, is an evolutionary novelty? *Philos. Sci.* **75**, 887–898 (2008).
- Jacob, F. Evolution and tinkering. *Science* **196**, 1161–1166 (1977).
- Jacob, F. *The Possible and the Actual*. (Univ. Washington Press, 1982).
- Gould, S. J. & Vrba, E. S. Exaptation—a missing term in the science of form. *Paleobiol.* **8**, 4–15 (1982).
- Taylor, J. S. & Raes, J. Duplication and divergence: the evolution of new genes and old ideas. *Annu. Rev. Genet.* **38**, 615–643 (2004).
- Patthy, L. Genome evolution and the evolution of exon-shuffling—a review. *Gene* **238**, 103–114 (1999).
- True, J. R. & Carroll, S. B. Gene co-option in physiological and morphological evolution. *Annu. Rev. Cell Dev. Biol.* **18**, 53–80 (2002).
- Zhang, J. Evolution by gene duplication: an update. *Trends Ecol. Evol.* **18**, 292–298 (2003).
- Bergthorsson, U., Andersson, D. I. & Roth, J. R. Ohno's dilemma: evolution of new genes under continuous selection. *Proc. Natl Acad. Sci. USA* **104**, 17004–17009 (2007).
- Lenski, R. E., Ofria, C., Pennock, R. T. & Adami, C. The evolutionary origin of complex features. *Nature* **423**, 139–144 (2003).
- Elena, S. F. & Lenski, R. E. Evolution experiments with microorganisms: the dynamics and genetic bases of adaptation. *Nature Rev. Genet.* **4**, 457–469 (2003).
- Lenski, R. E. Phenotypic and genomic evolution during a 20,000-generation experiment with the bacterium *Escherichia coli*. *Plant Breed. Rev.* **24**, 225–265 (2004).
- Beaumont, H. J. E., Gallie, J., Kost, K., Ferguson, G. C. & Rainey, P. B. Experimental evolution of bet hedging. *Nature* **462**, 90–93 (2009).
- Meyer, J. R., Dobias, D. T., Weitz, J. S., Barrick, J. E. & Lenski, R. E. Repeatability and contingency in the evolution of a key innovation in phage lambda. *Science* **335**, 428–432 (2012).
- Bentley, D. R. Whole-genome resequencing. *Curr. Opin. Genet. Dev.* **16**, 545–552 (2006).
- Hegreness, M. & Kishony, R. Analysis of genetic systems using experimental evolution and whole-genome sequencing. *Genome Biol.* **8**, 201 (2007).
- Barrick, J. E. et al. Genome evolution and adaptation in a long-term experiment with *E. coli*. *Nature* **461**, 1243–1247 (2009).
- Barrick, J. E. & Lenski, R. E. Genome-wide mutational diversity in an evolving population of *Escherichia coli*. *Cold Spring Harb. Symp. Quant. Biol.* **74**, 119–129 (2009).
- Blount, Z. D., Borland, C. Z. & Lenski, R. E. Historical contingency and the evolution of a key innovation in an experimental population of *Escherichia coli*. *Proc. Natl Acad. Sci. USA* **105**, 7899–7906 (2008).
- Koser, S. A. Correlation of citrate-utilization by members of the colon-aerogenes group with other differential characteristics and with habitat. *J. Bacteriol.* **9**, 59–77 (1924).
- Lütgens, M. & Gottschalk, G. Why a co-substrate is required for anaerobic growth of *Escherichia coli* on citrate. *J. Gen. Microbiol.* **119**, 63–70 (1980).
- Scheut, F. & Strockbine, N. A. In *Bergey's Manual of Systematic Bacteriology, Volume 2: The Proteobacteria* (eds Garrity, G. M., Brenner, D. J., Kreis, N. R. & Staley, J. R.) 607–624 (Springer, 2005).

24. Hall, B. G. Chromosomal mutation for citrate utilization by *Escherichia coli* K-12. *J. Bacteriol.* **151**, 269–273 (1982).
25. Jeong, H. et al. Genome sequences of *Escherichia coli* B strains REL606 and BL21(DE3). *J. Mol. Biol.* **394**, 644–652 (2009).
26. Fogle, C. A., Nagle, J. L. & Desai, M. M. Clonal interference, multiple mutations and adaptation in large asexual populations. *Genetics* **180**, 2163–2173 (2008).
27. Treves, D. S., Manning, S. & Adams, J. Repeated evolution of an acetate-crossfeeding polymorphism in long-term populations of *Escherichia coli*. *Mol. Biol. Evol.* **15**, 789–797 (1998).
28. Rozen, D. E., Schneider, D. & Lenski, R. E. Long-term experimental evolution in *Escherichia coli*. XIII. Phylogenetic history of a balanced polymorphism. *J. Mol. Evol.* **61**, 171–180 (2005).
29. Glickman, B. W. & Radman, M. *Escherichia coli* mutator mutants deficient in methyl-instructed DNA mismatch correction. *Proc. Natl Acad. Sci. USA* **77**, 1063–1067 (1980).
30. Sniegowski, P. D., Gerrish, P. J. & Lenski, R. E. Evolution of high mutation rates in experimental populations of *E. coli*. *Nature* **387**, 703–705 (1997).
31. Lara, F. J. S. & Stokes, J. L. Oxidation of citrate by *Escherichia coli*. *J. Bacteriol.* **63**, 415–420 (1952).
32. Pos, K. M., Dimroth, P. & Bott, M. The *Escherichia coli* citrate carrier CitT: a member of a novel eubacterial transporter family related to the 2-oxoglutarate/malate translocator from spinach chloroplasts. *J. Bacteriol.* **180**, 4160–4165 (1998).
33. Zhu, L. & Deutscher, M. P. The *Escherichia coli* *rna* gene encoding RNase I: sequence and unusual promoter structure. *Gene* **119**, 101–106 (1992).
34. Shankar, S., Schlichtman, D. & Chakrabarty, A. M. Regulation of nucleoside diphosphate kinase and an alternative kinase in *Escherichia coli*: role of the *sspA* and *mk* genes in nucleoside triphosphate formation. *Mol. Microbiol.* **17**, 935–943 (1995).
35. Usakin, L. A., Kogan, G. L., Kalmykova, A. I. & Gvozdev, V. A. An alien promoter capture as a primary step of the evolution of testes-expressed repeats in the *Drosophila melanogaster* genome. *Mol. Biol. Evol.* **22**, 1555–1560 (2005).
36. Adam, D., Dimitrijevic, N. & Scharlt, M. Tumor suppression in *Xiphophorus* by an accidentally acquired promoter. *Science* **259**, 816–819 (1993).
37. Bock, R. & Timmis, J. N. Reconstructing evolution: gene transfer from plastids to the nucleus. *Bioessays* **30**, 556–566 (2008).
38. Whoriskey, S. K., Nghiem, V., Leong, P., Masson, J. & Miller, J. H. Genetic rearrangements and gene amplification in *Escherichia coli*: DNA sequences at the junctions of amplified gene fusions. *Genes Dev.* **1**, 227–237 (1987).
39. Janausch, I. G., Zientz, E., Tran, Q. H., Kroger, A. & Uuden, G. C₄-dicarboxylate carriers and sensors in bacteria. *Biochim. Biophys. Acta* **1553**, 39–56 (2002).
40. Andersson, D. I., Slechta, E. S. & Roth, J. R. Evidence that gene amplification underlies adaptive mutability of the bacterial *lac* operon. *Science* **282**, 1133–1135 (1998).
41. Reams, A. B., Kofoed, E., Savageau, M. & Roth, J. R. Duplication frequency in a population of *Salmonella enterica* rapidly approaches steady state with or without recombination. *Genetics* **184**, 1077–1094 (2010).
42. Yanisch-Perron, C., Vieira, J. & Messing, J. Improved M13 phage cloning vectors and host strains: nucleotide sequences of the M13mp18 and pUC19 vectors. *Gene* **33**, 103–119 (1985).
43. Gunsalus, R. P. & Park, S. J. Aerobic-anaerobic gene regulation in *Escherichia coli*: control by the ArcAB and Fnr regulons. *Res. Microbiol.* **145**, 437–450 (1994).
44. Nizam, S. A., Zhu, J., Ho, P. Y. & Shimizu, K. Effects of *arcA* and *arcB* genes knockout on the metabolism in *Escherichia coli* under aerobic condition. *Biochem. Eng. J.* **44**, 240–250 (2009).
45. Charlier, D., Piette, J. & Glansdorff, N. IS3 can function as a mobile promoter. *Nucleic Acids Res.* **10**, 5935–5948 (1982).
46. Lenski, R. E., Rose, M. R., Simpson, S. C. & Tadler, S. C. Long-term experimental evolution in *Escherichia coli*. I. Adaptation and divergence during 2,000 generations. *Am. Nat.* **138**, 1315–1341 (1991).
47. Barrick, J. E. & Kuoester, D. B. breseq. <http://barricklab.org/breseq> (2010).
48. Camin, J. H. & Sokal, R. R. A method for deducing branching sequences in phylogeny. *Evolution* **19**, 311–326 (1965).
49. Bjarnason, J., Southward, C. M. & Surette, M. G. Genomic profiling of iron-responsive genes in *Salmonella enterica* serovar Typhimurium by high-throughput screening of a random promoter library. *J. Bacteriol.* **185**, 4973–4982 (2003).

Supplementary Information is available in the online version of the paper.

Acknowledgements We thank N. Hajela, M. Kauth and S. Sleight for assistance, J. Meyer and J. Plucain for discussion, and C. Turner for comments on the paper. Sequencing services were provided by the MSU Research Technology Support Facility. We acknowledge support from the US National Science Foundation (DEB-1019989 to R.E.L.) including the BEACON Center for the Study of Evolution in Action (DBI-0939454), the US National Institutes of Health (K99-GM087550 to J.E.B.), the Defense Advanced Research Projects Agency (HR0011-09-1-0055 to R.E.L.), a Rudolf Hugh Fellowship (to Z.D.B.), a DuVall Family Award (to Z.D.B.), a Ronald M. and Sharon Rogowski Fellowship (to Z.D.B.) and a Barnett Rosenberg Fellowship (to Z.D.B.).

Author Contributions J.E.B. and Z.D.B. performed genome sequencing and analyses. J.E.B. performed phylogenetic analyses and developed code for sequence analyses. Z.D.B. performed growth curves, molecular experiments and sequenced specific genes. C.J.D. performed gene expression experiments. R.E.L. conceived and directs the long-term experiment. Z.D.B., J.E.B., C.J.D. and R.E.L. analysed data, wrote the paper and prepared figures.

Author Information All genome data have been deposited in the NCBI Sequence Read Archive database (SRA026813). Other data have been deposited in the DRYAD database (<http://dx.doi.org/10.5061/dryad.8q6n4>). R.E.L. will make strains available to qualified recipients, subject to a material transfer agreement that can be found at <http://www.technologies.msu.edu/inventors/mta-cda/mta/mta-forms>. Reprints and permissions information is available at www.nature.com/reprints. The authors declare no competing financial interests. Readers are welcome to comment on the online version of the paper. Correspondence and requests for materials should be addressed to Z.D.B. (blountza@msu.edu) or R.E.L. (lenski@msu.edu).

METHODS

Evolution experiment. The long-term experiment is described in detail elsewhere^{13,46}. In brief, twelve populations of *E. coli* B were started in 1988 and have evolved since under conditions of daily 100-fold dilutions in a minimal medium, DM25, containing 139 μ M glucose and 1,700 μ M citrate⁴⁶. The populations undergo ~ 6.64 generations per day and had been evolving for 40,000 generations when this study began. Every 500 generations, samples were frozen at -80°C with glycerol as a cryoprotectant. The focus of this study was population Ara-3, in which the ability to grow aerobically on citrate evolved by 31,500 generations²⁰.

Genomic DNA isolation. Clones were revived from frozen stocks by overnight growth in LB medium at 37°C with aeration. DNA was extracted and purified using the Qiagen Genomic-tip 100/G kit (Qiagen).

Whole-genome sequencing and mutation detection. Clones were sequenced on Illumina GA, GA II and GA IIx instruments. The resulting reads were deposited in the NCBI SRA database (SRA026813). Most data sets contain single-end reads only, but additional mate-paired libraries were obtained for ZDB30 and ZDB172. Reads were mapped to the reference genome of the ancestral strain (REL606)²⁵, and mutations were predicted using the breseq computational pipeline⁴⁷. This pipeline detects point mutations, deletions and new sequence junctions that may indicate IS-element insertions or other rearrangements, as described in its online documentation. Large duplications and amplifications were predicted manually by examining the depth of read coverage across each genome.

Mutation lists (Supplementary Table 2) were further refined by manually reconstructing the most plausible series of events generating the observed differences. This procedure involved: (1) splitting predicted changes into multiple mutations based on phylogenetic relationships, (2) assigning mutations to genomes when a subsequent mutational event prevented their detection (for example, an SNP within a later deletion), and (3) correcting false positives for a handful of difficult-to-predict mutations by examining alignments and coverage in all clones. After these procedures, 17 homoplasies remained in the phylogeny, most of which seem to indicate mutational hot spots: 9 are IS-element insertions at specific sites, 7 are insertions or deletions at the boundaries of IS elements, and only 1 is a single-base substitution not associated with an IS element. Given these signatures, it is likely that these mutations occurred independently in multiple lineages.

The copy number and configuration of the *citT* module were estimated from the number of reads overlapping the new *rnk-citT* sequence junction relative to the two original flanking-sequence junctions, and from the average read-depth in this region relative to a single-copy region (Supplementary Table 9).

Phylogenetic analysis. An initial parsimony-based tree was calculated using presence-absence data for all mutational events in each genome using the *dnaps* program from PHYLIP. Branch lengths were recalculated using an irreversible Camin–Sokal model⁴⁸, because the ancestral states are known and reversions unlikely given the genome size and number of mutations observed. A maximum-likelihood model was then used to estimate branching times and two mutation rates, one for non-mutator branches and one for mutator branches. The model fixed the generation when each clone was sampled and assumed that mutations accumulated on branches according to a Poisson process.

Ten mutations in nine genes (*ybaL*, *nadR*, *hemE*, *cspC*, *yaaH*, *leuA*, *tolR*, *arcB* and *gltA*) were identified as phylogenetically informative based on their association with particular clades in the Ara-3 population (Supplementary Table 10). Sanger sequencing of PCR-amplified gene fragments was used to determine the presence or absence of these mutations in replay clones, which were then mapped onto the phylogeny using the keys in Supplementary Fig. 4. Owing to the large number of clones and genes under consideration, not all genes were sequenced for all clones. Supplementary Table 11 shows the data and phylogenetic assignments. Supplementary Table 14 shows the primer pairs used to amplify each locus.

PCR screens for *cit* amplifications. The *cit* amplification was detected in population samples and clones by PCR amplification across the *rnk-citG* junction using outward-directed primers specific to *citT* (Supplementary Table 14). When screening population samples, three reactions were run for each time point, and the template was a 1:10 dilution of the frozen sample for that generation.

Expression experiments. Expression was measured using luciferase-based reporter constructs. The complete upstream regions for the native *citT* and *rnk* genes were PCR-amplified from the cognate reporters from the *E. coli* transcriptional library⁵⁰ using the primers pZE05 and pZE07. The intergenic region of the evolved *rnk-citT* module was amplified from *Cit*⁺ clone ZDB172 using primers nctForward and nctReverse (Supplementary Table 14). The PCR products were cloned into the low-copy (1–2) plasmid pCS26-pac, which contains a kanamycin resistance gene and the luciferase operon (*luxCDABE*)⁴⁹. Each plasmid was transformed into clones REL606, ZDB30 and ZDB172.

Before the expression assays, strains were grown in a 96-well plate (BD Biosciences) in 200 μ l per well of DM25 supplemented with 50 μ g ml⁻¹ kanamycin, with constant shaking at 37°C for two 24-h cycles for acclimation. Fresh overnight cultures were then diluted 100-fold into a black, clear-bottomed 96-well plate (9520 Costar, Corning), with 150 μ l per well of DM25, and covered with a breathable sealing membrane (Nunc) to prevent evaporation. Light emission was measured using a Wallac Victor² plate reader (Perkin Elmer Life Sciences) every 20 min for 19 h with 90 s of 2-mm orbital shaking before each reading. Assays were run in quadruplicate in the same plate.

Isogenic strain construction. A single-copy chromosomal *rnk-citT* module was placed in a *Cit*⁻ background using the ‘gene gorging’ method⁵¹. Owing to problems inherent to the manipulation of amplified genes, we did not attempt to move an entire *citT* amplification segment. Instead, we engineered a *cit* amplification junction containing the *rnk* promoter from three smaller fragments that were PCR-amplified from the 32,000-generation *Cit*⁺ clone ZDB172. The first fragment contained the *cit* amplification junction (*citAmpJ*), including the *rnk* promoter region, and was PCR-amplified using the primers *citAmpJ* F and *citAmpJ* R (Supplementary Table 14). The second fragment contained the *citT-citG* junction (*citT-citG*) and was PCR-amplified using the primers *citT-citG* F and *citT-citG* R. The third fragment contained sequence internal to the *citG* gene (*citGfrag*) and was PCR-amplified using *citGfrag* F and *citGfrag* R. Each primer pair was designed with restriction sites that allowed ligation of the fragments to a hybrid construct in which the *cit* amplification junction, including the *rnk* promoter, was embedded within >500 bp of the *citG* flanking sequence. The assembled module was then PCR-amplified using *citT-citG* Gorge F and *citGfrag* R (Supplementary Table 14). The forward primer incorporated an *I-SceI* restriction site required for the gene-gorging procedure, which was then performed as described elsewhere⁵¹. We screened for putative transformants by performing PCR and testing for a *Cit*⁺ phenotype based on a positive reaction on Christensen’s Citrate Agar⁵². Successful constructs were confirmed by Sanger sequencing.

Growth trajectories. Strains of interest (Supplementary Table 15) were revived from frozen stocks by growing them in LB, and they were then acclimated by two 24-h culture cycles in DM25. Next, 100 μ l of each culture was diluted into 9.9 ml of DM25, and 200 μ l aliquots were placed into randomly assigned wells in a 96-well plate. For all pZBrnk-*citT* transformants, the medium was supplemented with 100 μ g ml⁻¹ ampicillin to ensure plasmid retention. Growth trajectories were replicated six- to eightfold for each strain. To limit evaporation, strains were grown in the innermost 60 wells, whereas the outermost 36 wells were filled with 300 μ l of saline buffer. When assays ran longer than 96 h, the buffer was replenished after 96 h. OD_{420 nm} was measured every 10 min by a VersaMax automated plate reader (Molecular Devices). Plates were shaken orbitally for 5 s before each measurement, but were otherwise stationary.

Fitness assays. Relative fitness was measured in competition experiments described elsewhere⁴⁶. In brief, we inoculated 0.05 ml each of acclimated cultures of ZDB595 and ZDB63, an Ara⁺ mutant of ZDB30, into 9.9 ml of DM25 with tenfold replication. Initial densities were measured by dilution plating on tetrazolium arabinose (TA) plates, on which ZDB595 and ZDB63 made red and white colonies, respectively. The cultures were then propagated for three daily transfer cycles, and the final densities were measured using TA plates. Relative fitness was calculated as the ratio of the realized growth rates of the competitors over the course of the experiment⁴⁶.

Isolation of *Cit*⁻ revertants. Three 10-ml LB broth cultures were inoculated with 15 μ l from the frozen stock of 33,000-generation *Cit*⁺ clone CZB154. After overnight growth at 37°C , the cultures were diluted 10⁶-fold, and 100 μ l was transferred to 30 flasks, ten containing 9.9 ml of DM25, ten containing 9.9 ml of DM25 without citrate, and ten containing 9.9 ml of M9 broth (a citrate-free minimal medium) with 25 μ g ml⁻¹ glucose. The 30 cultures were incubated at 37°C , and propagated through six daily 1:100 serial dilutions. Each culture was then diluted 10⁴-fold, and 100 μ l were spread onto each of eight TA plates. The plates were incubated for ~ 24 h at 37°C , and colonies were patched onto TA and Minimal Citrate (MC) plates. Clones that grew on TA plates, but not on MC plates, were then streaked onto Christensen’s agar. Those clones that did not produce a *Cit*⁺ reaction on Christensen’s agar were retained as *Cit*⁻ revertants. Up to 512 colonies per replicate culture were tested for loss of the *Cit*⁺ phenotype, but only one *Cit*⁻ revertant was retained from any culture. *Cit*⁻ revertants were found in 8/10 citrate-free DM25 cultures and in 5/10 cultures containing M9 medium. No revertants were isolated from any cultures in normal DM25 medium, presumably because of the advantage that *Cit*⁺ cells have when citrate is present. The 13 *Cit*⁻ revertants were tested for the presence or absence of the *cit* amplification by performing both PCR with the *citT*out F/R primer pair and *citT*-specific Southern blotting with EcoRV-digested genomic DNA (Supplementary Fig. 2 and Supplementary Table 14).

Plasmid construction. A DNA fragment containing the complete *rnk-citT* module was PCR-amplified from Cit⁺ clone ZDB172 using primers *citT*AmpX F and *citT*AmpX R (Supplementary Table 14). The fragment was then inserted into the cloning site of pUC19 (NEB), and sequencing confirmed that the resulting plasmid, pZBrnk-citT, had the corresponding region. The plasmid was transformed into strains REL606, ZDB30, ZDB199 and ZDB200. Cit⁺ transformants were identified by positive reactions on Cristensen's Citrate Agar⁵².

Identification of mutations in Cit⁺ replays. Nineteen Cit⁺ mutants isolated in replay and related experiments²⁰ were analysed for mutations. The mutants were first checked for large changes in the *citT* region by Southern hybridization with *citT*-specific probes. Genomic DNA was digested with EcoRV (NEB); fragments were separated on 0.8% agarose gels with a 1-kb ladder (NEB), then transferred to nylon membranes. Hybridizations were performed at 68 °C. The *citT*-specific probe was an internal fragment amplified by PCR using primers in Supplementary Table 14, purified using an Illustra GFX PCR DNA purification kit (GE Healthcare), and labelled using the DIG DNA labelling and detection kit (Roche). Most, but not all, mutants had enlarged *citT* bands. We tried to PCR-amplify across possible amplification boundaries of each mutant using the same

outward-directed *citT* primers used to screen for the original amplification in the Ara-3 population (Supplementary Table 14). PCR products were thus obtained for 8 clones. Sanger sequencing of the products showed novel junctions consistent with amplifications similar but not identical to the original case. For 7 other clones, PCR products of altered size were obtained when the region immediately upstream of *citT* was amplified, and sequencing showed that each alteration was caused by either a small deletion or an IS3 insertion in *citG*. To identify mutations at other loci, as well as mutations affecting the *cit* region, we sequenced the genomes of six mutants, as described above. These genomes included three of the four mutants for which the mutations conferring the Cit⁺ trait were not resolved using the approaches described above.

50. Zaslaver, A. *et al.* A comprehensive library of fluorescent transcriptional reporters for *Escherichia coli*. *Nature Methods* **3**, 623–628 (2006).
51. Herring, C. D., Glasner, J. D. & Blattner, F. R. Gene replacement without selection: regulated suppression of amber mutations in *Escherichia coli*. *Gene* **311**, 153–163 (2003).
52. Christensen, W. B. Hydrogen sulfide production and citrate utilization in the differentiating of enteric pathogens and coliform bacteria. *Res. Bull. Weld County Health Dept. Greeley Colo.* **1**, 3–16 (1949).

Comprehensive genomic characterization of squamous cell lung cancers

The Cancer Genome Atlas Research Network*

Lung squamous cell carcinoma is a common type of lung cancer, causing approximately 400,000 deaths per year worldwide. Genomic alterations in squamous cell lung cancers have not been comprehensively characterized, and no molecularly targeted agents have been specifically developed for its treatment. As part of The Cancer Genome Atlas, here we profile 178 lung squamous cell carcinomas to provide a comprehensive landscape of genomic and epigenomic alterations. We show that the tumour type is characterized by complex genomic alterations, with a mean of 360 exonic mutations, 165 genomic rearrangements, and 323 segments of copy number alteration per tumour. We find statistically recurrent mutations in 11 genes, including mutation of *TP53* in nearly all specimens. Previously unreported loss-of-function mutations are seen in the *HLA-A* class I major histocompatibility gene. Significantly altered pathways included *NFE2L2* and *KEAP1* in 34%, squamous differentiation genes in 44%, phosphatidylinositol-3-OH kinase pathway genes in 47%, and *CDKN2A* and *RB1* in 72% of tumours. We identified a potential therapeutic target in most tumours, offering new avenues of investigation for the treatment of squamous cell lung cancers.

Lung cancer is the leading cause of cancer-related mortality worldwide, leading to an estimated 1.4 million deaths in 2010 (ref. 1). The discovery of recurrent mutations in the epidermal growth factor receptor (*EGFR*) kinase, as well as fusions involving anaplastic lymphoma kinase (*ALK*), has led to a marked change in the treatment of patients with lung adenocarcinoma, the most common type of lung cancer^{2–5}. More recent data have suggested that targeting mutations in *BRAF*, *AKT1*, *ERBB2* and *PIK3CA* and fusions that involve *ROS1* and *RET* may also be successful^{6,7}. Unfortunately, activating mutations in *EGFR* and *ALK* fusions are typically not present in the second most common type of lung cancer, lung squamous cell carcinoma (SQCC)⁸, and targeted agents developed for lung adenocarcinoma are largely ineffective against lung SQCC.

Although no comprehensive genomic analysis of lung SQCCs has been reported, single-platform studies have identified regions of somatic copy number alterations in lung SQCCs, including amplification of *SOX2*, *PDGFRA* and *FGFR1* and/or *WHSC1L1* and deletion of *CDKN2A*^{9,10}. DNA sequencing studies of lung SQCCs have reported recurrent mutations in several genes, including *TP53*, *NFE2L2*, *KEAP1*, *BAI3*, *FBXW7*, *GRM8*, *MUC16*, *RUNX1T1*, *STK11* and *ERBB4* (refs 11, 12). *DDR2* mutations and *FGFR1* amplification have been nominated as therapeutic targets^{13–15}.

We have conducted a comprehensive study of lung SQCCs from a large cohort of patients as part of The Cancer Genome Atlas (TCGA) project. The twin aims are to characterize the genomic and epigenomic landscape of lung SQCC and to identify potential opportunities for therapy. We report an integrated analysis based on DNA copy number, somatic exonic mutations, messenger RNA sequencing, mRNA expression and promoter methylation for 178 histopathologically reviewed lung SQCCs, in addition to whole genome sequencing (WGS) of 19 samples and microRNA sequencing of 159 samples (Supplementary Table 1.1). Demographic and clinical data and results of the genomic analyses can be downloaded from the TCGA data portal (https://tcga-data.nci.nih.gov/docs/publications/lusc_2012/).

Samples and clinical data

Tumour samples were obtained from 178 patients with previously untreated stage I–IV lung SQCC. Germline DNA was obtained from

adjacent, histologically normal tissues resected at the time of surgery ($n = 137$) or from peripheral blood ($n = 41$). All patients provided written informed consent to conduct genomic studies in accordance with local Institutional Review Boards. The demographic characteristics are described in Supplementary Table 1.2. The median follow-up for the cohort was 15.8 months, and 60% of patients were alive at the time of the last follow-up (data updated in November 2011). Ninety-six per cent of the patients had a history of tobacco use, similar to previous reports for North American patients with lung SQCC¹⁶. DNA and RNA were extracted from patient specimens and measured by several genomic assays, which included standard quality-control assessments (Supplementary Methods, sections 2–8). A committee of experts in lung cancer pathology performed a further review of all samples to confirm the histological subtype (Supplementary Fig. 1.1 and Supplementary Methods, section 1).

Somatic DNA alterations

The lung SQCCs analysed in this study display a large number and variety of DNA alterations, with a mean of 360 exonic mutations, 323 altered copy number segments and 165 genomic rearrangements per tumour.

Copy number alterations were analysed using several platforms. Analysis of single nucleotide polymorphism (SNP) 6.0 array data across the set of 178 lung SQCCs identified a high rate of copy number alteration (mean of 323 segments) when compared with other TCGA projects (as of 1 February 2012), including ovarian cancer (477 segments)¹⁷, glioblastoma multiforme (282 segments)¹⁸, colorectal carcinoma (213 segments), breast carcinoma (282 segments) and renal cell carcinoma (156 segments) ($P < 1 \times 10^{-15}$ by Fisher's exact test). These segments gave rise to regions of both focal and broad somatic copy number alterations (SCNAs), with a mean of 47 focal and 23 broad events per tumour (broad events defined as $\geq 50\%$ of the length of the chromosome arm). There was strong concordance between the three independent copy number assays for all regions of SCNA (Supplementary Figs 2.1–2.4).

At the level of whole chromosome arm SCNAs, lung SQCCs exhibit many similarities to 205 cases of lung adenocarcinoma analysed by

*Lists of participants and their affiliations appear at the end of the paper.

TCGA (Supplementary Fig. 2.1a). The most notable difference between these cancers is selective amplification of chromosome 3q in lung SQCC, as has been reported^{9,19}. Using the SNP 6.0 array platform and GISTIC 2.0 (refs 20, 21), we identified regions of significant copy number alteration (Supplementary Methods, section 2). There were 50 peaks of significant amplification or deletion ($Q < 0.05$), several of which included SCNAs previously seen in lung SQCCs including *SOX2*, *PDGFRA* and/or *KIT*, *EGFR*, *FGFR1* and/or *WHSC1L1*, *CCND1* and *CDKN2A*^{9,10,19} (Supplementary Fig. 2.1b and Supplementary Data 2.1 and 2.2). Other peaks defined regions of SCNA reported for the first time, including amplifications of chromosomal segments containing *NFE2L2*, *MYC*, *CDK6*, *MDM2*, *BCL2L1* and *EYS* and deletions of *FOXP1*, *PTEN* and *NF1* (Supplementary Fig. 2.1b).

Whole exome sequencing of 178 lung SQCCs and matched germline DNA targeted 193,094 exons from 18,863 genes. The mean sequencing coverage across targeted bases was 121 \times , with 83% of target bases above 30 \times coverage. We identified a total of 48,690 non-silent mutations with a mean of 228 non-silent and 360 total exonic mutations per tumour, corresponding to a mean somatic mutation rate of 8.1 mutations per megabase (Mb) and median of 8.4 per Mb. That rate is higher than rates observed in other TCGA projects including acute myelogenous leukaemia (0.56 per Mb), breast carcinoma (1.0 per Mb), ovarian cancer¹⁷ (2.1 per Mb), glioblastoma multiforme¹⁸ (2.3 per Mb) and colorectal carcinoma (3.2 per Mb) (data as of 1 February 2012, $P < 2.2 \times 10^{-16}$ by *t*-test or Wilcoxon's rank sum test for lung SQCC versus all others). In lung SQCC, CpG transitions and transversions were the most commonly observed mutation types, with mean rates of 9.9 and 10.7 per sequenced megabase of CpG context, respectively, for a total mutation rate of 20.6 per Mb. At non-CpG sites, transversions at C:G sites were more common than transitions (7.3 versus 2.9 per Mb; total = 10.2 per Mb) and more common than transversions or transitions at A:T sites (1.5 versus 1.3 per Mb; total = 2.8 per Mb).

Significantly mutated genes were identified using a modified version of the MutSig algorithm (Supplementary Methods, section 3)^{22,23}. We identified 10 genes with a false discovery rate (FDR) Q value < 0.1 (Supplementary Table 3.1): *TP53*, *CDKN2A*, *PTEN*, *PIK3CA*, *KEAP1*, *MLL2*, *HLA-A*, *NFE2L2*, *NOTCH1* and *RB1*, all of which demonstrated robust evidence of gene expression as defined by reads per kilobase of exon model per million mapped reads (RPKM) > 1 (Fig. 1). *TP53* mutation was observed in 81% of samples by automated analysis; visual review of sequencing reads identified a further 9% of samples with potential mutations in regions of sub-optimal coverage or in samples with low purity. Most observed mutations in *NOTCH1* (8 out of 17) were truncating alterations, suggesting loss-of-function, as has recently been reported for head and neck SQCCs^{22,24}. Mutations in *HLA-A* were also almost exclusively nonsense or splice site events (7 out of 8).

To increase our statistical power to detect mutated genes in the setting of the observed high background mutation rate, we performed a secondary MutSig analysis only considering genes previously observed to be mutated in cancer according to the COSMIC database.

This yielded 12 other genes with FDR < 0.1 : *FAM123B* (also known as *WTX*), *HRAS*, *FBXW7*, *SMARCA4*, *NF1*, *SMAD4*, *EGFR*, *APC*, *TSC1*, *BRAF*, *TNFAIP3* and *CREBBP* (Supplementary Table 3.1). Both the spectrum and the frequency of *EGFR* mutations differed from those seen in lung adenocarcinomas. The two most common alterations in lung adenocarcinoma, Leu858Arg and inframe deletions in exon 19, were absent, whereas two Leu861Gln mutations were detected in *EGFR*.

As described in Supplementary Fig. 3.1, we verified somatic mutations by performing an independent hybrid-recapture of 76 genes in all samples. A total of 1,289 mutations were assayed, and we achieved satisfactory coverage to have power to verify at 1,283 positions. We validated 1,235 mutations (96.2%) (Supplementary Fig. 3.1 and Supplementary Methods, section 3). We also verified mutation calls using WGS and RNA sequencing data with similar results (Supplementary Figs 3.1, 4.3 and Supplementary Methods, sections 3 and 4).

WGS was performed for 19 tumour/normal pairs with a mean computed coverage of 54 \times . A mean of 165 somatic rearrangements was found per lung SQCC tumour pair (Supplementary Fig. 3.2), a value in excess of that reported for WGS studies of other tumour types including colorectal carcinoma (75)²⁵, prostate carcinoma (108)²⁶, multiple myeloma (21)²³ and breast cancer (90)²⁷. Although most inframe coding fusions detected in WGS were validated by RNA sequencing, no recurrent rearrangements predicted to generate fusion proteins were identified (Supplementary Data 3.1 and 4.1).

Somatically altered pathways

Many of the somatic alterations we have identified in lung SQCCs seem to be drivers of pathways important to the initiation or progression of the cancer. Specifically, genes involved in the oxidative stress response and squamous differentiation were frequently altered by mutation or SCNA. We observed mutations and copy number alterations of *NFE2L2* and *KEAP1* and/or deletion or mutation of *CUL3* in 34% of cases (Fig. 2). *NFE2L2* and *KEAP1* code for proteins that bind to each other, have been shown to regulate the cell response to oxidative damage, chemo- and radiotherapy, and are somatically altered in a variety of cancer types^{28,29}. We found mutations in *NFE2L2* almost exclusively in one of two *KEAP1* interaction motifs, DLG or ETGE. Mutations in *KEAP1* and *CUL3* showed a pattern consistent with loss-of-function and were mutually exclusive with mutations in *NFE2L2* (Figs 1c and 2). PARADIGM SHIFT³⁰ analysis predicts that mutations in *NFE2L2* and *KEAP1* exert a considerable functional effect (Supplementary Fig. 7.C.1, 7.C.2 and Supplementary Methods, section 7).

We also found alterations in genes with known roles in squamous cell differentiation in 44% of samples, including overexpression and amplification of *SOX2* and *TP63*, loss-of-function mutations in *NOTCH1*, *NOTCH2* and *ASCL4* and focal deletions in *FOXP1* (Fig. 2). Although *NOTCH1* has been well characterized as an oncogene in haematological cancers³¹, *NOTCH1* and *NOTCH2* truncating mutations have been reported in cutaneous SQCCs and lung SQCCs³². Truncating mutations in *ASCL4* are the first to be reported in human

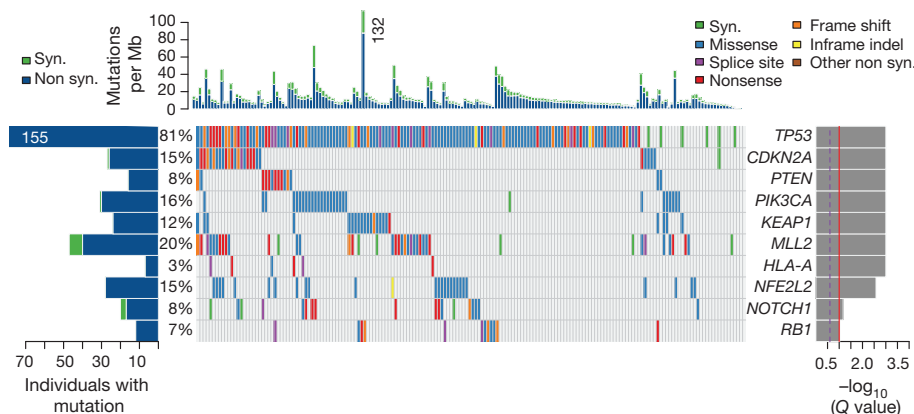


Figure 1 | Significantly mutated genes in lung SQCC. Significantly mutated genes (Q value < 0.1) identified by exome sequencing are listed vertically by Q value. The percentage of lung SQCC samples with a mutation detected by automated calling is noted at the left. Samples displayed as columns, with the overall number of mutations plotted at the top, and samples are arranged to emphasize mutual exclusivity among mutations. Syn., synonymous.

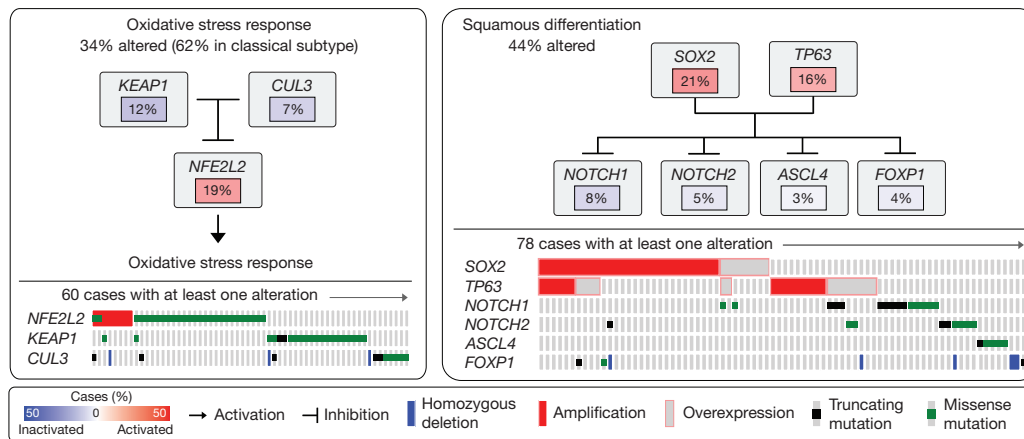


Figure 2 | Somatically altered pathways in squamous cell lung cancer. Left, alterations in oxidative stress response pathway genes as defined by somatic mutation, copy number alteration or up- or downregulation. Frequencies of alteration are expressed as a percentage of all cases, with background in red for activated genes and blue for inactivated genes. Right, alterations in genes that regulate squamous differentiation, as defined in the left panel.

cancer and may have a lineage role given the requirement for *ASCL1* for survival of small-cell lung cancer cells³³. Alterations in *NOTCH1*, *NOTCH2* and *ASCL4* were mutually exclusive and exhibited minimal overlap with amplification of *TP63* and/or *SOX2* (Fig. 2), suggesting that aberrations in those modulators of squamous cell differentiation have overlapping functional consequences.

mRNA expression profiling and subtype classification

Whole-transcriptome expression profiles were generated by RNA sequencing for the entire cohort and by microarrays for a 121-sample subset. Of 20,502 genes analysed, the mean RNA coverage indices were 19× and 6,420 RPKM (Supplementary Fig. 4.1 and Supplementary Methods, section 4). Previously reported lung SQCC gene expression-subtype signatures³⁴ were applied to both of the expression platforms, yielding four subtypes designated as classical (36%), basal (25%), secretory (24%) and primitive (15%). The concordance of subtypes between the two platforms was high (94% agreement) (Supplementary Fig. 4.2). Considerable correlations were found between the expression subtypes and genomic alterations in copy number, mutation and methylation (Fig. 3). The classical subtype was characterized by alterations in *KEAP1*, *NFE2L2* and *PTEN*, as well as pronounced hypermethylation and chromosomal instability. The 3q26 amplicon was present in all of the subtypes, but it was most characteristic of the classical subtype, which also showed the greatest overexpression of three known oncogenes on 3q: *SOX2*, *TP63* and *PIK3CA*. RNA sequencing data suggested that high expression levels of *TP63*, in samples with and without amplification of *TP63*, were associated with dominant expression of the deltaN isoform (also called p40), which lacks the amino-terminal transactivation domain, compared with the longer isoform, called tap63 (89% of tumours overexpressed deltaN compared with

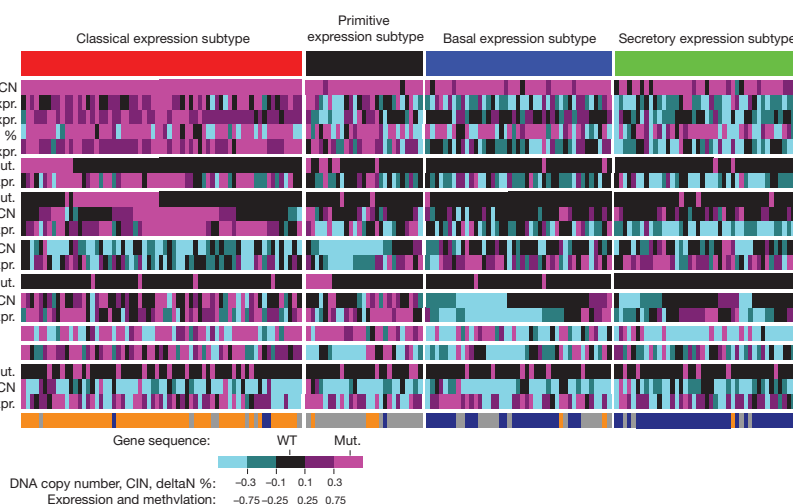
tap63; $P < 2.2 \times 10^{-16}$). The short deltaN isoform is thought to function as an oncogene^{35,36}, and its expression was most enriched in the classical subtype. By contrast, the primitive expression subtype more commonly exhibited *RB1* and *PTEN* alterations, and the basal expression subtype showed *NF1* alterations (Fig. 3). Amplification of *FGFR1* and *WHSC1L1* was anticorrelated with the classical subtype and specifically with *NFE2L2* or *KEAP1* mutated samples. Although *CDKN2A* alterations are common in lung SQCCs, they are not associated with any particular expression subtype (Fig. 3).

Independent clustering of miRNA and methylation data indicated association with expression subtypes. The highest overall methylation was seen in the classical subtype (Fig. 3, Supplementary Figs 5.1 and 6.1, Supplementary Methods, sections 5 and 6, Supplementary Data 6.1 and 6.2 and Supplementary Table 5.1). Integrative clustering (iCluster)³⁷ of mRNA, miRNA, methylation, SCNA and mutation data demonstrated concordance with the mRNA expression subtypes and associated alterations (Fig. 3, Supplementary Fig. 7.A.1 and Supplementary Methods, section 7). Independent correlation of somatic mutations, copy number alterations and gene expression signatures revealed notable subtype associations with alterations in the *TP53*, *PI3K*, *RB1* and *NFE2L2/KEAP1* pathways (Supplementary Fig. 7.B.1 and Supplementary Methods, section 7).

Analysis of the *CDKN2A* locus

Integrated multiplatform analyses showed that *CDKN2A*, a known tumour suppressor gene in lung SQCC³⁸ that encodes the p16^{INK4A} and p14^{ARF} proteins, is inactivated in 72% of cases of lung SQCC (Fig. 4a and Supplementary Data 7.1)—by epigenetic silencing by methylation (21%), inactivating mutation (18%), exon 1β skipping (4%) and homozygous deletion (29%).

Figure 3 | Gene expression subtypes integrated with genomic alterations. Tumours are displayed as columns, grouped by gene expression subtype. Subtypes were compared by Kruskal–Wallis tests for continuous features and by Fisher's exact tests for categorical features. Displayed features showed significant association with gene expression subtype ($P < 0.05$), except for *CDKN2A* alterations. deltaN percentage represents transcript isoform usage between the *TP63* isoforms, deltaN and tap63, as determined by RNA sequencing. Chromosomal instability (CIN) is defined by the mean of the absolute values of chromosome arm copy numbers (CN) from the GISTIC^{23,24} output. Absolute values are used so that amplification and deletion alterations are counted equally. Hypermethylation scores and iCluster assignments are described in Supplementary Figs 6.1 and 7.A.1, respectively. CIN, methylation, gene expression and deltaN values were standardized for display using z-score transformation. Expr., expression; mut., mutation; WT, wild type.



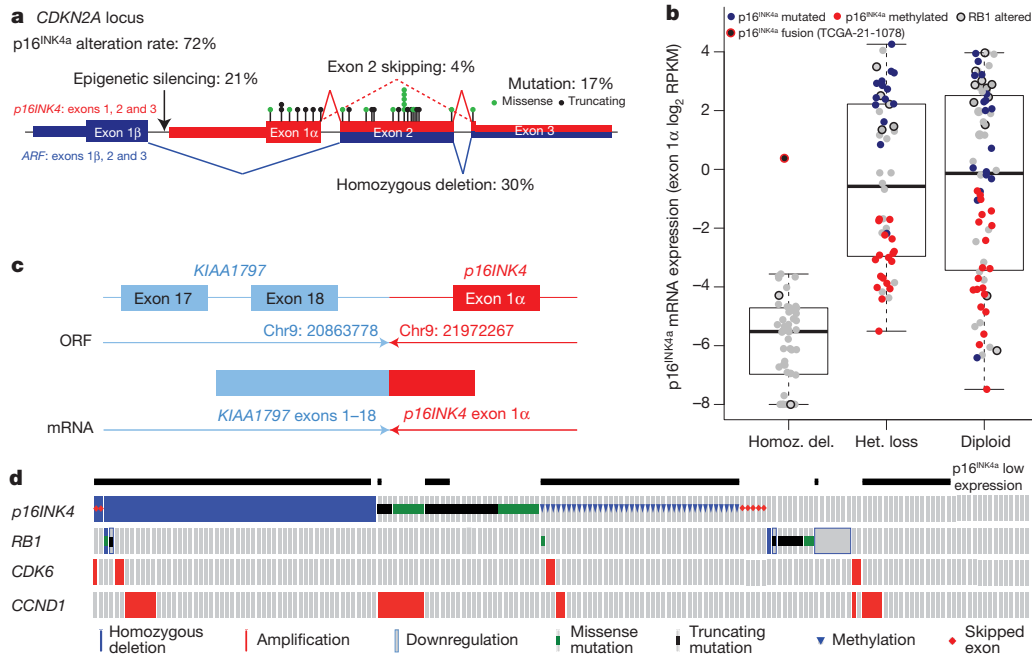


Figure 4 | Multi-faceted characterization of mechanisms of *CDKN2A* loss. **a**, Schematic view of the exon structure of *CDKN2A* demonstrating the types of alterations identified in the study. The locations of point mutation are denoted by black and green circles. **b**, *CDKN2A* expression (y axis) versus *CDKN2A* copy number (x axis). Samples are represented by circles and colour-coded by specific type of *CDKN2A* alteration. Del., deletion; het., heterozygous; homoz., homozygous. **c**, Diagram of the *KIAA1797*-*p16INK4* fusion identified by WGS. ORF, open reading frame. **d**, *CDKN2A* alterations and expression levels (binary) in each sample.

Analysis of mRNA expression across the *CDKN2A* locus revealed four distinct patterns of expression: complete absence of both *p16INK4* and *ARF* (33%); expression of high levels of both *p16INK4* and *ARF* (31%); high expression of *ARF* and absence of *p16INK4* (31%); or expression of a transcript that represents a splicing of exon 1β from *ARF* with the shared exon 3 of *ARF* and *p16INK4*, generating a premature stop codon (4%) (Supplementary Fig. 4.4). Almost all of the cases completely lacking *p16INK4* and *ARF* expression showed homozygous deletion (Fig. 4b and Supplementary Data 7.1). In one case, *p16INK4* expression was detected but analysis of WGS data demonstrated an intergenic fusion event that resulted in detectable transcription between exon 1α *p16INK4* and exon 18 of *KIAA1797* (Fig. 4b, c). Interestingly, combined analysis of WGS and RNA sequencing data identified tumour suppressor gene inactivation by intra- or interchromosomal rearrangement in *PTEN*, *NOTCH1*, *ARID1A*, *CTNNA2*, *VHL* and *NF1*, in eight further cases (Supplementary Data 3.1 and 4.1).

In addition to homozygous deletion, there are frequent mutational events in *CDKN2A* (Fig. 4b and Supplementary Data 7.1). These account for 45% of the 56 cases with high *p16INK4* and *ARF* expression. Furthermore, methylation of the exon 1α promoter accounts for many other cases of *CDKN2A* inactivation (70% of lung SQCCs with *ARF* expression in the absence of detectable *p16INK4*). Seven other tumours in the high-*ARF*/low-*INK4A* group had documented mutations of *INK4A*, primarily nonsense mutations, suggesting nonsense-mediated decay as a mechanism. Of the 28% of tumours without *CDKN2A* alterations, *RB1* mutations were identified in eight cases and *CDK6* amplification in one case (Fig. 4d).

Therapeutic targets

Molecularly targeted agents are now commonly used in patients with adenocarcinoma of the lung, whereas no effective targeted agents have been developed specifically for lung SQCCs¹³. We analysed our genomic data for evidence of the two common genomic alterations in adenocarcinomas of the lung: *EGFR* and *KRAS* mutations. Only one sample had a *KRAS* codon 61 mutation, and there were no exon 19 deletions or Leu585Arg mutations in *EGFR*. However, amplifications of *EGFR* were found in 7% of cases, as were two instances of the Leu861Gln *EGFR* mutation, which confers sensitivity to erlotinib and gefitinib³⁹.

The presence of new potential therapeutic targets in lung SQCC was suggested by the observation that 96% (171 out of 178) of tumours

contain one or more mutations in tyrosine kinases, serine/threonine kinases, phosphatidylinositol-3-OH kinase (PI(3)K) catalytic and regulatory subunits, nuclear hormone receptors, G-protein-coupled receptors, proteases and tyrosine phosphatases (Supplementary Fig. 7.D.1a and Supplementary Data 7.2 and 7.3). From 50 to 77% of the mutations were predicted to have a medium or high functional effect as determined by the mutation assessor score⁴⁰ (Supplementary Fig. 7.D.1a), and 39% of tyrosine and 42% of serine/threonine kinase mutations were located in the kinase domain. Many of the alterations were in known oncogenes and tumour suppressors, as defined in the COSMIC database (Supplementary Data 7.3).

We selected potential therapeutic targets based on several features, including (1) availability of a US Food and Drug Administration (FDA)-approved targeted therapeutic agent or one under study in current clinical trials (Supplementary Data 7.2); (2) confirmation of the altered allele in RNA sequencing; and (3) the mutation assessor score⁴⁰. Using those criteria, we identified 114 cases with somatic alteration of a potentially targetable gene (64%) (Supplementary Fig. 7.D.1b and Supplementary Data 7.4). Among these, we identified three families of tyrosine kinases, the erythroblastic leukaemia viral oncogene homologues (ERBBs), fibroblast growth factor receptors (FGFRs) and Janus kinases (JAKs), all of which were found to be mutated and/or amplified⁴¹. As discussed for *EGFR*, the mutational spectra in these potential therapeutic targets differed from those in lung adenocarcinoma (Supplementary Fig. 7.D.2)⁴².

To complement a gene-centred search for potential therapeutic targets, we analysed core cellular pathways known to represent potential therapeutic vulnerabilities: PI(3)K/AKT, receptor tyrosine kinase (RTK) and RAS. Analysis of the 178 lung SQCCs revealed alteration in at least one of those pathways in 69% of samples after restriction of the analysis to mutations confirmed by RNA sequencing and to amplifications associated with overexpression of the target gene (Fig. 5). Mutational events that have been curated in COSMIC are also shown in Supplementary Fig. 7D.2, as is the distribution of mutations, amplifications and overexpression of the genes depicted in Fig. 5. (A summary of all samples and their significant mutations and copy number alterations, including alterations in Fig. 5, is shown in Supplementary Data 7.5.) Specifically, one of the components of the PI(3)K/AKT pathway was altered in 47% of tumours and RTK signalling probably affected by events such as *EGFR* amplification, *BRAF* mutation or *FGFR* amplification or mutation in 26% of tumours

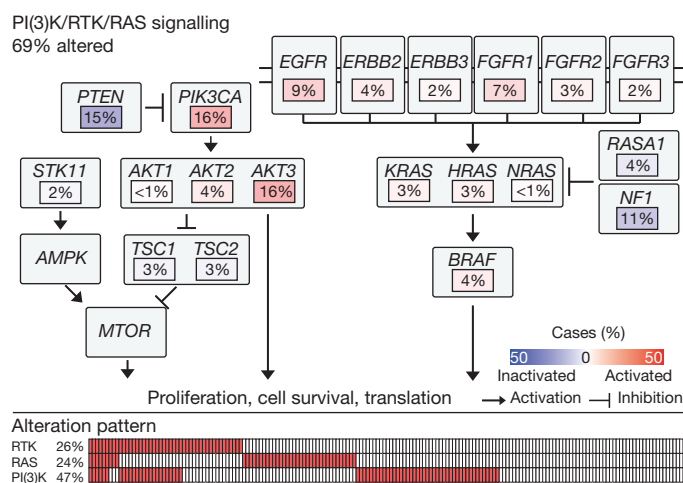


Figure 5 | Alterations in targetable oncogenic pathways in lung SQCCs. Pathway diagram showing the percentage of samples with alterations in the PI(3)K/RTK/RAS pathways. Alterations are defined by somatic mutations, homozygous deletions, high-level, focal amplifications, and, in some cases, by significant up- or downregulation of gene expression (AKT3, FGFR1, PTEN).

(Fig. 5 and Supplementary Fig. 7.D.3). Alterations in the PI(3)K/AKT pathway genes were mutually exclusive with *EGFR* alterations as identified by MEMo⁴³ (Supplementary Fig. 7.D.4). Although the dependence of lung SQCC on many of these individual alterations remains to be defined functionally, this analysis suggests new areas for potential therapeutic development in this cancer.

Discussion

Lung SQCCs are characterized by a high overall mutation rate of 8.1 mutations per megabase and marked genomic complexity. Similar to high-grade serous ovarian carcinoma¹⁷, almost all lung SQCCs display somatic mutation of *TP53*. There were also frequent alterations in the following pathways: *CDKN2A/RB1*, *NFE2L2/KEAP1/CUL3*, *PI3K/AKT* and *SOX2/TP63/NOTCH1* pathways, providing evidence of common dysfunction in cell cycle control, response to oxidative stress, apoptotic signalling and/or squamous cell differentiation. Pathway alterations clustered according to expression-subtype in many cases, suggesting that those subtypes have a biological basis.

A role for somatic mutation in the cancer hallmark of avoiding immune destruction⁴⁴ is suggested by the presence of inactivating mutations in the *HLA-A* gene. Somatic loss-of-function alterations of *HLA-A* have not been reported previously in genomic studies of lung cancer. Given the recently reported efficacy of anti-programmed death 1 (PD1)⁴⁵ and anti-cytotoxic T-lymphocyte antigen 4 (CTLA4) antibodies in non-small-cell lung cancer⁴⁶, these *HLA-A* mutations suggest a possible role for genotypic selection of patients for immunotherapies.

Targeted kinase inhibitors have been successfully used for the treatment of lung adenocarcinoma but minimally so in lung SQCC. The observations reported here suggest that a detailed understanding of the possible targets in lung SQCCs may identify targeted therapeutic approaches. Whereas *EGFR* and *KRAS* mutations, the two most common oncogenic aberrations in lung adenocarcinoma, are extremely rare in lung SQCC, alterations in the FGFR kinase family are common. Lung SQCCs also share many alterations in common with head and neck squamous cell carcinomas without evidence of human papilloma virus infection, including mutation in *PIK3CA*, *PTEN*, *TP53*, *CDKN2A*, *NOTCH1* and *HRAS*^{22,24}, suggesting that the biology of these two diseases may be similar.

The current study has identified a potentially targetable gene or pathway alteration in most lung SQCC samples studied. The data presented here can help to organize efforts to analyse lung SQCC clinical tumour specimens for a panel of specific, actionable mutations to select patients for appropriately targeted clinical trials. These

data could thereby help to facilitate effective personalized therapy for this deadly disease.

METHODS SUMMARY

All specimens were obtained from patients with appropriate consent from the relevant Institutional Review Board. DNA and RNA were collected from samples using the Allprep kit (Qiagen). We used commercial technology for capture and sequencing of exomes from tumour DNA and normal DNA and whole-genome shotgun sequencing. Significantly mutated genes were identified by comparing them with expectation models based on the exact measured rates of specific sequence lesions. GISTIC^{23,24} analysis of the circular-binary-segmented Affymetrix SNP 6.0 copy number data was used to identify recurrent amplification and deletion peaks. Consensus clustering approaches were used to analyse mRNA, miRNA and methylation subtypes using previous approaches^{20,21,34,38,41,44}.

Received 9 March; accepted 9 July 2012.

Published online 9 September 2012.

1. World Health Organization. Cancer, fact sheet no. 297 (<http://www.who.int/mediacentre/factsheets/fs297/en/>) (accessed February 2012).
2. Soda, M. *et al.* Identification of the transforming *EML4-ALK* fusion gene in non-small-cell lung cancer. *Nature* **448**, 561–566 (2007).
3. Paez, J. G. *et al.* EGFR mutations in lung cancer: correlation with clinical response to gefitinib therapy. *Science* **304**, 1497–1500 (2004).
4. Lynch, T. J. *et al.* Activating mutations in the epidermal growth factor receptor underlying responsiveness of non-small-cell lung cancer to gefitinib. *N. Engl. J. Med.* **350**, 2129–2139 (2004).
5. Pao, W. *et al.* EGF receptor gene mutations are common in lung cancers from “never smokers” and are associated with sensitivity of tumors to gefitinib and erlotinib. *Proc. Natl Acad. Sci. USA* **101**, 13306–13311 (2004).
6. Felip, E., Gridelli, C., Baas, P., Rosell, R. & Stahel, R. Metastatic non-small-cell lung cancer: consensus on pathology and molecular tests, first-line, second-line, and third-line therapy. *Ann. Oncol.* **22**, 1507–1519 (2011).
7. Ju, Y. S. *et al.* A transforming *KIF5B* and *RET* gene fusion in lung adenocarcinoma revealed from whole-genome and transcriptome sequencing. *Genome Res.* **22**, 436–445 (2012).
8. Rekhtman, N. *et al.* Clarifying the spectrum of driver oncogene mutations in biomarker-verified squamous carcinoma of lung: lack of *EGFR/KRAS* and presence of *PIK3CA/AKT1* mutations. *Clin. Cancer Res.* **18**, 1167–1176 (2012).
9. Bass, A. J. *et al.* *SOX2* is an amplified lineage-survival oncogene in lung and esophageal squamous cell carcinomas. *Nature Genet.* **41**, 1238–1242 (2009).
10. Ramos, A. H. *et al.* Amplification of chromosomal segment 4q12 in non-small cell lung cancer. *Cancer Biol. Ther.* **8**, 2042–2050 (2009).
11. Shibata, T. *et al.* Cancer related mutations in *NRF2* impair its recognition by Keap1-Cul3 E3 ligase and promote malignancy. *Proc. Natl Acad. Sci. USA* **105**, 13568–13573 (2008).
12. Kan, Z. *et al.* Diverse somatic mutation patterns and pathway alterations in human cancers. *Nature* **466**, 869–873 (2010).
13. Hammerman, P. S., Sos, M. L., Ramos, A. & Xu, C. Mutations in the *DDR2* kinase gene identify a novel therapeutic target in squamous cell lung cancer. *Cancer Discovery* **1**, 78 (2011).
14. Weiss, J. *et al.* Frequent and focal *FGFR1* amplification associates with therapeutically tractable *FGFR1* dependency in squamous cell lung cancer. *Sci. Transl. Med.* **2**, 62ra93 (2010).
15. Dutt, A. *et al.* Inhibitor-sensitive *FGFR1* amplification in human non-small cell lung cancer. *PLoS One* **6**, e20351 (2011).
16. Kenfield, S. A., Wei, E. K., Stampfer, M. J., Rosner, B. A. & Colditz, G. A. Comparison of aspects of smoking among the four histological types of lung cancer. *Tob. Control* **17**, 198–204 (2008).
17. The Cancer Genome Atlas Research Network. Integrated genomic analyses of ovarian carcinoma. *Nature* **474**, 609–615 (2011).
18. The Cancer Genome Atlas Research Network. Comprehensive genomic characterization defines human glioblastoma genes and core pathways. *Nature* **455**, 1061–1068 (2008).
19. Tonon, G. *et al.* High-resolution genomic profiles of human lung cancer. *Proc. Natl Acad. Sci. USA* **102**, 9625–9630 (2005).
20. Beroukhi, R. *et al.* The landscape of somatic copy-number alteration across human cancers. *Nature* **463**, 899–905 (2010).
21. Mermel, C. H. *et al.* GISTIC2.0 facilitates sensitive and confident localization of the targets of focal somatic copy-number alteration in human cancers. *Genome Biol.* **12**, R41 (2011).
22. Stransky, N. *et al.* The mutational landscape of head and neck squamous cell carcinoma. *Science* **333**, 1157–1160 (2011).
23. Chapman, M. A. *et al.* Initial genome sequencing and analysis of multiple myeloma. *Nature* **471**, 467–472 (2011).
24. Agrawal, N. *et al.* Exome sequencing of head and neck squamous cell carcinoma reveals inactivating mutations in *NOTCH1*. *Science* **333**, 1154–1157 (2011).
25. Bass, A. J. *et al.* Genomic sequencing of colorectal adenocarcinomas identifies a recurrent *VTI1A-TCF7L2* fusion. *Nature Genet.* **43**, 964–968 (2011).
26. Berger, M. F. *et al.* The genomic complexity of primary human prostate cancer. *Nature* **470**, 214–220 (2011).
27. Stephens, P. J. *et al.* Complex landscapes of somatic rearrangement in human breast cancer genomes. *Nature* **462**, 1005–1010 (2009).

28. Singh, A. *et al.* Dysfunctional KEAP1–NRF2 interaction in non-small-cell lung cancer. *PLoS Med.* **3**, e420 (2006).
29. Singh, A., Bodas, M., Wakabayashi, N., Bunz, F. & Biswal, S. Gain of Nrf2 function in non-small-cell lung cancer cells confers radioresistance. *Antioxid. Redox Signal.* **13**, 1627–1637 (2010).
30. Vaske, C. J. *et al.* Inference of patient-specific pathway activities from multi-dimensional cancer genomics data using PARADIGM. *Bioinformatics* **26**, i237–i245 (2010).
31. Aster, J. C., Blacklow, S. C. & Pear, W. S. Notch signalling in T-cell lymphoblastic leukaemia/lymphoma and other haematological malignancies. *J. Pathol.* **223**, 263–274 (2011).
32. Wang, N. J. *et al.* Loss-of-function mutations in Notch receptors in cutaneous and lung squamous cell carcinoma. *Proc. Natl Acad. Sci. USA* **108**, 17761–17766 (2011).
33. Osada, H., Tatematsu, Y., Yatabe, Y., Horio, Y. & Takahashi, T. *ASH1* gene is a specific therapeutic target for lung cancers with neuroendocrine features. *Cancer Res.* **65**, 10680–10685 (2005).
34. Wilkerson, M. D. *et al.* Lung squamous cell carcinoma mRNA expression subtypes are reproducible, clinically important, and correspond to normal cell types. *Clin. Cancer Res.* **16**, 4864–4875 (2010).
35. Bishop, J. A. *et al.* p40 (Δ Np63) is superior to p63 for the diagnosis of pulmonary squamous cell carcinoma. *Mod. Pathol.* **25**, 405–415 (2011).
36. Massion, P. P. *et al.* Significance of p63 amplification and overexpression in lung cancer development and prognosis. *Cancer Res.* **63**, 7113–7121 (2003).
37. Shen, R., Olshen, A. B. & Ladanyi, M. Integrative clustering of multiple genomic data types using a joint latent variable model with application to breast and lung cancer subtype analysis. *Bioinformatics* **25**, 2906–2912 (2009).
38. Wikman, H. & Kettunen, E. Regulation of the G1/S phase of the cell cycle and alterations in the RB pathway in human lung cancer. *Expert Rev. Anticancer Ther.* **6**, 515–530 (2006).
39. Kancha, R. K., Peschel, C. & Duyster, J. The epidermal growth factor receptor-L861Q mutation increases kinase activity without leading to enhanced sensitivity toward epidermal growth factor receptor kinase inhibitors. *J. Thorac. Oncol.* **6**, 387–392 (2011).
40. Reva, B., Antipin, Y. & Sander, C. Predicting the functional impact of protein mutations: application to cancer genomics. *Nucleic Acids Res.* **39**, e118 (2011).
41. Govindan, R. Summary of the proceedings from the 10th annual meeting of molecularly targeted therapy in non-small cell lung cancer. *J. Thorac. Oncol.* **5**, S433 (2010).
42. Ding, L. *et al.* Somatic mutations affect key pathways in lung adenocarcinoma. *Nature* **455**, 1069–1075 (2008).
43. Ciriello, G., Cerami, E., Sander, C. & Schultz, N. Mutual exclusivity analysis identifies oncogenic network modules. *Genome Res.* **22**, 398–406 (2012).
44. Hanahan, D. & Weinberg, R. A. Hallmarks of cancer: the next generation. *Cell* **144**, 646–674 (2011).
45. Brahmer, J. R. *et al.* Phase I study of single-agent anti-programmed death-1 (MDX-1106) in refractory solid tumors: safety, clinical activity, pharmacodynamics, and immunologic correlates. *J. Clin. Oncol.* **28**, 3167–3175 (2010).
46. Lynch, T. J. *et al.* Phase II trial of ipilimumab (IPI) and paclitaxel/carboplatin (P/C) in first-line stage IIIb/IV non-small cell lung cancer (NSCLC). *J. Clin. Oncol.* **28**, 7531 (2010).

Supplementary Information is available in the online version of the paper.

Acknowledgements This study was supported by NIH grants U24 CA126561, U24 CA126551, U24 CA126554, U24 CA126543, U24 CA126546, U24 CA126563, U24 CA126544, U24 CA143845, U24 CA143858, U24 CA144025, U24 CA143882, U24 CA143866, U24 CA143867, U24 CA143848, U24 CA143840, U24 CA143835, U24 CA143799, U24 CA143883, U24 CA143843, U54 HG003067, U54 HG003079 and U54 HG003273.

Author Contributions The TCGA research network contributed collectively to this study. Biospecimens were provided by the tissue source sites and processed by the biospecimen core resource. Data generation and analyses were performed by the genome sequencing centres, cancer genome characterization centres and genome data analysis centres. All data were released through the data coordinating centre. Project activities were coordinated by the National Cancer Institute and National Human Genome Research Institute project teams. We also acknowledge the following TCGA investigators who made substantial contributions to the project: P.S.H. and D.N.H. (manuscript coordinators); M.D.W. (data coordinator); P.S.H. and N.S. (analysis coordinators); P.S.H., M.S.L., A. Sivachenko, B.H. and G.G. (DNA sequence analysis); M.D.W., J.L. and D.N.H. (mRNA sequence analysis); L. Cope, J.G.H. and L. Danilova (DNA methylation analysis); A.C., G.S., N.H.P., R.K. and M.L. (copy number analysis); N.S., R. Bose, C.J.C., R. Sinha, C.M., S.N., E.A.C., R. Shen, J.N.W. and C. Sander (pathway analysis); A.C. and G.R. (miRNA sequence analysis); W.D.T., B.E.J., D.A.W. and M.-S.T. (pathology and clinical expertise); S.B.B., R. Govindan and M. Meyerson (project chairs).

Author Information The primary and processed data used to generate the analyses presented here can be downloaded by registered users from The Cancer Genome Atlas (<https://tcga-data.nci.nih.gov/tcga/tcgaDownload.jsp>, <https://cghub.ucsc.edu/> and https://tcga-data.nci.nih.gov/docs/publications/lusc_2012/). Reprints and permissions information is available at www.nature.com/reprints. This paper is distributed under the terms of the Creative Commons Attribution-Non-Commercial-Share Alike licence, and the online version of the paper is freely available to all readers. The authors declare no competing financial interests. Readers are welcome to comment on the online version of the paper. Correspondence and requests for materials should be addressed to M. Meyerson (matthew_meyerson@dfci.harvard.edu).

The Cancer Genome Atlas Research Network (Participants are arranged by area of contribution and then by institution.)

Genome sequencing centres: **Broad Institute** Peter S. Hammerman^{1,2}, Michael S. Lawrence¹, Douglas Voet¹, Rui Jing¹, Kristian Cibulskis¹, Andrey Sivachenko¹, Petar Stojanov¹, Aaron McKenna¹, Eric S. Lander^{1,3,4}, Stacey Gabriel⁵, Gad Getz^{1,5}, Carrie Sougnez⁵, Marcin Imielinski^{1,6}, Elena Helman¹, Bryan Hernandez¹, Nam H. Pho¹, Matthew Meyerson^{1,2,6}

Genome characterization centres: **BC Cancer Agency** Andy Chu⁷, Hye-Jung E. Chun⁷, Andrew J. Mungall⁷, Erin Pleasance⁷, A. Gordon Robertson⁷, Payal Sipahimalani⁷, Dominik Stoll⁷, Miruna Balasundaram⁷, Inanc Birol⁷, Yaron S. N. Butterfield⁷, Eric Chuah⁷, Robin J. N. Coope⁷, Richard Corbett⁷, Noreen Dhalla⁷, Ranabir Guin⁷, An He⁷, Carrie Hirst⁷, Martin Hirst⁷, Robert A. Holt⁷, Darlene Lee⁷, Haiyan I. Li⁷, Michael Mayo⁷, Richard A. Moore⁷, Karen Mungall⁷, Ka Ming Nip⁷, Adam Olshen⁸, Jacqueline E. Schein⁷, Jared R. Slobodan⁷, Angela Tam⁷, Nina Thiessen⁷, Richard Varhol⁷, Thomas Zeng⁷, Yongjun Zhao⁷, Steven J. M. Jones⁷, Marco A. Marra⁷; **Broad Institute** Gordon Saksena¹, Andrew D. Cherniack¹, Stephen E. Schumacher^{1,2}, Barbara Tabak^{1,2}, Scott L. Carter¹, Nam H. Pho¹, Huy Nguyen¹, Robert C. Onofrio³, Andrew Crenshaw¹, Kristin Ardlie⁵, Rameen Beroukhi^{1,2}, Wendy Winckler^{1,5}, Peter S. Hammerman^{1,2}, Gad Getz^{1,5}, Matthew Meyerson^{1,2,6}; **Brigham & Women's Hospital/Harvard Medical School** Alexei Protopopov^{9,10}, Jianhua Zhang^{9,10}, Angela Hadjipanayis^{11,12}, Semin Lee¹³, Ruibin Xi¹³, Lixing Yang¹³, Xiaojia Ren^{9,11,12}, Hailei Zhang^{1,9}, Sachet Shukla^{1,9}, Peng-Chieh Chen^{11,12}, Psalm Haseley^{12,13}, Eunjung Lee^{12,13}, Lynda Chin^{1,2,9,10,14}, Peter J. Park^{12,13,15}, Raju Kucheralapati^{11,12}; **Memorial Sloan-Kettering Cancer Center (TCGA pilot phase only)** Nicholas D. Socci¹⁶, Yupu Liang¹⁶, Nikolaus Schultz¹⁶, Laetitia Borsu¹⁶, Alex E. Lash¹⁶, Agnes Viale¹⁶, Chris Sander¹⁶, Marc Ladanyi^{17,18}; **University of North Carolina at Chapel Hill** J. Todd Auman^{19,20}, Katherine A. Hoadley^{21,22,23}, Matthew D. Wilkerson²³, Yan Shi²³, Christina Liquori²³, Shaowu Meng²³, Ling Li²³, Yidi J. Turman²³, Michael D. Topal^{22,23}, Donghui Tan²⁴, Scot Waring²³, Elizabeth Buda²³, Jesse Walsh²³, Corbin D. Jones²⁵, Piotr A. Mieczkowski²¹, Darshan Singh²³, Junyuan Wu²³, Anisha Gulabani²³, Peter Dolina²³, Tom Bodenheimer²³, Alan P. Hoyle²³, Janae V. Simons²³, Matthew G. Soloway²³, Lisle E. Mose²², Stuart R. Jefferys²², Saianand Balu²³, Brian D. O'Connor²³, Jan F. Prins²⁶, Jinze Liu²⁷, Derek Y. Chiang^{21,23}, D. Neil Hayes^{23,28}, Charles M. Perou^{21,22,23}; **University of Southern California/Johns Hopkins** Leslie Cope²⁹, Ludmila Danilova²⁹, Daniel J. Weisenberger³⁰, Dennis T. Maglinte³⁰, Fei Pan³⁰, David J. Van Den Berg³⁰, Timothy Triche Jr³⁰, James G. Herman²⁹, Stephen B. Baylin²⁹, Peter W. Laird³⁰

Genome data analysis centres: **Broad Institute** Gad Getz^{1,5}, Michael Noble¹, Doug Voet¹, Gordon Saksena¹, Nils Gehlenborg^{1,13}, Daniel DiCara¹, Jinhua Zhang^{9,10}, Hailei Zhang¹, Chang-Jiun Wu^{2,10}, Spring Yingchun Liu², Michael S. Lawrence¹, Lihua Zou¹, Andrey Sivachenko¹, Pei Lin¹, Petar Stojanov¹, Rui Jing¹, Juok Cho¹, Marc-Danie Nazaire¹, Jim Robinson¹, Helga Thorvaldsdottir¹, Jill Mesirov¹, Peter J. Park^{12,13,15}, Lynda Chin^{12,9,10,14}; **Memorial Sloan-Kettering Cancer Center** Nikolaus Schultz¹⁶, Rileen Sinha¹⁶, Giovanni Ciriello¹⁶, Ethan Cerami¹⁶, Benjamin Gross¹⁶, Anders Jacobsen¹⁶, Jianjiang Gao¹⁶, B. Arman Aksoy¹⁶, Nils Weinhold¹⁶, Ricardo Ramirez¹⁶, Barry S. Taylor¹⁶, Yevgeniy Antipin¹⁶, Boris Reva¹⁶, Ronglai Shen³¹, Qianxing Mo³¹, Venkatraman Seshan³¹, Paul K. Paik³², Marc Ladanyi^{17,18}, Chris Sander¹⁶; **The University of Texas MD Anderson Cancer Center** Rehan Akbani³³, Nianxiang Zhang³³, Bradley M. Broom³³, Tod Casasent³³, Anna Unruh³³, Chris Wakefield³³, R. Craig Cason³⁴, Keith A. Baggerly³³, John N. Weinstein^{33,35}; **University of California Santa Cruz/Buck Institute** David Haussler^{36,37}, Christopher C. Benz³⁸, Joshua M. Stuart³⁶, Jingchun Zhu³⁶, Christopher Szeto³⁶, Gary K. Scott³⁸, Christina Yau³⁸, Sam Ng³⁶, Ted Goldstein³⁶, Peter Waltman³⁶, Artem Sokolov³⁶, Kyle Ellrott³⁶, Eric A. Collisson³⁹, Daniel Zerbino³⁶, Christopher Wilks³⁶, Singer Ma³⁶, Brian Craft³⁶; **University of North Carolina at Chapel Hill** Matthew D. Wilkerson²³, J. Todd Auman^{19,20}, Katherine A. Hoadley^{21,22,23}, Ying Du²³, Christopher Cabanski²³, Vonn Walter²³, Darshan Singh²³, Junyuan Wu²³, Anisha Gulabani²³, Tom Bodenheimer²³, Alan P. Hoyle²³, Janae V. Simons²³, Matthew G. Soloway²³, Lisle E. Mose²², Stuart R. Jefferys²², Saianand Balu²³, J. S. Marron⁴⁰, Yufeng Liu²⁴, Kai Wang²⁷, Jinze Liu²⁷, Jan F. Prins²³, D. Neil Hayes^{23,28}, Charles M. Perou^{21,22,23}; **Baylor College of Medicine** Chad J. Creighton⁴¹, Yiqun Zhang⁴¹

Pathology committee William D. Travis⁴², Natasha Rekhtman⁴², Joanne Yi⁴³, Marie C. Aubry⁴⁵, Richard Cheney⁴⁴, Sanja Dacic⁴⁵, Douglas Flieder⁴⁶, William Funkhouser⁴⁷, Peter Illei⁴⁸, Jerome Myers⁴⁹, Ming-Sound Tsao⁵⁰

Biospecimen core resources: **International Genomics Consortium** Robert Penny⁵¹, David Mallery⁵¹, Troy Shelton⁵¹, Martha Hatfield⁵¹, Scott Morris⁵¹, Peggy Yena⁵¹, Candace Shelton⁵¹, Mark Sherman⁵¹, Joseph Paulauskis⁵¹

Disease working group Matthew Meyerson^{1,2,6}, Stephen B. Baylin²⁹, Ramaswamy Govindan⁵², Rehan Akbani³³, Ijeoma Azodo⁵³, David Beer⁵⁴, Ron Bose⁵², Lauren A. Byers⁵⁵, David Carbone⁵⁶, Li-Wei Chang⁵², Derek Chiang^{21,23}, Andy Chu⁷, Elizabeth Chun⁷, Eric Collisson³⁹, Leslie Cope²⁹, Chad J. Creighton⁴¹, Ludmila Danilova²⁹, Li Ding⁵², Gad Getz^{1,5}, Peter S. Hammerman^{1,2}, D. Neil Hayes^{23,28}, Bryan Hernandez¹, James G. Herman²⁹, John Heymach⁵⁵, Cristiane Ida⁴³, Marcin Imielinski^{1,6}, Bruce Johnson², Igor Jurisica⁵⁷, Jacob Kaufman⁵⁶, Farhad Kosari⁵³, Raju Kucheralapati^{11,12}, David Kwiatkowski^{17,18}, Marc Ladanyi^{17,18}, Michael S. Lawrence¹, Christopher A. Maher⁵², Andy Mungall⁷, Sam Ng³⁶, William Pao⁵⁶, Martin Peifer^{58,59}, Robert Penny⁵¹, Gordon Robertson⁷, Valerie Rusch⁶⁰, Chris Sander¹⁶, Nikolaus Schultz¹⁶, Ronglai Shen³¹, Jill Siegfried⁶¹, Rileen Sinha¹⁶, Andrey Sivachenko¹, Carrie Sougnez⁴, Dominik Stoll⁷, Joshua Stuart³⁶, Roman K. Thomas^{58,59,62}, Sandra Tomaszek⁵³, Ming-Sound Tsao⁵⁰,

William D. Travis⁴², Charles Vaske³⁶, John N. Weinstein^{33,35}, Daniel Weisenberger³⁰, David Wheeler⁶³, Dennis A. Wigle⁵³, Matthew D. Wilkerson²³, Christopher Wilks⁵⁰, Ping Yang⁵³, Jianjua John Zhang^{9,10}

Data coordination centre Mark A. Jensen⁶⁴, Robert Sfeir⁶⁴, Ari B. Kahn⁶⁴, Anna L. Chu⁶⁴, Prachi Kothiyal⁶⁴, Zhining Wang⁶⁴, Eric E. Snyder⁶⁴, Joan Pontius⁶⁴, Todd D. Pihl⁶⁴, Brenda Ayala⁶⁴, Mark Backus⁶⁴, Jessica Walton⁶⁴, Julien Baboud⁶⁴, Dominique L. Berton⁶⁴, Matthew C. Nicholls⁶⁴, Deepak Srinivasan⁶⁴, Rohini Raman⁶⁴, Stanley Girshik⁶⁴, Peter A. Kigonya⁶⁴, Shelley Alonso⁶⁴, Rashmi N. Sanbhadhi⁶⁴, Sean P. Barletta⁶⁴, John M. Greene⁶⁴, David A. Pot⁶⁴

Tissue source sites Ming-Sound Tsao⁵⁰, Bizhan Bandarchi-Chamkhaleh⁵⁰, Jeff Boyd⁴⁶, JoEllen Weaver⁴⁶, Dennis A. Wigle⁵³, Jeoma A. Azodo⁵³, Sandra C. Tomaszek⁵³, Marie Christine Aubry⁶⁵, Christiane M. Ida⁶⁵, Ping Yang⁶⁶, Farhad Kosari⁵³, Malcolm V. Brock⁶⁷, Kristen Rogers⁶⁷, Marian Rutledge⁶⁸, Travis Brown⁶⁷, Beverly Lee⁶⁸, James Shin⁶⁹, Dante Trusty⁶⁹, Rajiv Dhir⁷⁰, Jill M. Siegfried⁶¹, Olga Potapova⁷¹, Konstantin V. Fedosenko⁷², Elena Nemirovich-Danchenko⁷¹, Valerie Rusch⁶⁰, Maureen Zakowski⁷³, Mary V. Iacocca⁷⁴, Jennifer Brown⁷⁴, Brenda Rabeno⁷⁴, Christine Czerwinski⁷⁴, Nicholas Petrelli⁷⁴, Zhen Fan⁷⁵, Nicole Todaro⁷⁵, John Eckman⁷⁵, Jerome Myers⁷⁵, W. Kimryn Rathmell⁷⁵, Leigh B. Thorne⁷⁶, Mei Huang⁷⁶, Lori Boice⁷⁶, Ashley Hill²³, Robert Penny⁵¹, David Mallory⁵¹, Erin Curley⁵¹, Candace Shelton⁵¹, Peggy Yena⁵¹, Carl Morrison⁴⁴, Carmelo Gaudioso⁴⁴, John M. S. Bartlett⁷⁷, Sugy Kodeeswaran⁷⁷, Brent Zanke⁷⁷, Harman Sekhon⁷⁸, Kerstin David⁷⁹, Hartmut Juhl⁸⁰, Xuan Van Le⁸¹, Bernard Koh⁸¹, Richard Thorp⁸¹, Nguyen Viet Tien⁸², Nguyen Van Bang⁸³, Howard Sussman⁸⁴, Bui Duc Phu⁸³, Richard Hajek⁸⁵, Nguyen Phi Hung⁸⁶, Khuram Z. Khan⁸⁷, Thomas Muley⁸⁸

Project team: National Cancer Institute Kenna R. Mills Shaw⁸⁹, Margi Sheth⁸⁹, Liming Yang⁸⁹, Ken Buetow⁹⁰, Tanja Davidson⁹⁰, John A. Demchok⁸⁹, Greg Eley⁹⁰, Martin Ferguson⁹¹, Laura A. L. Dillon⁸⁹, Carl Schaefer⁹⁰, **National Human Genome Research Institute** Mark S. Guyer⁹², Bradley A. Ozenberger⁹², Jacqueline D. Palchik⁹², Jane Peterson⁹², Heidi J. Sofia⁹², Elizabeth Thomson⁹²

Writing committee Peter S. Hammerman^{1,2}, D. Neil Hayes^{23,28}, Matthew D. Wilkerson²³, Nikolaus Schultz¹⁶, Ron Bose⁵², Andy Chu⁷, Eric A. Collisson³⁹, Leslie Cope²⁹, Chad J. Creighton⁴¹, Gad Getz^{1,5}, James G. Herman²⁹, Bruce E. Johnson², Raju Kucheralapati^{11,12}, Marc Ladanyi^{17,18}, Christopher A. Maher⁵², Gordon Robertson⁷, Chris Sander¹⁶, Ronglai Shen¹⁶, Rileen Sinha¹⁶, Andrey Sivachenko³, Roman K. Thomas^{58,59,62}, William D. Travis⁴², Ming-Sound Tsao⁵⁰, John N. Weinstein^{33,35}, Dennis A. Wigle⁵³, Stephen B. Baylin²⁹, Ramaswamy Govindan⁵², Matthew Meyerson^{1,2,6}

¹The Eli and Edythe L. Broad Institute of Massachusetts Institute of Technology and Harvard University Cambridge, Massachusetts 02142, USA. ²Department of Medical Oncology, Dana-Farber Cancer Institute, Boston, Massachusetts 02215, USA. ³Department of Biology, Massachusetts Institute of Technology, Cambridge, Massachusetts 02142, USA. ⁴Department of Systems Biology, Harvard University, Boston, Massachusetts 02115, USA. ⁵Genetic Analysis Platform, The Eli and Edythe L. Broad Institute of Massachusetts Institute of Technology and Harvard University, Cambridge, Massachusetts 02142, USA. ⁶Department of Pathology, Harvard Medical School, Boston, Massachusetts 02115, USA. ⁷Canada's Michael Smith Genome Sciences Centre, BC Cancer Agency, Vancouver, British Columbia V5Z, Canada. ⁸Department of Epidemiology and Biostatistics, University of California, San Francisco, San Francisco, California 94143, USA. ⁹Belfer Institute for Applied Cancer Science, Department of Medical Oncology, Dana-Farber Cancer Institute, Boston, Massachusetts 02115, USA. ¹⁰Institute for Applied Cancer Science, Department of Genomic Medicine, The University of Texas MD Anderson Cancer Center, Houston, Texas 77030, USA. ¹¹Department of Genetics, Harvard Medical School, Boston, Massachusetts 02115, USA. ¹²Division of Genetics, Brigham and Women's Hospital, Boston, Massachusetts 02115, USA. ¹³The Center for Biomedical Informatics, Harvard Medical School, Boston, Massachusetts 02115, USA. ¹⁴Department of Dermatology, Harvard Medical School, Boston, Massachusetts 02115, USA. ¹⁵Informatics Program, Children's Hospital, Boston, Massachusetts 02115, USA. ¹⁶Computational Biology Center, Memorial Sloan-Kettering Cancer Center, New York, New York 10065, USA. ¹⁷Department of Molecular Oncology, Memorial Sloan-Kettering Cancer Center, New York, New York 10065, USA. ¹⁸Department of Pathology and Human Oncology & Pathogenesis Program, Memorial Sloan-Kettering Cancer Center, New York, New York 10065, USA. ¹⁹Eshelman School of Pharmacy, University of North Carolina at Chapel Hill, Chapel Hill, North Carolina 27599, USA. ²⁰Institute for Pharmacogenetics and Individualized Therapy, University of North Carolina at Chapel Hill, Chapel Hill, North Carolina 27599, USA. ²¹Department of Genetics, University of North Carolina at Chapel Hill, Chapel Hill, North Carolina 27599, USA. ²²Department of Pathology and Laboratory Medicine, University of North Carolina at Chapel Hill, Chapel Hill, Chapel Hill, North Carolina 27599, USA. ²³Lineberger Comprehensive Cancer Center, University of North Carolina at Chapel Hill, Chapel Hill, North Carolina 27599, USA. ²⁴Carolina Center for Genome Sciences, University of North Carolina at Chapel Hill, Chapel Hill, North Carolina 27599, USA. ²⁵Department of Biology, University of North Carolina at Chapel Hill, Chapel Hill, North Carolina 27599, USA. ²⁶Department of Computer Science, University of North Carolina at Chapel Hill, Chapel Hill, North Carolina 27599, USA. ²⁷Department of Computer Science, University of

Kentucky, Lexington, Kentucky 40506, USA. ²⁸Department of Internal Medicine, Division of Medical Oncology, University of North Carolina at Chapel Hill, Chapel Hill, North Carolina 27599, USA. ²⁹Cancer Biology Division, The Sidney Kimmel Comprehensive Cancer Center at Johns Hopkins University, Baltimore, Maryland 21231, USA. ³⁰University of Southern California Epigenome Center, University of Southern California, Los Angeles, California 90033, USA. ³¹Department of Epidemiology and Biostatistics, Memorial Sloan-Kettering Cancer Center, New York, New York 10065, USA. ³²Department of Medicine, Memorial Sloan-Kettering Cancer Center, New York, New York 10065, USA. ³³Department of Bioinformatics and Computational Biology, The University of Texas MD Anderson Cancer Center, Houston, Texas 77030, USA. ³⁴Division of Pathology and Laboratory Medicine, The University of Texas MD Anderson Cancer Center, Houston, Texas 77030, USA. ³⁵Department of Systems Biology, The University of Texas MD Anderson Cancer Center, Houston, Texas 77030, USA. ³⁶Department of Biomolecular Engineering and Center for Biomolecular Science and Engineering, University of California Santa Cruz, Santa Cruz, California 95064, USA. ³⁷Howard Hughes Medical Institute, University of California Santa Cruz, Santa Cruz, California 95064, USA. ³⁸Buck Institute for Age Research, Novato, California 94945, USA. ³⁹Division of Hematology/Oncology, University of California San Francisco, San Francisco, California 94143, USA. ⁴⁰Department of Statistics and Operations Research, University of North Carolina Medical Center, Chapel Hill, North Carolina 27599, USA. ⁴¹Human Genome Sequencing Center and Dan L. Duncan Cancer Center Division of Biostatistics, Baylor College of Medicine, Houston, Texas 77030, USA. ⁴²Department of Pathology, Memorial Sloan Kettering Cancer Center, New York, New York 10065 USA. ⁴³Department of Pathology, Mayo Clinic, Rochester, Minnesota 55905, USA. ⁴⁴Department of Pathology, Roswell Park Cancer Institute, Buffalo, New York 14263, USA. ⁴⁵Department of Pathology, University of Pittsburgh Cancer Center, Pittsburgh, Pennsylvania 15213, USA. ⁴⁶Department of Pathology, Fox Chase Cancer Center, Philadelphia, Pennsylvania 19111, USA. ⁴⁷Department of Pathology, University of North Carolina Medical Center, Chapel Hill, North Carolina 27599, USA. ⁴⁸Department of Pathology, Johns Hopkins University School of Medicine, Baltimore, Maryland 21287, USA. ⁴⁹Department of Pathology, Penrose-St. Francis Health System, Colorado Springs, Colorado 80907, USA. ⁵⁰Department of Pathology and Medical Biophysics, Ontario Cancer Institute and Princess Margaret Hospital, Toronto, Ontario M5G 2M9, Canada. ⁵¹International Genomics Consortium, Phoenix, Arizona 85004, USA. ⁵²Division of Oncology, Department of Medicine and The Genome Institute, Washington University School of Medicine, St. Louis, Missouri 63110, USA. ⁵³Center for Individualized Medicine, Mayo Clinic, Rochester, Minnesota 55905, USA. ⁵⁴Department of Surgery, University of Michigan, Ann Arbor, Michigan 48109, USA. ⁵⁵The University of Texas MD Anderson Cancer Center, Houston, Texas 77030, USA. ⁵⁶Departments of Hematology/Oncology and Cancer Biology, Vanderbilt University School of Medicine, Nashville, Tennessee 37232, USA. ⁵⁷Ontario Cancer Institute, IBM Life Sciences Discovery Centre, Toronto, Ontario M5G 1L7, Canada. ⁵⁸Department of Translational Genomics, University of Cologne, Cologne D-50931, Germany. ⁵⁹Max Planck Institute for Neurological Research, Cologne D-50866, Germany. ⁶⁰Department of Surgery, Memorial Sloan Kettering Cancer Center, New York, New York 10065, USA. ⁶¹Department of Pharmacology and Chemical Biology, University of Pittsburgh Medical Center, Pittsburgh, Pennsylvania 15232, USA. ⁶²Department of Translational Cancer Genomics, Center of Integrated Oncology, University of Cologne, Cologne D-50924, Germany. ⁶³Human Genome Sequencing Center, Baylor College of Medicine, Houston, Texas 77030, USA. ⁶⁴SRA International, Fairfax, Virginia 22033, USA. ⁶⁵Department of Laboratory Medicine and Pathology, Mayo Clinic, Rochester, Minnesota 55905, USA. ⁶⁶Department of Health Sciences Research, Mayo Clinic, Rochester, Minnesota 55905, USA. ⁶⁷Department of Surgery, Johns Hopkins School of Medicine, 600 North Wolfe Street, Baltimore, Maryland 21287, USA. ⁶⁸Department of Oncology, Johns Hopkins School of Medicine, 600 North Wolfe Street, Baltimore, Maryland 21287, USA. ⁶⁹Department of Pathology, Johns Hopkins School of Medicine, 600 North Wolfe Street, Baltimore, Maryland 21287, USA. ⁷⁰Department of Pathology, University of Pittsburgh, Pittsburgh, Pennsylvania 15213, USA. ⁷¹Cureline, South San Francisco, California 94080, USA. ⁷²City Clinical Oncology Dispensary, St Petersburg 197022, Russia. ⁷³Department of Pathology, Memorial Sloan Kettering Cancer Center, New York, New York 10065, USA. ⁷⁴Helen F. Graham Cancer Center, Newark, Delaware 19713, USA. ⁷⁵St Joseph Medical Center, Towson, Maryland 21204, USA. ⁷⁶UNC Tissue Procurement Facility, Department of Pathology, UNC Lineberger Cancer Center, Chapel Hill, North Carolina 27599, USA. ⁷⁷Ontario Tumour Bank, Ontario Institute for Cancer Research, Toronto, Ontario M5G 0A3, Canada. ⁷⁸Ontario Tumour Bank – Ottawa site, The Ottawa Hospital, Ottawa, Ontario K1H 8L6, Canada. ⁷⁹Indivumed GmbH, Hamburg, Falkenried 88, Haus D D-20251, Germany. ⁸⁰Indivumed Inc, Kensington, Maryland 20895, USA. ⁸¹ILSBio, LLC, Chestertown, Maryland 21620, USA. ⁸²Ministry of Health, 138A Giang Vo Street, Hanoi, Vietnam. ⁸³Hue Central Hospital, Hue City, 16 Le Loi, Hue, Vietnam. ⁸⁴Stanford University Medical Center, Stanford, California 94305, USA. ⁸⁵Center for Minority Health Research, University of Texas, M.D. Anderson Cancer Center, Houston, Texas 77030, USA. ⁸⁶National Cancer Institute, 43 Quan Su Street, Hanoi, Vietnam. ⁸⁷ILSBio LLC, Chestertown, Maryland 21620, USA. ⁸⁸ThoraxKlinik, Heidelberg University Hospital, Heidelberg 69126, Germany. ⁸⁹The Cancer Genome Atlas Program Office, National Cancer Institute, National Institutes of Health, Bethesda, Maryland 20892, USA. ⁹⁰Center for Biomedical Informatics and Information Technology (CBIIIT), National Cancer Institute, National Institutes of Health, Rockville, Maryland 20852, USA. ⁹¹MLF Consulting, Arlington, Maryland 02474, USA. ⁹²National Human Genome Research Institute, National Institutes of Health, Bethesda, Maryland 20892, USA.

Cross-neutralization of influenza A viruses mediated by a single antibody loop

Damian C. Ekiert^{1†*}, Arun K. Kashyap^{2*}, John Steel^{3†}, Adam Rubrum⁴, Gira Bhabha¹, Reza Khayat¹, Jeong Hyun Lee¹, Michael A. Dillon^{2†}, Ryann E. O'Neil^{2†}, Aleksandr M. Faynboym², Michael Horowitz², Lawrence Horowitz², Andrew B. Ward¹, Peter Palese³, Richard Webby⁴, Richard A. Lerner^{5,6}, Ramesh R. Bhatt² & Ian A. Wilson^{1,6}

Immune recognition of protein antigens relies on the combined interaction of multiple antibody loops, which provide a fairly large footprint and constrain the size and shape of protein surfaces that can be targeted. Single protein loops can mediate extremely high-affinity binding, but it is unclear whether such a mechanism is available to antibodies. Here we report the isolation and characterization of an antibody called C05, which neutralizes strains from multiple subtypes of influenza A virus, including H1, H2 and H3. X-ray and electron microscopy structures show that C05 recognizes conserved elements of the receptor-binding site on the haemagglutinin surface glycoprotein. Recognition of the haemagglutinin receptor-binding site is dominated by a single heavy-chain complementarity-determining region 3 loop, with minor contacts from heavy-chain complementarity-determining region 1, and is sufficient to achieve nanomolar binding with a minimal footprint. Thus, binding predominantly with a single loop can allow antibodies to target small, conserved functional sites on otherwise hypervariable antigens.

Antibody recognition of protein antigens is predominantly mediated by four to six complementarity-determining regions (CDRs), which are the variable loops at the tip of each Fab. The relatively large footprint of antibodies on their target antigens (~700–900 Å² for proteins) generally correlates with high-affinity binding. However, for neutralizing antibodies against variable pathogens, a larger footprint may result in increased opportunity for escape mutations that reduce antibody binding. Moreover, functionally conserved sites on otherwise variable antigens may be small, as for the influenza virus receptor-binding site; partially protected by glycans, as with both the HIV-1 glycoprotein gp120 and influenza; or are sterically restricted and difficult for antibodies to access, such as the picornavirus 'canyon'¹ or the gp120 co-receptor-binding site on HIV-1 (ref. 2). By contrast, non-immunoglobulin proteins can also achieve high-affinity binding in other ways that may have distinct advantages for targeting small, constrained surfaces. For example, bovine pancreatic trypsin inhibitor (BPTI) attains exceptionally high-affinity binding (K_d at fM levels) to serine proteases by inserting a single loop into the enzyme active site³. In light of the increasingly long heavy-chain CDR3 (HCDR3) loops being found in humans^{4–6}, a BPTI-like binding mechanism may be structurally accessible to antibodies, allowing insertion of a single loop into a pocket. However, no clear example of an antibody using such a binding mechanism has been reported.

Two conserved and functionally important sites on the haemagglutinin (HA) stem have been targeted by antibodies previously, including epitopes recognized by the broadly neutralizing antibodies A06 (refs 7 and 8), CR6261 (refs 9 and 10), F10 (ref. 11), CR8020 (ref. 12) and F16 (ref. 13). Several recent studies have suggested that stem antibodies may be present in a greater number of individuals than

previously thought^{14,15}, and the ability to re-elicite stem antibodies by immunization¹⁶ has raised hopes that a universal vaccine for influenza A may be achievable. Although such antibodies against the stem are highly cross-reactive, most antibodies that target the more variable receptor-binding domain (RBD) of the HA1 subunit show limited breadth of neutralization. Crystal structures show that, although a few antibody footprints on the HA1 RBD sometimes coincide with the receptor-binding site^{17–20}, many of the essential interactions are made with hypervariable regions well outside of the functionally conserved region involved in sialic acid recognition^{21,22}. However, recent work suggests that some rare antibodies against the HA1 RBD can achieve modest cross-reactivity^{20,23,24}. Thus, identification and structural understanding of heterosubtypic antibodies against the RBD with broad activity, particularly against human pandemic viruses (influenza H1, H2 and H3 subtypes), would be a major advance and facilitate development of new therapeutics complementary to those targeting the stem. Here we report the functional and structural characterization of one such antibody, C05, which neutralizes multiple subtypes by inserting an extended CDR loop into the receptor-binding pocket.

Isolation and characterization of C05

Previously, we isolated antibodies from phage-displayed combinatorial libraries derived from Turkish patients who survived H5N1 avian flu infection^{7,8} and identified a new class of antibodies effective against a broad range of group 1 influenza A viruses. Here we used a similar approach to identify antibodies that would neutralize both group 1 and group 2 viruses. Phage libraries constructed from the immune repertoires of seasonal influenza infection survivors were doubly selected

¹Department of Molecular Biology, The Scripps Research Institute, 10550 North Torrey Pines Road, La Jolla, California 92037, USA. ²Sea Lane Biotechnologies, 2450 Bayshore Parkway, Mountain View, California 94043, USA. ³Department of Microbiology, Mount Sinai School of Medicine, 1 Gustave Levy Place, New York, New York 10029-6574, USA. ⁴Department of Infectious Diseases, St Jude Children's Research Hospital, 262 Danny Thomas Place, Memphis, Tennessee 38105, USA. ⁵Department of Chemistry, The Scripps Research Institute, 10550 North Torrey Pines Road, La Jolla, California 92037, USA. ⁶The Skaggs Institute for Chemical Biology, The Scripps Research Institute, 10550 North Torrey Pines Road, La Jolla, California 92037, USA. †Present addresses: Department of Microbiology and Immunology, University of California-San Francisco, 600 16th Street, San Francisco, California 94143, USA (D.C.E.); Genentech Inc., 1 DNA Way, South San Francisco, California 94080, USA (M.A.D.); Novartis Institutes for Biomedical Research, 4560 Horton Street, Emeryville, California 94608, USA (R.E.O.); Department of Microbiology and Immunology, Emory University School of Medicine, 3103 Rollins Research Center, 1510 Clifton Road, 194-001-1AD, Atlanta, Georgia 30322, USA (J.S.).

*These authors contributed equally to this work.

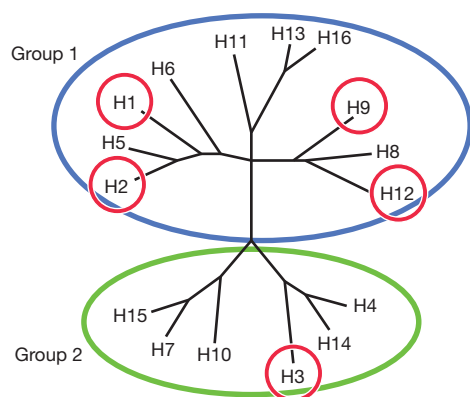


Figure 1 | C05 neutralizes multiple influenza virus subtypes from groups 1 and 2. Phylogenetic tree with the two main viral lineages indicated; group 1 is circled in blue and group 2 is circled in green. Strains from subtypes circled in red are bound or neutralized by C05.

against HA proteins from H1 (group 1) and H3 (group 2). This process yielded a limited number of clones that reacted broadly with both H1 and H3 HA proteins. One clone, C05, which uses the V_{H3-23} and $V_{K1-33*01}$ heavy- and light-chain V genes, respectively, has two distinctive structural features: a long 24-amino-acid HCDR3 (Supplementary Fig. 1) and a five-residue somatic insertion in HCDR1. C05 potently neutralizes viruses from H1, H2, H3 and H9 subtypes *in vitro* (Fig. 1 and Table 1a), including the influenza A subtypes that have caused human pandemics. However, C05 had no detectable activity against the H5 subtype, as well as some of the H1 viruses tested. In sharp contrast to most broadly neutralizing antibodies to influenza^{9–11,25}, which bind the more conserved stem region, C05 inhibits receptor binding and haemagglutination (Table 1a), indicating recognition of an epitope in the HA1 globular head domain.

Protection *in vivo*

To explore the *in vivo* efficacy of C05, we examined its ability to protect mice from lethal challenge with H1N1 or H3N2 viruses. When administered prophylactically 24 h before challenge with the A/Memphis/3/2008 (H1N1) virus, 1 mg kg^{-1} C05 IgG protected 100% of mice from death and prevented substantial weight loss (Fig. 2a). Lower doses (0.025 – 0.25 mg kg^{-1}) still afforded proportional protection (Supplementary Fig. 2a). For the A/X-31/1968 (H3N2) virus, a 10 mg kg^{-1} dose protected 100% of the mice from death (Fig. 2b), and both 0.25 and 1.0 mg kg^{-1} doses afforded protection to the majority (Supplementary Fig. 2b).

Next we determined the therapeutic potential of C05 against an established H1N1 or H3N2 infection. A single 15 mg kg^{-1} IgG dose was administered at 1, 2, 3, 4 or 5 days after lethal challenge with the aforementioned H1N1 or H3N2 viruses. In both instances, mice treated up to 3 days after infection were completely protected (Fig. 2c, d). We then evaluated the minimal dose needed to overcome established infection 3 days after inoculation, the latest time at which C05 treatment was completely protective against death. As little as a single 3 mg kg^{-1} dose of antibody prevented infection-related death in 80% of the animals (Supplementary Fig. 2c). These *in vivo* results indicate the utility of C05 in both prevention and treatment.

Avidity is critical for C05 function

To further profile its breadth of activity, we tested C05 Fab binding to a large panel of HAs by biolayer interferometry (BLI), including representative members of most of the 16 influenza subtypes. C05 Fab binds to a number of diverse HAs spanning both group 1 and group 2 viruses, including members of the H1, H2, H3, H9 and H12 subtypes (Table 1b). Notably, many HAs from viruses neutralized by IgG C05 are bound with only intermediate-to-low affinity by the Fab ($K_d \sim 100 \text{ nM}$ – $10 \mu\text{M}$),

Table 1 | C05 binds and neutralizes multiple group 1 and group 2 influenza A viruses

a C05 neutralizes group 1 and group 2 influenza viruses <i>in vitro</i>				
Group	Subtype	Strain	MIC (μg ml ⁻¹)	
1	H1N1	A/Virginia/670/1987	>100*	
		A/Texas/36/1991	>100*	
		A/New Caledonia/20/1999	<0.1*	
		A/Solomon Islands/2006	1.56*	
		A/Brisbane/59/2007	1.56*	
		A/Memphis/3/2008	<2.3*	
		A/California/04/2009	>100*	
		A/Guizhou/1/1957	18†	
	H5N1	A/Vietnam/1203/2004	>100*	
H9N2	A/Hong Kong/1073/1999	90†		
2	H3N2	A/X-31/1968	<0.1*	
		A/Panama/2007/1999	0.39*	
		A/Wisconsin/67/2005	<0.1*	
		A/Brisbane/10/2007	12.5*	

b C05 binding to group 1 and group 2 influenza HAs					
Group	Subtype	Strain	C05	CR6261	CR8020
1	H1N1	A/South Carolina/1/1918	—	++++	—
1	H1N1	A/New York/1/1918	—	++++	—
1	H1N1	A/AA/Marton/1943	—	++++	—
1	H1N1	A/USSR/90/1977	—	++++	—
1	H1N1	A/Singapore/6/1986	+	++++	—
1	H1N1	A/Texas/36/1991	—	++++	—
1	H1N1	A/Beijing/262/1995	+++	++++	—
1	H1N1	A/Solomon Islands/3/2006	+++	++++	—
1	H2N2	A/Japan/305/1957	+++	++	—
1	H2N2	A/Adachi/2/1957	+++	++	—
1	H5N1	A/Vietnam/1203/2004	—	++++	—
1	H5N1	A/Indonesia/05/2005	—	++++	—
1	H6N2	A/turkey/Massachusetts/3740/1965	—	++++	—
1	H9N2	A/turkey/Wisconsin/1/1966	+++	++++	—
1	H12N5	A/duck/Alberta/60/1976	+	—	—
1	H13N6	A/gull/Maryland/704/1977	—	++++	—
1	H16N3	A/black-headed gull/Sweden/4/99	—	+++	—
2	H3N2	A/duck/Ukraine/1/1963	—	—	++++
2	H3N2	A/Hong Kong/1/1968	++	—	++++
2	H3N2	A/Bangkok/1/1979	—	—	++++
2	H3N2	A/Victoria/3/1975	—	—	++++
2	H3N2	A/Beijing/353/1989	—	—	++++
2	H3N2	A/Shangdong/9/1993	—	—	++++
2	H3N2	A/Panama/2007/1999	++	—	++++
2	H3N2	A/Moscow/10/1999	++	—	++++
2	H3N2	A/Brisbane/10/2007	+	—	++++
2	H3N2	A/Perth/16/2009	++++	—	++++
2	H4N6	A/duck/Czechoslovakia/1956	—	—	++
2	H7N7	A/Netherlands/219/2003	—	—	++++
2	H10N7	A/chicken/Germany/N/1949	—	—	++++
2	H14N5	A/mallard/Astrakhan/263/1982	—	—	++
2	H15N8	A/shearw./W.Australia/2576/1979	—	—	+++

c C05 shows unusually low affinity for some HAs from neutralized viruses

Group	Subtype	Strain	C05 K_d (nM)		MIC ($\mu\text{g ml}^{-1}$)
			BLI	ITC	
2	H3N2	A/Perth/16/2009	18	26	ND
		A/Hong Kong/1/1968	430	100	<0.1
		A/Panama/2007/1999	720	225	0.4
		A/Brisbane/10/2007	>5,000	~10,000	12.5

Dissociation constants: ++ $K_d \geq 5,000 \text{ nM}$; +++ $K_d = 500$ – $5,000 \text{ nM}$; ++++ $K_d = 50$ – 500 nM ;

+++++ $K_d \leq 50 \text{ nM}$.

MIC, minimum inhibitory concentration; ND, not determined.

* Haemagglutination inhibition.

† Microneutralization.

well outside the range typically required for effective neutralization, such as by stem antibodies ($K_d < 100 \text{ nM}$)^{10,12}. To confirm these unexpected results, we selected four HAs from neutralized viruses that bound C05 Fab with a range of affinities ($K_d = 18 \text{ nM}$, 430 nM , 720 nM , and one with no detectable Fab binding by BLI) and assessed C05 binding in solution by isothermal titration calorimetry (ITC). The ITC results were in good agreement with the K_d measured by BLI (Table 1c). Notably,

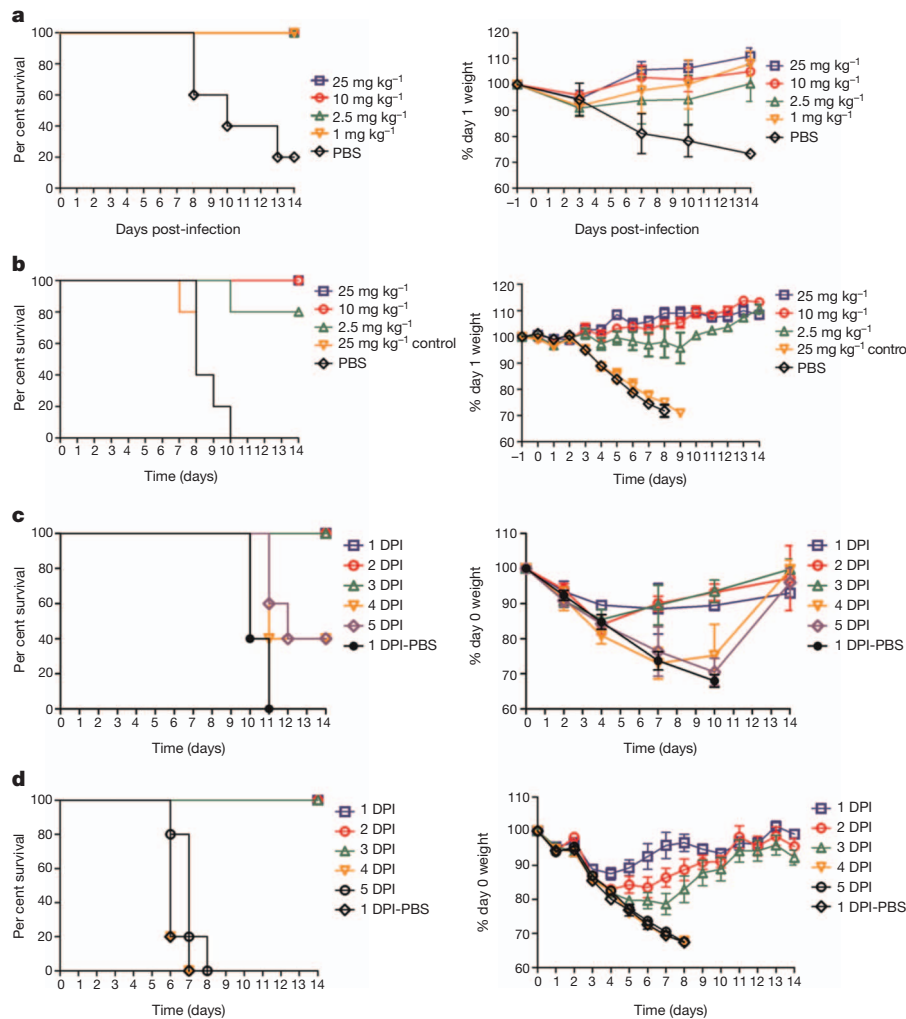


Figure 2 | C05 protects mice from lethal virus challenge. **a, b,** Survival and weight loss were monitored in response to varying amounts of C05 IgG administered prophylactically to mice 24 h before challenge with 25× the 50% mouse lethal dose (MLD_{50}) of A/Memphis/3/2008 (H1N1) (**a**) or 33× MLD_{50}

of A/X-31/1968 (H3N2) viruses (**b**). **c, d,** A single therapeutic dose of 15 mg kg^{-1} C05 IgG was delivered 1, 2, 3, 4 or 5 days post-infection (DPI) with 25× MLD_{50} of A/Memphis/3/2008 (**c**) or 33× MLD_{50} of A/X-31/1968 viruses (**d**). $n = 5$ mice for all studies. Error bars denote \pm s.d.

although only very weak binding ($K_d \sim 10 \mu\text{M}$) of C05 Fab to A/Brisbane/10/2007 (H3N2) HA was detected by ITC (undetectable by BLI), the corresponding virus was neutralized by C05 IgG *in vitro* (Table 1c). Thus, despite the unusually low affinity of C05 Fab for many of its targets, C05 IgG potentially neutralizes virus replication *in vitro* and is protective *in vivo*. To the best of our knowledge, only one other neutralizing antibody has been reported with such a considerable discrepancy between binding affinity and neutralization. The broadly neutralizing anti-HIV antibody 2G12 binds a high-mannose glycan cluster on the gp120 subunit of the HIV surface spike, but its affinity for a single high-mannose glycan is very low (K_d at μM levels)²⁶. However, a highly unusual domain-swapping of the Fabs allows 2G12 to bind multiple glycans simultaneously and thereby achieve high-affinity binding (nM levels) through avidity²⁷. For C05, the presence of multiple antibody-binding sites on each trimeric HA spike and the high density of HA on the virus surface may facilitate simultaneous engagement of both arms of the C05 IgG, resulting in much higher avidity compared with Fab. Electron microscopy experiments with H1, H2 and H3 HAs show that three C05 Fabs are bound per trimer (Fig. 3f), but their geometry is inconsistent with bivalent attachment by an IgG antibody. Indeed, C05 IgG binds to an array of immobilized HA with much higher affinity (nM to \sim pM levels) than its Fab, consistent with the single-particle electron microscopy analysis confirming the ability of IgG to cross-link HA spikes (Supplementary Fig. 3). Thus,

some antibodies with low-affinity Fab interactions can still have strong activity *in vitro* and *in vivo* and may represent an under-appreciated component of the immune repertoire. The role of avidity may be more or less pronounced depending on the nature of the epitope and the density of the antigen on the viral surface, with clustered epitopes, such as those on the HA1 RBD, benefiting most from avidity, whereas sterically crowded (for example, HA stem) or sparse epitopes (HIV envelope spikes) probably prevent bivalent binding. In the latter case, high-affinity binding must be achieved by the Fab or by heterologation of two different antigens, which may have a more prominent role in the neutralization of human viruses such as HIV²⁸.

Crystal structure of the C05–HA complex

To understand how the antibody C05 achieves heterosubtypic neutralization, we determined the crystal structure of C05 Fab in complex with the HA1 subunit from the A/Hong Kong/1/1968 (HK68/H3) influenza strain at 2.95 Å resolution, and Fab C05 in complex with the complete, trimeric ectodomain of HK68/H3 at 4.25 Å (Supplementary Table 1). In addition, high-resolution structures of HK68/H3 HA (1.90 Å) and C05 Fab (2.30 Å) provided high-quality starting models for refinement of the complexes. Few differences are apparent between the isolated HA1 and the HA1 subunit in trimeric HA, as in other HA1 crystal structures¹⁸. Further, the C05–HA1 and C05–HA trimer structures are in excellent

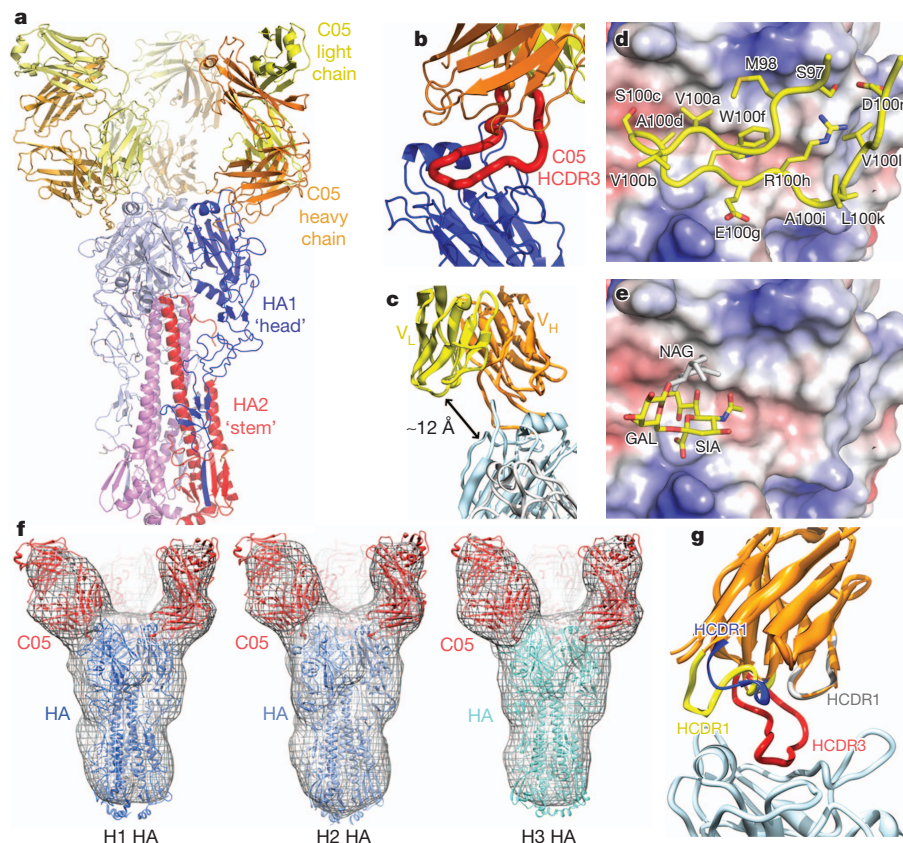


Figure 3 | C05 binds the receptor-binding site on the HA1 head. **a**, Crystal structures of C05 Fab in complex with trimeric HA and an HA1 fragment reveal the location of the C05 epitope in the HA1 'head' region. The C05 Fab heavy (orange) and light (yellow) chains and the HA1 (blue) and HA2 (red) subunits are depicted as ribbons. **b**, C05 inserts its long HCDR3 (red) into the receptor-binding site. **c**, C05 binds HA using only its heavy chain. **d**, **e**, Interaction of the HA receptor-binding pocket (in a solid electrostatic surface representation) with HCDR3 from C05 (in yellow backbone with side chains labelled by residue type and number) (**d**) and with an $\alpha 2,6$ sialoglycan receptor (derived from Protein Data Bank entry 1MQN), with an additional carbohydrate residue

modelled in grey (**e**). The binding site for the C05 H3 loop and the glycan receptor overlap extensively. **f**, Three-dimensional electron microscopy reconstructions of C05 Fab (red) bound, from left to right, to H1 (blue), H2 (light blue) and H3 (cyan) HAs. The fitting of H1, H2 and H3 crystal structures into the reconstructions support a common binding mode of C05 to each of the HAs studied. **g**, In addition to its long HCDR3 (red), C05 has a five-residue insertion in HCDR1 (yellow), extending the tip of this loop relative to the germline-encoded canonical conformation. For comparison, a sequence-related Fab structure (Protein Data Bank code 2VXS) without an insertion in HCDR1 (blue loop) is superimposed onto C05.

agreement (Supplementary Fig. 4), indicating that the C05–HA1 complex faithfully recapitulates the native interaction.

Three C05 Fabs bind near the membrane-distal end of the HA trimeric spike (Fig. 3a), and HCDR3 penetrates the receptor-binding site (Fig. 3b). Several notable features of the C05 interaction are immediately apparent, and the exceptionally long 24-residue HCDR3 of C05 dominates the antibody–antigen interaction (Fig. 3b). Although $\sim 1.5\%$ of human antibodies in the Abys database have an HCDR3 of 24 or more residues, only 3 of the over 1,000 Fab structures in the Protein Data Bank have more than 24-residue HCDR3s (Supplementary Fig. 5). Very long CDRs can adopt unusual conformations, such as the 'hammerhead' structure in PG9 and PG16^{4,6,29}, and these long loops are presumably crucial for antigen recognition, yet few structures of such antibodies bound to antigen have been reported. The C05 structure therefore gives us a valuable glimpse at how long HCDR3s can be used to target recessed or evolutionarily constrained epitopes.

The long HCDR3 of C05 extends far from the antibody surface, with its most distal end forming a β -hairpin. The long HCDR3 holds the V_H and V_L domains at a distance from the HA surface (Fig. 3c), preventing the light chain from contacting the epitope, reminiscent of the heavy-chain-dominant recognition by stem-directed V_{H1-69} antibodies^{9,11}. At a first approximation, the C05 HCDR3 resembles the PG9 and PG16 hammerheads, but with its shorter carboxy-terminal branch truncated (Supplementary Fig. 6). The HCDR3 β -hairpin inserts into the shallow HA receptor-binding pocket near

the HA spike apex (Fig. 3d). HCDR3 overlaps with the binding site for glycan receptors, indicating that C05 inhibits virus attachment by direct competition with sialic acid (Fig. 3e). However, C05 interaction with the receptor-binding site differs considerably from sialic acid binding to HA.

Aside from HCDR3, only HCDR1 makes additional minor interactions with HA, in part owing to a five-residue somatic insertion (Fig. 3g and Supplementary Fig. 1). Insertions and deletions (indels) within the V gene coding region are relatively rare^{30,31}, but recent work suggests that these indels may be selected during affinity maturation and can be important for antibody function^{32,33}. Consistent with the minor contacts made by HCDR1, removal of the five-residue insert (del(FGEST)) or scanning mutagenesis of HCDR1 had no detectable effect on C05 binding to HK68/H3 and several other H1, H2 and H3 HAs (Table 2 and Supplementary Table 2), whereas binding of C05(del(FGEST)) to the HA of H3 influenza subtype strain Perth09 was reduced nearly 100-fold compared with wild-type C05 (Table 2), indicating that HCDR1 may make additional interactions with Perth09 (see discussion in Supplementary Information and Supplementary Fig. 7). Thus, the HCDR1 insertion is dispensable for binding to most HAs tested, whereas the HCDR3 loop alone is sufficient for full activity. However, nearby antibody CDRs and framework regions probably contribute to binding by supporting HCDR3, as the loop conformation is essentially identical in the crystal structure of C05 Fab alone. In particular, the tip of HCDR2 interacts with the

Table 2 | Effect of HCDR1 mutations on C05 binding

Strain	Dissociation constants (K_d , nM)							
	C05 variant							
	WT	del(FGEST)	F27bA	G27cA	E27dA	T31F	T31L	T31A
A/Hong Kong/1/1968 (H3N2)	500	690	610	450	540	420	1,400	640
A/Perth/13/2009 (H3N2)	18	1,300	460	33	28	6.8	560	550

WT, wild type.

backside of the HCDR3 loop and harbours several somatic mutations that may have arisen to best position and stabilize HCDR3 for HA binding (Supplementary Fig. 8). By contrast, HCDR1 seems to have a lesser role, as the above mutations above did not prevent C05 binding.

Loop-insertion binding mechanism

Despite high sequence diversity immediately surrounding the receptor-binding site, the functional constraints imposed by binding to sialic acid receptors restrict variation within the pocket itself. Thus, although other antibodies can bind in or near the receptor-binding site, a typical antibody footprint would extend well beyond the conserved functional region and contact at least some variable positions around the receptor-binding site, rendering them largely strain specific and susceptible to escape through antigenic drift. A notable exception is CH65, which cross-neutralizes an unusually large subset of H1N1 viruses, but not other subtypes²⁰. However, unlike C05, CH65 binds HA using both heavy and light chains (including five of the six CDR loops), which increases contact with these more variable surfaces (Supplementary Fig. 9). By contrast, the long HCDR3 of C05 targets the conserved elements of the receptor-binding site, and enters and exits the pocket without contacting many of the surrounding variable positions (Fig. 4a, b). Indeed, we were unable to generate C05 escape mutants with an H3 virus despite repeated attempts.

Loop insertion is a common mechanism for achieving high-affinity protein–protein interactions, as notably illustrated by BPTI³. Owing to the restricted, single-CDR-driven interaction of C05 with HK68/H3 HA, only 550 Å² of surface area is buried on the HA by C05, which is unusually small for an antibody–protein interaction. This small footprint allows C05 to achieve broader cross-reactivity compared with other antibodies that extend their interface outside of the receptor-binding site (for example, ~650 Å² buried surface on HA for CH65 and 740 Å² for 2D1; Supplementary Table 3). Single-particle three-dimensional electron microscopy reconstructions of C05 bound to H1, H2 and H3 HAs (Fig. 3f and Supplementary Fig. 10), along with binding experiments probing the effect of several mutations in the HCDR3 loop (Supplementary Fig. 11), clearly illustrate that binding to other subtypes is probably very similar to that in the H3 crystal structure.

Epitope conservation and variation linked to escape

The wide range of affinities for C05 against a panel of HAs indicates that epitope variation has a considerable effect on C05 activity. Therefore, we examined that sequence diversity contained within all full-length, non-redundant human H1, H2 and H3 HA sequences in the NCBI Flu database³⁴. An analysis including all 16 virus subtypes yielded similar results (Supplementary Table 4). Of 17 C05 contact residues on HA, 6 core residues are ≥99% conserved across human H1, H2 and H3 viruses, including 98, 134, 136, 153, 190 and 194 (Fig. 4a, b). The remaining 11 positions are generally <50% conserved (ranging from 42 to 76%). Therefore, the C05 epitope is markedly less conserved (mean % identity/mean % conservation across all contact residues is 59%/64%) compared with stem epitopes recognized by broadly neutralizing antibodies (76%/86% for CR6261 and 71%/80% for CR8020), owing to greater variation within the receptor-binding site. Thus, the range of observed affinities for C05 binding to H3 HAs may arise from multiple, subtle mutations (increasing K_d two- to tenfold) that in combination tune C05 affinity for HA and ultimately reduce binding below the threshold of detection in some cases. Substitutions at HA1 190, 225, 226 and 228 are important for determining receptor specificity in HAs adapted to particular hosts (for example, α2-3 versus α2-6 sialoglycans for avian versus human viruses, respectively), and mutations modulating receptor affinity are a well-documented mechanism of antibody escape³⁵. C05 makes only minor contacts with Leu 226 and does not contact residues 225 or 228. C05 interacts more extensively with Asp 190 in HK68/H3, but Asp, Glu and Val are present at position 190 in our panel of HAs bound by C05. Thus, C05 may bind equally well to HAs with either α2,3 or α2,6 receptor specificity, but variability within the receptor-binding site may account for some of the observed heterogeneity in C05 binding.

Several common indels are close to the receptor-binding site and may affect antibody binding (Supplementary Fig. 12). Insertions at position 133a result in a local bulge that clashes directly with C05 HCDR3 and probably abrogates binding. This insertion is observed in 100% of all H6 and H10, 96% of all H5 and 66% of all H1 subtype sequences. Consistent with this observation, no H5 viruses tested were

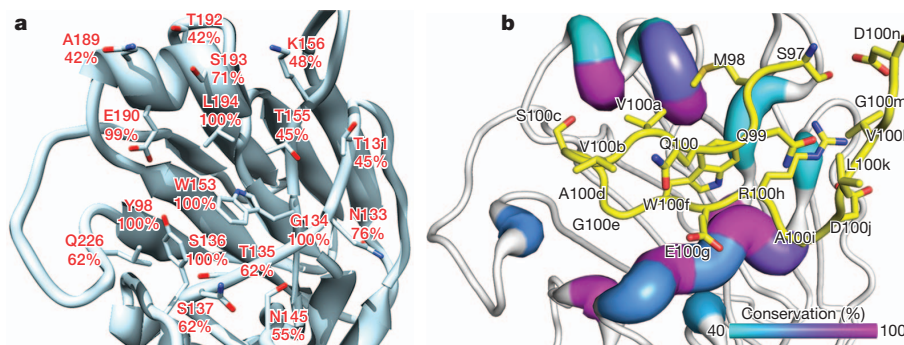


Figure 4 | C05 epitope conservation across influenza A viruses. **a**, Owing to the functional constraints imposed on the receptor-binding site by interaction with sialoglycans, many of the residues that make up the C05 epitope are conserved among human influenza viruses. C05 contact residues are depicted as sticks and the per cent conservation of each position across human H1, H2 and H3 viruses—the subtypes that have caused pandemics and epidemics in

humans—is shown. **b**, Similar to the view in **a**, but includes the position of the C05 HCDR3 (yellow ribbon and sticks) relative to the epitope variation that is colour coded on the HA backbone (with warmer colours indicating higher conservation). Contact residues on HA are depicted with a thick tube for their backbone, and non-contacting regions of HA are shown as a thin white ribbon.

neutralized and binding to H6, H10 and multiple H5 isolates was undetectable, even with 10 μ M IgG. Similarly, C05 binding to five different H1 HAs with the 133a insertion was undetectable with 10 μ M IgG, and only very weak binding was observed to a sixth (A/Singapore/6/1986); no viruses with the insertion were neutralized. By contrast, all H1 HAs without the 133a insertion were bound and/or neutralized by C05. Thus, the 133a insertion seems to negatively affect binding of C05, similar to the effect of the 133a insertion on CH65 (ref. 20). In addition, indels near position 158 and the 220-loop correlate with poor activity against H4, H6, H7, H10, H14 and H16 subtypes (Supplementary Fig. 12). These insights have enabled us to delineate the most important structural requirements for high-affinity cross-reactive binding to the receptor-binding site.

Implications for antiviral therapeutics and vaccine design

Because C05 binding is accomplished exclusively through the heavy chain, and primarily through HCDR3, its interaction with HA defines a minimal set of contacts sufficient for cross-group neutralization, which may be exploited to develop antiviral therapeutics. The ability of a broadly neutralizing antibody, such as C05, to penetrate the shallow receptor-binding site with relatively high affinity (μ M to nM levels) and avidity (nM) compared with its natural receptor (mM) makes such an antibody extremely attractive for therapeutics and diagnostics. C05 was discovered from a single human donor source library using the power of phage-display library technology to isolate this rare antibody-binding interaction. Owing to the combinatorial nature of antibody library construction, we cannot determine explicitly whether the C05 heavy chain and light chain pairing previously existed in the donor. However, other receptor-binding site antibodies, such as CH65 (ref. 20), have been isolated from B cells, showing that receptor-binding site antibodies can be found naturally and are potentially inducible by vaccination strategies. Thus, the design of HA immunogens to elicit more broadly neutralizing head antibodies may now be more feasible and will complement the arsenal of already promising stem antibodies for use in a more universal vaccine, as well as in structure-based and computational approaches to design small proteins and other possible therapeutics against flu, such as already achieved against the stem epitope³⁶.

METHODS SUMMARY

Isolation of C05. Phage antibody libraries were cloned from the bone marrow of donors with confirmed influenza virus exposure. Phages were selected by sequential panning against A/Wisconsin/67/05 (H3N2) followed by A/New Caledonia/20/1999 (H1N1).

Neutralization. Microneutralization and HA-inhibition assays were carried out according to standard protocols, as described in detail in Methods.

In vivo protection in mice. Animal experiments were performed in accordance with the guidelines of the Mount Sinai School of Medicine and St Jude Children's Research Hospital Institutional Animal Care and Use Committees (IACUC). All animal experiments were done essentially as described in ref. 8. Virus strains used in these studies were A/Memphis/3/2008 (H1N1) and A/X-31/1968 (H3N2). 5–6-week-old BALB/c mice were used for the H1N1 studies and 8-week-old DBA/2 mice for the H3N2 studies.

Proteins. Antibodies were expressed in *Escherichia coli*, baculovirus and mammalian cells as described in Methods. HAs were expressed in baculovirus as previously described in ref. 12 or purchased from Protein Sciences Corp.

Binding data. Binding of C05 IgG or Fab to recombinant HAs and K_d determination was performed by BLI, ITC and enzyme-linked immunosorbent assay.

Structure determination. Robotic crystal screening was carried out using the Rigaku Crystalman system at the Joint Center for Structural Genomics. Diffraction data were collected at the Advanced Photon Source GM/CA-CAT 23ID-B and 23ID-D and SSRL 11-1 beamlines and processed using HKL2000 (HKL Research) and XPREP (Bruker). Structures were solved by molecular replacement using Phaser, adjusted using Coot and refined in Phenix. Kabat numbering was applied using Abnum³⁷. Structural analyses were performed using programs MS and CONTACSYM.

Sequences. PDB antibody sequences were analysed through the Abysis database. HA sequence data sets were downloaded from the NCBI Flu database³⁴, aligned

with MUSCLE³⁸ and analysed using Genetics Computer Group (Accelrys) and custom shell scripts.

Full Methods and any associated references are available in the online version of the paper.

Received 23 December 2011; accepted 13 July 2012.

Published online 16 September 2012.

- Smith, T. J., Chase, E. S., Schmidt, T. J., Olson, N. H. & Baker, T. S. Neutralizing antibody to human rhinovirus 14 penetrates the receptor-binding canyon. *Nature* **383**, 350–354 (1996).
- Labrijn, A. F. *et al.* Access of antibody molecules to the conserved coreceptor binding site on glycoprotein gp120 is sterically restricted on primary human immunodeficiency virus type 1. *J. Virol.* **77**, 10557–10565 (2003).
- Rühlmann, A., Kukla, D., Schwager, P., Bartels, K. & Huber, R. Structure of the complex formed by bovine trypsin and bovine pancreatic trypsin inhibitor. Crystal structure determination and stereochemistry of the contact region. *J. Mol. Biol.* **77**, 417–436 (1973).
- McLellan, J. S. *et al.* Structure of HIV-1 gp120 V1/V2 domain with broadly neutralizing antibody PG9. *Nature* **480**, 336–343 (2011).
- Pejchal, R. *et al.* A potent and broad neutralizing antibody recognizes and penetrates the HIV glycan shield. *Science* **334**, 1097–1103 (2011).
- Pejchal, R. *et al.* Structure and function of broadly reactive antibody PG16 reveal an H3 subdomain that mediates potent neutralization of HIV-1. *Proc. Natl Acad. Sci. USA* **107**, 11483–11488 (2010).
- Kashyap, A. K. *et al.* Combinatorial antibody libraries from survivors of the Turkish H5N1 avian influenza outbreak reveal virus neutralization strategies. *Proc. Natl Acad. Sci. USA* **105**, 5986–5991 (2008).
- Kashyap, A. K. *et al.* Protection from the 2009 H1N1 pandemic influenza by an antibody from combinatorial survivor-based libraries. *PLoS Pathogens* **6**, e1000990 (2010).
- Ekiert, D. C. *et al.* Antibody recognition of a highly conserved influenza virus epitope. *Science* **324**, 246–251 (2009).
- Throsby, M. *et al.* Heterosubtypic neutralizing monoclonal antibodies cross-protective against H5N1 and H1N1 recovered from human IgM⁺ memory B cells. *PLoS ONE* **3**, e3942 (2008).
- Sui, J. *et al.* Structural and functional bases for broad-spectrum neutralization of avian and human influenza A viruses. *Nature Struct. Mol. Biol.* **16**, 265–273 (2009).
- Ekiert, D. C. *et al.* A highly conserved neutralizing epitope on group 2 influenza A viruses. *Science* **333**, 843–850 (2011).
- Corti, D. *et al.* A neutralizing antibody selected from plasma cells that binds to group 1 and group 2 influenza A hemagglutinins. *Science* **333**, 850–856 (2011).
- Corti, D. *et al.* Heterosubtypic neutralizing antibodies are produced by individuals immunized with a seasonal influenza vaccine. *J. Clin. Invest.* **120**, 1663–1673 (2010).
- Wrammert, J. *et al.* Broadly cross-reactive antibodies dominate the human B cell response against 2009 pandemic H1N1 influenza virus infection. *J. Exp. Med.* **208**, 181–193 (2011).
- Wei, C. J. *et al.* Induction of broadly neutralizing H1N1 influenza antibodies by vaccination. *Science* **329**, 1060–1064 (2010).
- Barbey-Martin, C. *et al.* An antibody that prevents the hemagglutinin low pH fusogenic transition. *Virology* **294**, 70–74 (2002).
- Fleury, D., Wharton, S. A., Skehel, J. J., Knossow, M. & Bizebard, T. Antigen distortion allows influenza virus to escape neutralization. *Nature Struct. Biol.* **5**, 119–123 (1998).
- Xu, R. *et al.* Structural basis of preexisting immunity to the 2009 H1N1 pandemic influenza virus. *Science* **328**, 357–360 (2010).
- Whittle, J. R. *et al.* Broadly neutralizing human antibody that recognizes the receptor-binding pocket of influenza virus hemagglutinin. *Proc. Natl Acad. Sci. USA* **108**, 14216–14221 (2011).
- Fleury, D. *et al.* A complex of influenza hemagglutinin with a neutralizing antibody that binds outside the virus receptor binding site. *Nature Struct. Biol.* **6**, 530–534 (1999).
- Fleury, D., Daniels, R. S., Skehel, J. J., Knossow, M. & Bizebard, T. Structural evidence for recognition of a single epitope by two distinct antibodies. *Proteins* **40**, 572–578 (2000).
- Yoshida, R. *et al.* Cross-protective potential of a novel monoclonal antibody directed against antigenic site B of the hemagglutinin of influenza A viruses. *PLoS Pathog.* **5**, e1000350 (2009).
- Ohshima, N. *et al.* Naturally occurring antibodies in humans can neutralize a variety of influenza virus strains, including H3, H1, H2, and H5. *J. Virol.* **85**, 11048–11057 (2011).
- Okuno, Y., Isegawa, Y., Sasao, F. & Ueda, S. A common neutralizing epitope conserved between the hemagglutinins of influenza A virus H1 and H2 strains. *J. Virol.* **67**, 2552–2558 (1993).
- Lee, H. *et al.* Reactivity-based one-pot synthesis of oligomannoses: defining antigens recognized by 2G12, a broadly neutralizing anti-HIV-1 antibody. *Angew. Chem. Int. Ed.* **43**, 1000–1003 (2004).
- Calarese, D. A. *et al.* Antibody domain exchange is an immunological solution to carbohydrate cluster recognition. *Science* **300**, 2065–2071 (2003).
- Mouquet, H. *et al.* Polyreactivity increases the apparent affinity of anti-HIV antibodies by heterologation. *Nature* **467**, 591–595 (2010).
- Pancera, M. *et al.* Crystal structure of PG16 and chimeric dissection with somatically related PG9: structure–function analysis of two quaternary-specific antibodies that effectively neutralize HIV-1. *J. Virol.* **84**, 8098–8110 (2010).

30. Wilson, P. C. *et al.* Somatic hypermutation introduces insertions and deletions into immunoglobulin V genes. *J. Exp. Med.* **187**, 59–70 (1998).
31. de Wildt, R. M., van Venrooij, W. J., Winter, G., Hoet, R. M. & Tomlinson, I. M. Somatic insertions and deletions shape the human antibody repertoire. *J. Mol. Biol.* **294**, 701–710 (1999).
32. Krause, J. C. *et al.* An insertion mutation that distorts antibody binding site architecture enhances function of a human antibody. *mBio* **2**, e00345–10 (2011).
33. Zhou, T. *et al.* Structural basis for broad and potent neutralization of HIV-1 by antibody VRC01. *Science* **329**, 811–817 (2010).
34. Bao, Y. *et al.* The influenza virus resource at the National Center for Biotechnology Information. *J. Virol.* **82**, 596–601 (2008).
35. Hensley, S. E. *et al.* Hemagglutinin receptor binding avidity drives influenza A virus antigenic drift. *Science* **326**, 734–736 (2009).
36. Fleishman, S. J. *et al.* Computational design of proteins targeting the conserved stem region of influenza hemagglutinin. *Science* **332**, 816–821 (2011).
37. Abhinandan, K. R. & Martin, A. C. Analysis and improvements to Kabat and structurally correct numbering of antibody variable domains. *Mol. Immunol.* **45**, 3832–3839 (2008).
38. Edgar, R. C. MUSCLE: multiple sequence alignment with high accuracy and high throughput. *Nucleic Acids Res.* **32**, 1792–1797 (2004).

Supplementary Information is available in the online version of the paper.

Acknowledgements We thank H. Tien and D. Marciano for automated crystal screening, the staff of the Advanced Photon Source (APS) GM/CA-CAT and Stanford Synchrotron Radiation Lightsource (SSRL) BL11-1 for beamline support, X. Dai and R. Stanfield for assistance with data collection and processing, M. Hothorn for assistance with ITC experiments, J. Paulson and D. Burton for comments and discussion, A. Estelles and R. Briante, L. Xu, S. Wang and D. Corn for technical support and P. Foreman for assistance with animal study design. This project was funded in part by National Institutes of Health (NIH) grant P01AI058113 (I.A.W.), a predoctoral fellowship from the Achievement Rewards for College Scientists Foundation (D.C.E.), grant GM080209 from the NIH Molecular Evolution Training Program (D.C.E.), the Skaggs Institute (I.A.W.), a career development fellowship from the Northeast Biodefense Center (U54-AI057158-Lipkin) (J.S.), National Institute of Allergy and Infectious Diseases (NIAID) grant U01AI070373 (R.W.), and Center for Research on Influenza Pathogenesis NIAID contract HHSN266200700010C (P.P.). Portions of this

research were carried out at the SSRL, a national user facility operated by Stanford University on behalf of the US Department of Energy (DOE), Office of Basic Energy Sciences. The SSRL Structural Molecular Biology Program is supported by the DOE Office of Biological and Environmental Research and by the NIH, National Center for Research Resources, Biomedical Technology Program, and the National Institute of General Medical Sciences (NIGMS). The GM/CA-CAT 23-ID-B beamline has been funded in whole or in part with federal funds from the National Cancer Institute (Y1-CO-1020) and NIGMS (Y1-GM-1104). Use of the APS was supported by the US Department of Energy, Basic Energy Sciences, Office of Science, under contract no. DE-AC02-06CH11357. The electron microscopy data presented here was collected at the National Resource for Automated Molecular Microscopy, which is supported by the NIH through the P41 program (RR017573) at the National Center for Research Resources. The JCSG is supported by NIH grant U54 GM094586. The content is solely the responsibility of the authors and does not necessarily represent the official views of NIGMS or the NIH. This is publication 21421 from The Scripps Research Institute.

Author Contributions A.K.K., M.A.D., R.E.O., A.M.F., M.H., L.H., R.A.L. and R.R.B. isolated and performed the initial characterization of C05; A.K.K., J.S., A.R., P.P. and R.W. designed and performed virus neutralization and *in vivo* experiments; D.C.E., M.A.D., R.E.O., A.M.F. and A.K.K. expressed and purified proteins; D.C.E. determined and analysed the crystal structures with guidance from I.A.W.; G.B., D.C.E., M.A.D., R.E.O., A.M.F. and A.K.K. performed binding experiments; R.K., J.H.L. and A.B.W. carried out electron microscopy studies; D.C.E. and A.K.K. analysed the sequence data sets and D.C.E., I.A.W., R.R.B. and A.K.K. wrote the manuscript. All authors commented on the paper.

Author Information Coordinates and structure factors have been deposited in the Protein Data Bank under PDB codes 4FNK, 4FNL, 4FP8 and 4FQR. Electron microscopy maps have been deposited in the Electron Microscopy Data Bank (accession numbers 2138, 2139 and 2140). Nucleotide sequences for the C05 variable regions have been deposited in GenBank under accession numbers JX206996 and JX206997. Reprints and permissions information is available at www.nature.com/reprints. The authors declare competing financial interests: details are available in the online version of the paper. Readers are welcome to comment on the online version of the paper. Correspondence and requests for materials should be addressed to I.A.W. (wilson@scripps.edu) or R.R.B. (ramesh.bhatt@sealanebio.com).

METHODS

HA protein and whole-virus enzyme-linked immunosorbent assay. Recombinant HA proteins: H5 protein, A/Vietnam/1203/2004 (Protein Sciences), 10 ng per well; recombinant HA H1 protein, A/ New Caledonia/20/99 (Protein Sciences), 10 ng per well; recombinant HA H3 protein, A/Wisconsin/67/05 (Protein Sciences), 10 ng per well; H1N1 virus, A/New Caledonia (BioSource), 70 ng per well; H3N2 virus, A/Panama/2007/99 (BioSource), 10 ng per well.

Enzyme-linked immunosorbent assay (ELISA)-inactivated virus was incubated overnight at room temperature (20–22 °C). The next day plates were blocked (1% bovine serum albumin in PBS buffer and 0.05% Tween-20) and 0.1 ml serum samples (diluted in blocking buffer) were incubated, washed and detected using a peroxidase-conjugated anti-human Fc antibody (Jackson ImmunoResearch) and tetramethyl benzidine detection (BioFX). Attenuance at $D_{450\text{ nm}}$ was read, and data recorded is reported herein.

Library construction. Antibody phage-display libraries were created from the individual immune repertoires of confirmed influenza infection survivors. Bone marrow aspirates were collected and stored in RNAlater (Ambion) to preserve RNA integrity until processing for library construction. Serum samples were taken from each individual and used to confirm antibody reactivity to various HA proteins or inactivated influenza viruses by ELISA (Supplementary Fig. 13). The phage-display libraries were constructed as previously described in ref. 7.

Selection of HA-binding clones. Phage antibody library panning was done essentially as described in ref. 7. Cross-reactive antibodies were identified by selection on both H3 and H1 HA protein antigens. After two rounds of panning on H3 HA A/Wisconsin/67/05, H1 HA protein from A/New Caledonia/20/1999 replaced the H3 HA protein for two additional rounds. A fifth and final round of selection was performed on the H3 HA protein.

IgG expression and Fabs. The C05 heavy- and light-chain regions were mammalian-codon-optimized, synthesized (GeneArt) and cloned into the pTT5-based expression vectors. Expression was done essentially as described in ref. 7. The C05 Fab fragment was obtained by Lys-C digestion of IgG, followed by purification by protein A (GE Healthcare), protein G (GE Healthcare), cation exchange (MonoS, GE Healthcare) and gel filtration (Superdex 200, GE Healthcare). For binding studies, C05 Fab was expressed recombinantly using the baculovirus system. A DNA fragment derived from the promoter region of pFastBac-Dual (Invitrogen) was fused to the gp67 and the honey bee melittin (HBM) signal peptides by overlap PCR, yielding a fragment with head-to-head p10 and polyhedrin promoters upstream of the HBM and gp67 signal peptides, respectively (that is, HBM-p10-pPolyH-gp67). C05 Fab heavy- and light-chain regions were synthesized (GenScript), fused to the promoter-signal peptide cassette by overlap PCR (heavy chain downstream of pPolyH-gp67 and light chain downstream of p10-HBM) and ligated into the SfiI sites of a derivative of pFastBacDual. A His₆ tag was introduced at the C terminus of the light chain to facilitate purification.

Mutations to probe the importance of the CDR H1 insertion were generated by site-directed mutagenesis using the QuikChange Lightning Multi kit (Agilent). The resulting baculovirus transfer vectors were used to generate recombinant bacmids using the Bac-to-Bac system (Invitrogen) and virus was rescued by transfecting purified bacmid DNA into Sf9 cells using Cellfectin II (Invitrogen). C05 Fab proteins were produced by infecting suspension cultures of Hi5 cells (Invitrogen) with recombinant baculovirus at a multiplicity of infection (MOI) of 5–10 and incubating at 28 °C, shaking at 110 r.p.m. After 72 h, the cultures were clarified by two rounds of centrifugation at 2,000g and 10,000g at 4 °C. The supernatant containing secreted, soluble Fab was concentrated and buffer exchanged into 1 × PBS, pH 7.4. After metal-affinity chromatography using nickel-nitrilotriacetic acid (Ni-NTA) resin, Fabs were purified by protein G affinity chromatography (GE Healthcare) and gel filtration (Superdex 200).

ELISA. Microtitre plates were coated with 0.1 ml of the following HA antigens diluted in coating buffer and incubated overnight at room temperature: 100 ng ml⁻¹ H5N1 Vietnam 1203/04, 700 ng ml⁻¹ H1N1 New Caledonia/20/99 and 100 ng ml⁻¹ H3N2 Wisconsin/67/05. Blocking was done with 0.3 ml of blocking buffer (4% non-fat dry milk in PBS and 0.05% Tween-20). After blocking, antibodies were diluted to 0.5 µg ml⁻¹ in 2% non-fat dry milk blocking buffer and were incubated for 2 h at 4 °C, washed and later detected using a 1:3,000 dilution of peroxidase-conjugated anti-human Fc antibody (Jackson ImmunoResearch) in 2% non-fat dry milk blocking buffer and standard TMB substrate detection. Attenuance at $D_{450\text{ nm}}$ was read, and data recorded are reported herein.

Viruses. Recombinant influenza viruses were generated using reverse genetics as previously described in ref. 39. In brief, 1 µg each of ten plasmids was transfected into 293T cells in monolayer. Each transfection contained ambisense plasmids (for the expression of both viral RNAs and messenger RNAs) for the A/Puerto

Rico/8/34/PA, PB1, PB2, NP, M and NS segments, in addition to viral RNA (pPOL1 type) and protein expression plasmids (pCAGGS type) for A/X-31/1968 HA and NA (pCAGGS expression plasmid was kindly provided by J. Miyazaki⁴⁰). Twenty hours after transfection, 293T cells were re-suspended in cell culture supernatant and used to inoculate 10-day-old embryonated eggs.

Microneutralization. Antibodies were screened for neutralizing activity against viruses as follows. Twofold serial dilutions of each monoclonal antibody were incubated with 100 50% tissue culture infective doses of virus in PBS at 37 °C for 1 h. Madin-Darby canine kidney cell monolayers in 24-well plates were washed once with PBS and inoculated with virus-antibody mixtures. After incubation for 1 h at 37 °C in 5% CO₂, the inoculum was removed and monolayers were again washed once with PBS. Opti-MEM supplemented with 0.3% BSA, 0.01% FBS and 1 µg ml⁻¹ tosyl phenylalanyl chloromethyl ketone-treated trypsin was added and cells were incubated for 72 h at 37 °C. The presence of virus in cell culture supernatants was assessed by HA assays using 0.5% chicken red blood cells.

Haemagglutination inhibition. Haemagglutination-inhibition titres were determined using four haemagglutinating units of HA protein or virus. HA protein or virus was incubated for 1 h at room temperature with serial twofold dilutions of C05 IgG in 96-well, V-bottom microtitre plates (Costar) followed by addition of 0.5% chicken red blood cells and mixing. The mixture was incubated for 30 min at room temperature followed by brief centrifugation at 1,000 r.p.m. to pellet the red blood cells.

Generation of escape mutants. In brief, H3N2 A/X-31/1968 virus was incubated with a neutralizing excess of monoclonal antibody for 45 min at room temperature. The virus-monoclonal mix was inoculated into 10-day-old embryonated eggs and incubated at 37 °C for 48 h. Eggs were inoculated in triplicate. The virus (allantoic fluid) grown under these conditions was collected and tested for virus outgrowth by HA assay. No viral growth was observed by haemagglutination of chicken red blood cells. The experiment was performed twice.

In vivo protection. Animal experiments were performed in accordance with the guidelines of the Mount Sinai School of Medicine and St Jude Children's Research Hospital Institutional Animal Care and Use Committees (IACUC). All animal experiments were done essentially as described in ref. 8. Virus strains and titres used in these studies were H1N1 A/Memphis/3/2008 (25 MLD₅₀, 1 × 10⁵ 50% egg infective doses) and H3N2 A/X-31/1968 (33 MLD₅₀, 300 plaque-forming units). Mice were 5–6-week-old BALB/c for the H1N1 studies and DBA/2 for the H3N2 studies.

Cloning, expression and purification of influenza A HAs. On the basis of H3 numbering, complementary DNAs corresponding to residues 11–329 (HA1) and 1–176 (HA2) of the influenza A HA ectodomain were fused to an amino-terminal gp67 signal peptide and to a C-terminal biotinylation site (amino acid sequence: GGGLNDIFEAQKIEWHE), trimerization domain and His₆-tag by overlap PCR, essentially as previously described in ref. 12. The trimerization domain and His₆-tag were separated from the HA ectodomain by a thrombin cleavage site. In the case of the HK68/H3 trimer construct used for crystallization, the biotinylation site was omitted from the construct. For the HK68/HA1 subunit used for crystallization, HA1 residues 43–309 were fused to the gp67 signal peptide (N terminus) and a C-terminal His₆-tag. The resulting PCR products were digested with SfiI and inserted into a custom baculovirus transfer vector (pDCE198). The production of virus and expression conditions were essentially as above for the C05 Fabs. After metal-affinity chromatography using Ni-NTA resin, trimeric HAs for crystallography were digested with trypsin (New England Biolabs, 5 mU trypsin per mg HA, 16 h at 17 °C) to produce uniformly cleaved (HA1/HA2), and to remove the trimerization domain and His₆-tag. After quenching the digests with 2 mM phenylmethylsulphonyl fluoride, the digested material was further purified by anion-exchange chromatography (MonoQ, GE Healthcare, 10 mM Tris, pH 9.0, 50–1,000 mM NaCl) and size-exclusion chromatography (Superdex 200, GE Healthcare, 10 mM Tris, pH 8.0, 150 mM NaCl).

Expression and purification of BirA. *Escherichia coli* biotin ligase (BirA enzyme) was expressed and purified in a manner similar to previous reports⁴¹, but with an N-terminal His tag, essentially as previously described in ref. 12. In brief, a pET21a derivative containing the *E. coli birA* gene (pDCE095) was transformed into BL21(DE3) cells, grown in shake flasks in low salt LB medium at 37 °C to an attenuance (at $D_{600\text{ nm}}$) of ~0.7, then shifted to 23 °C and induced with the addition of isopropyl-β-D-thiogalactopyranoside (IPTG) to a final concentration of 1 mM. The culture was incubated at 23 °C for ~16 h after induction. The cells were lysed and homogenized by two passes through an EmulsiFlex C-3 cell disruptor (15kPSI), and birA was purified by nickel affinity (NiNTA resin, Qiagen), anion exchange (MonoQ column, GE Healthcare) and gel filtration. Purified BirA protein was concentrated to 5 mg ml⁻¹ in 50 mM Tris, pH 7.5, 200 mM potassium chloride and 5% glycerol, aliquoted, flash frozen in liquid nitrogen and stored at –80 °C.

Biotinylation and purification of influenza HAs for binding studies. After expression and Ni-NTA purification of influenza A HA as described above, proteins for binding studies were concentrated to $\sim 2\text{--}5\text{ mg ml}^{-1}$ total protein. The HAs were biotinylated by the addition of 25 μg BirA enzyme per mg total protein, in a buffer of the following composition: 100 mM Tris, pH 8.0, 10 mM ATP, 10 mM magnesium acetate and 50 μM biotin, with less than 50 mM NaCl. The biotinylation reactions were incubated at 37 °C for 1–2 h. Biotinylated HAs were purified by size-exclusion chromatography and concentrated to $\sim 5\text{--}20\text{ mg ml}^{-1}$.

K_d determination by BLI. K_d was determined by BLI using an Octet Red instrument (ForteBio). Biotinylated HAs, purified as described above, were used for these measurements. HAs at $\sim 10\text{--}50\text{ }\mu\text{g ml}^{-1}$ in $1\times$ kinetics buffer ($1\times$ PBS, pH 7.4, 0.01% BSA and 0.002% Tween 20) were loaded onto streptavidin-coated biosensors and incubated with varying concentrations of C05 Fab in solution. All binding data were collected at 30 °C. The experiments comprised five steps: (1) baseline acquisition (60 s); (2) HA loading onto sensor (300–600 s); (3) second baseline acquisition (180–200 s); (4) association of C05 for the measurement of k_{on} (180 s); and (5) dissociation of C05 for the measurement of k_{off} (180 s). Four to six concentrations of C05 were used, with the highest concentration varying, depending on the HA affinity, from 50 to 1,000 nM. Baseline and dissociation steps were carried out in buffer only. The ratio of k_{on} to k_{off} determines the K_d reported here. The sequences of all proteins used in this work are available in FASTA format at the end of this document. All binding traces and curves used for fitting k_{on} and k_{off} are reported in Supplementary Figs 14 and 15.

K_d determination by ITC. ITC was performed using an ITC₂₀₀ calorimeter (Microcal). All proteins were dialysed extensively against PBS buffer before the titrations. The experiments were performed at 25 °C. A typical titration consisted of injecting 1.6 μl aliquots of C05 Fab (0.5 mM) into 70 μM HA solution in the cell at time intervals of 90 s to ensure that the titration peak returned to the baseline. ITC data were corrected for the heat of dilution by subtracting the mixing enthalpies for titrant solution injections into protein-free buffer. ITC data were analysed using program Origin (Version 7.0) as provided by the manufacturer using a single set of identical binding sites model.

Owing to the high molecular weight of the system and the very poor expression of the A/Brisbane/10/2007 (H3N2) HA, we were unable to achieve a high enough molar concentration of HA in the ITC cell to obtain a complete, high-quality titration curve. For a K_d of 10 μM , the manufacturer's guidelines suggest 0.5 mM HA in the cell and 5 mM Fab in the syringe. This would correspond to $\sim 30\text{ mg ml}^{-1}$ HA ($\sim 10\text{ mg}$ total) and $\sim 250\text{ mg ml}^{-1}$ Fab ($\sim 20\text{ mg}$ total). However, we were only able to obtain $\sim 1\text{ mg}$ of the A/Brisbane/10/2007 (H3N2) HA from 10 l of insect cell culture, precluding the possibility of obtaining the quantity of protein required for an optimal experiment. In addition, although C05 Fab could be obtained in good yields and could be concentrated to at least 50 mg ml^{-1} ($\sim 1\text{ mM}$), clear self-association between C05 molecules was apparent even at $\sim 19\text{ mg ml}^{-1}$ ($\sim 0.38\text{ mM}$), the concentrations used in the experiment reported here. However, after subtraction of Fab injections into a buffer-filled cell to correct for the heat of dilution resulting from the Fab self-association at high concentrations, the resulting data could still be fit reasonably well and an approximate value for the K_d could be obtained (see Supplementary Fig. 16).

Electron microscopy of C05 Fab with H1, H2 and H3 HAs. Negative-stained grids were prepared by applying 0.1 mg ml^{-1} of the purified complex to a freshly glow-discharged carbon-coated 400 Cu mesh grid and stained with Nano-W. Grids were viewed using a FEI Tecnai TF20 electron microscope operating at an accelerating voltage of 120 kV and imaged at a magnification of $\times 100,000$. Images were acquired on a Gatan 4k \times 4k charge-coupled device (CCD) camera in five-degree tilt increments from 0 to 55° using a de-focus range of 700 to 900 nm. The tilt angles provided additional particle orientations to improve the image reconstruction. The pixel size of the CCD camera was calibrated at this magnification to be 1.09 Å using a two-dimensional catalase crystal with known cell parameters.

Image processing. For each complex, particles were automatically selected from micrographs using the DoG Picker software through the Appion package^{42,43}. The contrast transfer function estimation for micrographs was completed using ctfind3 and ctfilt^{42,44}. Particles were binned by four (80×80 -sized boxes) and reference free two-dimensional class averages were calculated using the Sparx package, without imposing symmetry⁴⁵. An unliganded 25 Å hemagglutinin (H1) volume generated with Sparx was used as the initial model for the image reconstruction process, with the reference-free class averages as the experimental images. Density for the Fabs could be visualized after 3 cycles of refinement. Refinement was continued for 70 cycles with decreasing angular search parameters. The resultant model was then used as the initial model for the iterative image reconstruction process against the raw particles binned by two (160×160 -sized boxes). Contrast transfer function correction was applied during this procedure using the Sparx package. C3 symmetry was imposed throughout the image

reconstruction process. The final three-dimensional image reconstructions have an estimated resolution of 17 Å according to a Fourier shell correlation (FSC) of 0.5.

Model fitting. Coordinates of HA from A/Solomon Islands/3/2006 (H1N1) and A/Japan/305/1957 (H2N2) in addition to C05 were fitted into the respective electron microscopy reconstructions. For H3, the coordinates of HA from A/Hong Kong/1/1968 (H3N2) were used in the electron microscopy reconstruction of HA from A/Perth/16/2009 (H3N2) with C05 Fab. The automated fit of each component was manually improved through rigid body movement using the program UCSF Chimera to minimize the number of clashes between HA and the Fabs while maintaining the highest possible correlation coefficient value with the chimera fit tool. This resulted in a portion at the base of the stem region of HA being excluded from the image reconstruction. Coincidentally, this region of HA possesses high B-factors in the crystal structures and may adopt distinct conformations on the electron microscope grid. The density for this region can be seen at lower contour thresholds.

Crystallization and structure determination of the HK68/H3 HA. Gel-filtration fractions containing HK68/H3 HA were concentrated to $\sim 9\text{ mg ml}^{-1}$ in 10 mM Tris, pH 8.0, and 50 mM NaCl. Initial crystallization trials were set up using the automated Rigaku CrystalMation robotic system at the Joint Center for Structural Genomics (<http://www.jcsg.org>). The crystal used for data collection was grown by the sitting drop vapour diffusion method with a reservoir solution (200 μl) containing 2.0 M ammonium sulphate, 100 mM sodium cacodylate, pH 6.5, and 200 mM NaCl. Drops consisting of 100 nl protein + 100 nl precipitant were set up at 20 °C, and crystals appeared within 3–7 days. The resulting crystals were cryoprotected by brief immersion in well solution supplemented with 35% glycerol, then flash-cooled and stored in liquid nitrogen until data collection.

Diffraction data for the HK68/H3 HA were collected on beamline 11-1 at the SSRL. The data were indexed in space group C22₁, integrated and scaled using HKL2000 (HKL Research). The structure was solved by molecular replacement to 1.90 Å resolution using Phaser⁴⁶. A protomer from 2VIU¹⁸ (A/X-31/1968 (H3N2) HA) was used as the initial search model and three copies (forming a non-crystallographic trimer) were found in the asymmetric unit. At this point, poorly defined regions of the model were trimmed and the HA was mutated *in silico* to match the HK68/H3 sequence. Rigid body refinement, simulated annealing and restrained refinement (including translation-libration-screw (TLS) refinement, with one group for each HA1 or HA2 domain) were carried out in Phenix⁴⁷. Riding hydrogens were used during refinement and are included in the final model. Between rounds of refinement, the model was built and adjusted using Coot⁴⁸. Waters were built automatically using the 'ordered_solvent' modelling function in Phenix⁴⁷. Refinement statistics can be found in Supplementary Table 1.

Crystallization and structure determination of the C05 Fab. Gel-filtration fractions containing the C05 Fab were concentrated to $\sim 11\text{ mg ml}^{-1}$ in 10 mM Tris, pH 8.0, and 50 mM NaCl. Initial crystallization trials were set up using the automated Rigaku CrystalMation robotic system at the Joint Center for Structural Genomics (<http://www.jcsg.org>). Several hits were obtained, with the most promising candidates grown in $\sim 2.0\text{--}2.5\text{ M}$ ammonium sulphate between pH 5 and 7. Optimization of these conditions resulted in diffraction-quality crystals. The crystals used for data collection were grown by the sitting drop vapour diffusion method with a reservoir solution (1 ml) containing 1.8 M ammonium sulphate, 100 mM sodium acetate, pH 5.4, and 50 mM NaCl. Drops consisting of 0.5 μl protein + 0.5 μl precipitant were set up at 4 °C and crystals appeared within 3–7 days. The resulting crystals were cryoprotected by soaking in well solution supplemented with increasing concentrations of ethylene glycol (5% steps, 1 h per step) to a final concentration of 20%, then flash-cooled and stored in liquid nitrogen until data collection.

Diffraction data for the C05 Fab crystals were collected on the GM/CA-CAT 23ID-D beamline at the Advanced Photo Source (APS) at Argonne National Laboratory. The data were indexed in space group P4₁2₁2, integrated, scaled, and merged using HKL2000 (HKL Research). The structure was solved by molecular replacement to 2.30 Å resolution using Phaser⁴⁶. PDB codes 1AQK and 1VGE were used as search models for the variable and constant domains, respectively, and 2 complete Fabs were found in the asymmetric unit. Rigid body refinement, simulated annealing and restrained refinement (including TLS refinement, with one group for each Ig domain) were carried out in Phenix⁴⁷. Riding hydrogens were used during refinement and are included in the final model. Between rounds of refinement, the model was built and adjusted using Coot⁴⁸. Waters were built automatically using the 'ordered_solvent' modelling function in Phenix⁴⁷. Refinement statistics can be found in Supplementary Table 1.

Crystallization and structure determination of the C05-HK68-H3 HA1 complex. Gel-filtration fractions containing the C05-HK68/H3 HA1 complex were concentrated to $\sim 9 \text{ mg ml}^{-1}$ in 10 mM Tris, pH 8.0, and 50 mM NaCl. Initial crystallization trials were set up using the automated Rigaku CrystalMation robotic system at the Joint Center for Structural Genomics (<http://www.jcsg.org>). The crystals used for data collection were grown by the sitting drop vapour diffusion method with a reservoir solution (200 μl) containing 10% (w/v) polyethylene glycol (PEG) 3000, 200 mM zinc acetate and 100 mM sodium acetate, pH 4.5. Drops consisting of 100 nl protein + 100 nl precipitant were set up at 4 °C, and crystals appeared within 3 days and continued to grow larger until approximately day 7. The resulting crystals were cryoprotected by brief immersion in well solution supplemented with 30% ethylene glycol, then flash-cooled and stored in liquid nitrogen until data collection.

Diffraction data for the C05-HK68/H3 HA1 complex were collected on the GM/CA-CAT 23ID-D beamline at the APS at Argonne National Laboratory. The data were indexed in space group $P2_1$, integrated, scaled and merged using HKL2000 (HKL Research). The structure was solved by molecular replacement to 2.95 Å resolution using Phaser⁴⁶. The isolated HA1 subunit from the HK68/H3 structure reported here was used as a search model and four copies were found in the asymmetric unit. A subsequent search with the variable and constant domains from the un-liganded C05 Fab structure yielded good solutions for four complete Fab fragments. Rigid body refinement, simulated annealing and restrained refinement (including TLS refinement, with one group for HA1 and one for each immunoglobulin domain) were carried out in Phenix⁴⁷. Riding hydrogens were used during refinement and are included in the final model. Between rounds of refinement, the model was built and adjusted using Coot⁴⁸. Refinement statistics can be found in Supplementary Table 1.

Crystallization and structure determination of the C05-HK68-H3 HA trimer complex. Gel-filtration fractions containing the C05-HK68-H3 trimeric HA complex were concentrated to $\sim 10 \text{ mg ml}^{-1}$ in 10 mM Tris, pH 8.0, and 50 mM NaCl. Initial crystallization trials were set up using the automated Rigaku CrystalMation robotic system at the Joint Center for Structural Genomics (<http://www.jcsg.org>). Only two hits were obtained (in related conditions) and neither could be reproduced or optimized further. Thus, the crystals from the initial screen were used for data collection. The best crystal was grown by the sitting drop vapour diffusion method with a reservoir solution (200 μl) containing 28% (w/v) PEG 400, 200 mM calcium chloride and 100 mM HEPES buffer, pH 7.5. Drops consisting of 100 nl protein + 100 nl precipitant were set up at 4 °C and a very small crystal was visible after 14 days. Over the course of a further 2 weeks, the crystal reached its maximum size. The crystal was cryoprotected by brief immersion in well solution supplemented with 10% ethylene glycol, then flash-cooled and stored in liquid nitrogen until data collection.

Diffraction data for the C05-HK68/H3 trimer complex were collected on the GM/CA-CAT 23ID-B beamline at the APS at Argonne National Laboratory. Owing to poor crystal quality (cluster of stacked plates), the diffraction images were noisy and highly anisotropic. The data were indexed in space group $P1$, integrated and scaled using HKL2000 (HKL Research) and merged using XPREP (Bruker). The structure was solved by molecular replacement to a nominal resolution of 4.25 Å using Phaser⁴⁶. However, owing to the anisotropy of the diffraction, many reflections were observed at a higher resolution (~ 3.2 Å) than the nominal resolution reported, and these additional data were included in refinement. A HK68-H3 trimer from the high-resolution structure reported here was

used as the initial search model and total of four trimers (12 HA protomers) were found in the asymmetric unit. The C05-HK68-H3 HA1 complex was docked onto each of the 12 HA1 subunits in the asymmetric unit to position the C05 Fab. Rigid body refinement, simulated annealing and restrained refinement (including TLS refinement, with one group for HA1, one for HA2 and one for each immunoglobulin domain) were carried out in Phenix⁴⁷. Riding hydrogens were used during refinement and are included in the final model. Between rounds of refinement, the model was built and adjusted using Coot⁴⁸. Refinement statistics can be found in Supplementary Table 1.

Structural analyses. Hydrogen bonds and van der Waals contacts between C05 and the HK68/H3 HA1 domain HA were calculated using HBPLUS and CONTACTSYM, respectively. Surface area buried on Fab binding was calculated with MS. MacPyMol (DeLano Scientific) and UCSF Chimera⁴⁹ was used to render structure figures and for general manipulations. Kabat numbering was applied to the coordinates using the AbNum server³⁷. The final coordinates were validated using the JCSG quality-control server (v2.7), which includes MolProbity⁵⁰.

Sequence analysis of C05 epitope conservation in all HA proteins. All full-length, non-redundant and non-lab-strain influenza A HA sequences were downloaded from the NCBI Flu database³⁴. At the time of download (7 August, 2010), the data set included 8,720 sequences encompassing all 16 influenza A subtypes, of which 5,813 and 2,907 sequences were from group 1 and group 2 viruses, respectively. The sequences were aligned using MUSCLE³⁸ and analysed using Genetics Computer Group (Accelrys) and custom shell scripts (available from the authors on request). In this analysis, residues are considered conserved if substitutions are restricted to other amino acids in the same group: (1) Asp, Asn, Glu, Gln (negatively charged or isosteric polar substitutions); (2) Val, Ile, Leu, Met (small hydrophobic); (3) Phe and Tyr (aromatic); and (4) Ser and Thr (small polar/hydroxyl). The values reported for percent conservation are the number to sequences with an identical or conservative change at a position divided by the total number of sequences and multiplied by 100.

39. Fodor, E. *et al.* Rescue of influenza A virus from recombinant DNA. *J. Virol.* **73**, 9679–9682 (1999).
40. Miyazaki, J. *et al.* Expression vector system based on the chicken β -actin promoter directs efficient production of interleukin-5. *Gene* **79**, 269–277 (1989).
41. Brown, P. H., Cronan, J. E., Grotli, M. & Beckett, D. The biotin repressor: modulation of allostery by corepressor analogs. *J. Mol. Biol.* **337**, 857–869 (2004).
42. Lander, G. C. *et al.* Appion: an integrated, database-driven pipeline to facilitate EM image processing. *J. Struct. Biol.* **166**, 95–102 (2009).
43. Voss, N. R., Yoshioka, C. K., Radermacher, M., Potter, C. S. & Carragher, B. DoG Picker and TiltPicker: software tools to facilitate particle selection in single particle electron microscopy. *J. Struct. Biol.* **166**, 205–213 (2009).
44. Mindell, J. A. & Grigorieff, N. Accurate determination of local defocus and specimen tilt in electron microscopy. *J. Struct. Biol.* **142**, 334–347 (2003).
45. Hohn, M. *et al.* SPARX, a new environment for cryo-EM image processing. *J. Struct. Biol.* **157**, 47–55 (2007).
46. McCoy, A. J. *et al.* Phaser crystallographic software. *J. Appl. Cryst.* **40**, 658–674 (2007).
47. Adams, P. D. *et al.* PHENIX: a comprehensive Python-based system for macromolecular structure solution. *Acta Crystallogr. D* **66**, 213–221 (2010).
48. Emsley, P., Lohkamp, B., Scott, W. G. & Cowtan, K. Features and development of Coot. *Acta Crystallogr. D* **66**, 486–501 (2010).
49. Pettersen, E. F. *et al.* UCSF Chimera—a visualization system for exploratory research and analysis. *J. Comput. Chem.* **25**, 1605–1612 (2004).
50. Chen, V. B. *et al.* MolProbity: all-atom structure validation for macromolecular crystallography. *Acta Crystallogr. D* **66**, 12–21 (2010).

No surviving evolved companions of the progenitor of SN 1006

Jonay I. González Hernández^{1,2}, Pilar Ruiz-Lapuente^{3,4}, Hugo M. Tabernero⁵, David Montes⁵, Ramon Canal⁴, Javier Méndez^{4,6} & Luigi R. Bedin⁷

Type Ia supernovae are thought to occur when a white dwarf made of carbon and oxygen accretes sufficient mass to trigger a thermonuclear explosion¹. The accretion could be slow, from an unevolved (main-sequence) or evolved (subgiant or giant) star^{2,3} (the single-degenerate channel), or rapid, as the primary star breaks up a smaller orbiting white dwarf^{3,4} (the double-degenerate channel). A companion star will survive the explosion only in the single-degenerate channel⁵. Both channels might contribute to the production of type Ia supernovae^{6,7}, but the relative proportions of their contributions remain a fundamental puzzle in astronomy. Previous searches for remnant companions have revealed one possible case for SN 1572 (refs 8, 9), although that has been questioned¹⁰. More recently, observations have restricted surviving companions to be small, main-sequence stars^{11–13}, ruling out giant companions but still allowing the single-degenerate channel. Here we report the results of a search for surviving companions of the progenitor of SN 1006 (ref. 14). None of the stars within 4 arc minutes of the apparent site of the explosion is associated with the supernova remnant, and we can firmly exclude all giant and subgiant stars from being companions of the progenitor. In combination with previous results, our findings indicate that fewer than 20 per cent of type Ia supernovae occur through the single-degenerate channel.

Together with SN 1572 (Tycho Brahe's supernova), SN 1604 (Kepler's supernova) and the recently identified SN 185, SN 1006 is one of only four known historical Galactic type Ia supernova events. It is also the only one whose type has never been disputed. Whereas a survey of the stars close to the centre of Tycho's supernova remnant (SNR) produced a likely candidate for the companion^{8,9}, and the supernova may thus be attributed to accretion via the single-degenerate channel, the absence of a surviving companion in the supernova remnant SNR 0509–67.5, in the Large Magellanic Cloud, down to very faint magnitudes, strongly suggests that the supernova there was the result of accretion via the double-degenerate channel¹⁵. Although the aforementioned direct searches have excluded, up to now, red giant companions, there is some evidence from nearby spiral galaxies that a fraction of type Ia supernovae may have had companions of this type¹⁶. This hypothesis, however, is challenged by the absence of ultraviolet emission, which would be expected at the beginning of the supernova outburst¹⁷.

The distance to the remnant of SN 1006 (2.18 ± 0.08 kpc away, as determined from the expansion velocity and the proper motion of the ejecta¹⁸) is much more precisely known than that of the remnant of SN 1572 (2.83 ± 0.70 kpc). The interstellar extinction is also much smaller, which makes the distances to the stars less uncertain. To be a possible candidate, a star must be at the correct distance and, depending on its spectral type and luminosity class, must show some spectral peculiarity or an enhancement of the abundances of Fe-peak elements

such as that seen in star G of Tycho's supernova⁹. Because of its relative proximity compared with SN 1572, and the lower extinction (V-band extinction of $A_V = 0.3$ mag, versus 2.0–2.4 mag in Tycho's supernova), going down to an R-band magnitude of $m_R = 15$ mag allows us to include, out to the supernova distance and beyond, all red giants,

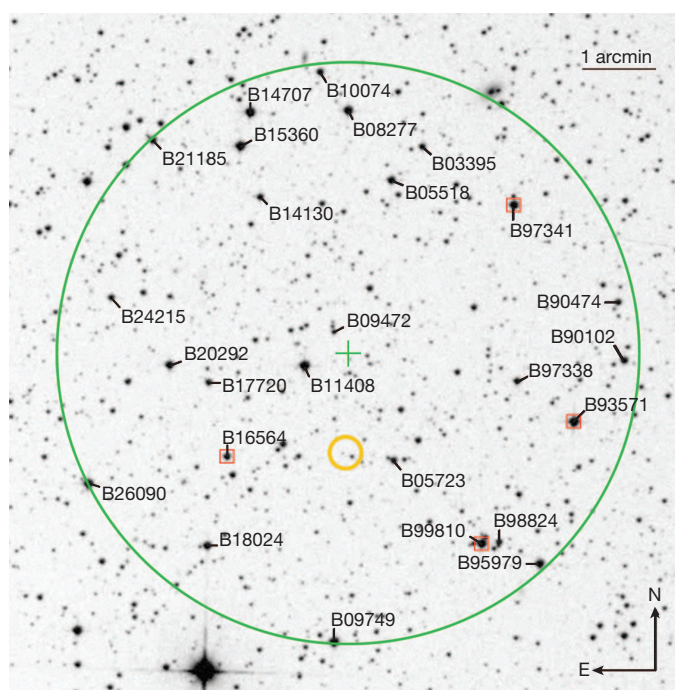


Figure 1 | R-band image of the SN 1006 field. Image from the Digitized Sky Survey 2. The positions and names of the 26 stars included in the spectroscopic survey (selected from the USNO-A2.0 catalogue²⁸) are given. The centre of our search is the geometrical centre of the quite symmetrical X-ray emission of the SNR²⁹ (green cross), at RA = 15 h 2 min 55 s, dec. = $-41^\circ 55' 12''$. Also shown are the boundary of the surveyed region (large green circle) and the geometrical centre of the H α emission¹⁸ (small yellow circle). Giant stars are marked by red squares. See also Supplementary Fig. 1, for a full view of the SNR. Another centre has been proposed more recently³⁰, on the basis of the distribution of the ejecta along the line of sight. It is, however, still located within our surveyed area. For a star at a distance of $d \approx 2.2$ kpc and with a velocity of ~ 100 km s⁻¹ (roughly the orbital velocity before the explosion) perpendicular to the line of sight, the angular displacement on the sky in 1,000 yr would be only $10''$. However, given the asymmetry of the SNR, and also that in core-collapse supernovae the distance between the compact object and the X-ray centroid of the SNR can be 15% or more of the radius of the SNR, we adopted a much wider radius for the search: $4'$. That amounts to 27% of the radius of the SNR, which is $15'$ (Supplementary Fig. 1). Positions, magnitudes and angular distances to the centre of the survey are given in Supplementary Table 1.

¹Instituto de Astrofísica de Canarias, E-38205 La Laguna, Tenerife, Spain. ²Departamento de Astrofísica, Universidad de La Laguna, E-38206 La Laguna, Tenerife, Spain. ³Instituto de Física Fundamental, CSIC, E-28006 Madrid, Spain. ⁴Department of Astronomy, Institut de Ciències del Cosmos, Universitat de Barcelona, Martí i Franquès 1, E-08028 Barcelona, Spain. ⁵Departamento de Astrofísica y Ciencias de la Atmósfera, Facultad de Ciencias Físicas, Universidad Complutense de Madrid, E-28040 Madrid, Spain. ⁶Isaac Newton Group of Telescopes, PO Box 321, E-38700 Santa Cruz de La Palma, Spain.

⁷INAF-Osservatorio Astronomico di Padova, Vicolo dell'Osservatorio 5, I-35122 Padova, Italy.

Table 1 | Parameters of the sample stars

Name	T_{eff} (K)	$\log[g]$ (cm s^{-2})	v_{turb} (km s^{-1})	[Fe/H] (dex)	v_{rad} (km s^{-1})	d (kpc)
B09472	5853 \pm 75	4.52 \pm 0.17	1.211 \pm 0.105	-0.04 \pm 0.06	-20.74 \pm 2.14	1.23 \pm 0.53
B11408	4677 \pm 68	2.91 \pm 0.23	2.136 \pm 0.082	-0.29 \pm 0.05	-123.54 \pm 1.48	1.62 \pm 0.68
B05723	5910 \pm 87	4.50 \pm 0.23	1.249 \pm 0.107	0.30 \pm 0.07	-12.81 \pm 3.06	0.76 \pm 0.32
B17720	5300 \pm 86	4.65 \pm 0.22	1.190 \pm 0.193	0.33 \pm 0.06	-60.13 \pm 1.30	0.58 \pm 0.25
B16564	4845 \pm 39	3.13 \pm 0.16	1.607 \pm 0.049	-0.37 \pm 0.03	-116.07 \pm 1.86	3.03 \pm 1.27
B97338	5707 \pm 42	4.21 \pm 0.12	1.292 \pm 0.054	0.01 \pm 0.04	-5.53 \pm 2.25	1.05 \pm 0.45
B05518	6327 \pm 63	4.85 \pm 0.13	1.386 \pm 0.090	0.14 \pm 0.04	-4.38 \pm 1.92	0.50 \pm 0.21
B20292	5196 \pm 33	3.67 \pm 0.09	1.372 \pm 0.051	-0.66 \pm 0.03	2.92 \pm 2.52	1.13 \pm 0.48
B14130	6177 \pm 44	4.61 \pm 0.09	1.528 \pm 0.052	0.31 \pm 0.03	-21.26 \pm 2.09	0.89 \pm 0.38
B03395	5517 \pm 49	4.36 \pm 0.13	1.165 \pm 0.074	0.22 \pm 0.04	-56.18 \pm 5.21	0.95 \pm 0.41
B97341	4881 \pm 51	2.98 \pm 0.18	1.641 \pm 0.057	-0.16 \pm 0.04	-41.76 \pm 1.96	2.48 \pm 1.04
B99810	4658 \pm 39	2.51 \pm 0.15	1.782 \pm 0.039	-0.72 \pm 0.03	33.53 \pm 1.50	2.42 \pm 1.02
B15360	4960 \pm 70	3.40 \pm 0.21	1.886 \pm 0.086	0.07 \pm 0.05	-37.03 \pm 1.61	1.29 \pm 0.54
B93571	4579 \pm 58	2.51 \pm 0.22	2.182 \pm 0.066	-0.21 \pm 0.05	-100.33 \pm 1.58	2.39 \pm 1.01
B18024	6083 \pm 58	4.44 \pm 0.13	1.545 \pm 0.095	-0.36 \pm 0.04	22.61 \pm 2.35	0.60 \pm 0.26
B08277	5693 \pm 34	4.39 \pm 0.09	1.123 \pm 0.044	0.17 \pm 0.03	-49.50 \pm 2.08	0.45 \pm 0.19
B24215	5729 \pm 45	4.44 \pm 0.12	1.189 \pm 0.058	0.16 \pm 0.04	3.02 \pm 2.39	0.95 \pm 0.41
B14707	5065 \pm 47	3.36 \pm 0.15	1.270 \pm 0.060	0.16 \pm 0.04	22.14 \pm 1.83	1.37 \pm 0.58
B90474	5051 \pm 38	3.05 \pm 0.12	1.874 \pm 0.046	-0.29 \pm 0.03	-98.10 \pm 1.95	4.78 \pm 2.00
B90102	5650 \pm 33	4.21 \pm 0.10	1.076 \pm 0.049	-0.11 \pm 0.03	85.57 \pm 1.16	0.91 \pm 0.39
B10074	5601 \pm 63	4.52 \pm 0.14	1.036 \pm 0.102	0.05 \pm 0.05	-30.26 \pm 1.38	0.71 \pm 0.30
B95979	6776 \pm 94	4.19 \pm 0.16	1.832 \pm 0.131	0.02 \pm 0.06	-32.94 \pm 6.81	0.94 \pm 0.40
B09749	6163 \pm 65	4.53 \pm 0.14	1.362 \pm 0.082	0.14 \pm 0.05	-13.15 \pm 2.60	0.40 \pm 0.17
B26090	6101 \pm 39	4.58 \pm 0.09	1.238 \pm 0.053	0.15 \pm 0.03	-48.08 \pm 2.52	0.37 \pm 0.16

We provide the stellar atmosphere parameters (effective temperature, T_{eff} ; surface gravity, $\log g$; microturbulent velocity, v_{turb}), metallicities ([Fe/H]), radial velocities (v_{rad}) and distances (d) of the sample stars, together with 1σ uncertainties. The stellar parameters and metallicities were obtained from Fe I and Fe II excitation and ionization equilibria, using the $S_{\text{TE}}\text{PAR}^{25}$ code, which makes use of the MOOG²⁶ code and ATLAS9 model atmospheres²⁷. Our analysis has been performed assuming local thermodynamic equilibrium. SN 1006 is located about 500 pc above the Galactic plane, which lies close to the Galactic plane, the radial velocities of the stars along the line of sight do not follow a regular pattern (this can be seen in the sixth column), because most of them belong either to the thick disc or to the halo of the Galaxy (see the dispersion in metallicities in the fifth column). Two of the observed stars, B98824 and B21185, are spectroscopic binaries and were discarded as possible companion stars of the progenitor of SN 1006 (Supplementary Information).

all subgiants and also main-sequence stars down to an absolute magnitude of $M_R \approx +3.1$ mag. Inspecting the Two Micron All Sky Survey¹⁹ photometric catalogue for possible unevolved companions (Supplementary Information), we found no main-sequence stars brighter than $m_R \approx 16.4$ mag, which brings the limit down to $M_R \approx +4.5$ mag, corresponding to a V-band absolute magnitude of $M_V \approx +4.9$ (approximately equal to, or slightly less than, solar luminosity). Slightly evolved companions could be somewhat brighter: $m_R \approx 16.0$ (about twice as luminous as the Sun). Only the case of SNR 0509-67.5 in the Large Magellanic Cloud¹⁵ has a fainter limit and has been reached in a direct search.

We derive the stellar atmosphere parameters of the sample stars (Fig. 1) using high-resolution spectroscopic data from the Ultraviolet and Visual Echelle Spectrograph (UVES) (Table 1). The spectra of four giants in the sample are shown in Fig. 2, and those of F- and G-type dwarfs are shown in Supplementary Fig. 2. In Table 1, we also provide the radial velocities of sample stars measured from the UVES spectra, and distances determined from five photometric magnitudes, taking into account the stellar parameters (Supplementary Information). In Fig. 3, we compare the abundances of Fe-peak elements in the stars of our sample with the Galactic trends²⁰, for F-, G- and K-type unevolved stars. Unlike in SN 1572, where star G shows an overabundance of Ni ($[\text{Ni}/\text{Fe}] = \log(N_{\text{Ni}}/N_{\text{Fe}}) - \log(N_{\text{Ni}}/N_{\text{Fe}})_{\odot} = 0.16 \pm 0.04$, where N_X is the number of atoms of element X and the second logarithm involves solar values), the stars in SN 1006 are all within the dispersion of the Galactic [Ni/Fe] trend. No enhancement is seen for any other element. In Supplementary Fig. 3, we also show the Galactic trends of several α -elements and we do not see any clear anomaly in these element abundances either.

None of the stars in the sample shows any noteworthy rotation. High rotation speeds have been claimed to be a characteristic of the surviving companions of type Ia supernovae¹⁰, on the assumptions that, first, owing to tidal interaction and in spite of the angular momentum loss due to mass transfer, the rotation periods before explosion are equal to the (short) orbital periods, and, second, the radius of the star remains basically unchanged after the explosion⁹. It has recently been shown²¹, however, that in a type Ia supernova the impact of the ejecta on the companion does indeed reduce those speeds by a large factor, which would make the rotation criterion irrelevant.

Only four stars are at distances (marginally) compatible with that of the remnant of SN 1006. All of them are red giants: B16564 (G9-K0 III), B97341 (G9 III), B99810 (K1 III) and B93571 (K1 III) and none shows any spectroscopic peculiarity.

Two-dimensional hydrodynamic simulations of the impact of the ejecta of a type Ia supernova on a red giant binary companion have been performed²². More recently, the emission of supernova debris, arising from their impact with a similar companion, has been also considered¹⁷. In terms of the effects of the explosion on the companion

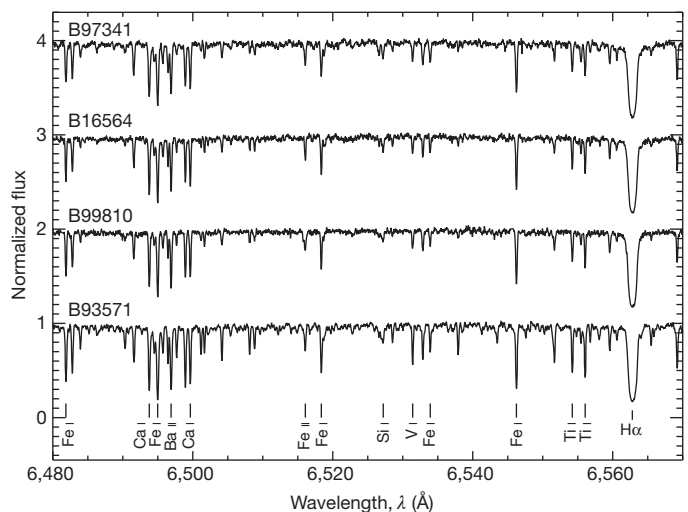


Figure 2 | Observed UVES spectra of the candidate giant stars. The spectra are labelled by their names in Table 1 and sorted in order of decreasing effective temperature from top to bottom. These high-resolution spectra were obtained at the 8.2-m Kueyen VLT (UT2) telescope equipped with UVES at the Cerro Paranal Observatory, Chile. They were obtained on 13, 14, 25 and 28–30 April 2002 and on 1 May 2002, and cover the spectral regions 3,295–5,595 Å, 5,680–6,645 Å, 6,705–8,515 Å and 8,675–10,420 Å at a resolving power of $\lambda/\Delta\lambda \approx 43,000$. The signal-to-noise ratio of the spectra is in the range 50–170 and is typically 80. The data were reduced in a standard manner, and later normalized with the software IRAF, using low-order polynomial fits to the observed continuum.

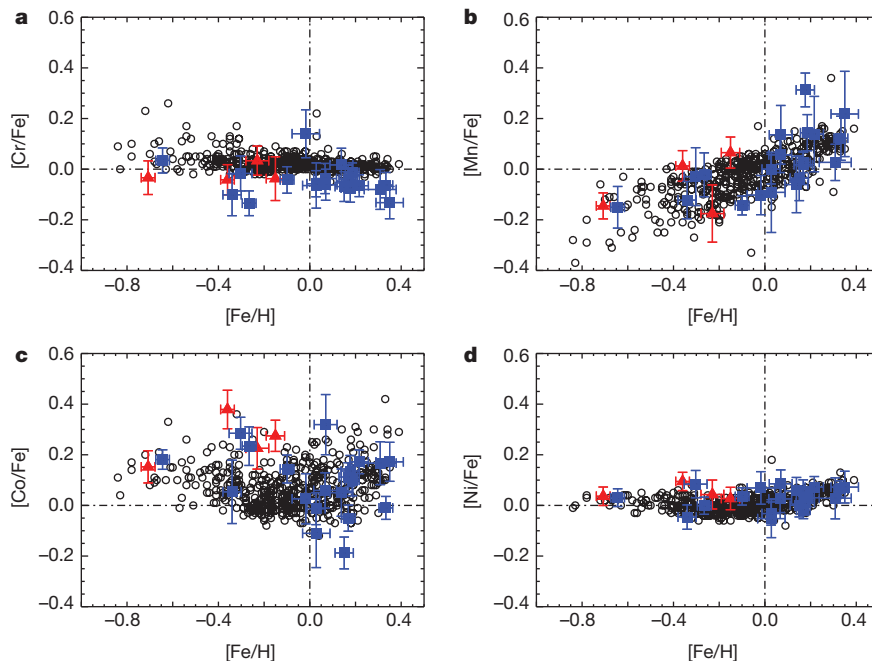


Figure 3 | Stellar abundance ratios $[X/Fe]$ of several Fe-peak elements. The chemical abundances have been derived using the equivalent-width technique for each element: chromium (a), manganese (b), cobalt (c) and nickel (d). We performed a differential analysis on a line-by-line basis, using the solar UVES spectrum of the Moon as reference (see Supplementary Information, section 3, for more details). The abundances of several Fe-peak elements relative to iron

(Supplementary Table 4b) are compared with the Galactic trends of these elements (black circles) in the relevant range of metallicities²⁰. Red triangles correspond to the four giant stars whose distances are marginally compatible with that of the remnant of SN 1006. Blue squares correspond to the rest of the stars in the sample. The error bars are the 1σ uncertainties associated with the dispersion of the measurements from different spectral features.

star, the results agree: most of the envelope is stripped away and what is left are the degenerate core and a very small fraction (amounting to a few per cent) of the original envelope. This hydrogen-rich envelope initially extends out to a radius of ~ 350 solar radii and then contracts on a thermal timescale. The star should be evolving at constant luminosity (of about 1,000 times the solar luminosity) towards increasing effective temperatures for 10^5 – 10^6 yr. The same conclusion is reached when extrapolating to the red giant case the results of simulations of the impact of type Ia supernova ejecta on a main-sequence companion²³: the red giant should have been stripped of most of its hydrogen envelope.

Nothing similar to any of the above four normal red giants would be seen. However, the peculiar type of object that would result from the interaction of the ejecta with a red giant companion would be luminous enough to have been seen at the distance of SN 1006 and within our magnitude limit. A subgiant star similar to star G in Tycho's supernova would equally have been seen, but the only three subgiants in the sample (B20292, B15360 and B14707) lie much closer than the SNR. We are thus left with only main-sequence stars, which lie at shorter distances than the SNR; have luminosities similar to, or lower than, the solar luminosity; and are not predicted by any of the hydrodynamic simulations of the impact of type Ia supernova ejecta with either a main-sequence star or a subgiant. In these hydrodynamic simulations²², a main-sequence companion of one solar mass is expanded and heated, reaching $\sim 5,000$ times the solar luminosity; it is then predicted to contract and cool down on a thermal timescale. It has been found that the return to luminosities of the order of those before the explosion could be faster because of the short cooling times of the outermost layers of the star²⁴, but, even so, in only $\sim 1,000$ yr the object does not have enough time to become dimmer than the Sun (Supplementary Information).

Accordingly, SN 1006, the brightest event so far observed in our Galaxy, should have been produced either by mass accretion from an unevolved star similar to, or less massive than, the Sun (with the above caveats), or by merging with another white dwarf. Adding this

result to the evidence from the other direct searches, the single-degenerate channel seems either to encompass only a clear minority of cases (20% or fewer) or preferentially involves main-sequence companions with masses more probably below that of the Sun.

Received 27 February; accepted 26 July 2012.

- Nomoto, K., Saio, H., Kato, M. & Hachisu, I. Thermal stability of white dwarfs accreting hydrogen-rich matter and progenitors of type Ia supernovae. *Astrophys. J.* **663**, 1269–1276 (2007).
- Whelan, J. & Iben, I. Jr. Binaries and supernovae of type I. *Astrophys. J.* **186**, 1007–1014 (1973).
- Branch, D., Livio, M., Yungelson, L. R., Boffi, F. & Baron, E. In search of the progenitors of type Ia supernovae. *Publ. Astron. Soc. Pacif.* **107**, 1019–1029 (1995).
- Pakmor, R. *et al.* Sub-luminous type Ia supernovae from the mergers of equal-mass white dwarfs with mass $0.9M_{\odot}$. *Nature* **463**, 61–64 (2010).
- Ruiz-Lapuente, P. The quest for a supernova companion. *Science* **276**, 1813–1814 (1997).
- Greggio, L. The rates of Type Ia supernovae – II. Diversity of events at low and high redshifts. *Mon. Not. R. Astron. Soc.* **406**, 22–42 (2010).
- Brandt, T. D. *et al.* The ages of type Ia supernova progenitors. *Astrophys. J.* **140**, 804–816 (2010).
- Ruiz-Lapuente, P. *et al.* The binary progenitor of Tycho Brahe's 1572 supernova. *Nature* **431**, 1069–1072 (2004).
- González Hernández, J. I. *et al.* The chemical abundances of Tycho G in supernova remnant 1572. *Astrophys. J.* **691**, 1–15 (2009).
- Kerzendorf, W. *et al.* Subaru high resolution spectroscopy of star G in the Tycho supernova remnant. *Astrophys. J.* **701**, 1665–1672 (2009).
- Nugent, P. E. *et al.* Supernova SN 2011fe from an exploding carbon–oxygen white dwarf star. *Nature* **480**, 344–347 (2011).
- Li, W. *et al.* Exclusion of a luminous red giant as a companion star to the progenitor of supernova SN 2011fe. *Nature* **480**, 348–350 (2011).
- Edwards, Z. I., Pagnotta, A. & Schaefer, B. E. The progenitor of the type Ia supernova that created SNR 0519–69.0 in the Large Magellanic Cloud. *Astrophys. J.* **747**, L19–L23 (2012).
- Stephenson, F. R. SN 1006: the brightest supernova. *Astron. Geophys.* **51**, 527–532 (2010).
- Schaefer, B. E. & Pagnotta, A. An absence of ex-companion stars in the type Ia supernova remnant SNR 0509–67.5. *Nature* **481**, 164–166 (2012).
- Sternberg, A. *et al.* Circumstellar material in type Ia supernovae via sodium absorption features. *Science* **333**, 856–859 (2011).
- Kasen, D. Seeing the collision of a supernova with its companion star. *Astrophys. J.* **708**, 1025–1031 (2010).

18. Winkler, P. F., Gupta, G. & Long, K. S. The SN 1006 remnant: optical proper motions, deep imaging, distance, and brightness at maximum. *Astrophys. J.* **585**, 324–335 (2003).
19. Cutri, R. M. *et al.* 2MASS All-Sky Catalog of point sources. *VizieR Online Data Catalog II/246* <http://vizier.u-strasbg.fr/viz-bin/VizieR?-source=II/246> (2003).
20. Neves, V., Santos, N. C., Sousa, S. G., Correia, A. C. M. & Israelian, G. Chemical abundances of 451 stars from the HARPS GTO planet search program. Thin disk, thick disk, and planets. *Astron. Astrophys.* **497**, 563–581 (2009).
21. Pan, K.-C., Ricker, P. & Taam, R. Impact of type Ia supernova ejecta on the binary companions in the single-degenerate scenario. *Astrophys. J.* **750**, 151 (2012).
22. Marietta, E., Burrows, A. & Fryxell, B. Type Ia supernova explosions in binary systems: the impact on the secondary star and its consequences. *Astrophys. J.* **128** (suppl.), 615–650 (2000).
23. Pakmor, R., Röpke, F. K., Weiss, A. & Hillebrandt, W. The impact of type Ia supernovae on main sequence binary companions. *Astron. Astrophys.* **489**, 943–951 (2008).
24. Podsiadlowski, P. On the evolution and appearance of a surviving companion after a Type Ia supernova explosion. Preprint at <http://arxiv.org/abs/astro-ph/0303660> (2003).
25. Tabernero, H. M., Montes, D. & González Hernández, J. I. Chemically tagging the Hyades Supercluster: a homogeneous sample of F6-K4 kinematically selected northern stars. *Astron. Astrophys.* (in the press); preprint at <http://arxiv.org/abs/1205.4879> (2012).
26. Sneden, C. *Carbon and Nitrogen Abundances in Metal-Poor Stars*. PhD thesis, Univ. Texas, Austin (1973).
27. Kurucz, R. L. ATLAS9 stellar atmospheres programs and 2 km s⁻¹ grid. (Smithsonian Astrophysical Observatory, 1993).
28. Monet, D. G. The 526,289,881 objects in the USNO-A2.0 catalogue. *Bull. Am. Astron. Soc.* **30**, 1427 (1998).
29. Allen, G. E., Petre, R. & Gotthelf, E. V. X-ray synchrotron emission from 10–100 TeV cosmic ray electrons in the supernova remnant SN 1006. *Astrophys. J.* **558**, 739–752 (2001).
30. Winkler, P. F., Long, K. S., Hamilton, A. J. S. & Fesen, R. A. Probing multiple sight lines through the SN 1006 remnant by ultraviolet absorption spectroscopy. *Astrophys. J.* **624**, 189–197 (2005).

Supplementary Information is available in the online version of the paper.

Acknowledgements This work was supported by the Spanish Ministerio de Ciencia e Innovación (MICINN), the Universidad Complutense de Madrid (UCM) and the Comunidad de Madrid, and is based on observations collected with the UVES spectrograph at the VLT/UT2 8.2-m Kueyen Telescope (ESO run ID, 69.D-0397(A)) at the Paranal Observatory, Chile. We are grateful to the Cerro Paranal Observatory staff and to the User Support Department of ESO for their help.

Author Contributions J.I.G.H. performed the chemical abundance analysis of the observed UVES spectra and determined the distances to the targets. J.I.G.H. and P.R.-L. wrote the paper. P.R.-L. was the Principal Investigator of the ESO proposal. R.C. and J.M. also participated in the ESO proposal. H.M.T. and D.M. derived the stellar parameters and created figures showing the observed spectra. R.C. and P.R.-L. contributed to the astrophysical interpretation of the results. J.M. and L.R.B. collected the photometric data and created figures showing the field and the supernova remnant. All the authors provided comments and contributed to the text of the final manuscript.

Author Information Reprints and permissions information is available at www.nature.com/reprints. The authors declare no competing financial interests. Readers are welcome to comment on the online version of the paper. Correspondence and requests for materials should be addressed to J.I.G.H. (jonay@iac.es) or P.R.-L. (pilar@am.ub.es).

Popularity versus similarity in growing networks

Fragkiskos Papadopoulos¹, Maksim Kitsak², M. Ángeles Serrano³, Marián Boguñá³ & Dmitri Krioukov²

The principle¹ that ‘popularity is attractive’ underlies preferential attachment², which is a common explanation for the emergence of scaling in growing networks. If new connections are made preferentially to more popular nodes, then the resulting distribution of the number of connections possessed by nodes follows power laws^{3,4}, as observed in many real networks^{5,6}. Preferential attachment has been directly validated for some real networks (including the Internet^{7,8}), and can be a consequence of different underlying processes based on node fitness, ranking, optimization, random walks or duplication^{9–16}. Here we show that popularity is just one dimension of attractiveness; another dimension is similarity^{17–24}. We develop a framework in which new connections optimize certain trade-offs between popularity and similarity, instead of simply preferring popular nodes. The framework has a geometric interpretation in which popularity preference emerges from local optimization. As opposed to preferential attachment, our optimization framework accurately describes the large-scale evolution of technological (the Internet), social (trust relationships between people) and biological (*Escherichia coli* metabolic) networks, predicting the probability of new links with high precision. The framework that we have developed can thus be used for predicting new links in evolving networks, and provides a different perspective on preferential attachment as an emergent phenomenon.

Nodes that are similar have a higher chance of getting connected, even if they are not popular. This effect is known as homophily in social sciences^{17,18}, and it has been observed in many real networks^{19–24}. In the web^{23,24}, for example, an individual creating her new homepage tends to link it not only to popular sites such as Google or Facebook, but also to not-so-popular sites that are close to her special interests—for example, sites devoted to the composer Tartini or to free solo climbing. These observations suggest the introduction of a measure of attractiveness that would somehow balance popularity and similarity.

The simplest proxy for popularity is the node birth time. All other things being equal, older nodes have more chances to become popular and attract connections^{3,4}. If nodes join the network one by one, then the node birth time is simply the node number $t = 1, 2, \dots$. To model similarity, we randomly place nodes on a circle that represents the simplest similarity space. That is, the angular distances between nodes model their similarity distances, such as the cosine similarity or any other measure^{22–24}. The simplest way to model a balance between popularity and similarity is then to establish new connections that optimize the product between popularity and similarity. In other words, the model is simply as follows: (1) initially the network is empty; (2) at time $t \geq 1$, new node t appears at a random angular position θ_t on the circle; and (3) new node t connects to a subset of existing nodes s , $s < t$, consisting of the m nodes with the m smallest values of product $s\theta_{st}$, where m is a parameter controlling the average node degree $\bar{k} = 2m$, and θ_{st} is the angular distance between nodes s and t (Fig. 1a, b). At early times $t \leq m$, node t connects to all the existing nodes.

This model has an interesting geometric interpretation, shown in Fig. 1c. Specifically, after mapping birth time t of a node to its radial coordinate r_t via $r_t = \ln t$, all nodes lie not on a circle but on a plane—their polar coordinates are (r_t, θ_t) . It then turns out that new nodes

connect simply to the closest m nodes on the plane, except that distances are not Euclidean but hyperbolic²⁵. The hyperbolic distance between two nodes at polar coordinates (r_s, θ_s) and (r_t, θ_t) is approximately $x_{st} = r_s + r_t + \ln(\theta_{st}/2) = \ln(st\theta_{st}/2)$. Therefore the sets of nodes s minimizing x_{st} or $s\theta_{st}$ for each t are identical. The hyperbolic

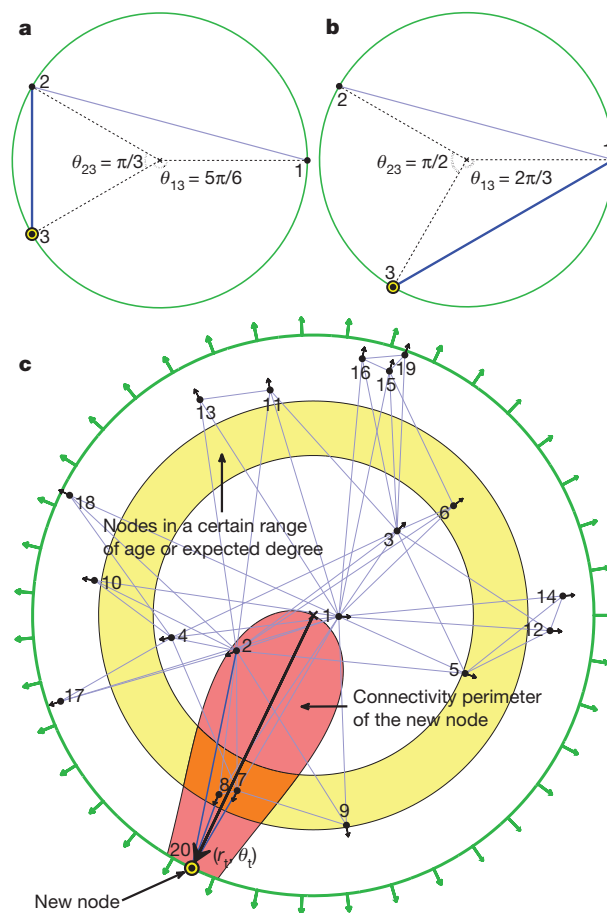


Figure 1 | Geometric interpretation of popularity × similarity optimization. The nodes (dots) are numbered by their birth times, and located at random angular (similarity) coordinates. On its birth, the new circled node t in the yellow annulus connects to m old nodes s minimizing $s\theta_{st}$. The new connections are shown by the thicker blue links. In **a** and **b**, $t = 3$ and $m = 1$. In **a**, node 3 connects to node 2 because $2\theta_{23} = 2\pi/3 < 10_{13} = 5\pi/6$. In **b**, node 3 connects to node 1 because $1\theta_{13} = 2\pi/3 < 2\theta_{23} = \pi$. In **c**, an optimization-driven network with $m = 3$ is simulated for up to 20 nodes. The radial (popularity) coordinate of new node $t = 20$ is $r_t = \ln t$, shown by the long thick arrow. This node connects to the three hyperbolic closest nodes. The red shape marks the set of points located at hyperbolic distances less than r_t from the new node. Arrows on dots show all nodes drifting away from the crossed origin, emulating popularity fading as explained in the text. The drift speed in the network shown corresponds to the degree distribution exponent $\gamma = 2.1$. The outer green circle shows the current network boundary of radius $r_t = \ln t$ expanding with time t as indicated by green arrows.

¹Department of Electrical Engineering, Computer Engineering and Informatics, Cyprus University of Technology, 33 Saripolou Street, 3036 Limassol, Cyprus. ²Cooperative Association for Internet Data Analysis (CAIDA), University of California, San Diego (UCSD), La Jolla, California 92093, USA. ³Departament de Física Fonamental, Universitat de Barcelona, Martí i Franquès 1, 08028 Barcelona, Spain.

distance is then nothing but a convenient single-metric representation of a combination of the two attractiveness attributes, radial popularity and angular similarity. We will use this metric extensively below.

The networks grown as described may seem to have nothing in common with preferential attachment (PA)^{2–4}. Yet we show in Fig. 2a that the probability $\Pi(k)$ that an existing node of degree k attracts a connection from a new node is the same linear function of k in the described model and in PA. It is not surprising then that the degree distributions in PA and in our model are the same power laws. In Supplementary Information section IV, we prove that the exponent γ of this power law approaches 2. Preferential attachment thus emerges as a process originating from optimization trade-offs between popularity and similarity.

However, there are crucial differences between such optimization and PA. In the latter, new nodes connect with the same probability $\Pi(k)$ to any nodes of degree k in the network. In the former, new nodes connect only to specific subsets of such k -degree nodes that are closest to the new node along the similarity dimension θ (Fig. 1c). To quantify, we compare in Fig. 2b the probability of connection between a pair of nodes as a function of their hyperbolic distance in the two cases. We see that close nodes are almost always connected in the optimization model, whereas in PA the probability of their connection is lower by an order of magnitude. On the other hand, nodes that are far apart are never connected in the optimization model, whereas they can be connected in PA. These differences manifest themselves in the strength of clustering, which is the probability that two nodes connected to the same node are also connected to each other. In PA, clustering is asymptotically zero²⁶, whereas it is strong in many real networks^{5,6}.

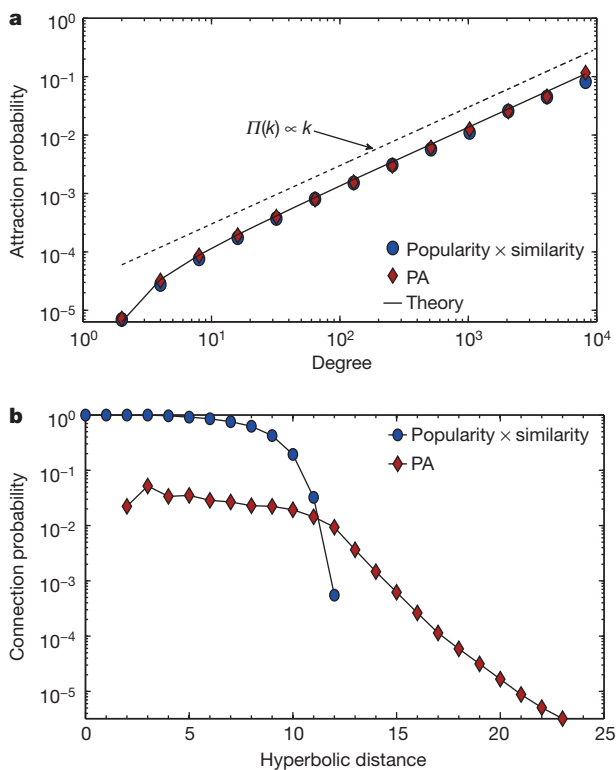


Figure 2 | Emergence of PA from popularity × similarity optimization.

Two growing networks have been simulated up to $t = 10^5$ nodes, one growing according to the described optimization model, and the other according to PA. In both networks, each new node connects to $m = 2$ existing nodes. The $\gamma \rightarrow 2$ limit is not well-defined in PA, so that $\gamma = 2.1$ is used instead as described in the text. **a**, The probability $\Pi(k)$ that an existing node of degree k attracts a new link. The solid line is the theoretical prediction, while the dashed line is a linear function, $\Pi(k) \propto k$. **b**, The probability $p(x)$ that a pair of nodes located at hyperbolic distance x are connected. The average clustering (over all nodes) in the optimization and PA networks is $\bar{c} = 0.83$ and $\bar{c} = 0.12$, respectively.

We show in Supplementary Information section IV that the described optimization model leads to clustering that is the strongest possible for networks with a given degree distribution.

The strength of clustering and the power-law exponent can both be adjusted to arbitrary values via the following model modifications. We first consider the effect of popularity fading, observed in many real networks^{27,28}. We note that the closer the node to the centre in Fig. 1c, the more popular it is: the higher its degree, and the more new connections it attracts, which explains why PA emerges in the model. Therefore to model popularity fading, we let all nodes drift away from the centre such that the radial coordinate of node s at time $t > s$ is increasing as $r_s(t) = \beta r_s + (1 - \beta)r_t$, where $r_s = \ln s$ and $r_t = \ln t$, and parameter $\beta \in [0, 1]$. This modification is identical to minimizing $s^\beta \theta_{st}$ (or $s^b \theta_{st}^a$ with $\beta = b/a$) instead of $s\theta_{st}$. It changes the power-law exponent to $\gamma = 1 + 1/\beta \geq 2$. If $\beta = 1$, the nodes do not move and $\gamma = 2$. If $\beta = 0$, all nodes move with the maximum speed, always lying on the circle of radius r_t , while the network degenerates to a random geometric graph growing on the circle. PA emerges at any $\gamma = 1 + 1/\beta$ since the attraction probability $\Pi(k)$ is a linear function of degree k , $\Pi(k) \propto k + m(\gamma - 2)$, the same as in PA⁴. We prove these statements in Supplementary Information sections IV–VII, where we also show that the popular fitness model¹⁰ can be mapped to our geometric optimization framework by letting different nodes drift away with different speeds (Supplementary Information section V).

Because the strongest clustering is due to connections to the closest nodes, to weaken clustering we allow connections to more-distant nodes. Connecting to the m closest nodes is approximately the same as connecting to nodes lying within distance $R_t \approx r_t$ (see Fig. 1c and Supplementary Information section IV, where we derive the exact expression for R_t , which controls the average degree in the network). If new nodes t establish connections to existing nodes s at hyperbolic distance x_{st} with probability $p(x_{st}) = 1/\{1 + \exp[(x_{st} - R_t)/T]\}$, where parameter $T \geq 0$ is the network temperature (see Supplementary Information sections IV and VI), then clustering is a decreasing function of temperature. That is, temperature is the parameter controlling clustering in the network. At zero temperature, the connection probability $p(x_{st})$ is either 1 or 0 depending on whether distance x_{st} is less or greater than R_t , so that we recover the strongest clustering case above, where new nodes connect only to the closest existing nodes. Clustering gradually decreases to zero at $T = 1$, and remains asymptotically zero for any $T \geq 1$ (Supplementary Information sections IV, VI). At high temperatures $T \rightarrow \infty$, the model degenerates either to growing random graphs, or, remarkably, to standard PA (Supplementary Information section VII).

To investigate if similarity shapes the structure and dynamics of real networks as our model predicts, we consider a series of historical snapshots of the Internet, the *E. coli* metabolic network, and the social network of trust relationships between people, also known as the web of trust (WoT). The first two networks are disassortative (nodes of dissimilar degrees are connected with a higher probability), while the third is assortative (nodes of similar degrees are connected with a higher probability), and its degree distribution deviates from a power law. We map these networks to their popularity × similarity spaces (Methods Summary). The mapping infers the radial (popularity) and angular (similarity) coordinates for all nodes, so that we can compute the hyperbolic distances between all node pairs, and the probabilities of new connections as functions of the hyperbolic distance between corresponding nodes. These probabilities are shown in Fig. 3. In all the three networks, they are close to the theoretical predictions of our model.

This finding is important for several reasons. First, it shows that real-world networks evolve as our framework predicts. Specifically, given the popularity and similarity coordinates of two nodes, they link with probability close to the theoretical value predicted by the model. The framework may thus be used for link prediction, a notoriously difficult and important problem in many disciplines²⁹, with applications

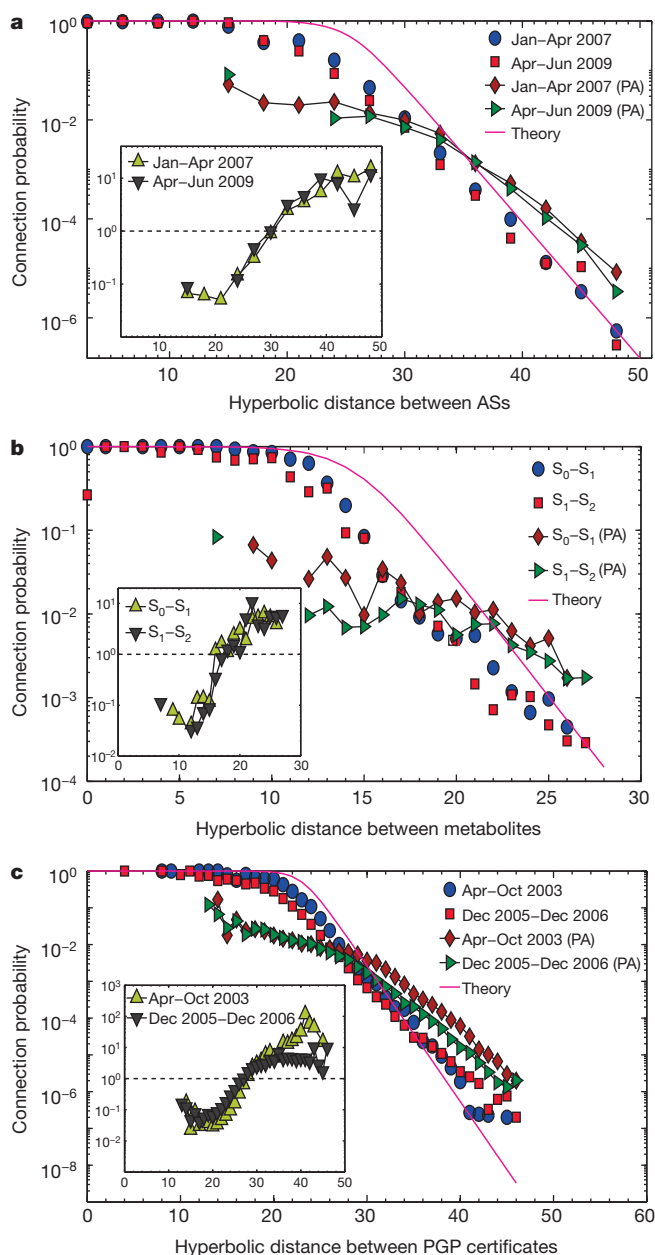


Figure 3 | Popularity \times similarity optimization for three different networks. **a**, The growing Internet; **b**, *E. coli* metabolic network; and **c**, pretty-good-privacy (PGP) web of trust (WoT) between people. Each plot shows the probability of connections between new and old nodes, as a function of the hyperbolic (popularity \times similarity) distance x between them in the real networks (circles and squares) and in PA emulations (diamonds and triangles). To emulate PA, new links are disconnected from old nodes to which these links are connected in the real networks, and reconnected to old nodes according to PA. For a pair of historical network snapshots S_0 (older) and S_1 (newer), new nodes are the nodes present in S_1 but not in S_0 , and old nodes are the nodes present both in S_1 and S_0 . Each plot shows the data for two pairs of such historical snapshots. The solid curve in each plot is the theoretical connection probability in the optimization model with the parameters corresponding to a given real network. Because the probability of new connections in the real networks is close to the theoretical curves, the shown data demonstrate that these networks grow as the popularity \times similarity optimization model predicts, whereas PA, accounting only for popularity, is off by orders of magnitude in predicting the connections between similar (small x) or dissimilar (large x) nodes. To quantify this inaccuracy, the insets show the ratio between the connection probabilities in PA emulations and in the real networks, that is, the ratios of the values shown by diamonds and circles, and by triangles and squares in the main plots. The x -axes in the insets are the same as in the main plots.

ranging from predicting protein interactions or terrorist connections to designing recommender and collaborative filtering systems³⁰. Second, Fig. 3 directly validates our framework and its core mechanism. It is not surprising then that, as a consequence, the synthetic graphs that the model generates are remarkably similar to real networks across a range of metrics (Supplementary Information section IX), implying that the framework can be also used for accurate modelling of real network topologies. We review related work in Supplementary Information section X, and to the best of our knowledge, there is no other model that would simultaneously: (1) be simple and universal, that is, applicable to many different networks, (2) have a similarity space as its core component, (3) cast PA as an emergent phenomenon, (4) generate graphs similar to real networks across a wide range of metrics, and (5) validate the proposed growth mechanism directly. Validation is usually limited to comparing certain graph metrics, such as degree distribution, between modelled and real networks; however, this ‘validates’ a consequence of the mechanism, not the mechanism itself. Direct validation is usually difficult, because proposed mechanisms tend to incorporate many unmeasurable factors—economic or political factors in Internet evolution, for example. Our approach is no different in that it cannot measure all the factors or node attributes contributing to node similarity in any of the considered real networks. Yet, the angular distances between nodes in our approach can be considered as projections of properly weighted combinations of all such similarity factors affecting network evolution, and we can infer these distances using statistical inference methods, directly validating the growth mechanism.

To summarize, popularity is attractive, but so is similarity. Neglecting the latter would lead to severe aberrations. Within the Internet, for example, a local network in Nebraska would connect directly to a local network in Tibet, in the same way as on the web, a person not even knowing about Tartini or free solo climbing would suddenly link her page to these subjects. The probability of such dissimilar connections is very low in reality, and the stronger the similarity forces, the smaller this probability is. Neglecting the network similarity structure leads to overestimations or underestimations of the probability of dissimilar or similar connections by orders of magnitude (Fig. 3). However, one cannot tell the difference between our framework and PA by examining node degrees only. The probability that an existing node of degree k attracts a new link optimizing popularity \times similarity is exactly the same linear function of k as in PA (Fig. 2a). Supplementary Fig. 1 shows that this function is indeed realized in the considered real networks, re-validating effective PA for these networks. Therefore the popularity \times similarity optimization approach provides a natural geometric explanation for the following ‘dilemmas’ characteristic of PA. On the one hand, PA has been validated for many real networks, while on the other hand, it requires exogenous mechanisms to explain not only strong clustering, but also linear popularity preference, and how such preference can emerge in real networks, where nodes do not have any global information about the network structure. As PA appears as an emergent phenomenon in the framework developed here, our framework provides a simple and natural resolution to these dilemmas, and this resolution is directly validated against large-scale evolution of very different real networks.

We conclude with the observation that to know the closest nodes in the hyperbolic popularity \times similarity space requires precise global information about all node locations. However, non-zero temperatures smooth out the sharp connectivity perimeter threshold in Fig. 1c, thus modelling reality where this proximity information is not precise and mixed with errors and noise. In that respect, PA is a limiting regime with similarity forces reduced to nothing but noise.

METHODS SUMMARY

To infer the radial r_i and angular θ_i coordinates for each node i in a real network snapshot with adjacency matrix a_{ij} , $i, j = 1, 2, \dots, t$, we use the Markov Chain Monte Carlo (MCMC) method described in detail in Supplementary Information.

Specifically, we derive there the exact relation between the expected current degree k_i of node i and its current radial coordinate r_i , which scales as $k_i \sim e^{r_i - r_i}$. To infer the radial coordinates we use the same expression substituting in it the real degrees k_i of nodes instead of their expected degrees. Having inferred the radial coordinates, we then execute the Metropolis-Hastings algorithm to find the node angular coordinates that maximize likelihood $\mathcal{L} = \prod_{i < j} p(x_{ij})^{a_{ij}} [1 - p(x_{ij})]^{1 - a_{ij}}$, where $p(x_{ij}) = 1 / [1 + e^{(x_{ij} - R)/T}]$ is the connection probability in the model, and parameters R and T are defined by the average node degree and clustering in the network via expressions in Supplementary Information section IV. Likelihood \mathcal{L} is the probability that the network snapshot with node coordinates (r_i, θ_i) , defining the hyperbolic distances x_{ij} between all nodes, is produced by the model. The algorithm employs an MCMC process, which finds coordinates θ_i for all i that approximately maximize \mathcal{L} . Further details are in Supplementary Information sections II and III, where we also show that the method yields meaningful results for the considered networks, but not for a network (movie actor collaborations) to which popularity \times similarity optimization does not apply.

The nodes in Fig. 3a, b and c are respectively autonomous systems (ASs), metabolites and Pretty Good Privacy (PGP) certificates associating users' email addresses with their cryptographic keys. Parameters (R, T) used to infer the coordinates and to draw the theoretical connection probabilities are (25.2, 0.79), (14.4, 0.77) and (23, 0.59). Each panel of Fig. 3 shows data for two pairs of snapshots: Fig. 3a, January–April 2007 and April–June 2009; Fig. 3b, S_0 – S_1 and S_1 – S_2 defined in Supplementary Information section I; and Fig. 3c, April–October 2003 and December 2005–December 2006. The few missing data points in the empirical curves (circles and squares) indicate that there are no node pairs at the corresponding distances after the mapping, whereas extra missing points in the PA emulation curves (diamonds and triangles) indicate that all node pairs at those distances are not connected after PA emulations, meaning that the PA connection probability is zero there.

Received 25 April; accepted 26 July 2012.

Published online 12 September 2012.

- Dorogovtsev, S., Mendes, J. & Samukhin, A. WWW and Internet models from 1955 till our days and the “popularity is attractive” principle. Preprint at <http://arXiv.org/abs/cond-mat/0009090> (2000).
- Barabási, A.-L. & Albert, R. Emergence of scaling in random networks. *Science* **286**, 509–512 (1999).
- Krapivsky, P. L., Redner, S. & Leyvraz, F. Connectivity of growing random networks. *Phys. Rev. Lett.* **85**, 4629–4632 (2000).
- Dorogovtsev, S. N., Mendes, J. F. F. & Samukhin, A. N. Structure of growing networks with preferential linking. *Phys. Rev. Lett.* **85**, 4633–4636 (2000).
- Dorogovtsev, S. N. *Lectures on Complex Networks* (Oxford Univ. Press, 2010).
- Newman, M. E. J. *Networks: An Introduction* (Oxford Univ. Press, 2010).
- Pastor-Satorras, R., Vázquez, A. & Vespignani, A. Dynamical and correlation properties of the internet. *Phys. Rev. Lett.* **87**, 258701 (2001).
- Jeong, H., Neda, Z. & Barabási, A. L. Measuring preferential attachment in evolving networks. *Europhys. Lett.* **61**, 567–572 (2003).
- Dorogovtsev, S. N., Mendes, J. & Samukhin, A. Size-dependent degree distribution of a scale-free growing network. *Phys. Rev. E* **63**, 062101 (2001).
- Bianconi, G. & Barabási, A.-L. Bose-Einstein Condensation in complex networks. *Phys. Rev. Lett.* **86**, 5632–5635 (2001).
- Caldarelli, G., Capocci, A., Rios, P. D. L., & Muñoz, M. A. Scale-free networks from varying vertex intrinsic fitness. *Phys. Rev. Lett.* **89**, 258702 (2002).
- Vázquez, A. Growing network with local rules: preferential attachment, clustering hierarchy, and degree correlations. *Phys. Rev. E* **67**, 056104 (2003).
- Pastor-Satorras, R., Smith, E. & Sole, R. V. Evolving protein interaction networks through gene duplication. *J. Theor. Biol.* **222**, 199–210 (2003).
- Fortunato, S., Flammini, A. & Menczer, F. Scale-free network growth by ranking. *Phys. Rev. Lett.* **96**, 218701 (2006).
- D'Souza, R. M., Borgs, C., Chayes, J. T., Berger, N. & Kleinberg, R. D. Emergence of tempered preferential attachment from optimization. *Proc. Natl Acad. Sci. USA* **104**, 6112–6117 (2007).
- Motter, A. E. & Toroczkai, Z. Introduction: optimization in networks. *Chaos* **17**, 026101 (2007).
- McPherson, M., Smith-Lovin, L. & Cook, J. M. Birds of a feather: homophily in social networks. *Annu. Rev. Sociol.* **27**, 415–444 (2001).
- Simsek, O. & Jensen, D. Navigating networks by using homophily and degree. *Proc. Natl Acad. Sci. USA* **105**, 12758–12762 (2008).
- Redner, S. How popular is your paper? An empirical study of the citation distribution. *Eur. Phys. J. B* **4**, 131–134 (1998).
- Watts, D. J., Dodds, P. S. & Newman, M. E. J. Identity and search in social networks. *Science* **296**, 1302–1305 (2002).
- Börner, K., Maru, J. T. & Goldstone, R. L. The simultaneous evolution of author and paper networks. *Proc. Natl Acad. Sci. USA* **101**, 5266–5273 (2004).
- Crandall, D., Cosley, D., Huttenlocher, D., Kleinberg, J. & Suri, S. in *Proc. 14th ACM SIGKDD International Conference on Knowledge Discovery and Data Mining (KDD 2008)* (eds Li, Y., Liu, B. & Sarawagi, S.) 160–168 (ACM, 2008).
- Menczer, F. Growing and navigating the small world Web by local content. *Proc. Natl Acad. Sci. USA* **99**, 14014–14019 (2002).
- Menczer, F. Evolution of document networks. *Proc. Natl Acad. Sci. USA* **101**, 5261–5265 (2004).
- Bonahon, F. *Low-Dimensional Geometry* (AMS, 2009).
- Bollobás, B. & Riordan, O. in *Handbook of Graphs and Networks* (eds Bornholdt, S. & Schuster, H. G.) Ch. 1 1–34 (Wiley-VCH, 2003).
- Adamic, L. A. & Huberman, B. A. Power-law distribution of the World Wide Web. *Science* **287**, 2115 (2000).
- van Raan, A. F. J. On growth, ageing, and fractal differentiation of science. *Scientometrics* **47**, 347–362 (2000).
- Clauset, A., Moore, C. & Newman, M. E. J. Hierarchical structure and the prediction of missing links in networks. *Nature* **453**, 98–101 (2008).
- Menon, A. K. & Elkan, C. in *Machine Learning and Knowledge Discovery in Databases (ECML)* (eds Gunopulos, D., Hofmann, T., Malerba, D. & Vazirgiannis, M.) 437–452 (Lecture Notes in Computer Science, Vol. 6912, Springer, 2011).

Supplementary Information is available in the online version of the paper.

Acknowledgements We thank C. Elkan, G. Bianconi, P. Krapivsky, S. Redner, S. Havlin, E. Stanley and A.-L. Barabási for discussions and suggestions. This work was supported by a Marie Curie International Reintegration Grant within the 7th European Community Framework Programme; MICINN Projects FIS2010-21781-C02-02 and BFU2010-21847-C02-02; Generalitat de Catalunya grant 2009SGR838; the Ramón y Cajal programme of the Spanish Ministry of Science; ICREA Academia prize 2010, funded by the Generalitat de Catalunya; NSF grants CNS-0964236, CNS-1039646, CNS-0722070; DHS grant N66001-08-C-029; DARPA grant HR0011-12-1-0012; and Cisco Systems.

Author Contributions F.P. and D.K. planned research, performed research and wrote the paper; M.K., M.A.S. and M.B. planned and performed research. All authors discussed the results and reviewed the manuscript.

Author Information Reprints and permissions information is available at www.nature.com/reprints. The authors declare no competing financial interests. Readers are welcome to comment on the online version of the paper. Correspondence and requests for materials should be addressed to F.P. (f.papadopoulos@cut.ac.cy) or D.K. (dima@ucsd.edu).

A single-atom electron spin qubit in silicon

Jarryd J. Pla¹, Kuan Y. Tan^{1†}, Juan P. Dehollain¹, Wee H. Lim¹, John J. L. Morton^{2†}, David N. Jamieson³, Andrew S. Dzurak¹ & Andrea Morello¹

A single atom is the prototypical quantum system, and a natural candidate for a quantum bit, or qubit—the elementary unit of a quantum computer. Atoms have been successfully used to store and process quantum information in electromagnetic traps¹, as well as in diamond through the use of the nitrogen-vacancy-centre point defect². Solid-state electrical devices possess great potential to scale up such demonstrations from few-qubit control to larger-scale quantum processors. Coherent control of spin qubits has been achieved in lithographically defined double quantum dots in both GaAs (refs 3–5) and Si (ref. 6). However, it is a formidable challenge to combine the electrical measurement capabilities of engineered nanostructures with the benefits inherent in atomic spin qubits. Here we demonstrate the coherent manipulation of an individual electron spin qubit bound to a phosphorus donor atom in natural silicon, measured electrically via single-shot read-out^{7–9}. We use electron spin resonance to drive Rabi oscillations, and a Hahn echo pulse sequence reveals a spin coherence time exceeding 200 μ s. This time should be even longer in isotopically enriched ²⁸Si samples^{10,11}. Combined with a device architecture¹² that is compatible with modern integrated circuit technology, the electron spin of a single phosphorus atom in silicon should be an excellent platform on which to build a scalable quantum computer.

There have been a number of proposals for the implementation of a spin-based qubit in silicon¹³, though none have been studied in as much detail as the phosphorus atom qubit¹⁴. This interest has been motivated by the knowledge, developed over half a century from electron spin resonance experiments on bulk-doped phosphorus in silicon¹⁵, that spin coherence times can be exceptionally long, exceeding seconds¹¹. This is due to the availability of silicon in an enriched nuclear spin-zero (²⁸Si) form, as well as the low spin-orbit coupling in silicon¹⁵. The use of donor electron spins has further advantages of consistency (because each atom is identical) and tuneability (for example, through the Stark shift¹⁶), and the donor atom's nuclear spin can be employed as a quantum memory for longer term storage¹⁷.

Using methods compatible with existing complementary metal-oxide-semiconductor (CMOS) technology, we fabricated a nanostructure device on the SiO₂ surface to enable read-out and control of an electron spin¹² (Fig. 1a). In this work, the donor is intentionally implanted into the silicon substrate, with future options including the use of deterministic ion implantation¹⁸ or atomic precision in donor placement through scanning probe lithography¹⁹. The device is placed in a magnetic field of approximately 1 T, yielding well-defined electron spin-down and spin-up states ($|\downarrow\rangle$ and $|\uparrow\rangle$).

Transitions between the electron $|\downarrow\rangle$ and $|\uparrow\rangle$ states are driven by an oscillating magnetic field generated by applying microwaves to an on-chip broadband transmission line^{4,20}. By operating at a high magnetic field and low temperature ($T_{\text{electron}} \approx 300$ mK), we can detect these transitions through single-shot projective measurements on the electron spin with a process known as spin-to-charge conversion^{7,8}. Here the donor electron is both electrostatically coupled and tunnel-coupled to the island of a single electron transistor (SET), with the SET

serving as both a sensitive charge detector and an electron reservoir for the donor. Using gates PL and TG (Fig. 1a) to tune the electrochemical potentials of the donor electron spin states (μ_{\downarrow} and μ_{\uparrow} for states $|\downarrow\rangle$ and $|\uparrow\rangle$) and the Fermi level in the SET island (μ_{SET}), we can discriminate between a $|\downarrow\rangle$ or $|\uparrow\rangle$ electron as well as perform electrical initialization of the qubit, following the procedure introduced in ref. 8.

Our experiments use a two-step cyclical sequence of the donor potential, alternating between a spin read-out/initialization phase and a coherent control phase (see Supplementary Video). The qubit is first initialized in the $|\downarrow\rangle$ state through spin-dependent loading by satisfying the condition $\mu_{\downarrow} < \mu_{\text{SET}} < \mu_{\uparrow}$ (Fig. 1b). After this, the system is brought into a regime where the spin is a stable qubit ($\mu_{\downarrow}, \mu_{\uparrow} \ll \mu_{\text{SET}}$) and manipulated with various microwave pulse schemes resonant with the spin transition (Fig. 1c). The spin is then read out electrically via spin-to-charge conversion (Fig. 1b), a process which produces a pulse in the current through the SET (that is, I_{SET}) if the electron was $|\uparrow\rangle$, and leaves the qubit initialized $|\downarrow\rangle$ for the next cycle.

The electron spin resonance frequency can be extracted from the spin Hamiltonian describing this system (see also Fig. 1d):

$$H = \gamma_e B_0 S_z - \gamma_n B_0 I_z + AS \cdot I \quad (1)$$

where γ_e (or γ_n) is the gyromagnetic ratio of the electron (or nucleus), B_0 is the externally applied magnetic field, S (or I) is the electron (or nuclear) spin operator with z -component S_z (or I_z) and A is the hyperfine constant. If $\gamma_e B_0 \gg A$, the states shown in Fig. 1d are good approximations for the eigenstates of equation (1). Allowed transitions involving flips of the electron spin only (identified by arrows in Fig. 1d) exhibit resonance frequencies that depend on the state of the ³¹P nuclear spin: $\nu_{e1} \approx \gamma_e B_0 - A/2$ for nuclear spin-down; and $\nu_{e2} \approx \gamma_e B_0 + A/2$ for nuclear spin-up. The transition frequencies ν_{e1} and ν_{e2} are found by conducting an electron spin resonance (ESR) experiment²¹, which is described in the Supplementary Information.

To demonstrate coherent control, we apply a single microwave pulse of varying duration t_p to perform Rabi oscillations of the electron spin. For each t_p the cyclic pulse sequence (Fig. 1e, f) is repeated 20,000 times, first with a microwave frequency ν_{e1} , and immediately after at ν_{e2} . It is necessary to pulse on both ESR transitions as the ³¹P nuclear spin can flip several times during acquisition of the data in Fig. 2a. Figure 1g displays single-shot traces of the SET output current I_{SET} for four consecutive repetitions of the measurement sequence, for an arbitrary pulse length. A threshold detection method⁸ is used to determine the fraction of shots that contain a $|\uparrow\rangle$ electron for the measurements at both frequencies. Figure 2a shows the electron spin-up fraction f_{\uparrow} as a function of the microwave pulse duration for different applied powers P_{ESR} . The fits through the data are derived from simulations assuming Gaussian fluctuations of the local field (see Supplementary Information). Confirmation that these are Rabi oscillations comes from the linear dependence of the Rabi frequency with the applied microwave amplitude ($P_{\text{ESR}}^{1/2}$), that is, $f_{\text{Rabi}} = \gamma_e B_1$. Here B_1 is taken as half of the total linear oscillating magnetic field amplitude generated by the transmission line at the site of the donor,

¹Centre for Quantum Computation and Communication Technology, School of Electrical Engineering & Telecommunications, University of New South Wales, Sydney, New South Wales 2052, Australia.

²Department of Materials, Oxford University, Oxford OX1 3PH, UK. ³Centre for Quantum Computation and Communication Technology, School of Physics, University of Melbourne, Melbourne, Victoria 3010, Australia. [†]Present addresses: Department of Applied Physics/COMP, Aalto University, PO Box 13500, FI-00076 Aalto, Finland (K.Y.T.); London Centre for Nanotechnology, University College London, London WC1H 0AH, UK (J.J.L.M.).

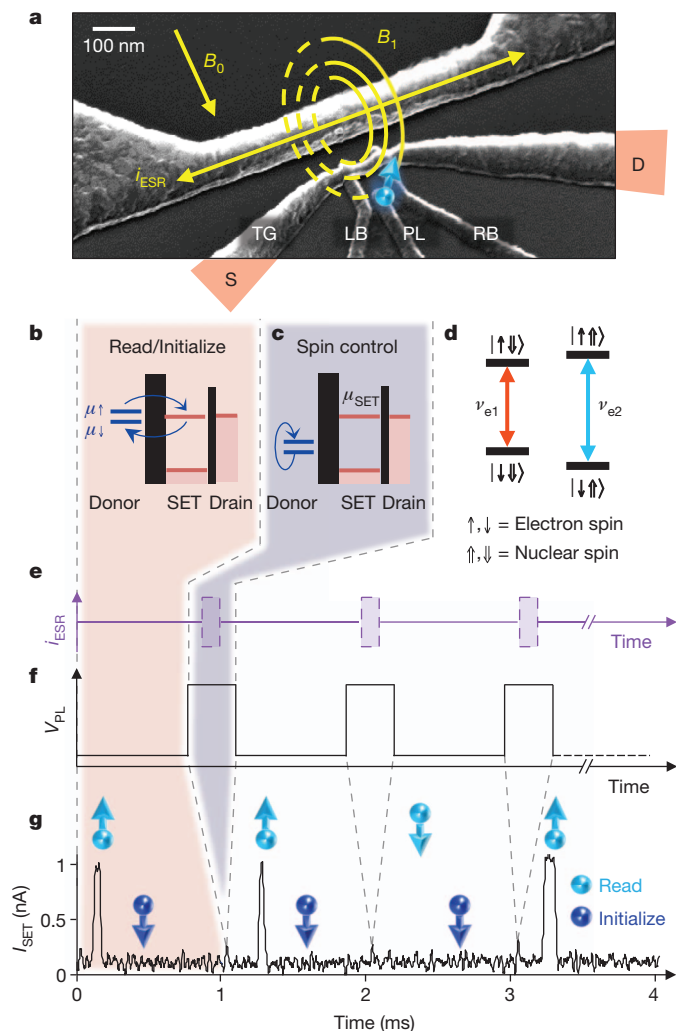


Figure 1 | Qubit device and pulsing scheme. **a**, Scanning electron micrograph of a qubit device similar to the one used in the experiment. The SET (lower right portion) consists of a top gate (TG), plunger gate (PL), left and right barrier gates (LB and RB) and source/drain contacts (S and D). The microwave transmission line is shown in the upper left portion. The donor (blue) is subject to an oscillating magnetic field B_1 from the transmission line which is perpendicular to the in-plane external field B_0 . **b** and **c**, Pulse sequence for the qubit initialization, control and read-out. **b**, Read/initialization phase $\mu_1 < \mu_{\text{SET}} < \mu_2$: a spin-up electron will tunnel from the donor to the SET island, to be later replaced by a spin-down electron, causing a pulse of current through the SET. A spin-down electron remains trapped on the donor throughout the entire phase. **c**, Control phase $\mu_1, \mu_2 \ll \mu_{\text{SET}}$: electron spin states are plunged well below the SET island Fermi level while microwaves are applied to the transmission line to perform electron spin resonance. **d**, Energy level diagram of the ^{31}P electron-nuclear system. **e** and **f**, Microwave pulse sequence (**e**) and synchronized PL gate voltage waveform (**f**) for performing and detecting spin manipulations (not drawn to scale). An arbitrary ESR pulse sequence is represented by each of the dashed purple boxes in panel **e**. **g**, Example of I_{SET} response to four consecutive read/control events where a single microwave pulse of duration t_p is applied, taken at $B_0 = 1.07$ T. The pulse duration t_p has been set to give a high probability of flipping the electron spin. The duration of the pulses in I_{SET} gives the electron spin-down tunnel-in time (about 33 μs), while their delay from the beginning of the read phase gives the spin-up tunnel-out time (about 295 μs).

assuming the rotating-wave approximation. Figure 2b shows the expected linear behaviour with microwave amplitude of the Rabi frequencies extracted from the data in Fig. 2a. The largest Rabi frequency attained was 3.3 MHz ($B_1 \approx 0.12$ mT), corresponding to a $\pi/2$ rotation in about 75 ns.

The qubit manipulation time should be contrasted with the coherence lifetime of the qubit, termed T_2 . Possible sources of decoherence

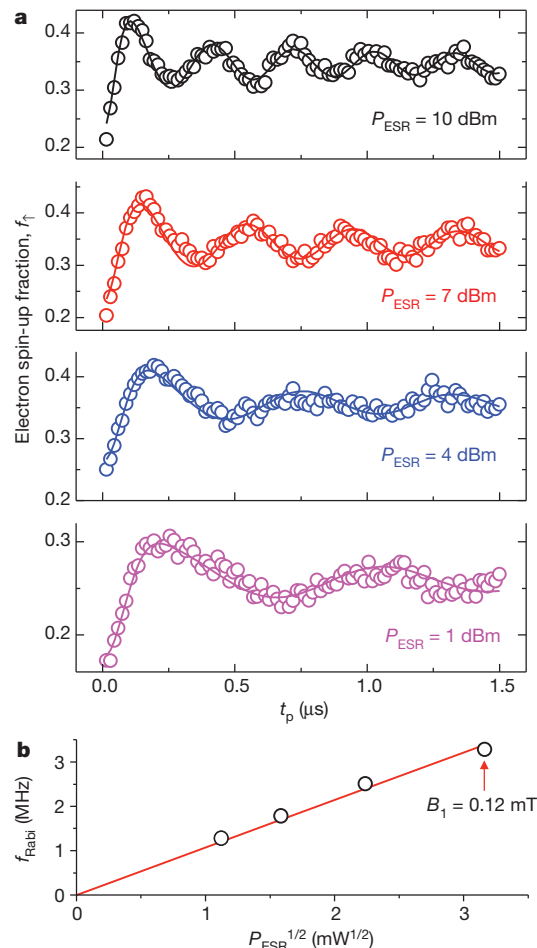


Figure 2 | Rabi oscillations and power dependence of the Rabi frequency.

a, Electron spin-up fraction as a function of the microwave burst duration for varying input powers P_{ESR} . Measurements were performed at an external field of $B_0 = 1.07$ T where the ESR frequencies are $\nu_{e1} = 29.886$ GHz and $\nu_{e2} = 30.000$ GHz. Each point represents an average of 20,000 single-shot measurements, with each shot about 1 ms in duration (see Supplementary Information for further details). The solid lines are fits generated from simulations of the measurements (Supplementary Information). **b**, Rabi frequency versus the microwave excitation amplitude, with a fit displaying the linear relationship.

include spectral diffusion of the ^{29}Si bath spins^{15,22,23}, noise in the external magnetic field, and paramagnetic defects and charge traps at the Si/SiO₂ interface²⁴. These mechanisms can, to a degree, be compensated for by using spin echo techniques (Fig. 3a), as long as the fluctuations are slow compared with the electron spin manipulation time (typically around 100 ns).

Figure 3a presents the gate voltage and microwave pulsing scheme for a Hahn echo measurement. Dephasing resulting from static local contributions to the total effective field during an initial period τ_1 is (partially or fully) refocused by a π rotation followed by a second period τ_2 (see Fig. 3c for a Bloch sphere state evolution). A spin echo is observed by varying the delay τ_2 and recording the spin-up fraction. In Fig. 3e we plot the difference in delay times ($\tau_2 - \tau_1$) against f_1 . For $\tau_1 = \tau_2$, we expect to recover a $|\downarrow\rangle$ electron at the end of the sequence if little dephasing occurs (that is, for short τ), and hence observe a minimum in f_1 . When $\tau_2 - \tau_1 \neq 0$, imperfect refocusing results in an increase in the recovered spin-up fraction. The echo shape is approximated as being Gaussian and the half-width at half-maximum implies a pure dephasing time of $T_2^* = 55 \pm 5$ ns.

We now set $\tau = \tau_1 = \tau_2$ and monitor the spin-up fraction as a function of τ , to obtain the spin echo decay curve of Fig. 3f. A fit of the form

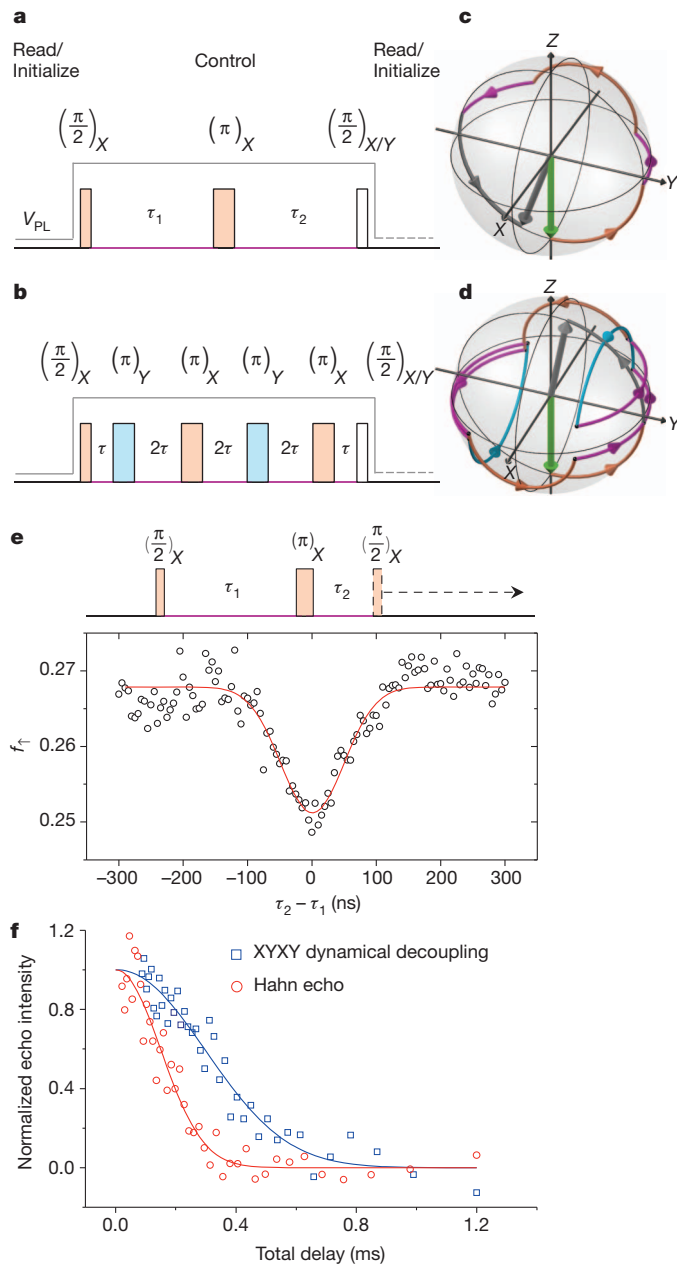


Figure 3 | Coherence time and dynamical decoupling. **a** and **b**, Pulse protocols for the Hahn echo (**a**) and XYXY dynamical decoupling (**b**) sequences with accompanying PL gate voltage waveforms, as described in the main text. The rotation angles are displayed above each pulse in brackets, with the subscript (X or Y) denoting the axis on the Bloch sphere about which the rotation is applied. The read/initialization time is 1 ms. All measurements were performed at $B_0 = 1.07$ T and with $P_{\text{ESR}} = 10$ dBm, where a $\pi/2$ rotation takes around 75 ns. **c** and **d**, Bloch sphere representation of the evolution in the rotating frame for the Hahn echo (**c**) and XYXY (**d**) sequences. The green arrow represents the initial spin state $| \downarrow \rangle$, while the grey arrow represents the final state for the case when the second $\pi/2$ pulse is about X (Y is not shown). The purple path represents dephasing in between pulses, the orange path represents a rotation about X, and the blue path is a rotation about Y. We have included rotation angle errors of 5° and 15° for the $\pi/2$ and π pulses respectively. **e**, An echo curve, obtained by applying the depicted pulse sequence with a fixed τ_1 ($= 10$ ns) and varying τ_2 . Each point represents the electron spin-up fraction f_\uparrow calculated from 50,000 single shots acquired at both ESR frequencies ($\nu_{e1} = 29.886$ GHz and $\nu_{e2} = 30.000$ GHz) and summed. The fit in red is Gaussian and of the form $f_\uparrow = B \exp[-(\tau_2 - \tau_1)/C]^2] + D$. **f**, Hahn echo (or XYXY dynamical decoupling) decay in red circles (or blue squares), measured via simulated quadrature detection (see the Methods for details). A fit through the data is given by $y = \exp[-(N\tau/T_2)^b]$, where $N = 2$ (or $N = 8$) for the Hahn echo (or XYXY dynamical decoupling) experiment. Parameter values are discussed in the main text.

$y = \exp(-(2\tau/T_2)^b)$, where T_2 and b are free parameters, yields $T_2 = 206 \pm 12$ μs and $b = 2.1 \pm 0.4$. The coherence time T_2 is almost a factor of 2,000 times longer than T_2^* , and is remarkably close to the value (300 μs) measured in bulk-doped natural silicon samples²⁵. Variations in T_2 can be expected, depending on the exact distribution of ^{29}Si nuclei within the extent of the donor electron wavefunction. This indicates that the presence of a nearby SET and the close proximity of the Si/SiO₂ interface have little, if any, effect on the electron spin coherence. This is not entirely surprising, because paramagnetic centres at the Si/SiO₂ interface are expected to be fully spin-polarized under our experimental conditions $g\mu_B B_0 \gg k_B T$ (where g is the donor electron Landé g-factor, μ_B is the Bohr magneton and k_B is the Boltzmann constant), leading to an exponential suppression of their spin fluctuations²⁶. Direct flip-flop transitions between the donor qubit and nearby interface traps are suppressed by the difference in g-factor ($g = 1.9985$ for the donor, $g > 2$ for the traps²¹), whereas dipolar flip-flops with nearby donors²⁷ can appear as a T_1 process⁸ on a much longer timescale. We measured $T_1 \approx 0.7$ s at $B_0 = 2.5$ T (data not shown), implying that this process has no bearing on T_2 . The echo decay is Gaussian in shape ($b = 2.1 \pm 0.4$), consistent with decoherence dominated by ^{29}Si spectral diffusion²².

We have extended the coherence time by applying an XYXY dynamical decoupling ESR pulse sequence²⁸ (Fig. 3b and d). This sequence substitutes the single π rotation of the Hahn echo with a series of four π rotations alternating about the X and Y axes, achieved by applying adjacent π pulses that are 90° out of phase. The resulting echo decay is shown in Fig. 3f, with a fit to the data yielding $T_2 = 410 \pm 20$ μs and $b = 2.1 \pm 0.4$. As well as representing a factor-of-two improvement in T_2 , the XYXY sequence demonstrates the ability to perform controlled rotations about two orthogonal axes on the Bloch sphere (X and Y), permitting arbitrary one-qubit gates for universal quantum computing²⁹.

Next we consider the fidelity of our electron spin qubit, broken down into three components: measurement, initialization and control. The measurement fidelity F_M comprises errors resulting from detection limitations of the experimental set-up as well as thermally induced read-out events. The electrical spin-down and spin-up read errors (γ_\downarrow and γ_\uparrow respectively) arise from a finite measurement bandwidth and signal-to-noise ratio. They depend on the threshold current I_T used for detecting the spin-up pulses. Figure 4a shows the results of a numerical model based on our experimental data (see Supplementary Information for details), where $\gamma_{\downarrow, \uparrow}$ are plotted as a function of I_T . At $I_T = 370$ pA we achieve a best-case error of $\gamma = \gamma_\downarrow + \gamma_\uparrow = 18\%$.

Thermal broadening of the Fermi distribution in the SET island produces the read/load errors, as depicted in Fig. 4b. The process of a spin-down electron tunnelling into an empty state in the SET occurs with a probability α , whereas β denotes the probability of incorrectly initializing the qubit in the spin-up state. The parameters α and β are sensitive to the device tuning and can vary slightly between measurements. We have extracted α and β from simulations of the Rabi oscillations in Fig. 2a, and for $P_{\text{ESR}} = 10$ dBm we find $\alpha = 28 \pm 1\%$ and $\beta = 1^{+9}_{-1}\%$. This gives an average measurement fidelity for the electron spin-up and spin-down states of $F_M = 1 - (\gamma + \alpha(1 - \gamma_\downarrow))/2 = 77 \pm 2\%$ and an initialization fidelity F_I of at least 90% (see Supplementary Information for full details).

The qubit control fidelity F_C is reduced by random field fluctuations from the ^{29}Si nuclear bath spins. These produce an effective field B_{eff} in the rotating frame that is tilted out of the X-Y plane (Fig. 4d), and lead to imperfect pulses. We now estimate the strength of these fluctuations. Figure 4c presents a series of ESR spectra, where the electron spin-up fraction is monitored as a function of the microwave frequency. The top three traces of Fig. 4c contain individual sweeps with each point obtained over a timescale of around 250 ms. We attribute the shift in peak position between sweeps to slow fluctuations of a few strongly coupled ^{29}Si nuclei, with hyperfine coupling strengths of the order of 1 MHz. The width of the peaks is most probably the result of

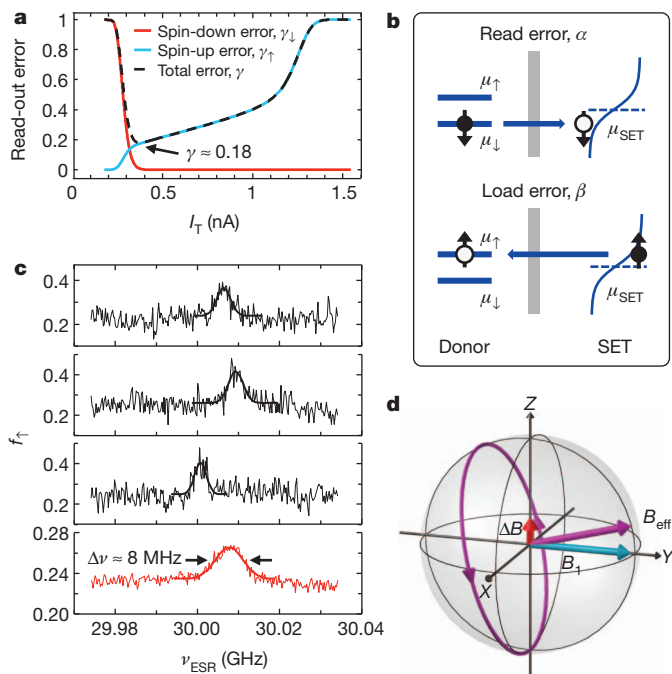


Figure 4 | Qubit fidelity analysis. **a**, Electrical read-out errors generated from a numerical model. The red curve gives the error γ_{\downarrow} involved in identifying a $|\downarrow\rangle$ electron as a function of the threshold current I_T , caused by noise in I_{SET} exceeding I_T . The blue curve represents the error γ_{\uparrow} for detecting a $|\uparrow\rangle$ electron, which occurs as a result of detection bandwidth limitations and a finite $|\uparrow\rangle I_{\text{SET}}$ pulse height⁸. The dashed curve depicts the combined electrical error, $\gamma = \gamma_{\downarrow} + \gamma_{\uparrow}$. **b**, Mechanisms by which read (top) and load (bottom) errors are produced as a result of thermal broadening in the SET island (discussed in the main text). The solid circles represent full electron states with spin indicated by the arrow, while the empty circles signify unoccupied states. **c**, Sweeps of the frequency ν_{ESR} in the vicinity of the nuclear spin-up ESR transition ν_{e2} . The top three traces are individual sweeps where f_1 at each ν_{ESR} is calculated from 250 single-shot measurements. The bottom trace is an average of 100 sweeps. **d**, Illustration of the rotation errors created by hyperfine field fluctuations of the ^{29}Si nuclear bath. For simplicity, only the Z-component of the hyperfine field has been shown. The bath nuclear spins produce an offset from resonance, ΔB , which causes rotations about a new axis aligned with B_{eff} .

distant, weakly coupled ^{29}Si nuclear spins that fluctuate on the single-shot timescale (see Supplementary Information for further discussion). The bottom trace of Fig. 4c contains an average of 100 sweeps, representing many nuclear spin configurations. From this we extract a full-width at half-maximum $\Delta\nu = 7.5 \pm 0.5$ MHz. This is consistent with the observed T_2^* , where $\Delta\nu = 1/(\pi T_2^*) = 6 \pm 1$ MHz. To calculate the rotation angle error, we simulate a Rabi experiment assuming the largest B_1 achieved (0.12 mT) and Gaussian fluctuations of the nuclear bath with a standard deviation of $\sigma = \Delta\nu / (2\sqrt{2 \ln(2)}) = 3.2 \pm 0.2$ MHz (see Supplementary Information). From this we infer an average tip angle of $102 \pm 3^\circ$ for an intended π rotation, corresponding to an average control fidelity of $F_C = 57 \pm 2\%$.

The processes that contribute to the measurement, initialization and control fidelity degradation can be mitigated with foreseeable adjustments to the device architecture and experimental set-up. Significant improvements in the read/load errors would follow from enhanced electrical filtering to lower the electron temperature, thus enabling the high read-out fidelities ($>90\%$) already achieved⁸. Moving to an enriched ^{28}Si (nuclear spin-zero) substrate¹⁰ would remove the primary source of rotation angle error, and allow for the exceptional coherence times already demonstrated in bulk-doped samples¹¹.

Future experiments will focus on the coupling of two donor electron spin qubits through the exchange interaction¹⁴, a key requirement in proposals for scalable quantum computing architectures in this system³⁰. Taken together with the single-atom doping technologies^{18,19}

now demonstrated in silicon, the advances reported here open the way for a spin-based quantum computer using single atoms, as first envisaged by Kane¹⁴ more than a decade ago.

METHODS SUMMARY

Device fabrication and experimental set-up. For information relating to the device fabrication and experimental set-up, see the Supplementary Information.

Simulated quadrature detection for T_2 measurements. For each τ ($\tau = \tau_1 = \tau_2$ for the Hahn echo), the sequence of Fig. 3a (or Fig. 3b) is repeated 30,000 times (or 75,000 times) for the Hahn echo (or XYXY dynamical decoupling) measurement at both ν_{e1} and ν_{e2} , and for X and Y phases of the final $\pi/2$ rotation. The resulting signal amplitude is given by $(f_1(\nu_{e1}, Y) - f_1(\nu_{e1}, X)) + (f_1(\nu_{e2}, Y) - f_1(\nu_{e2}, X))$, where $f_1(\nu_{e1}, Y)$ represents the electron spin-up fraction of the single-shot traces taken at ν_{e1} with a final $\pi/2$ pulse about the Y-axis, and so on. The data points in Fig. 3f have been re-normalized with the amplitudes and offsets extracted from free-exponential fits through the decays. A 30% reduction in signal amplitude was observed for the XYXY dynamical decoupling decay, relative to that of the Hahn echo.

Received 16 May; accepted 27 July 2012.

Published online 19 September 2012.

- Biercuk, M. J. *et al.* Optimized dynamical decoupling in a model quantum memory. *Nature* **458**, 996–1000 (2009).
- van der Sar, T. *et al.* Decoherence-protected quantum gates for a hybrid solid-state spin register. *Nature* **484**, 82–86 (2012).
- Petta, J. R. *et al.* Coherent manipulation of coupled electron spins in semiconductor quantum dots. *Science* **309**, 2180–2184 (2005).
- Koppens, F. H. L. *et al.* Driven coherent oscillations of a single electron spin in a quantum dot. *Nature* **442**, 766–771 (2006).
- Nowack, K. C., Koppens, F. H. L., Nazarov, Y. V. & Vandersypen, L. M. K. Coherent control of a single electron spin with electric fields. *Science* **318**, 1430–1433 (2007).
- Maune, B. M. *et al.* Coherent singlet-triplet oscillations in a silicon-based double quantum dot. *Nature* **481**, 344–347 (2012).
- Elzerman, J. M. *et al.* Single-shot read-out of an individual electron spin in a quantum dot. *Nature* **430**, 431–435 (2004).
- Morello, A. *et al.* Single-shot readout of an electron spin in silicon. *Nature* **467**, 687–691 (2010).
- Simmons, C. B. *et al.* Tunable spin loading and T_1 of a silicon spin qubit measured by single-shot readout. *Phys. Rev. Lett.* **106**, 156804 (2011).
- Ager, J. W. *et al.* High-purity, isotopically enriched bulk silicon. *J. Electrochem. Soc.* **152**, G448–G451 (2005).
- Tyryshkin, A. M. *et al.* Electron spin coherence exceeding seconds in high purity silicon. *Nature Mater.* **11**, 143–147 (2012).
- Morello, A. *et al.* Architecture for high-sensitivity single-shot readout and control of the electron spin of individual donors in silicon. *Phys. Rev. B* **80**, 081307(R) (2009).
- Morton, J. J. L., McCamey, D. R., Eriksson, M. A. & Lyon, S. A. Embracing the quantum limit in silicon computing. *Nature* **479**, 345–353 (2011).
- Kane, B. E. A silicon-based nuclear spin quantum computer. *Nature* **393**, 133–137 (1998).
- Feher, G. & Gere, E. A. Electron spin resonance experiments on donors in silicon. II. Electron spin relaxation effects. *Phys. Rev.* **114**, 1245–1256 (1959).
- Bradbury, F. R. *et al.* Stark tuning of donor electron spins in silicon. *Phys. Rev. Lett.* **97**, 176404 (2006).
- Morton, J. J. L. *et al.* Solid-state quantum memory using the ^{31}P nuclear spin. *Nature* **455**, 1085–1088 (2008).
- Jamieson, D. N. *et al.* Controlled shallow single-ion implantation in silicon using an active substrate for sub-20-keV ions. *Appl. Phys. Lett.* **86**, 202101 (2005).
- Fuechsle, M. *et al.* A single-atom transistor. *Nature Nanotechnol.* **7**, 242–246 (2012).
- Dehollain, J. P. *et al.* Nanoscale broadband transmission lines for spin qubit control. Preprint at <http://arxiv.org/abs/1208.2421v1> (2012).
- Xiao, M., Martin, I., Yablonovitch, E. & Jiang, H. W. Electrical detection of the spin resonance of a single electron in a silicon field-effect transistor. *Nature* **430**, 435–439 (2004).
- Chiba, M. & Hirai, A. Electron spin echo decay behaviours of phosphorus doped silicon. *J. Phys. Soc. Jpn* **33**, 730–738 (1972).
- Witzel, W. M. & Das Sarma, S. Quantum theory for electron spin decoherence induced by nuclear spin dynamics in semiconductor quantum computer architectures: Spectral diffusion of localized electron spins in the nuclear solid-state environment. *Phys. Rev. B* **74**, 035322 (2006).
- Schenkel, T. *et al.* Electrical activation and electron spin coherence of ultralow dose antimony implants in silicon. *Appl. Phys. Lett.* **88**, 112101 (2006).
- Tyryshkin, A. M. *et al.* Coherence of spin qubits in silicon. *J. Phys. Condens. Matter* **18**, S783–S794 (2006).
- Morello, A., Stamp, P. C. E. & Tupsitsyn, I. S. Pairwise decoherence in coupled spin qubit networks. *Phys. Rev. Lett.* **97**, 207206 (2006).
- Witzel, W. M., Carroll, M. S., Morello, A., Cywiński, Ł. & Das Sarma, S. Electron spin decoherence in isotope-enriched silicon. *Phys. Rev. Lett.* **105**, 187602 (2010).
- Tyryshkin, A. M. *et al.* Dynamical decoupling in the presence of realistic pulse errors. Preprint at <http://arxiv.org/abs/1011.1903v2> (2010).
- Barenco, A. *et al.* Elementary gates for quantum computation. *Phys. Rev. A* **52**, 3457–3467 (1995).

30. Hollenberg, L. C. L., Greentree, A. D., Fowler, A. G. & Wellard, C. J. Two-dimensional architectures for donor-based quantum computing. *Phys. Rev. B* **74**, 045311 (2006).

Supplementary Information is available in the online version of the paper.

Acknowledgements We thank R. P. Starrett, D. Barber, C. Y. Yang and R. Szymanski for technical assistance. We also thank A. Laucht for the Bloch sphere artwork and D. Reilly for comments on the manuscript. This research was funded by the Australian Research Council Centre of Excellence for Quantum Computation and Communication Technology (project number CE11E0096) and the US Army Research Office (W911NF-08-1-0527). We acknowledge support from the Australian National Fabrication Facility.

Author Contributions K.Y.T. and W.H.L. fabricated the device; D.N.J. designed the phosphorus implantation experiments; J.J.P., K.Y.T., J.J.L.M. and J.P.D. performed the measurements; J.J.P., A.M., A.S.D. and J.J.L.M. designed the experiments and discussed the results; J.J.P. analysed the data; J.J.P. wrote the manuscript with input from all co-authors.

Author Information Reprints and permissions information is available at www.nature.com/reprints. The authors declare no competing financial interests. Readers are welcome to comment on the online version of the paper. Correspondence and requests for materials should be addressed to J.J.P. (jarryd@unsw.edu.au) or A.M. (a.morello@unsw.edu.au).

Ocean oxygenation in the wake of the Marinoan glaciation

Swapan K. Sahoo¹, Noah J. Planavsky², Brian Kendall^{3†}, Xinqiang Wang⁴, Xiaoying Shi⁴, Clint Scott⁵, Ariel D. Anbar^{3,6}, Timothy W. Lyons² & Ganqing Jiang¹

Metazoans are likely to have their roots in the Cryogenian period^{1–3}, but there is a marked increase in the appearance of novel animal and algae fossils shortly after the termination of the late Cryogenian (Marinoan) glaciation about 635 million years ago^{4–6}. It has been suggested that an oxygenation event in the wake of the severe Marinoan glaciation was the driving factor behind this early diversification of metazoans and the shift in ecosystem complexity^{7,8}. But there is little evidence for an increase in oceanic or atmospheric oxygen following the Marinoan glaciation, or for a direct link between early animal evolution and redox conditions in general⁹. Models linking trends in early biological evolution to shifts in Earth system processes thus remain controversial¹⁰. Here we report geochemical data from early Ediacaran organic-rich black shales (~635–630 million years old) of the basal Doushantuo Formation in South China. High enrichments of molybdenum and vanadium and low pyrite sulphur isotope values ($\Delta^{34}\text{S}$ values ≥ 65 per mil) in these shales record expansion of the oceanic inventory of redox-sensitive metals and the growth of the marine sulphate reservoir in response to a widely oxygenated ocean. The data provide evidence for an early Ediacaran oxygenation event, which pre-dates the previous estimates for post-Marinoan oxygenation^{11–13} by more than 50 million years. Our findings seem to support a link between the most severe glaciations in Earth's history, the oxygenation of the Earth's surface environments, and the earliest diversification of animals.

The increase of oxygen in Earth's surface environments was protracted and is thought to have proceeded in two major steps. The ocean–atmosphere system was essentially devoid of oxygen until very early in the Proterozoic eon, when atmospheric oxygen rose to $>1\%$ of the present atmospheric level (PAL)^{14,15}. The timing and dynamics of this initial oxygenation are under active investigation, but there is little doubt that a major atmospheric transition, the 'Great Oxidation Event' (GOE), occurred about 2.4 billion years (Gyr) ago^{14,15}. It is commonly assumed that there was a second significant oxygen rise to near PAL during the late Neoproterozoic (~750–542 Myr ago)^{14,15}; however, the timing and magnitude of this second oxygenation event remain elusive^{9,15}.

The appearance of metazoan fossils has traditionally been used as a minimum estimate for the timing of the late Neoproterozoic oxygenation event¹⁶. Molecular clock estimates place the origin of crown-group animals in the Cryogenian period (850–635 Myr ago)¹. There are also sponge biomarkers² and sponge-like fossils³ in Cryogenian or older rocks, but these are only simple metazoans with limited oxygen demands (see Supplementary Information). Novel micro- and macrofossils interpreted as early metazoans appear immediately above Marinoan-age (~635 Myr ago) glacial deposits in South China^{4–6} (see Supplementary Information). Further, there is a radiation in marine algae following the Marinoan glaciation, which is probably linked to a

metazoan-driven shift in trophic structure and ecosystem complexity¹⁷. It has been proposed that this biological innovation is linked to an oxygenation event following the extensive Marinoan glaciation^{7,8}. However, there is no direct geochemical evidence for an increase in ocean oxygenation in the immediate aftermath of the Marinoan glaciation. Most existing geochemical evidence for a late Neoproterozoic redox shift is much younger (~580–550 Myr old), controversial, or records a local shift in redox conditions that may not be globally representative^{9,11–13}.

Trace-metal enrichments in black shales can record information about the global ocean redox state^{13,18–20}. Following the establishment of pervasive oxidative weathering after the GOE at ~2.4 Gyr ago^{14,15}, the size of the global marine reservoir of redox-sensitive elements (RSEs) was primarily controlled by the spatial extent of anoxic versus oxic marine conditions^{18,19}. In reducing marine environments, the burial fluxes of many RSEs, notably molybdenum (Mo) and vanadium (V), exceed those in oxygenated settings by several orders of magnitude. Hence, it follows that when oxic conditions are more widespread, the global seawater concentrations of these RSEs will be higher¹⁸. For example, in today's predominantly oxygenated oceans, Mo is the most abundant transition metal (~105 nM; ref. 18), despite its very low crustal abundance (~1 p.p.m.; ref. 21). Because the residence time of Mo (800–440 kyr)^{18,22} and V (~50 kyr)¹⁸ in seawater is much longer than the ocean mixing time (~1.5 kyr), Mo and V in marine basins track the global average conditions^{18–20,22}. This concept is well-grounded in an understanding of the modern Mo and V global mass balances^{18,19}.

The magnitude of RSE enrichments in anoxic marine sediments reflect dissolved RSE concentrations in seawater^{20,23}. In general, RSE enrichments also scale with the organic carbon flux because reduced, particle-reactive metal species (for example, thiomolybdate or vanadyl ions) are bound by organic particles, resulting in strong correlations between the metal and total organic carbon (TOC) contents in modern anoxically deposited sediments and black shales^{20,23}. Therefore, authigenic enrichments are commonly normalized to TOC concentrations (for example, Mo/TOC and V/TOC)²³. RSE enrichments in anoxic shales may also depend on other factors, such as sedimentation rates and sulphide levels. However, studies in modern anoxic basins with access to the open ocean^{18–20,23} have shown that the dissolved metal concentrations exert a first-order control on the degree of the enrichment (see Supplementary Information). This relationship sets the stage for using RSE enrichments in anoxic shales to track Earth's oxygenation history and specifically the extents of anoxia in the ocean^{9,13,23}.

The temporal record of RSE enrichments in shales deposited beneath an anoxic water column currently provides the least controversial and most direct geochemical signal for a significant redox shift in the late Neoproterozoic^{9,13}. However, the existing data only show a jump in RSE enrichments to Phanerozoic values near the end of the Ediacaran

¹Department of Geoscience, University of Nevada, Las Vegas, Nevada 89154, USA. ²Department of Earth Sciences, University of California, Riverside, California 92521, USA. ³School of Earth and Space Exploration, Arizona State University, Tempe, Arizona 85287, USA. ⁴School of Earth Science and Resources, China University of Geosciences, Beijing 10008, China. ⁵Department of Earth and Planetary Sciences, McGill University, Montreal, Quebec H3A 2A7, Canada. ⁶Department of Chemistry and Biochemistry, Arizona State University, Tempe, Arizona 85287, USA. [†]Present address: Department of Earth and Environmental Sciences, University of Waterloo, Waterloo, Ontario N2L 3G1, Canada.

period (~ 551 Myr ago)^{9,13,24}, long after the radiation of complex metazoans including triploblastic animals^{4–6,25}. There is a pronounced data gap between this time and 663 Myr ago in previous analyses due to the lack of suitable open-marine, deep-water black shale samples^{9,13}. Here we fill this gap by analysing organic-rich black shales of the basal Doushantuo Formation in South China that were probably deposited between 635 and 630 Myr ago (see Supplementary Information). We found very high, Phanerozoic-like RSE enrichments within a few million years after the Marinoan glaciation, coincident with the appearance of the earliest non-poriferan metazoan fossils^{4,5}.

In South China, Marinoan-age glacial diamictites of the Nantuo Formation are overlain by a 3-to-6-m thick, 635.2 ± 0.6 Myr old²⁶ cap carbonate commonly referred to as Member I of the Doushantuo Formation (Fig. 1)²⁷. The cap carbonate is conformably overlain by organic-rich black shales (Member II of the Doushantuo Formation), with subordinate carbonate layers and phosphorite-chert nodules in shelf and upper-slope environments²⁷ (see Supplementary Information). Putative metazoan fossils were found 6 m above the Doushantuo cap carbonate in the Yangtze Gorges area^{4,5}, less than two metres above an ash bed that has been dated as 632.5 ± 0.5 Myr old²⁶. Morphologically complex macroscopic fossils of the Lantian biota⁶ were reported from slope-basinal black shales, approximately 15 m above the cap carbonate (Fig. 1). Our geochemical analyses focus on the basal Member II black shales, which are roughly equivalent or slightly below these fossil horizons.

The basal Member II black shales have a transitional contact with the underlying cap carbonate²⁸. Their widespread occurrence across the basin and lack of event beds (for example, turbidites and olistostromes) suggest that they were deposited during the latest stage of postglacial transgression or sea-level highstand, with the shelf-to-basin topography inherited from the Cryogenian²⁷ (see Supplementary Information). We focused on deepwater Member II samples collected from three sections in an open-marine, slope/basinal setting (Fig. 1 and Supplementary Fig. 1). The black shales in the lower slope and basin sections contain an average of ~ 2.0 wt% of both pyrite iron ($\text{Fe}_{\text{pyrite}}$) and total organic carbon (TOC). The upper slope section has comparatively lower $\text{Fe}_{\text{pyrite}}$ (~ 0.3 wt% on average) and higher TOC (2.3 wt% on average); see Supplementary Table 1.

Slope and basin post-glacial black shales of Member II show strong Mo and V enrichments (Fig. 2). Mo enrichments in these sections commonly exceed the average Phanerozoic euxinic (anoxic and sulphidic) shale concentration of ~ 100 p.p.m. and the Phanerozoic

average Mo/TOC ratio (p.p.m./wt%) of ~ 25 (refs 9, 13). These high Mo enrichments show that the local water column was not only anoxic but also had free dissolved sulphide (euxinic conditions)²³. Vanadium enrichments of several thousand p.p.m. are common and equivalent to the largest values observed in the Phanerozoic anoxic shale record⁹ (Fig. 3). Similarly, uranium (U) in the lower Doushantuo Formation (Fig. 2) exceeds 30 p.p.m.—equivalent to the largest enrichments observed in modern anoxic basins²⁹. Therefore, the magnitude of RSE enrichments used previously to argue for a late Neoproterozoic oxygenation event at ~ 551 Myr ago^{9,13} are now found in >630 -Myr-old, early Ediacaran black shales (Fig. 3). It is well established that basin restriction, if anything, decreases the extent of RSE enrichment^{20,23}, ruling out the possibility that the large enrichments have only local significance (see Supplementary Information). Also, other factors, such as persistent or transient occurrences of oxygen in overlying waters, consistently mute the magnitude of RSE enrichment²³. Hence, the large RSE enrichments in the lower Doushantuo Formation provide strong evidence for a significant global marine oxygenation event in the aftermath of the Marinoan glaciation.

Simple mass-balance calculations confirm that the observed Mo and V enrichments in the lower Doushantuo Formation require a well-oxidized ocean (see Supplementary Information). Building from the global Mo and V cycles^{18,19}, it is possible to estimate the effects of increasing riverine RSE flux on the marine Mo and V reservoirs. Even with a very elevated riverine flux of Mo and V, the marine redox landscape will control RSE reservoir sizes and thus RSE enrichments. For instance, based on mass-balance calculations, even a doubling of the riverine Mo or V flux can be compensated for by relatively small growth in the extent of euxinia (for example, 1–2% of the seafloor area; see Supplementary Fig. 3). Although continental Mo and V fluxes may have been elevated for short periods (thousands of years) during the most rapid stages of glacial retreat, glacially elevated fluxes are not expected during deposition of the examined black shales, which span a period of millions of years after glacial retreat. Mass-balance calculations also indicate that even a relatively small areal increase (for example, 2–3%) in anoxic seafloor would crash the Mo and V reservoirs on a timescale of ≤ 0.5 Myr (see Supplementary Information). Thus, the observed Mo and V enrichments in lower Doushantuo Formation black shales suggest that oxic waters bathed the vast majority of the ocean. Oxygen-deficient conditions must have been spatially limited and only located where high organic matter loading caused oxygen depletion along ocean margins, such as in the Nanhua basin.

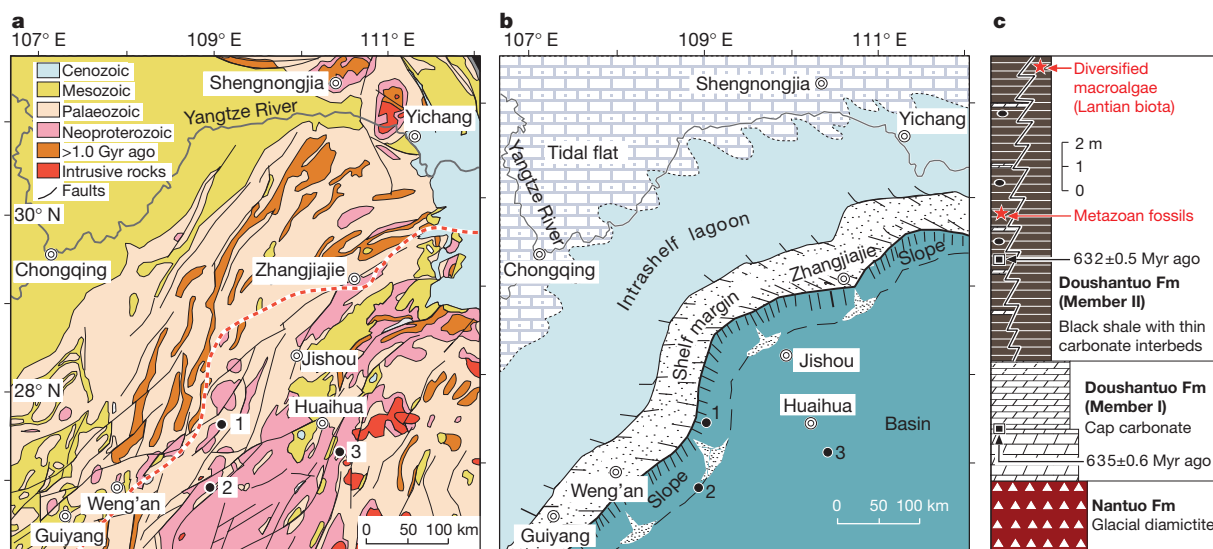


Figure 1 | Locality maps and stratigraphy. **a**, Simplified geological map with location of sections (1, Taoying; 2, Wuhe; 3, Yuanjia). The dashed red line marks the shelf margin during deposition of the Doushantuo Formation.

b, Palaeogeographic model for the Doushantuo Formation (simplified from ref. 27). **c**, Stratigraphy of the lower Doushantuo Formation with radiometric ages²⁶ and important fossil horizons^{4–6} marked.

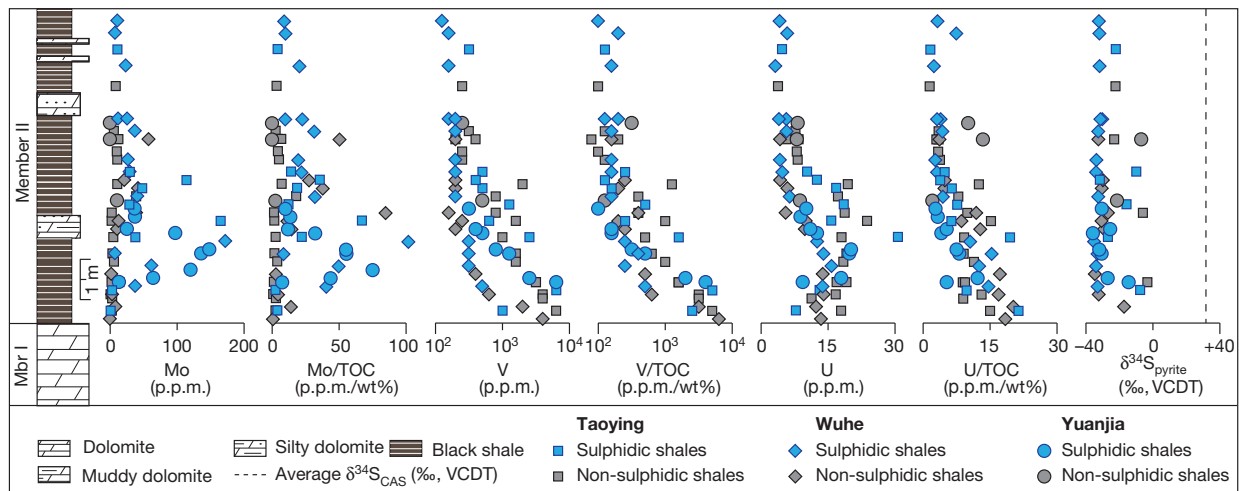


Figure 2 | Trace-metal abundances (Mo, Mo/TOC, V, V/TOC, U, U/TOC) and pyrite sulphur isotopes ($\delta^{34}\text{S}_{\text{pyrite}}$) from the lower Doushantuo Formation black shales. The shape of the data symbols indicates sample locations: Taoying (upper-slope section; squares), Wuhe (lower-slope section; diamonds), and Yuanjia (basin section; circles). The colour of the data symbols is used to distinguish sulphidic ($\text{Fe}_{\text{pyrite}}/\text{Fe}_{\text{HR}} > 0.8$; grey) from non-sulphidic ($\text{Fe}_{\text{pyrite}}/\text{Fe}_{\text{HR}} < 0.8$; light green) shales (Supplementary Fig. 2). Because a large

portion of the Doushantuo samples have unusually low total iron (Fe_T)/aluminium (Al) ratios (Supplementary Table 1), we do not use highly reactive iron (Fe_{HR})/total iron (Fe_T) ratios as a quantitative palaeoredox proxy (see Supplementary Information). The dashed line in the $\delta^{34}\text{S}_{\text{pyrite}}$ panel marks the average $\delta^{34}\text{S}_{\text{CAS}}$ value of the analysed stratigraphic interval^{5,24}. Sulphur isotope data are reported as per mil (‰) deviations from the isotope composition of Vienna Cañon Diablo Troilite (VCDT).

Large variability in the magnitude of RSE enrichments in lower Doushantuo Formation black shales suggests locally variable redox conditions. There are intervals with high RSE enrichments adjacent (<0.2 m) to intervals with near-crustal, un-enriched RSE concentrations, despite apparently constant physical conditions (that is, absence of wave-, storm- and gravity-generated beds) well below the storm wave base (see Supplementary Information). These variations suggest significant redox shifts in environments and thus deposition of the units under mixed oxic, suboxic-ferruginous, and euxinic conditions. Redox fluctuations in deep-water environments well below the mixed

layer, including those at an estimated depth of $>1,000$ m in the basinal section^{27,28} (see Supplementary Information), are consistent with a well-oxygenated global ocean–atmosphere system.

All Mo, V and U concentrations shift to lower values in the upper part of the basal Doushantuo black shales (Fig. 2). Given the observed variability in RSE enrichments within the basal unit, this drop in RSE enrichments may record a local environmental shift towards less reducing conditions that are not conducive to redox-sensitive metal sequestration (see Supplementary Information). Alternatively, the decrease of RSE values may record a shift back to more reducing ocean conditions

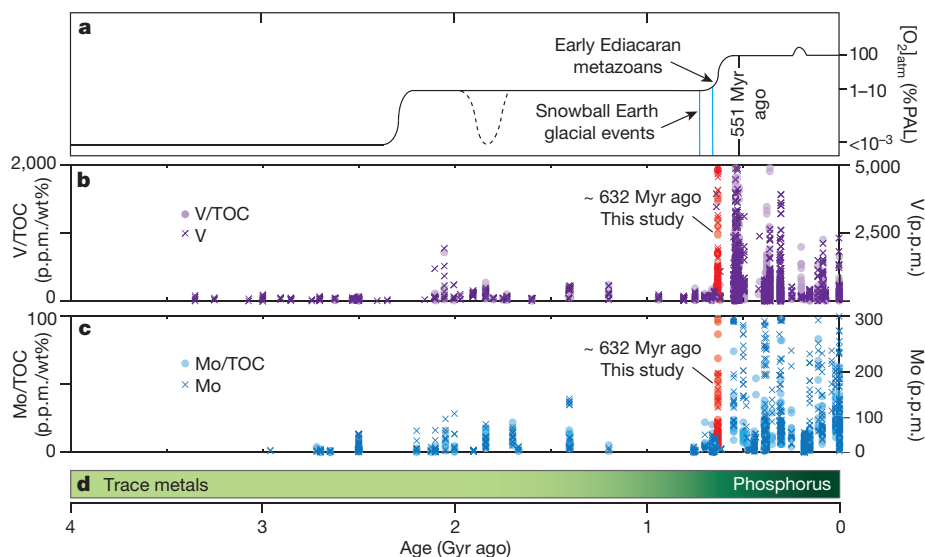


Figure 3 | Summary of redox-sensitive trace elements and evolution of the ocean–atmosphere redox state. **a**, Atmospheric oxygen levels compared with present atmospheric level (PAL). The early Ediacaran metazoans^{4,5} appeared shortly after the Marinoan glaciation, during an increase in ocean–atmosphere oxygen level (modified from ref. 8). **b**, Temporal trends in V enrichments (crosses) and V/TOC ratios (circles) in euxinic black shales (Supplementary Tables 2 and 3). **c**, Temporal trends in Mo enrichments (crosses) and Mo/TOC ratios (circles) in euxinic black shales (Supplementary Tables 2 and 3). The spikes of V, V/TOC, Mo and Mo/TOC from the lower Doushantuo black shales (this study) are marked. **d**, Potential shift in nutrient-limiting factor from trace metals

to phosphorus after the Marinoan glaciation^{8,32}. Data compilation, stratigraphic and chronological details are provided in the Supplementary Information. The Mo and V records indicate that the ocean experienced a late Neoproterozoic growth in the inventory of redox-sensitive trace elements, which can be linked to ocean ventilation. This redox shift was previously thought to have occurred at ~ 551 Myr ago^{9,13}. Our study provides evidence for an oxygenation event associated with increased seawater Mo–V enrichments and Mo/TOC and V/TOC ratios in the aftermath of the Marinoan glaciation, synchronous with or slightly pre-dating the earliest non-poriferan metazoan fossil record at ~ 632 Myr ago.

typical of the mid-Proterozoic (~1,800–700 Myr ago)—implying that the early Ediacaran oxygenation was not a unidirectional process (see Supplementary Information). However, this possibility requires a more comprehensive test in broader palaeogeographic settings of the Nanhua basin and in other global successions.

Highly negative pyrite sulphur isotope ($\delta^{34}\text{S}_{\text{pyrite}}$) values down to -35‰ from the basal samples (Fig. 2; Supplementary Table 1) further support our interpretation of an oxygenated ocean–atmosphere system following Marinoan deglaciation. Coeval (~635–630 Myr) carbonate-associated sulphate sulphur isotope ($\delta^{34}\text{S}_{\text{CAS}}$) values from shelf sections^{5,24} have an average of $\sim 34\text{‰}$. In this framework, the calculated isotope fractionation between pyrite and coeval sulphate ($\Delta^{34}\text{S}$) in the deep basin section is $>65\text{‰}$ —equivalent to maximum fractionations by modern sulphate reducing bacteria³⁰ and the maximum pyrite–coeval sulphate offset observed in the Phanerozoic rock record^{9,31} (Supplementary Fig. 4). An increase in the isotopic offset between pyrite and seawater sulphate in the late Neoproterozoic has been commonly linked to growth of the global marine sulphate reservoir and surface oxidation^{9,31}. The large sulphur isotope fractionation in the basal Member II shales therefore points towards a pervasively oxygenated ocean with lower associated pyrite burial, consistent with the conclusion drawn from RSE enrichments.

The shift to pervasively oxygenated oceans and, by inference, higher atmosphere O_2 conditions following the Marinoan glaciation may be linked to high nutrient availability⁸. It has been proposed that there was a large marine phosphate reservoir during and following the Cryogenian glacial events^{7,8}. Phosphate is commonly considered as the ultimate limiting nutrient on geological timescales, as nitrogen (N) can be supplied by biological nitrogen fixation from an essentially limitless atmospheric supply. Therefore, glacially induced perturbations to the phosphorus cycle may have triggered an organic carbon burial event²⁸ that induced a shift towards higher oxygen levels.

This model, however, overlooks the potential for persistent N stress linked to trace-metal biolimitation³². In a broadly anoxic ocean, chalcophilic trace metals (for example, Mo, Cu, Cd) may be co-limiting nutrients and inhibit efficient N fixation—just as in the modern oxic marine system Fe stress limits N fixation over broad swaths of the ocean³². Significant Mo biolimitation may have limited the organic carbon production and stabilized the redox state of the oceans through the mid-Proterozoic³². In this light, a jump in sulphidic black shale Mo enrichments at the Cryogenian–Ediacaran transition probably records a shift in nutrient regimes as well as in global redox conditions.

Marine chalcophilic trace-metal levels following glacial retreat must have been sufficient to allow for significant organic carbon burial and the switch to a more pervasively oxygenated ocean. Dissolved marine Mo may have built up to the critical levels needed to move out of a marine system with chronic Mo-induced N stress during glaciation. A brief episode (for example, thousands of years) of increased Mo delivery associated with high rates of postglacial weathering before the deposition of the Doushantuo Member II shales may have also helped to provide the perturbation needed to overcome persistent Mo biolimitation. Mitigating coupled Mo–N stress would have allowed for efficient utilization of a large marine phosphate reservoir^{7,8}—ultimately promoting organic carbon burial and oxygen release. Ventilation of the ocean would lead to significant growth of the Mo reservoir (and other RSE reservoirs) as manifest in the Member II shales deposited several million years after glacial retreat. The formerly enigmatic association of the ‘Snowball Earth’ glaciations and early metazoan and algal diversification could thus be linked to shifts in nutrient availability, burial of organic carbon, and ultimately the shift to a more oxygenated ocean–atmosphere system that favoured the early diversification of metazoan life and ecosystems.

Received 3 March; accepted 26 July 2012.

1. Erwin, D. H. *et al.* The Cambrian conundrum: early divergence and later ecological success in the early history of animals. *Science* **334**, 1091–1097 (2011).

2. Love, G. D. *et al.* Fossil steroids record the appearance of Demospongiae during the Cryogenian period. *Nature* **457**, 718–721 (2009).
3. Maloof, A. C. *et al.* Possible animal-body fossils in pre-Marinoan limestones from South Australia. *Nature Geosci.* **3**, 653–659 (2010).
4. Yin, L. *et al.* Doushantuo embryos preserved inside diapause egg cysts. *Nature* **446**, 661–663 (2007).
5. McFadden, K. A. *et al.* Pulsed oxidation and biological evolution in the Ediacaran Doushantuo Formation. *Proc. Natl Acad. Sci. USA* **105**, 3197–3202 (2008).
6. Yuan, X. *et al.* An early Ediacaran assemblage of macroscopic and morphologically differentiated eukaryotes. *Nature* **470**, 390–393 (2011).
7. Hoffman, P. F. & Schrag, D. P. The snowball Earth hypothesis: testing the limits of global change. *Terra Nova* **14**, 129–155 (2002).
8. Planavsky, N. J. *et al.* The evolution of the marine phosphate reservoir. *Nature* **467**, 1088–1090 (2010).
9. Och, L. M. & Shields-Zhou, G. A. The Neoproterozoic oxygenation event: environmental perturbations and biogeochemical cycling. *Earth Sci. Rev.* **110**, 26–57 (2012).
10. Butterfield, N. J. Oxygen, animals and oceanic ventilation: an alternative view. *Geobiology* **7**, 1–7 (2009).
11. Fike, D. A. *et al.* Oxidation of the Ediacaran ocean. *Nature* **444**, 744–747 (2006).
12. Canfield, D. E., Poulton, S. W. & Narbonne, G. M. Late-Neoproterozoic deep-ocean oxygenation and the rise of animal life. *Science* **315**, 92–95 (2007).
13. Scott, C. *et al.* Tracing the stepwise oxygenation of the Proterozoic ocean. *Nature* **452**, 456–459 (2008).
14. Holland, H. D. The oxygenation of the atmosphere and oceans. *Phil. Trans. R. Soc. B* **361**, 903–915 (2006).
15. Canfield, D. E. The early history of atmospheric oxygen: homage to Robert A. Garrels. *Annu. Rev. Earth Planet. Sci.* **33**, 1–36 (2005).
16. Knoll, A. H. & Carroll, S. E. Early animal evolution: emerging views from comparative biology and geology. *Science* **284**, 2129–2137 (1999).
17. Peterson, K. J. & Butterfield, N. J. Origin of the Eumetazoa: testing ecological predictions of molecular clocks against the Proterozoic fossil record. *Proc. Natl Acad. Sci. USA* **102**, 9547–9552 (2005).
18. Emerson, S. R. & Huested, S. S. Ocean anoxia and the concentrations of molybdenum and vanadium in seawater. *Mar. Chem.* **34**, 177–196 (1991).
19. Hastings, D. W., Emerson, S. R. & Mix, A. C. Vanadium in foraminiferal calcite as a tracer for changes in the areal extent of reducing sediments. *Paleoceanography* **11**, 665–678 (1996).
20. Algeo, T. J. & Lyons, T. W. Mo-total organic carbon covariation in modern anoxic marine environments: implications for analysis of paleoredox and paleohydrographic conditions. *Paleoceanography* **21**, PA1016, <http://dx.doi.org/10.1029/2004PA001112> (2006).
21. Wedepohl, K. H. The composition of the continental crust. *Geochim. Cosmochim. Acta* **59**, 1217–1232 (1995).
22. Miller, C. A., Peucker-Ehrenbrink, B., Walker, B. D. & Marcantonio, F. Re-assessing the surface cycling of molybdenum and rhenium. *Geochim. Cosmochim. Acta* **75**, 7146–7179 (2011).
23. Lyons, T. W. *et al.* Tracking euxinia in the ancient ocean: a multiproxy perspective and Proterozoic case study. *Annu. Rev. Earth Planet. Sci.* **37**, 507–534 (2009).
24. Li, C. *et al.* A stratified redox model for the Ediacaran ocean. *Science* **328**, 80–83 (2010).
25. Pecoits, E. *et al.* Bilateral burrows and grazing behavior at >585 million years ago. *Science* **336**, 1693–1696 (2012).
26. Condon, D. *et al.* U–Pb ages from the Neoproterozoic Doushantuo Formation, China. *Science* **308**, 95–98 (2005).
27. Jiang, G. *et al.* Stratigraphy and paleogeography of the Ediacaran Doushantuo Formation (ca. 635–551 Ma) in South China. *Gondwana Res.* **19**, 831–849 (2011).
28. Jiang, G. *et al.* Organic carbon isotope constraints on the dissolved organic carbon (DOC) reservoir at the Cryogenian–Ediacaran transition. *Earth Planet. Sci. Lett.* **299**, 159–168 (2010).
29. Calvert, S. E. & Pedersen, T. F. Geochemistry of recent oxic and anoxic marine sediments: implications for the geological record. *Mar. Geol.* **113**, 67–88 (1993).
30. Sim, M. S., Bosak, T. & Ono, S. Large sulfur isotope fractionation does not require disproportionation. *Science* **333**, 74–77 (2011).
31. Canfield, D. E. & Raiswell, R. The evolution of the sulfur cycle. *Am. J. Sci.* **299**, 697–723 (1999).
32. Anbar, A. D. & Knoll, A. H. Proterozoic ocean chemistry and evolution: a bioinorganic bridge? *Science* **297**, 1137–1142 (2002).

Supplementary Information is available in the online version of the paper.

Acknowledgements This study was supported by the National Science Foundation Division of Earth Science, NASA Astrobiology programme and National Natural Science Foundation of China. We are grateful to S. Xiao for input, discussions and editing the palaeontological text. We thank C. Reinhard, G. Love, A. Mix, J. Morford, D. Adams, J. Owens, C. Li and L. Och for discussions and S. Bates, G. Gordon and J. Owens for assistance with laboratory analyses. We thank M. Wille for comments and suggestions.

Author Contributions The research was planned by G.J., T.W.L., A.D.A., X.S., S.K.S., N.J.P., B.K. and X.W. Samples were collected by S.K.S., X.W. and G.J. The manuscript was prepared by S.K.S., N.J.P. and G.J., with important contributions from all co-authors. Analyses were carried out by S.K.S. with contributions from N.J.P. and B.K.

Author Information Reprints and permissions information is available at www.nature.com/reprints. The authors declare no competing financial interests. Readers are welcome to comment on the online version of the paper. Correspondence and requests for materials should be addressed to G.J. (Ganqing.Jiang@unlv.edu).

Response of salt-marsh carbon accumulation to climate change

Matthew L. Kirwan¹ & Simon M. Mudd^{2,3}

About half of annual marine carbon burial takes place in shallow water ecosystems where geomorphic and ecological stability is driven by interactions between the flow of water, vegetation growth and sediment transport¹. Although the sensitivity of terrestrial and deep marine carbon pools to climate change has been studied for decades, there is little understanding of how coastal carbon accumulation rates will change and potentially feed back on climate^{2,3}. Here we develop a numerical model of salt marsh evolution, informed by recent measurements of productivity and decomposition, and demonstrate that competition between mineral sediment deposition and organic-matter accumulation determines the net impact of climate change on carbon accumulation in intertidal wetlands. We find that the direct impact of warming on soil carbon accumulation rates is more subtle than the impact of warming-driven sea level rise, although the impact of warming increases with increasing rates of sea level rise. Our simulations suggest that the net impact of climate change will be to increase carbon burial rates in the first half of the twenty-first century, but that carbon-climate feedbacks are likely to diminish over time.

Salt marshes, mangroves and seagrass meadows are among the most valuable ecosystems in the world, yet vulnerable to climate change and direct anthropogenic disturbance^{2,4,5}. Understanding how coastal ecosystems and their carbon pools react to climate change and sea level rise is difficult because landscape-forming processes and biological processes work on similar timescales and are thoroughly intertwined. For example, vegetation growth depends on physical conditions such as sea level rise and inundation duration, but can also mediate physical conditions because plants influence their elevation by accreting peat and trapping mineral sediment⁶. Rates of carbon accumulation are therefore dependent on ecosystem engineering processes, and in some cases, determine whether a marsh survives sea level rise.

Recent work suggests that some individual aspects of global change may increase the resiliency of coastal wetlands facing sea level rise and their ability to sequester carbon. For example, increased CO₂, warmer temperatures, and moderate increases in rates of sea level rise all tend to increase rates of plant productivity, marsh accretion, and presumably the ability of marshes to survive sea level rise^{7–13}. However, accelerated sea level rise also leads to more mineral sediment deposition, which influences the elevation of coastal wetlands in ways that might limit their ability to sequester carbon^{12,14}. Increases in decay rates may accompany increased CO₂ and warmer temperatures^{15,16}. Finally, the accumulation rate of labile organic matter tends to equilibrate through time because decay rates are proportional to the size of the active carbon pool¹². Here we model these ecogeomorphic feedbacks to explore how one of the most complex carbon sinks responds to interactive components of global change including temperature warming and sea level rise.

Our numerical model couples two previous models that separately simulated the influence of vegetation on the deposition of mineral sediment¹⁷ and the interactions between inundation, root zone processes and carbon accumulation¹². In our model, inundation stimulates

plant growth up to a threshold water depth, as observed in long-term records of salt marsh biomass and field experiments^{7,12,13}. Increased temperatures tend to increase rates of productivity and decay in the model according to sensitivities determined from a latitudinal gradient and field experimentation^{10,16}. Organic matter produced by root growth is distributed throughout the soil profile when productivity exceeds decay, and changes in soil volume (that is, marsh elevation) affect both mineral and organic components of accretion. Whereas previous modelling efforts focused on the influence of mineral sedimentation on marsh evolution, we deliberately chose parameter values (sediment grain size, suspended sediment concentrations) that allowed us to explore the evolution of organic-matter-rich marshes dominated by root-zone processes (Table 1). In the discussion below, we refer to organic-matter accumulation and carbon accumulation interchangeably, given that the two are intrinsically linked¹⁸.

We first performed model experiments that explored how competition between enhanced productivity and decay associated with warmer temperatures determine carbon accumulation rates. We took a hypothetical marsh dominated by the macrophyte *Spartina alterniflora* in equilibrium with a slow, constant rate of sea level rise (1 mm yr⁻¹), and subjected it to an instantaneous 4 °C increase in temperature. After the temperature change, we found that rates of organic-matter decomposition exceeded rates of root production, leading to a slight decrease in organic-matter accumulation (Fig. 1a). Concurrently, warming enhanced aboveground productivity and its ability to trap mineral sediment, leading to a small increase in vertical accretion rate and marsh elevation relative to sea level (Fig. 1b). When temperature was perturbed under a higher rate of sea level rise (3 mm yr⁻¹), ambient plant productivity was relatively high, so that warming led to an increase in productivity that was greater than the increase in decay rate. Thus, rates of carbon accumulation and vertical accretion both increased after the step change in temperature (Fig. 1c, d). Accretion rates were momentarily higher than the rate of sea level rise, so the marsh platform built up elevation relative to sea level, and reduced inundation led to progressive reduction of plant productivity and vertical accretion. Consistent with a variety of numerical models of salt marsh evolution⁶, vertical accretion rates decreased until they approached a new equilibrium with the rate of sea level rise. Our results predict that the new equilibrium condition (under a moderate rate of sea level rise and warmer temperature) will be characterized by a higher elevation of the platform relative to sea level, a small increase in the rate

Table 1 | Parameter values used in model simulations

Parameter	Value
Sediment concentration, <i>C</i>	1 mg l ⁻¹
Particle diameter	0.03 mm
Maximum biomass, <i>B</i>	2,500 g m ⁻²
Fast decay, <i>k_f</i>	2 yr ⁻¹
Slow decay, <i>k_r</i>	0.001 yr ⁻¹
Spring tidal range	1.4 m

Parameters not listed have values identical to those in refs 12 and 16.

¹Department of Environmental Sciences, University of Virginia, PO Box 400123, Charlottesville, Virginia 24151, USA. ²School of GeoSciences, University of Edinburgh, Edinburgh EH8 9XP, UK. ³Earth Research Institute, University of California, Santa Barbara, California 93106, USA.

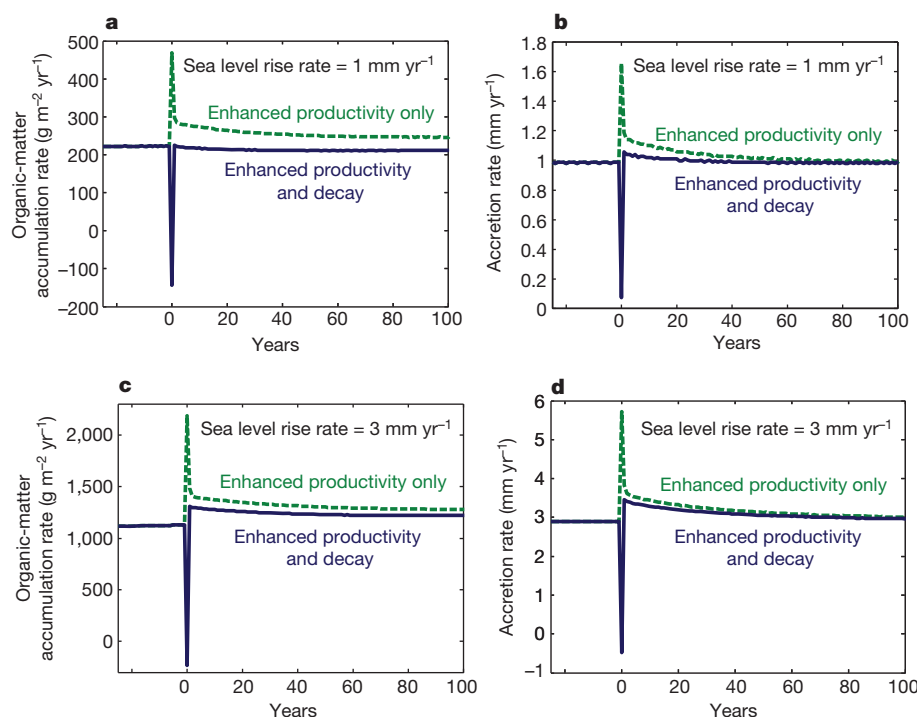


Figure 1 | Response of organic-matter accumulation and vertical accretion rates to an instantaneous 4 °C change in temperature at year 0.

a, b, 1 mm yr⁻¹ rate of sea level rise. **c, d,** 3 mm yr⁻¹ rate of sea level rise. The solid line denotes the model with temperature influence on productivity and decay, and the dashed line denotes the model with no effect of temperature on decay. The sharply negative accretion and organic accumulation rates at year 0

should be considered a model artefact arising from enhanced decay that takes place immediately, whereas enhanced productivity takes one year to reach the soil profile in the model. Enhanced productivity and decay have no long-term effect on accretion rate (**b, d**), but have moderate impacts on organic-matter accumulation (**a, c**).

of plant productivity and organic-matter accretion, but no change in vertical accretion rate.

This simple experiment provides two important insights into carbon dynamics in salt marshes. First, it illustrates that if plant productivity drives changes in wetland elevation, then the results of short-term experiments are likely to overestimate the long-term effect of climate change on carbon burial and vertical accretion. Field and laboratory experiments, for example, demonstrate that increased CO₂ leads to an increase in productivity and marsh accretion^{8,9}. Our model results are consistent with these observations because enhanced productivity via warming also leads to an increase in marsh accretion rate. The response was most pronounced when the effect of temperature on decomposition was not modelled (dashed line in Fig. 1b, d), analogous to

increased-CO₂ experiments that do not warm soil temperatures⁸. However, our experiments indicate that the enhanced vertical accretion rate quickly returns to the rate of sea level rise because the progressive building of wetland elevations ultimately limits plant productivity. At the same time, losses of labile soil carbon increase in proportion to the size of the growing carbon pool. Together, decreasing rates of plant productivity and increasing rates of decay cause carbon burial rates to decline after their initial increase (Fig. 1d).

A second implication of our results is that the rate of sea level rise, and its influence on ambient plant productivity, determines the net response of organic accumulation rates to climate change. Warming leads to reductions in organic matter accumulation at low rates of sea level rise (Fig. 1a), while warming leads to increases in organic-matter

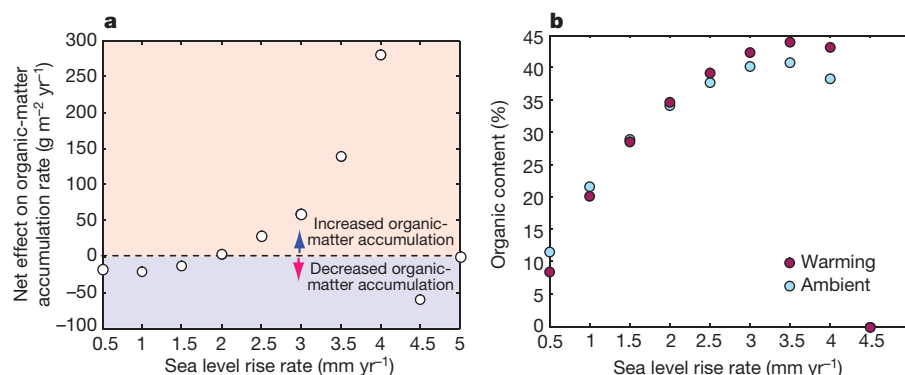


Figure 2 | Impact of warming under constant sea-level-rise rates. **a,** Net impact of warming on organic-matter accumulation rate defined as the deviation from ambient accumulation rate 100 years after the step change in temperature modelled in Fig. 1. The net influence of warming is negative at low rates of sea level rise, but positive at high rates of sea level rise. For experiments with different decay coefficients see the Supplementary Information. **b,** Impact

of warming on the fraction of organic material deposited at the soil surface. Warming leads to an increase in mineral content at low rates of sea level rise, but an increase in organic content at high rates of sea level rise. In general, warming temperatures and accelerating sea-level-rise rates lead to more organic-enriched soils until the marsh submerges (4.5 mm yr⁻¹ in this experiment).

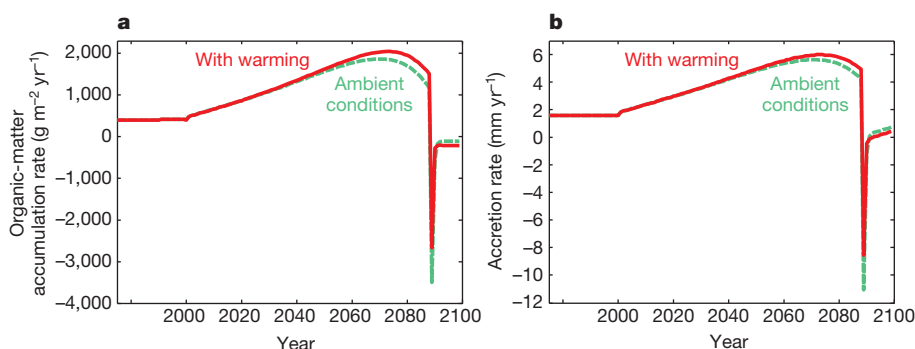


Figure 3 | Impact of warming under accelerating sea-level-rise rates.

a. Response of organic-matter accumulation rate to temperature-driven changes in productivity, decay and sea-level-rise rates over the next century. **b.** Response of accretion rate to the same warming and sea-level-rise scenario. For most of the twenty-first century, plant productivity and organic-matter accumulation rates increase with progressive inundation of the marsh surface.

accumulation at high rates of sea level rise (Fig. 1c). Although the net impact of warming declines through time in either case, discernible differences in carbon accumulation persist for centuries. Figure 2 summarizes the impact of warmer temperature on long-term (100-year) carbon accumulation rates over a variety of sea-level-rise rates. Vertical accretion rates equilibrate to the rate of sea level rise within 100 years, so the response of carbon accumulation rates to warming is driven by competition between organic-matter production and mineral sediment trapping efficiency. More productive plants in a warmer climate can have a positive influence on either process. At low rates of sea level rise, the marsh starts high in the tidal frame with little productivity. Enhanced productivity associated with warming leads to more inorganic trapping at the expense of organic accumulation (Fig. 2a), and marsh soils become more mineral-rich (Fig. 2b). At high rates of sea level rise, the marsh starts low in the tidal frame with high plant productivity and high organic-matter accumulation rates. Enhanced productivity leads to an increase in organic accumulation at the expense of inorganic sediment trapping (Fig. 2a), and the marsh becomes more organic-matter-rich (Fig. 2b). Thus, the effect of increased productivity on organic-matter accumulation depends on the background rate of sea level rise, and the elevation of the marsh relative to sea level. These processes suggest that predicting carbon cycling in rapidly accreting landscapes such as deltas, floodplains and wetlands requires knowledge not just of how plants respond to climate change, but also of how vegetation and geomorphic processes interact.

Given that sea-level-rise rates influence the net impact of warming on carbon accumulation, but are themselves a function of temperature, we considered a final experiment that simulated the evolution of a hypothetical marsh over the next century in which these variables interact (Fig. 3). Temperature projections followed the IPCC A2 scenario¹⁹ (an increase of 3.7 °C by 2100), and drove the rate of sea level rise according to a second-order semi-empirical relationship²⁰. The experiment began with a 100-year spin-up period in which carbon pools and marsh elevations grow and equilibrate with the historical rate of global sea level rise, which we take to be 1.7 mm yr⁻¹ (ref. 19). Although plant productivity accelerated with inundation and temperature throughout the experiment, more complex behaviour related to the influences of temperature and carbon pool size on decay rates emerged late in the simulation. As in Fig. 2, warmer temperatures led to little change in the organic accumulation rate when the rate of sea level rise was 1.7 mm yr⁻¹. As sea level rise accelerated, and ambient productivity increased owing to relative marsh lowering, the effect of enhanced productivity became more pronounced. For most of the twenty-first century, warmer temperatures and faster sea level rise rates led to an increase in organic-matter production, carbon accumulation, and vertical accretion. This increasing organic

The abrupt decline in organic-matter accumulation and marsh accretion near 2085 is due to plant mortality as plants cross an inundation threshold. At this point, carbon ceases to be deposited into marsh sediment, even as existing carbon near the soil surface continues to decay. For alternative climate scenarios and the impacts of varying suspended sediment concentrations, see the Supplementary Information.

production led to a growing carbon pool, and with it a growing loss of labile organic matter through decay. Eventually the combined effects of a larger carbon pool and enhanced decay outstripped organic production, leading to decelerating rates of organic accumulation after 2050 and declining rates of organic accumulation after 2075. Although enhanced plant productivity facilitated faster mineral sediment deposition, root zone processes dominated elevation change in this organic-matter-rich marsh, and vertical accretion rates also declined after 2075. With an accelerating rate of sea level rise and a declining rate of vertical accretion, the hypothetical marsh quickly lost elevation relative to sea level and vegetation drowned around 2085.

For more than 30 years, the debate on whether carbon stored in ecosystems will exacerbate or mediate climate change has focused on the biogeochemical evolution of terrestrial and open-ocean systems^{21,22}. However, coastal ecosystems such as salt marshes have only recently been recognized as important components of the global carbon cycle^{2,3}. Our results illustrate potential feedbacks between climate and carbon in the rapidly evolving coastal zone. We find that the net impact of temperature warming and sea level rise is to increase carbon burial rates in the first half of the twenty-first century (negative feedback with climate), but to slightly decrease carbon burial rates in the second half of the century (positive feedback with climate). In contrast, terrestrial ecosystems are likely to absorb a progressively smaller fraction of anthropogenic carbon dioxide emissions through the twenty-first century^{23,24}. Thus, transient increases in carbon burial rates near the coast could potentially help offset the reduced uptake of carbon from terrestrial ecosystems. Interestingly, our model results suggest that a switch in feedback direction takes place even in marshes that are surviving sea level rise, and where rates of plant productivity accelerate in response to climate change. If sea level rises by more than a metre by 2100, most models of marsh evolution indicate that marshes will be submerged and lose productivity²⁵. Our model considers only the temporal evolution of a single point within a hypothetical marsh. If the spatial extent of global marshes were to decline owing to sea level rise or anthropogenic modifications, then our prediction of long-term declining carbon burial rates would be amplified.

METHODS SUMMARY

To explore the temporal evolution of a hypothetical salt marsh platform, we coupled a model that simulates the influence of vegetation on the accumulation of mineral sediment¹⁷ with a model that focuses on interactions between inundation, root zone processes, and carbon accumulation¹². The model is generally suited to represent salt marshes in protected microtidal–mesotidal estuaries, most explicitly those colonized by *Spartina alterniflora*, the dominant macrophyte in North American marshes. In the model, inundation stimulates plant growth up to a threshold water depth^{7,12,13} and increased temperatures tend to increase rates of productivity and decay^{10,16}. Standing biomass varies throughout the growing

season, and affects marsh accretion by trapping sediments during periods of marsh inundation and by depositing belowground carbon owing to root mortality. Belowground organic-matter production is estimated from aboveground biomass according to a depth-dependent root-to-shoot ratio¹². Compaction is computed on the basis of sediment overburden and organic content¹². Dead biomass decays according to a linear decay model, where decay is influenced by the concentration of organic carbon, its depth below the soil surface, and temperature. For simplicity, we consider only two pools of soil carbon in our simulations: a quickly decaying pool of organic matter that reflects the decomposition of cellulose and amino-acids (k_1), and a slowly decaying pool that reflects the decomposition of more refractory materials such as lignins (k_r).

Full Methods and any associated references are available in the online version of the paper.

Received 27 February; accepted 25 July 2012.

- Duarte, C. M., Middelburg, J. J. & Caraco, N. Major role of marine vegetation on the oceanic carbon cycle. *Biogeochemistry* **2**, 1–8 (2005).
- Mcleod, E. *et al.* A blueprint for blue carbon: towards an improved understanding of the role of vegetated coastal habitats in sequestering CO₂. *Front. Ecol. Environ.* **9**, 552–560 (2011).
- Chmura, G. L. What do we need to assess the sustainability of the tidal salt marsh carbon sink? *Ocean Coast. Manage.* doi:10.1016/j.ocecoaman.2011.09.006 (2011).
- Gedan, K. B., Silliman, B. R. & Bertness, M. D. Centuries of human-driven change in salt marsh ecosystems. *Annu. Rev. Mar. Sci.* **1**, 117–141 (2009).
- Barbier, E. B. *et al.* The value of estuarine and coastal ecosystem services. *Ecol. Monogr.* **81**, 169–193 (2011).
- Fagherazzi, S. *et al.* Numerical models of salt marsh evolution: ecological, geomorphic, and climatic factors. *Rev. Geophys.* **50**, RG1002 (2012).
- Morris, J. T., Sundareshwar, P. V., Nich, C. T., Kjerfve, B. & Cahoon, D. R. Responses of coastal wetlands to rising sea level. *Ecology* **83**, 2869–2877 (2002).
- Langley, J. A., McKee, K. L., Cahoon, D. R., Cherry, J. A. & Megonigal, J. P. Elevated CO₂ stimulates marsh elevation gain, counterbalancing sea-level rise. *Proc. Natl Acad. Sci. USA* **106**, 6182–6186 (2009).
- Cherry, J. A., McKee, K. L. & Grace, J. B. Elevated CO₂ enhances biological contributions to elevation change in coastal wetlands by offsetting stressors associated with sea-level rise. *J. Ecol.* **97**, 67–77 (2009).
- Kirwan, M. L., Guntenspergen, G. R. & Morris, J. T. Latitudinal trends in *Spartina alterniflora* productivity and the response of coastal marshes to global change. *Glob. Change Biol.* **15**, 1982–1989 (2009).
- Charles, H. & Dukes, J. S. Effects of warming and altered precipitation on plant and nutrient dynamics of a New England salt marsh. *Ecol. Appl.* **19**, 1758–1773 (2009).
- Mudd, S. M., Howell, S. M. & Morris, J. T. Impact of dynamic feedbacks between sedimentation, sea-level rise, and biomass production on near-surface marsh stratigraphy and carbon accumulation. *Estuar. Coast. Shelf Sci.* **82**, 377–389 (2009).
- Kirwan, M. L. & Guntenspergen, G. R. Feedbacks between inundation, root production, and shoot growth in a rapidly submerging brackish marsh. *J. Ecol.* **100**, 764–770 (2012).
- Else-Quirk, T., Seliskar, D. M., Sommerfield, C. K. & Gallagher, J. L. Salt marsh carbon pool distribution in a mid-Atlantic lagoon, USA: sea level rise implications. *Wetlands* **31**, 87–99 (2011).
- Wolf, A. A., Drake, B. G., Erickson, J. E. & Megonigal, J. P. An oxygen-mediated positive feedback between elevated carbon dioxide and soil organic matter decomposition in a simulated anaerobic wetland. *Glob. Change Biol.* **13**, 2036–2044 (2007).
- Kirwan, M. L. & Blum, L. K. Enhanced decomposition offsets enhanced productivity and soil carbon accumulation in coastal wetlands responding to climate change. *Biogeochemistry* **8**, 987–993 (2011).
- Mudd, S. M., D'Alpaos, A. & Morris, J. T. How does vegetation affect sedimentation on tidal marshes? Investigating particle capture and hydrodynamic controls on biologically mediated sedimentation. *J. Geophys. Res.* **115**, F03029 (2010).
- Craft, C. B., Seneca, E. D. & Broome, S. W. Loss on ignition and Kjeldahl digestion for estimating organic carbon and total nitrogen in estuarine marsh soils: calibration with dry combustion. *Estuaries* **14**, 175–179 (1991).
- Bindoff, N. L. *et al.* in *Climate Change 2007: The Physical Science Basis. Contribution of Working Group I to the Fourth Assessment Report of the Intergovernmental Panel on Climate Change* (eds Solomon, S. *et al.*) 385–432 (Cambridge Univ. Press, 2007).
- Vermee, M. & Rahmstorf, S. Global sea level linked to global temperature. *Proc. Natl Acad. Sci. USA* **106**, 21527–21532 (2009).
- Baer, C. F., Goeller, H. E., Olson, J. S. & Rotty, R. M. Carbon dioxide and climate: The uncontrolled experiment. *Am. Sci.* **65**, 310–320 (1977).
- Riebesell, U., Kortzinger, A. & Oschlies, A. Sensitivities of marine carbon fluxes to ocean change. *Proc. Natl Acad. Sci. USA* **106**, 20602–20609 (2009).
- Shugart, H. H. & Woodward, F. I. *Global Change and the Terrestrial Biosphere: Achievements and Challenges* (Wiley-Blackwell, 2011).
- Friedlingstein, P. *et al.* Climate-carbon cycle feedback analysis: results from the (CMIP)-M-4 model intercomparison. *J. Clim.* **19**, 3337–3353 (2006).
- Kirwan, M. L. *et al.* Limits on the adaptability of coastal marshes to rising sea level. *Geophys. Res. Lett.* **37**, L23401 (2010).

Supplementary Information is available in the online version of the paper.

Acknowledgements We appreciate reviews by S. Bridgman and L. Larsen. This work was supported by the USGS Global Change Research Program.

Author Contributions Both M.L.K. and S.M.M. designed the experiments, interpreted their results, and wrote the paper.

Author Information Reprints and permissions information is available at www.nature.com/reprints. The authors declare no competing financial interests. Readers are welcome to comment on the online version of the paper. Correspondence and requests for materials should be addressed to M.L.K. (mlk4n@virginia.edu).

METHODS

Vegetation modelling. To explore the temporal evolution of a hypothetical salt marsh platform, we coupled a model that simulates the influence of vegetation on the accumulation of mineral sediment¹⁷ with a model that focuses on interactions between inundation, root zone processes, and carbon accumulation¹². The model is generally suited to represent salt marshes in protected microtidal–mesotidal estuaries, most explicitly those colonized by *Spartina alterniflora*, the dominant macrophyte in North American marshes. In the model, inundation stimulates plant growth up to a threshold water depth^{7,12,13} and increased temperatures tend to increase rates of productivity¹⁰. Between a minimum and maximum depth, measured below mean high high water (MHHW), the biomass during the peak growing season is:

$$B_{\text{peak}} = \frac{B_{\text{max}}}{D_{\text{max}} - D_{\text{min}}} (D - D_{\text{min}}) (1 + \Delta T \sigma_B) \quad (1)$$

(Dimensions are denoted in square brackets of [M] for mass, [L] for length and [T] for time). Here, D_{min} [L] and D_{max} [L] are the minimum and maximum depths below MHHW, B_{peak} is the peak season biomass [M L⁻²], B_{max} [M L⁻²] is the biomass at the optimal depth below mean high tide, ΔT is the change in temperature from a reference temperature, and σ_B is a factor that accounts for the increase in biomass due to an increase in temperature. From a latitudinal gradient of *S. alterniflora* productivity in 56 North American marshes¹⁰, we determine that $\sigma_B \approx 0.06$ °C⁻¹, in general agreement with experimental warming studies that also demonstrate a positive response to warming^{11,26,27}. The time-varying standing biomass B [M L⁻²] is calculated on the basis of on a sinusoidal approximation of the annual variation in marsh productivity (B fluctuates between 0 and B_p during the year)¹². Standing biomass can then affect marsh accretion by trapping sediments during periods of marsh inundation and by depositing belowground carbon owing to root mortality.

Sediment trapping. We model the trapping of mineral sediment as the sum of plant-mediated particle settling Q_s [M L⁻² T⁻¹] and direct capture of sediment by plant stems Q_c [M L⁻² T⁻¹] using the method of ref. 16. In *S. alterniflora* marshes, the mass flux from plant mediated settling is much greater than that from direct particle capture under typical flow conditions (<10 cm s⁻¹) (ref. 17). The particle settling flux is:

$$Q_s = (w_s - w_{\text{up}}) C \quad (3)$$

where C [M L⁻³] is the suspended sediment concentration, w_s [L T⁻¹] is the settling velocity of particles in still water and w_{up} [L T⁻¹] is the upward velocity of particles due to turbulence. The upward velocity of particles is:

$$w_{\text{up}} = \kappa_{\text{VK}} \sqrt{\frac{0.20 \alpha_k u^2 (C_D a_c d_c)^{2/3}}{\rho_w}} \quad (4)$$

where u [L T⁻¹] is the flow velocity, κ_{VK} is von Karman's constant, assumed to be 0.4, α_k is a coefficient reported to be 0.9 (ref. 28) and C_D is the depth-averaged drag coefficient. a_c [L⁻¹] is the projected plant area per unit volume, calculated as $a_c = \alpha B^{\beta}$, and d_c is the stem diameter calculated by $d_c = \mu B^{\phi}$. The drag coefficient is calculated using:

$$C_D = 2 \left(\frac{\alpha_0 v}{\mu B^{\phi}} + \chi + \zeta \frac{\alpha \mu \pi}{4} B^{\beta + \phi} \right) \quad (5)$$

where χ and ζ are empirical coefficients reported to be 0.46 ± 0.11 and 3.8 ± 0.5 , respectively²⁹. During the rising limb of the tide we make the simplification that sediment concentrations are fixed owing to a supply of sediment-laden water from tidal creeks, and during the falling limb of the tide suspended sediment concentrations are calculated by solving the sediment continuity equation¹⁷.

Compaction plays a significant part in determining the absolute elevation of marsh surfaces because the sediments that make up salt marsh soils are compressible. Here we use a constitutive equation verified by laboratory experimentation to model the compaction of the vertical soil profile. Following ref. 12:

$$E = E_0 - \text{CI} \log \left(\frac{\sigma_{\text{eff}}}{\sigma_0} \right)$$

where E [dimensionless] is the void ratio, CI [dimensionless] is the compression index, E_0 [dimensionless] is the void ratio at the reference stress, σ_0 [M T⁻² L⁻¹], and σ_{eff} [M T⁻² L⁻¹] is the effective stress. Following ref. 12, we assume the column

is under hydrostatic pressure and that the effective stress at any depth below the surface is simply the buoyant weight of the material above it. The compression index and reference void ratio depend on the substrate, where organic material in the modelled soil column is far more compressible than inorganic material¹².

Organic-matter production. Carbon is deposited in the subsurface via root mortality. The belowground biomass B_{bg} [M L⁻²] is related to the aboveground biomass through:

$$\frac{B_{\text{bg}}}{B} = \theta_{\text{bg}} D + D_{\text{mbm}} \quad (6)$$

where θ_{bg} and D_{mbm} are the slope [L⁻¹] and the intercept [dimensionless] of the relationship between the roots-to-shoots ratio and the depth below MHHW. These parameter values were determined from field experiments that examined the change in roots-to-shoots ratio with inundation for *S. alterniflora*¹².

The difference between growth rate and mortality rate determines the change in standing biomass through the year. Mudd *et al.*¹² approximated the measured growth of *S. alterniflora* as a sinusoidal function based on field data from North Inlet, South Carolina. This yields a mortality rate, M [M L⁻² T⁻¹] of:

$$M = \frac{1}{2} \left[G_{\text{min}} + G_{\text{peak}} + (G_{\text{peak}} - G_{\text{min}}) \cos \left(\frac{2\pi[\text{JD} - \text{JD}_{\text{peak}} + \phi]}{365} \right) \right] + \frac{\pi}{365} (B_{\text{peak}} - B_{\text{min}}) \sin \left(\frac{2\pi[\text{JD} - \text{JD}_{\text{peak}}]}{365} \right) \quad (7)$$

where JD is the Julian day (1 Jan = 1, 31 Dec = 365), JD_{peak} is the day of the year when aboveground biomass is at its peak and B_{min} [M L⁻²] is the minimum aboveground biomass, G_{ag} [M L⁻² T⁻¹] is the rate of aboveground biomass production per unit area, G_{min} [M L⁻² T⁻¹] is the minimum growth rate, G_{peak} [M L⁻² T⁻¹] is the peak growth rate, ϕ is the phase shift (in days) between the peak growing season and the date of peak biomass⁷. The mortality rate is then integrated over a time step and multiplied by the ratio between aboveground and belowground biomass.

Organic-matter decay. Fresh organic matter enters the soil profile upon mortality. Dead biomass decays according to a linear decay model ($\partial C_i / \partial t = -k_i C_i$) where C_i [M L⁻³] is the concentration in pool i , and k_i [T⁻¹] is the decay coefficient in pool i (refs 12, 30). The decay coefficient of pool i is calculated as $k_i = (1 + \Delta T \sigma_k) k_{i,0} \exp[d/\mu_i]$ where $k_{i,0}$ is the decay coefficient at a reference temperature, σ_k is a coefficient that describes the increase in decay coefficient as temperature increases, d [L] is the depth below the marsh surface and μ_i (0.4 m) is a coefficient that describes the reduction in decomposition with depth as organic sediments are buried under anoxic conditions¹². Kirwan and Blum¹⁶ found the coefficient σ_k to be about 0.25 °C⁻¹ for a mid-Atlantic *S. alterniflora* marsh. This result is qualitatively consistent with other observations of decay that are more rapid in marshes during warmer portions of the year, and with observations from terrestrial ecosystems (see references within ref. 16). In our simulations, we consider two pools of soil carbon: a quickly decaying pool of organic matter that reflects the decomposition of cellulose and amino acids (k_1), and a slowly decaying pool that reflects the decomposition of more refractory materials such as lignins (k_r). Experimental studies of decay in salt marshes are limited to durations less than five years, so this approach is necessarily guided by terrestrial models of carbon dynamics³¹. Nevertheless, slow decay over timescales of decades to millennia is apparent in the salt marsh stratigraphic record³².

26. Gedan, K. B., Altieri, A. H. & Bertness, M. D. Uncertain future of New England salt marshes. *Mar. Ecol. Prog. Ser.* **434**, 229–237 (2011).
27. Idaszkin, Y. L. & Bortolus, A. Does low temperature prevent *Spartina alterniflora* from expanding toward the austral-most salt marshes? *Plant Ecol.* **212**, 553–561 (2011).
28. Nepf, H. M. Drag, turbulence, and diffusion in flow through emergent vegetation. *Wat. Resour. Res.* **35**, 479–489 (1999).
29. Tanino, Y. & Nepf, H. M. Laboratory investigation on mean drag in a random array of rigid, emergent cylinders. *J. Hydraul. Eng.* **134**, 34–41 (2008).
30. Powlson, D. S., Smith, P. & Smith, J. U. (eds) *Evaluation of Soil Organic Matter Models, using Existing Long-Term Datasets* 237–246 (Springer, 1996).
31. Baisden, W. T. *et al.* A multi-isotope C and N modeling analysis of soil organic matter turnover and transport as a function of soil depth in a California annual grassland soil chronosequence. *Glob. Biogeochem. Cycles* **16**, 1135 (2002).
32. Choi, Y. & Wang, Y. Dynamics of carbon sequestration in a coastal wetland using radiocarbon measurements. *Glob. Biogeochem. Cycles* **18**, GB4016 (2004).

Delayed phenology and reduced fitness associated with climate change in a wild hibernator

Jeffrey E. Lane^{1,2,3}, Loeske E. B. Kruuk¹, Anne Charmantier², Jan O. Murie³ & F. Stephen Dobson^{2,4}

The most commonly reported ecological effects of climate change are shifts in phenologies, in particular of warmer spring temperatures leading to earlier timing of key events^{1,2}. Among animals, however, these reports have been heavily biased towards avian phenologies, whereas we still know comparatively little about other seasonal adaptations, such as mammalian hibernation. Here we show a significant delay (0.47 days per year, over a 20-year period) in the hibernation emergence date of adult females in a wild population of Columbian ground squirrels in Alberta, Canada. This finding was related to the climatic conditions at our study location: owing to within-individual phenotypic plasticity, females emerged later during years of lower spring temperature and delayed snowmelt. Although there has not been a significant annual trend in spring temperature, the date of snowmelt has become progressively later owing to an increasing prevalence of late-season snowstorms. Importantly, years of later emergence were also associated with decreased individual fitness. There has consequently been a decline in mean fitness (that is, population growth rate) across the past two decades. Our results show that plastic responses to climate change may be driven by climatic trends other than increasing temperature, and may be associated with declines in individual fitness and, hence, population viability.

The timings of key periodic events, or phenologies, in wild animal populations are assumed to have evolved to synchronize life cycles with seasonal availabilities of resources³. As temporal resource distributions are shifting rapidly owing to climate change⁴, the extent to which phenologies respond should therefore have important consequences for both the fitness of individuals and the viability of populations^{5,6}. Phenological shifts are indeed the most often cited ecological responses to climate change^{1,2}, with estimates of the mean responses across groups of species ranging from advances of 0.23 days (ref. 7) to 0.55 days (ref. 8) per year. Moreover, there is evidence that populations that have either not shown a phenological advance⁹, or have exhibited insufficient advances to remain synchronized with their primary food sources^{10,11}, are more likely to be in decline.

Unlike many bird species that undertake extensive migrations to cope with seasonal variation in resource availability, most mammals are sedentary and must therefore rely on adaptations to cope *in situ*. Hibernation is one such adaptation that is widespread across mammalian orders¹² and is assumed to have evolved in response to environmental resource shortages¹³. However, the environment in which hibernation has most often been studied, is the laboratory. Our understanding of the causes and consequences of natural variation in hibernation expression thus lags considerably behind that of its underlying physiological and biochemical mechanisms. The phenology of hibernation, particularly the date of emergence, is considered to have important consequences for individual fitness¹⁴, but the relative lack of data from wild populations currently limits our ability to adequately test this hypothesis and, by extension, make predictions as to how hibernating species will be affected by climate change. We

report here an analysis of hibernation phenology in a wild population of Columbian ground squirrels (*Urocitellus columbianus*).

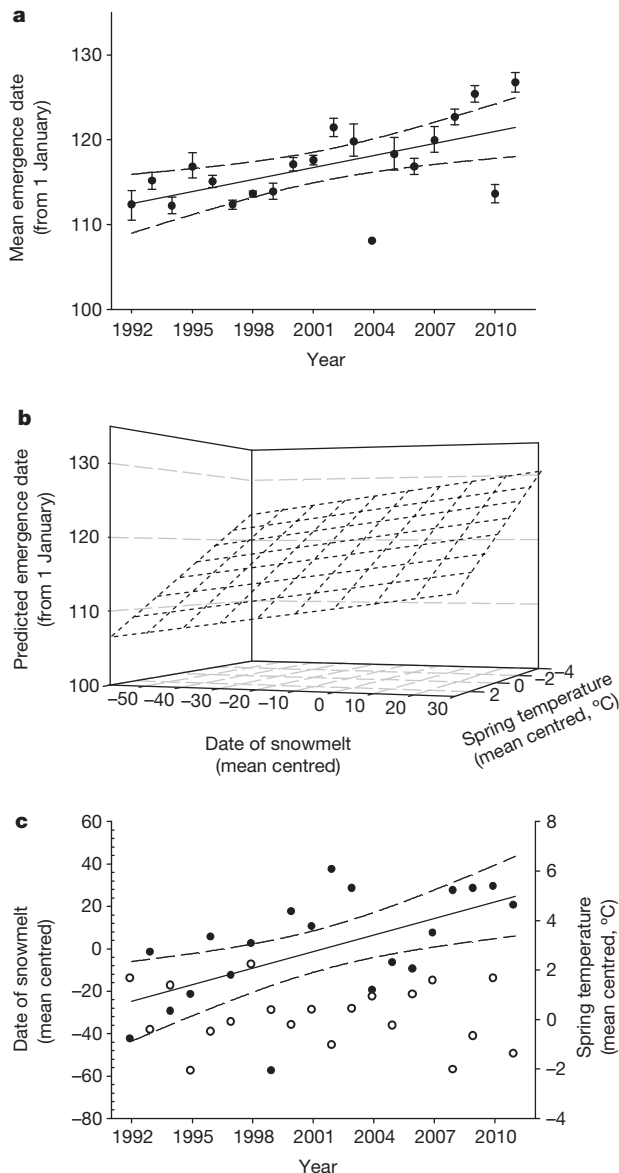
Columbian ground squirrels are small (less than 1 kg), obligate hibernators resident in the Rocky Mountains of North America. The short growing seasons of plants in the alpine and subalpine regions that they inhabit require that they spend the majority of the year (8–9 months) hibernating¹⁵. Over the past 20 years, the mean date of emergence from hibernation of adult females in our study population in Alberta, Canada, has become later by 0.47 ± 0.15 days (\pm s.e.m.) per year ($F_{1,18} = 9.68$, $r^2 = 0.35$, $P = 0.006$; general linear model; Fig. 1a). To investigate the environmental factors contributing to this delay, we quantified the phenotypic responses of individuals to variation in two weather variables (date of snowmelt and spring temperature; see Methods for definitions) previously shown to influence emergence date in hibernating mammals^{6,16}, as well as the annual trends in these predictors.

Individuals responded plastically to both weather variables. Female ground squirrels emerged 0.07 ± 0.03 days (\pm s.e.m.) later with each 1-day delay in snowmelt, and 1.51 ± 0.47 days (\pm s.e.m.) later with each 1-°C decrease in temperature (Table 1, Fig. 1b and Supplementary Fig. 1). There was also significant variation between individuals in their average emergence date (partly because emergence date is heritable in this population¹⁷), but not in individual plasticity in response to either climatic variable (that is, a significant difference in intercept, but not slopes of individual reaction norms¹⁸; Table 1).

Date of snowmelt has been delayed by 2.83 ± 0.88 days (\pm s.e.m.) per year over the course of the study ($F_{1,18} = 10.38$, $r^2 = 0.37$, $P = 0.005$; general linear model; Fig. 1c), but there has not been a significant trend in spring temperature (-0.10 ± 0.05 °C (\pm s.e.m.) per year; $F_{1,18} = 3.00$, $r^2 = 0.10$, $P = 0.101$; general linear model; Fig. 1c). The delay in snowmelt has been caused by an increasing likelihood of late-season snowstorms ($\chi^2_1 = 8.97$, $P = 0.003$; generalized linear model). During the first decade of the study, there was only 1 year that experienced a substantial snowfall event (that is, ≥ 5 cm of snow deposited over > 1 day) after the middle of April, whereas in the most recent decade 7 years experienced such late snowstorms. This result follows consensus projections from current climate models of elevated atmospheric moisture flux and, over most of North America, increased precipitation. Specifically, an overall increase in both total winter precipitation and the frequency of heavy precipitation events is projected¹⁹.

Adult females are engaged in reproduction for approximately half of the 3–4-month active season (that is, 51 days: 24 days of gestation and 27 days of lactation²⁰), after which females and offspring must accumulate sufficient fat resources to endure the ensuing hibernation period. Therefore, we predicted that delayed emergence dates would have fitness costs for adult females. We calculated an annual contribution to individual fitness (hereafter referred to as ‘annual fitness’) from both individual over-winter survival (*S*) and reproductive success (*R*) as $S + 0.5 \times R$ (ref. 21) (analyses of *S* and *R* separately are provided in Supplementary Tables 1 and 2, and Supplementary Fig. 2). *S* was

¹Institute of Evolutionary Biology, School of Biological Sciences, University of Edinburgh, Edinburgh EH9 3JT, UK. ²Centre d'Ecologie Fonctionnelle et Evolutive, Unité Mixte de Recherche, CNRS 5175, 1919 Route de Mende, 34293 Montpellier Cedex 5, France. ³Department of Biological Sciences, University of Alberta, Edmonton, Alberta T6G 2E9, Canada. ⁴Department of Biological Sciences, Auburn University, Auburn, Alabama 36849, USA.



scored as 0 or 1 depending on whether a female with a known emergence date in year_t survived to the spring of year_{t+1} (average across all years: $77.1 \pm 3.3\%$ (\pm s.e.m.)). Adult females are philopatric²² and the study population is fully censused; we were thus confident that all females surviving the winter were captured the following spring. *R* was calculated as the number of offspring that a female produced in a given year that survived over the winter. Average litter size is

Figure 1 | Variation in emergence date from hibernation and two environmental predictors of emergence (spring temperature and date of snowmelt) for adult female Columbian ground squirrels during the past 20 years. **a**, Annual trend in mean emergence date ($b_{\text{year}} = 0.47$, $P = 0.006$). **b**, The influence of date of snowmelt (b_{W} (the within-subject effect) = 0.07 , $P = 0.031$ (from within-subject mean centred analysis)) and spring temperature ($b_{\text{W}} = -1.51$, $P = 0.003$ (from within-subject mean centred analysis)) on emergence date. **c**, annual variation in the date of snowmelt (black circles; mean centred; $b_{\text{year}} = 2.83$, $P = 0.005$) and spring temperature (open circles; mean centred; $b_{\text{year}} = -0.10$ °C, $P = 0.101$). Regression lines (with 95% confidence intervals) are indicated for all significant relationships in **a** and **c**. Data are shown as mean \pm s.e.m.

approximately 3 (ref. 23) and the average over-winter survival rate of juveniles is 30–35%²⁴; average *R* across all females and years was therefore 0.91 ± 0.05 (\pm s.e.m.) surviving offspring. Individuals of neither sex disperse as juveniles²⁵, and all animals surviving their first winter were therefore captured as yearlings the following spring.

We considered effects of variation both between and within years when investigating the relationship between annual fitness and emergence date. Years with late average emergence dates were associated with lower annual fitness of females (Table 2 and Fig. 2a), but there was no evidence of further effects of variation within years (Table 2; that is, within a given year, there was not a significant difference in the fitness of early versus late emergers). As average emergence date has become later over the past 2 decades, there has been an associated decrease in mean annual fitness within the population ($b_{\text{year}} = -32.63$, $F_{1,16} = 7.58$, $P = 0.014$; general linear model (where b_{year} is the linear coefficient term for year)). Although the decrease has slowed down recently ($b_{\text{year}}^2 = 8.00 \times 10^{-3}$, $F_{1,16} = 6.71$, $P = 0.020$; general linear model, where b_{year}^2 is the quadratic coefficient term for year), partly owing to two recent years in which emergence was relatively early (2004 and 2010; Fig. 1a), mean fitness has also become more volatile (Fig. 2b). During the first decade of the study, only 1 of the 10 years (10%) exhibited a mean fitness value of less than 1 (that is, population decrease), whereas 4 out of 9 years (44%) exhibited such values in the most recent decade.

Declines in population viability resulting from insufficient phenological advances can theoretically be mitigated by adaptive phenotypic plasticity²⁶ or microevolution⁵ serving to resynchronize populations with their food resources. However, the phenological shift in Columbian ground squirrels is in the very direction that seems to be detrimental to fitness (Fig. 2a). Heavy snow cover prevents access to the squirrels' vegetative food sources. Therefore, squirrels are unable to resume above-ground activity earlier. However, delayed emergence presumably challenges their ability to subsequently accumulate the necessary fat resources to survive ensuing hibernation. This challenge could be from a shortening of the active season and/or from the squirrels attempting to fatten during a less energetically favourable period (for example, after vegetative senescence). Regardless of the mechanism, the documented association between emergence date and individual fitness suggests that, should the projections of increased winter

Table 1 | Effect of date of snowmelt and spring temperature on hibernation emergence date of female Columbian ground squirrels.

Effects	Model terms	Coefficient (s.e.m.)	χ^2 (d.f.)	P value
Fixed effects	Intercept	118.46 (0.77)		
	Between-subject effect (snowmelt)	0.06 (0.04)	2.71 (1)	0.100
	Within-subject effect (snowmelt)	0.07 (0.03)	4.65 (1)	0.031
	Between-subject effect (spring temperature)	-2.77 (0.76)	12.40 (1)	<0.001
	Within-subject effect (spring temperature)	-1.51 (0.47)	8.66 (1)	0.003
Random effects	Age	Range: -4.93 (1.81; age = 9) to 0.95 (5.04; age = 11)	24.56 (9)	0.004
	Year	6.38	59.45 (1)	<0.001
	Random intercept	8.28	34.62 (3)	<0.001
	Random slope (snowmelt)	1.12×10^{-3}	0.77 (3)	0.856
	Random slope (spring temperature)	0.05	0.35 (3)	0.950
	Residual error	21.08		

Model outputs are from a random regression model with within-subject mean centring ($n = 512$ records from 150 females, across 20 years). The influences of date of snowmelt and spring temperature are partitioned into between- and within-subject effects. Age, in years (as a 10-level categorical factor), is included as a fixed effect to control for age-related influences on emergence date and we report the maximum and minimum of the 10 age coefficients. The random effect structure estimates the variance in both the intercept and slopes of individuals in response to the two environmental variables (see Methods for details). *P* values are based on likelihood ratio tests. d.f., degrees of freedom.

Table 2 | Influence of variation in hibernation emergence date on annual fitness of female Columbian ground squirrels.

Effects	Model term	Coefficient	95% Highest posterior density intervals
Fixed effects	Intercept	1.23	0.88 to 1.52
	Between-year gradient	-0.14	-0.27 to -0.03
	Within-year gradient	-0.03	-0.08 to 0.02
	Density	-9.68×10^{-3}	-2.04×10^{-2} to 1.90×10^{-3}
	Age	Range: -0.76 (age = 10) to 0.20 (age = 4)	-1.01 to -0.15 (age = 10); 0.09 to 0.43 (age = 4)
Random effects	Identity	0.06	
	Year	0.09	

Standardized linear (between-years and within-years) gradients, based on annual fitness, for hibernation emergence date of adult female Columbian ground squirrels. Age in years (as a 10-level categorical factor) is included as a fixed effect to control for age-related influences on fitness and we report the maximum and minimum of the 10 age coefficients. Density (number of adult females in the population) is included as a continuous fixed effect to control for density-dependent influences. Analyses are based on a sample size of $n = 459$ records, collected from 145 females for which we had both an emergence date phenotype and fitness estimate. The 95% highest posterior density intervals (from 1,000 Markov chain Monte Carlo samples) are indicated. Individuals are represented in the data set multiple times, and multiple records were produced each year, therefore the variances associated with the random effects of identity and year are also included. Complete definitions for all terms are provided in the Methods.

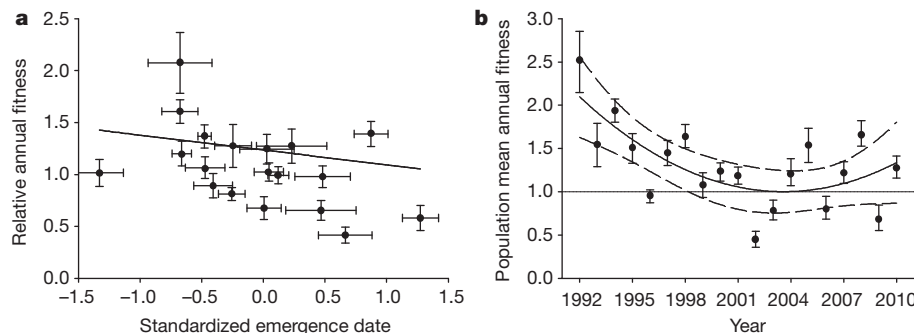


Figure 2 | Influence of mean emergence date from hibernation on, and the annual trend in, mean annual fitness of adult female Columbian ground squirrels over the past 20 years. **a**, The influence of standardized emergence date (standardized to a mean of zero and unit variance) on mean relative annual fitness (individual values divided by the population mean) (from mean-centred selection analysis, β_B (between-individual selection gradient) = -0.14; highest

posterior density interval, -0.27 - -0.03). **b**, The annual trend ($b_{\text{year}} = -32.63$, $P = 0.014$; $b_{\text{year}}^2 = 8.00 \times 10^{-3}$, $P = 0.020$) in mean annual fitness. Regression lines (with 95% confidence intervals) are indicated for both significant relationships and the threshold between population growth and decline (mean annual fitness = 1.0) is indicated in **b**. Data are shown as mean \pm s.e.m.

precipitation hold true, continued phenological delays will lead to diminished and more volatile population dynamics.

A recent study has shown that earlier snowmelts led to advances in emergence date from hibernation and concordant increases in overwinter survival of yellow-bellied marmots (*Marmota flaviventris*)⁶. Thus, although the direction of the trend is directly opposite to what we observed in Columbian ground squirrels, the links between the environmental predictor, emergence phenology and fitness are consistent. This is important because the overwhelming majority of research to date on the effects of climate change in natural systems has focused on increasing temperatures (for example, a previous study² summarized over 25,000 climate-change-induced phenological shifts and all of these were in response to temperature). Spring temperature is certainly the most ecologically relevant cue for many species, but over many areas of the globe its influence will be moderated by the date of snowmelt. Historically, these two cues should have been correlated as warmer springs led to earlier melting of the snow pack. However, over the past 20 years, this correlation has been weak at our study site ($t_{18} = -1.85$, $r = -0.40$, $P = 0.081$; Pearson correlation) as the date of snowmelt is now heavily influenced by an increasing prevalence of late-season snowstorms. The results presented here highlight the extent to which aspects of climate change other than increasing temperature may affect natural populations.

METHODS SUMMARY

We documented dates of emergence from hibernation and annual fitness of all adult females ($n = 512$ records from 150 females) within a fully censused population of Columbian ground squirrels in Alberta, Canada (50° N, 114° W and 1,500 m above sea level) from 1992 to 2011. Unique alphanumeric ear tags enabled individuals to be identified, and maternity assignment protocols are as described previously¹⁷. The date of snowmelt and spring temperature were recorded at a nearby weather station and a complete explanation of the treatment of climatic data are provided in the Methods. We used general linear models to quantify

annual trends in mean emergence date, the two environmental variables and mean fitness ($n = 20$ years, except for analyses involving fitness as 2011 data are not yet available). We also fit a generalized linear model with a binomial error structure to examine whether late-season snowstorms have become more likely in recent years. Plasticity of individuals was quantified using a random regression model with within-subject mean centering^{18,27}. We used a mean-centred mixed-effects model, implemented in a traditional linear selection analysis^{27,28}, to examine the influence of hibernation phenology on annual fitness both within, and across, years. Nonlinear and correlational selection gradients are presented in Supplementary Table 3.

Full Methods and any associated references are available in the online version of the paper.

Received 15 December 2011; accepted 18 June 2012.

Published online 8 August 2012.

1. Parmesan, C. Ecological and evolutionary responses to recent climate change. *Annu. Rev. Ecol. Syst.* **37**, 637–669 (2006).
2. Thackeray, S. J. *et al.* Trophic level asynchrony in rates of phenological change for marine, freshwater and terrestrial environments. *Glob. Change Biol.* **16**, 3304–3313 (2010).
3. Both, C., van Asch, M., Bijlsma, R. G., van den Burg, A. B. & Visser, M. E. Climate change and unequal phenological changes across four trophic levels: constraints or adaptations? *J. Anim. Ecol.* **78**, 73–83 (2009).
4. Intergovernmental Panel on Climate Change. *The Physical Science Basis: Contribution of Working Group I to the Fourth Assessment Report of the Intergovernmental Panel on Climate Change* (Cambridge Univ. Press, 2007).
5. Visser, M. E. Keeping up with a warming world: assessing the rate of adaptation to climate change. *Proc. R. Soc. B.* **275**, 649–659 (2008).
6. Ozgul, A. *et al.* Coupled dynamics of body mass and population growth in response to environmental change. *Nature* **466**, 482–485 (2010).
7. Parmesan, C. & Yohe, G. A globally coherent fingerprint of climate change impacts across natural systems. *Nature* **421**, 37–42 (2003).
8. Root, T. L. *et al.* Fingerprints of global warming on wild animals and plants. *Nature* **421**, 57–60 (2003).
9. Møller, A. P., Rubolini, D. & Lehikoinen, E. Populations of migratory bird species that did not show a phenological response to climate change are declining. *Proc. Natl Acad. Sci. USA* **105**, 16195–16200 (2008).
10. Both, C., Bouwhuis, S., Lessells, C. M. & Visser, M. E. Climate change and population declines in a long-distance migratory bird. *Nature* **441**, 81–83 (2006).

11. Saino, N. *et al.* Climate warming, ecological mismatch at arrival and population decline in migratory birds. *Proc. R. Soc. B.* **278**, 835–842 (2011).
12. Geiser, F. & Ruf, T. Hibernation versus daily torpor in mammals and birds: physiological variables and classification of torpor patterns. *Physiol. Zool.* **68**, 935–966 (1995).
13. Humphries, M. M., Thomas, D. W. & Kramer, D. L. The role of energy availability in mammalian hibernation: a cost-benefit approach. *Physiol. Biochem. Zool.* **76**, 165–179 (2003).
14. Michener, G. R. Spring emergence schedules and vernal behaviour of Richardson's ground squirrels: why do males emerge from hibernation before females? *Behav. Ecol. Sociobiol.* **14**, 29–38 (1983).
15. Dobson, F. S., Badry, M. J. & Geddes, C. Seasonal activity and body mass of Columbian ground squirrels. *Can. J. Zool.* **70**, 1364–1368 (1992).
16. Michener, G. R. Effects of climatic conditions on the annual activity and hibernation cycle of Richardson's ground squirrels and Columbian ground squirrels. *Can. J. Zool.* **55**, 693–703 (1977).
17. Lane, J. E. *et al.* A quantitative genetic analysis of hibernation emergence date in a wild population of Columbian ground squirrels. *J. Evol. Biol.* **24**, 1949–1959 (2011).
18. Nussey, D. H., Wilson, A. J. & Brommer, J. E. The evolutionary ecology of individual phenotypic plasticity in wild populations. *J. Evol. Biol.* **20**, 831–844 (2007).
19. Christensen, J. H. *et al.* in *The Physical Science Basis. Contribution of Working Group I to the Fourth Assessment Report of the Intergovernmental Panel on Climate Change* (eds Solomon, S. *et al.*) 847–940 (Cambridge Univ. Press, 2007).
20. Murie, J. O. & Harris, M. A. Annual variation of spring emergence and breeding in Columbian ground squirrels (*Spermophilus columbianus*). *J. Mamm.* **63**, 431–439 (1982).
21. Qvarnström, A., Brommer, J. E. & Gustafsson, L. Testing the genetics underlying the co-evolution of mate choice and ornament in the wild. *Nature* **441**, 84–86 (2006).
22. Wiggett, D. R. & Boag, D. A. Intercolony natal dispersal in the Columbian ground squirrel. *Can. J. Zool.* **67**, 42–50 (1989).
23. Murie, J. O., Boag, D. A. & Kivett, V. K. Litter size in Columbian ground squirrels (*Spermophilus columbianus*). *J. Mamm.* **61**, 237–244 (1980).
24. Dobson, F. S. & Murie, J. O. Interpretation of intraspecific life history patterns: evidence from Columbian ground squirrels. *Am. Nat.* **129**, 382–397 (1987).
25. Boag, D. A. & Murie, J. O. Weight in relation to sex, age and season in Columbian ground squirrels (Sciuridae: Rodentia). *Can. J. Zool.* **59**, 999–1004 (1981).
26. Charmantier, A. *et al.* Adaptive phenotypic plasticity in response to climate change in a wild bird population. *Science* **320**, 800–803 (2008).
27. van de Pol, M. & Wright, J. A simple method for distinguishing within- versus between-subject effects using mixed models. *Anim. Behav.* **77**, 753–758 (2009).
28. Lande, R. & Arnold, S. J. The measurement of selection on correlated characters. *Evolution* **37**, 1210–1226 (1983).

Supplementary Information is linked to the online version of the paper at www.nature.com/nature.

Acknowledgements We thank the volunteers and assistants who helped with fieldwork, and the University of Calgary for providing accommodation at the Biogeosciences Institute (E. Johnson and J. Buchanan-Mappin). D. Stralberg, S. Boutin and E. Bayne provided comments and assistance that improved an earlier version of this paper, and M. Low wrote the R script to calculate the spring temperature climate window. Funding was provided by the Natural Sciences and Engineering Research Council of Canada (NSERC) (J.O.M. and S. Boutin (University of Alberta)), National Science Foundation (DEB-0089473) (F.S.D.), the Royal Society of London (J.E.L. and L.E.B.K.) and Agence Nationale de la Recherche de France (ANR-08-JCJC-0041-01) (A.C., F.S.D. and J.E.L.) and the Alberta Conservation Association (J.E.L.). All protocols were approved by the Life and Environmental Sciences Animal Care Committee at the University of Calgary as well as the Animal Care and Use Committee at the University of Alberta (1992 to 1998) or the Institutional Animal Care and Use Committee at Auburn University (1999 to 2011).

Author Contributions J.E.L., L.E.B.K., A.C. and F.S.D. developed the concept of the paper, and F.S.D. and J.O.M. collected the field data. J.E.L. performed all analyses and wrote the paper, and all other authors provided intellectual insight and detailed comments. All authors obtained funding.

Author Information Reprints and permissions information is available at www.nature.com/reprints. The authors declare no competing financial interests. Readers are welcome to comment on the online version of this article at www.nature.com/nature. Correspondence and requests for materials should be addressed to J.E.L. (u.columbianus@hotmail.com).

METHODS

Study system. We used previously established protocols¹⁷ to document dates of hibernation emergence of adult female Columbian ground squirrels (≥ 2 years of age). In brief, we began conducting daily surveys from observation towers before the emergence of the first individuals. As they emerged, squirrels were caught in live traps and identified with alphanumeric eartags. Almost all individuals ($n = 136$) were originally handled as juveniles and their ages were known with certainty. Adults in the first year of the study (1992; $n = 4$) and any immigrating animals ($n = 10$) received eartags on first capture and their ages were estimated either as yearlings or 2 years and older, based on body size and reproductive condition.

Weather variables. The date of snowmelt for each year was determined from data collected at a nearby weather station in Okotoks, Alberta (Environment Canada, <http://climate.weatheroffice.gc.ca>; 50° N, 114° W, and 1,081 m above sea level; approximately 40 km from the study site). Patterns of snowmelt in this area can be extremely variable owing to adiabatic warming of winds from the Pacific Ocean²⁹ and frequent late-season snowstorms. We therefore chose the first day of the year with 0 cm of snow on the ground after continuous snow cover. However, if a substantial snowfall event (that is, ≥ 5 cm deposited over >1 day) occurred after this date, we selected the first day with 0 cm of snow after this event. The restriction to >1 day was chosen so that only snowfall events providing relatively consistent ground cover (as opposed to short-duration snow flurries) were included. A relatively moderate definition of ≥ 5 cm was chosen because the weather station, although relatively close in distance to the field site, is >400 m lower in elevation. Snowfall at the field site is therefore expected to be more severe. In 2 separate years (2002 and 2004) a substantial snowfall event occurred following the emergence of all females. The dates of snowmelt after these events were considered in the analyses of annual trends in weather variables. However, as they could not influence ground squirrel phenology, the dates of snowmelt before these events were used in the plasticity analyses.

Mean spring ambient temperatures (T_a) were calculated based on daily temperature recordings taken at the Okotoks station and a sliding window approach was used to determine the relevant period over which to calculate average temperature. We varied the window from 2 to 30 days and considered all possible windows from 1 January to 15 June. We selected the window (Julian days: 102–123 (12 April to 3 May in non-leap years)) that provided the highest r^2 with the mean annual emergence date ($r^2 = 0.54$). We used a Pearson's product-moment correlation test to estimate the correlation between the two weather variables.

Plasticity analyses. We used a random regression model to evaluate the influence of the two weather variables on the emergence dates of females¹⁷. Because we wished to quantify the extent of within-individual plastic responses to environmental variation, we used a within-subject mean centring approach that decomposes the environmental effects into those associated with the average environment experienced by an individual over its lifetime (a 'between-individual' effect), versus deviations of the environment in a given year from the individual's lifetime average (the 'within-individual' plastic effect)²⁷.

Emergence date (y_{ij}) for each individual i in year j was modelled as a continuous response to variation in the two weather variables, T_a and snow:

$$y_{ij} = b_0 + b_B \bar{T}_{a_i} + b_W (T_{a_{ij}} - \bar{T}_{a_i}) + b_B \bar{\text{snow}}_i + b_W (\text{snow}_{ij} - \bar{\text{snow}}_i) + \text{age} + [\text{year}] + [\text{ID}_i] + [\text{ID}_i \cdot (\text{snow}_{ij} - \bar{\text{snow}}_i)] + [\text{ID}_i \cdot (T_{a_{ij}} - \bar{T}_{a_i})] + e_{ij}$$

where b_0 represents the intercept and, as the weather variables were standardized to zero mean, is equivalent to the expected emergence date in the average environment. The between-subject effect (b_B) is estimated as the slope of y_{ij} on the mean value of each weather variable for each individual, i . The within-subject (b_W) effect is estimated as the slope of y_{ij} on the annual deviation of the weather variable from the subject mean. The random effects are shown in square brackets: $[\text{ID}_i]$ quantifies the variation in within-subject intercepts, and $[\text{ID}_i \cdot (T_{a_{ij}} - \bar{T}_{a_i})]$ and $[\text{ID}_i \cdot (\text{snow}_{ij} - \bar{\text{snow}}_i)]$ quantify the variation in the within-subject slopes for

the effects of the two weather variables (that is, the reaction norms¹⁸). Year [year] was included in order to model variation across years that is not explained by the weather variables and to account for multiple measures per year. Age in years was included as a 10-level fixed effect and e_{ij} represents the residual error. Significance of model terms was assessed with likelihood ratio tests ($-2 \times$ difference in log-likelihood between hierarchical models, tested against a chi-square distribution with the number of degrees of freedom that corresponded to the difference in the number of terms estimated).

Annual trends. We used general linear models implemented in R (ver. 2.10.0; R Core Development Team) to determine whether there was a significant annual trend (year fitted as a continuous fixed effect) in mean emergence date or in either of the weather variables. We also fit a generalized linear model with a binomial error structure to examine whether late-season snowstorms have become more likely in recent years. The female that emerged the earliest over the 20 years did so on 9 April. Therefore, whether a snowstorm, which deposited at least 5 cm of snow, was observed following 9 April (scored as 0 or 1) was entered as the dependent variable, with year fitted as a continuous fixed effect.

Fitness implications of variation in emergence date. We calculated annual contributions to lifetime fitness (which, for simplicity, we refer to as a measure of 'annual fitness') for individuals as $S + 0.5 \times R$, following a previous study²¹. S represents over-winter survival and R represents annual reproductive success (defined in the main text). Prior to the analysis, emergence dates were standardized to a mean of zero and unit variance, and relative fitness was calculated by dividing by the overall mean²⁸. Because we wished to test whether any association between annual fitness and emergence date was driven by between- versus within-year variation, for each individual we considered effects of the annual mean emergence date (\bar{y}_j) and the deviation of that individual from the annual mean ($y_{ij} - \bar{y}_j$).

$$\omega_{ij} = \beta_0 + \beta_B \bar{y}_j + \beta_W (y_{ij} - \bar{y}_j) + \text{age} + \text{density} + [\text{year}] + [\text{ID}_i] + e_{ij}$$

In this model, ω_{ij} represents relative annual fitness (divided by the overall population mean) of individual i at time j . β_0 is the intercept, β_B represents the influence of the annual mean emergence date that year and β_W represents the within-year variation. Age in years was included as a 10-level fixed effect. Population density (estimated as the number of adult females) varied substantially across the study period (range: 4–56) and was therefore included as a fixed effect to control for potential density-dependent effects on fitness. Explanations and results of quadratic and correlational analyses are included in Supplementary Table 3. Highest posterior density intervals were generated from 1,000 Markov chain Monte Carlo samples and are reported instead of standard errors and P values, as we cannot assume normality^{28,30}. The random effects of identity $[\text{ID}_i]$ and [year] were fitted to account for multiple records per individual and per year, respectively.

We used a general linear model to determine whether there has been a significant trend across years in the average annual fitness within the population and whether this trend has changed over time (by fitting both the linear and quadratic coefficients for year, respectively). Female survival rate (\bar{S}) was calculated as the percentage of females surviving over the winter and annual reproductive success (\bar{R}) was calculated as the mean number of pups surviving over the winter per female. Mean annual fitness across the population was then calculated as $\bar{S} + 0.5 \times \bar{R}$. Note that this also provides an approximation of population growth rate³¹.

29. Whiteman, C. D. *Mountain Meteorology: Fundamentals and Applications*. (Oxford University Press, 2000).
30. Bates, D. M., Maechler, M. & Dai, B. lme4: Linear mixed-effects models using Eigen and Eigen. <http://r-forge.r-project.org/> (2008).
31. Sæther, B.-E., Ringsby, T. H., Bakke, O. & Solberg, E. J. Spatial and temporal variation in demography of a house sparrow metapopulation. *J. Anim. Ecol.* **68**, 628–637 (1999).

Evidence for dietary change but not landscape use in South African early hominins

Vincent Balter¹, José Braga², Philippe Télouk¹ & J. Francis Thackeray³

The dichotomy between early *Homo* and *Paranthropus* is justified partly on morphology^{1,2}. In terms of diet, it has been suggested that early *Homo* was a generalist but that *Paranthropus* was a specialist³. However, this model is challenged and the issue of the resources used by *Australopithecus*, the presumed common ancestor, is still unclear. Laser ablation profiles of strontium/calcium, barium/calcium and strontium isotope ratios in tooth enamel are a means to decipher intra-individual diet and habitat changes. Here we show that the home range area was of similar size for species of the three hominin genera but that the dietary breadth was much higher in *Australopithecus africanus* than in *Paranthropus robustus* and early *Homo*. We also confirm that *P. robustus* relied more on plant-based foodstuffs than early *Homo*. A South African scenario is emerging in which the broad ecological niche of *Australopithecus* became split, and was then occupied by *Paranthropus* and early *Homo*, both consuming a lower diversity of foods than *Australopithecus*.

The dietary specialization of *Paranthropus* is thought to have contributed to its demise because it was unable to adapt to the changing environmental conditions that took place approximately 1 million years ago¹. From an ecological point of view, a small dietary breadth is generally correlated with narrow habitat preferences³. The evaluation of the size of the home range area, in addition to the estimation of the dietary breadth, would provide a detailed picture of resource use by the hominins. Using tooth enamel, the present work investigates the dietary breadth and the home range area of South African hominins with strontium/calcium (Sr/Ca) and barium/calcium (Ba/Ca) ratios, and strontium isotope (⁸⁷Sr/⁸⁶Sr) compositions. Dietary Sr/Ca and Ba/Ca proxies are based on the biological discrimination of Sr and Ba relative to Ca (that is, Ca biopurification), resulting in predictably lower Sr/Ca and Ba/Ca in a consumer, relative to its diet⁴. In bones, Sr/Ca and Ba/Ca decrease concomitantly up trophic chains⁴, but in enamel, and for a reason that is not yet fully understood, only low Ba/Ca ratios are characteristic in carnivores. Low Sr/Ca ratios are representative of browsers and carnivores⁵, whereas high Sr/Ca or Ba/Ca ratios in enamel are characteristic in grazers⁵. In contrast, the ⁸⁷Sr/⁸⁶Sr of a consumer is free of any trophic process⁶. It only reflects the ⁸⁷Sr/⁸⁶Sr composition of the bedrock (substrate) on which the consumer fed because the abundance of radiogenic ⁸⁷Sr is determined by normalization of the stable isotope variations relative to a reference ⁸⁶Sr/⁸⁸Sr ratio of 0.1194.

The Sr/Ca, Ba/Ca and ⁸⁷Sr/⁸⁶Sr ratios are assessed using laser ablation profiles in permanent molars from the dentine enamel junction to outer enamel following the direction of the enamel growth prism^{7–9}. The specimens include *Australopithecus africanus* ($n = 4$), *Paranthropus robustus* ($n = 7$) and early *Homo* ($n = 3$) from Sterkfontein, Swartkrans and Kromdraai B, South Africa (Supplementary Table 1). For comparison, we also measured the Sr/Ca, Ba/Ca and ⁸⁷Sr/⁸⁶Sr ratios in tooth enamel of grazers and browsers ($n = 3$) from Sterkfontein and Swartkrans. In most cases, several profiles were analysed for a given tooth to assess intra-tooth variability. The diagenetic effects on Sr/Ca,

Ba/Ca and ⁸⁷Sr/⁸⁶Sr of the Sterkfontein Valley fossil material are negligible (Supplementary Information). Several lines of evidence support this conclusion. First, if a sizeable pool of biological Sr is exchanged with a diagenetic component, this would affect the Sr isotopic composition and the samples would fall on a Sr/Ca versus ⁸⁷Sr/⁸⁶Sr line representing the mixing between the biological and the diagenetic Sr components. Taking the whole data set into account, it is evident that Sr/Ca and ⁸⁷Sr/⁸⁶Sr ratios are not correlated ($R^2 = 0.008$, $P = 0.260$). As well as Ca, Sr and Ba, we also measured a suite of other trace elements (Mn, Zn, Rb, Y, La, Sm, Yb, Th and U), which are present at the sub-p.p.b. level in modern enamel, and which are taken up easily post mortem¹⁰. No co-variation between Ca, Sr or Ba and the diagenetic proxies was found for any of the profiles (Supplementary Information). Last, the concentrations of the diagenetic proxies are very low, typically at the p.p.b. level, which is characteristic of pristine enamel and in accordance with previous results obtained using solution inductively coupled plasma mass spectrometry (ICPMS)¹¹.

The ⁸⁷Sr/⁸⁶Sr ratio ranges from 0.7197 to 0.7412 for the hominins and the bovids, with a mean value of 0.7309 ± 0.0048 (± 1 s.d.) (Fig. 1 and Supplementary Table 1). Recently, a study¹² reported ⁸⁷Sr/⁸⁶Sr ratios in the enamel of hominins and animals from Sterkfontein and Swartkrans (min = 0.7197, max = 0.7454, mean = 0.7305 ± 0.0054 (± 1 s.d.)). The ⁸⁷Sr/⁸⁶Sr values of the two sets of data for hominins are indistinguishable (Fig. 1; Student's t -test, $P = 0.240$). However, the data sets differ in the variability of the intra-tooth ⁸⁷Sr/⁸⁶Sr ratio, which is provided by the coefficient of variation associated with the mean ⁸⁷Sr/⁸⁶Sr value for a given tooth. In this study, the mean ⁸⁷Sr/⁸⁶Sr values and their associated coefficients of variation are normally distributed (Shapiro–Wilk test, $P = 0.306$ and $P = 0.107$, for mean and standard deviation, respectively) and are not correlated ($R^2 = 0.007$, $P = 0.659$). In contrast, in the study mentioned above¹², the mean ⁸⁷Sr/⁸⁶Sr values are normally distributed (Shapiro–Wilk test, $P = 0.111$), whereas the coefficient of variation values are log-normally distributed (Shapiro–Wilk test, $P = 0.972$) and the mean ⁸⁷Sr/⁸⁶Sr values are positively correlated with their log-normalized coefficient of variation values ($R^2 = 0.546$, $P < 10^{-3}$). The two data sets were obtained using different laser-sampling strategies, and this probably explains the observed patterns of intra-tooth ⁸⁷Sr/⁸⁶Sr variability.

As in the majority of studies using laser-ablation ICPMS on tooth samples^{7,8,13–17}, we carried out laser sampling on flat enamel surfaces. To do this, we used naturally broken teeth or teeth that had already been cross-sectioned mechanically. However, in the study mentioned previously¹², sampling was carried out using laser scans on the external surface of the enamel of whole teeth, which is a curved surface. This would have inevitably resulted in the sampling of laser-unfocused areas, an analytical bias that is known to produce variations of the size of the ablated particles and instrumental isotopic fractionation during ionization, leading to artificially scattered isotopic ratios¹⁸. The sampling strategy that was used¹² could explain why the smallest teeth were found to exhibit the highest intra-tooth ⁸⁷Sr/⁸⁶Sr variability.

¹Laboratoire de Géologie de Lyon, UMR 5276, CNRS, Ecole Normale Supérieure de Lyon, 15 parvis René Descartes BP 7000, 69342 Lyon Cedex 07, France. ²Computer-assisted Palaeoanthropology Team, UMR 5288, CNRS, Université de Toulouse Paul Sabatier, 37 Allées Jules Guesde, 31000 Toulouse, France. ³Institute for Human Evolution, University of the Witwatersrand, PO Wits, Johannesburg 2050, South Africa.

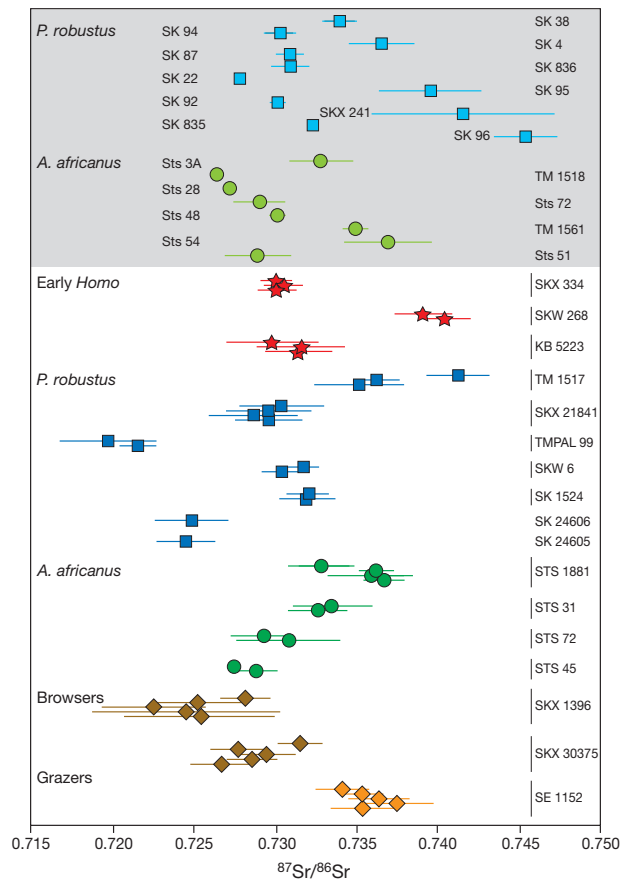


Figure 1 | $^{87}\text{Sr}/^{86}\text{Sr}$ ratios of hominin and bovid enamel. The shaded area contains data from a previous study¹². Error bars are 2-sigma standard deviations of the mean.

Finally, we do not find statistically significant differences of the $^{87}\text{Sr}/^{86}\text{Sr}$ ratio between hominin groups (Kruskal–Wallis, $P = 0.266$), or between the hominin group as a whole and the fauna (Kruskal–Wallis, $P = 0.259$). Thus, the South African hominins do not show clear systematic variation of the enamel $^{87}\text{Sr}/^{86}\text{Sr}$ ratio, and we conclude, on the basis of present results, that the home range areas of the three hominins were of similar size and composed of identical geological substrates.

The Sr/Ca and Ba/Ca ratios tend to decrease from the enamel dentine junction to the outer enamel, in accordance with previous findings⁸ (Supplementary Data). These trends have been interpreted to result from a positive gradient of mineralization, which favours Ca against Sr and Ba during the enamel secretory and maturation phases. In contrast to the Sr isotopic data, the elemental Sr/Ca and Ba/Ca data in the enamel of South African hominins display differences between the three genera, with a certain degree of overlap (Figs 2 and 3). The Sr/Ca ratio of *A. africanus* is significantly higher than that obtained for other hominin taxa, and the Ba/Ca ratio of early *Homo* is significantly lower than that obtained for other hominin taxa (Supplementary Table 2). The *P. robustus* specimens are characterized by Sr/Ca and Ba/Ca values that are intermediate between those of *A. africanus* and early *Homo*. Compared to the fauna, and taking into account both the Sr/Ca and Ba/Ca ratios, early *Homo* and *P. robustus* are indistinguishable from carnivores and browsers, respectively (Supplementary Table 2). With regard to *A. africanus*, the Sr/Ca and Ba/Ca ratios are indistinguishable from grazers and browsers, respectively (Supplementary Table 3). A possible interpretation is that the diets of early *Homo* and *P. robustus* were typical of carnivores and browsers, respectively, whereas the diet of *A. africanus* was more complex.

Taking the intra-tooth variability of Sr/Ca and Ba/Ca into account gives a more complete picture of the dietary habits of hominins. The

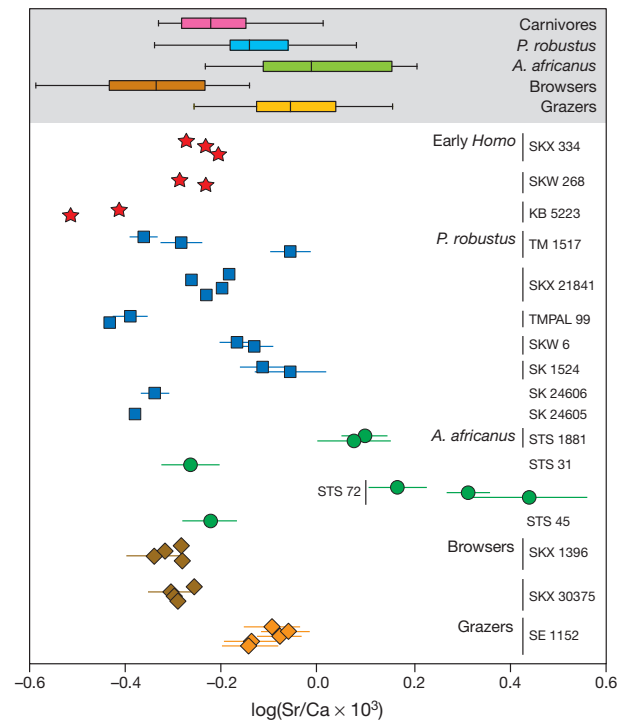


Figure 2 | Sr/Ca ratios of hominin and bovid enamel. For both ratios, error bars are 2-sigma standard deviations of the mean, and the shaded areas contain data from a previous study²⁰.

variability of intra-tooth Sr/Ca ratios provided by the coefficient of variation of the mean Sr/Ca value for a given sample is higher for *A. africanus* ($29.5 \pm 11.3\%$ (± 1 s.d.)) than for the other hominin groups (*P. robustus*, $13.8 \pm 7.6\%$; early *Homo*, $8.6 \pm 2.7\%$; Supplementary Table 3). This is also the case for the variability of the intra-tooth

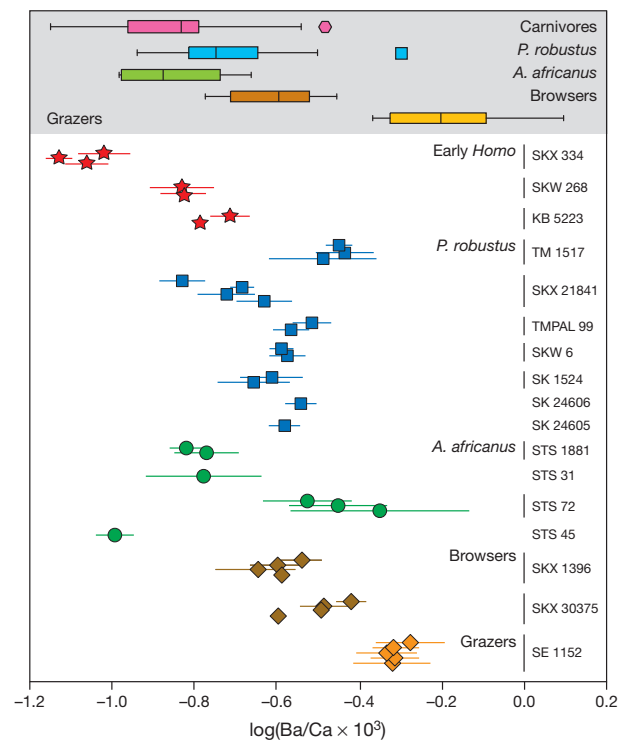


Figure 3 | Ba/Ca ratios of hominin and bovid enamel. For both ratios, error bars are 2-sigma standard deviation of the mean, and the shaded areas contain data from a previous study²⁰.

Ba/Ca ratio (*A. africanus*, $47.7 \pm 25.6\%$; *P. robustus*, $26.0 \pm 12.5\%$; early *Homo*, $23.8 \pm 8.0\%$; Supplementary Table 3).

The diet of *A. africanus* has a high Sr/Ca and a low Ba/Ca ratio, but a monotonous consumption of a Sr-enriched and Ba-depleted diet would not have produced the observed high intra-tooth Sr/Ca and Ba/Ca variability of *A. africanus*. It is more likely that the diet of *A. africanus* resulted from the combination of two distinct dietary sources. An association of woody plants represented by leaves and fruits of trees and bushes, which are Sr-enriched and Ba-depleted⁴, and meat, which is both Sr- and Ba-depleted, could explain the enamel Sr/Ca and Ba/Ca patterns of *A. africanus*. Woody plants and meat products could have been consumed alternately by *A. africanus* on a seasonal scale. This is regarded as the most probable dietary association for the genus *Australopithecus* because it is the only way to reconcile conflicting results based on tooth morphology¹⁹, dental microwear² and carbon isotope ratios²⁰. This scenario is compatible with the idea of fallback resource use, by which it is proposed that food items of poor nutritional quality become an increasing food component as preferred foods become rare^{21,22}. However, at this stage, it is not possible to state whether the fallback food was the woody plant or the meat component.

The diet of *P. robustus* seems to have been less variable than that of *A. africanus* and was mainly based on woody plant foodstuffs. This is consistent with the measured average Sr/Ca and Ba/Ca ratios, which are indistinguishable from browsers, the reduced intra-tooth Sr/Ca and Ba/Ca ratio variability, and with dental microwear and tooth morphology data^{2,23}. Similar to *P. robustus*, the diet of early *Homo* was less variable than that of *A. africanus*, but contrary to the diet of *P. robustus*, it was based more on meat products. Our results support the idea that the degree by which woody plants and underground storage organs²¹ were consumed by *A. africanus* was reduced in the *Homo* lineage, whereas the more specialized masticatory apparatus of the robust australopithecines enabled them to have subsisted mostly on this type of food. However, this constitutes a South African scenario for which the diet of the *Homo*-like australopithecine *A. sediba* remains to be tested²⁴.

METHODS SUMMARY

The analysed tooth samples were housed at the Transvaal Museum (Ditsong National Museum of Natural History) in Pretoria, South Africa. The hominid teeth that were selected were naturally broken or already cut for microstructural studies purposes. This strategy of sampling enables chemical variations to be measured along profiles from the enamel dentin junction to the outer enamel. Sintered standard SRM-1400 ('Bone Ash') was used as a bracketing reference, both for elemental and isotopic measurements, to correct for instrumental biases. A quadrupole-ICPMS (ThermoElement X7) was used for the measurement of trace elements concentrations. Selected monitored elements were Ca, Mn, Zn, Rb, Sr, Y, Ba, La, Sm, Yb, Th and U. The $^{87}\text{Sr}/^{86}\text{Sr}$ ratio was measured on a Nu-HR (Nu-instrument) multicollector-ICPMS. The laser is a 157-nm F_2/He excimer laser LPF202 of Lambda Physik⁹. Contrary to our previous study⁷, we did not measure trace element concentrations and isotopic ratios on the same laser spot, because the Sr concentrations were too low in some of the samples, resulting in poor signal intensity on the multicollector-ICPMS. The trace elements and the isotopic ratios were therefore measured separately in two different sessions. The main operational conditions are summarized in Supplementary Table 1. The standard bone ash SRM-1400, which is certified to contain 250 p.p.m. of Sr, produces typical signals of ^{88}Sr of approximately 5×10^4 counts per second (c.p.s.) on the quadrupole-ICPMS and approximately 700 mV on the multicollector-ICPMS. We obtain an average $\text{Sr}/\text{Ca} \times 10^3$ value of 0.668 ± 0.042 (± 2 s.d.) and an average $\text{Ba}/\text{Ca} \times 10^3$ value of 0.578 ± 0.054 (± 2 s.d.) for the standard SRM-1400 ($n = 16$). These numbers are close to the certified values of 0.652 and 0.629, respectively²⁵. We obtain an average $^{87}\text{Sr}/^{86}\text{Sr}$ value of 0.713068 ± 0.000728 (± 2 s.d.) for the standard SRM-1400 ($n = 17$), which is close to a thermal ionization mass spectrometry (TIMS) value of 0.713104 ± 0.000019 (± 2 s.d.) that was reported previously²⁶. The method is described fully in the Supplementary Information.

Received 19 March; accepted 21 June 2012.

Published online 8 August 2012.

1. Wood, B. Reconstructing human evolution: Achievements, challenges, and opportunities. *Proc. Natl Acad. Sci. USA* **107**, 8902–8909 (2010).

2. Kay, R. F. & Grine, F. E. in *Evolutionary History of the "Robust" Australopithecines* (ed. Grine, F. E.) 427–447 (Aldine de Gruyter, 1988).
3. Wood, B. & Strait, D. Patterns of resource use in early *Homo* and *Paranthropus*. *J. Hum. Evol.* **46**, 119–162 (2004).
4. Balter, V. Allometric constraints on Sr/Ca and Ba/Ca partitioning in terrestrial mammalian trophic chains. *Oecologia* **139**, 83–88 (2004).
5. Sponheimer, M. & Lee-Thorp, J. A. Enamel diagenesis at South African Australopithecine sites: Implications for paleoecological reconstruction with trace elements. *Geochim. Cosmochim. Acta* **70**, 1644–1654 (2006).
6. Hobson, K. A. Tracing origins and migration of wildlife using stable isotopes: a review. *Oecologia* **120**, 314–326 (1999).
7. Balter, V. et al. Analysis of coupled Sr/Ca and $^{87}\text{Sr}/^{86}\text{Sr}$ variations in enamel using laser-ablation tandem quadrupole-multicollector ICPMS. *Geochim. Cosmochim. Acta* **72**, 3980–3990 (2008).
8. Humphrey, L. T., Dean, M. C., Jeffries, T. E. & Penn, T. E. M. Unlocking evidence of early diet from tooth enamel. *Proc. Natl Acad. Sci. USA* **105**, 6834–6839 (2008).
9. Télouk, P., Rose-Koga, E. & Albarède, F. Preliminary results from a new 157nm laser ablation ICP-MS instrument: new opportunities in the analysis of solid samples. *Geostand. News* **27**, 5–11 (2003).
10. Kohn, M. J., Schoeninger, M. J. & Barker, W. W. Altered states: effects of diagenesis on fossil tooth chemistry. *Geochim. Cosmochim. Acta* **63**, 2737–2747 (1999).
11. Balter, V. et al. U-Pb dating of fossil enamel from the Swartkrans Pleistocene hominid site, South Africa. *Earth Planet. Sci. Lett.* **267**, 236–246 (2008).
12. Copeland, S. R. et al. Strontium isotope evidence for landscape use by early hominins. *Nature* **474**, 76–78 (2011).
13. Prohaska, T. et al. Investigation of Sr isotope ratios in prehistoric human bones and teeth using laser ablation ICP-MS and ICP-MS after Rb/Sr separation. *J. Anal. At. Spectrom.* **17**, 887–891 (2002).
14. Kang, D. et al. Application of laser ablation-inductively coupled plasma-mass spectrometry (LA-ICP-MS) to investigate trace metal spatial distributions in human tooth enamel and dentine growth layers and pulp. *Anal. Bioanal. Chem.* **378**, 1608–1615 (2004).
15. Dolphin, A. E. et al. Variation in elemental intensities among teeth and between pre- and postnatal regions of enamel. *Am. J. Phys. Anthropol.* **128**, 878–888 (2005).
16. Grün, R., Aubert, M., Joannes-Boyau, R. & Moncel, M. H. High resolution analysis of uranium and thorium concentration as well as U-series isotope distributions in a Neanderthal tooth from Payre (Ardèche, France) using laser ablation ICP-MS. *Geochim. Cosmochim. Acta* **72**, 5278–5290 (2008).
17. Hinz, E. A. & Kohn, M. J. The effect of tissue structure and soil chemistry on trace element uptake in fossils. *Geochim. Cosmochim. Acta* **74**, 3213–3231 (2010).
18. Jackson, S. E. & Günther, D. The nature and sources of laser induced isotopic fractionation in laser ablation-multicollector-inductively coupled plasma-mass spectrometry. *J. Anal. At. Spectrom.* **18**, 205–212 (2003).
19. McHenry, H. M. Relative cheek-tooth size in *Australopithecus*. *Am. J. Phys. Anthropol.* **64**, 297–306 (1984).
20. Sponheimer, M. & Lee-Thorp, J. A. Isotopic evidence for the diet of an early hominid, *Australopithecus africanus*. *Science* **283**, 368–370 (1999).
21. Laden, G. & Wrangham, R. The rise of the hominids as an adaptive shift in fallback foods: Plant underground storage organs (USOs) and australopithecine origins. *J. Hum. Evol.* **49**, 482–498 (2005).
22. Wolpoff, M. H. Posterior tooth size, body size, and diet in South African gracile australopithecines. *Am. J. Phys. Anthropol.* **39**, 375–393 (1973).
23. Scott, R. S. et al. Dental microwear texture analysis shows within species diet variability in fossil hominins. *Nature* **436**, 693–695 (2005).
24. Berger, L. R. et al. *Australopithecus sediba*: a new Species of *Homo*-like australopithecine from South Africa. *Science* **328**, 195–204 (2010).
25. Hinnert, T. A. et al. Interlaboratory comparison of mass spectrometric methods for lead isotopes and trace elements in NIST SRM 1400 Bone Ash. *J. Anal. At. Spectrom.* **13**, 963–970 (1998).
26. Schweissing, M. M. & Grupe, G. Stable strontium isotopes in human teeth and bone: a key to migration events of the late Roman period in Bavaria. *J. Archaeol. Sci.* **30**, 1373–1383 (2003).

Supplementary Information is linked to the online version of the paper at www.nature.com/nature.

Acknowledgements The authors thank F. Albarède, J. Blichert-Toft, B. Bourdon and G. Escarguel for helpful comments on the manuscript. This work was supported by the South African National Research Foundation, the French Ministry of Foreign Affairs, the French Embassy in South Africa through the Cultural and Cooperation Services, and the French Institut National des Sciences de l'Univers through the programs ECLIPSE II and PALEO2. The authors are grateful to S. Potze and the Ditsong National Museum of Natural History (formerly Transvaal Museum, Northern Flagship Institution), and the South African Heritage Resources Agency for facilitating access to the fossil samples.

Author Contributions V.B., J.B. and J.F.T. designed the study, V.B. and P.T. carried out the analysis, V.B. wrote the manuscript with J.B. and J.F.T. All authors discussed the results.

Author Information Reprints and permissions information is available at www.nature.com/reprints. The authors declare no competing financial interests. Readers are welcome to comment on the online version of this article at www.nature.com/nature. Correspondence and requests for materials should be addressed to V.B. (Vincent.Balter@ens-lyon.fr).

Skin shedding and tissue regeneration in African spiny mice (*Acomys*)

Ashley W. Seifert^{1,2,3}, Stephen G. Kiama², Megan G. Seifert^{1,3}, Jacob R. Goheen^{3,4}, Todd M. Palmer^{1,3} & Malcolm Maden¹

Evolutionary modification has produced a spectrum of animal defence traits to escape predation, including the ability to autotomize body parts to elude capture^{1,2}. After autotomy, the missing part is either replaced through regeneration (for example, in urodeles, lizards, arthropods and crustaceans) or permanently lost (such as in mammals). Although most autotomy involves the loss of appendages (legs, chelipeds, antennae or tails, for example), skin autotomy can occur in certain taxa of scincid and gekkonid lizards³. Here we report the first demonstration of skin autotomy in Mammalia (African spiny mice, *Acomys*). Mechanical testing showed a propensity for skin to tear under very low tension and the absence of a fracture plane. After skin loss, rapid wound contraction was followed by hair follicle regeneration in dorsal skin wounds. Notably, we found that regenerative capacity in *Acomys* was extended to ear holes, where the mice exhibited complete regeneration of hair follicles, sebaceous glands, dermis and cartilage. Salamanders capable of limb regeneration form a blastema (a mass of lineage-restricted progenitor cells⁴) after limb loss, and our findings suggest that ear tissue regeneration in *Acomys* may proceed through the assembly of a similar structure. This study underscores the importance of investigating regenerative phenomena outside of conventional model organisms, and suggests that mammals may retain a higher capacity for regeneration than was previously believed. As re-emergent interest in regenerative medicine seeks to isolate molecular pathways controlling tissue regeneration in mammals, *Acomys* may prove useful in identifying mechanisms to promote regeneration in lieu of fibrosis and scarring.

Among mammals, autotomy seems to have evolved several times, but is taxonomically sparse. Documented autotomy is typically restricted to the tail and occurs through loss of the tail sheath (false autotomy) or through breakage across the vertebra (true autotomy)^{2,5}. In addition to tail autotomy, casual reference has been made to mammalian species with weak or fragile skin, although whether these animals are capable of skin autotomy remains unknown. Thus, we first sought to investigate anecdotal evidence that two species of African spiny mouse (*Acomys kemp*i and *Acomys percival*i) readily shed portions of their skin as a predator escape behaviour.

To test the hypothesis that *A. kemp*i and *A. percival*i are capable of skin autotomy, we live-trapped individuals on rocky outcroppings (kopjes) in central Kenya. In addition to guard hairs, species in the genus *Acomys* are notable for the presence of spine-like hairs on the dorsum (Fig. 1a, b). Handling both species in the field confirmed that vigorous movement often led to tearing of the skin. Tearing resulted in large open wounds or skin loss ranging from small pieces to areas approximating 60% of the total dorsal surface area (Fig. 1c). In addition to integumentary loss, both species exhibited autotomy of the tail sheath as previously reported for other *Acomys* species, and individuals were often captured with missing tails². Among captive individuals, we observed severe skin wounds to heal quickly, and rapid regrowth of spiny hairs totally obscured the wounded area (Fig. 1d, e). Field-captured individuals showed similar healing and, in some cases,

patterned hair follicles in anagen (growth phase) that seemed to have regenerated in wounded areas (Fig. 1f).

To evaluate how *Acomys* skin tears so easily, we asked whether the mechanical properties of *Acomys* skin might underlie its observed weakness. On the basis of experiments investigating skin autotomy in geckos³, weak skin (that is, skin possessing uniform structural properties that fails or breaks under relatively low induced loading) can be differentiated from fragile skin (that is, skin possessing specific morphological characterizations such as a fracture plane that allows the outer layers to be released). To assess skin weakness, we compared mechanical properties of *Acomys* and *Mus* skin. During mechanical loading, *Mus* skin displayed elastic properties before breaking, whereas *Acomys* skin was brittle and began tearing shortly after load was applied (Fig. 2a). We derived stress-strain curves from dorsal skin to determine the mean tensile strength (σ_m) and found that *Mus* skin was 20 times stronger than *Acomys* skin (2.3 ± 0.19 MPa and

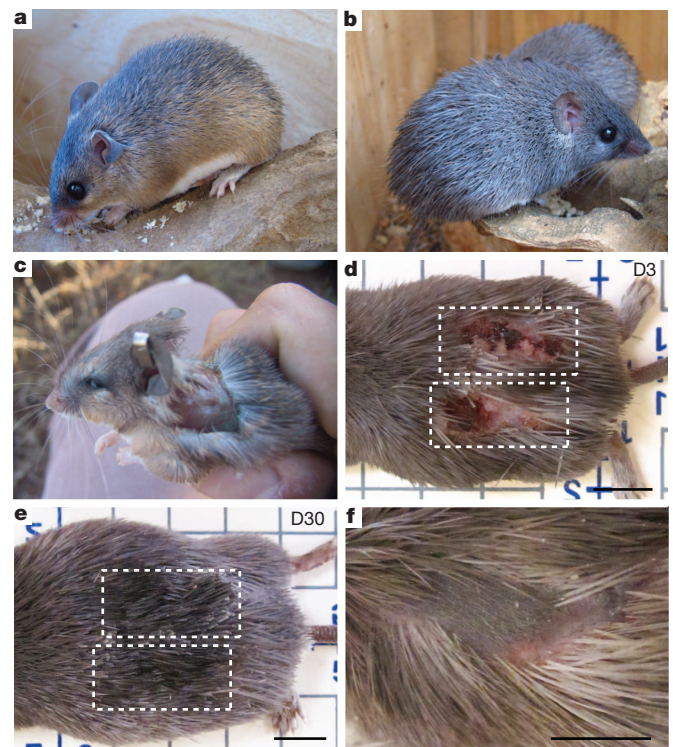


Figure 1 | *A. kemp*i and *A. percival*i exhibit skin autotomy and subsequent rapid healing. **a, b**, *A. kemp*i (**a**) and *A. percival*i (**b**) possess stiff, spine-like hairs on the dorsum. **c**, *A. kemp*i after loss of dorsal skin. **d, e**, Scab formation after full-thickness skin injury visible at D3 (**d**). The same wounds in **d** are no longer visible at D30 (**e**), and new spiny hairs cover the damaged area at D30 (**e**). **f**, Healing wound in field-caught specimen showing new hair follicles within the wound bed. Scale bars, 1 cm.

¹Department of Biology, University of Florida, 223 Bartram Hall, PO Box 118525 Gainesville, Florida 32610, USA. ²Department of Veterinary Anatomy and Physiology, University of Nairobi, PO Box 30197, 00010 Nairobi, Kenya. ³Mpala Research Centre, PO Box 555 Nanyuki 10400, Kenya. ⁴Department of Zoology and Physiology, and Department of Botany, University of Wyoming, 1000 East University Avenue, Laramie, Wyoming 82071, USA.

0.11 ± 0.03 MPa (mean \pm s.e.m.)) (Fig. 2a, b). Lastly, by calculating mean toughness (W), we found that nearly 77 times more energy was required to break *Mus* skin relative to *Acomys* skin (Fig. 2b). These results demonstrate that *Acomys* possess skin that tears (or breaks) easily in response to low applied tension and provide a mechanical basis for the weakness of their skin.

To evaluate whether structural properties of *Acomys* skin contributed to its mechanical weakness, we examined cellular features of *A. percivali* skin and found that it was anatomically comparable to that of *Mus* and other rodents, albeit with much larger hair follicles (Fig. 2c, d). We found no evidence of a fracture plane, which is the mechanism of skin autonomy in geckos and skinks³. Examining elastin fibres, which enhance skin elasticity, we found all three species possessed a similar distribution and abundance of elastin in the dermis and beneath the panniculus carnosus (Supplementary Fig. 1a–f). We tested whether larger hair follicles in *Acomys* skin reduced the total dermal area occupied by connective tissue by examining the proportion of adnexa (that is, follicles and associated glands) within the dermis and found it was greater in *A. percivali* ($55.61 \pm 4.28\%$) compared with *M. musculus* ($43.65 \pm 4.62\%$) ($t = 1.9$, $P = 0.043$) (Fig. 2e, f). These findings suggest that although the basic tissue structure of *Acomys* skin is similar to *Mus*, the space occupied by adnexa in the dermis reduces the absolute connective tissue content, potentially contributing to the decreased elasticity and lower tensile strength when the skin is placed under tension⁶. The lack of a fracture plane underscores this finding and supports an inherent structural difference underlying the observed weakness of *Acomys* skin.

Given its inherent structural weakness and propensity to tear, we assessed the ability of *Acomys* to heal skin wounds using small (4 mm) and large (1.5 cm), full-thickness excisional wounds. Scab formation and haemostasis was rapid in wounds of both sizes and the wound area in large wounds was reduced by $64 \pm 3.1\%$ 24 h after injury (Supplementary Fig. 2a). During scar-free healing in terrestrial salamanders⁷ and mammalian fetuses⁸, the wound bed is re-epithelialized within several days, whereas a 4-mm wound in adult rat skin takes between

5 and 7 days to re-epithelialize⁹. In *Acomys*, we found that five out of six 4-mm wounds had completely re-epithelialized by day 3 after injury (D3), whereas *Mus* wounds failed to re-epithelialize this quickly (Fig. 2g, h). After re-epithelialization, loose-skinned mammals (such as rodents and rabbits, for example) rely primarily on contraction to heal their wounds¹⁰. Similarly, we observed high contraction rates, which accounted for 95% of wound closure after 17 days (Supplementary Fig. 2a–c). In contrast to scarring, in which collagen fibres organize into a dense network parallel to the epidermis, during scar-free healing collagen fibres assume a pattern similar to unwounded dermis¹⁰. Examining the extracellular matrix (ECM) at D10, we observed scarring in *Mus*, whereas in *Acomys*, collagen fibres were less densely packed and contained a more porous structure (Fig. 2i, j). Using picrosirius red we found collagen type I predominated the wound bed at D10 in *Mus*, whereas collagen type III was in greater abundance in *Acomys* (Fig. 2k, l). This difference was even more pronounced in 1.5-cm wounds (Supplementary Fig. 3a–b'). Together, these data show that rapid re-epithelialization and wound edge contraction greatly reduce the size of open skin tears in *Acomys*. Our findings, that wound ECM is deposited slowly, has a porous configuration and is dominated by type III collagen, suggest that this composition favours regeneration over fibrosis during skin repair in *Acomys*.

To test the regenerative capacity of the wound environment we sampled large healing wounds for evidence of hair follicle neogenesis and dermal regeneration. In association with the more porous ECM, we observed folliculogenesis of normal pelage hairs and large spiny hairs in the wound bed between D21 and D28 and we could distinguish old, large follicles near the wound margins from newly regenerated follicles within the wound bed (Fig. 3a–d and Supplementary Fig. 3c–e). New follicles seemed to regenerate throughout the uncontracted portion of the wound bed not just in the central region (Fig. 3c and Supplementary Fig. 3e), and we observed regenerating hair follicles in various stages of development (Fig. 3a–m and Supplementary Fig. 4a–c). A localized and highly proliferative population of epidermal cells drives hair follicle development

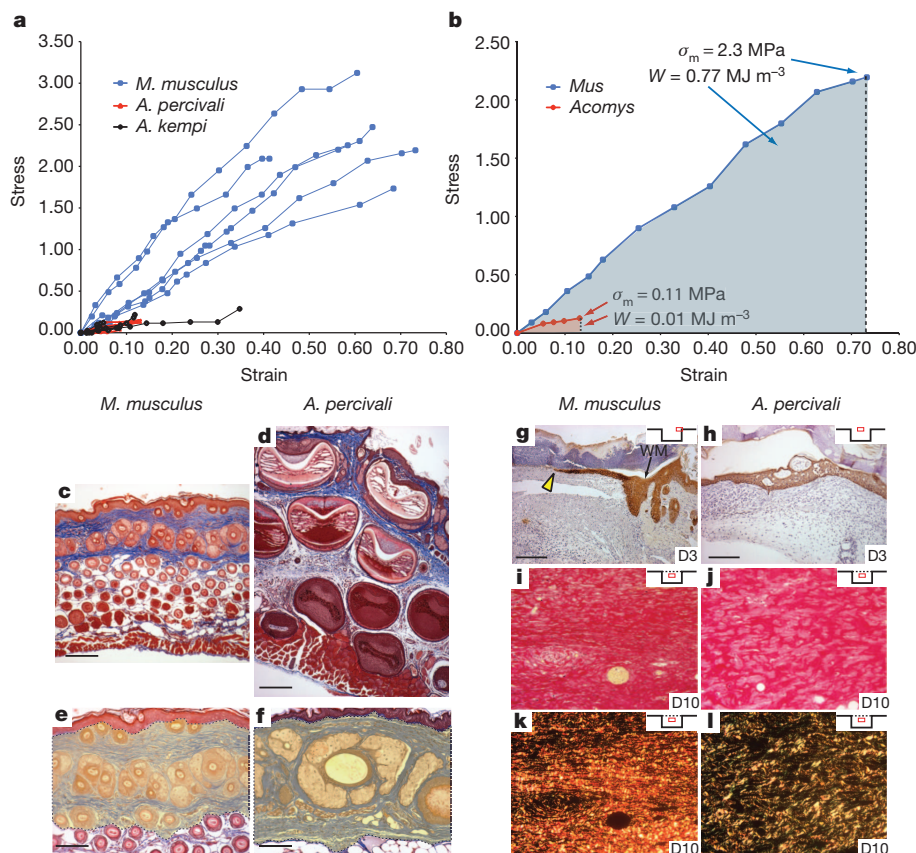


Figure 2 | *Acomys* skin is weak, tears easily, and during repair develops a porous ECM rich in collagen type III. **a, b**, Stress–strain curves for *M. musculus* ($n = 6$), *A. kempi* ($n = 5$) and *A. percivali* ($n = 5$), depicted up to the failure strain (**a**) and for one individual (**b**) approximating the real mean tensile strength (σ_m) and mean toughness (W) (represented as shaded area). **c, d**, Masson's trichrome staining of unwounded back skin from *M. musculus* (**c**) and *A. percivali* (**d**). **e, f**, The proportion of adnexa (hair follicles and associated glands) in the dermis (yellow shading) of *M. musculus* (**e**) and *A. percivali* (**f**). **g**, Cytochrome-stained keratinocytes (yellow arrowhead) just beginning to migrate in small wounds at D3 in *M. musculus*. **h**, Completely re-epithelialized wounds in *Acomys* at D3. WM, wound margin. Insets show relative wound position of the pictured tissue. **i–l**, Picrosirius red staining of small wounds in *M. musculus* (**i, k**) and *A. percivali* (**j, l**). Birefringence of picrosirius stain (**k, l**) differentiates thick collagen type I fibres (red/orange) from thin collagen type III fibres (green). Collagen fibres in *M. musculus* are predominantly type I, densely packed and run parallel to the epidermis (**k**). Collagen fibres in *A. percivali* are more porous with a greater proportion of collagen type III (**l**). Scale bars, 100 μ m.

and we observed a similar phenomenon during follicle regeneration (Fig. 3e and Supplementary Fig. 4a–c). To investigate whether embryonic signalling networks used during hair follicle development were used during hair follicle regeneration, we examined keratin 17 (KRT17), which is diffusely expressed within the epidermis during skin development and becomes progressively restricted to developing hair follicles¹¹. After re-epithelialization, KRT17 was highly enriched throughout the neoepidermis overlying the wound bed at D14, and as new hair follicles formed in the wound bed, KRT17 became restricted to follicular epithelium (Fig. 3f and Supplementary Fig. 5). During wound repair in *Mus*, we found KRT17 was also highly upregulated in the re-epithelialized epidermis at D14 (Supplementary Fig. 5), and although KRT17 localized to some basal keratinocytes in *Mus* epidermis at D21, these sites failed to aggregate into placodes or new hair follicles such that KRT17 was completely absent from the new epidermis by D26 (Fig. 3f). The disappearance of KRT17 from basal keratinocytes in *Mus*, together with our observation of continued localization in new placodes and hair follicles in *Acomys*, suggests the underlying dermal signals required to induce placode formation in *Mus* are lacking.

Although the precise signal for placode formation remains obscure, there is an absolute requirement for Wnt-signalling during normal follicle formation¹². Nuclear localization of LEF1 protein has been used as a readout of this inductive signalling¹³. We detected nuclear accumulation of LEF1 in regenerating epidermal placodes, condensing dermal fibroblasts beneath the hair germ, and in dermal papilla and matrix cells (Fig. 3g, h and Supplementary Fig. 6a). We also detected nuclear LEF1 staining at low levels in some non-placode basal keratinocytes, whereas we did not detect nuclear LEF1 in the epidermis during wound healing in *Mus*, suggesting epidermal Wnt-activation in *Acomys* may partially underlie our observation of hair follicle regeneration (Supplementary Fig. 6b, c).

Regulation of canonical Bmp-signalling also has a role during hair follicle induction and differentiation of follicular progenitor populations into the mature hair follicle (reviewed in ref. 14). Phosphorylation of SMAD proteins 1, 5 and 8 (pSMAD1, 5 and 8) is a robust readout of canonical Bmp signalling. We detected pSMAD1/5/8 (the antibody detects the phosphorylated forms of all of these proteins but does not exclusively differentiate any particular one) at low levels during follicle induction and later at higher levels in dermal papilla and matrix cells undergoing differentiation in the hair bulb (Fig. 3i, j). Furthermore, we detected SOX2-positive dermal papilla in some regenerating hair follicles, which is consistent with its role in specifying various hair types during mouse hair follicle development¹⁵ (Fig. 3k). Taken together, these results demonstrate that regenerating hair follicles in *Acomys* progress through defined stages of hair follicle development, exhibit high rates of proliferation, and reuse molecular pathways used during embryonic hair follicle development to regenerate new hair follicles.

Adult mammal skin is normally unable to regenerate epidermally-derived structures in response to wounding (for example, glands and hair follicles). An exception to this is the observation of spontaneous folliculogenesis in large excisional wounds in rabbits, and more recently in laboratory mice (C57BL6/SJ, SJL or mixed strain)^{16–18}. Rabbits are also one of the few mammalian species that can regenerate large ear punch wounds¹⁹. We proposed that the regenerative capacity observed in *Acomys* might extend to their ear tissue as well. To test this we made 4-mm punches through the ears of both *Acomys* species and, to our surprise, found that they were able to close these large punches (Fig. 4a–c and Supplementary Fig. 7a–c). Uninjured ear tissue contains skin (epidermis and dermis), associated hair follicles, adipose cells, muscle and cartilage; we found that *Acomys* were capable of completely regenerating all of these tissues with high fidelity except muscle (Fig. 4b, c). Twelve days after injury we observed an accumulation of cells around the circumference of the wound beneath the epidermis, and, although regeneration of new tissue was centripetal, cells accumulated to a greater degree on the proximal side of the punch. Hair follicle and cartilage regeneration proceeded in a proximal to

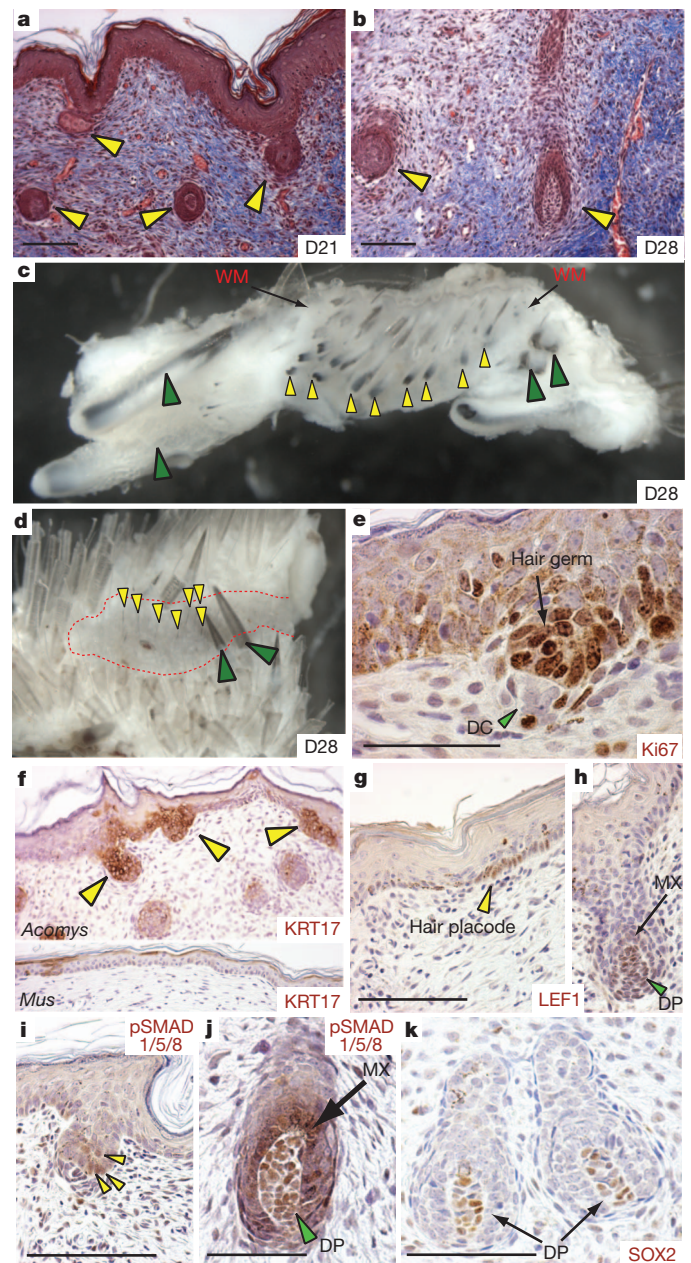


Figure 3 | *Acomys* exhibit *de novo* hair follicle regeneration in wounded skin. **a–d**, Hair follicles regenerating in *A. percivali* (yellow arrowheads) between D21 and D28 in large skin wounds. New hair follicles (yellow arrowheads) are present throughout the wound bed (red dotted area) at D28 (**c**, **d**). Green arrowheads indicate old follicles. **e–k**, Regenerating hair follicles express proteins associated with development and differentiation. Ki67 labels proliferating hair germ (**e**). KRT17 (yellow arrowheads) is present in *Acomys* but absent in *Mus* at D26 (**f**). Nuclear-localized LEF1 is present in follicle placodes (**g**) and later in dermal papilla cells (DP) and surrounding matrix cells (MX) (**h**). Phosphorylated SMAD1, 5 and 8 (as a readout of Bmp-signalling) is present in epidermal hair germ cells (**i**) and later in dermal papilla and matrix cells of regenerating follicles (**j**). SOX2 is present in dermal papilla cells (**k**). Scale bars, 100 μ m (**a–d**, **f–k**) and 50 μ m (**e**).

distal wave (Fig. 4d, e) and similar to the skin, follicular epidermis in the ear activated Wnt-signalling (Supplementary Fig. 6d, e). In contrast to *Acomys*, we found *Mus* were incapable of regenerating 4-mm ear punches and instead formed scar tissue (Supplementary Fig. 8a, b). Notably, despite scar formation, *Mus* ear repair resulted in the *de novo* formation of cartilage condensations distal to the cut cartilage suggesting *Mus* might initiate, but not maintain, a regenerative response after ear wounding (Supplementary Fig. 8b).

It remains unclear whether mammalian regeneration proceeds through formation of a blastema, or is instead an exaggerated version of hyperplastic growth^{20–22}. Blastema formation is considered a hallmark of epimorphic regeneration. One characteristic of a regeneration blastema is that it contains proliferating cells and maintains proliferation during regeneration²³. We observed widespread proliferation throughout the ear regenerate in *Acomys* and surprisingly, throughout healing ear tissue in *Mus* (Fig. 4f, g). However, we noted a lack of proliferation in the distal epidermis of *Acomys*, whereas we detected proliferation throughout *Mus* epidermis extending to the distal tip (Fig. 4f, g). Although proliferation was maintained in *Acomys* ears, we observed almost no proliferating cells in later-staged *Mus* ears (Fig. 4h, i).

A second characteristic of a blastema is the formation of a specialized epidermal signalling centre (the wound epidermis), which is required for proliferating blastemal cells to remain in the cell cycle²⁴ and is characterized by a loss of epidermal stratification, loss of basal keratinocyte polarity, and lack of a mature basal lamina²⁵. After re-epithelialization in *Acomys*, we noted a thickening of the distal epidermis, disorganization of basal keratinocytes and absence of a mature basement membrane (Fig. 4j). Comparatively, the epidermis near the amputation plane exhibited normal stratification and possessed a prominent basement membrane (Fig. 4k). By contrast,

Mus seemed to form a wound epidermis only transiently after re-epithelialization, with a proportionately smaller distal area exhibiting these characteristics for a short time (data not shown). By D12 in *Mus*, collagen type IV staining revealed a mature basement membrane beneath the entire epidermis of the healing ear (Fig. 4l). In addition, the epidermis exhibited normal stratification and proper apical-basal polarity of the basal keratinocytes (Fig. 4g, l).

In addition to sustained proliferation and formation of the wound epidermis, ECM molecules have a key role in supporting proliferation and directing subsequent differentiation during regeneration²⁶. By contrast, molecules such as laminin and collagen type I, which favour differentiation, are downregulated in the blastema during amphibian limb regeneration and are expressed as differentiation of the musculoskeletal system proceeds^{26,27}. Histological examination of *Acomys* ears at D12 revealed high levels of fibronectin, some tenascin-C (TN-C) surrounding densely packed cells, but very low levels of collagen type I (Supplementary Fig. 9a–c). Collagen type III was also more abundant than collagen type I during regeneration (Supplementary Fig. 9d–d'). TN-C became restricted from areas where new cartilage began differentiating and within these differentiating cells we found activation of the Bmp-signalling pathway in cells giving rise to new auricular cartilage (Fig. 4o and Supplementary Fig. 10). During hyperplastic growth in *Mus* ears, the ECM initially displayed

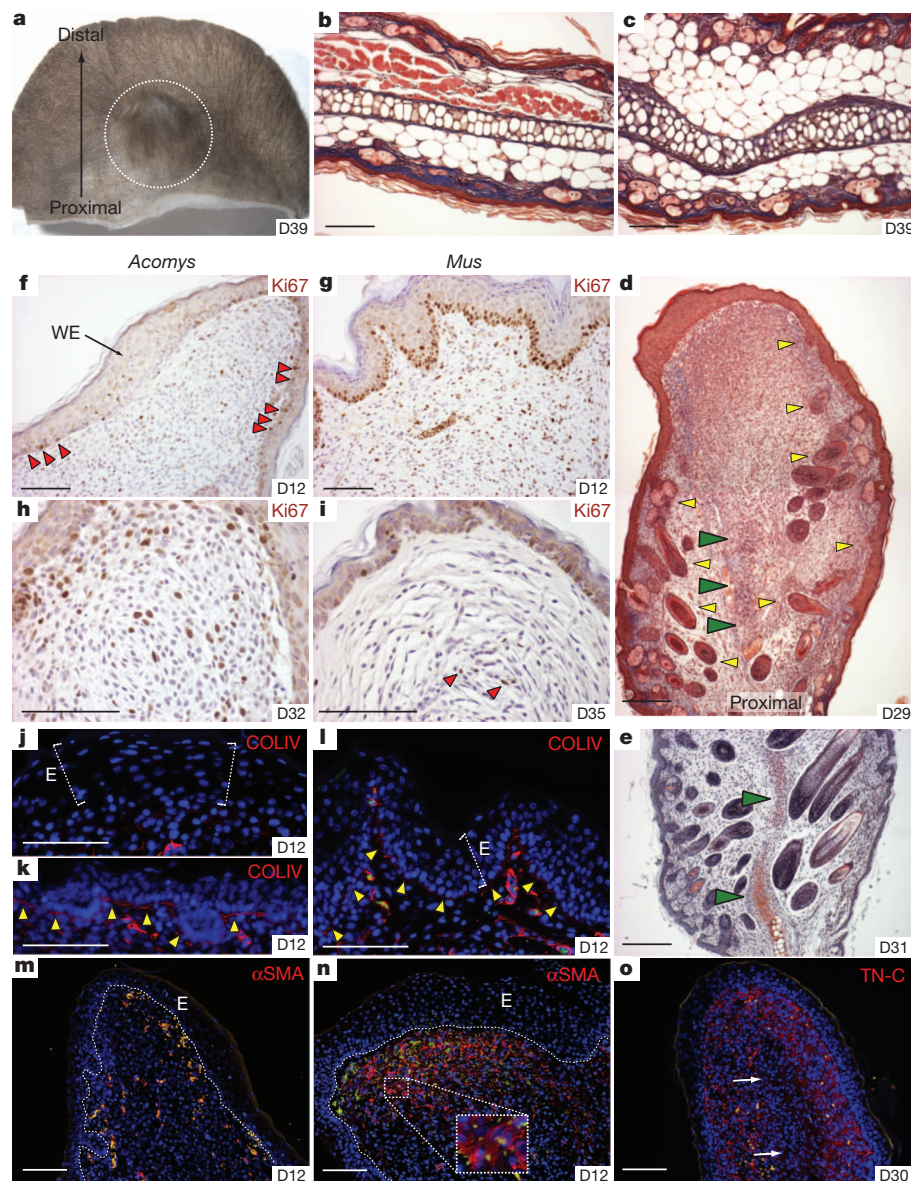


Figure 4 | *Acomys* regenerate hair follicles, sebaceous glands, dermis, adipose tissue and cartilage in 4-mm ear punches. **a**, A regenerated 4-mm ear punch in *A. percivali*. **b**, Unwounded tissue in *Acomys* ear pinna. **c**, Regenerated dermis, hair follicles, cartilage and adipose tissue within biopsy punched area. White circle denotes the original punch area. **d**, Regenerating hair follicles (yellow arrowheads) and cartilage (green arrowheads) differentiate proximal to distal. **e**, Safranin-O and fast green staining indicates chondrogenesis (green arrowheads). **f–i**, Proliferating cells (Ki67⁺) in early (**f**, **g**) and late (**h**, **i**) *Acomys* and *Mus* ears. Proliferation is restricted proximal to the wound epidermis (WE) (red arrowheads) in *Acomys* (**f**) and is continuous in basal keratinocytes of *Mus* (**g**). Proliferation is maintained in *Acomys* at D32 (**h**) with very few proliferating cells persisting in *Mus* (**i**) (red arrowheads). **j–l**, Collagen-IV-stained mature basement membrane is absent beneath the wound epidermis (E) in *Acomys* (**j**), but is present near the amputation (**k**) and distally in *Mus* (**l**). Yellow arrowheads indicate basement membrane, and white lines indicate epidermal thickness. **m**, **n**, Almost no α SMA-positive fibroblasts are present in *Acomys* (**m**), whereas α SMA-positive myofibroblasts are present in healing *Mus* ear (**n**). Inset shows stress fibres in individual myofibroblasts. **o**, TN-C disappears where new cartilage differentiates (white arrows) in *Acomys*. Yellow/green cells (**j–o**) are autofluorescing blood cells in the green fluorescent protein (GFP) channel. Scale bars, 100 μ m.

high levels of fibronectin and low levels of TN-C as did *Acomys* ears, but produced relatively higher levels of collagen type I (Supplementary Fig. 9e–g). Collagen production in *Mus* was not only faster and more abundant, but also exhibited a higher ratio of collagen type I to type III (Supplementary Fig. 9h, h'). Given the exuberant production of collagen type I in *Mus*, we asked whether resident fibroblasts were differentiating into myofibroblasts, which contribute to scarring in lieu of regeneration (reviewed in ref. 28). Using α -smooth muscle actin (α SMA), we found myofibroblasts in high abundance throughout ear tissue in *Mus*, whereas they were almost completely absent in *Acomys* ears (Fig. 4m, n). These data corroborate the importance of the wound ECM to promote proliferation while antagonizing differentiation and support previous work showing precocious collagen type I formation antagonizes appendage regeneration²⁷.

Our data suggest that reparative ear regeneration in *Acomys* is a balance between premature reformation of the dermis (scarring) and maintenance of cell proliferation within a pro-regenerative environment. By contrast, *Mus* fails to form (or maintain) a wound epidermis, which is coincident with precocious formation of the basement membrane and stratification of the epidermis. This leads to a loss of cell proliferation, increased collagen type I deposition (in lieu of collagen type III), myofibroblast activation and ultimately, scar formation. Although our data suggest ear regeneration shares similar characteristics with blastema formation, understanding the molecular signals required to organize and maintain a wound epidermis and identifying the lineage of regenerating cells is crucial to address how regeneration occurs in these animals. Future work investigating how *Acomys* can control fibrosis will shed light on how regeneration and scarring can be balanced in the face of infection and inflammation in wild mammals, and provides an ideal model system in which to examine epimorphic regeneration in mammals.

METHODS SUMMARY

Animals. Specimens of *A. kempi* and *A. percivali* were live-captured in Laikipia, Kenya, at the Mpala Research Centre. Experimental animals were held in an open-air field laboratory under ambient conditions. For comparative experiments, Swiss Webster mice were obtained from a local supplier in Nairobi and in the United States from Charles River.

Wounding. All experiments conducted in Kenya were performed in accordance with approved animal practices. Experiments performed in the United States were approved by the Institutional Review Board on Animal Care at the University of Florida and in Kenya by the University of Nairobi. Spiny mice were halothane-anesthetized and small (4 mm) and large (1.5 cm) full-thickness excisional wounds were made on the dorsum.

Strength measurements. Strength measures were made using a Hounsfield tensometer equipped with an automatic motor and stretched at a rate of 20 mm min⁻¹. Full-thickness skin strips (including the panniculus carnosus) measuring approximately 20 × 40 mm were used. Force (N) and displacement (mm) were measured on a xy plotter and these points were subsequently recorded as stress (σ = force per cross-sectional area) and strain (ϵ = change in length/initial length) and replotted in Excel. The work (W) required to achieve the breaking strength was calculated as the area under each stress–strain curve and expressed as the mean work for each genus.

Histology and immunohistochemistry. For histological analysis, samples were fixed in 10% neutral buffered formalin at 4 °C for 16–24 h, washed in PBS, dehydrated in ethanol and infiltrated with paraffin. Samples were cut at 5 μ m. For immunohistochemistry, slides were incubated with primary antibodies (see Methods) and visualized using either 3,3'-diaminobenzidine (DAB) or Alexa-Fluor 594. Negative controls were run using appropriate Ig isotypes at the same concentration as the primary antibody. For all immunohistochemistry comparisons, a minimum of $n = 4$ per species was used.

Full Methods and any associated references are available in the online version of the paper.

Received 27 November 2011; accepted 10 August 2012.

- Maginnis, T. L. The costs of autotomy and regeneration in animals: a review and framework for future research. *Behav. Ecol.* **17**, 857–872 (2006).

- Shargal, E., Rath-Wolfson, L., Kronfeld, N. & Dayan, T. Ecological and histological aspects of tail loss in spiny mice (Rodentia: Muridae, *Acomys*) with a review of its occurrence in rodents. *J. Zool.* **249**, 187–193 (1999).
- Bauer, A. M., Russell, A. P. & Shadwick, R. E. Mechanical properties and morphological correlates of fragile skin in gekkonid lizards. *J. Exp. Biol.* **145**, 79–102 (1989).
- Kragl, M. et al. Cells keep a memory of their tissue origin during axolotl limb regeneration. *Nature* **460**, 60–65 (2009).
- Dubost, G. & Gasc, J.-P. The process of total tail autotomy in the South-American rodent, *Proechimys*. *J. Zool.* **212**, 563–572 (1987).
- Vogel, H. G. Correlation between tensile-strength and collagen content in rat skin — effect of age and cortisol treatment. *Connect. Tissue Res.* **2**, 177–182 (1974).
- Seifert, A. W., Monaghan, J. R., Voss, S. R. & Maden, M. Skin regeneration in adult axolotls: a blueprint for scar-free healing in vertebrates. *PLoS One* **7**, e32875 (2012).
- Dang, C. M. et al. Scarless fetal wounds are associated with an increased matrix metalloproteinase-to-tissue-derived inhibitor of metalloproteinase ratio. *Plast. Reconstr. Surg.* **111**, 2273–2285 (2003).
- Soo, C. et al. Differential expression of matrix metalloproteinases and their tissue-derived inhibitors in cutaneous wound repair. *Plast. Reconstr. Surg.* **105**, 638–647 (2000).
- Yannas, I. V. *Tissue and Organ Regeneration in Adults* (Springer, 2001).
- McGowan, K. M. & Coulombe, P. A. Onset of keratin 17 expression coincides with the definition of major epithelial lineages during skin development. *J. Cell Biol.* **143**, 469–486 (1998).
- Andl, T., Reddy, S. T., Gaddapara, T. & Millar, S. E. WNT signals are required for the initiation of hair follicle development. *Dev. Cell* **2**, 643–653 (2002).
- DasGupta, R. & Fuchs, E. Multiple roles for activated LEF/TCF transcription complexes during hair follicle development and differentiation. *Development* **126**, 4557–4568 (1999).
- Botchkarev, V. A. & Sharov, A. A. BMP signaling in the control of skin development and hair follicle growth. *Differentiation* **72**, 512–526 (2004).
- Driskell, R. R., Giangreco, A., Jensen, K. B., Mulder, K. W. & Watt, F. M. Sox2-positive dermal papilla cells specify hair follicle type in mammalian epidermis. *Development* **136**, 2815–2823 (2009).
- Billingham, R. E. & Russell, P. S. Incomplete wound contracture and the phenomenon of hair neogenesis in rabbits' skin. *Nature* **177**, 791–792 (1956).
- Breidis, C. Regeneration of hair follicles and sebaceous glands from the epithelium of scars in the rabbit. *Cancer Res.* **14**, 575–579 (1954).
- Ito, M. et al. Wnt-dependent de novo hair follicle regeneration in adult mouse skin after wounding. *Nature* **447**, 316–320 (2007).
- Vorontsova, M. A. & Liozner, L. D. *Asexual propagation and Regeneration* 377–379 (Pergamon, 1960).
- Borgens, R. B. Mice regrow the tips of their foretoes. *Science* **217**, 747–750 (1982).
- Muneoka, K., Allan, C. H., Yang, X., Lee, J. & Han, M. Mammalian regeneration and regenerative medicine. *Birth Defects Res. C Embryo Today* **84**, 265–280 (2008).
- Clark, L. D., Clark, R. K. & Heber-Katz, E. A new murine model for mammalian wound repair and regeneration. *Clin. Immunol. Immunopathol.* **88**, 35–45 (1998).
- Chalkley, D. T. A quantitative histological analysis of forelimb regeneration in *Triturus viridescens*. *J. Morphol.* **94**, 21–70 (1954).
- Globus, M., Vethamany-Globus, S. & Lee, Y. C. Effect of apical epidermal cap on mitotic cycle and cartilage differentiation in regeneration blastemata in the newt, *Notophthalmus viridescens*. *Dev. Biol.* **75**, 358–372 (1980).
- Neufeld, D. A. & Day, F. A. Perspective: a suggested role for basement membrane structures during newt limb regeneration. *Anat. Rec.* **246**, 155–161 (1996).
- Calve, S., Odelberg, S. J. & Simon, H. G. A transitional extracellular matrix instructs cell behavior during muscle regeneration. *Dev. Biol.* **344**, 259–271 (2010).
- Sato, A., Makanae, A., Hirata, A. & Satou, Y. Blastema induction in aneurogenic state and Prrx-1 regulation by MMPs and FGFs in *Ambystoma mexicanum* limb regeneration. *Dev. Biol.* **355**, 263–274 (2011).
- Hinz, B. Formation and function of the myofibroblast during tissue repair. *J. Invest. Dermatol.* **127**, 526–537 (2007).

Supplementary Information is available in the online version of the paper.

Acknowledgements We thank John Kahiro for assisting during materials testing and the Department of Mechanical Engineering, University of Nairobi, for use of their equipment. We thank John Kimani, Stanley Marete and Jackson Mugweru, for help with animal care and materials procurement in Nairobi, Ekiro Ekanar for field assistance, and Bernard Agwanda, Darcy Ogada, and Hillary Young for help with identification and natural history of *Acomys*. Conversations with Steve Takata and Truman Young drew our attention to this phenomenon.

Author Contributions A.W.S., J.R.G., T.M.P. and M.M. formulated the research. A.W.S., M.G.S., M.M. and S.G.K., performed the research and analysed the data. A.W.S. wrote the manuscript and all authors discussed the results, commented on and edited the manuscript.

Author Information Reprints and permissions information is available at www.nature.com/reprints. The authors declare no competing financial interests. Readers are welcome to comment on the online version of the paper. Correspondence and requests for materials should be addressed to A.W.S. (seifert@ufl.edu).

METHODS

Animals. Male and female *A. kempi* and *A. percivali* were live-captured using Sherman traps in Laikipia, Kenya, at the Mpala Research Centre, between 2009 and 2011. Fifty traps were set in the late afternoon at various kopjes (rock outcroppings), and traps were checked the next morning for animals. Captured animals were transported to an open-air field laboratory and held under ambient conditions in species-specific groups with access to water *ad libitum*. Animals were fed twice daily on peanut butter and oats. Some animals were transported to the University of Nairobi, where they were maintained under similar conditions. For comparative experiments, Swiss Webster mice were obtained from a local supplier in Nairobi and in the United States from Charles River.

Wounding. All experiments conducted in Kenya were performed in accordance with approved animal practices. Experiments performed in the United States were approved by the Institutional Review Board on Animal Care at the University of Florida and in Kenya by the University of Nairobi. Both male and female mice were used, but pregnant females were excluded. Three types of wounds were used for this study: natural wounds, small circular wounds (4 mm diameter), and large circular wounds (1.5 cm diameter). Spiny mice were halothane-anaesthetized and shaved at least 1 day before wounding. Natural wounds were not made by the investigators and occurred either in the field or in captivity. Full-thickness excisional wounds were made by pinching the skin with forceps and cutting beneath to form a 4-mm circle (small) or cutting with iridectomy scissors a 1.5-cm diameter circle (large). For small wounds, four wounds were made on the dorsum posterior to the forelimbs and anterior to the hindlimbs. Wounds were allowed to heal and were not treated during healing. Calipers were used to measure wound width (mm) and wounds were recorded using a Canon S900 ($\times 1\text{--}\times 4$ Macro zoom).

Strength measurements. After culling, the entire dorsal skin including the panniculus carnosus was removed and placed face down in PBS. Two strips of dorsal skin measuring 20×40 mm were excised from this preparation maintaining the anteroposterior orientation, and the second strip was returned to PBS while the first strip was measured. Strips for mechanical testing were placed in metal screw clamps with rubber pieces covering the clamped ends. Clamps were placed in a Hounsfield tensiometer equipped with an automatic motor and stretched at a rate of 20 mm min^{-1} . Tissue measurements for width (mm) and length (mm) between clamps were measured before stretching, and PBS was applied before loading to keep the samples moist. Force (N) and displacement (mm) were measured on a xy plotter, and these points were subsequently recorded as stress (σ = force per cross-sectional area) and strain (ε = change in length/initial length) and replotted in Excel.

Load was applied to skin strips parallel to the long body axis and the tensile strength (σ_m) and failure strain (ε_f) were recorded (*M. musculus* ($n = 6$), *A. kempi* ($n = 5$) and *A. percivali* ($n = 5$)). The work (W) required to achieve the breaking strength was calculated as the area under each stress–strain curve and expressed as the mean work for each genus.

Histology and immunochemistry. For histological analysis, samples were fixed in 10% neutral buffered formalin at 4°C for 16–24 h, washed in PBS, dehydrated in ethanol and infiltrated with paraffin. Samples were cut at $5 \mu\text{m}$. For immunohistochemistry, slides were incubated with primary antibodies (see Methods) and visualized using either 3,3'-diaminobenzidine (DAB) or Alexa-Fluor 594. Negative controls were run using appropriate Ig isotypes at the same concentration as the primary antibody. For all immunohistochemistry comparisons, a minimum of $n = 4$ per species was used.

Primary antibodies and antigen retrieval used were: tenascin-C (1:50; Abcam; ab3970) with pronase at $1 \mu\text{g ml}^{-1}$ for 10 min at room temperature; fibronectin (1:500; Abcam; ab23750) with heat-induced epitope retrieval (HIER) in citrate buffer (pH 6.0); pan-cytokeratin (1:1,000; DAKO; Z0622) with proteinase K (DAKO) for 2 min at room temperature; cytokeratin 17 (1:400; Abcam; ab53707) with proteinase K for 2 min; Ki67 (1:2,000; Abcam; ab15580) with HIER in Tris-EDTA (pH 9.0); LEF1 (1:4,000; gift from O. Huber) with HIER in citrate buffer (pH 6.0) followed by treatment with 0.1% trypsin for 10 min room temperature; β -catenin (1:1,000; Sigma; HPA 029159) with HIER in citrate buffer (pH 6.0); pSMAD1/5/8 (1:200; Cell Signaling; 9511) with HIER in Tris-EDTA (pH 9.0); SOX2 (1:150; Abcam; ab97959) with HIER in citrate buffer (pH 6.0); collagen type IV (1:500; Rockland; 600-401-106-0.1) with proteinase K for 2 min; α SMA (1:200; Abcam; ab32575) with HIER in citrate buffer (pH 6.0); collagen type I (1:500; Abcam; ab34710) with HIER in citrate buffer (pH 6.0) followed by proteinase K for 2 min. For detection of rabbit antibodies, Vector Elite anti-rabbit kits were used, and for mouse monoclonal antibodies (TN-C) Vector M.O.M. kits were used. Antibodies were visualized with either diaminobenzidine (DAB) (Vector) or a streptavidin-conjugated Alexa-Fluor 594 antibody after incubation with biotinylated anti-secondary.

Estimation of the proportion of the adnexa in the dermis. The volume density of the adnexa in the dermis $V_{V(\text{adnexa, dermis})}$ is the ratio of the total volume of follicles and sebaceous glands to the total volume of the dermis. This ratio can be estimated by point counting on plane sections^{29–31}. For this purpose, one histological section was randomly sampled from each animal ($n = 6$ per species). The corresponding micrographs were projected on a screen, and a transparent test grid bearing a square lattice of points overlaid with random positions on each projected image:

$$V_{V(\text{adnexa, dermis})} = P_a/P_d$$

The total number of test points falling on profiles of the adnexa P_a and on the entire dermis P_d was counted. An estimator of the volume density of the adnexa was then calculated that is unbiased (that is, there is no systematic error due to the sampling or counting procedures) provided that the plane section and the test grid are randomly positioned.

Statistical analysis. To test for significant differences between percentage adnexa, the Student's two-tailed t -test function in Excel was used to calculate P values. Alpha was set at 0.05 and data are mean \pm standard error.

Descriptive statistics. For strength measure, $n = 6$ for *M. musculus* and $n = 5$ for *A. kempi* and *A. percivali*. The following data are mean \pm s.e.m. Mean failure strain (ε_f): *Mus* (0.61 ± 0.05), *A. kempi* (0.14 ± 0.05) and *A. percivali* (0.08 ± 0.02). Mean tensile strength (MPa): *Mus* (2.3 ± 0.19), *A. kempi* (0.15 ± 0.04), *A. percivali* (0.08 ± 0.03) and *Acomys* (both species) (0.11 ± 0.03). Mean toughness (MJ m^{-3}): *Mus* (0.77 ± 0.08), *A. kempi* (0.012 ± 0.006), *A. percivali* (0.005 ± 0.003) and *Acomys* (both species) (0.01 ± 0.004). The percentage of adnexa, $n = 6$ for each species. *A. percivali* ($55.61 \pm 4.28\%$) compared with *M. musculus* ($43.65 \pm 4.62\%$) ($t = 1.9$, $P = 0.043$). The percentage of wound contraction, $n = 12$ for *A. percivali* ($95.5 \pm 0.7\%$).

29. Gundersen, H. J. G. Notes on the estimation of the numerical density of arbitrary profiles: the edge effect. *J. Microsc.* **111**, 219–223 (1977).
30. Kiama, S. G., Maina, J. N., Bhattacharjee, J. & Weyrauch, K. D. Functional morphology of the pecten oculi in the nocturnal spotted eagle owl (*Bubo bubo africanus*), and the diurnal black kite (*Milvus migrans*) and domestic fowl (*Gallus gallus* var. *domesticus*): a comparative study. *J. Zool.* **254**, 521–528 (2001).
31. Weibel, E. R. *Stereological Methods* (Academic, 1979).

Structural and genetic basis for development of broadly neutralizing influenza antibodies

Daniel Lingwood^{1*}, Patrick M. McTamney^{1*}, Hadi M. Yassine^{1*}, James R. R. Whittle¹, Xiaoti Guo¹, Jeffrey C. Boyington¹, Chih-Jen Wei¹ & Gary J. Nabel¹

Influenza viruses take a yearly toll on human life despite efforts to contain them with seasonal vaccines. These viruses evade human immunity through the evolution of variants that resist neutralization. The identification of antibodies that recognize invariant structures on the influenza haemagglutinin (HA) protein have invigorated efforts to develop universal influenza vaccines. Specifically, antibodies to the highly conserved stem region of HA neutralize diverse viral subtypes. These antibodies largely derive from a specific antibody gene, heavy-chain variable region *IGHV1-69*, after limited affinity maturation from their germline ancestors^{1,2}, but how HA stimulates naive B cells to mature and induce protective immunity is unknown. To address this question, we analysed the structural and genetic basis for their engagement and maturation into broadly neutralizing antibodies. Here we show that the germline-encoded precursors of these antibodies act as functional B-cell antigen receptors (BCRs) that initiate subsequent affinity maturation. Neither the germline precursor of a prototypic antibody, CR6261 (ref. 3), nor those of two other natural human *IGHV1-69* antibodies, bound HA as soluble immunoglobulin-G (IgG). However, all three *IGHV1-69* precursors engaged HA when the antibody was expressed as cell surface IgM. HA triggered BCR-associated tyrosine kinase signalling by germline transmembrane IgM. Recognition and virus neutralization was dependent solely on the heavy chain, and affinity maturation of CR6261 required only seven amino acids in the complementarity-determining region (CDR) H1 and framework region 3 (FR3) to restore full activity. These findings provide insight into the initial events that lead to the generation of broadly neutralizing antibodies to influenza, informing the rational design of vaccines to elicit such antibodies and providing a model relevant to other infectious diseases, including human immunodeficiency virus/AIDS. The data further suggest that selected immunoglobulin genes recognize specific protein structural 'patterns' that provide a substrate for further affinity maturation.

Antibodies to the conserved stem region of HA block membrane fusion and prevent productive infection by diverse influenza viruses. The structural basis of HA stem recognition of two such monoclonal antibodies, CR6261 and F10, has been defined^{3,4}. These antibodies bind with nanomolar affinity to a highly conserved hydrophobic groove at the interface of HA1 and HA2, the two polypeptides that constitute HA, and neutralize several influenza group 1 subtypes including H1, H5, H6, H8 and H9 (ref. 3). Among the anti-stem antibodies isolated so far, the *IGHV1-69* gene segment is observed more frequently than expected by chance^{2,5}. To understand the development of these antibodies, we studied the prototypic *IGHV1-69*-derived broadly neutralizing antibody CR6261, isolated by phage display of human immunoglobulin genes, as well as two others cloned from single human cells, FE53 and 1009-3B05 (refs 1–3). Influenza *IGHV1-69*-based broadly neutralizing antibodies undergo a relatively low degree of somatic mutation (an average of 14 amino acids in the

heavy chain, $n = 9$)^{1–4} (Fig. 1a). We first asked whether their germline antibody precursors might recognize HA with measurable affinity. Notably, the *IGHV1-69* germline ancestors of CR6261, FE53 and 1009-3B05 failed to bind HA as soluble IgG, even at concentrations as high as 100 $\mu\text{g ml}^{-1}$ (Fig. 1b).

To define the molecular basis for affinity maturation of these antibodies, we analysed the respective contributions of heavy and light chains to antigen recognition. We compared chimaeric antibodies that consisted of somatic heavy (sH) and germline light (gL) chains to the mature antibody (sHsL). The chimaeric sHgL of all three antibodies bound to a recombinant H1 HA with affinities similar to their respective matured sHsL (Fig. 1b). Maturation of the light chain thus does not affect binding to H1 HA. Rather, somatic mutation of the *IGHV1-69* heavy chain gene alone mediates the increase in binding affinity. This finding is consistent with the lack of light-chain interaction observed in the crystal structures of both CR6261–HA and F10–HA complexes^{3,4}, suggesting that *IGHV1-69* light-chain somatic mutation may be incidental and is not required for heavy–light-chain pairing or improved neutralization function.

We next investigated the minimum requirements of heavy-chain loop maturation that lead to somatic activity. We chose to focus this

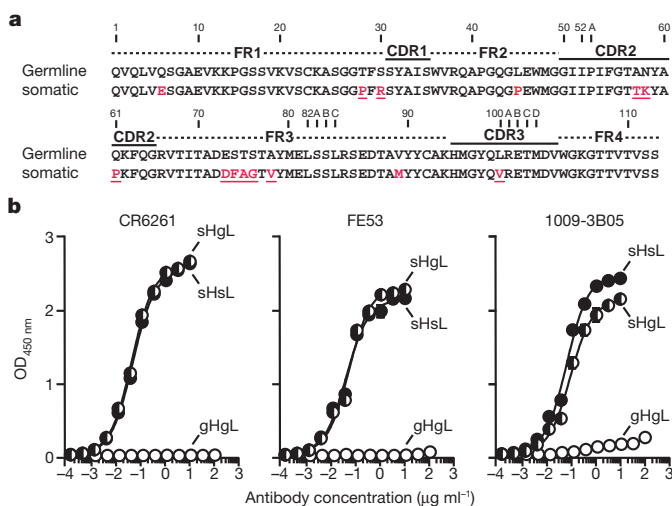


Figure 1 | Somatic maturation of heavy chain confers HA reactivity. **a**, Amino acid alignment of somatic CR6261 heavy-chain variable region (including the D and J regions) with JOINSOLVER²⁵ predicted germline precursor (Kabat²⁶ convention). Somatic mutations are shown in red. Those incorporated into germline variants are underlined. Mutations T28P and S30R are in close proximity to the Kabat-defined CDR H1 and are CR6261 contact residues, and therefore defined as CDR H1 somatic mutations in the remaining text. **b**, ELISA binding of somatic (sHsL, filled circles), respective germline (gHgL, open circles), and chimaeric (sHgL, half-filled circles) indicated HA-stem-specific antibodies to H1 1999 NC. OD, optical density. Error bars represent standard deviations of the mean for each antibody concentration.

¹Vaccine Research Center, National Institute of Allergy and Infectious Diseases, National Institutes of Health, Bethesda, Maryland 20892-3005, USA.

*These authors contributed equally to this work.

analysis on CR6261, the first IGHV1-69 anti-stem broadly neutralizing antibody discovered, for which the structure is known. The sH of CR6261 differs from the germline heavy (gH) chain by only 14 amino acids (11.6%) (Fig. 1a). Four of these amino acids (Pro 28, Arg 30, Lys 58 and Phe 74) contact the HA stem in the crystal structure (Fig. 2a). We generated several CR6261 germline variants by introducing residues from sH, including CDR H1, CDR H2, CDR H3 or FR3, into gH, singly or in combination. The resulting antibodies were analysed for their ability to bind HA and neutralize virus in an HA-pseudotyped lentiviral system⁶ (Table 1). Tested individually, only the somatic CDR H1 (sCDR H1: Thr28Pro/Ser30Arg) increased binding, but it was more than 100-fold less than sH. Furthermore, sCDR H1 alone did not confer detectable activity in our neutralization assay (Table 1). Although sFR3 alone did not improve the potency of germline CR6261, sCDR H1 and sFR3 together restored full activity for both binding and neutralization against H1N1 and H5N1 viruses (Table 1, Fig. 2b and Supplementary Fig. 1). This finding suggests that the

mutation of only a small number of germline residues enables potent neutralization.

Because CDR H1 and FR3 sit adjacent to one another in the folded protein, we examined the protein structure further. In most IGHV1-69 antibodies with no CDR H1 mutations, Phe 29 is buried in the 'canonical' conformation of the CDR H1 (ref. 7). In contrast, the somatically mutated CDR H1 of CR6261 flips the hydrophobic residue Phe 29 out, placing this residue in contact with HA. To determine whether the position of Phe 29 in CR6261 is due to maturation or binding, we solved the crystal structure of unliganded CR6261(sHgL), and compared it to both a IGHV1-69 antibody with no mutations in CDR H1, and HA-liganded CR6261 (Fig. 2c). In the unliganded structure, Phe 29 is exposed on the surface, suggesting that the somatic mutations Thr28Pro and Ser30Arg lead to its placement there—a hydrophobic residue from the interior of the antibody is made available to contribute to the interface by mutation of adjacent residues. The CDR H1 of IGHV1-69 in both germline and affinity-matured states is not well ordered unless bound to antigen. However, the CDR H1 loop in CR6261 favours the non-canonical conformation, with Phe 29 exposed, whether or not HA is bound. The solved structure suggests that the main consequence of somatic CDR H1 mutation is to favour this non-canonical state. Comparison of these structures also explains the synergistic effect of mutations in CDR H1 and FR3; somatic mutation in FR3 introduces Phe 74 on the surface of CR6261 adjacent to Phe 29 in CDR H1, and these two sets of mutations increase the hydrophobicity of the contact surface more than either alone.

The minimal somatic mutation of the CR6261 germ line required to confer full activity made it surprising that the germline antibody did not recognize HA with any measurable affinity in solution. We proposed that antibody recognition by the low-affinity germline IGHV1-69 revertant requires a more physiological presentation, for example, on the cell surface where such antibodies would normally be expressed. A naturally bivalent transmembrane IgM form of the CR6261 germ line was transfected into human embryonic kidney 293F cells. Cell surface expression was confirmed by staining with an anti-lambda-chain antibody. Fluorescent-labelled HA stained CR6261-germline-expressing cells but not mock transfected cells, as measured by flow cytometry (Fig. 3a). In contrast, no binding was seen in solution with CR6261 germline Fab monomer, bivalent IgG, or decameric IgM antibody derivatives (Supplementary Fig. 2). The specificity of CR6261 germline binding to the HA stem was further confirmed by its minimum reactivity to a mutant HA probe that blocks anti-stem-antibody binding (Supplementary Fig. 3). FE53 and 1009-3B05 each showed similar membrane-dependent recognition (Fig. 3a). Our results suggest that membrane presentation of antibody provides a mechanism by which low-affinity germline B cells achieve sufficient binding to recognize antigens before affinity maturation, and are consistent with experiments showing that two-dimensional confinement and clustering at the plasma membrane can increase the apparent affinity of cell surface receptors^{8,9}.

Two amino acids at the tip of CDR H2, Ile 53 and Phe 54, seem to be an anchor by which germline IGHV1-69 might attach to HA (Fig. 2a). Indeed, mutation of these two amino acids to alanines abolished HA germline binding for all V_H-1-69 antibodies (Fig. 3a). Individual mutation of Ile 53 and Phe 54 also abolished binding of unmodified/native HA trimer (binding in the presence of 6'-sialyllactose to prevent sialic acid mediated cell adhesion; Fig. 3b and Supplementary Fig. 4). In the CR6261-HA co-crystal structure, CDR H2 inserts into a hydrophobic pocket between HA1 and HA2 (ref. 3) (Fig. 3c). These data suggest that this interaction of the germline CDR H2 has a central role in recognition and engagement of the HA stem.

To determine whether binding of antigen to germline antibodies displayed on the cell surface could induce BCR activation and signalling, the transmembrane IgM version of the CR6261 germline was transfected into a transformed human B cell capable of expressing a functional BCR^{10,11}, a Ramos cell clone whose endogenous IgM is not

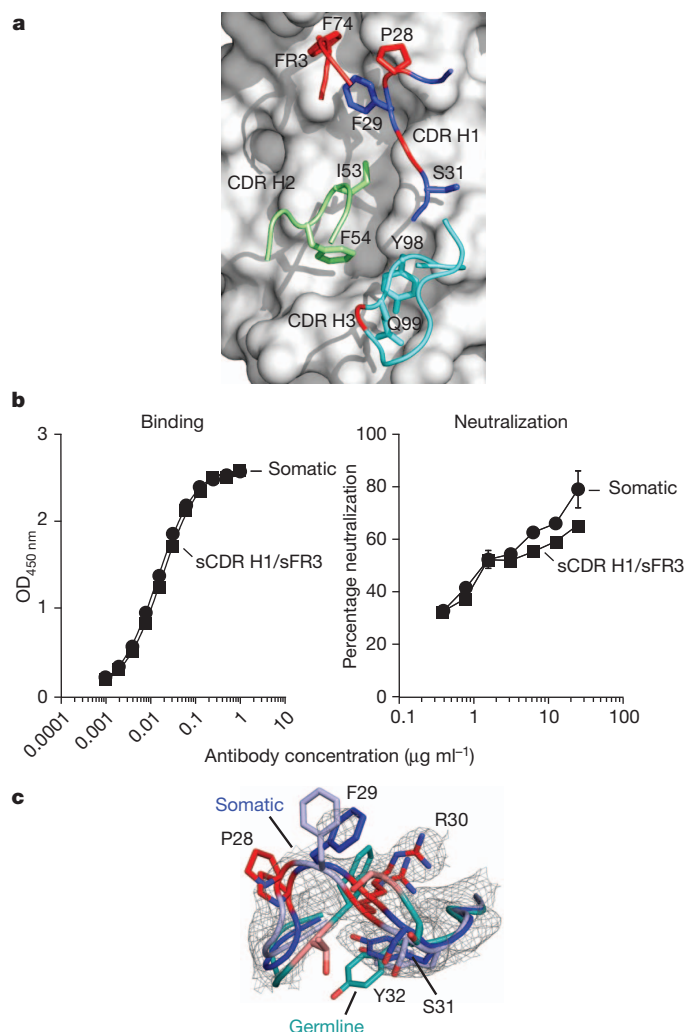


Figure 2 | CDR H1 maturation confers CR6261 neutralization activity. **a**, CR6261 interaction with H1 A/South Carolina/1/1918 (1918 SC) HA stem (grey, PDB accession 3GBN). Side chains with at least 10 Å² of interaction are depicted as sticks, with somatically mutated residues coloured red. **b**, ELISA binding and neutralization of H1 1999 NC by mature (filled circles) and sCDR H1/sFR3 germline-mutated CR6261 (filled squares). Error bars represent standard deviations of the mean for each antibody concentration. **c**, CDR H1 of CR6261 uncomplexed (blue) or with HA (light blue, PDB accession 3GBN) compared with unmutated CDR H1 from 47e (cyan, PDB accession 1RZI); mutated residues are in red (CR6261) or pink (47e). A non-crystallographic symmetry (NCS)-averaged electron density map (grey) is contoured at 1.0σ.

Table 1 | HA binding and pseudovirus neutralization analysis

Germline revertants	Mutations	H1 1999 NC	
		Titre ($\mu\text{g ml}^{-1}$)	IC ₅₀ ($\mu\text{g ml}^{-1}$)
Somatic	Full	0.00133	1.9
Germline	None	>100	>25
sCDR H1	T28P S30R	0.150	>25
sCDR2 H2	A57T N58K Q61P	>100	>25
sFR3	D73E F74S A75T G76S V78A	63.2	>25
sCDR H3	V100L	>100	>25
sCDR H1/sCDR H2	T28P S30R A57T N58K Q61P	0.150	>25
sCDR H1/sFR3	T28P S30R D73E F74S A75T G76S V78A	0.00133	2.0
sCDR H1/sCDR H3	T28P S30R V100L	0.250	>25
sCDR H2/sFR3	A57T N58K Q61P D73E F74S A75T G76S V78A	0.950	>25
sCDR H2/sCDR H3	A57T N58K Q61P V100L	0.150	>25
sFR3/sCDR H3	D73E F74S A75T G76S V78A V100L	>100	>25
sCDR H1/sCDR H2/sFR3	T28P S30R A57T N58K Q61P D73E F74S A75T G76S V78A	0.00133	1.4

Binding was determined by ELISA endpoint dilution titres. Half-maximum inhibitory concentration (IC₅₀) values represent 50% neutralization of pseudotyped lentiviruses by the respective antibodies. Mutations incorporated into germline-revertant antibodies correspond to the variable regions indicated.

expressed (Methods). We found that proteoliposome-arrayed HA (Supplementary Fig. 5) selectively triggered tyrosine phosphorylation of BCR effector proteins HS1 and SLP-65 (ref. 12) (Fig. 3d). Signalling by HA was comparable to that induced by IgM cross-linking. Furthermore, mutation of Ile53Ala/Phe54Ala in CDR H2 abolished the response to

HA stimulation, consistent with the binding data and confirming the importance of the germline CDR H2 structure in naive B-cell activation. These findings indicate that engagement of low-affinity germline IGHV1-69 antibody can lead to BCR activation, thus triggering further maturation and the subsequent humoral immune response.

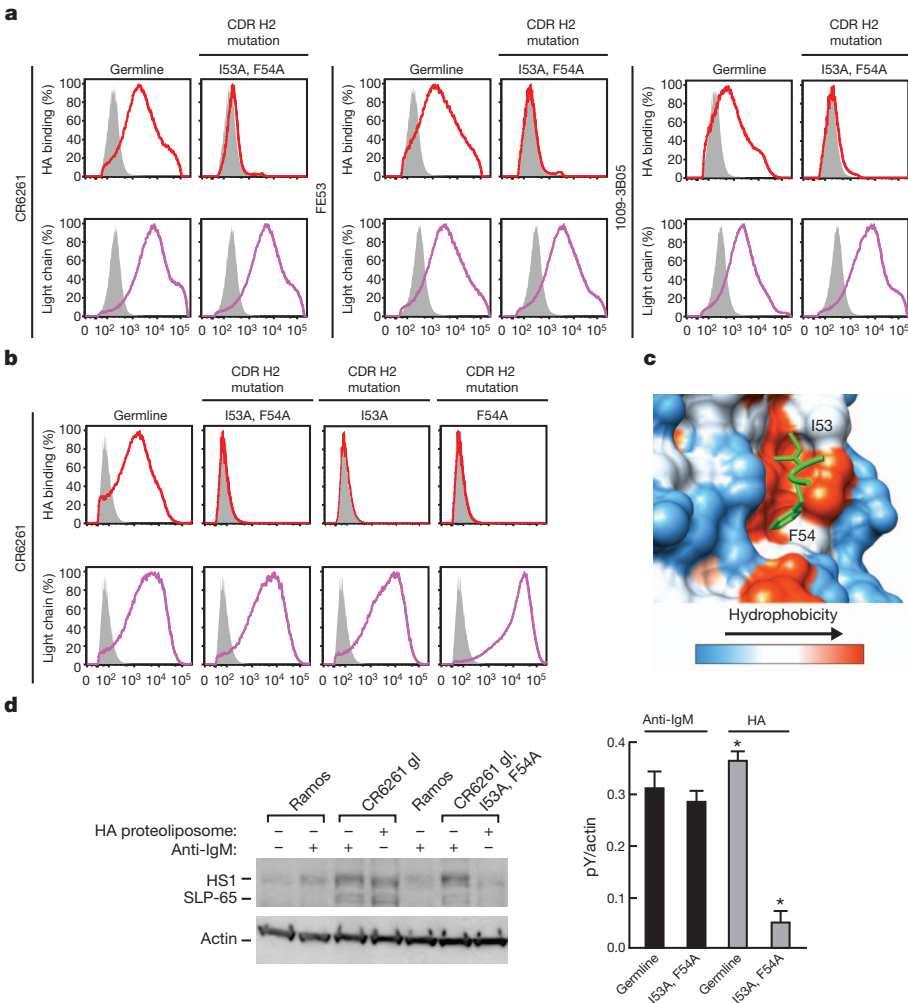


Figure 3 | HA engages and activates membrane-presented germline antibody. **a**, 293F cells expressing membrane IgMs (VRC01 (grey), IGHV1-69 germ lines (wild-type and Ile53Ala/Phe54Ala mutants, coloured lines)) exposed to HA with an N-linked glycan introduced to block the sialic-acid-binding site (Δ BS) (red) and anti-light-chain expression controls (purple) analysed by flow cytometry. **b**, Unmodified HA trimer also engages germline

(30 mM 6'-sialyllactose present) by flow cytometry. **c**, CR6261 CDR H2 interactions with 1918 SC HA stem (PDB accession 3GBN). **d**, HA proteoliposomes selectively activate tyrosine phosphorylation (pY) by CR6261 germline BCR ($P < 0.0002$, ANOVA); wild-type and mutant CDR H2 receptor activity differed for HA (asterisk) but not for anti-IgM (Tukey's HSD, $\alpha = 0.05$). Presented are the mean values and standard errors of pY intensity.

We have shown in this study that IGHV1-69 antibodies, with no mutation of the germline-encoded VH sequence, engage influenza HA with sufficient affinity to trigger B-cell activation. In all cases, engagement depends on membrane presentation of antibodies with the same structural determinant—two specific hydrophobic residues in the CDR H2. Mutational analysis further revealed that just a few mutations convert a germline IGHV1-69 into an antibody with the full activity of CR6261. Taken together, these results suggest that the IGHV1-69 germ line is poised to form, with a varied set of CDR H3 sequences, broadly neutralized antibodies directed against the highly conserved stem of influenza HA.

Having an antibody with the inherent potential to recognize a common feature of influenza virus would seem to offer obvious evolutionary advantages. Although neutralizing antibodies against other viruses such as human immunodeficiency virus (HIV), SARS and hepatitis C virus also use the IGHV1-69 gene for recognition^{13–18}, these interactions differ. For example, 17b antibody binding to the CD4-induced site on HIV-1 Env¹⁴ and 8066 antibody binding to HIV-1 gp41 (ref. 19) orient the CDR H2 into a hydrophobic cleft whereas others such as the SARS neutralizing antibody M396 orient CDR H2 into a more hydrophilic site¹⁶. In each case, the actual fold recognized by the CDR H2 is distinct from that recognized on the HA stem. Together, the data suggest that the IGHV1-69 CDR H2 motif is particularly well adapted to recognize the specific protein fold that is highly conserved on the stem of diverse influenza virus HAs.

This germline VH gene, although expressed as part of the adaptive immune response, may therefore serve as a primordial pattern recognition receptor, structurally adapted to participate in recognition of such hydrophobic grooves³. As no other heavy-chain V genes have a hydrophobic CDR H2 (ref. 14), we speculate that influenza may have exerted selection pressure leading to retention of this VH gene. It is also conceivable that the adaptive immune system retains this innate capacity for hydrophobic contact to facilitate the generation of high-affinity antibodies after only a limited degree of somatic mutation. This situation contrasts with the considerable somatic mutation (31%) observed in broadly neutralizing antibodies directed to the CD4-binding site of HIV²⁰, a more recently evolved virus for which there has been less opportunity to select for protective antiviral genes.

The majority of current vaccine-elicited influenza antibodies are directed to the globular head region of viral surface glycoprotein HA, which undergoes considerable antigenic drift to evade the human immune system. Thus, influenza vaccination requires annual assessment of the strains likely to circulate in the coming year to generate protective immunity for the world population. Consequently, there is great interest in the development of a universal influenza vaccine^{21,22}. Antibodies targeting the highly conserved HA stem epitope represent the vast majority of all broadly neutralized antibodies isolated against influenza so far^{1–4}. We have previously demonstrated that it is possible to elicit CR6261-like stem-directed antibodies by vaccination^{22,23}. Despite sequence variations in the CDRs and FR regions, IGHV1-69 antibodies evolve with a relatively small number of somatic mutations. At the same time, robust induction of these neutralizing antibodies in humans remains a challenge. Analysis of current genomics data (1000 Genome Project) reveals a polymorphism in the IGHV1-69 allele at the contact site in CDR H2 where Leu replaces Phe 54 at a predicted homozygous frequency of 13% in the general population. This substitution abolishes HA recognition by all three germline antibodies (Supplementary Fig. 6). This finding underscores the remarkable specificity in the CDR H2 contact and raises the possibility that some vaccine recipients may not mount a IGHV1-69 response. At the same time, ~30% of stem antibodies isolated until now derive from other VH gene segments^{1,2}, and it remains possible that such individuals might develop responses from other IgG loci. Taken together, knowledge of the initial engagement of the HA stem with the IGHV1-69 V gene, its subsequent BCR stimulation and somatic mutation will aid in the rational design of universal influenza vaccines.

METHODS SUMMARY

The genes encoding wild-type HA proteins (H1 A/New Caledonia/20/1999 (1999 NC) and H5 A/Indonesia/05/2005 (2005 IND)) and somatically mutated and inferred germline antibodies of CR6261, FE53, and 1009-3B05 were synthesized. Somatic mutated CR6261 germline revertants and germline CDR H2 Ala mutations of Ile and Phe were constructed by introducing mutations to germline heavy chains by site-directed mutagenesis. Plasmids encoding these proteins were transfected into the human embryonic kidney cell line 293F and isolated from expression supernatants 72–96 h after transfection. HA trimeric proteins were purified as previously described²⁴. Soluble Fab, IgG and IgM antibodies were purified using HisTrap, Protein G and IgM affinity columns, respectively, with additional gel-exclusion chromatography performed on IgM samples (GE Healthcare).

The purified antibody variants (1.7×10^{-4} – $100 \mu\text{g ml}^{-1}$) were assayed for binding to H1 1999 NC and in some cases to H5 2005 IND by enzyme-linked immunosorbent assay (ELISA) with purified trimeric HA proteins. The various antibodies were detected by peroxidase-conjugated goat anti-human IgG unless otherwise noted. Endpoint dilutions were determined from nonlinear fit dose-response curves using a detection limit of $4 \times$ background absorbance. CR6261 variants (0.39 – $25 \mu\text{g ml}^{-1}$) were also assayed for neutralization of pseudotyped recombinant lentiviruses expressing wild-type HA with the corresponding neuraminidase (NA) with a luciferase reporter gene as previously described²².

The crystal structure of CR6261 sHgL Fab at 2.85 Å resolution was determined by molecular replacement (Methods).

For membrane presentation of antibody, IGHV1-69 germ lines were expressed in membrane IgM format in 293F cells, which were then subject to a FACS-based HA cell surface binding assay 72 h after transfection (Methods). For BCR triggering, membrane IgM germ lines were transiently expressed in an IgM-negative Ramos B cell line and exposed to proteoliposome-arrayed H1 1999 NC (Methods). Activation was assessed by extent of tyrosine phosphorylation using the 4G10 pY antibody as described¹².

Full Methods and any associated references are available in the online version of the paper.

Received 5 May; accepted 29 June 2012.

Published online 29 August; corrected online 26 September 2012 (see full-text HTML version for details).

1. Corti, D. *et al.* Heterosubtypic neutralizing antibodies are produced by individuals immunized with a seasonal influenza vaccine. *J. Clin. Invest.* **120**, 1663–1673 (2010).
2. Wrammert, J. *et al.* Broadly cross-reactive antibodies dominate the human B cell response against 2009 pandemic H1N1 influenza virus infection. *J. Exp. Med.* **208**, 181–193 (2011).
3. Ekiert, D. C. *et al.* Antibody recognition of a highly conserved influenza virus epitope. *Science* **324**, 246–251 (2009).
4. Sui, J. *et al.* Structural and functional bases for broad-spectrum neutralization of avian and human influenza A viruses. *Nature Struct. Mol. Biol.* **16**, 265–273 (2009).
5. Sui, J. *et al.* Wide prevalence of heterosubtypic broadly neutralizing human anti-influenza A antibodies. *Clin. Infect. Dis.* **52**, 1003–1009 (2011).
6. Yang, Z. Y. *et al.* Immunization by avian H5 influenza hemagglutinin mutants with altered receptor binding specificity. *Science* **317**, 825–828 (2007).
7. Al-Lazikani, B., Lesk, A. M. & Chothia, C. Standard conformations for the canonical structures of immunoglobulins. *J. Mol. Biol.* **273**, 927–948 (1997).
8. Fahmy, T. M., Bieler, J. G., Edidin, M. & Schneck, J. P. Increased TCR avidity after T cell activation: a mechanism for sensing low-density antigen. *Immunity* **14**, 135–143 (2001).
9. Huppa, J. B. *et al.* TCR-peptide–MHC interactions in situ show accelerated kinetics and increased affinity. *Nature* **463**, 963–967 (2010).
10. Klein, G., Giovanella, B., Westman, A., Stehlin, J. S. & Mumford, D. An EBV-genome-negative cell line established from an American Burkitt lymphoma; receptor characteristics. EBV infectibility and permanent conversion into EBV-positive sublines by *in vitro* infection. *Intervirology* **5**, 319–334 (1975).
11. Benjamin, D. *et al.* Immunoglobulin secretion by cell lines derived from African and American undifferentiated lymphomas of Burkitt's and non-Burkitt's type. *J. Immunol.* **129**, 1336–1342 (1982).
12. Muller, R., Wienands, J. & Reth, M. The serine and threonine residues in the Ig- α cytoplasmic tail negatively regulate immunoreceptor tyrosine-based activation motif-mediated signal transduction. *Proc. Natl Acad. Sci. USA* **97**, 8451–8454 (2000).
13. Chan, C. H., Hadlock, K. G., Fong, S. K. & Levy, S. IGHV1-69 gene is preferentially used by hepatitis C virus-associated B cell lymphomas and by normal B cells responding to the E2 viral antigen. *Blood* **97**, 1023–1026 (2001).
14. Huang, C. C. *et al.* Structural basis of tyrosine sulfation and V_H gene usage in antibodies that recognize the HIV type 1 coreceptor-binding site on gp120. *Proc. Natl Acad. Sci. USA* **101**, 2706–2711 (2004).
15. Luftig, M. A. *et al.* Structural basis for HIV-1 neutralization by a gp41 fusion intermediate-directed antibody. *Nature Struct. Mol. Biol.* **13**, 740–747 (2006).

16. Prabakaran, P. *et al.* Structure of severe acute respiratory syndrome coronavirus receptor-binding domain complexed with neutralizing antibody. *J. Biol. Chem.* **281**, 15829–15836 (2006).
17. Haid, S., Pietschmann, T. & Pecheur, E. I. Low pH-dependent hepatitis C virus membrane fusion depends on E2 integrity, target lipid composition, and density of virus particles. *J. Biol. Chem.* **284**, 17657–17667 (2009).
18. Xiao, X. *et al.* Germline-like predecessors of broadly neutralizing antibodies lack measurable binding to HIV-1 envelope glycoproteins: implications for evasion of immune responses and design of vaccine immunogens. *Biochem. Biophys. Res. Commun.* **390**, 404–409 (2009).
19. Gustchina, E. *et al.* Structural basis of HIV-1 neutralization by affinity matured Fabs directed against the internal trimeric coiled-coil of gp41. *PLoS Pathog.* **6**, e1001182 (2010).
20. Wu, X. *et al.* Rational design of envelope identifies broadly neutralizing human monoclonal antibodies to HIV-1. *Science* **329**, 856–861 (2010).
21. Nabel, G. J. & Fauci, A. S. Induction of unnatural immunity: prospects for a broadly protective universal influenza vaccine. *Nature Med.* **16**, 1389–1391 (2010).
22. Wei, C. J. *et al.* Induction of broadly neutralizing H1N1 influenza antibodies by vaccination. *Science* **329**, 1060–1064 (2010).
23. Ledgerwood, J. E. *et al.* DNA priming and influenza vaccine immunogenicity: two phase 1 open label randomised clinical trials. *Lancet Infect. Dis.* **11**, 916–924 (2011).
24. Wei, C. J. *et al.* Comparative efficacy of neutralizing antibodies elicited by recombinant hemagglutinin proteins from avian H5N1 influenza virus. *J. Virol.* **82**, 6200–6208 (2008).
25. Souto-Carneiro, M. M., Longo, N. S., Russ, D. E., Sun, H. W. & Lipsky, P. E. Characterization of the human Ig heavy chain antigen binding complementarity determining region 3 using a newly developed software algorithm, JOINSOLVER. *J. Immunol.* **172**, 6790–6802 (2004).
26. Kabat, E. A., Wu, T. T., Perry, H. M., Gottesman, K. S. & Foeller, C. *Sequences of Proteins of Immunological Interest* (US Dept. of Health and Human Services, Public Health Service, National Institutes of Health, 1991).

Supplementary Information is linked to the online version of the paper at www.nature.com/nature.

Acknowledgements We thank N. Longo for help with JOINSOLVER analysis, Z.-Y. Yang for the design of membrane-bound IgM antibody, and X. Chen for technical support. We also thank A. Tislerics for manuscript preparation, B. Hartman and J. Farrar for preparation of figures, members of the G.J.N. laboratory and P. Kwong for advice and discussions. Use of the Advanced Photon Source was supported by the US Department of Energy, Office of Science, Office of Basic Energy Sciences, under contract no. W-31-109-Eng-38. This research was supported by the Intramural Research Program of the Vaccine Research Center, NIAID, National Institutes of Health.

Author Contributions D.L., P.M.M., H.M.Y., J.C.B., C.-J.W. and G.J.N. designed the research studies; D.L., P.M.M., H.M.Y., J.R.W., X.G., J.C.B. and C.-J.W. performed the research; D.L., P.M.M., H.M.Y., J.R.W., J.C.B., C.-J.W. and G.J.N. analysed data and wrote the paper.

Author Information Structure factors and coordinates for CR6261 sHgL Fab were deposited with the Protein Data Bank under accession 4EVN. Reprints and permissions information is available at www.nature.com/reprints. The authors declare no competing financial interests. Readers are welcome to comment on the online version of this article at www.nature.com/nature. Correspondence and requests for materials should be addressed to G.J.N. (gnabel@nih.gov).

METHODS

Plasmid construction. Genes encoding HA proteins A/New Caledonia/20/1999 (H1 1999 NC; GenBank AY289929) and A/Indonesia/05/2005 (H5 2005 IND; GenBank ABW06108.1), the corresponding neuraminidase proteins, monoclonal antibodies CR6261, FE53, 1009-3B05 and the respective inferred germline antibodies³ were synthesized using human preferred codons as described²⁷ by GeneArt (Regensburg, Germany). The germ lines were predicted using JOINSOLVER²⁵ and were created from the following segments: *IGHV1-69*01*, *IGHD2-02*02*, *IGHJ6*03* (CR6261); *IGHV1-69*01*, *IGHD2-08*02*, *IGHJ4*02* (FE53); and *IGHV1-69*06*, *IGHD2-08*01*, *IGHJ3*02* (1009-3B05). The genes were cloned into a CMV/R vector for efficient expression in mammalian cells²⁷. Soluble and membrane IgM and Fab genes were generated by overlapping PCR (IgG and IgM class switch region was identified through sequence alignment of GenBank available sequences for cloning of soluble and membrane-bound IgM antibodies). Mutations to germline antibodies were introduced using the QuikChange Site-Directed Mutagenesis kit (Agilent Technologies). The following mutations of germline CR6261 heavy chain were generated to probe maturation: CDR H1 (Thr28Pro and Ser30Arg), CDR H2 (Ala57Thr, Asn58Lys and Gln61Pro), CDR H2-61P that lacks the mutation at amino acid 61 (Ala57Thr and Asn58Lys), CDR H3 (Val100Leu) and FR3 (Asp73Glu, Phe74Ser, Ala75Thr, Gly76Ser and Val78Ala). Germline variant antibodies constructed to probe engagement correspond to the following mutations: CDR H2 mutations Ile53Ala, Phe54Ala and Phe54Leu.

Cell surface binding. To evaluate the role that cell surface presentation has in the recognition of low-affinity antigens at the initial contacting germline stage, soluble germline antibodies were expressed as receptor IgMs on the surface of 293F cells (293fectin Reagent, Invitrogen). For the HA ligand, an N-linked glycan (HA1 Arg192Thr, H3 numbering) was introduced into the receptor binding site (IGRBs) of wild-type or HA stem binding mutant (Ile45Arg/Thr49Arg mutations in HA2, Δ stem) H1 1999 NC to prevent sialic-acid-mediated cell binding. The resulting avi-tagged trimer was biotinylated, purified by size-exclusion chromatography, and labelled with a streptavidin-linked PE fluorophore²⁰. Two days after transfection, 2×10^6 cells expressing membrane IgM versions of CR6261 germ line (gl), FE53 gl, 1009-3B05 gl (all \pm CDR H2 mutations Ile53Ala and Phe54Ala), or VRC01 (mock) were placed on ice, stained with violet fluorescent reactive dye (ViViD, catalogue no. L34955, Invitrogen) for 30 min in PBS, washed, and then incubated (1 h, 4 °C, in PBS containing 1% FBS) with either: PE-HA Δ RBS (4 μ g ml⁻¹); PE-HA Δ RBS Δ stem (4 μ g ml⁻¹); PE-anti-human kappa chain (catalogue no. 12-9970-42, eBioscience) (FE53 gl, 1009-3B05 gl); PE mouse anti-human lambda chain (catalogue no. 555797, BD Biosciences) (CR6261 gl). For unmodified/native HA binding, cells were incubated with 4 μ g ml⁻¹ trimer along with 30 mM 6'-sialyllactose to prevent sialic-acid-mediated cell binding (Supplementary Fig. 4) (1 h, 4 °C, in PBS). Cells were washed twice and then fixed in PBS containing 0.5% PFA. ViViD-negative cell surface PE intensity was quantified by flow cytometry (ViViD excitation at 407 nm, bandpass filter 450/50 nm; PE excitation at 532 nm; BD LSR II, BD Biosciences).

HA proteoliposome preparation. This platform was used to provide both the multivalent antigen display needed to oligomerize and activate the BCR²⁸ and the synaptic engagement architecture that underscores naive B-cell stimulation by antigen-presenting cells in the lymph node germinal centre²⁹. One gram of 1,2-dioleoyl-*sn*-glycero-3-phosphocholine:1,2-dioleoyl-*sn*-glycero-3-[(N-(5-amino-1-carboxypentyl)iminodiacetic acid)] succinyl (Avanti Polar Lipids) in a 1:1 molar ratio was evaporated under a stream of nitrogen for 1 h. The dry lipid film was then rehydrated in 1,000 μ l of liposome buffer (50 mM HEPES, 150 mM NaCl, pH 7.25 (HBS)) and shaken for 40 min, all the time being heated above the membrane melting temperature of the lipid mixture. The resulting homogeneous suspension was subjected to ten freeze-thaw cycles and then extruded 21 times through a 100-nm pore polycarbonate membrane using the Avanti mini-extruder (Avanti Polar Lipids). HA proteoliposomes were produced by incubating the resultant liposomes with His-tagged Δ RBS H1 1999 NC trimer for 1 h at room temperature (HA trimer:lipid molar ratio of 1:900). The sample was then adjusted to 15% iodixanol (in 1.25 ml HBS) and overlaid with 1.75 ml, 0.5 ml and 0.5 ml of 10%, 2.5% and 0% iodixanol in HBS, respectively. Samples were then centrifuged at

200,000g in a TH660 rotor (Sorvall) for 2 h. The proteoliposome fraction, which concentrated at the 2.5–0% iodixanol interface (Supplementary Fig. 5), was collected and dialysed overnight (Slide-A-Lyzer Dialysis Cassette, 10000 MWCO, catalogue no. 66380, Thermo Scientific) to remove density gradient material. After dialysis, proteoliposomes were pelleted (200,000g, 2 h, TH660 rotor), resuspended in HBS and measured by the Pierce BCA protein assay (catalogue no. 23227, Thermo Scientific).

B-cell activation. Ramos B lymphocytes (ATCC) were initially stained with fluorescently conjugated anti-lambda chain and anti-IgM monoclonal antibodies (mouse PE-anti-human lambda chain, catalogue no. 555797, BD Biosciences; APC-anti-human IgM, catalogue no. 314510, BioLegend) to isolate a B-cell clone with no functional BCR at the cell surface. Such a clone was identified by flow cytometry (BD FACSAria, BD Biosciences), expanded and re-sorted for IgM and light-chain negativity for a further six generations before use. For activation studies, 2×10^6 IgM-negative cells were transfected (Cell Line Nucleofector Kit V, Lonza Group) with wild-type or Ile53Ala and Phe54Ala (CDR H2 mutated) versions of germline CR6261 receptor IgM. Twenty-four hours after transfection, cells were exposed to either 0.5 μ g ml⁻¹ mouse anti-human IgM F(ab')₂ (catalogue no. 9023-01, SouthernBiotech) in HBS as a positive control or HA proteoliposomes (HA trimer diluted to 2.5 μ M in HBS). After 15 min exposure at room temperature, cells were placed at 4 °C, washed two times with HBS and then lysed for 10 min in lysis buffer (Cell Lysis Buffer, Cell Signaling Technology) supplemented with protease inhibitors (Complete Protease Inhibitor Cocktail, catalogue no. 13352700, Roche Applied Science). After SDS-PAGE, BCR activation was assessed by western blot analysis of the cell lysate: 4G10 pY (catalogue no. 05-0321, Millipore) reactivity to phosphotyrosine-SLP-65 (p65) and phosphotyrosine HS1 (p75) as described^{12,30,31}. Total phosphotyrosine intensity from three independent experiments was measured by densitometry (Image Processing in Java (Image J) software with curve area density calculation performed in Microsoft Excel). Phosphotyrosine intensity was standardized to the level of cell lysate actin (monoclonal anti- β -actin, catalogue no. A5316, Sigma), with the background value for BCR activation being defined as the extent of stimulation in untransfected IgM-negative Ramos exposed to 0.5 μ g ml⁻¹ mouse anti-human IgM F(ab')₂.

Crystallography. The Fab fragment of CR6261 sHgL was concentrated to 7 mg ml⁻¹ in PBS and crystallized in a hanging drop over a reservoir containing 100 mM imidazole pH 6.5, 17.5% polyethylene glycol 8,000, and 3% 2-methyl-2,4-pentanediol. Crystals were cryoprotected by transfer through paratone-N and vitrified in liquid nitrogen. Data to 2.85 Å resolution were collected at Southeast Regional Collaborative Access Team (SER-CAT) 22-ID beamline at the Advanced Photon Source, Argonne National Laboratory. The structure was determined by molecular replacement using the program PHASER with the structure of CR6261 bound to influenza HA (3GBN) as the search model, and refined using the program PHENIX (Supplementary Table 1). The asymmetric unit contains eight copies of the Fab. The CDR H1 was deleted from the model before refinement. An electron density map calculated before modelling the CDR H1 showed only weak density corresponding to this loop; however, an NCS-averaged map calculated in COOT, which is shown in Fig. 2c, indicated clearly that the CDR H1 loop adopts a non-canonical conformation similar to that observed in the co-crystal structure with HA.

27. Kong, W. P. *et al.* Protective immunity to lethal challenge of the 1918 pandemic influenza virus by vaccination. *Proc. Natl Acad. Sci. USA* **103**, 15987–15991 (2006).
28. Metzger, H. Transmembrane signaling: the joy of aggregation. *J. Immunol.* **149**, 1477–1487 (1992).
29. Liu, W., Sohn, H. W., Tolar, P. & Pierce, S. K. It's all about change: the antigen-driven initiation of B-cell receptor signaling. *Cold Spring Harb. Perspect. Biol.* **2**, a002295 (2010).
30. Wienands, J., Larbolette, O. & Reth, M. Evidence for a preformed transducer complex organized by the B cell antigen receptor. *Proc. Natl Acad. Sci. USA* **93**, 7865–7870 (1996).
31. Heizmann, B., Reth, M. & Infantino, S. Syk is a dual-specificity kinase that self-regulates the signal output from the B-cell antigen receptor. *Proc. Natl Acad. Sci. USA* **107**, 18563–18568 (2010).

Genotoxic consequences of endogenous aldehydes on mouse haematopoietic stem cell function

Juan I. Garaycoechea^{1*}, Gerry P. Crossan^{1*}, Frederic Langevin¹, Maria Daly¹, Mark J. Arends² & Ketan J. Patel^{1,3}

Haematopoietic stem cells (HSCs) regenerate blood cells throughout the lifespan of an organism. With age, the functional quality of HSCs declines, partly owing to the accumulation of damaged DNA^{1–3}. However, the factors that damage DNA and the protective mechanisms that operate in these cells are poorly understood. We have recently shown that the Fanconi anaemia DNA-repair pathway counteracts the genotoxic effects of reactive aldehydes^{4,5}. Mice with combined inactivation of aldehyde catabolism (through *Aldh2* knockout) and the Fanconi anaemia DNA-repair pathway (*Fancd2* knockout) display developmental defects, a predisposition to leukaemia, and are susceptible to the toxic effects of ethanol—an exogenous source of acetaldehyde⁴. Here we report that aged *Aldh2*^{−/−} *Fancd2*^{−/−} mutant mice that do not develop leukaemia spontaneously develop aplastic anaemia, with the concomitant accumulation of damaged DNA within the haematopoietic stem and progenitor cell (HSPC) pool. Unexpectedly, we find that only HSPCs, and not more mature blood precursors, require *Aldh2* for protection against acetaldehyde toxicity. Additionally, the aldehyde-oxidizing activity of HSPCs, as measured by Aldefluor stain, is due to *Aldh2* and correlates with this protection. Finally, there is more than a 600-fold reduction in the HSC pool of mice deficient in both Fanconi anaemia pathway-mediated DNA repair and acetaldehyde detoxification. Therefore, the emergence of bone marrow failure in Fanconi anaemia is probably due to aldehyde-mediated genotoxicity restricted to the HSPC pool. These findings identify a new link between endogenous reactive metabolites and DNA damage in HSCs, and define the protective mechanisms that counteract this threat.

Reactive aldehydes, such as acetaldehyde, are by-products of metabolism. These molecules readily react with DNA and proteins within cells, leading to both mutagenesis and cell death⁴. Recent work has identified a critical requirement for the aldehyde-catabolising enzyme *Aldh2* and the Fanconi anaemia DNA-repair pathway in protecting against damage caused by these toxic molecules. The majority of mice deficient in both acetaldehyde catabolism (*Aldh2*^{−/−}) and the Fanconi anaemia DNA-repair pathway (*Fancd2*^{−/−}), spontaneously succumb to acute T-cell leukaemia⁴. Flow cytometric analysis revealed that the maturation of haematopoietic lineages was intact (Supplementary Fig. 1). However, double-mutant mice, without leukaemia, consistently have reduced numbers of all blood constituents and bone marrow cellularity, compared to wild-type controls (Supplementary Fig. 2). Furthermore, a small proportion of these double-mutant mice developed anaemia with age ($n = 6/29$) (Fig. 1a). These mice showed profound pancytopenia, and histological analysis of the bone marrow revealed hypocellularity (Fig. 1b, c and Supplementary Fig. 3a). Furthermore, these mice showed extramedullary haematopoiesis (Supplementary Fig. 3b). These clinical and pathological features are consistent with aplastic anaemia—a hallmark of human Fanconi anaemia but, until now, not a feature observed in Fanconi anaemia knockout mice. Immunohistochemistry revealed that the bone

marrow of the aged *Aldh2*^{−/−} *Fancd2*^{−/−} mice had increased numbers of cells that were positive for γ -H2AX, a well-established marker of DNA double-strand breaks⁶. There was also an increased proportion of cells undergoing apoptosis, as measured by cleaved caspase-3 (Fig. 1c). The data in Fig. 1d, e show that there was a significant induction in γ -H2AX, as measured by flow cytometry, within the total bone marrow of aged aplastic double-mutant mice. However, γ -H2AX induction within the Lineage (Lin)[−] c-Kit⁺ Sca-1⁺ (LKS) population, which is enriched for HSPCs, was much greater. Analysis of young *Aldh2*^{−/−} *Fancd2*^{−/−} mice indicated that the induction in γ -H2AX was greater in long-term HSCs (LT-HSCs; Lin[−] c-Kit⁺ Sca-1⁺ Flt3[−] CD34[−]) than in other haematopoietic progenitors (Supplementary Fig. 4). Taken together this suggests that there is a requirement for acetaldehyde catabolism and Fanconi anaemia pathway-mediated DNA repair for blood homeostasis, and that this activity may be restricted to a subset of haematopoietic cells.

We therefore set out to test systematically how haematopoietic cells at different stages of maturity respond to exogenous acetaldehyde—the key substrate of *Aldh2*. In the first instance we found that B cells, erythroid progenitor and granulocyte–macrophage progenitor cells from three different strains of mice deficient in the Fanconi anaemia DNA-repair pathway (*Fanca*^{−/−}, see Supplementary Fig. 5; *Fancd2*^{−/−}, ref. 7; and *Fancp*^{−/−} (*Fancp* is also known as *Slx4*); ref. 8) were all more sensitive to acetaldehyde than congenic controls (Fig. 2a). Surprisingly, when we tested the resistance of haematopoietic cells deficient in both *Aldh2* and *Fancd2*, we noted that all three lineages tested were no more sensitive than those deficient in *Fancd2* alone (Fig. 2b). In contrast, we have previously shown that *Aldh2*^{−/−} *Fancd2*^{−/−} mice developed bone marrow failure after ethanol exposure, but that this did not occur in single-mutant mice⁴. We speculated that this was because aldehyde catabolism and the Fanconi anaemia repair pathway specifically protected the HSC compartment, and therefore aldehyde accumulation would be most toxic to this vital cell population. Progressive attrition of the HSC pool is considered to be the reason why most Fanconi anaemia patients develop bone marrow failure⁹.

To test this, we modified the classic colony-forming unit spleen (c.f.u.-S) assay, which is used to quantify short-term HSCs (ST-HSCs), a subset of HSPCs^{10–12}. As shown in Fig. 2c, we exposed the bone marrow of mutant and wild-type mice to acetaldehyde *in vitro*, before transplantation into lethally irradiated recipients. Ten days after transplantation we killed the mice and counted the number of spleen colonies. This assay therefore allows us to measure directly the survival of ST-HSCs after exposure to acetaldehyde. The data in Fig. 2d show that ST-HSCs use both aldehyde detoxification and Fanconi anaemia pathway-mediated DNA repair to counteract the genotoxic effects of acetaldehyde. This is in contrast to the more mature haematopoietic cells, in which *Aldh2* is dispensable for resistance to acetaldehyde.

For many years it has been appreciated that potent aldehyde dehydrogenase activity is associated with certain normal and cancer stem cells^{13–15}. This activity can be quantified by the commercial assay

¹MRC Laboratory of Molecular Biology, Hills Road, Cambridge CB2 0QH, UK. ²University of Cambridge, Department of Pathology, Addenbrooke's Hospital, Cambridge CB2 2QQ, UK. ³University of Cambridge, Department of Medicine, Level 5, Addenbrooke's Hospital, Cambridge CB2 0QQ, UK.

*These authors contributed equally to this work.

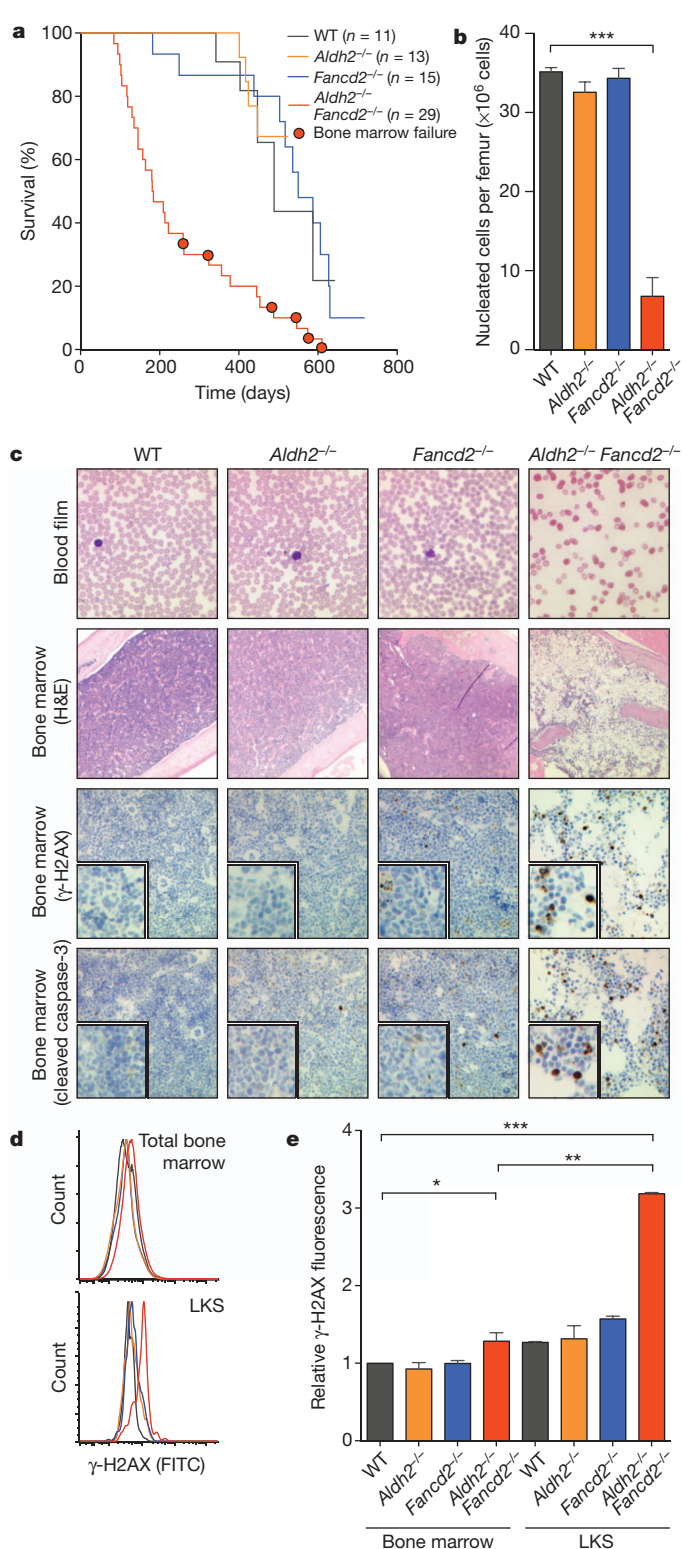


Figure 1 | Aged *Aldh2*^{-/-} *Fancd2*^{-/-} mice succumb to bone marrow failure. **a**, Kaplan-Meier curve showing the survival of a cohort of *Aldh2*^{-/-} *Fancd2*^{-/-} mice and congenic controls. Red dots denote mice with bone marrow failure ($n = 6/29$). WT, wild type. **b**, Bar chart representing the number of nucleated cells per femur of aged *Aldh2*^{-/-} *Fancd2*^{-/-} mice ($n = 6$) with bone marrow failure and controls. Error bars represent s.e.m. **c**, Peripheral blood film ($\times 400$), bone marrow histology stained with haematoxylin and eosin (H&E; $\times 50$) and immunohistochemistry for cleaved caspase-3 or γ -H2AX ($\times 200$, inset $\times 400$) from an *Aldh2*^{-/-} *Fancd2*^{-/-} mouse with bone marrow failure and controls. **d**, **e**, Flow cytometric analysis of γ -H2AX in total bone marrow and LKS populations with quantification of the relative induction in *Aldh2*^{-/-} *Fancd2*^{-/-} (error bars represent s.e.m., $n = 2$, $*P < 0.05$, $**P < 0.01$, $***P < 0.001$).

strict in mouse than in man^{17,18}. The identity of the enzyme responsible for Aldefluor activity was unknown, although it has recently been shown that it is not due to *Aldh1a1* (ref. 17). In contrast, we find that the Aldefluor activity is greatly abrogated in *Aldh2*^{-/-} mice. There is a marked reduction in the Aldefluor activity of total bone marrow and of the HSPC pool, with an intermediate reduction in *Aldh2*^{+/-} mice (Fig. 3b, c). Furthermore, *Aldh2* is the most highly expressed member of the aldehyde dehydrogenase family in the LT-HSC population^{17,19}. These data suggest that *Aldh2* is the major source of Aldefluor activity and acetaldehyde detoxification within the HSPC pool.

Having established that *Aldh2* and *Fancd2* protect HSPCs against acetaldehyde-mediated genotoxicity, we set out to establish the direct physiological consequences of disruption of both genes on HSPC function in young 8–12-week-old mice. First we used immunophenotyping to determine the frequency of HSPCs within the bone marrow of young double-mutant mice that had not developed leukaemia or bone marrow failure^{20–22}. The data in Fig. 4a show a 30-fold reduction in the LKS population, in contrast to the mild twofold reduction in *Fancd2*^{-/-} mice. Further analysis of this population revealed that there was a tenfold reduction in the frequency of LT-HSCs ($\text{Lin}^- \text{c-Kit}^+ \text{Sca-1}^+ \text{Flt3}^- \text{CD34}^-$) in *Aldh2*^{-/-} *Fancd2*^{-/-} mice compared to wild-type littermates, with *Fancd2*^{-/-} or *Aldh2*^{-/-} mice again showing only a mild reduction (Fig. 4b and Supplementary Fig. 6a). Similarly, bone marrow from *Aldh2*^{-/-} *Fancd2*^{-/-} mice showed a significant reduction in the frequency of HSCs defined by SLAM markers ($\text{Lin}^- \text{CD41}^- \text{CD48}^- \text{CD150}^+$)¹⁹. However, when SLAM markers were combined with canonical HSC surface markers (SLAM + LKS: $\text{Lin}^- \text{CD41}^- \text{CD48}^- \text{CD150}^+ \text{c-Kit}^+ \text{Sca-1}^+$), a more pronounced 251-fold reduction in the frequency of HSCs was observed in *Aldh2*^{-/-} *Fancd2*^{-/-} mice (Supplementary Fig. 6b–d).

Analysis of cell cycle dynamics revealed an accumulation in the S–G2–M phase of the cell cycle in double-mutant LT-HSCs. Furthermore, we noticed a marked reduction in the number of quiescent (G_0) LT-HSCs in *Aldh2*^{-/-} *Fancd2*^{-/-} mice ($P < 0.0001$). The majority of LT-HSCs were actively cycling, in contrast to wild-type LT-HSCs, which are mainly quiescent (Fig. 4c). It has previously been demonstrated that damage to the bone marrow compartment leads to a loss of quiescence and entry of HSCs into the cell cycle^{21,23,24}.

Finally, we functionally tested the HSPC pool of young *Aldh2*^{-/-} *Fancd2*^{-/-} mice. Bone marrow obtained from *Aldh2*^{-/-} *Fancd2*^{-/-} mice and congenic controls was transplanted into lethally irradiated recipients. These recipients were then killed at day 10 and the number of spleen colony forming units (c.f.u.-S₁₀) was quantified. The data in Fig. 4d and Supplementary Fig. 7a clearly show that the number of c.f.u.-S₁₀ was greatly reduced (28-fold) in mice reconstituted with *Aldh2*^{-/-} *Fancd2*^{-/-} marrow compared with wild type, in contrast to the mild reductions in the single mutants (*Aldh2*^{-/-}, 1.8-fold; *Fancd2*^{-/-}, 3.2-fold compared with wild type). The *in vitro* cobblestone-area-forming cell (CAFC) assay corroborates this decreased frequency of HSPCs in *Aldh2*^{-/-} *Fancd2*^{-/-} marrow (Supplementary Fig. 7b). However, these assays have limitations because we cannot draw any conclusions about the long-term repopulating potential of the HSCs. To assess this function, we carried out the

known as Aldefluor¹⁶. Briefly, cells are incubated with a fluorescent aldehyde substrate that, when oxidized by aldehyde dehydrogenases, cannot efflux from the cell (Fig. 3a). The amount of fluorescence reflects the aldehyde dehydrogenase activity in that cell. The addition of 4-diethylaminobenzaldehyde (DEAB), which is an inhibitor of *Aldh* enzymes, prevents enzymatic oxidation and the accumulation of this product, therefore providing a negative control for fluorescence. In human bone marrow, the Aldefluor activity of HSCs is sufficient to enable their identification and isolation¹⁶. However, the restriction of this aldehyde dehydrogenase activity to the HSC pool seems to be less

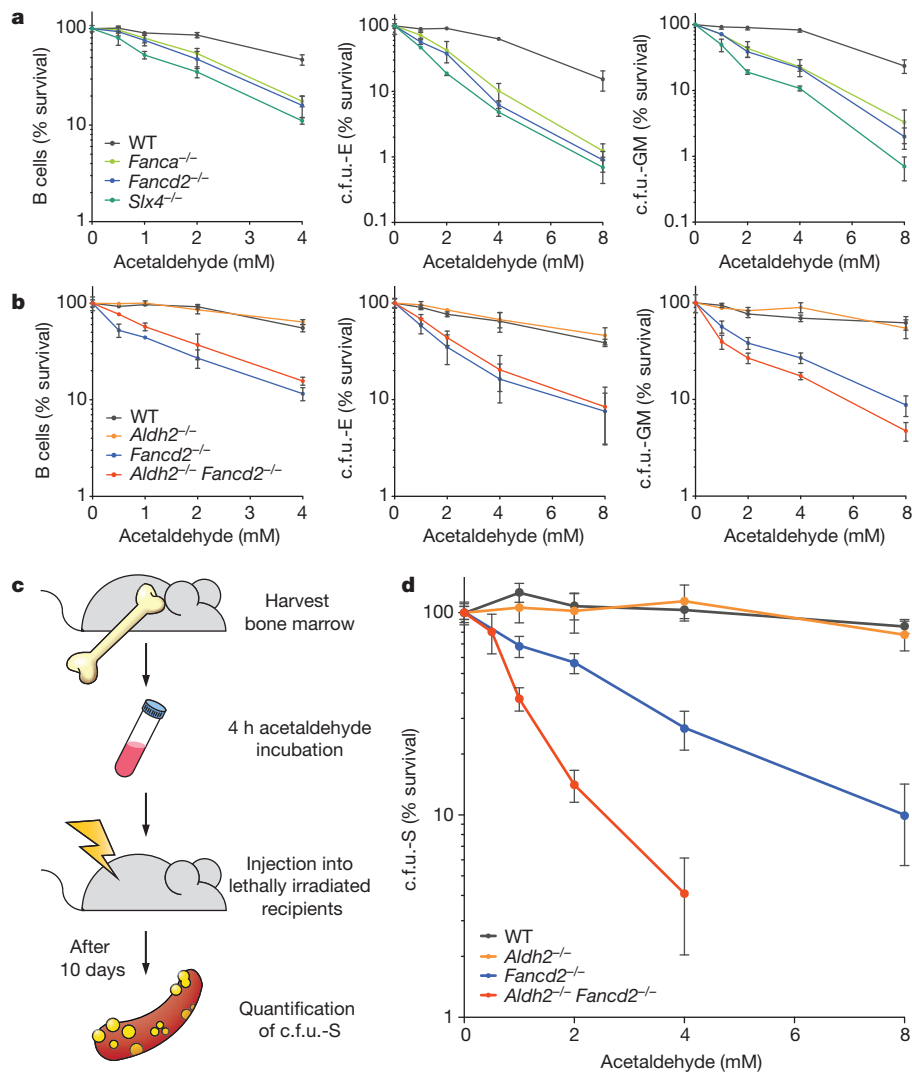


Figure 2 | *Aldh2* is critical for protecting *Fancd2*^{-/-} ST-HSCs from exogenous acetaldehyde. **a–d**, Survival of B cells, erythroid (c.f.u.-E) and granulocyte-macrophage (c.f.u.-GM) progenitors following exposure to acetaldehyde *in vitro*. **a**, **b**, Cells were obtained from wild-type (WT), *Fanca*^{-/-}, *Fancd2*^{-/-} and *Slx4*^{-/-} mice (**a**) or wild-type, *Aldh2*^{-/-}, *Fancd2*^{-/-} and *Aldh2*^{-/-} *Fancd2*^{-/-} mice (**b**). Each data point represents the mean of two independent experiments, each carried out in duplicate, error bars represent s.e.m. **c**, Scheme outlining the assay to determine survival of ST-HSCs (c.f.u.-S₁₀) after exposure to acetaldehyde. **d**, c.f.u.-S₁₀ survival was made relative to the untreated controls of each genotype. Each data point represents the mean c.f.u.-S₁₀ survival among eight recipient mice. Error bars represent s.e.m.

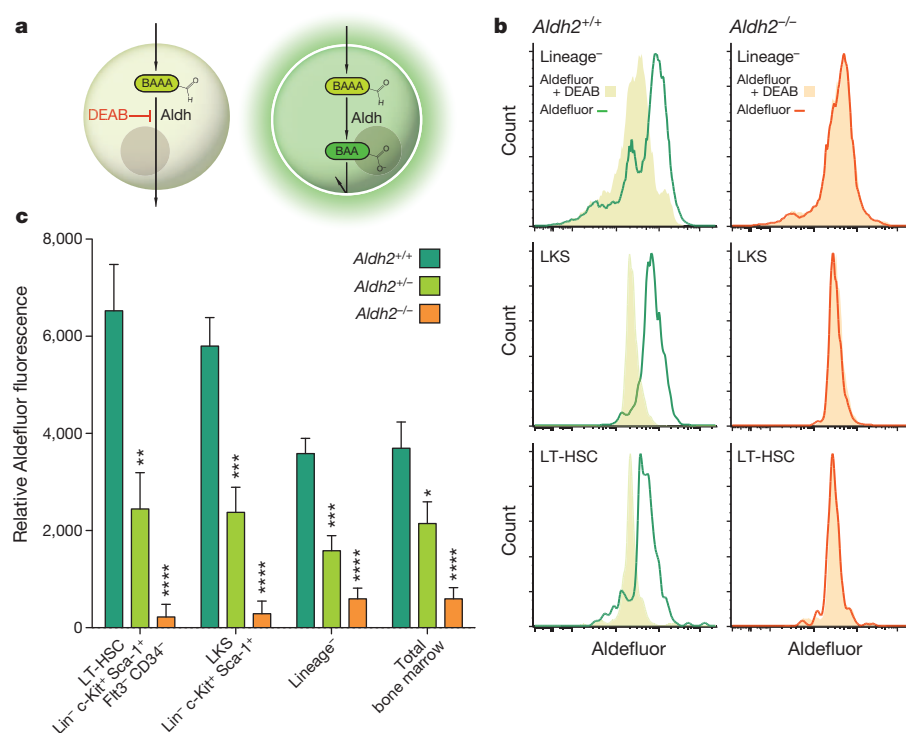


Figure 3 | *Aldh2* is responsible for Aldefluor activity in murine HSPCs. **a**, Scheme outlining the Aldefluor assay. The substrate is oxidized by Aldh enzymes and the charged fluorescent product accumulates. DEAB, a general inhibitor of Aldh enzymes, was used as a control for background fluorescence. **b**, Flow cytometric analysis of the lineage-negative, LKS and long-term HSC (LT-HSC) populations of *Aldh2*^{+/+} and *Aldh2*^{-/-} bone marrow treated with the Aldefluor reagent with and without DEAB. **c**, Quantification of Aldefluor fluorescence in bone marrow subpopulations from *Aldh2*^{+/+}, *Aldh2*^{+/-} and *Aldh2*^{-/-} mice. The data were made relative to DEAB control and represents the mean of three independent experiments. Error bars represent s.e.m., *n* = 10. **P* < 0.05, ***P* < 0.01, ****P* < 0.001 and *****P* < 0.0001 compared with *Aldh2*^{+/+} control for each population.

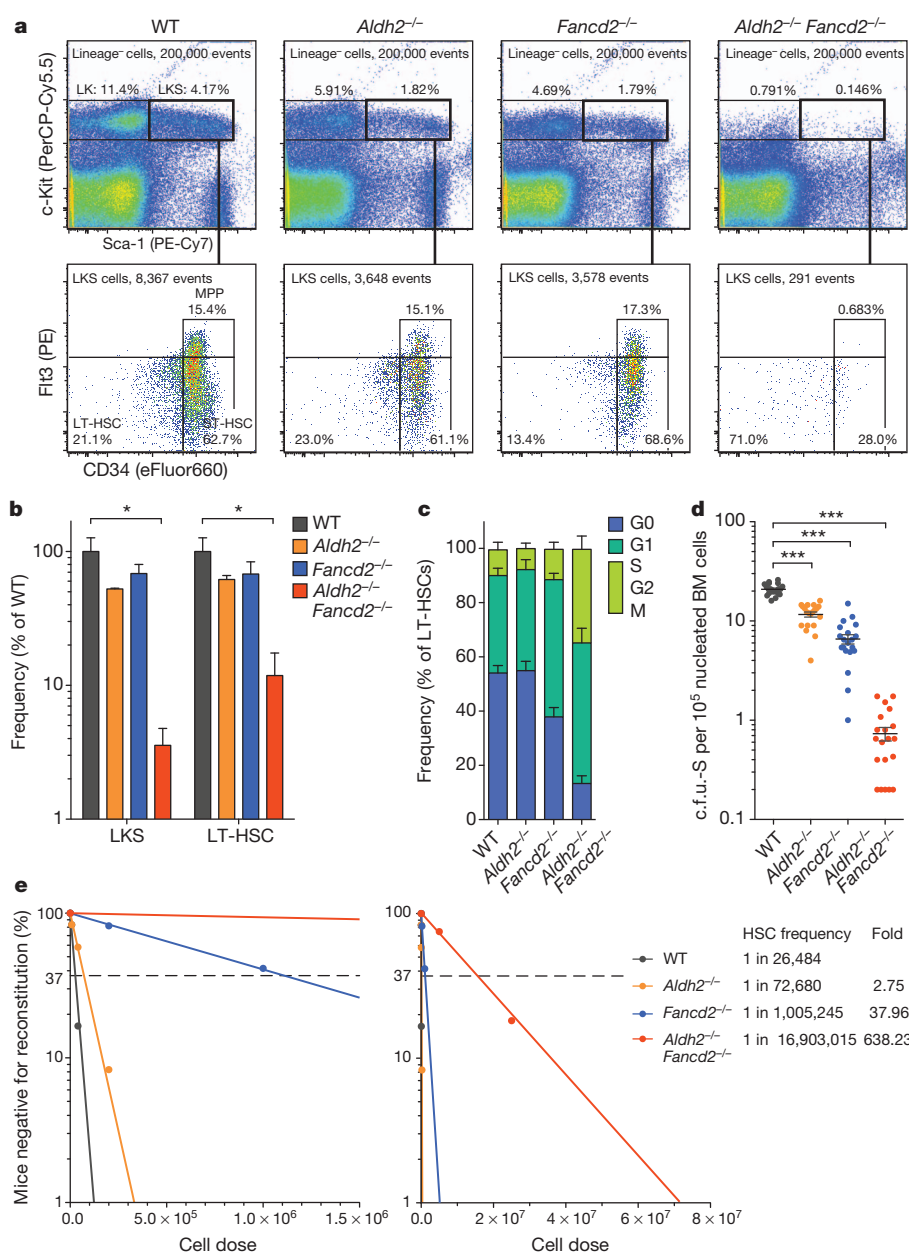


Figure 4 | The HSC pool of young *Aldh2*^{-/-} *Fancd2*^{-/-} mice is severely compromised. **a**, Representative FACS profiles of HPSCs of 8–12-week-old *Aldh2*^{-/-} *Fancd2*^{-/-} mice, showing LKS, LT-HSC, ST-HSC and multipotent progenitor (MPP) populations. WT, wild type. **b**, Quantification of HPSC populations assessed by FACS. **P* < 0.05, error bars represent s.e.m., *n* = 3 per genotype. **c**, Cell cycle analysis of the LT-HSCs in *Aldh2*^{-/-} *Fancd2*^{-/-} mice and controls (*n* = 5 per genotype) determined by Ki-67 and 4',6-diamidino-2-phenylindole (DAPI) staining. **d**, Frequency of c.f.u.-S₁₀ in the bone marrow of *Aldh2*^{-/-} *Fancd2*^{-/-} and control mice. Each point represents the number of c.f.u.-S₁₀ counted in the spleen of a single recipient. *n* = 20 per genotype, central line represents the mean, error bars represent the s.e.m., ****P* < 0.001. **e**, Limiting dilution assay was carried out by transplanting six concentrations of mutant bone marrow and a set concentration of wild-type competitor cells (12 recipients were used per test cell dose). Young *Aldh2*^{-/-} *Fancd2*^{-/-} bone marrow exhibited a 638-fold reduction in the frequency of HSCs compared to wild type (*P* < 0.0001).

long-term competitive repopulation assay. This assay allows the frequency of LT-HSCs within mutant bone marrow to be calculated (defined as competitive repopulation units, CRU) and is based on their functional ability to reconstitute all blood lineages in lethally irradiated mice²⁵. The data in Fig. 4e and Supplementary Fig. 7c reveal that double-mutant marrow is profoundly compromised, showing a 638-fold reduction in the frequency of CRU compared with wild type (*P* < 1 × 10⁻²⁰). It is also worth noting that the long-term repopulating ability in *Aldh2*^{-/-} bone marrow was reduced 2.75-fold (*P* = 0.0156), demonstrating the functional importance of aldehyde dehydrogenase activity associated with the HSC compartment. Furthermore, there was a 38-fold reduction in the HSC pool of *Fancd2*^{-/-} mice compared to wild type (*P* = 5 × 10⁻¹⁸). It is notable that the combined inactivation of both acetaldehyde catabolism and the Fanconi anaemia DNA-repair pathway leads to a synergistic functional HSC defect.

The data presented here reveal that HSPCs use two parallel mechanisms for protection from the irreversible genetic damage caused by reactive aldehydes. Recently, numerous studies have identified critical roles for a variety of DNA-repair pathways in HSC homeostasis, with

defective DNA repair leading to age-dependent dysfunction of these cells in mice^{1,2,26,27}. We show that the combined inactivation of aldehyde detoxification and the Fanconi anaemia DNA-repair pathway results in persistent DNA damage in HSCs. This leads to the loss of a functional HSC pool, and precipitates spontaneous bone marrow failure. Children with Fanconi anaemia often succumb to bone marrow failure and leukaemia, in both instances due to genetic damage to the stem cells^{9,28}. This study also provides the first evidence, to our knowledge, about what drives the Fanconi anaemia haematological phenotype, and has the potential to inform future therapeutic interventions for this lethal human illness. Perhaps the most important implication of this work is the revelation that naturally produced aldehydes can be potently genotoxic to HSCs, and without the necessary protection, these stem cells malfunction or die, the two key features that typify a process of accelerated ageing.

METHODS SUMMARY

Mice. *Aldh2*^{-/-} *Fancd2*^{-/-} mice were described previously⁴. All animals were maintained in specific pathogen-free conditions. In individual experiments, all mice were matched for age and gender. All animal experiments undertaken in this study were done so with the approval of the UK Home Office.

Haematopoietic progenitor. Survival of lineage-restricted progenitors was assessed using methylcellulose-based media, and survival of short-term HSCs was assessed using the c.f.u.-S assay, as described previously^{10–12}. Total bone marrow was treated with acetaldehyde *in vitro* for 4 h before plating in methylcellulose-based media or injection into lethally irradiated recipients (see Methods).

Aldefluor stain. The Aldefluor stain was performed according to the manufacturer's instructions, using bone marrow cells pre-stained for surface markers to define HSCs, as described in Methods. Aldefluor fluorescence was quantified using the geometric mean.

Limiting dilution assay. The limiting dilution assay was performed essentially as described previously¹⁹. Varying amounts of male 'test' bone marrow (8×10^3 , 4×10^4 , 2×10^5 , 1×10^6 , 5×10^6 and 2.5×10^7 cells) were mixed with a fixed amount (2×10^5) of wild-type female bone marrow and injected into lethally irradiated (900 Gy, split between two doses) female F₁ C57B6/J α 1a \times 129/SV recipients. Twelve recipients were used for each dose of test bone marrow. After 16 weeks, mice were assessed for multi-lineage reconstitution (see Methods).

Statistical analysis. Unless otherwise stated, data reflect the mean \pm s.e.m., and a two-tailed Student's *t*-test was used to assess the statistical significance (**P* < 0.05, ***P* < 0.01, ****P* < 0.001, *****P* < 0.0001).

Full Methods and any associated references are available in the online version of the paper.

Received 4 April; accepted 29 June 2012.

Published online 26 August 2012.

- Nijnik, A. *et al.* DNA repair is limiting for haematopoietic stem cells during ageing. *Nature* **447**, 686–690 (2007).
- Rossi, D. J. *et al.* Deficiencies in DNA damage repair limit the function of haematopoietic stem cells with age. *Nature* **447**, 725–729 (2007).
- Niedernhofer, L. J. DNA repair is crucial for maintaining hematopoietic stem cell function. *DNA Repair (Amst.)* **7**, 523–529 (2008).
- Langevin, F., Crossan, G. P., Rosado, I. V., Arends, M. J. & Patel, K. J. Fancd2 counteracts the toxic effects of naturally produced aldehydes in mice. *Nature* **475**, 53–58 (2011).
- Rosado, I. V., Langevin, F., Crossan, G. P., Takata, M. & Patel, K. J. Formaldehyde catabolism is essential in cells deficient for the Fanconi anemia DNA-repair pathway. *Nature Struct. Mol. Biol.* **18**, 1432–1434 (2011).
- Rogakou, E. P., Pilch, D. R., Orr, A. H., Ivanova, V. S. & Bonner, W. M. DNA double-stranded breaks induce histone H2AX phosphorylation on serine 139. *J. Biol. Chem.* **273**, 5858–5868 (1998).
- Houghtaling, S. *et al.* Epithelial cancer in Fanconi anemia complementation group D2 (*Fancd2*) knockout mice. *Genes Dev.* **17**, 2021–2035 (2003).
- Crossan, G. P. *et al.* Disruption of mouse Slx4, a regulator of structure-specific nucleases, phenocopies Fanconi anemia. *Nature Genet.* **43**, 147–152 (2011).
- Kutler, D. I. *et al.* A 20-year perspective on the International Fanconi Anemia Registry (IFAR). *Blood* **101**, 1249–1256 (2003).
- McCulloch, E. A. & Till, J. E. The radiation sensitivity of normal mouse bone marrow cells, determined by quantitative marrow transplantation into irradiated mice. *Radiat. Res.* **13**, 115–125 (1960).
- Meagher, R. C., Sieber, F. & Spivak, J. L. Suppression of hematopoietic-progenitor-cell proliferation by ethanol and acetaldehyde. *N. Engl. J. Med.* **307**, 845–849 (1982).
- Becker, A. J., Mc, C. E. & Till, J. E. Cytological demonstration of the clonal nature of spleen colonies derived from transplanted mouse marrow cells. *Nature* **197**, 452–454 (1963).
- Balber, A. E. Concise review: aldehyde dehydrogenase bright stem and progenitor cell populations from normal tissues: characteristics, activities, and emerging uses in regenerative medicine. *Stem Cells* **29**, 570–575 (2011).
- Armstrong, L. *et al.* Phenotypic characterization of murine primitive hematopoietic progenitor cells isolated on basis of aldehyde dehydrogenase activity. *Stem Cells* **22**, 1142–1151 (2004).
- Storms, R. W. *et al.* Distinct hematopoietic progenitor compartments are delineated by the expression of aldehyde dehydrogenase and CD34. *Blood* **106**, 95–102 (2005).
- Storms, R. W. *et al.* Isolation of primitive human hematopoietic progenitors on the basis of aldehyde dehydrogenase activity. *Proc. Natl Acad. Sci. USA* **96**, 9118–9123 (1999).
- Levi, B. P., Yilmaz, O. H., Duester, G. & Morrison, S. J. Aldehyde dehydrogenase 1a1 is dispensable for stem cell function in the mouse hematopoietic and nervous systems. *Blood* **113**, 1670–1680 (2009).
- Hess, D. A. *et al.* Selection based on CD133 and high aldehyde dehydrogenase activity isolates long-term reconstituting human hematopoietic stem cells. *Blood* **107**, 2162–2169 (2006).
- Kiel, M. J., Yilmaz, O. H., Iwashita, T., Terhorst, C. & Morrison, S. J. SLAM family receptors distinguish hematopoietic stem and progenitor cells and reveal endothelial niches for stem cells. *Cell* **121**, 1109–1121 (2005).
- Purton, L. E. & Scadden, D. T. Limiting factors in murine hematopoietic stem cell assays. *Cell Stem Cell* **1**, 263–270 (2007).
- Rossi, D. J. *et al.* Cell intrinsic alterations underlie hematopoietic stem cell aging. *Proc. Natl Acad. Sci. USA* **102**, 9194–9199 (2005).
- Sudo, K., Ema, H., Morita, Y. & Nakauchi, H. Age-associated characteristics of murine hematopoietic stem cells. *J. Exp. Med.* **192**, 1273–1280 (2000).
- Wilson, A. *et al.* Hematopoietic stem cells reversibly switch from dormancy to self-renewal during homeostasis and repair. *Cell* **135**, 1118–1129 (2008).
- Mohrin, M. *et al.* Hematopoietic stem cell quiescence promotes error-prone DNA repair and mutagenesis. *Cell Stem Cell* **7**, 174–185 (2010).
- Szilyassy, S. J., Humphries, R. K., Lansdorp, P. M., Eaves, A. C. & Eaves, C. J. Quantitative assay for totipotent reconstituting hematopoietic stem cells by a competitive repopulation strategy. *Proc. Natl Acad. Sci. USA* **87**, 8736–8740 (1990).
- Milyavsky, M. *et al.* A distinctive DNA damage response in human hematopoietic stem cells reveals an apoptosis-independent role for p53 in self-renewal. *Cell Stem Cell* **7**, 186–197 (2010).
- Seita, J., Rossi, D. J. & Weissman, I. L. Differential DNA damage response in stem and progenitor cells. *Cell Stem Cell* **7**, 145–147 (2010).
- Crossan, G. P. & Patel, K. J. The Fanconi anaemia pathway orchestrates incisions at sites of crosslinked DNA. *J. Pathol.* **226**, 326–337 (2012).

Supplementary Information is linked to the online version of the paper at www.nature.com/nature.

Acknowledgements We thank M. Grompe for *Fancd2*-deficient mice and M. Milsom and D. Walter for technical advice. We are grateful to T. Langford, R. Berks, A. Middleton, C. Knox and J. Wiles for their help with mouse experimental work. We would also like to thank the Biomed services and ARES staff for animal husbandry and assistance. We thank N. Grant for photography. We thank the Human Research Tissue Bank (NIHR Cambridge Biomedical Research Centre) for processing histology. We also thank F. Zhang for help with FACS. G.P.C. is supported by CRUK and Homerton College, Cambridge. J.I.G. is supported by the Milstein Fund and the Darwin Trust of Edinburgh. F.L. is supported by the March of Dimes Foundation.

Author Contributions The study was conceived by K.J.P., G.P.C. and J.I.G. The manuscript was written by K.J.P., G.P.C. and J.I.G. All experiments were planned and executed by J.I.G. and G.P.C. Cell sorting was performed by M.D. Additional analysis of mice with bone marrow failure was conducted by F.L. M.J.A. analysed histological samples and provided useful discussion.

Author Information Reprints and permissions information is available at www.nature.com/reprints. The authors declare no competing financial interests. Readers are welcome to comment on the online version of this article at www.nature.com/nature. Correspondence and requests for materials should be addressed to K.J.P. (kjp@mrc-lmb.cam.ac.uk).

METHODS

Mice. *Aldh2*^{-/-} *Fancd2*^{-/-} mice on a C57/B6Jol1a × 129SV hybrid background were described previously⁴. *Fancd2*-deficient mice (*Fancd2*^{tm1Hou}, Mouse Genome Informatics (MGI) code: 2673422, 129S4/SvJae) were a gift from M. Grompe. *Aldh2*-deficient mice were generated from embryonic stem (ES) cells obtained from EUCOMM (*Aldh2*^{tm1a(EUCOMM)Wtsi}, MGI code: 4431566, C57BL/6N). Mice carrying both the *Fancd2*^{tm1Hou} and *Aldh2*^{tm1a(EUCOMM)Wtsi} synthetic alleles were generated by crossing *Fancd2*^{tm1Hou} and *Aldh2*^{tm1a(EUCOMM)Wtsi} heterozygous mice. These progeny were subsequently intercrossed to obtain double-mutant mice and control genotypes as described previously⁴. *Fanca*-deficient mice were generated from ES cells, carrying a targeted disruption of the *Fanca* locus, obtained from the EUCOMM consortium (Supplementary Fig. 5b). Targeting was confirmed by long-range PCR using the following oligonucleotides. LAR3: CACAACGGGTCTCTCTGTTAGTCC; GF4: GCTAACACTAGTAAGAGTCACAATAATCTC; RAF5: CACACCTCCCCCTGAACCTGAAAC; and GR3: CTTGTTGGTGGTGGATATCTTGATGGTTG (Supplementary Fig. 5b). Germline transmission was achieved and progeny were genotyped using the following oligonucleotides. FL033: GCCTTTGCTGCTCTAATTCCATGT; FL040: TCAGTCACTGAGACGCAACCTTTACACT; and En2A: GCTTCACTGAGTCTCTGGCATCTC (Supplementary Fig. 5c). Furthermore, cells derived from *Fanca*-deficient mice were unable to mono-ubiquitinate Fancd2 after damage with MMC (Supplementary Fig. 5d). All animals were maintained in specific pathogen-free conditions. In individual experiments all mice were matched for age and gender. All animal experiments undertaken in this study were done so with the approval of the UK Home Office.

Aldefluor stain. Aldefluor stain was performed according to the manufacturer's instructions, using bone marrow cells pre-stained for surface markers to define HSPCs as described below. Fluorescence was quantified using the geometric mean. **Limiting dilution assay.** The limiting dilution assay was performed essentially as described previously¹⁹. Varying amounts of male 'test' bone marrow (8×10^3 , 4×10^4 , 2×10^5 , 1×10^6 , 5×10^6 and 2.5×10^7 cells) were mixed with a fixed amount (2×10^5) of wild-type female bone marrow and injected into lethally irradiated (900 Gy, split between two doses) female F₁ C57B6/Jo1a × 129/SV recipients. Twelve recipients were used for each dose of test bone marrow. After 16 weeks, these recipients were killed and peripheral blood was fractionated by FACS into T cells (CD4⁺ or CD8⁺, B220⁻Gr-1⁻Mac-1⁻), B cells (B220⁺CD4⁻CD8⁻Gr-1⁻Mac-1⁻) and myeloid cells (Gr-1⁺ or Mac-1⁺, B220⁻CD4⁻CD8⁻) using surface markers described previously²⁹. The relative contribution of the test and wild-type bone marrow to peripheral blood chimaerism was then assessed using quantitative PCR (qPCR) for the Y chromosome with oligonucleotides described previously³⁰. Recipients were considered reconstituted with test bone marrow if all three lineages showed $\geq 1\%$ chimaerism for the test bone marrow. The frequency of non-reconstituted mice is plotted against the dose of test cells injected. The frequency of CRU was calculated using L-Calcul and *P* values were calculated using ELDA software at <http://bioinf.wehi.edu.au/software/elda>.

Statistical analysis. Unless otherwise stated, data reflect the mean \pm s.e.m., and a two-tailed Student's *t*-test was used to assess the statistical significance (**P* < 0.05, ***P* < 0.01, ****P* < 0.001, *****P* < 0.0001).

Histological analysis. Histological analysis was performed on tissues that had been fixed in neutral buffered formalin for 24 h. The samples were then paraffin embedded and 4 μ m sections were cut before staining with haematoxylin and eosin. Immunohistochemistry was performed as described previously³¹, using rabbit anti-phospho-histone H2AX (Cell Signaling 2577; 1:50) and rabbit anti-cleaved caspase-3 (Cell Signaling Asp175 9661L; 1:100).

Peripheral blood. Peripheral blood was collected from mice at 8–12 weeks of age or from aged mice as indicated. Whole blood (50–100 μ l) was collected in EDTA microvette tubes (Startedt) and analysed on a VetABC analyser (Horiba).

γ -H2AX staining. γ -H2AX staining by flow cytometry was performed using the total bone marrow of aged mutant mice and appropriate controls. Cells were resuspended at a concentration of 3×10^6 cells per 100 μ l. The cells were stained for surface markers using biotin lineage cocktail (Miltenyi Biotec), anti-c-Kit (PerCP-Cy5.5), and anti-Sca-1 (PE-Cy7). The samples were incubated for 15 min at 4 °C in the dark. Anti-Flt3 (PE) and anti-CD34 (eFluor660) were also added to the stain of lineage-depleted bone marrow of young mice, and these samples were incubated for 75 min at 4 °C in the dark. Brilliant violet-421 streptavidin was added and the cells incubated for a further 15 min. Cells were fixed and permeabilized using Intraprep (Beckman Coulter) following the manufacturer's instructions. The cells were then stained for 15 min with a FITC-conjugated anti- γ -H2AX antibody (JBW301, Upstate).

Survival assays of primary mouse B cells. Survival assays of primary mouse B cells were performed with lymphocytes purified from the spleen using Lympholyte M (Cederlane). Lymphocytes were stimulated with LPS (Sigma L4391) at a final

concentration of 40 μ g ml⁻¹. A total of 4×10^5 cells were plated with acetaldehyde in one well of a 24-well plate. After 7 days the viable cells were enumerated by trypan blue exclusion, counting 100 images using a ViCell XR (Beckman Coulter). Each data point represents the mean of three independent experiments, each carried out in triplicate.

Methylcellulose c.f.u. survival assays. Methylcellulose c.f.u. survival assays were carried out as described previously^{10–12}. Briefly, total bone marrow was flushed in IMDM (GIBCO) from the femora and tibiae of mutant mice and controls. The number of nucleated cells was enumerated using a solution of 3% acetic acid and methylene blue, and counted using a ViCell XR Cell counter. Equal numbers of total bone marrow cells were then exposed to various concentrations of acetaldehyde *in vitro* for 4 h in a sealed CryoVial. After treatment, two tenfold serial dilutions of the bone marrow were made, and these cells were plated into 6-well plates with methylcellulose-based media containing cytokines.

For c.f.u.-GM, cells were plated at final concentrations of 2×10^6 , 2×10^5 and 2×10^4 cells per well in MethoCult M3534 (StemCell Technologies). Colonies were counted 7 days after incubation at 37 °C and 5% CO₂. For c.f.u.-E, cells were treated in the same manner, but were plated into MethoCult M3334 (StemCell Technologies) and colonies were counted after 2 days. In all cases survival was made relative to the untreated control for each genotype. Each point represents the mean of two independent experiments, each carried out in duplicate.

c.f.u.-S assays. c.f.u.-S assays were performed as described previously^{10–12}. To assess the frequency of c.f.u.-S in mutant mice, total bone marrow was flushed from the femora and tibiae of mutant mice and appropriate controls. Nucleated cells were enumerated using a solution of 3% acetic acid and methylene blue. The mutant bone marrow was then injected intravenously into 20 recipient irradiated mice that had been lethally irradiated. 1×10^5 nucleated bone marrow cells were used for wild-type, *Aldh2*^{-/-} and *Fancd2*^{-/-} bone marrow, and 5×10^5 cells for *Aldh2*^{-/-} *Fancd2*^{-/-} bone marrow. After 10 days the spleens were fixed in Bouin's solution (Sigma), the number of colonies were counted and made relative to the number of total bone marrow cells injected.

To assess the survival of c.f.u.-S after exposure to acetaldehyde, we treated total bone marrow cells with various acetaldehyde concentrations for 4 h *in vitro* before injecting them into lethally irradiated recipient mice. After 10 days, the number of c.f.u.-S were counted. The survival was made relative to the untreated control for each genotype. Each data point represents the mean c.f.u.-S survival in eight recipient mice.

Irradiation of mice. Irradiation of mice was performed using a Cs-137 GSR C1m blood irradiator (Gamma-Service Recycling GmbH; Germany). Mice received a dose of 900 Gy of total body irradiation, split between two equal doses, separated by 4 h. Mice received prophylactic enrofloxacin (Baytril, Bayer) in the drinking water for 7 days before irradiation and for 5 weeks after irradiation.

Flow cytometry. Flow cytometry was performed on bone marrow cells that were isolated from the femora and tibiae of mutant mice and appropriate controls by flushing cells and passing them through a 70- μ m filter. The following antibodies were used to stain for HSCs: FITC-conjugated lineage cocktail with antibodies anti-CD4 (clone H129.19, BD Pharmingen), CD3e (clone 145-2C11, eBioscience), Ly-6G/Gr-1 (clone RB6-8C5, eBioscience), CD11b/Mac-1 (clone M1/70, BD Pharmingen), CD45R/B220 (clone RA3-6B2, BD Pharmingen), Fc ϵ R1 α (clone MAR-1, eBioscience), CD8a (clone 53-6.7, BD Pharmingen), CD11c (clone N418, eBioscience) and TER-119 (clone Ter119, BD Pharmingen), anti-c-Kit (PerCP-Cy5.5, clone 2B8, eBioscience), anti-Sca-1 (PE-Cy7, clone D7, eBioscience), anti-Flt3 (PE, clone A2F10, eBioscience) and anti-CD34 (eFluor660, clone RAM34, eBioscience). When staining for SLAM markers the same lineage cocktail was used (FITC) with the addition of the following antibodies: anti-CD48 (FITC, clone HM48-1, BioLegend), anti-CD41 (FITC, clone MWReg30, BD Pharmingen), anti-CD150 (APC, clone TC15-12F12.2, BioLegend) and anti-c-Kit and Sca-1 as above. Maturation of B cells was assessed using anti-CD45R/B220 (PE, clone RA3-6B2, BD Pharmingen) and anti-IgM (APC, clone II/41, BD Pharmingen). The maturation of the erythroid lineage was analysed using antibodies anti-TER-119 (APC, clone Ter-119, BD Pharmingen) and anti-CD71 (PE, clone C2, BD Pharmingen). Granulocyte-macrophage maturation was assessed with antibodies anti-CD11b/Mac-1 (APC, clone M1/70, BD Pharmingen) and anti-Ly-6G/Gr-1 (PE, clone RB6-8C5, eBioscience). Thymic T-cell maturation was assessed using CD4 (FITC, clone H129.19, BD Pharmingen) and CD8a (PE, clone 53-6.7, BD Pharmingen) antibodies. For the FACS sorting of peripheral white blood cells the following antibodies were used: anti-CD4 (FITC, clone H129.19, BD Pharmingen), anti-CD8a (FITC, clone 53-6.7, BD Pharmingen), anti-CD45R/B220 (APC, clone RA3-6B2, BD Pharmingen), anti-CD11b/Mac-1 (PE, clone M1/70, BD Pharmingen) and anti-Ly-6G/Gr-1 (PE, clone 1A8, BD Pharmingen). The samples were incubated for 15 min at 4 °C in the dark with the exception of samples containing anti-CD34 (RAM34), which were incubated for 90 min. Samples were run on a

LSRII flow cytometer (BD Pharmingen) and the data were analysed with FlowJo 9.3.1 (Tree Star).

Y chromosome qPCR. Y chromosome qPCR was performed on genomic DNA from total peripheral blood or FACS-sorted peripheral blood cells (T cells (B220⁻ Gr-1⁻ Mac-1⁻ CD4⁺ or CD8⁺), B cells (Gr-1⁻ Mac-1⁻ CD4⁻ CD8⁻ B220⁺) or myeloid cells (CD4⁻ CD8⁻ B220⁻ Gr-1⁺ or Mac-1⁺)) using QIAamp DNA micro kit (Qiagen). qPCR was performed using SYBR GreenER qPCR Supermix (Invitrogen). The level of male chimaerism was calculated using oligonucleotides to amplify the genomic regions of the *Tsyt* and β -actin genes and the $\Delta\Delta C_T$ method³⁰. qPCR was performed in triplicate using the following conditions: 50 °C for 2 min and 95 °C for 10 min, followed by 50 cycles of 95 °C for 15 s, and 60 °C for 1 min, on a 7900HT Fast Real-Time system (Applied Biosystems).

Ki-67 staining. Ki-67 staining was performed on total bone marrow that was lineage depleted using a magnetic bead lineage depletion kit (Miltenyi Biotec). The cells were then stained for surface markers: biotin lineage cocktail (Miltenyi Biotec), streptavidin (APC-Cy7), c-Kit (PerCP-Cy5.5), Sca-1 (PE-Cy7), CD34 (eFluor660) and Flt3 (PE). The cells were fixed and permeabilized using the Cytotfix/Cytoperm kit (BD Pharmingen) following the manufacturer's instructions. The cells were then stained overnight at 4 °C with FITC mouse anti-human Ki-67 (B56, BD Pharmingen). The samples were washed and resuspended in PBS plus 3% FCS with DAPI, at a final concentration of 3 μ M, and analysed immediately.

CAFC assay. The CAFC assay was performed on a layer of freshly established wild-type murine stromal cells, as described previously³². The stromal layer was cultured at 33 °C and 5% CO₂ until confluency was reached and was then inactivated by irradiation with 15 Gy. Single-cell suspensions of whole bone marrow were prepared at various concentrations and seeded on the stromal layer in 96-well plates with MyeloCult Media (StemCell Technologies) as described previously^{32,33}. The plates were incubated at 33 °C and 5% CO₂ for 21 days, and colonies scored as described previously³⁴. The CAFC frequency was calculated based on the Poisson distribution using L-Cal software (StemCell Technologies).

29. Ema, H. *et al.* Adult mouse hematopoietic stem cells: purification and single-cell assays. *Nature Protocols* **1**, 2979–2987 (2006).
30. Wang, L. J. *et al.* Engraftment assessment in human and mouse liver tissue after sex-mismatched liver cell transplantation by real-time quantitative PCR for Y chromosome sequences. *Liver Transpl.* **8**, 822–828 (2002).
31. Drost, R. *et al.* BRCA1 RING function is essential for tumor suppression but dispensable for therapy resistance. *Cancer Cell* **20**, 797–809 (2011).
32. Lo Celso, C., Klein, R. J. & Scadden, D. T. Analysis of the hematopoietic stem cell niche. *Curr. Protoc. Stem Cell Biol.* Chapter 2, Unit 2A 5 (2007).
33. Zhang, Q. S. *et al.* *Fancd2*^{-/-} mice have hematopoietic defects that can be partially corrected by resveratrol. *Blood* **116**, 5140–5148 (2010).
34. Amrani, Y. M. *et al.* The *Paf* oncogene is essential for hematopoietic stem cell function and development. *J. Exp. Med.* **208**, 1757–1765 (2011).

The Fun30 nucleosome remodeller promotes resection of DNA double-strand break ends

Xuefeng Chen¹, Dandan Cui², Alma Papusha¹, Xiaotian Zhang¹, Chia-Dwo Chu¹, Jiangwu Tang^{2†}, Kaifu Chen², Xuewen Pan² & Grzegorz Ira¹

Chromosomal double-strand breaks (DSBs) are resected by 5' nucleases to form 3' single-stranded DNA substrates for binding by homologous recombination and DNA damage checkpoint proteins. Two redundant pathways of extensive resection have been described both in cells^{1–3} and *in vitro*^{4–6}, one relying on Exo1 exonuclease and the other on Sgs1 helicase and Dna2 nuclease. However, it remains unknown how resection proceeds within the context of chromatin, where histones and histone-bound proteins represent barriers for resection enzymes. Here we identify the yeast nucleosome-remodelling enzyme Fun30 as a factor promoting DSB end resection. Fun30 is the major nucleosome remodeller promoting extensive Exo1- and Sgs1-dependent resection of DSBs. The RSC and INO80 chromatin-remodelling complexes and Fun30 have redundant roles in resection adjacent to DSB ends. ATPase and helicase domains of Fun30, which are needed for nucleosome remodelling⁷, are also required for resection. Fun30 is robustly recruited to DNA breaks and spreads along the DSB coincident with resection. Fun30 becomes less important for resection in the absence of the histone-bound Rad9 checkpoint adaptor protein known to block 5' strand processing⁸ and in the absence of either histone H3 K79 methylation or γ -H2A, which mediate recruitment of Rad9 (refs 9, 10). Together these data suggest that Fun30 helps to overcome the inhibitory effect of Rad9 on DNA resection.

To identify novel proteins that are important in homologous recombination, we screened a pool of 4,836 homozygous diploid yeast deletion mutants¹¹ for those with altered rates of integration of a *URA3* cassette at two independent loci (*ISU1* and *SOD2*) (Fig. 1a). These screens identified most of the genes known to be essential in homologous recombination, genes that are known to suppress gene targeting, such as *SGS1* and *EXO1*, as well as several novel genes (Fig. 1b and Supplementary Table 1). Higher rates of gene integration in the *sgs1Δ* and *exo1Δ* mutants are probably attributable to increased stability of the transformed linear DNA fragments¹² because Sgs1 helicase and Exo1 nuclease enzymes are involved in the degradation of 5' strands at DSB ends^{2,3}. The Mph1 helicase that was also identified in the screen may inhibit gene targeting by unwinding early recombination intermediates¹³. Thus, degradation of a transformed integration cassette by resection enzymes and disruption of early recombination intermediates by DNA helicases probably prevents efficient integration in cells. In addition to the *sgs1Δ*, *exo1Δ* and *mph1Δ* mutants, gene targeting was significantly increased in the *fun30Δ* mutant (Fig. 1b), suggesting that Fun30 may also be involved either in DSB end resection or in processing recombination intermediates. Fun30 is a member of the well conserved yet poorly characterized Etl1 subfamily of Snf2 nucleosome-remodelling factors¹⁴, acts as a homodimeric ATP-dependent nucleosome-remodelling enzyme⁷ and has been implicated in gene silencing^{15,16}.

To assess a possible role for Fun30 in resection, we deleted *FUN30* in a haploid strain where a DSB was induced by HO (homothallic

switching endonuclease) at the *MAT* locus and the *HML* and *HMR* homologous sequences were deleted to prevent repair by homologous recombination. Southern blot analysis with multiple probes on both sides of the break allowed us to follow the loss of restriction fragments as a measure of 5' strand resection at varying distances from the DSB³.

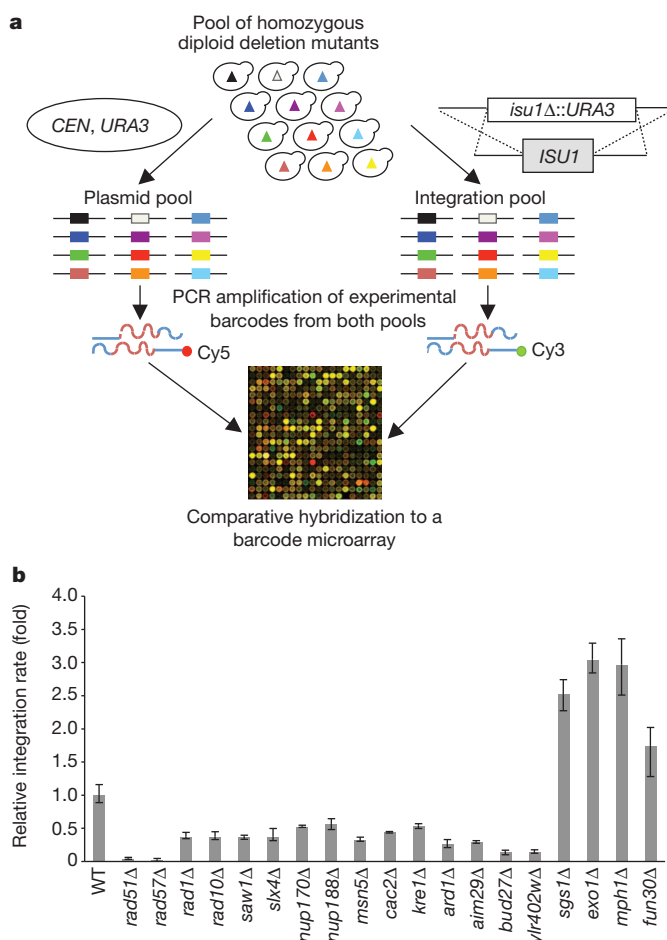


Figure 1 | A genome-wide screen identifies novel genes that regulate gene integration in yeast. **a**, A barcode microarray-based screen for mutants with altered frequency of gene integration. A mixed population of 4,836 homozygous diploid deletion mutant strains was transformed with an integrating cassette (that is, *isu1Δ::URA3*) or a centromeric plasmid (control). Molecular barcodes representing the deletion mutants were PCR-amplified from genomic DNA samples isolated from both transformed pools using Cy5- or Cy3-labelled primers and co-hybridized to a barcode microarray to reveal mutants with altered gene integration efficiencies. **b**, Integration frequency in selected mutants. WT, wild type; error bars, s.d. ($n = 3$).

¹Department of Molecular & Human Genetics, Baylor College of Medicine, One Baylor Plaza, Houston, Texas 77030, USA. ²Verna and Marrs McLean Department of Biochemistry and Molecular Biology, Baylor College of Medicine, One Baylor Plaza, Houston, Texas 77030, USA. [†]Present address: Institute of Plant Protection and Microbiology, Zhejiang Academy of Agricultural Sciences, Hangzhou 310021, China.

Deletion of *FUN30* only mildly affected the initial resection next to the DSB but severely delayed resection at regions 5, 10 and 27–28 kilobases (kb) from the break site (Fig. 2A). Consistently, *fun30Δ* mutants failed to repair DSBs by single-strand annealing¹⁷, a mechanism of DSB repair between two direct repeats that requires extensive resection followed by annealing of the repeats (Fig. 2B). In contrast, the mutants deficient in *INO80*, *SWR1* or *RSC*, which were previously implicated in resection^{18–20}, were proficient in single-strand annealing, suggesting that Fun30 has a unique function in extensive resection (Fig. 2B). Consistent with defects in resection in *fun30Δ* mutants, loading of the single-stranded DNA binding protein RPA, and the Rad51 recombinase, was moderately decreased within 1 kb of the DSB but greatly diminished 5 kb from the break site (Fig. 2C).

To test whether Fun30 affects processing of homologous recombination intermediates, we tested crossover frequency using an ectopic recombination assay involving *MATa* and *MATa-inc* sequences located on chromosomes V and III, respectively²¹. Crossover and non-crossover products can be distinguished on the basis of restriction fragment size (Supplementary Fig. 1). In this assay, the *fun30Δ* mutant showed a repair efficiency comparable to that of wild-type cells and to other single mutants that affect extensive resection³. However, a two-fold increase in crossover frequency was found in *fun30Δ* cells but not in mutants of the other tested remodelers (Supplementary Fig. 1). This is the first evidence linking a nucleosome-remodelling enzyme to recombination pathway choice. In this study, we focused on the role of Fun30 in resection.

There are two pathways of extensive resection in yeast, one that depends on Exo1 and one that depends on Sgs1 (refs 1–3). To test whether Fun30 works in either one or both pathways, we compared resection in *exo1Δ*, *sgs1Δ* and *fun30Δ* single mutants with that in *sgs1Δfun30Δ* and *exo1Δfun30Δ* double mutants. Both double mutants exhibited more severe resection defects and DNA damage

sensitivities than any of the single mutants (Supplementary Fig. 2), and the triple mutant *sgs1Δexo1Δfun30Δ* had the same pattern of resection as *sgs1Δexo1Δ* double-mutant cells (Supplementary Fig. 2 and ref. 3). Therefore, we conclude that Fun30 contributes to both the Exo1 and the Sgs1 resection pathways.

Fun30 probably regulates resection directly, because we observed robust Fun30 recruitment to DSBs which spread in both directions along the DSB coincident with resection (Fig. 3a). Also, Fun30 co-immunoprecipitates with other resection proteins including Exo1, Dna2 and RPA (Supplementary Fig. 4). Further evidence comes from the observation that in *fun30Δ* cells resection enzymes were recruited next to DSB ends but failed to spread efficiently farther from the break site (Fig. 3b), suggesting that Fun30 is important for the progression of resection. Finally, both helicase and ATPase domains needed for nucleosome remodelling by Fun30 (ref. 7) are also required for efficient resection (Fig. 3c and Supplementary Fig. 5). It is unlikely that Fun30 has an indirect role in resection via changing the general chromatin structure, because the patterns of nucleosome positioning at multiple loci around an HO cut site in *fun30Δ* and the wild-type cells are comparable (Supplementary Fig. 3). Also, microarray analysis of genome-wide gene expression showed that *FUN30* deletion cause only modest changes in expression of 14 genes unrelated to DNA damage response^{15,16} (Supplementary Table 2), and cellular levels of proteins involved in resection were comparable in wild-type and *fun30Δ* cells (Supplementary Fig. 3).

Chromatin remodelling at DSBs could occur independently of resection or in a way coupled with resection. The second possibility is more likely because recruitment of Fun30 to DSBs is severely impaired in mutants defective in resection, such as *sgs1Δexo1Δ* and *mre11Δ*, and in the absence of active Cdk1 kinase^{22,23} (Fig. 3d). This defect is unlikely to be due to poor checkpoint activation because Fun30 was efficiently recruited in checkpoint-deficient cells

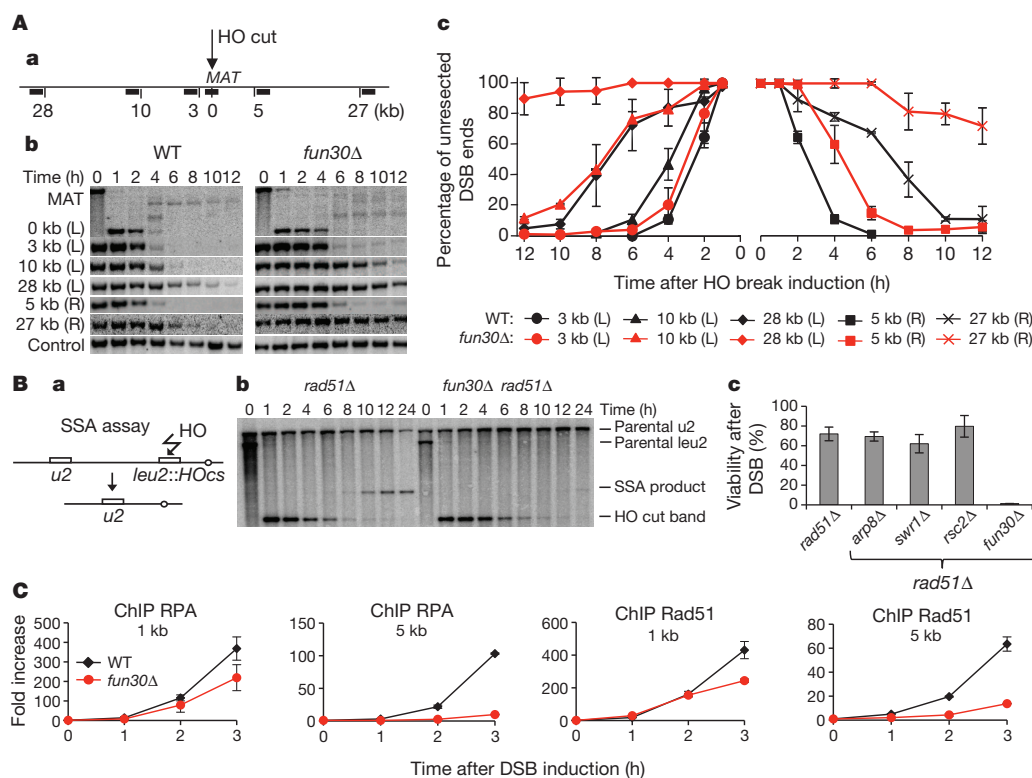


Figure 2 | *fun30Δ* mutants are deficient in resection. **A**, **a**, Diagram of the *MAT* locus and probes used to follow resection kinetics. **b**, **c**, Southern blot analysis (**b**) and kinetics (**c**) of DSB end resection in wild-type and *fun30Δ* mutants. Plotted in this and all following graphs are mean values of three independent experiments with error bars denoting s.d. **B**, **a**, Schematic

representation of single-strand annealing assay¹⁷ (SSA) **b**, **c**, Southern blot analysis of SSA kinetics (**b**) and cell viability in response to a DSB repaired by SSA (**c**). **C**, The relative enrichment of Rad51 and RPA at DSBs in wild-type and *fun30Δ* cells analysed by chromatin immunoprecipitation (ChIP).

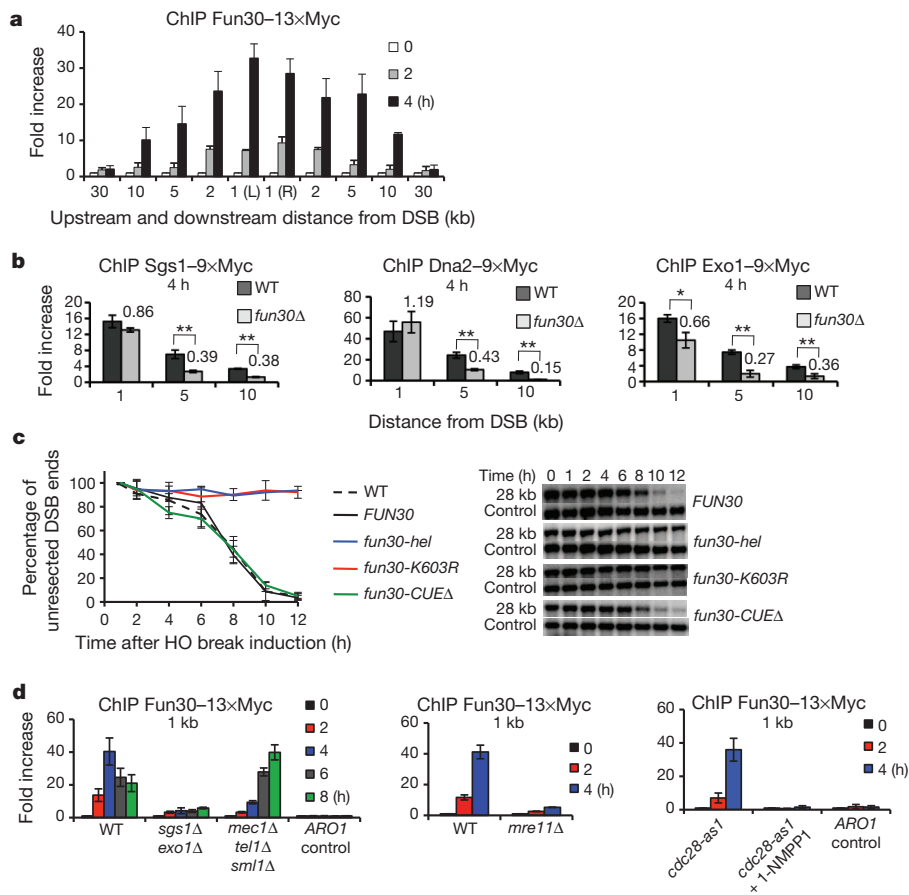


Figure 3 | Fun30 is directly involved in DSB end resection. **a**, ChIP analysis of Fun30-13xMyc recruitment at a DSB. **b**, Recruitment of resection enzymes analysed by ChIP. Statistically significant differences in protein enrichment are indicated: * $P < 0.05$, ** $P < 0.01$, t -test. Relative enrichment in *fun30Δ* is shown. **c**, Analysis of resection kinetics in indicated *FUN30* mutants. The levels

of mutant proteins and their recruitment to DSBs were comparable to wild-type Fun30 (Supplementary Fig. 5). **d**, ChIP analysis of Fun30-13xMyc recruitment in mutants deficient in resection or DNA damage checkpoint. Recruitment at the *ARO1* locus was used as a control. Au error bars, s.d. ($n = 3$).

(*mec1Δ tel1Δ sml1Δ*), albeit with a delay (Fig. 3d). Together with the observation that Fun30 spreads along the DSB coincident with resection and is required for efficient spreading of resection enzymes away from the DSB, we reason that Fun30-mediated chromatin remodelling and resection appear in a coupled manner. Consistent with this view, there is no detectable change in histone H3 occupancy before resection as monitored by histone H3 chromatin immunoprecipitation. We note that histones remain bound to DSB ends longer in *fun30Δ* or *sgs1Δ exo1Δ* mutants, but this can be attributed to slower resection (Supplementary Fig. 6 and ref. 24).

Previous studies indicated an important role for the INO80 (ref. 20), RSC¹⁹ and SWR1 (ref. 18) ATP-dependent nucleosome-remodelling complexes in resection. To examine possible redundant activities in resection, we created single mutants lacking individual components of these and other complexes and the corresponding double mutants additionally lacking Fun30. No significant resection defect was observed in mutants deficient in CHD1, ISW1a/b or SWR1 activity alone, and in the double mutants the defect was comparable to that in the *fun30Δ* single mutant (Supplementary Figs 7 and 8). Also, Rad54, a Snf2-like protein²⁵, has no role in resection. However, the damage sensitivity of *rad54Δ* is epistatic with *fun30Δ*, providing further evidence for Fun30's role in the homologous recombination pathway (Supplementary Fig. 9). A very mild defect was observed in *arp8Δ* (INO80 complex) mutant cells, and in *rsc2Δ* mutant cells initial resection was significantly delayed, a phenotype similar to but weaker than that observed in MRX mutants³. The *arp8Δ fun30Δ* and *rsc2Δ fun30Δ* double mutants showed more dramatic defects in resection and DNA damage response than the single mutants (Supplementary Figs 7 and

8). Elimination of all three remodelling factors impaired resection and checkpoint activation very severely (Fig. 4A). Taken together, these results indicate that Fun30 is the most important remodeller promoting extensive resection, and that initial resection close to DSBs is stimulated by RSC and to lesser extent by Fun30 and INO80.

Along with tight histone–DNA interactions, the histone-bound checkpoint mediator protein Rad9 represents an additional barrier for resection. Rad9 is recruited to histone H2A phosphorylated at Ser 129 (also called γ -H2A) and histone H3 methylated at Lys 79 by Dot1 (refs 9, 10), and it inhibits resection both at DSBs and at telomeres^{8,26}, a phenomenon conserved in evolution^{27,28}. We examined the possible role of nucleosome remodellers in resection within nucleosomes associated with Rad9. In *rad9Δ* cells extensive resection is markedly increased, with an average rate of 10 kb h^{-1} compared with 4 kb h^{-1} in wild-type cells³, and in *hml1/2-S129** or *dot1Δ* mutant cells resection is moderately increased ($6\text{--}7 \text{ kb h}^{-1}$) (Fig. 4B). Resection in *fun30Δ rad9Δ* cells was much faster than in *fun30Δ* cells and, similarly, Fun30 becomes partly dispensable for resection in the absence of γ -H2A or Dot1 (Fig. 4B and Supplementary Fig. 10). Accordingly, deletion of *DOT1* partly suppressed the DNA damage sensitivity of *fun30Δ* mutants, indicating that the observed sensitivity of *fun30Δ* cells is at least partly due to a resection defect (Supplementary Fig. 10). Faster resection in *fun30Δ rad9Δ* cells was not due to increased INO80 or RSC activity within Rad9-free chromatin, because resection kinetics in the *fun30Δ rad9Δ rsc2Δ* and *fun30Δ rad9Δ arp8Δ* triple mutants was still increased (Fig. 4B) relative to *fun30Δ* cells. These data suggest that Fun30 is particularly important for remodelling and resection within Rad9-bound

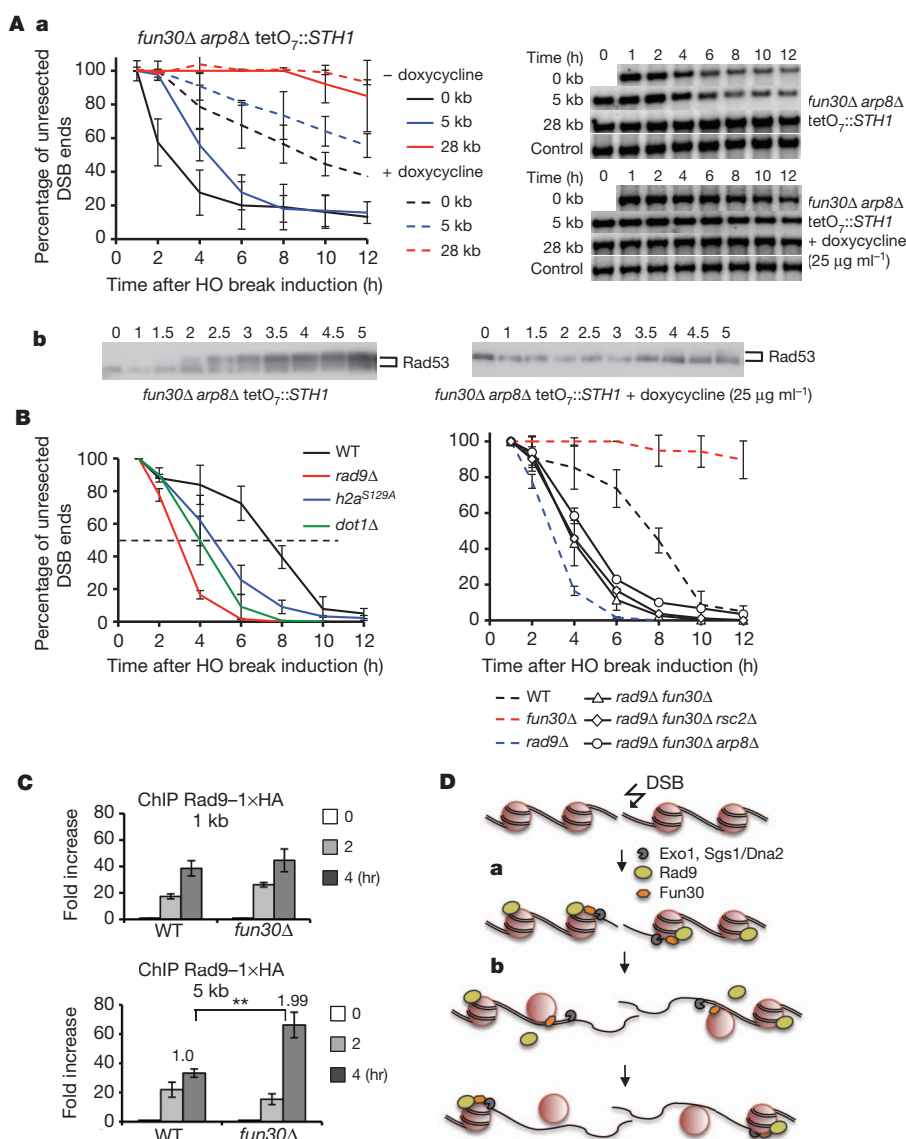


Figure 4 | Fun30 chromatin-remodelling factor promotes resection within Rad9-bound nucleosomes. **A**, Analysis of DSB end resection (**a**) and western blot showing Rad53 phosphorylation (**b**). *STH1* expression (component of RSC) was eliminated by adding doxycycline. **B**, Analysis of resection at 28 kb from a DSB. Southern blots are shown in Supplementary Fig. 10. Error bars, s.d.

chromatin. One possibility is that Fun30 helps to overcome the resection barrier formed by Rad9. Accordingly, more Rad9 was accumulated at DSB ends in *fun30Δ* cells than in wild-type cells (Fig. 4C and model in Fig. 4D).

We have identified Fun30 as a novel regulator of homologous recombination that promotes resection in the context of chromatin. Our findings in yeast shed light on the coordinated processes of DNA repair and chromatin remodelling and should provide insights into possible roles of the human homologue, SMARCAD1 (ref. 29), in DNA repair.

METHODS SUMMARY

All experiments were performed on the *Saccharomyces cerevisiae* strains listed in Supplementary Table 3. The resection kinetics were analysed by Southern blotting using probes specific to broken chromosome. Protein recruitment was followed by chromatin immunoprecipitation, and protein interactions were studied by co-immunoprecipitation and western blotting. Detailed methods are presented in Supplementary Information.

($n = 3$). **C**, ChIP analysis of Rad9–HA binding. $^{**}P < 0.01$. **D**, Model of coupled resection and chromatin remodelling. **a**, Nucleases and helicases resect DNA within a nucleosome-free region next to a break. Histones or histone-bound Rad9 impedes further resection. **b**, Fun30 is recruited to nucleosomes being resected and increases the access to nucleosomal DNA.

Full Methods and any associated references are available in the online version of the paper.

Received 29 September 2011; accepted 27 June 2012.

Published online 9 September 2012.

- Gravel, S., Chapman, J. R., Magill, C. & Jackson, S. P. DNA helicases Sgs1 and BLM promote DNA double-strand break resection. *Genes Dev.* **22**, 2767–2772 (2008).
- Mimitou, E. P. & Symington, L. S. Sae2, Exo1 and Sgs1 collaborate in DNA double-strand break processing. *Nature* **455**, 770–774 (2008).
- Zhu, Z., Chung, W. H., Shim, E. Y., Lee, S. E. & Ira, G. Sgs1 helicase and two nucleases dna2 and exo1 resect DNA double-strand break ends. *Cell* **134**, 981–994 (2008).
- Cejka, P. *et al.* DNA end resection by Dna2–Sgs1–RPA and its stimulation by Top3–Rmi1 and Mre11–Rad50–Xrs2. *Nature* **467**, 112–116 (2010).
- Nicolette, M. L. *et al.* Mre11–Rad50–Xrs2 and Sae2 promote 5' strand resection of DNA double-strand breaks. *Nature Struct. Mol. Biol.* **17**, 1478–1485 (2010).
- Niu, H. *et al.* Mechanism of the ATP-dependent DNA end-resection machinery from *Saccharomyces cerevisiae*. *Nature* **467**, 108–111 (2010).
- Awad, S., Ryan, D., Prochasson, P., Owen-Hughes, T. & Hassan, A. H. The Snf2 homolog Fun30 acts as a homodimeric ATP-dependent chromatin-remodeling enzyme. *J. Biol. Chem.* **285**, 9477–9484 (2010).

8. Lazzaro, F. *et al.* Histone methyltransferase Dot1 and Rad9 inhibit single-stranded DNA accumulation at DSBs and uncapped telomeres. *EMBO J.* **27**, 1502–1512 (2008).
9. Hammet, A., Magill, C., Heierhorst, J. & Jackson, S. P. Rad9 BRCT domain interaction with phosphorylated H2AX regulates the G1 checkpoint in budding yeast. *EMBO Rep.* **8**, 851–857 (2007).
10. Toh, G. W. *et al.* Histone H2A phosphorylation and H3 methylation are required for a novel Rad9 DSB repair function following checkpoint activation. *DNA Repair (Amst.)* **5**, 693–703 (2006).
11. Giaever, G. *et al.* Functional profiling of the *Saccharomyces cerevisiae* genome. *Nature* **418**, 387–391 (2002).
12. Chung, W. H., Zhu, Z., Papusha, A., Malkova, A. & Ira, G. Defective resection at DNA double-strand breaks leads to de novo telomere formation and enhances gene targeting. *PLoS Genet.* **6**, e1000948 (2010).
13. Prakash, R. *et al.* Yeast Mph1 helicase dissociates Rad51-made D-loops: implications for crossover control in mitotic recombination. *Genes Dev.* **23**, 67–79 (2009).
14. Flaus, A., Martin, D. M., Barton, G. J. & Owen-Hughes, T. Identification of multiple distinct Snf2 subfamilies with conserved structural motifs. *Nucleic Acids Res.* **34**, 2887–2905 (2006).
15. Neves-Costa, A., Will, W. R., Vetter, A. T., Miller, J. R. & Varga-Weisz, P. The SNF2-family member Fun30 promotes gene silencing in heterochromatic loci. *PLoS ONE* **4**, e8111 (2009).
16. Yu, Q., Zhang, X. & Bi, X. Roles of chromatin remodeling factors in the formation and maintenance of heterochromatin structure. *J. Biol. Chem.* **286**, 14659–14669 (2011).
17. Vaze, M. *et al.* Recovery from checkpoint-mediated arrest after repair of a double-strand break requires srs2 helicase. *Mol. Cell* **10**, 373–385 (2002).
18. Kalocsay, M., Hiller, N. J. & Jentsch, S. Chromosome-wide Rad51 spreading and SUMO-H2A.Z-dependent chromosome fixation in response to a persistent DNA double-strand break. *Mol. Cell* **33**, 335–343 (2009).
19. Shim, E. Y. *et al.* RSC mobilizes nucleosomes to improve accessibility of repair machinery to the damaged chromatin. *Mol. Cell Biol.* **27**, 1602–1613 (2007).
20. van Attikum, H., Fritsch, O., Hohn, B. & Gasser, S. M. Recruitment of the INO80 complex by H2A phosphorylation links ATP-dependent chromatin remodeling with DNA double-strand break repair. *Cell* **119**, 777–788 (2004).
21. Ira, G., Malkova, A., Liberi, G., Foiani, M. & Haber, J. E. Srs2 and Sgs1-Top3 suppress crossovers during double-strand break repair in yeast. *Cell* **115**, 401–411 (2003).
22. Ira, G. *et al.* DNA end resection, homologous recombination and DNA damage checkpoint activation require CDK1. *Nature* **431**, 1011–1017 (2004).
23. Ivanov, E. L., Sugawara, N., White, C. I., Fabre, F. & Haber, J. E. Mutations in XRS2 and RAD50 delay but do not prevent mating-type switching in *Saccharomyces cerevisiae*. *Mol. Cell Biol.* **14**, 3414–3425 (1994).
24. Chen, C. C. *et al.* Acetylated lysine 56 on histone H3 drives chromatin assembly after repair and signals for the completion of repair. *Cell* **134**, 231–243 (2008).
25. Alexeev, A., Mazin, A. & Kowalczykowski, S. C. Rad54 protein possesses chromatin-remodeling activity stimulated by the Rad51-ssDNA nucleoprotein filament. *Nature Struct. Biol.* **10**, 182–186 (2003).
26. Lydall, D. & Weinert, T. Yeast checkpoint genes in DNA damage processing: implications for repair and arrest. *Science* **270**, 1488–1491 (1995).
27. Bothmer, A. *et al.* Regulation of DNA end joining, resection, and immunoglobulin class switch recombination by 53BP1. *Mol. Cell* **42**, 319–329 (2011).
28. Bunting, S. F. *et al.* 53BP1 inhibits homologous recombination in Brca1-deficient cells by blocking resection of DNA breaks. *Cell* **141**, 243–254 (2010).
29. Okazaki, N. *et al.* The novel protein complex with SMARCAD1/KIAA1122 binds to the vicinity of TSS. *J. Mol. Biol.* **382**, 257–265 (2008).

Supplementary Information is available in the online version of the paper.

Acknowledgements We thank P. Sung, W.-D. Heyer and A. Pellicioli for antibodies; S.-E. Lee, S. Kron and M. Osley for strains; B. Llorente for sharing unpublished data; and J. Tyler, P. Sung and S. E. Lee for comments on the manuscript. This work was supported by the National Institutes of Health grants GM080600 (to G.I.) and HG004840 (to X.P.).

Author Contributions X.C. and D.C. contributed equally to this work. X.C. constructed most of the strains and analysed chromatin structure, protein interactions, protein recruitment to DSBs, histone loss at DSBs, activation of the DNA damage checkpoint and DNA damage sensitivity. X.Z. and K.C. performed microarray analysis of gene expression. D.C., J.T. and X.P. performed the genetic screen and constructed *FUN30* point mutants. A.P. and C.-D.C. analysed resection and crossover frequency. X.C., X.P. and G.I. designed the experiments, discussed the data and wrote the manuscript.

Author Information Microarray data for gene expression and gene targeting have been deposited in the Gene Expression Omnibus under accession number GSE38601. Reprints and permissions information is available at www.nature.com/reprints. The authors declare no competing financial interests. Readers are welcome to comment on the online version of the paper. Correspondence and requests for materials should be addressed to X.P. (xuewenp@bcm.edu) or G.I. (gira@bcm.edu).

METHODS

Yeast strains and plasmids. All strains used are listed in Supplementary Table 3. The *FUN30* ATPase dead mutants, helicase-domain deletion mutants and Cue-domain deletion mutants were first constructed using fusion PCR with a high-fidelity Phusion DNA polymerase (NEB). In each case, the mutation or deletion was introduced via a pair of overlapping PCR primers. The PCR products were subsequently cloned onto pXP735, a derivative of the plasmid pFA6a-kanMX6 (ref. 30) with a *TRP1* promoter inserted between the *pTEF* and *kanMX* coding sequences. Wild-type *FUN30* was similarly cloned into pXP735. In each case, the *FUN30* gene, including 490 bp of the 5' untranslated region (5' UTR), the coding sequence and 300 bp of the 3' UTR was inserted between the *pTEF* and *TRP1* promoter sequences on the vector and verified with DNA sequencing. The resultant plasmid was then used as the template to amplify an integration cassette containing the 5' UTR, the coding region, the 3' UTR of *FUN30*, the *TRP1* promoter that directs expression of the *kanMX* gene and a *tTEF* fragment. The PCR products were transformed into a *fun30Δ::natMX* mutant. The 5' UTR of *FUN30* and the *tTEF* sequences at both ends of the PCR products direct their integration into the genome by replacing the existing *fun30Δ::natMX* cassette via homologous recombination. As a result, the wild-type or mutant alleles were integrated at the endogenous *FUN30* locus, with its expression controlled by the endogenous regulatory elements. Integrants were selected for G418 resistance and Clonate sensitivity, PCR amplified and verified with DNA sequencing. The sequences of all oligonucleotide primers used for constructing and sequencing these alleles are available upon request.

Genome-wide screens for mutants that regulate gene integration efficiency. Both *isu1Δ::URA3* and *sod2Δ::URA3* gene knockout cassettes containing ~1.5 kb of flanking sequence on each side of the endogenous *ISU1* or *SOD2* locus were separately transformed into a pool of 4,836 homozygous diploid deletion mutants. About 8×10^5 independent *Ura*⁺ transformants were obtained for each cassette. As a control, the centromeric circular plasmid pRS416 (*URA3*), which is maintained in yeast cells ectopically, was also transformed into the pool. For each transformation reaction, all *Ura*⁺ transformants were pooled and a genomic DNA sample was extracted. An integration sample and the control sample were analysed with the barcode microarray to identify deletion mutants with altered integration frequency. Results of both the *isu1Δ::URA3* and *sod2Δ::URA3* screens were combined to compile a list of mutants with reduced or increased integration efficiency (by twofold or more). These mutants were then individually validated for relative integration efficiency using a third integration cassette, *can1Δ::URA3*, in a well-controlled manner. Briefly, both the *can1Δ::URA3* cassette and a *LEU2* plasmid (pRS415) were transformed into each strain within the same transformation reaction. Cells from such a reaction were split and plated on both SC-*Ura* plates to select for transformants resulting from integration and SC-*Leu* plates to select for cells containing the plasmid. The numbers of *Ura*⁺ and *Leu*⁺ transformants obtained from each reaction were compared to calculate the relative integration rate for each strain, with that of a wild-type strain arbitrarily set to 1.0 as a reference. Four such independent transformation reactions were carried out with each strain and the results were averaged.

Microarray analysis of gene expression. Both the wild-type BY4741 and an isogenic *fun30Δ* mutant were grown in 10 ml of synthetic complete medium until log phase. Cells were collected and resuspended in 400 μl of TES solution (10 mM Tris-HCl, pH 7.5, 10 mM EDTA, 0.5% SDS). Cells were lysed by vortexing with glass beads after adding 400 μl of acidic phenol to the cell suspension. Cell lysates were clarified by centrifugation at 16,000g for 10 min at 4 °C. Protein in the supernatant was extracted once with an equal volume of phenol:chloroform (1:1) solution, followed by extraction once with an equal volume of chloroform. The resulting supernatant was mixed with three volumes of 100% ethanol and 0.1 volume of 3 M NaOAc (pH 5.2) and incubated at -80 °C for 2 h. Total RNA was precipitated by centrifugation at 16,000g for 20 min at 4 °C and this was followed by washing once with 70% ethanol. After a brief air dry (5 min), RNA was dissolved in 50 μl of DEPC-treated water and analysed with an Affimetrix microarray. Two independent experiments were carried out for each strain and the results were combined.

Chromatin immunoprecipitation. ChIP assays were carried out as previously described^{31,32}, with modification. Briefly, cultures were grown to a density of about 1×10^7 cells ml⁻¹ in pre-induction medium (YEP-*raffinose*) and HO was induced by adding 2% galactose. Protein-DNA complexes were crosslinked with 1% (final concentration) formaldehyde and incubated for 10 min at room temperature (23 °C) with rotation. The reaction was quenched by adding glycine to a final concentration of 125 mM and incubated at room temperature for 5 min with rotation. Cells were lysed with glass beads in lysis buffer (50 mM HEPES, pH 7.5, 1 mM EDTA, 140 mM NaCl, 1% Triton X-100, 0.1% NaDOC, 1 mg ml⁻¹ Bacitracin, 1 mM Benzamidin and 1 mM PMSF) supplemented with Roche protease inhibitor tablets. Cell extracts were sonicated to shear the DNA to an

average size of 0.5 kb. Cell debris was removed by centrifugation at 16,000g for 10 min. Supernatant was collected and incubated with affinity-purified anti-Myc (Sigma M4439), anti-FLAG (Sigma M2), anti-Rad51 (gift from Dr Patrick Sung) or anti-Rfa2 (gift from Dr Wolf-Dietrich Heyer) antibodies overnight at 4 °C, followed by incubation with protein G agarose beads for 4 h at 4 °C. The protein-bound beads were washed twice with lysis buffer (as above), twice with lysis buffer containing 500 mM NaCl, twice in wash buffer (10 mM Tris-HCl, pH 8.0, 1 mM EDTA, 0.25 M LiCl, 0.5% NP-40 substitute and 0.5% NaDOC) and twice in $\times 1$ TE. Protein-DNA complexes were eluted with elution buffer (10 mM Tris-HCl, pH 8.0, 10 mM EDTA, pH 8.0, and 1% SDS) and incubated at 65 °C overnight to reverse crosslinking. Samples were digested with proteinase K at 37 °C for 6 h. DNA was purified by phenol extraction and ethanol precipitation. Purified DNA samples were analysed by real-time quantitative PCR (ABI 7900HT) with primers that specifically anneal to DNA sequences located at indicated distances from the DSB, using the following conditions: 95 °C for 10 min; 40 cycles of 95 °C for 15 s, 60 °C for 1 min and 72 °C for 30 s. Histone loss was measured according to the method described in ref. 24.

Co-immunoprecipitation. To examine the potential interaction between *Fun30* and resection enzymes, we performed co-immunoprecipitation as described in ref. 33, with modification. Yeast cells ($\sim 2 \times 10^7$ ml⁻¹) grown in YEPD medium were treated with 0.1% methyl methanesulfonate (MMS) for 90 min. Treated cells or untreated control cells were lysed on a bead beater in lysis buffer (100 mM HEPES, pH 8.0, 20 mM Mg(Ac)₂, 150 mM NaCl, 10% glycerol (v/v), 0.4% Nonidet P-40, 10 mM EGTA, 0.1 mM EDTA, plus protease and phosphatase inhibitors). The extracts were gently clarified by centrifugation at 1,800g for 10 min at 4 °C. The supernatant for each sample was collected and split into two aliquots. One thousand units of Benzonase (Sigma) were added to one of the aliquots (~1.5 ml) to digest genomic DNA and RNA. The supernatant was then incubated with protein G agarose beads for 3 h at 4 °C to capture the proteins or protein-DNA complexes that bind nonspecifically to the beads. Beads were discarded after centrifugation at 1,800g for 5 min. The supernatant was incubated with 10 μg of anti-Myc or anti-FLAG antibody at 4 °C overnight with agitation. In parallel, a mock immunoprecipitation was established for each set of co-immunoprecipitation reactions by incubating one aliquot of MMS-treated sample with an appropriate IgG. Protein G agarose beads were added to each sample and the mixtures were incubated for another 3 h at 4 °C. Then the beads were subjected to extensive washing at 4 °C with wash buffer (100 mM HEPES, pH 7.4, 20 mM Mg(Ac)₂, 150 mM NaCl, 10% glycerol (v/v), 0.5% Nonidet P-40, 10 mM EGTA, 0.1 mM EDTA, plus protease and phosphatase inhibitors). Immunoprecipitated proteins were eluted by boiling beads in $\times 2$ SDS loading buffer for 5 min.

Western blotting. Whole-cell extracts (WCE) were prepared as previously described³¹. Yeast cells grown overnight in rich medium (YEPD) or pre-induction medium (YEP-*raffinose*: 1% yeast extract, 2% peptone, 2% *raffinose*) either before or at different times following HO break induction were collected. WCEs were prepared using trichloroacetic acid. Pelleted cells from 5 ml of culture were washed once with water and resuspended in 10% trichloroacetic acid. The cells were lysed by vortexing with acid-washed glass beads and the protein lysates were pelleted by centrifugation at 20,000g for 15 min. The pellets were washed with ice-cold 80% acetone and proteins were dissolved in $\times 2$ SDS sample loading buffer by boiling for 5 min. Samples were centrifuged for 5 min at 13,200g in a microcentrifuge and the supernatant was retained as the protein extract. WCEs or immunoprecipitated samples were resolved on a 7.5% or 8.5% SDS-PAGE gel and transferred onto a polyvinylidene difluoride membrane (Immobilon-P, Millipore). To examine the expression levels of Sgs1-9×Myc, Exo1-9×Myc, Mre11-13×Myc or Dna2-9×Myc in wild-type and *fun30* cells, the membrane was probed with mouse monoclonal anti-Myc antibody (M4439, Sigma). To monitor checkpoint activation during DSB repair, the membrane was probed with anti-Rad53 antibody (gift from Dr Achille Pelliccioli). Anti-mouse and anti-rabbit IgG HRP-conjugated secondary antibodies were obtained from Santa Cruz Biotechnology. Blots were developed using the ECL Plus Western Blotting System (GE Healthcare).

Analysis of resection at DSB ends. Resection of DSB ends was analysed at an HO-induced DSB at the *MAT* locus on chromosome III using Southern blots as previously described³. Briefly, genomic DNA was isolated by glass bead disruption using a standard phenol extraction method. Purified DNA was digested with *EcoRI* and separated on a 0.8% agarose gel. Southern blotting and hybridization with radiolabelled DNA probes specific for the *MAT* locus was performed as described previously³⁴. The band signal intensities were analysed with IMAGEQUANT TL software (Amersham Biosciences) and normalized to the *TRA1* probe. DSB end resection beyond each *EcoRI* site for each time point was estimated as the percentage of the band signal intensity corresponding to the *EcoRI* fragment of interest at 1 h after break induction.

Single-strand annealing and ectopic recombination assays. Repair by single-strand annealing between two partial *LEU2* gene repeats was followed by Southern

blot analysis using a *leu2* sequence probe as previously described¹⁷. Experiments were done in a *rad51Δ* background to prevent repair by break-induced replication. Repair by ectopic recombination between chromosome V and chromosome III was followed by Southern blot analysis using a *MATa* sequence probe. Crossing-over was measured at an 8-h time point as previously described²¹. To test cell viability in response to a DSB repaired by single-strand annealing or by ectopic recombination, cells were grown in pre-induction medium (YEP- raffinose) overnight to an early log phase. Cells were then diluted to a concentration of $\sim 1 \times 10^3$ cells ml⁻¹ and equal amounts of cells were plated on YEPD and YEP-Gal plates. Plates were incubated at 30 °C for 3 d. Viability was calculated by dividing the number of colonies grown on YEP-Gal by the number of colonies grown on YEPD multiplied by 100%. Three independent experiments were performed for each strain.

Spot assays for analysing sensitivity to DNA-damaging agents. Yeast cells were grown in YEPD rich medium overnight to saturation. Undiluted and 1/10 serial dilutions of each cell culture were spotted onto plates containing camptothecin or phleomycin DNA-damaging agent at the indicated concentrations. Plates were incubated at 30 °C for 2–3 d before being photographed.

Micrococcal nuclease digestion. Yeast cells from 80 ml of culture ($\sim 2 \times 10^7$ ml⁻¹) were collected by centrifugation at 4,000g and washed twice with distilled de-ionized H₂O. The cell pellet was resuspended in 900 μl of sorbitol solution (1 M Sorbitol, 50 mM Tris-Cl, pH 7.5). Then 0.56 μl of 14.3 M β-mercaptoethanol and 100 μl of Zymolase 20T stock (dissolved in sorbitol solution, 25 mg ml⁻¹) were added to each sample. Samples were then incubated at 30 °C with rotation for 25 min to digest cell wall. Spheroplasts were collected by centrifugation at 14,000g for 2 min and washed twice with ice-cold sorbitol solution. The pellet was resuspended with 1.3 ml of lysis buffer (0.5 mM spermidine,

1 mM β-mercaptoethanol, 0.075% Nonidet P-40, 50 mM NaCl, 10 mM Tris-HCl, pH 8.0, 5 mM MgCl₂, 5 mM CaCl₂, plus protease inhibitors). Micrococcal nuclease (Roche Applied Science) was added to each sample to a final concentration of 100 U ml⁻¹. After mixing, 200 μl of nuclei suspension was immediately taken out as an undigested control. The remaining samples were subjected to MNase digestion at 37 °C. Aliquots of nuclei suspension were taken out at 2, 4, 8 and 16 min, and the reactions were immediately stopped by addition of 20 mM EDTA, pH 8.0, and 1% SDS. The supernatants were collected by centrifugation at 14,000g for 10 min, followed by Proteinase K digestion (0.1 mg ml⁻¹) at 50 °C for 3 h. The resultants were purified by phenol-chloroform extraction, and DNA was recovered by ethanol precipitation. DNA pellets were washed once with 70% ethanol, and then dissolved in $\times 1$ TE. After RNase treatment, samples were separated on a 1.4% agarose gel. Nucleosome mapping at specific loci was examined by Southern blotting and hybridization with DNA probes specific for sequences located at the HO cleavage site or 5, 10 or 27 kb from the DSB.

30. Wach, A., Brachat, A., Pohlmann, R. & Philippsen, P. New heterologous modules for classical or PCR-based gene disruptions in *Saccharomyces cerevisiae*. *Yeast* **10**, 1793–1808 (1994).
31. Chen, X. *et al.* Cell cycle regulation of DNA double-strand break end resection by Cdk1-dependent Dna2 phosphorylation. *Nature Struct. Mol. Biol.* **18**, 1015–1019 (2011).
32. Sugawara, N., Wang, X. & Haber, J. E. In vivo roles of Rad52, Rad54, and Rad55 proteins in Rad51-mediated recombination. *Mol. Cell* **12**, 209–219 (2003).
33. Lambert, J. P. *et al.* Defining the budding yeast chromatin-associated interactome. *Mol. Syst. Biol.* **6**, 448 (2010).
34. Church, G. M. & Gilbert, W. Genomic sequencing. *Proc. Natl Acad. Sci. USA* **81**, 1991–1995 (1984).

The yeast Fun30 and human SMARCAD1 chromatin remodellers promote DNA end resection

Thomas Costelloe^{1*}, Raphaël Louge^{2,3*}, Nozomi Tomimatsu^{4*}, Bipasha Mukherjee⁴, Emmanuelle Martini⁵, Basheer Khadaroo^{2,3}, Kenny Dubois^{2,3}, Wouter W. Wiegant¹, Agnès Thierry⁶, Sandeep Burma⁴, Haico van Attikum¹ & Bertrand Llorente^{2,3}

Several homology-dependent pathways can repair potentially lethal DNA double-strand breaks (DSBs). The first step common to all homologous recombination reactions is the 5'–3' degradation of DSB ends that yields the 3' single-stranded DNA required for the loading of checkpoint and recombination proteins. In yeast, the Mre11–Rad50–Xrs2 complex (Xrs2 is known as NBN or NBS1 in humans) and Sae2 (known as RBBP8 or CTIP in humans) initiate end resection, whereas long-range resection depends on the exonuclease Exo1, or the helicase–topoisomerase complex Sgs1–Top3–Rmi1 together with the endonuclease Dna2 (refs 1–6). DSBs occur in the context of chromatin, but how the resection machinery navigates through nucleosomal DNA is a process that is not well understood⁷. Here we show that the yeast *Saccharomyces cerevisiae* Fun30 protein and its human counterpart SMARCAD1 (ref. 8), two poorly characterized ATP-dependent chromatin remodellers of the Snf2 ATPase family, are directly involved in the DSB response. Fun30 physically associates with DSB ends and directly promotes both Exo1- and Sgs1-dependent end resection through a mechanism involving its ATPase activity. The function of Fun30 in resection facilitates the repair of camptothecin-induced DNA lesions, although it becomes dispensable when Exo1 is ectopically overexpressed. Interestingly, SMARCAD1 is also recruited to DSBs, and the kinetics of recruitment is similar to that of EXO1. The loss of SMARCAD1 impairs end resection and recombinational DNA repair, and renders cells hypersensitive to DNA damage resulting from camptothecin or poly(ADP-ribose) polymerase inhibitor treatments. These findings unveil an evolutionarily conserved role for the Fun30 and SMARCAD1 chromatin remodellers in controlling end resection, homologous recombination and genome stability in the context of chromatin.

Fun30 possesses intrinsic ATP-dependent chromatin-remodelling activity⁸, which is required to promote gene silencing in heterochromatin⁹. *FUN30* deletion renders cells hypersensitive to camptothecin (CPT)⁹, whereas overexpression results in genomic instability¹⁰. A role for Fun30 in the DSB response, however, remains enigmatic. While performing a genomic screen using a plasmid-based assay, we discovered that the *fun30Δ* mutant shows an increased efficiency in one-ended homologous recombination or break-induced replication (BIR) (Fig. 1, Supplementary Fig. 1 and Supplementary Table 1). We also found that gap repair, which is a two-ended homologous recombination reaction, is increased in the *fun30Δ* mutant (Supplementary Fig. 2). This shows that Fun30 affects a step common to all homologous recombination reactions. Interestingly, the *fun30Δ* mutant shares this phenotype with the resection mutants *sgs1Δ* and *exo1Δ*¹¹, in which impaired resection slows down the degradation of transformed plasmids, favouring plasmid-based recombination¹¹ (Fig. 1 and Supplementary Fig. 2). Altogether, this indicates that Fun30 promotes DNA end processing.

To test whether Fun30 contributes to 5'–3' DNA end resection, we analysed single-stranded (ss)DNA formation at an HO endonuclease-induced DSB at the *MAT* locus¹². Because ssDNA is resistant to cleavage by restriction enzymes, 5'–3' resection at the DSB generates a ladder of ssDNA bands after restriction digestion of the genomic DNA and electrophoresis under alkaline conditions. In the absence of Fun30, the shortest ssDNA intermediate is formed with normal kinetics, but the formation of longer ssDNA intermediates is either delayed or abolished (Fig. 2a and Supplementary Fig. 3a). Chromatin immunoprecipitation (ChIP) of the ssDNA-binding replication protein A (RPA) complex at the HO-induced DSB confirmed these results (Supplementary Fig. 3c, d). Notably, we detected a similar resection defect at an I-SceI endonuclease cut site inserted at the *HIS3* locus (Fig. 2c), ruling out a locus-specific effect. Our results indicate that Fun30 facilitates long-range end resection, which is further supported by a delay in the kinetics of DSB repair by single-strand annealing (SSA) in the *fun30Δ* mutant (Supplementary Fig. 4).

In the combined absence of Fun30 and either Sgs1 or Exo1, the resection defect was stronger than the defects in the corresponding single mutants (Fig. 2b and Supplementary Fig. 3b), leading to a more pronounced defect in RPA loading at the HO-induced DSB (Supplementary Fig. 3c). This correlated with higher plasmid-based

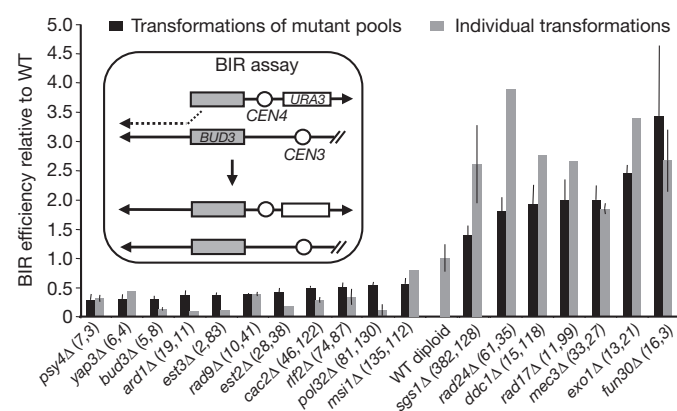


Figure 1 | *fun30Δ* and DNA end-resection mutants show high BIR efficiencies. BIR efficiencies of selected homozygous diploid null mutants relative to wild type (WT; BY4743). Mutants have been ranked according to their BIR efficiencies. Two BIR experiments using transformations of mutant pools were performed (Supplementary Fig. 1). The rank of each mutant in these two BIR experiments is given in parentheses. This rank is bottom-up for mutants with BIR efficiencies lower than wild type, and top-down otherwise. A schematic of the BIR assay is provided in the box. Error bars denote \pm mean absolute deviation of two independent experiments.

¹Department of Toxicogenetics, Leiden University Medical Center, Einthovenweg 20, 2333 ZC Leiden, The Netherlands. ²Centre National de la Recherche Scientifique, Unité Mixte de Recherche 7258, Centre de Recherche en Cancérologie de Marseille, Marseille F-13009, France. ³Aix-Marseille University, Unité Mixte de Recherche 7258, Marseille F-13284, France. ⁴Division of Molecular Radiation Biology, Department of Radiation Oncology, University of Texas Southwestern Medical Center, 2201 Inwood Road, NC7.214E, Dallas, Texas 75390, USA. ⁵CEA-DSV-Institut de Radiobiologie Cellulaire et Moléculaire, 92265 Fontenay aux Roses, France. ⁶Institut Pasteur, Unité de Génétique Moléculaire des Levures, Centre National de la Recherche Scientifique and University Pierre and Marie Curie-Paris, 25 rue du Docteur Roux, F75724 Paris Cedex 15, France.

*These authors contributed equally to this work.

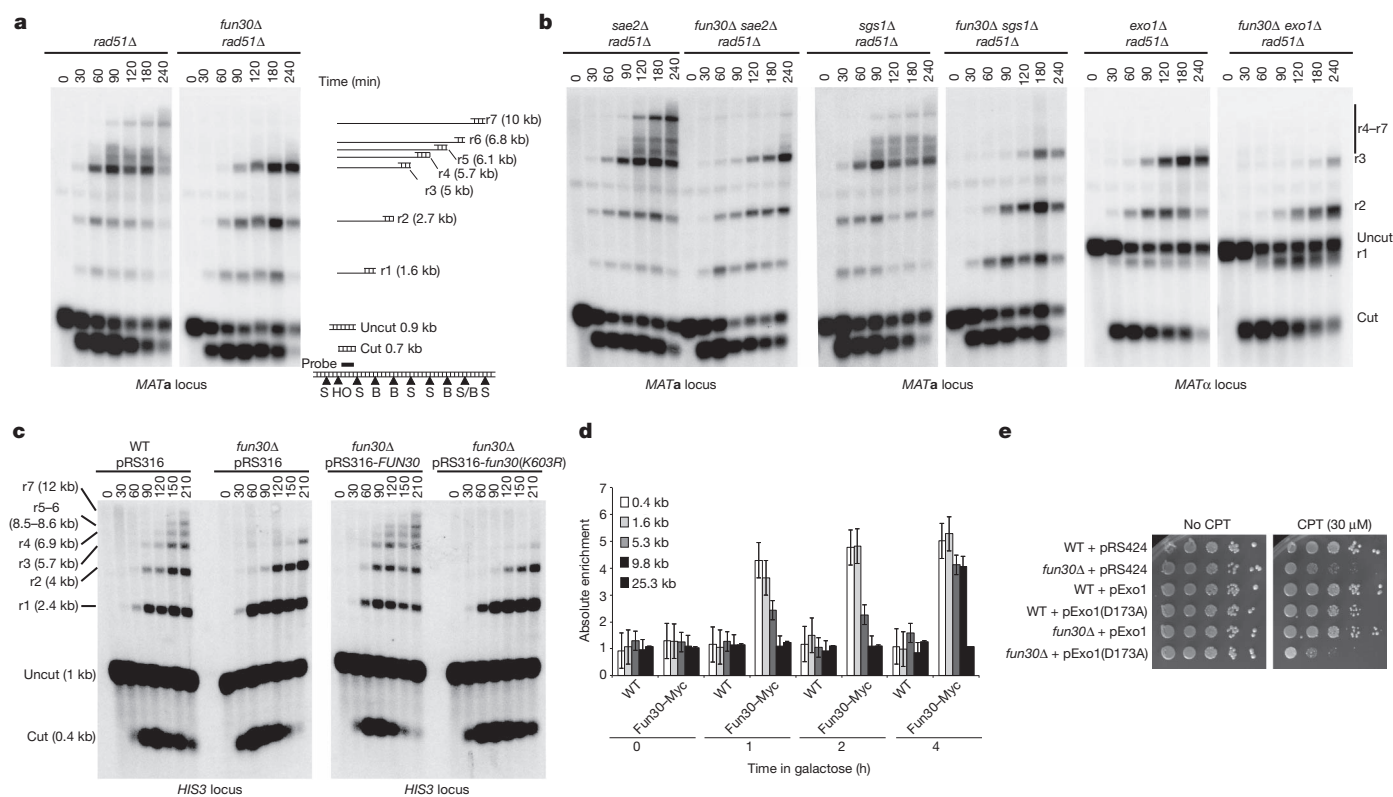


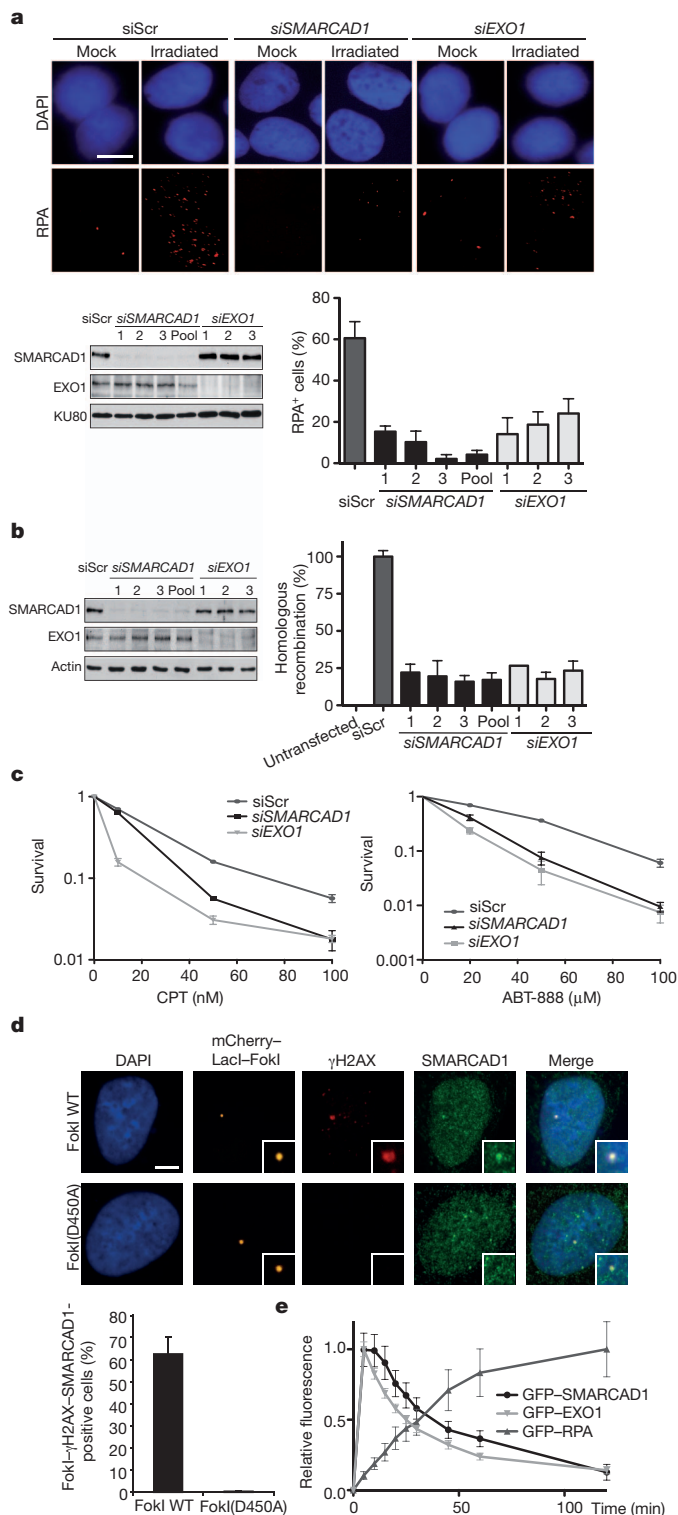
Figure 2 | Fun30 promotes long-range 5'–3' DNA end resection and is recruited to DSBs. **a**, Southern blot analysis of StyI (S) and BstXI (B)-digested genomic DNA after alkaline gel electrophoresis. r1–r7 denote partially ssDNA fragments. **b**, As in **a**, except that *exo1Δ* mutants were *MATα* strains, showing a longer uncut fragment (1.9 kb). **c**, Southern blot analysis of StyI-digested

BIR efficiencies and stronger delays in the kinetics of SSA (Supplementary Figs 2 and 4). These results demonstrate that Fun30 promotes both Sgs1- and Exo1-dependent resection of DSBs. Interestingly, we observed smeared cut fragments in the SSA assay in the *fun30Δ exo1Δ* double mutant (Supplementary Fig. 4b). These indicate severely impaired long-range resection¹, which suggests that the Sgs1 resection pathway depends more strongly on Fun30 than the Exo1 pathway.

The ATPase activity of Fun30 is essential for its chromatin-remodelling activity⁸. Expression of wild-type Fun30, but not ATPase-deficient Fun30(K603R), restored end resection to wild-type levels in *fun30Δ* mutants (Fig. 2c). This indicates that chromatin remodelling driven by Fun30 facilitates long-range resection, either directly or indirectly. After induction of an HO endonuclease-induced DSB at the *MAT* locus, Fun30 accumulated at sites near the DSB within 60 min and spread away at later time points (Fig. 2d), as previously observed for Sgs1, Dna2 and Exo1 (refs 2, 13). This supports a direct role for Fun30 in long-range resection, acting together with the Exo1 and Sgs1 resection machineries. However, Fun30 could affect end resection indirectly by regulating gene transcription or by establishing an abnormal chromatin structure. The loss of Fun30 neither led to any major change in transcript accumulation of end-resection factors (Supplementary Fig. 5), nor affected nucleosome positioning at the *HIS3* locus used to monitor resection (Supplementary Fig. 6). Together, these results implicate Fun30 in directly promoting long-range resection at DSBs. This is further supported by the fact that acute loss of Fun30 led to a long-range resection defect at the I-SceI break induced at the *HIS3* locus (Supplementary Fig. 7). Interestingly, ChIP analysis of histone H3 and H2B occupancy around an HO-induced DSB at *MAT* showed that the loss of the histone ChIP signal is coupled to long-range resection in both wild-type and *fun30Δ* cells (Supplementary Figs 8 and 9)¹⁴. This indicates that Fun30 does not

facilitate long-range resection by modulating histone occupancy, but rather by increasing access to DNA within DSB-associated chromatin⁸. We next investigated the physiological role of the resection function of Fun30. Gene conversion at a single HO-induced DSB at *MAT* is normal in a *fun30Δ* mutant, both in the presence and absence of Sgs1 or Exo1 (data not shown). This shows that long-range resection is not essential for efficient gene conversion^{1,3}. We confirmed that the *fun30Δ* mutant is hypersensitive to the topoisomerase I inhibitor CPT, but not to the ribonucleotide reductase inhibitor hydroxyurea or ultraviolet light (Supplementary Fig. 10)⁹. Expression of wild-type, but not ATPase-deficient Fun30(K603R), restored CPT resistance in *fun30Δ* mutants (Supplementary Fig. 10a), indicating that resection driven by Fun30 ATPase activity protects cells against CPT-induced DNA damage. To show directly that the resection function of Fun30 is responsible for CPT resistance, we ectopically expressed Exo1 in a *fun30Δ* mutant. Expression of wild-type Exo1, but not the Exo1(D173A) nuclease-deficient mutant, suppressed both the resection defect and the CPT hypersensitivity of the *fun30Δ* mutant (Fig. 2e and Supplementary Fig. 11). This confirms that the resection function of Fun30 is required for the repair of CPT-induced DNA damage. Interestingly, the *fun30Δ exo1Δ* and *fun30Δ sgs1Δ* mutants are more sensitive to CPT, but not to hydroxyurea, than are the *fun30Δ*, *exo1Δ* and *sgs1Δ* mutants (Supplementary Fig. 10b), which corroborates their stronger resection defects. However, the combined absence of Fun30 and Sae2 led to a synergistic hypersensitivity to both CPT and hydroxyurea (Supplementary Fig. 10b), despite a resection defect that is comparable to that in the *fun30Δ* mutant (Fig. 2b), indicating that the roles of Fun30 and Sae2 in genome maintenance do not rely exclusively on facilitating resection¹⁵.

Resection mutants are known to affect the type of yeast survivors that form by different recombination mechanisms in the absence of



functional telomerase^{16,17}. Under liquid culture conditions, cells lacking the Est2 subunit of telomerase accumulate mostly type II survivors. However, we detected almost equal proportions of type I and type II survivors in a *fun30Δ est2Δ* mutant, similar to what is observed in other resection-defective mutants (*rad24Δ*, *rad17Δ* (ref. 17) and *exo1Δ* (ref. 16)) (Supplementary Fig. 12). Introduction of the *cdc13-1* mutation that induces the formation of long ssDNA tracts at telomeres¹⁸ suppresses the *fun30Δ est2Δ* phenotype as it suppresses the phenotype of a *rad17Δ est2Δ* mutant¹⁷. Therefore, Fun30 affects recombination at unprotected telomeres, probably because of its role in resection.

Figure 3 | SMARCAD1 promotes end resection, homologous recombination and cell survival after genotoxic insults in U2OS cells.

a, Immunodetection (top) and quantification (bottom right) of RPA foci 3 h after 6 Gy of ionizing radiation. Scale bar, 10 μm. Western blot analysis of SMARCAD1 in cells transfected with individual or pooled short interfering RNAs (siRNAs) (bottom left). Knockdown of *EXO1* serves as a control. Nuclei with more than ten RPA foci were scored. **b**, Western blot analysis of SMARCAD1 (left) and quantification of homologous recombination frequencies using a DR-GFP assay (right). **c**, Clonogenic survival of SMARCAD1 knockdown cells treated with CPT or the PARP inhibitor ABT-888. **d**, Immunofluorescence staining of SMARCAD1 and γH2AX at DSBs induced by mCherry-LacI-FokI (FokI WT) at a 256× Lac operator genomic array (top). Nuclease-deficient mCherry-LacI-FokI(D450A) was used as a control. Quantification of cells showing co-localization of SMARCAD1 and γH2AX at FokI-induced DSBs (bottom). Scale bar, 5 μm. **e**, Quantification of GFP-SMARCAD1, GFP-EXO1 and GFP-RPA accumulation at sites of laser micro-irradiation in live cells. DAPI, 4',6-diamidino-2-phenylindole; siScr, scrambled siRNA. Error bars denote s.e.m. (**a**, **b** and **d**) and ± s.e.m. (**c** and **e**) of three independent experiments for all plots in **a**, **b**, **c** and **e**.

SMARCAD1 is the human Snf2 family member that has the highest sequence similarity with Fun30. SMARCAD1 may function in the DNA-damage response because it is phosphorylated at canonical (Ser/Thr-Gln) ATM/ATR phosphorylation sites, as well as at non-canonical sites, in response to genotoxic insults^{19,20}. We examined whether SMARCAD1 also promotes DNA end resection. SMARCAD1 knockdown reduced the accumulation of RPA into ionizing radiation-induced foci (IRIF) (Fig. 3a), as well as that of green fluorescent protein (GFP)-tagged RPA at laser micro-irradiation-induced DSBs in U2OS cells²¹ (Supplementary Fig. 13a). Accordingly, we found that SMARCAD1 knockdown reduced ssDNA formation as determined by directly staining ssDNA-associated 5-bromo-2'-deoxyuridine (BrdU) IRIF (Supplementary Fig. 13b). These phenotypes are similar to those seen after knockdown of *EXO1*, a major resection enzyme in human cells²¹, indicating that the absence of SMARCAD1 impairs resection. In accord with a resection defect, we found that the loss of SMARCAD1 also impaired recombinational DSB repair. SMARCAD1 knockdown cells (1) were defective in the repair of an I-SceI-induced DSB by gene conversion in the direct-repeat (DR)-GFP reporter²² (Fig. 3b); (2) showed a major reduction in the repair of CPT-induced DSBs as monitored by the disappearance of TP53BP1 foci in S/G2 phase cells (Supplementary Fig. 13c); and (3) were hypersensitive to DNA damage resulting from CPT or poly(ADP-ribose) polymerase (PARP) inhibitor (ABT-888) treatments (Fig. 3c). In addition, SMARCAD1 co-localized with

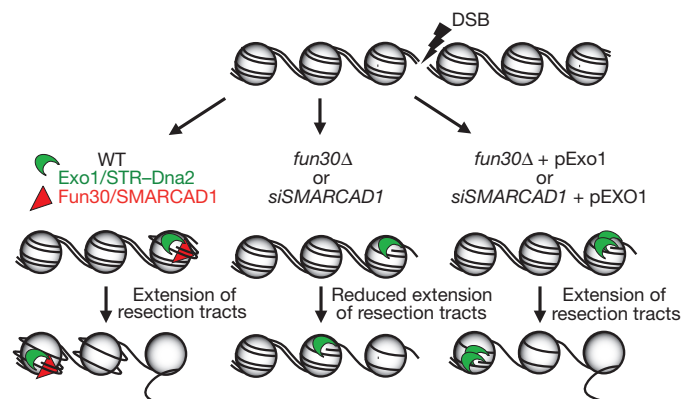


Figure 4 | Model for Fun30 and SMARCAD1 control of end resection through DSB-associated nucleosomes. Fun30 and SMARCAD1 weaken histone-DNA interactions in nucleosomes flanking DSBs, which facilitates ssDNA production by the Exo1- and Sgs1-Top3-Rmi1 (STR)-Dna2 resection machineries. In the absence of Fun30 and SMARCAD1, histone-DNA interactions limit the extent of resection, but plasmid-based overexpression of Exo1 (pExo1) or EXO1 (pEXO1) bypasses this impediment in yeast and U2OS cells, respectively.

γ H2AX at laser-induced DNA damage and at DNA breaks generated by the FokI nuclease (Fig. 3d and Supplementary Fig. 13d), demonstrating that SMARCAD1 is recruited to DSBs. Importantly, GFP-tagged SMARCAD1 was recruited to laser micro-irradiation-induced lesions before GFP-tagged RPA and with kinetics similar to that of GFP-tagged EXO1 (Fig. 3e)²¹, as expected for a factor that promotes resection. Finally, the defect in RPA IRIF formation in SMARCAD1-depleted cells could be partially rescued by overexpression of EXO1 (Supplementary Fig. 13e), indicating that SMARCAD1, like Fun30, has a direct role in DNA end resection and recombinational DSB repair.

Recent reports from budding yeast⁹, fission yeast²³ and human cells²⁴ have shown that the Fun30 or SMARCAD1 Snf2 family members have related roles in promoting heterochromatinization. We show that Fun30 and SMARCAD1 are new DNA-damage-response proteins that facilitate DNA end resection and DSB repair in chromatin (Fig. 4). Their precise modes of action and the extent of their functional conservation remain to be determined.

METHODS SUMMARY

The yeast strains used are derivatives of S288C, W303 and JKM179 (see Supplementary Table 2). Details of their construction are provided in Methods. The BIR genomic screen was adapted from ref. 25, except that pADW17 and pLS192 were used¹¹. Tag arrays were from C.-Y. Ho (Samuel Lunenfeld Research Institute, Toronto, Canada). The gap-repair assay used pSB110 (ref. 26), which contains an autonomous replication sequence but no centromere. Detection of ssDNA intermediates, SSA assays and ChIP experiments were performed as in refs 1 and 27. Transfection of U2OS cells, quantification of RPA foci after γ -irradiation, co-immunostaining for SMARCAD1 and γ H2AX after laser micro-irradiation, and live-cell imaging of GFP-tagged proteins to laser-induced breaks were carried out as described^{21,28}. SMARCAD1 localization studies at FokI-induced DSBs and DR-GFP assays were performed as previously reported^{22,29}. Survival of U2OS cells after CPT or ABT-888 treatment was quantified by the standard colony-formation assay.

Full Methods and any associated references are available in the online version of the paper.

Received 7 October 2011; accepted 28 June 2012.

Published online 9 September; corrected online 26 September 2012 (see full-text HTML version for details).

- Mimitou, E. P. & Symington, L. S. Sae2, Exo1 and Sgs1 collaborate in DNA double-strand break processing. *Nature* **455**, 770–774 (2008).
- Zhu, Z., Chung, W. H. S. h. i. m. E. Y., Lee, S. E. & Ira, G. Sgs1 helicase and two nucleases Dna2 and Exo1 resect DNA double-strand break ends. *Cell* **134**, 981–994 (2008).
- Gravel, S., Chapman, J. R., Magill, C. & Jackson, S. P. DNA helicases Sgs1 and BLM promote DNA double-strand break resection. *Genes Dev.* **22**, 2767–2772 (2008).
- Cejka, P. *et al.* DNA end resection by Dna2-Sgs1-RPA and its stimulation by Top3-Rmi1 and Mre11-Rad50-Xrs2. *Nature* **467**, 112–116 (2010).
- Nicolette, M. L. *et al.* Mre11–Rad50–Xrs2 and Sae2 promote 5' strand resection of DNA double-strand breaks. *Nature Struct. Mol. Biol.* **17**, 1478–1485 (2010).
- Niu, H. *et al.* Mechanism of the ATP-dependent DNA end-resection machinery from *Saccharomyces cerevisiae*. *Nature* **467**, 108–111 (2010).
- Sinha, M. & Peterson, C. L. Chromatin dynamics during repair of chromosomal DNA double-strand breaks. *Epigenomics* **1**, 371–385 (2009).
- Awad, S., Ryan, D., Prochasson, P., Owen-Hughes, T. & Hassan, A. H. The Snf2 homolog Fun30 acts as a homodimeric ATP-dependent chromatin-remodeling enzyme. *J. Biol. Chem.* **285**, 9477–9484 (2010).
- Neves-Costa, A., Will, W. R., Vetter, A. T., Miller, J. R. & Varga-Weisz, P. The SNF2-family member Fun30 promotes gene silencing in heterochromatic loci. *PLoS ONE* **4**, e8111 (2009).
- Ouspenski, I. I., Elledge, S. J. & Brinkley, B. R. New yeast genes important for chromosome integrity and segregation identified by dosage effects on genome stability. *Nucleic Acids Res.* **27**, 3001–3008 (1999).
- Marrero, V. A. & Symington, L. S. Extensive DNA end processing by Exo1 and Sgs1 inhibits break-induced replication. *PLoS Genet.* **6**, e1001007 (2010).
- White, C. I. & Haber, J. E. Intermediates of recombination during mating type switching in *Saccharomyces cerevisiae*. *EMBO J.* **9**, 663–673 (1990).
- Shim, E. Y. *et al.* *Saccharomyces cerevisiae* Mre11/Rad50/Xrs2 and Ku proteins regulate association of Exo1 and Dna2 with DNA breaks. *EMBO J.* **29**, 3370–3380 (2010).
- Chen, C. C. e. t. a. I. Acetylated lysine 56 on histone H3 drives chromatin assembly after repair and signals for the completion of repair. *Cell* **134**, 231–243 (2008).

- Clerici, M., Mantiero, D., Lucchini, G. & Longhese, M. P. The *Saccharomyces cerevisiae* Sae2 protein negatively regulates DNA damage checkpoint signalling. *EMBO Rep.* **7**, 212–218 (2006).
- Zubko, M. K. Exo1 and Rad24 differentially regulate generation of ssDNA at telomeres of *Saccharomyces cerevisiae* cdc13–1 mutants. *Genetics* **168**, 103–115 (2004).
- Grandin, N. & Charbonneau, M. Control of the yeast telomeric senescence survival pathways of recombination by the Mec1 and Mec3 DNA damage sensors and RPA. *Nucleic Acids Res.* **35**, 822–838 (2007).
- Garvik, B., Carson, M. & Hartwell, L. Single-stranded DNA arising at telomeres in cdc13 mutants may constitute a specific signal for the RAD9 checkpoint. *Mol. Cell. Biol.* **15**, 6128–6138 (1995).
- Matsuoka, S. *et al.* ATM and ATR substrate analysis reveals extensive protein networks responsive to DNA damage. *Science* **316**, 1160–1166 (2007).
- Beli, P. *et al.* Proteomic investigations reveal a role for RNA processing factor THRAP3 in the DNA damage response. *Mol. Cell* **46**, 212–225 (2012).
- Tomimatsu, N. *et al.* Exo1 plays a major role in DNA end resection in humans and influences double-strand break repair and damage signaling decisions. *DNA Repair* **11**, 441–448 (2012).
- Bolderson, E. *et al.* Phosphorylation of Exo1 modulates homologous recombination repair of DNA double-strand breaks. *Nucleic Acids Res.* **38**, 1821–1831 (2010).
- Strålfors, A., Walfridsson, J., Bhuiyan, H. & Ekwall, K. The FUN30 chromatin remodeler, Fft3, protects centromeric and subtelomeric domains from euchromatin formation. *PLoS Genet.* **7**, e1001334 (2011).
- Rowbotham, S. P. *et al.* Maintenance of silent chromatin through replication requires SWI/SNF-like chromatin remodeler SMARCAD1. *Mol. Cell* **42**, 285–296 (2011).
- Ooi, S. L., Shoemaker, D. D. & Boeke, J. D. DNA microarray-based genetic screen for nonhomologous end-joining mutants in *Saccharomyces cerevisiae*. *Science* **294**, 2552–2556 (2001).
- Bärtisch, S., Kang, L. E. & Symington, L. S. RAD51 is required for the repair of plasmid double-stranded DNA gaps from either plasmid or chromosomal templates. *Mol. Cell. Biol.* **20**, 1194–1205 (2000).
- van Attikum, H., Fritsch, O. & Gasser, S. M. Distinct roles for SWR1 and INO80 chromatin remodeling complexes at chromosomal double-strand breaks. *EMBO J.* **26**, 4113–4125 (2007).
- Tomimatsu, N., Mukherjee, B. & Burma, S. Distinct roles of ATR and DNA-PKcs in triggering DNA damage responses in ATM-deficient cells. *EMBO Rep.* **10**, 629–635 (2009).
- Shanbhag, N. M., Rafalska-Metcalf, I. U., Balane-Bolivar, C., Janicki, S. M. & Greenberg, R. A. ATM-dependent chromatin changes silence transcription in cis to DNA double-strand breaks. *Cell* **141**, 970–981 (2010).

Supplementary Information is linked to the online version of the paper at www.nature.com/nature.

Acknowledgements We thank G. Ira for sharing unpublished data and S. Janicki, R. Greenberg, L. Symington and all the laboratories from the Centre National de la Recherche Scientifique (CNRS) UPR3081 for providing reagents. We thank S. Coulon for help in the analysis of the *fun30* repressible allele, I. Lafontaine for support in statistical analyses, C. V. Camacho for generating the V5-EXO1 constructs and A. Guénolé, R. Srivas, T. Ideker, K. Vreeken and M. Vermeulen for help in searching for Fun30 interactors. B.L. is grateful to B. Dujon for hosting him and providing the opportunity to perform the BIR screen. S.B. is supported by grants from the National Institutes of Health (R01 CA149461), National Aeronautics and Space Administration (NNX10AE08G) and the Cancer Prevention and Research Institute of Texas (RP100644). H.v.A. receives funding from the Netherlands Organization for Scientific Research (NWO-VIDI grant) and Human Frontiers Science Program (HFSP-CDA grant). B.L. is supported by grants from the CNRS (ATIP) and the Agence Nationale de la Recherche (ANR-10-BLAN-1606-03).

Author Contributions B.L. and A.T. performed the genetic screen and B.L. identified the resection defect of *fun30Δ*. T.C. constructed yeast strains and plasmids and performed the yeast ChIP experiments. R.L. constructed yeast strains and performed ssDNA analysis by alkaline gels, BIR and gap-repair assays. R.L. and T.C. analysed SSA defects. N.T. and B.M. performed all of the SMARCAD1 knockdown experiments in human cells and the DR-GFP assays. E.M. designed and built the strain containing the inducible I-SceI cut site at *HIS3*, performed the micrococcal nuclease assay and contributed to data analysis. B.K. performed the analysis of survivors in the absence of telomerase. K.D. assisted R.L. and K.D., R.L. and T.C. performed *fun30* DNA-damage-sensitivity assays. W.W.W. examined the localization of SMARCAD1 at FokI-induced DSBs. T.C., S.B., H.v.A. and B.L. designed the experiments and analysed the data. H.v.A. and B.L. wrote the manuscript.

Author Information Microarray data have been deposited in the NCBI Gene Expression Omnibus and are accessible through accession numbers GSE38715 (BIR screen) and GSE38735 (*fun30Δ* transcriptome). Reprints and permissions information is available at www.nature.com/reprints. The authors declare no competing financial interests. Readers are welcome to comment on the online version of the paper. Correspondence and requests for materials should be addressed to B.L. (bllorente@ifr88.cnrs-mrs.fr) or H.v.A. (h.van.attikum@lumc.nl).

METHODS

Yeast strains and plasmids. The yeast strains used are derivatives of S288C, W303 and JKM179 and are listed in Supplementary Table 2. Details of the primers used for gene disruption and confirmation are available on request. *FUN30* was disrupted by one-step gene replacement using the *hphNT1*, *KanMX4* or *13MYC::KanMX4* cassettes³⁰. Using such a strategy, BLY187 and BLY188 were obtained from LSY1709-9D, BLY185 and BLY186 from LSY1709-4A, BLY189 from LSY1983-16B, BLY031 from BY4741, BLY033 from BY4742, BLK020 from W303, BLY137 from EM111, yHA629 from JKM179 and yHA630 from JKM179. *SAE2* was disrupted by one-step gene replacement using the *HIS3MX6* cassette to generate BLY195 and BLY196 from LSY1709-9D, and to generate BLY197 and BLY198 from BLY187. *rad51Δ* yeast strains used for CPT- and hydroxyurea-sensitivity assays in Supplementary Fig. 10b are of the W303 background and were obtained by crossing the corresponding *rad51Δ* mutants with the parental W303 reference strain.

Yeast strains used for the analysis of survivors in the absence of telomerase were built as follows: MNS961 was crossed with BLK020, the resulting diploid was grown on non-selective medium to lose pSD196 and obtain BLK018, and senescence was analysed on BLK018 ascospores. To perform these experiments in the presence of the *cdc13-1* mutation, YE1553 was crossed with MNS961 and the resulting diploid was sporulated to obtain BLK029. YE1552 was crossed with BLK020 and the resulting diploid was sporulated to obtain BLK026. BLK029 was eventually crossed with BLK026 and grown on non-selective medium to lose pSD196 and to obtain BLK033. Senescence was analysed on BLK033 ascospores. *cdc13-1* cells were grown at 25 °C, and the presence of the *cdc13-1* mutation was followed by its thermosensitivity at 30 °C. Senescence was analysed as described in the Supplementary Fig. 12 legend.

EM111 was built as follows: the 5'-ACATAATGAATTATACAT-3' sequence upstream of the regulated TATA box of *HIS3* from the JKM139 strain was replaced by the 5'-TAGGGATAACAGGTAAT-3' sequence containing the I-SceI cleavage site. This modified *HIS3* locus was then used to replace the *HIS3* locus from Lev488 (ref. 31), a W303 derivative strain containing the *lys2::PGAL-I-SceI* cassette.

A plasmid containing the wild-type *Fun30*-coding gene was generated by introducing a 4.5 kb *SpeI/NotI* fragment containing *FUN30* into pRS316. An ATPase-deficient version of the *Fun30*-coding gene, which contains a point mutation in the ATPase domain that replaces a lysine with an arginine at position 603 (*Fun30*(K603R)), was introduced by site-directed mutagenesis and confirmed by sequencing.

Exo1- and Exo1(D173A)-overexpressing plasmids are pSM502 and pSM638, respectively, described in ref. 32.

Media, growth conditions and genetic methods. Media, growth conditions and genetic methods are as described previously in ref. 33. Galactose induction of HO or I-SceI was performed as follows: one colony was grown overnight at 30 °C in either yeast extract peptone dextrose (YPD) or synthetic complete (SC) media. The next day cells were diluted and grown for about 8 h using the same media to mid-log phase. Cells were washed with water and grown overnight in YPLG (1% yeast extract, 2% peptone, 2% lactic acid, 3% glycerol, 0.05% glucose) or SC media, as indicated, to mid-log phase. HO or I-SceI expression was induced by adding 2% galactose, and switched off by adding 2% glucose. Note that HO expression in strains from the W303 background was driven from the centromeric plasmid pGAL:HO³⁴.

BIR genomic screen. Details of the screen are given in the Supplementary Fig. 1 legend. The pool of homozygous diploid null mutants was preferred instead of the pool of haploid null mutants because, in principle, the genetic quality of the diploid deletion strain is higher²⁵. Two independent experiments were carried out, each one included one transformation with circular pADW17 and one transformation with pLS192 linearized with *SnaBI* (Supplementary Table 3). For each mutant and for each experiment, the median of the normalized hybridization values of the different up-tag and down-tag spots was calculated³⁵. The mean absolute deviation from the two experiments is given in Fig. 1. Transformation ratios corresponding to BIR efficiencies were derived by dividing the median hybridization signal from the linear mini-chromosome pLS192 by that of the circular mini-chromosome pADW17 (Supplementary Table 1). The BIR defect of each mutant was confirmed by one or two individual transformations, and at least four individual transformations were performed for wild-type diploid, *sgs1Δ* and *fun30Δ*.

Alkaline electrophoresis. ssDNA intermediates were analysed by alkaline gel electrophoresis as described¹², and the blots were hybridized with double-stranded probes obtained by PCR. The coordinates of the *MAT* probe are 201176–201570 on chromosome 3, and the coordinates of the *HIS3* probe are 722025–722227 on chromosome 15.

ChIP. ChIP was performed as previously described²⁷. In brief, cells were grown overnight in YPAD, diluted in YPLG and grown to mid-log phase. Glucose was added to a fraction of the cells to repress HO, whereas galactose was added to the remainder of the cells to induce HO. Cells were fixed using formaldehyde and collected at 0, 1, 2, 4 and 6 h after galactose addition (cells grown in the presence of

glucose were collected at the 2-h time point). Extracts were prepared and subjected to ChIP using the following antibodies: anti-Myc (9B11; Cell Signaling Technology), rabbit anti-RPA (Agrisera) and rabbit anti-histone H2B or H3 (Abcam). An aliquot of each extract was not immunoprecipitated and served as input. Input and immunoprecipitated DNA were purified and analysed by quantitative PCR. Absolute fold enrichment for RPA or *Fun30*-Myc at the HO DSB was calculated as follows: for each time point, the signal from a site near the HO DSB at the *MAT* locus was normalized to that from the non-cleaved *SMC2* locus in ChIP and input DNA samples. For each time point and site, the normalized ChIP signals were normalized to the normalized input DNA signals, because end resection can reduce the available DNA template. Finally, relative-fold enrichment was calculated by dividing the absolute-fold enrichment from induced cells to that of uninduced cells.

DNA end resection and loss of histone H2B and H3 ChIP signals were calculated as follows: to measure end resection using input DNA from ChIP experiments, the input DNA value for each site near the DSB was normalized to that of the input DNA value from the non-cleaved *SMC2* locus. The ratios obtained for each time point after HO induction were normalized to that in uninduced cells. Similarly, to determine the loss of H2B and H3 ChIP signal, the ChIP value for each site near the DSB was normalized to that of the ChIP value from the non-cleaved *SMC2* locus. The ratios obtained for each time point after HO induction were normalized to that in uninduced cells. ChIP results are presented as the mean of at least two experiments \pm s.e.m.

Micrococcal nuclease digestion of chromatin. Micrococcal nuclease digestion of chromatin was performed as described in ref. 36. After purification, the DNA was digested by *HindIII* to show nucleosome positioning by indirect end-labelling. The *HIS3* proximal probe used for Southern blot hybridization is the same as for alkaline electrophoresis experiments. The coordinates of the *DED1* proximal probe are 722441–722809 on chromosome 15. Coordinates of the *NOC2* proximal probe are 727786–728097 on chromosome 15.

Irradiation of U2OS cells, *SMARCA1* knockdown, immunofluorescence staining and live-cell imaging. U2OS cells were irradiated with γ -rays from a caesium source (J.L. Shepherd & Associates) or were micro-irradiated with a pulsed nitrogen laser (Spectra-Physics; 365 nm, 10 Hz) with output set at 75% of the maximum, as described in ref. 28. *SMARCA1* was depleted using siRNA1 5'-AGGAUGCAUCUUGUCUGAAUUGAAA-3', siRNA2 5'-GGGACGAUUGAAGAAUCCAUGCUGAA-3' and siRNA3 5'-GAGAUGUAGUUAUAGGCUUAUGAA-3'. *EXO1* was depleted using siRNA1 5'-UGCCUUUGCUAAUCCAAUCCACGC-3', siRNA2 5'-UAGUGUUUACGGAUCCAAUCCUUCU-3' and siRNA3 5'-UUUGUUAGUAGGUCAUUUACCAGG-3'. The efficiency of knockdown for every experiment was verified by western blotting as described in ref. 28; cells transfected with scrambled siRNA (Invitrogen) served as controls. Immunofluorescence staining for γ H2AX and *SMARCA1* accumulation after laser irradiation or FokI expression, or for RPA or TP53BP1 foci after γ -irradiation was carried out as described previously in ref. 28. For demarcating cells in S/G2 phase, nuclei were co-immunostained with anti-cyclin A antibody²⁷. Quantification of foci was done as described in ref. 22. The following antibodies were used for immunofluorescence staining or western blotting: RPA (Abcam), *SMARCA1* (Bethyl Laboratories), *EXO1* (Thermo Fisher), cyclin A, TP53BP1 (Santa Cruz Biotechnology), actin (Sigma) and γ H2AX (Upstate Biotechnology). For live-cell imaging combined with laser micro-irradiation, U2OS cells were transfected with GFP-RPA³⁸, GFP-*EXO1* (ref. 21) or GFP-*SMARCA1* (OriGene), laser micro-irradiated and time-lapse imaged, and fluorescence intensities of micro-irradiated areas relative to non-irradiated areas calculated as described previously in ref. 21. To stain for BrdU and ssDNA foci, U2OS cells were grown in the presence of 10 μ M BrdU (Sigma) for 16 h, irradiated with 10 Gy of γ -rays, fixed at the indicated times and immunofluorescence-stained with an anti-BrdU antibody (BD Biosciences) under non-denaturing conditions to detect BrdU incorporated into ssDNA, as described in ref. 21. For ectopic expression of *EXO1* in U2OS cells, the gene coding for the b isoform of *EXO1* was sequentially cloned into pLenti6.3/V5-DEST by BP and LR clonase reactions (Invitrogen) using pEGFP-C1-*Exo1b*²² as a template. The final vector, pLenti6.3/*Exo1b*-V5/DEST, was confirmed by sequencing. The accumulation of *SMARCA1* at FokI-induced DSBs was monitored in U2OS cells containing 256 Lac operator repeats integrated into the genome as described in ref. 29. Vectors expressing wild-type mCherry-LacI-FokI or nuclease-deficient mCherry-LacI-FokI(D450A) were transfected into these cells, and 24 h later the cells were immunostained for *SMARCA1* and γ H2AX.

30. Janke, C. *et al.* A versatile toolbox for PCR-based tagging of yeast genes: new fluorescent proteins, more markers and promoter substitution cassettes. *Yeast* **21**, 947–962 (2004).

31. Pardo, B., Ma, E. & Marcand, S. Mismatch tolerance by DNA polymerase Pol4 in the course of nonhomologous end joining in *Saccharomyces cerevisiae*. *Genetics* **172**, 2689–2694 (2006).

32. Moreau, S., Morgan, E. A. & Symington, L. S. Overlapping functions of the *Saccharomyces cerevisiae* Mre11, Exo1 and Rad27 nucleases in DNA metabolism. *Genetics* **159**, 1423–1433 (2001).
33. Burke, D. & Strathern, J. in *Methods in Yeast Genetics: a Cold Spring Harbor Laboratory Course Manual* (eds Amberg, D. C., Burke, D. & Strathern, J. N.) (2005).
34. Herskowitz, I. & Jensen, R. E. Putting the HO gene to work: practical uses for mating-type switching. *Methods Enzymol.* **194**, 132–146 (1991).
35. Decourty, L. *et al.* Linking functionally related genes by sensitive and quantitative characterization of genetic interaction profiles. *Proc. Natl Acad. Sci. USA* **105**, 5821–5826 (2008).
36. Martini, E. M. D., Keeney, S. & Osley, M. A. A role for histone H2B during repair of UV-induced DNA damage in *Saccharomyces cerevisiae*. *Genetics* **160**, 1375–1387 (2002).
37. Bekker-Jensen, S. *et al.* Spatial organization of the mammalian genome surveillance machinery in response to DNA strand breaks. *J. Cell Biol.* **173**, 195–206 (2006).
38. Sporbert, A., Gahl, A., Ankerhold, R., Leonhardt, H. & Cardoso, M. C. DNA polymerase clamp shows little turnover at established replication sites but sequential *de novo* assembly at adjacent origin clusters. *Mol. Cell* **10**, 1355–1365 (2002).

Interaction landscape of membrane–protein complexes in *Saccharomyces cerevisiae*

Mohan Babu^{1,2*}, James Vlasblom^{3,4*}, Shuye Pu³, Xinghua Guo¹, Chris Graham¹, Björn D. M. Bean⁵, Helen E. Burston⁵, Franco J. Vizeacoumar¹, Jamie Snider¹, Sadhna Phanse¹, Vincent Fong¹, Yuen Yi C. Tam⁵, Michael Davey⁵, Olha Hnatshak¹, Navgeet Bajaj¹, Shamanta Chandran¹, Thanuja Punna¹, Constantine Christopoulos¹, Victoria Wong¹, Analyn Yu¹, Gouqing Zhong¹, Joyce Li¹, Igor Stagljar^{1,4,6}, Elizabeth Conibear⁵, Shoshana J. Wodak^{3,4,6}, Andrew Emili^{1,6} & Jack F. Greenblatt^{1,6}

Macromolecular assemblies involving membrane proteins (MPs) serve vital biological roles and are prime drug targets in a variety of diseases¹. Large-scale affinity purification studies of soluble-protein complexes have been accomplished for diverse model organisms, but no global characterization of MP-complex membership has been described so far. Here we report a complete survey of 1,590 putative integral, peripheral and lipid-anchored MPs from *Saccharomyces cerevisiae*, which were affinity purified in the presence of non-denaturing detergents. The identities of the co-purifying proteins were determined by tandem mass spectrometry and subsequently used to derive a high-confidence physical interaction map encompassing 1,726 membrane protein–protein interactions and 501 putative heteromeric complexes associated with the various cellular membrane systems. Our analysis reveals unexpected physical associations underlying the membrane biology of eukaryotes and delineates the global topological landscape of the membrane interactome.

Various experimental methods have been used to examine protein–protein interactions (PPIs) among MPs^{2–4}, but integral and lipid-anchored MPs are still notably under-represented in public interaction databases⁵. In contrast to the success of tandem affinity purification (TAP) procedures for characterizing soluble-protein complexes in yeast^{6,7}, native MP complexes are more difficult to purify owing to their hydrophobic nature¹. We therefore developed alternative TAP extraction and affinity isolation procedures, using buffers containing one of three different mild, non-denaturing detergents optimized for MP solubilization. Based on pilot studies, we selected Triton X-100, DDM (n-dodecyl- β -D-maltopyranoside), and C12E8 (octaethylene glycol monododecyl ether), as these were most effective and extracted complementary sets of yeast MPs (Supplementary Fig. 1a–c and Supplementary Text). For proteome-wide analysis, we used yeast strains bearing MP fusions with a carboxy-terminal chromosomal tag expressed at endogenous levels from native promoters⁸. The tagged MPs and stably associated proteins were purified essentially as described previously⁹, except that all steps were carried out in the presence of one of the three detergents.

Based on existing database annotations, transmembrane helix (TMH) predictions, subcellular localization, literature curation and other information sources (Supplementary Fig. 1d and Supplementary Table 1), we compiled a target list that encompassed 2,141 annotated or predicted MPs (Fig. 1a and Supplementary Table 2), of which 1,590 were tagged and processed (Supplementary Fig. 2a). These included 1,144 putative integral, 400 peripheral and 46 lipid-anchored MPs. Detection coverage ranged from approximately 81% for low abundance MPs ($<10^3$ molecules per cell) to approximately 94% for high-abundance proteins ($>10^4$ molecules per cell) (Supplementary Fig. 2b)⁸.

We did not attempt to purify 551 open reading frames (ORFs) because they were not detectably expressed⁸ or the growth of the tagged strains was impaired (Supplementary Table 2), although a substantial fraction ($\sim 66\%$; 362 of 551) were subsequently detected as interacting ‘preys’ in successful bait purifications.

The overall target recovery rates were comparable for each detergent ($\sim 50\%$), and we successfully purified 77% (1,228 out of 1,590) of the tagged MPs (Fig. 1b). In addition to bait abundance, success depended on the cellular compartment (Fig. 1c) and TMH number of each MP (Fig. 1d). The highest coverage was obtained for those MPs associated with the Golgi, endoplasmic reticulum or mitochondria with fewer than four TMH ($\sim 80\%$), whereas MPs associated with the bud neck or possessing ≥ 10 TMH had lower success ($\sim 70\%$). Nevertheless, we were successful in purifying baits harbouring characteristic membrane-associated Pfam domains such as the ABC transporter, SNARE (soluble NSF attachment protein receptor) and PX domains ($>90\%$ success; Supplementary Fig. 2c and Supplementary Table 3).

To assign confidence scores, the observed physical associations, including non-MPs, were first ranked using the purification enrichment score¹⁰, and then integrated with purification enrichment scores computed from published yeast TAP mass spectrometry (TAP-MS) surveys of soluble proteins^{6,7} to describe the cytoplasmic interface of membrane systems better. To optimize accuracy and coverage (Supplementary Text), we built a high-confidence ‘integrated network’ with the same precision (that is, a reference benchmark true positive to false positive ratio of approximately 22:1) as that of a highly accurate yeast soluble-protein interaction map (Supplementary Fig. 2a)¹¹.

The integrated network consists of 13,343 high-confidence associations among 2,875 proteins (Supplementary Table 4), representing two-thirds of the yeast proteome detectable by mass spectrometry¹². Notably, 6,082 of these PPIs are directly supported by the purification data described here and, for 1,726 PPIs involving at least one of 905 putative MPs (Supplementary Table 4), two-thirds (64%; 1,110 out of 1,726) have not been reported previously (Fig. 1e and Supplementary Fig. 2d). For example, we identified putative binding partners for 20 plasma membrane proteins with previously unreported interactions, including orthologues¹³ of 8 human therapeutic targets (Supplementary Table 5).

On average, the MPs have approximately half the number of interaction partners as yeast soluble proteins (geometric mean ~ 2.1 versus ~ 4.7 ; Supplementary Fig. 2e, f), possibly owing in part to partial detergent-induced dissociation. As with soluble proteins⁷, essential, highly expressed and evolutionarily conserved MPs exhibit greater connectivity (Supplementary Fig. 2g, h), particularly components of the bud, cortex and Golgi (mean connectivity of ≥ 2.8).

¹Banting and Best Department of Medical Research, Donnelly Centre, 160 College Street, University of Toronto, Toronto, Ontario M5S 3E1, Canada. ²Department of Biochemistry, Research and Innovation Centre, 3737 Wascana Parkway, University of Regina, Regina, Saskatchewan S4S 0A2, Canada. ³Hospital for Sick Children, 555 University Avenue, Toronto, Ontario M5G 1X8, Canada. ⁴Department of Biochemistry, 1 King's College Circle, Medical Science Building, University of Toronto, Toronto, Ontario M5S 1A8, Canada. ⁵Centre for Molecular Medicine and Therapeutics, Child and Family Research Institute, 950 West 28th Avenue, University of British Columbia, Vancouver, British Columbia V5Z 4H4, Canada. ⁶Department of Molecular Genetics, 1 King's College Circle, Medical Science Building, University of Toronto, Toronto, Ontario M5S 1A8, Canada.

*These authors contributed equally to this work.

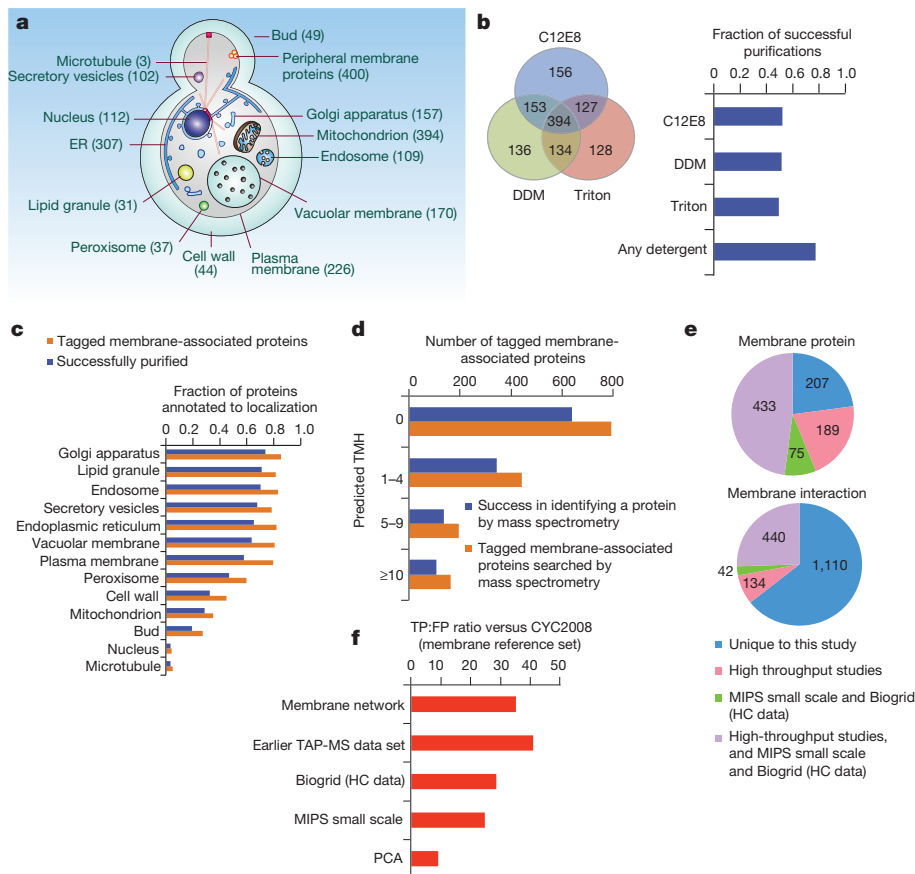


Figure 1 | Proteome-wide purification of yeast MPs. **a**, Yeast membrane compartments. Numbers indicate MPs (listed in Supplementary Table 2) whose purification was attempted. **b**, Overlap of tagged bait proteins identified by mass spectrometry after purification in three different detergents (left panel), and the proportion of successful bait recovery (right panel). **c**, Fraction of tagged and successfully purified MPs according to simplified Gene Ontology consortium cellular-component annotations. **d**, Number of tagged and purified yeast MPs according to TMH number. **e**, Overlap of MPs (top panel) and their interactions (bottom panel) in the MP sub-network, compared to previous high-throughput

Independent criteria support the reliability of the integrated and MP interaction networks, and the quality of the underpinning data. First, benchmarking against a reference set of PPIs derived from MPs in the CYC2008 catalogue of manually curated protein complexes¹¹ showed that the accuracy of the MP interactions was comparable to, or higher than, published small-scale experiments^{14,15}, protein-fragment complementation assay (PCA)³ and large-scale yeast PPI networks derived for soluble proteins in past TAP surveys^{6,7} (Fig. 1f). Second, we observed significant enrichment ($P < 0.05$) for interactions between MPs in the same, or related, subcellular compartments (Supplementary Fig. 3a and Supplementary Table 6). Third, the average semantic similarity of the Gene Ontology consortium annotations of the interacting proteins in the MP network (Supplementary Fig. 3b) was comparable to or higher than that obtained for several previous high-confidence PPI networks^{2,3,16}, although slightly lower than that obtained for soluble protein TAP¹⁷ or literature curation^{14,15}, probably reflecting the less complete annotations of MPs in general. Finally, we compared our integrated network with genetic interaction data derived for yeast membrane^{18,19} and non-membrane^{4,20} biological systems (Supplementary Text). We found significant enrichment ($P < 10^{-9}$) for highly correlated genetic interaction profiles between pairs of physically interacting proteins compared to random pairs (Supplementary Fig. 3c). Collectively, these results suggest that our high-confidence PPI are of similarly high quality as the most reliable soluble yeast interactome data sets published so far^{6,7,10,17}.

studies^{2,3,16,17} and high-confidence (HC) literature PPI from the MIPS (Munich Information Center for Protein Sequences) and BioGRID (Biological General Repository for Interaction Datasets) databases^{14,15}. **f**, Average true positive: false positive (TP:FP) ratio of this study (MP sub-network) versus an earlier TAP-MS-derived soluble yeast protein data set¹⁷, literature curated interactions^{14,15}, and a PCA yeast interactome study³, as measured against a random reference membrane PPI set (CYC2008 complex catalogue)¹¹. Note that the actual TP:FP ratio depends on the definition of the reference set and is given here only to compare data sets. ER, endoplasmic reticulum.

To deduce the membership of MP complexes, we used the Markov clustering algorithm²¹ to partition the integrated network into densely connected subgroups of interacting proteins, allowing for component sharing between clusters¹⁷ (Supplementary Text). In total, we identified 720 clusters representing putative multi-protein complexes (Supplementary Table 7 and Supplementary Fig. 3d), of which most (501) contain at least one MP (Fig. 2 and Supplementary Table 7). Many (99) of the 264 predicted heterodimeric MP-containing complexes consisted of only uncharacterized proteins or one uncharacterized factor with an annotated MP (Supplementary Table 7), which most commonly contained Pfam domains related to the cell wall or intracellular signalling (Supplementary Table 8).

Overlap between these clusters and the CYC2008 complex catalogue showed that of the curated yeast complexes containing an MP, 40% (67 out of 167) had 90% or more subunits matching a cluster, whereas only approximately 7% (12 out of 167) of known MP complexes were missed by our study, presumably indicating limitations of our isolation procedures (Supplementary Fig. 3e). Conversely, 280 of our predicted MP clusters had limited overlap (<5% of the components) with CYC2008 complexes (Supplementary Fig. 3f), representing a rich resource for biological discovery. Unexpected connections were uncovered that suggest new roles even for well-characterized MPs, such as the association between Tor2 and Vps8 (Supplementary Fig. 4j) that may mediate TOR signalling at endosomes²². Likewise, our study provides additional support for proteasome engagement with

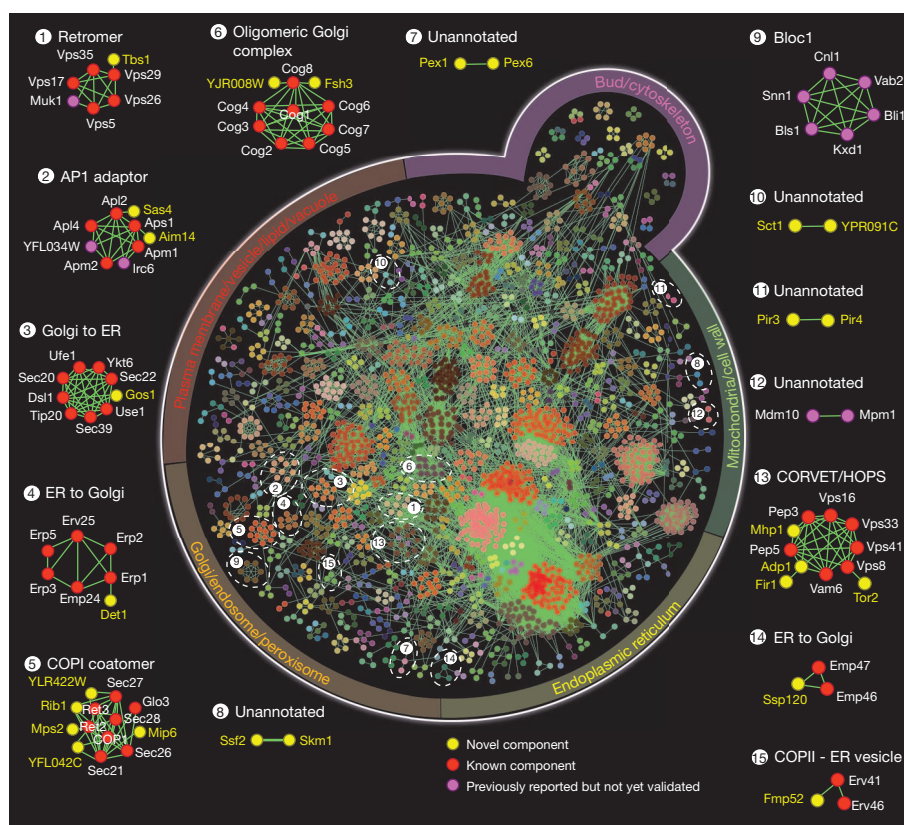


Figure 2 | Global organization of yeast MP complexes. Predicted MP clusters (subunits shown as similarly coloured nodes) inferred from the integrated network of high-confidence PPI (edges), demarcated according to primary compartment annotations. Representative complexes at the periphery highlight some of the findings of our study, including novel complexes and

known complexes with new components. Our purifications were most successful for MPs localized to the Golgi and endoplasmic reticulum, a bias reflected in the highlighted examples. For each complex, previously reported components (red nodes), novel subunits (yellow nodes) and previously reported but not yet validated interactors (pink nodes) are displayed.

organelles through the membrane fusion factor SEC18 (Supplementary Text and Supplementary Fig. 5a–c).

We independently evaluated 21 interactions involving MP components by co-immunoprecipitation and/or iMYTH²³ (integrated membrane yeast two-hybrid) assays and confirmed >90% (19 out of 21) (Fig. 2 and Supplementary Fig. 4a–k). For example, we validated the interaction of PIR (proteins with internal repeat) domain-containing envelope proteins Pir3 and Pir4 (Supplementary Fig. 4i), and the association of Sct1, an integral membrane acyltransferase involved in glycerolipid biosynthesis, and the uncharacterized integral MP YPR091C, which localizes to the endoplasmic reticulum (Supplementary Fig. 4h).

As complex subunits should exert a consistent biological role, we next used high-content fluorescence screening of mutant strains to systematically investigate the phenotypic consequences of deleting individual components of 26 different MP complexes (Supplementary Fig. 6a and Supplementary Table 9). Based on the patterns of compartment-specific fluorescent markers, subunit loss typically resulted in a discernible and consistent phenotype for most (20 out of 26) of the predicted complexes tested (representative data shown in Supplementary Fig. 6; see Supplementary Table 9 and Supplementary Text).

The association of 321 functionally uncharacterized proteins with putative MP complexes provides insight into their possible cellular roles (Supplementary Table 10), demonstrated by the identification of Irc6 as a binding partner of the heterotetrameric AP1 clathrin adaptor complex (Fig. 3a). AP1 is peripherally associated with Golgi and endosomal membranes, where it incorporates cargo proteins like Sna2 and chitin synthase Chs3 into clathrin-coated vesicles²⁴. As with loss of the AP1 subunit Apm1, we found that loss of Irc6 increased

cell-surface missorting of Chs3 and Sna2 (Fig. 3b–e). Irc6 is homologous to mammalian p34, which associates with soluble AP1 adaptors in human cells but has not been characterized in detail²⁵. Consistent with this, an Irc6–GFP (green fluorescent protein) fusion localizes to the cytosol (data not shown) and shows sub-stoichiometric binding to AP1 by co-immunoprecipitation (Fig. 3f). Although many AP1 regulators recognize the γ -adaptin (Apl4) appendage domain, yeast two-hybrid assays indicated that Irc6 interacts with the core domain of Apl4 and with a subunit of the AP2 complex (Fig. 3g), suggesting a wider role in regulating clathrin adaptors. Interestingly, the amino-terminal conserved domain of Irc6 (Fig. 3h), which is necessary and sufficient for the interaction with AP1 (Fig. 3i), has a predicted fold similar to that of regulatory Rab-like GTPases²⁶. These data suggest Irc6 is a conserved, functionally important AP1 interacting protein.

A second example is the interaction of the uncharacterized protein Ssp120 with the annotated MPs Emp46 and Emp47, which facilitate secretion by sorting cargo proteins into endoplasmic-reticulum-derived COPII-coated vesicles²⁷ (Fig. 4a). Ssp120 lacks a transmembrane domain but contains a signal sequence mediating endoplasmic reticulum translocation²⁸ and, like Emp47, localizes to early Golgi in wild-type yeast⁸. Ssp120 is missorted to the vacuole in *emp47* (but not *emp46*) mutants (Fig. 4b) and is secreted after additional deletion of Vps10, a receptor that directs vacuolar transport at the late Golgi (Fig. 4c). Ssp120 has a domain structure similar to human MCFD2 (Fig. 4d), which binds the mammalian Emp46 and Emp47 homologue LMAN1 and is a cargo-specific adaptor for secretion of the blood coagulation factors V and VIII. Mutations in LMAN1 or MCFD2 cause the bleeding disorder F5F8D, or combined factor V and factor VIII deficiency²⁹. Intriguingly, the C-terminal region but not the EF-hand motifs of Ssp120 (Fig. 4d) are important both for Golgi localization

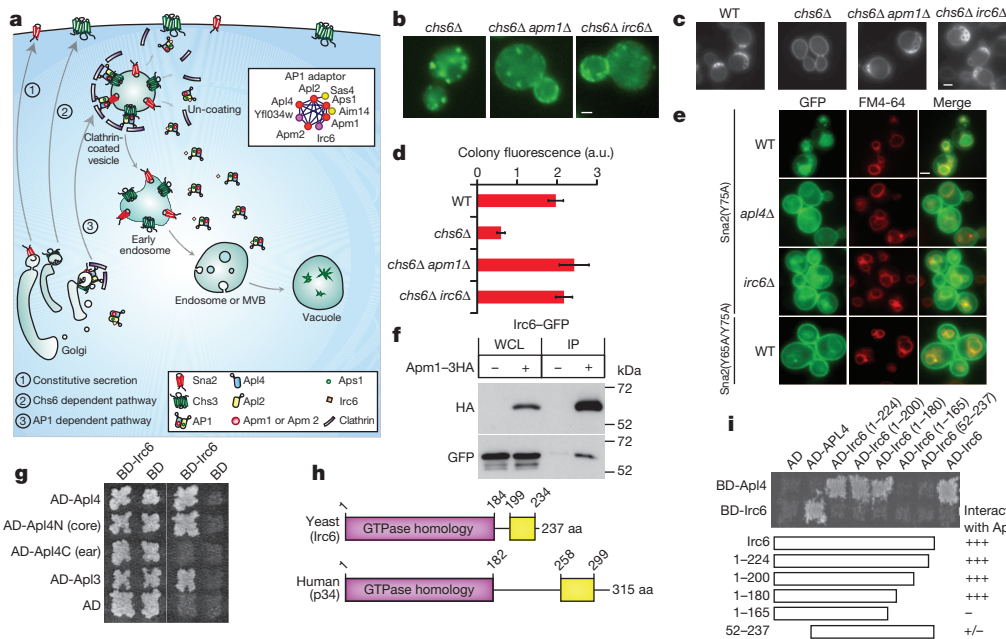


Figure 3 | Functional association of Irc6 with AP1. **a**, Model illustrating AP1 dependent incorporation of Chs3 and Sna2 into clathrin-coated vesicles at Golgi and endosomal compartments. Inset indicates subunit associations of the AP1 complex. MVB, multivesicular body. **b**, Fluorescence microscopy of Chs3-GFP. Mutation of AP1 (Apm1) or Irc6 in *chs6* mutants restores Chs3-dependent chitin ring formation. **d**, Quantification of chitin production. The graph shows the average colony fluorescence (arbitrary units, a.u.) \pm s.d. of at least six replicates. **e**, A Sna2(Y75A)-GFP mutant lacking an AP3 sorting motif mislocalizes to the cell surface in strains lacking AP1 (Apl2) or Irc6,

similar to a Sna2(Y65A/Y75A)-GFP mutant lacking both AP1 and AP3 motifs. **f**, Immunoblot analyses of epitope-tagged proteins in whole-cell lysates (WCL) and anti-haemagglutinin (HA) immunoprecipitates (IP). Molecular masses are indicated on the right. **g**, Two-hybrid assay of the indicated Gal4-activation domain (AD) and DNA-binding domain (BD) fusion proteins; cells were grown on medium containing histidine (left panel) or tested for activation of a *HIS3* reporter on medium lacking histidine (right panel). **h**, Sequence conservation between Irc6 and human p34. **i**, Two-hybrid analysis of interactions between AP1 subunit Apl4 and truncated forms of Irc6. aa, amino acid; WT, wild type.

(Fig. 4e) and interaction with Emp47 (Fig. 4f). Consistent with a shared role, both *ssp120* and *emp47* single mutants show calcium-sensitive growth, whereas *ssp120 emp47* double mutants do not display increased sensitivity (Fig. 4g)²⁷. Consistent with a conserved role for Ssp120 as a cargo-specific adaptor, Emp47 retained its ability to escort Emp46 from the endoplasmic reticulum in *ssp120* mutants (Fig. 4h).

Further elucidation of this and other novel predicted interactions should yield mechanistic insights into membrane system function, many of which are likely to be conserved.

To investigate the broader evolutionary conservation of MP complexes, we mapped homology relationships across 71 sequenced eukaryotic genomes using InParanoid and Compara (Supplementary

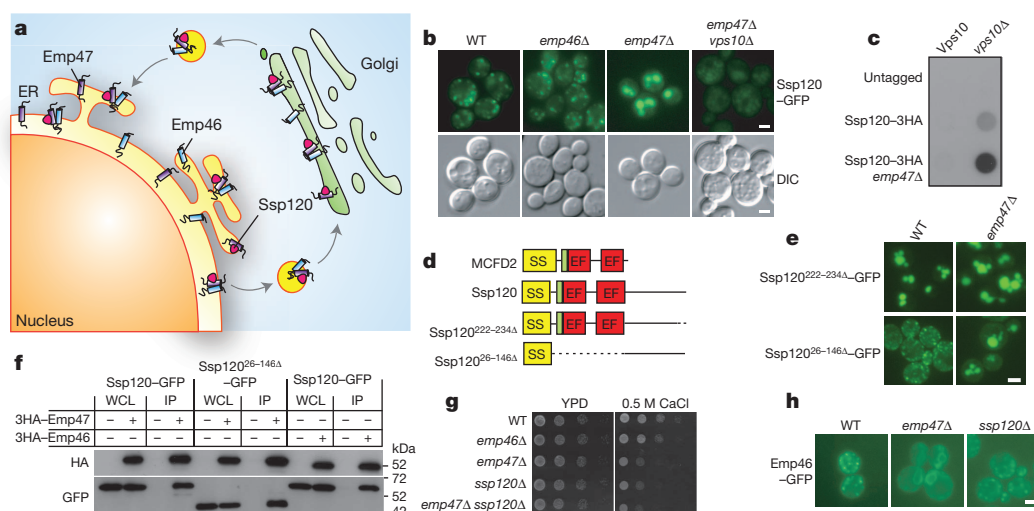


Figure 4 | Ssp120 participates in Golgi to ER recycling. **a**, Model showing recycling of the Emp46-Emp47-Ssp120 complex between endoplasmic reticulum and early Golgi. **b**, Fluorescence microscopy of GFP-tagged Ssp120 in wild-type and mutant strains. DIC, differential interference contrast. **c**, Immunoblot showing secretion of tagged Ssp120 constructs from indicated strains. **d**, Domain organization of human MCFD2 and yeast Ssp120 constructs. Signal sequences (SS) and EF-hand domains highlighted; green boxes indicate additional homology, dotted lines mark deleted regions. **e**, Localization of Ssp120-GFP constructs in wild-type cells and *emp47* mutants. **f**, Immunoblot analyses of epitope-tagged proteins in whole cell lysates (WCL) and anti-HA immunoprecipitates (IP). **g**, Strain growth on YPD media containing 0.5 M CaCl_2 . **h**, Fluorescence microscopy of GFP-tagged Emp46 in wild-type and mutant strains. Scale bars, 2 μm .

boxes indicate additional homology, dotted lines mark deleted regions. **e**, Localization of Ssp120-GFP constructs in wild-type cells and *emp47* mutants. **f**, Immunoblot analyses of epitope-tagged proteins in whole cell lysates (WCL) and anti-HA immunoprecipitates (IP). **g**, Strain growth on YPD media containing 0.5 M CaCl_2 . **h**, Fluorescence microscopy of GFP-tagged Emp46 in wild-type and mutant strains. Scale bars, 2 μm .

Table 11). Among our 501 MP-containing complexes, one-third (132) were present among >90% of organisms considered, whereas <10% (48) were restricted to fungi (Supplementary Table 12). Most MP complexes had at least half of their subunits conserved in worm (363), fly (374) and/or human (389) (Supplementary Fig. 7a), including 90 complexes whose components were fully conserved (Supplementary Fig. 7b).

The MP interactions reported here reveal the global modular architecture of the membrane systems of a model eukaryote. A key element was the parallel purification of endogenous MP complexes in the presence of three different detergents. Although TAP-MS offers exceptional coverage and accuracy, our approach has potential caveats. The affinity tag may interfere with protein localization or interactions, transient associations may be lost and the detergents may disrupt associations, potentially contributing to the smaller average size of MP complexes compared to non-membrane assemblies. The data presented here may also be impacted by missing, incomplete or conflicting information on functional annotations, genome sequences and subcellular localization information (Supplementary Fig. 1d), as well as the occurrence of spurious interactions. Nevertheless, the rate of false positive PPIs in the integrated network, as estimated from the reference benchmark precision (true positive:false positive ratio of 22:1), is just 4.3% (corresponding to 573 non-specific interactions), comparable to that for previous TAP studies of the soluble yeast interactome^{6,7}.

Although limitations exist, the systematic elaboration of a high-confidence MP interactome provides many opportunities for functional inference. Our results identify associations between un-annotated yeast MPs and functionally cohesive complexes involved in diverse biological processes. The conservation of many of these complexes provides insights into the membrane biology of eukaryotes, including humans. Just as genetic studies in yeast have led to the characterization of conserved human disease pathways, the network of MP complexes reported here predicts orthologous relationships that may be relevant to human disorders.

All of the experimental data, interactions and predicted complexes of this study are publicly accessible through a dedicated database (<http://wodaklab.org/membrane/>), complementing previous maps of the yeast soluble proteome as valuable community resources.

METHODS SUMMARY

MP target selection, strain construction, TAP-MS, derivation of the PPI network and protein complexes, conservation analysis, phenotypic assays and other experimental and bioinformatic procedures are detailed in Methods and Supplementary Information. Yeast strains used in this study are listed in Supplementary Table 13.

Full Methods and any associated references are available in the online version of the paper.

Received 2 May 2011; accepted 27 June 2012.

Published online 2 September 2012.

1. Bao, L., Redondo, C., Findlay, J. B., Walker, J. H. & Ponnambalam, S. Deciphering soluble and membrane protein function using yeast systems. *Mol. Membr. Biol.* **26**, 127–135 (2009).
2. Miller, J. P. *et al.* Large-scale identification of yeast integral membrane protein interactions. *Proc. Natl Acad. Sci. USA* **102**, 12123–12128 (2005).
3. Tarassov, K. *et al.* An *in vivo* map of the yeast protein interactome. *Science* **320**, 1465–1470 (2008).
4. Costanzo, M. *et al.* The genetic landscape of a cell. *Science* **327**, 425–431 (2010).
5. Turner, B. *et al.* iRefWeb: interactive analysis of consolidated protein interaction data and their supporting evidence. *Database (Oxford)* **2010**, baq023 (2010).
6. Gavin, A. C. *et al.* Proteome survey reveals modularity of the yeast cell machinery. *Nature* **440**, 631–636 (2006).
7. Krogan, N. J. *et al.* Global landscape of protein complexes in the yeast *Saccharomyces cerevisiae*. *Nature* **440**, 637–643 (2006).
8. Ghaemmaghami, S. *et al.* Global analysis of protein expression in yeast. *Nature* **425**, 737–741 (2003).

9. Babu, M., Krogan, N. J., Awrey, D. E., Emili, A. & Greenblatt, J. F. Systematic characterization of the protein interaction network and protein complexes in *Saccharomyces cerevisiae* using tandem affinity purification and mass spectrometry. *Methods Mol. Biol.* **548**, 187–207 (2009).
10. Collins, S. R. *et al.* Toward a comprehensive atlas of the physical interactome of *Saccharomyces cerevisiae*. *Mol. Cell. Proteomics* **6**, 439–450 (2007).
11. Pu, S., Wong, J., Turner, B., Cho, E. & Wodak, S. J. Up-to-date catalogues of yeast protein complexes. *Nucleic Acids Res.* **37**, 825–831 (2009).
12. de Godoy, L. M. *et al.* Comprehensive mass-spectrometry-based proteome quantification of haploid versus diploid yeast. *Nature* **455**, 1251–1254 (2008).
13. Ostlund, G. *et al.* InParanoid 7: new algorithms and tools for eukaryotic orthology analysis. *Nucleic Acids Res.* **38**, D196–D203 (2010).
14. Mewes, H. W. *et al.* MIPS: analysis and annotation of proteins from whole genomes in 2005. *Nucleic Acids Res.* **34**, D169–D172 (2006).
15. Regul, T. *et al.* Comprehensive curation and analysis of global interaction networks in *Saccharomyces cerevisiae*. *J. Biol.* **5**, 11 (2006).
16. Yu, H. *et al.* High-quality binary protein interaction map of the yeast interactome network. *Science* **322**, 104–110 (2008).
17. Pu, S., Vlasblom, J., Emili, A., Greenblatt, J. & Wodak, S. J. Identifying functional modules in the physical interactome of *Saccharomyces cerevisiae*. *Proteomics* **7**, 944–960 (2007).
18. Aguilar, P. S. *et al.* A plasma-membrane E-MAP reveals links of the eisosome with sphingolipid metabolism and endosomal trafficking. *Nature Struct. Mol. Biol.* **17**, 901–908 (2010).
19. Schuldiner, M. *et al.* Exploration of the function and organization of the yeast early secretory pathway through an epistatic miniarray profile. *Cell* **123**, 507–519 (2005).
20. Collins, S. R. *et al.* Functional dissection of protein complexes involved in yeast chromosome biology using a genetic interaction map. *Nature* **446**, 806–810 (2007).
21. Enright, A. J., Van Dongen, S. & Ouzounis, C. A. An efficient algorithm for large-scale detection of protein families. *Nucleic Acids Res.* **30**, 1575–1584 (2002).
22. Flinn, R. J. & Backer, J. M. mTORC1 signals from late endosomes: taking a TOR of the endocytic system. *Cell Cycle* **9**, 1869–1870 (2010).
23. Paumi, C. M. *et al.* Mapping protein-protein interactions for the yeast ABC transporter Ycf1p by integrated split-ubiquitin membrane yeast two-hybrid analysis. *Mol. Cell* **26**, 15–25 (2007).
24. Renard, H. F., Demaegd, D., Guerriat, B. & Morsomme, P. Efficient ER exit and vacuole targeting of yeast Sna2p require two tyrosine-based sorting motifs. *Traffic* **11**, 931–946 (2010).
25. Page, L. J., Sowerby, P. J., Lui, W. W. & Robinson, M. S. γ -synergins: an EH domain-containing protein that interacts with γ -adaptin. *J. Cell Biol.* **146**, 993–1004 (1999).
26. Pieper, U. *et al.* ModBase, a database of annotated comparative protein structure models, and associated resources. *Nucleic Acids Res.* **39**, D465–D474 (2011).
27. Sato, K. & Nakano, A. Emp47p and its close homolog Emp46p have a tyrosine-containing endoplasmic reticulum exit signal and function in glycoprotein secretion in *Saccharomyces cerevisiae*. *Mol. Biol. Cell* **13**, 2518–2532 (2002).
28. Sidhu, R. S., Mathewes, S. & Bollon, A. P. Selection of secretory protein-encoding genes by fusion with PHO5 in *Saccharomyces cerevisiae*. *Gene* **107**, 111–118 (1991).
29. Zhang, B. Recent developments in the understanding of the combined deficiency of FV and FVIII. *Br. J. Haematol.* **145**, 15–23 (2009).

Supplementary Information is linked to the online version of the paper at www.nature.com/nature.

Acknowledgements We thank H. Riezman, K. Sato and A. Nakano for providing strains and reagents, C. Ungermann for Sec18 antisera, A. Pierleoni for assistance with MemPype and R. Zheng for technical assistance. This research was supported by grants from the Canadian Foundation for Innovation, the Canadian Institutes of Health Research (CIHR MOP no. 81156, MOP no. 64394 and MOP no. 82940), the Canadian Cancer Society Research Institute, the Heart and Stroke Foundation, the Cystic Fibrosis Foundation, Novartis, the Ontario Genomics Institute and Genome Canada. E.C. is a CIHR New Investigator. S.J.W. is a Canada Research Chair Tier-I and acknowledges support from the SickKids Foundation.

Author Contributions J.F.G., A.E. and M.B. designed the project. M.B. coordinated and managed all experiments, and data analysis was coordinated by J.V. with guidance from S.J.W. and M.B. X.G., O.H., G.Z. and J.L. prepared the purification samples. S.C., N.B. and C.C. carried out mass spectrometry. V.F., T.P. and S.P. (CCBR) performed database searches and curation. J.V. and S.P. (CCBR) designed the web portal. J.V., M.B. and S.P. (SickKids) analysed the network data. M.B., C.G., B.D.M.B., J.S., V.W., A.Y., Y.Y.C.T., H.E.B., M.D. and F.J.V. carried out validation experiments. M.B., J.V., E.C., S.J.W. and A.E. jointly drafted the manuscript with critical input from J.F.G., and contributions from I.S., J.S. and B.D.M.B. All authors discussed the results and commented on the manuscript.

Author Information Reprints and permissions information is available at www.nature.com/reprints. The authors declare no competing financial interests. Readers are welcome to comment on the online version of this article at www.nature.com/nature. Correspondence and requests for materials should be addressed to E.C. (conibear@cmm.ubc.ca), S.J.W. (shoshana@sickkids.ca), A.E. (andrew.emili@utoronto.ca) or J.F.G. (jack.greenblatt@utoronto.ca).

METHODS

Yeast strains, media and plasmids. The yeast strains and plasmids used in this study are listed in Supplementary Table 13. For the large-scale purifications, the yeast strains were obtained from the Yeast-TAP-fusion library deposited in Open Biosystems⁸. Standard rich (YPD), synthetic medium plus dextrose lacking histidine, and synthetic complete medium containing 2% glucose as a carbon source were used for cell growth. Standard methods were used for the introduction of DNA into yeast³⁰.

Tandem affinity purification and mass spectrometry. Each tagged protein was purified from 4L yeast cultures grown in rich media (YPD) under native conditions and prepared for mass spectrometry essentially as described previously⁹, except with some modifications of our standard procedures. With the addition of non-ionic detergents to our buffers, we were able to solubilize and purify the majority of the yeast MPs. For most of the MPs, three purifications were carried out in parallel using three different non-ionic detergents, and two complementary mass-spectrometry techniques, MALDI-TOF (matrix assisted laser desorption/ionization time-of-flight) mass spectrometry and tandem LC-MS (liquid chromatography-electrospray ionization-mass spectrometry), were used to detect physically interacting proteins.

These detergents not only have different abilities to solubilize affinity-tagged proteins (Supplementary Text) but may differ in the extent to which they disrupt PPI. The detergents were removed from the purified protein samples before mass-spectrometric identification of co-purifying polypeptides using tandem LC-MS instruments that are more sensitive than those used previously to characterize soluble yeast protein complexes⁷. Gel images and confidence scores for protein identification by MALDI-TOF MS are made available in our database (<http://wodaklab.org/membrane/>). Confidence scores for protein identification by MALDI-TOF and tandem LC-MS were calculated essentially as described previously⁹. A tagged protein is considered successfully purified if either it or an annotated or putative MP with ≥ 2 TMH is identified by mass spectrometry (probability score $\geq 90\%$ for tandem LC-MS; Z score ≥ 1 for MALDI-TOF mass spectrometry). Details on the derivation of the PPI network and prediction of protein complexes are described in Supplementary Text.

Detergents. The following eleven detergents were used at a final concentration of 1% in the affinity purification of the initial test set of yeast MPs: Triton X-100, DDM (n-dodecyl- β -D-maltopyranoside), C12E8 (octaethylene glycol monododecyl ether), LDAO (lauryldimethylamine-oxide), CHAPS, (3-[(3-cholamidopropyl)dimethylammonio]-1-propanesulfonate), OG (octaethylene glycol monododecyl ether), DM (n-dodecyl- β -D-maltoside), CHAPSO (3-[(3-cholamidopropyl)dimethylammonio]-2-hydroxy-1-propanesulfonate), FC-12 (fos-choline-12), Nonidet P-40 (NP-40) and deoxycholate.

Colony overlay. The immunoblotting assay for secretion of haemagglutinin-tagged proteins was carried out essentially as described previously³¹ with antisera against haemagglutinin.

Fluorescence microscopy. The plasmids encoding fluorescent markers for actin, spindle and mitochondria (Supplementary Table 13) were constructed essentially as described previously³². The endoplasmic reticulum fluorescent plasmid, pScs2-RFP, was a gift from T. Levine. The Golgi Sec7-RFP fluorescent plasmid was constructed using a *SEC7* gene from the MORF (moveable ORF) library³³ through the Gateway recombining system. For the morphological study, each compartment-specific fluorescent plasmid was transformed into the Y7072 *MAT α can1 Δ ::STE2pr-spHIS5 lyp1 Δ ; his3 Δ 1 leu2 Δ 0 ura3 Δ 0 met15 Δ 0 LYS2+* strain background. The resulting query strain with the expressed fluorescent plasmid was then mated to an array of *MAT α* mutant strains through synthetic genetic array (SGA) technology⁴. After the subsequent standard SGA selections⁴, the mutants containing compartment-specific markers were visualized using high-content confocal fluorescent microscopy.

For vacuolar staining, cells were pulsed with 32 μ M of endocytic dye FM4-64 (Life Technologies) for 20 min in the dark at 30 °C, after which cells were resuspended in YPD and incubated for 30 min at 30 °C. Cells were subsequently washed twice in phosphate buffered saline (PBS) before visualization. When required, images were captured using a spinning disc confocal system (WaveFX; Quorum) with an ultra-cooled 512 back-tinned electron-multiplying charge-coupled device camera, or a microscope (E-600FN; Nikon) with an OrcaII camera (Hamamatsu). Alternatively, strains expressing GFP fusion proteins were viewed using an Axioplan 2 fluorescence microscope (Carl Zeiss). Images were captured with a CoolSNAP camera (Roper Scientific) using MetaMorph software (Molecular Devices) and adjusted using Adobe Photoshop (Adobe Systems).

Immunoprecipitation. The endogenously non-overproduced TAP-tagged proteins expressed in BY4741 by targeted homologous recombination⁹ were confirmed by western blot analysis using anti-TAP antibody that recognizes the protein A epitope of the TAP tag. TAP-tagged strains were transformed with plasmids expressing a galactose inducible overproduced haemagglutinin-tagged full-length protein. The transformants were selected on synthetic-defined media

lacking uracil. These strains were grown at 30 °C in synthetic-defined media lacking uracil with 2% sucrose as a carbon source. The cells were then sub-cultured and induced for 4 h at 30 °C in yeast peptone medium with 2% galactose. The cells were pelleted by centrifugation at 1,900g for 20 min and then resuspended in lysis buffer essentially as described previously⁹. The lysed yeast cells were incubated for 3 h in the presence of 1% Triton X-100 at 4 °C with immunoglobulin G (IgG) Sepharose 6 Fast Flow beads. The immunoprecipitation procedure was then carried out essentially as described previously⁹, except that in each purification step we added 1% Triton X-100. Alternatively, for the immunoprecipitation experiments in Figs 3 and 4, cell extracts were prepared from spheroplasts resuspended in lysis buffers (50 mM Tris-Cl pH 8.0; 50 mM NaCl; 0.1% Triton X-100; 1 mM DTT (dithiothreitol) and 1/100 EDTA-free protease inhibitor (Thermo) (Fig. 3); as well as 50 mM HEPES pH 7.9, 150 mM KCl, 1% Triton X-100, 1 mM DTT and 1/100 EDTA-free protease inhibitor (Thermo) (Fig. 4)) and incubated with rabbit anti-HA.11 (Santa Cruz) and protein A Sepharose beads. Western blot analysis of immunoprecipitated proteins was carried out using mouse anti-GFP (Roche) and mouse anti-HA.11 monoclonal antibodies (Covance).

In the case of co-immunoprecipitation with untagged proteins, the standard protocol was adapted with protein A resins (Pierce). The mouse Pre4 and rabbit Rpt1 polyclonal antibodies were obtained from Abcam, and the Sec18 rabbit polyclonal antibody was a gift from C. Ungermann.

Evaluation of Chs3 and Sna2 sorting. Assays to measure the function of the AP1 pathway were based on the localization of AP1 cargo proteins Sna2 and Chs3. Sna2-GFP is sorted to the vacuole by the binding of either AP1 or AP3 adaptors to distinct Sna2 motifs²⁴. The Sna2(Y75A)-GFP mutant, which lacks the AP3 motif, depends on AP1 for its vacuolar targeting and is mis-sorted to the cell surface in strains lacking AP1, similar to a Sna2 mutant (Sna2(Y65A/Y75A)-GFP) lacking both AP1 and AP3 motifs, thus providing a visual indication of AP1 function.

The chitin synthase Chs3, which requires Chs6 for transport to the cell surface, is retained in the cell by the AP1-dependent recycling pathway in *chs6* mutants³⁴, preventing chitin ring formation. Disruption of the AP1 complex restores Chs3 cell surface delivery through a bypass pathway and restores chitin ring formation in *chs6* mutants. Thus, chitin levels in *chs6* mutants provide a quantitative measure of AP1 function. Chitin levels were quantified by measuring the fluorescence of colonies grown on YPD plates containing 50 μ g ml⁻¹ calcofluor white at 30 °C for 3 days. Fluorescent-light images were captured with a Fluor S Max MultiImager (Bio-Rad Laboratories) using the 530DF60 filter and Quantity One software (version 4.2.1; Bio-Rad Laboratories), and image densitometry was performed as described previously³⁵. Alternatively, chitin rings were visualized by fluorescence microscopy of cells fixed with 3.7% formaldehyde, incubated in 100 μ g ml⁻¹ calcofluor white in 0.5 M Tris pH 9.6 for 30 min at 30 °C, and washed twice before analysis.

Yeast two-hybrid analysis. All plasmids for yeast two-hybrid analysis were generated by homologous recombination in pGAD-C2 and pGBDUC-2, essentially as described previously³⁶. Haploid strains expressing GAL4-AD fusion proteins were mated with strains expressing GAL4-BD fusion proteins. Diploid cells were tested for activation of the HIS3 reporter by growth on selective media lacking histidine.

iMYTH assay. SCT1 prey generation in the pPR3N vector, endogenous tagging of YPR091C with the Cub-LexA-VP16 MYTH tag and subsequent iMYTH screening were carried out as previously described³⁷. In brief, bait and artificial bait expressing variants of the *Saccharomyces cerevisiae* NMY51 or L40 MYTH reporter strains were generated and transformed with prey plasmid expressing either control construct or NubG-SCT1p construct. Control plasmids, expressing Nubi-tagged ('positive') and NubG-tagged ('negative') forms of the unrelated, plasma membrane-localized Fur4 uracil permease, were obtained from Dualsystems Biotech (<http://www.dsystems.ch/>). Transformed cells were picked from solid media, diluted into 150 μ l of sterile ddH₂O and spotted directly onto selective media. Plates were grown at 30 °C for 3–6 days and growth was scored.

30. Rose, M. D., Winston, F. & Hieter, P. *Methods in Yeast Genetics* (Cold Spring Harbor Laboratory Press, 1990).
31. Conibear, E. & Stevens, T. H. Studying yeast vacuoles. *Methods Enzymol.* **351**, 408–432 (2002).
32. Li, Z. *et al.* Systematic exploration of essential yeast gene function with temperature-sensitive mutants. *Nature Biotechnol.* **29**, 361–367 (2011).
33. Gelperin, D. M. *et al.* Biochemical and genetic analysis of the yeast proteome with a movable ORF collection. *Genes Dev.* **19**, 2816–2826 (2005).
34. Valdivia, R. H. & Schekman, R. The yeasts Rho1p and Pkc1p regulate the transport of chitin synthase III (Chs3p) from internal stores to the plasma membrane. *Proc. Natl Acad. Sci. USA* **100**, 10287–10292 (2003).
35. Lam, K. K. *et al.* Palmitoylation by the DHHC protein Pfa4 regulates the ER exit of Chs3. *J. Cell Biol.* **174**, 19–25 (2006).
36. James, P., Halladay, J. & Craig, E. A. Genomic libraries and a host strain designed for highly efficient two-hybrid selection in yeast. *Genetics* **144**, 1425–1436 (1996).
37. Snider, J. *et al.* Detecting interactions with membrane proteins using a membrane two-hybrid assay in yeast. *Nature Protocols* **5**, 1281–1293 (2010).

CAREERS

POSTGRADUATES US university offers career-planning course for credit **p.593**

CITATIONS Publisher links citation rates to scientific peer recognition **p.593**

NATUREJOBS For the latest career listings and advice www.naturejobs.com

GETTY



Bud Abbott and Lou Costello made disagreements about order in baseball the stuff of comedy legend.

AUTHORSHIP

Who's on first?

When scientists collaborate on an experiment and a paper, it can be hard to decide who gets the credit and how much.

BY AMBER DANCE

Stephen Kosslyn first started to consider how author lists come together when he found himself mediating a dispute. A postdoc and a graduate student each wanted to be listed as the first author on a study. “They both had a case,” recalls Kosslyn. “It got heated.”

Disagreements often happen when contributors put in similar amounts of effort on different aspects of a project, says Kosslyn, a psychologist at Stanford University in California. For example, one person might have developed the idea for the project and the other performed most of the data analysis. “The force of the dispute usually revolves around the feeling that whatever they did was more

important than what the other person did,” says Kosslyn.

Such disputes are common. “As authorship is our academic currency, it tends to be a hot-button topic,” says Karen Peterson, scientific ombudsman at the Fred Hutchinson Cancer Research Center in Seattle, Washington. She says that one-fifth of the disputes she adjudicates concern authorship. Similar conflicts are among the most common issues mediated by the Committee on Publication Ethics (COPE), says Virginia Barbour, the organization’s chairwoman and chief editor of *PLoS Medicine* in Cambridge, UK.

Authorship disagreements can be mitigated with careful discussions, explicit lab guidelines and a good understanding of authorship practices in one’s field. There is no

perfect approach, but deciding on who gets an authorship credit, and how they are ranked, is a crucial part of doing science responsibly.

Precise statistics on authorship disputes are hard to come by, says Mario Biagioli, a science historian at the University of California, Davis, who has studied authorship. Scientists may be reluctant to admit that they have demanded undeserved authorship or otherwise subverted the system, and the US Office of Research Integrity does not track such disagreements because they are not considered scientific misconduct, says Biagioli, who co-edited the book *Scientific Authorship: Credit and Intellectual Property in Science* (Routledge, 2002). However, in a 2005 survey¹ of researchers who had received a grant from the US National Institutes of Health (NIH), 10% of respondents admitted to assigning authorship “inappropriately”.

CREDIT CONFUSION

Questions of who deserves credit for a paper are a fairly recent phenomenon, says Biagioli. Once upon a time, a paper had one author, maybe two. But with modern big science and large collaborations, a study might have hundreds or even thousands of authors — as in the case of the ATLAS experiment² at the Large Hadron Collider at CERN, Europe’s particle-physics laboratory near Geneva, Switzerland.

And what authorship means varies by scientific discipline. For example, in particle physics, hundreds of researchers may contribute to the development and maintenance of a single piece of equipment, such as an accelerator. At big physics labs such as CERN, everyone who was working at the lab when the discovery was made gets a slot on the author list — even if they haven’t seen the paper, says Biagioli. The authors are usually listed alphabetically, regardless of how much they contributed.

In the biological sciences, by contrast, the author list is often strictly ranked. The top spot is at the end of the list, where the principal investigator gets credit for running the lab. The student or postdoc who actually did the work goes first. As for the authors in the middle, it is hard to tell whether they participated a lot or a little, says Biagioli.

The International Committee of Medical Journal Editors (ICMJE), headquartered in Philadelphia, Pennsylvania, has developed authorship guidelines that are used by many journals and institutions. These rules state that to be listed as an author, each researcher

► must meet three key criteria: they must have been involved in designing the project, collecting data or analysing the results; they must have participated in drafting or revising the manuscript; and they must have approved the final, published paper. Many universities that have their own guidelines base them on the ICMJE's wording, says Biagioli.

Kosslyn has his own definition: the crucial element, he says, is creativity. For example, a researcher could work with study participants in the lab, but just be following a protocol. "Anybody could have run the subjects, so running the subjects is not enough," says Kosslyn. To earn authorship, the researcher would be intellectually engaged: they might point out a feature of the data that leads the team to reshape the experiment. The paper wouldn't look the same without them.

THE AUTHOR IN QUESTION

COPE recommends that researchers decide who will be an author and what order they will be listed in before they even conduct experiments, and that the group revisits the author list as a project evolves. A handshake isn't enough to seal the deal — researchers should keep author agreements in writing.

Whenever they occur, authorship discussions need not be confrontational (see 'Aggravation-free authorship'). Mark Groudine, deputy director of the Hutchinson Center, says that the parties in a dispute should sit down and try to talk the matter over. "People get so locked into their positions that they don't make the effort to understand the other person's point of view," he says, "and therefore they don't understand why it's a dispute."

If talking doesn't work, Groudine suggests asking the opinion of an unbiased third party. For example, on one project he collaborated with another principal investigator. When it came to writing up the paper, both wanted



Ombudsman Karen Peterson says that one-fifth of the disputes she handles are about authorship.

to be senior author. They invited two trusted colleagues to mediate.

The jury awarded the senior slot to Groudine, but he felt uneasy about it. He suggested that the other investigator be the corresponding author, who communicates with the journal and any scientists who enquire about the work. "I consider corresponding author as equivalent, almost, to senior author," says Groudine. Co-senior authorship is also an option, he adds.

But sharing credit too broadly can be risky. Sometimes authors are listed more as a courtesy than because they made a key contribution, says Chris Sneden, an astronomer at the University of Texas at Austin, who will step down from his post as editor of *The Astrophysical Journal Letters* at the end of this year. Accepting courtesy authorship is a "double-edged sword," he says. If the paper becomes famous, "every author gets to claim credit". But if it becomes infamous, everyone gets a share of the blame. Researchers need to be aware of the potential risks of adding their names to manuscripts that

they know little about (see 'Ghosts and guests').

Gerald Schatten, a stem-cell researcher at the University of Pittsburgh in Pennsylvania, learned that lesson when he lent his good name to a high-profile but eventually discredited stem-cell paper by Woo Suk Hwang, then at Seoul National University. Schatten was investigated by his university, which cleared him of misconduct, but chastised him for 'research misbehaviour' because he failed to check the quality of the science³.

The decision to accept courtesy authorship is a matter of preference, says Sneden. "Personally, if I haven't actually contributed something to the specific paper, I just won't have my name on it," he says. In that case, he politely tells his colleagues that he shouldn't be on the list. "I make sure they understand that it's not a negative reflection on the paper," he says.

TAKEN IN VAIN

Sometimes, the recipient of this courtesy may not get the chance to bow out. A researcher who has been added to the author list without their permission might be surprised to see their name when the paper comes out, says Sneden, or even angry if they don't agree with the conclusions. Those who find themselves unexpectedly an author on a paper that they would prefer not to be associated with should contact the editor of the journal, he recommends. The editor will get in touch with the study's corresponding author, and decide whether a corrigendum is necessary to explain that the author in question was not involved with the work.

These kinds of conflicts shouldn't occur. Corresponding authors are expected to have the approval of their co-authors — but some don't realize it. "People, do you read the publication agreement that you sign?" Sneden asks his colleagues. (Often, the answer is no.)

Increasingly, journals are attempting to keep authors in line by asking for details on who did what. In cases of fraud, those descriptions should lay the blame at the right person's door.

Biagioli agrees that delineating each person's contribution should help, but he says that the descriptions are frequently too brief. As an example, he cites the study published this month in *Nature* by the ENCODE Project Consortium⁴. It ascribes generic tasks such as "data analysis", "writing" or "scientific management" to large sets of authors, making it impossible to tell, for example, who analysed which data. When scientists sit down to plan a project — and ideally draft the author list — they should also decide how to describe everyone's contributions, says Biagioli. The relevant details will probably vary by discipline, he adds.

In his own lab, Kosslyn has instituted a scheme to make authorship requirements explicit from the outset. As he listened to his student and postdoc arguing their cases several years ago, he started to develop what eventually

CONFLICT RESOLUTION

Aggravation-free authorship

When many scientists work together, determining authorship isn't always easy. Here are some tips for settling the line-up.

- Make sure that you choose collaborators with whom you can work well.
- Discuss authorship early, and keep doing so often as a project evolves. Put it in writing.
- When there are disputes, first try to talk it out amicably and understand the other person's point of view. For example, try to work out how the idea first came about.
- If you must approach your supervisor about an authorship decision that you don't like, keep the tone inquisitive, not accusatory. Explain that you want to understand how authorship was decided.

● If a contributor's authorship is in question, it can help to consider what the paper would have looked like without their efforts, and whether someone else could have made the same contribution.

● Familiarize yourself with your institution's or journal's authorship guidelines, or those of the International Committee of Medical Journal Editors. Use them to back up your case.

● Be prepared to compromise or share credit.

● If you can't agree among yourselves, engage a supervisor, trusted colleagues or an ombudsman to investigate the matter and make a recommendation. **A.D.**

COMMERCIAL PAPERS

Ghosts and guests

Authorship can be misused when there is money to be made. Medical journals contain a mixture of original scientific findings and veiled advertisements for drugs, and scientists and physicians must read papers critically to understand a medicine's true merits, says Alastair Matheson, a biomedical-research consultant in Toronto, Canada.

Some pharmaceutical companies make drugs and run clinical trials, then engage medical writers to draft manuscripts. These contributors are often ghostwriters not listed as authors on the paper. Instead, the company's marketing team finds a big academic name to headline the project — even if this guest author makes no contribution to the paper apart from scanning the final version. Companies sometimes use the same technique to produce reviews promoting their latest medicines, says Joseph Ross, a physician who studies health policy at Yale University in New Haven, Connecticut. One survey⁵ found that guests and ghosts haunted 21% of papers published in six leading medical journals in 2008.

"This vast production line of information about drugs is passed off as the work of academics rather than the work of industry," says Matheson. The companies get to advertise their products; the ghostwriters receive a pay cheque; and the academics get another line on their CVs. But the patients and the integrity of science all lose out, says Matheson.

For example, Merck, a pharmaceutical company based in Whitehouse Station, New Jersey, minimized reporting of the risks observed for its painkiller Vioxx (rofecoxib) until the drug was taken off the market in 2004. Ross was a

consultant to people who had taken Vioxx and developed heart problems, or their families, in two court cases against Merck, and he saw some of the company's internal documents⁶. "We were sort of shocked to find pretty rampant evidence that a lot of the trials were ghostwritten," says Ross. "We would stumble across a full draft of a manuscript that just said, 'external author?'"

There are ways to identify traces of guests and ghosts in a manuscript: "Check the small print," says Matheson. That is where a medical writer or communications company may be acknowledged. Funding from a drug-maker is another tell-tale sign. "These are pointers to the likelihood that this is something originated and planned by industry prior to the involvement of the headline authors," says Matheson. Author disclosures are less helpful, he adds, because academic authors may list several affiliations and it is difficult to tell which commercial relationship is relevant.

With commerce and medicine intimately intertwined, it would be impractical for academics to cut ties with companies, says Matheson. But, he adds, when academics are offered guest authorship, "I would advise them, for the sake of their reputation, to do two things". First, he says, be more than a guest: make sure that your contribution is author-level. Second, insist that company employees involved in the study are also listed as authors.

Matheson says it is the responsibility of journals to make participation by drug-makers more apparent. He would like to see papers marked right at the top with 'commercial article'. He also suggests that journals use labels to indicate who funded the study, and what drug it supports. **A.D.**

became a 1,000-point system. The researchers who come up with the idea get 250 points, split between them according to their contribution; writing the paper is worth the same. A further 500 points are available for designing and running the experiment and analysing the data. Researchers who score at least 100 points make the author list, with each person's point total determining their rank.

Disagreements still occur; in those cases, Kosslyn decides how the points are allocated. When the balance of contributions is unclear, he does his best. However, it rarely comes to tallying points. "Usually it's very obvious what the order's going to be," he says.

In recent years, no disputes have ever risen to the level of the argument that led to the

point system. "That," says Kosslyn, "was the last heated dispute we had in the lab." ■ **SEE WORLD VIEW P.475**

Amber Dance is a freelance science writer in Los Angeles, California.

1. Martinson, B. C., Anderson, M. S. & de Vries, R. *Nature* **435**, 737–738 (2005).
2. The ATLAS Collaboration *J. Instrum.* **3**, S08003 (2008).
3. Maris, E. & Check, E. *Nature* **439**, 768–769 (2006).
4. The ENCODE Project Consortium *Nature* **489**, 57–74 (2012).
5. Wislar, J. S., Flanagan, A., Fontanarosa, P. B. & DeAngelis, C. D. *Br. Med. J.* **343**, D6128 (2011).
6. Ross, J. S., Hill, K. P., Egilman, D. S. & Krumholz, H. M. *J. Am. Med. Assoc.* **299**, 1800–1812 (2008).

POSTGRADUATES

Career-planning course

The University of Pittsburgh in Pennsylvania has launched a course on career planning for graduate students, one of the first to offer degree credits. Planning for Scientific Success aims to help students to identify and develop skills based on their interests and values, and to create a lifelong career-development plan. Steven Wendell, a molecular biologist and assistant director of the postdoctoral office at the university, proposed the course. "The career problems I hear from graduate students and postdocs are based in their lack of a clear, authentic career vision," he says. The course lasts for two semesters and is required for oral-biology graduate students at the University of Pittsburgh dental school, but is open to all graduate students at the university. Each semester is worth one credit.

GRADUATES

Trouble with tracking

Universities across Europe want to improve how they track graduates' career progression, says the European University Association (EUA) in Brussels. In *Tracking Learners' and Graduates' Progression Paths*, published on 13 September, the EUA finds that if institutions follow career outcomes, they can take steps to improve them, such as revising curricula or establishing strategies to improve communication skills. But of 23 institutions surveyed, 77% did not systematically track PhD-holders' careers. Study co-author Michael Gaebel, head of higher-education policy at the EUA, says institutions should create a student database and team up to standardize data collection.

CITATIONS

Nobel prizes predicted

On 19 September, Thomson Reuters announced its annual 'citation laureates', whom it deems likely to win a Nobel prize. Since 2002, 26 of the predictions have come true. "We're trying to demonstrate that there is a strong correlation between citation at high frequency and peer esteem in science," says David Pendlebury, lead analyst for citation-laureate selection based in Eugene, Oregon. Each year, Reuters chooses up to nine candidates in each of the fields of chemistry, economics, physics and medicine. The 2012 laureates include researchers in genetic regulation, quantum teleportation and reducing the speed of light.

SOLIDARITY

A passing thought.

BY GEORGE ZEBROWSKI

Leo Wilson sat by the window and watched the insects passing through the glass.

It was an illusion of some sort, he told himself, unblinking to catch how it was done; a love of insects was fooling him. Dreaming, he had to wake up.

But they went through, unstoppable solid ghosts — mosquitoes, ladybirds, a bee and even a wasp; the mix made no sense, as if each kind of insect was showing off.

He watched sadly as the bugs came through and stuck to the sticky strips he had hung nearby to keep a record.

He touched the glass and drummed on it with his fingers, once again testing its solidity; the charge in the mass of his fingers, which produced the experience of solidity, was certainly related to what the insects were able to do. They knew the physics and could alter the well defined illusion of solidity by varying the resistance. Absolute solidity, non-atomistic matter, closely packed to forbid all space-like fields, did not exist. Nature had been too cheap to make an all-solid Universe. Ever parsimonious, it had inflated a pattern with space, not unlike Styrofoam. All the mass of Earth might be compressed into a thimble, an entire universe into a single point...

No, what the insects were doing was not a miraculous violation of natural law. But how were the bugs doing it? And why were they doing it?

Another group arrived at the window, passed through, and flew into his stickies. He stared in wonder, thinking that he might be helping them by watching, deluding himself into seeing the impossible-possible.

He checked the stickies again. Three were full now with writhing bodies struggling to break free of the glue.

He turned back to the window and saw with shock that the window was now covered with the bodies of dead insects that had failed to pass through — and feared that his turning away had caused the catastrophe.

To come through, they needed him.

He sat and waited for another group, thinking of the very small statistical chance that he might walk through a wall; quantum theory admitted as much.

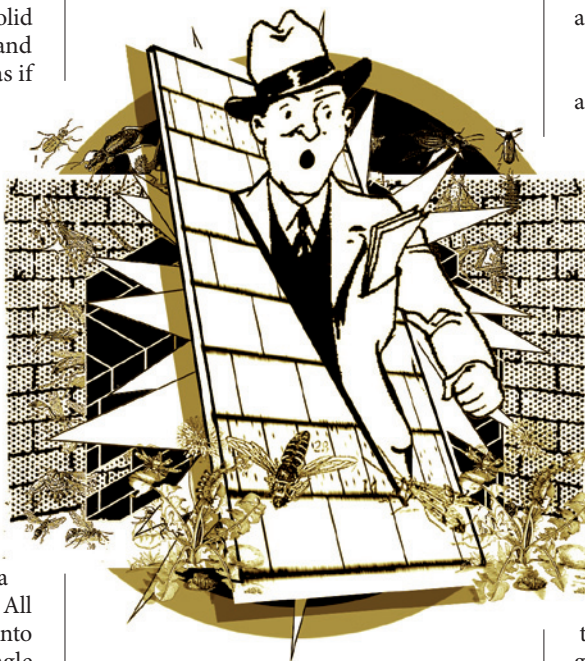
The insects, some of them, had found that moment.

And some had not.

Video would not do to witness the extraordinary event.

But just before he called in observers, he went outside and pushed a finger through the glass, then his whole hand, but resisted the urge to push through with his tongue.

Finally, he stood on tiptoes and went



through with his head, and felt a tingle as he withdrew, sure now that all it took was belief, derived from the fact that he had seen it done.

Being a patriotic sort, Leo convinced his government of the phenomenon. History did not need to record which governance, as it did not much matter after he walked through a wall for a few ministers. An advisory magician was sceptical until Leo took him by the hand and walked him through.

Quantum probabilities had a lot to offer.

Some months later, several heads of intelligence agencies went to lunch — a commonality among professionals in a world determined to quarrel instead of war, but this time each was asking the other what they were going to do about one another's agents, the ones who were now stuck in walls.

All the agency heads had the same problem. They all knew Leo

Wilson from his file, and asked for his help. Finally, after a number of agents had died in the

walls and others had to be fed by hand to survive, the agencies called a secret meeting somewhere in the Mediterranean and asked Leo Wilson to attend.

"What do you suggest?" they asked after telling him what had happened.

"Never had that problem myself," he said. "I've forgotten I have doors in my house."

"You do it without... difficulties?" they asked.

"Of course," he told them.

"What can you suggest to help us?" they asked.

"Read to them about the reality of probabilities," he said. "Might loosen up their imaginations."

Tried. It did not work.

"Ladies and gentlemen," Leo said, "I don't know what else to tell you. Insects are cooperative, and maybe they pool the energy of the hive." It occurred to Leo that the insects that had gone splat on the glass were the ones with individual tendencies, not unlike agency spies. "Or maybe it's something like..." he started to say.

"Like what, Mr Wilson?" they all asked at once, as if suspecting that he was holding back the vital answer.

He sighed. "Like bird navigation."

Our feathered friends have something in their brains that enables them to go anywhere on the globe without our kind of GPS.

"But you told us some of the insects failed to go through. Doesn't that suggest anything?"

"Yes, but they didn't hesitate and stick part way through the glass," Leo said, thinking about degrees of cooperation; the spies were, after all, company types.

"Help us, Mr Wilson, men are dying stuck in the walls!"

"Dying?" Leo asked.

"We have to feed these political embarrassments. What do you know, what do the bugs know how to do that we don't?"

Leo looked around at the anxious faces, shrugged and said: "They do it better than we do." ■

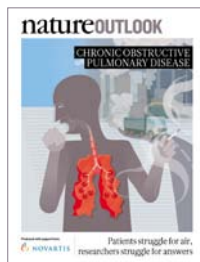
George Zebrowski is an award-winning novelist, story writer, essayist, editor and lecturer. He is the author of the novel Empties (Golden Gryphon Press) and the editor, with Gregory Benford, of Sentinels in Honor of Arthur C. Clarke (Hadley Rille Books).

➔ **NATURE.COM**
Follow Futures on
Facebook at:
go.nature.com/mtoodm

natureOUTLOOK

CHRONIC OBSTRUCTIVE PULMONARY DISEASE

27 September 2012 / Vol 489 / Issue No. 7417



Cover art: Nik Spencer

Editorial

Herb Brody,
Michelle Grayson,
Mary Carmichael,
Tony Scully, Davina
Dadley-Moore

Art & Design

Wes Fernandes,
Alisdair MacDonald,
Andrea Duffy

Production

Donald McDonald,
Kelly Hopkins, Leonora
Dawson-Bowling,
Yvonne Strong

Sponsorship

Will Piper, Yvette
Smith, Reya Silao

Marketing

Elena Woodstock,
Hannah Phipps

Project Manager

Claudia Deasy

Art Director

Kelly Buckheit Krause

Magazine Editor

Tim Appenzeller

Editor-in-Chief

Philip Campbell

Tens of millions of people around the world find it distressingly difficult to breathe owing to a combination of emphysema and chronic asthmatic bronchitis — a deadly duo known as chronic obstructive pulmonary disease (COPD).

Smoking is the most common trigger for COPD, and we have mapped the incidence of smoking and the prevalence of COPD in the United States, a country with fine-grained data on both phenomena (page S2). But there is more to COPD than smoking. Evidence is emerging that some people might be genetically susceptible to the disease (S7), while researchers are picking apart the involvement of errant immune cells (S15).

New treatments for COPD are in development. Hot areas of pursuit involve combinations of agents, as well as novel drug-delivery systems (S16). Most available treatments only abate COPD's debilitating flare-ups. One new line of enquiry is to stimulate the production of antioxidants to neutralize the free radicals that trigger the violent biochemical cascades that lead to the lungs' deterioration (S4). If the damage wrought is irreversible, artificial lungs might be an option (S12). And there are tantalizing early results that suggest that vitamin D supplements can at least slow the lungs' deterioration (S10).

No remedy for COPD will be effective if the condition is not properly diagnosed. Indeed, too often, the disease is mistaken for other, less serious ailments, and the standard doctor's office test is prone to error (S8).

While the decline in smoking in the West should lower the prevalence of COPD, other parts of the world have a rougher road to travel. COPD is expected to grow rapidly in China where tobacco use, smog and smoky cooking stoves portend a future of difficult breathing (S18).

We acknowledge the financial support of Novartis Pharma AG in producing this Outlook. As always, *Nature* has full responsibility for all editorial content.

Herb Brody

Supplements Editor

CONTENTS

S2 HEALTH IMPACT

Breathless

A closer look at the problem of COPD

S4 BIOCHEMISTRY

A radical treatment

Shielding the lungs with antioxidants

S7 PERSPECTIVE

How can genetics help?

Edwin K. Silverman sees hope for patients

S8 DIAGNOSIS

To catch a killer

Early detection to improve treatment

S10 NUTRITION

The vitamin D complex

Can dietary supplements abate the disease?

S12 DEVICES

Artificial inspiration

All options are on the operating table

S15 PERSPECTIVE

Clues, not conclusions

Steven R. Duncan summarizes the case against COPD–autoimmunity connection

S16 THERAPEUTICS

Strength in numbers

Drugs get tougher with COPD's symptoms

S18 PUBLIC HEALTH

Where there's smoke

Rates of COPD set to soar in China

COLLECTION

S21 Rtp801, a suppressor of mTOR signaling, is an essential mediator of cigarette smoke-induced pulmonary injury and emphysema
T. Yoshida *et al.*

S28 Involvement of surfactant protein D in emphysema revealed by genetic association study
T. Ishii *et al.*

S34 Association between fibroblast growth factor 7 and the risk of chronic obstructive pulmonary disease
Si-cheng Xu *et al.*

S40 Energy expenditure in chronic obstructive pulmonary disease — evaluation of simple measures
F. Slinde, A.M. Grönberg, U. Svantesson, L. Hulthén and S. Larsson

Nature Outlooks are sponsored supplements that aim to stimulate interest and debate around a subject of interest to the sponsor, while satisfying the editorial values of *Nature* and our readers' expectations. The boundaries of sponsor involvement are clearly delineated in the *Nature Outlook* Editorial guidelines available at http://www.nature.com/advertising/resources/pdf/outlook_guidelines.pdf

CITING THE OUTLOOK

Cite as a supplement to *Nature*, for example, *Nature* Vol XXX, No. XXXX Suppl, Sxx–Sxx (2012). To cite previously published articles from the collection, please use the original citation, which can be found at the start of each article.

VISIT THE OUTLOOK ONLINE

This supplement can be found at:
<http://www.nature.com/nature/outlook/COPD>

All featured articles will be freely available for 6 months.

SUBSCRIPTIONS AND CUSTOMER SERVICES

For UK/Europe (excluding Japan): Nature Publishing Group, Subscriptions, Brunel Road, Basingstoke, Hants, RG21 6XS, UK. Tel: +44 (0) 1256 329242. Subscriptions and customer services for Americas — including Canada, Latin America and the Caribbean: Nature Publishing Group, 75 Varick St, 9th floor, New York, NY 10013-1917, USA. Tel: +1 866 363 7860 (US/Canada) or +1 212 726 9223 (outside US/Canada). Japan/China/Korea: Nature Publishing Group — Asia-Pacific, Chiyoda Building 5-6th Floor, 2-37 Ichigaya Tamachi, Shinjuku-ku, Tokyo, 162-0843, Japan. Tel: +81 3 3267 8751.

CUSTOMER SERVICES

Feedback@nature.com
Copyright © 2012 Nature Publishing Group



HEALTH IMPACT

Breathless

COPD is one of the world's biggest killers, but awareness is low, diagnosis is often missed, and in many countries the extent of the problem is not even well-documented.

BY AMBER DANCE

Worldwide, 65 million people with chronic obstructive pulmonary disease (COPD) are gasping for air — and with the World Health Organization (WHO) predicting the disease will vault from fifth to third in the leading causes of death globally by 2030, their breathless ranks are set to swell. Governments, scientists and pharmaceutical companies are taking several approaches to ease the burden of COPD, both on the patients and on healthcare systems.

COPD encompasses both emphysema and chronic asthmatic bronchitis; patients can suffer either problem or both simultaneously. Emphysema eats away at the lung's air sacs, or alveoli, so that less surface area is available for gas exchange. Bronchitis constricts the airways entering the lungs and clogs them with mucus. The winded masses face a disease that is incurable, even for those fortunate enough to receive

a proper diagnosis and treatment for symptoms.

Surveys suggest that COPD is grossly underdiagnosed in both developed and developing nations. People don't always report the relevant clinical signs, and some doctors do not use spirometry, the gold-standard method of diagnosis, because they cannot afford the machine or haven't heard of it. A patient undiagnosed means a patient untreated, which could hasten death.

Although reliable numbers on global COPD rates are hard to come by, the WHO estimates that 90% of COPD cases occur in developing nations. COPD is likely to become an especially serious problem over the coming decades in China, the world's biggest producer and consumer of cigarettes. About a third of Chinese people smoke, among the highest rates in the world. Smoking-related diseases are the country's biggest killer, and COPD alone kills nearly two million people there each year.

Smoking is the major risk factor for COPD,

but it is not the only one. Just 15% of smokers develop the disease. Presumably, their genetic makeup predisposes them to lung maladies. Scientists have known for decades that a mutation in the enzyme α 1-antitrypsin, found in 1–2% of people with COPD, puts people at greater risk — especially smokers. In the past few years, genome-wide screens have netted a slew of new gene candidates, though not all have been confirmed as risk factors.

The manner in which smoke particles damage the lungs also remains uncertain. In addition to imbalances in enzymes such as antitrypsin, another potential culprit is the immune system. Most smokers suffer from inflamed airways. But those who develop COPD endure sustained inflammation, even after they quit smoking. Some scientists see this as evidence that COPD is an autoimmune disease. Supporting the hypothesis, researchers have found that some people with COPD possess antibodies against some of their own proteins.

Another potential modulator of the immune response in COPD is vitamin D. Several studies have shown that people with COPD are more likely to have a deficiency in the vitamin, and the less vitamin D they have, the worse their lungs work. Vitamin D may squelch the negative inflammatory response while promoting beneficial immunity, but researchers have yet to confirm its effect and work out the details.

Pharmaceutical companies are pursuing new and improved versions of current COPD treatments, such as the bronchodilators that relax airway muscles and ease breathing. Both Novartis, headquartered in Basel, Switzerland, and Pearl Therapeutics, headquartered in Redwood City, California, report promising data. And a collaboration between GlaxoSmithKline (GSK), headquartered in Brentford, UK, and Theravance, a biopharmaceutical company based in South San Francisco, California, is running several trials with a dual-drug combination. But another combined therapy from GSK and Theravance, Relovair, has yielded mixed results thus far. Fortunately, drugs are not the only option. Researchers are also at work on bioartificial lungs that they hope could reduce or even eliminate the need for donor organs.

Cigarette smoke is packed with free radicals, so antioxidants — which can neutralize their damaging effects — have also been tested in clinical trials. The results have been inconsistent, perhaps because each medicine only mops up a subset of the different types of free radicals ravaging the lungs. Some scientists have now turned their attention to Nrf2, a DNA-binding protein that switches on many of the body's own antioxidants.

These treatments will be important weapons in the fight against COPD. But most are still confined to the lab rather than nearing the clinic — and scientists and health professionals must take aim at COPD now if they are to stem its rise. ■

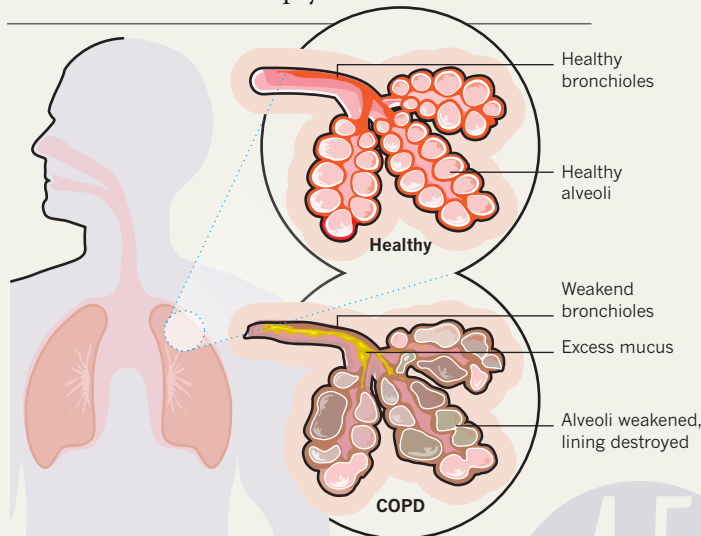
Amber Dance is a freelance science writer based in Los Angeles, California.

CHARLES THATCHER/GETTY IMAGES

COPD IN THE UNITED STATES

INSIDE THE LUNGS

It is not a single disease but a constellation of symptoms. And comes in two forms: emphysema and chronic bronchitis.



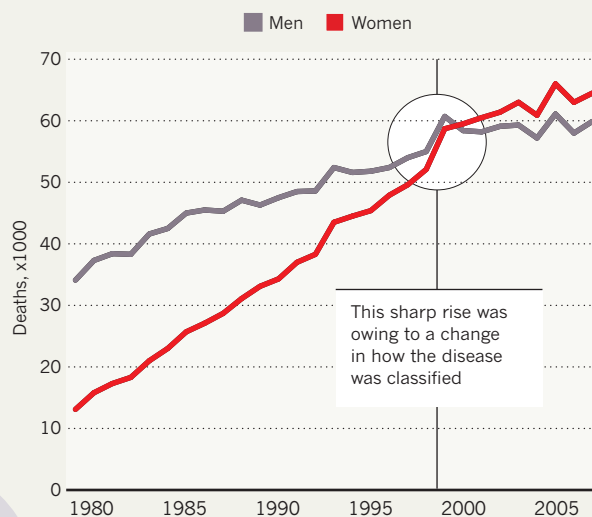
Patients with COPD suffer primarily because their alveoli, or air sacs, lose their elastic quality or are destroyed. The airways may also become thick and stiff, inflamed, or clogged with mucus, so that patients can take only shallow breaths.

4.5

A person dies of COPD-related illness every four to five minutes in the United States.

A DISEASE ON THE RISE

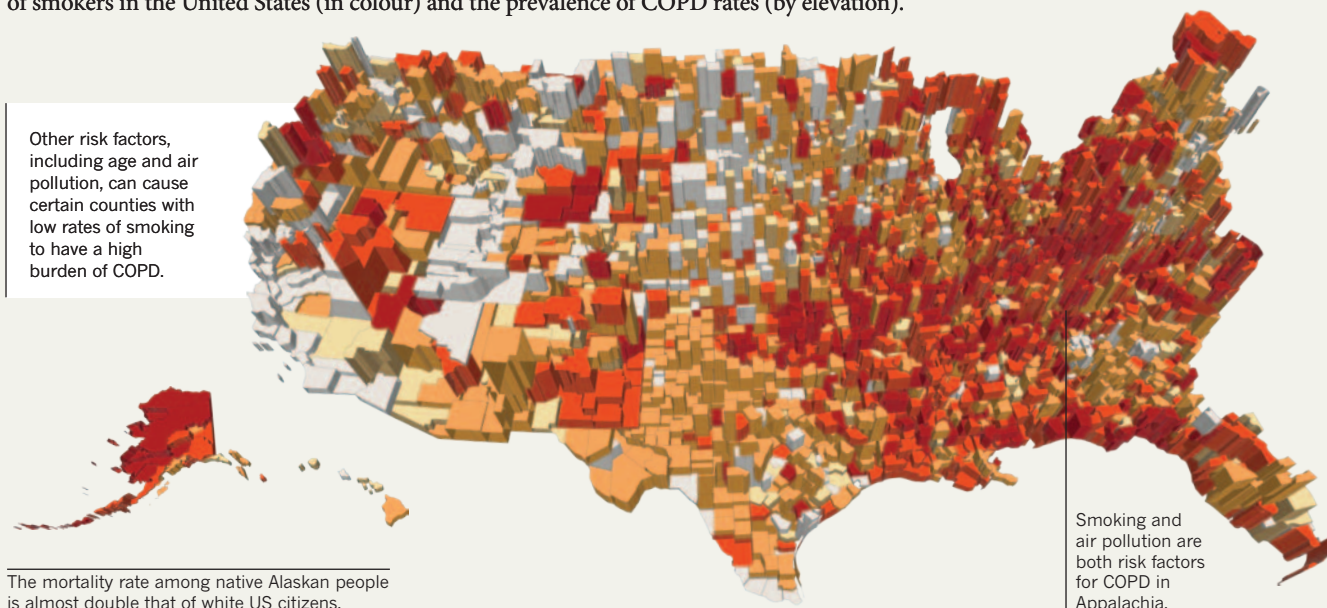
Of the ten most common causes of death in the United States, COPD is the only one with an increasing death rate.



The rise was fuelled partly by a sharp increase of COPD among women, who in 2000 became more likely than men to die of the disease owing to several trends including more women smoking at a younger age and doctors' increasing awareness of the syndrome.

SMOKE SCREEN

Tobacco smoking is the primary risk factor for COPD in industrialized countries. This map shows the prevalence of smokers in the United States (in colour) and the prevalence of COPD rates (by elevation).



The mortality rate among native Alaskan people is almost double that of white US citizens.

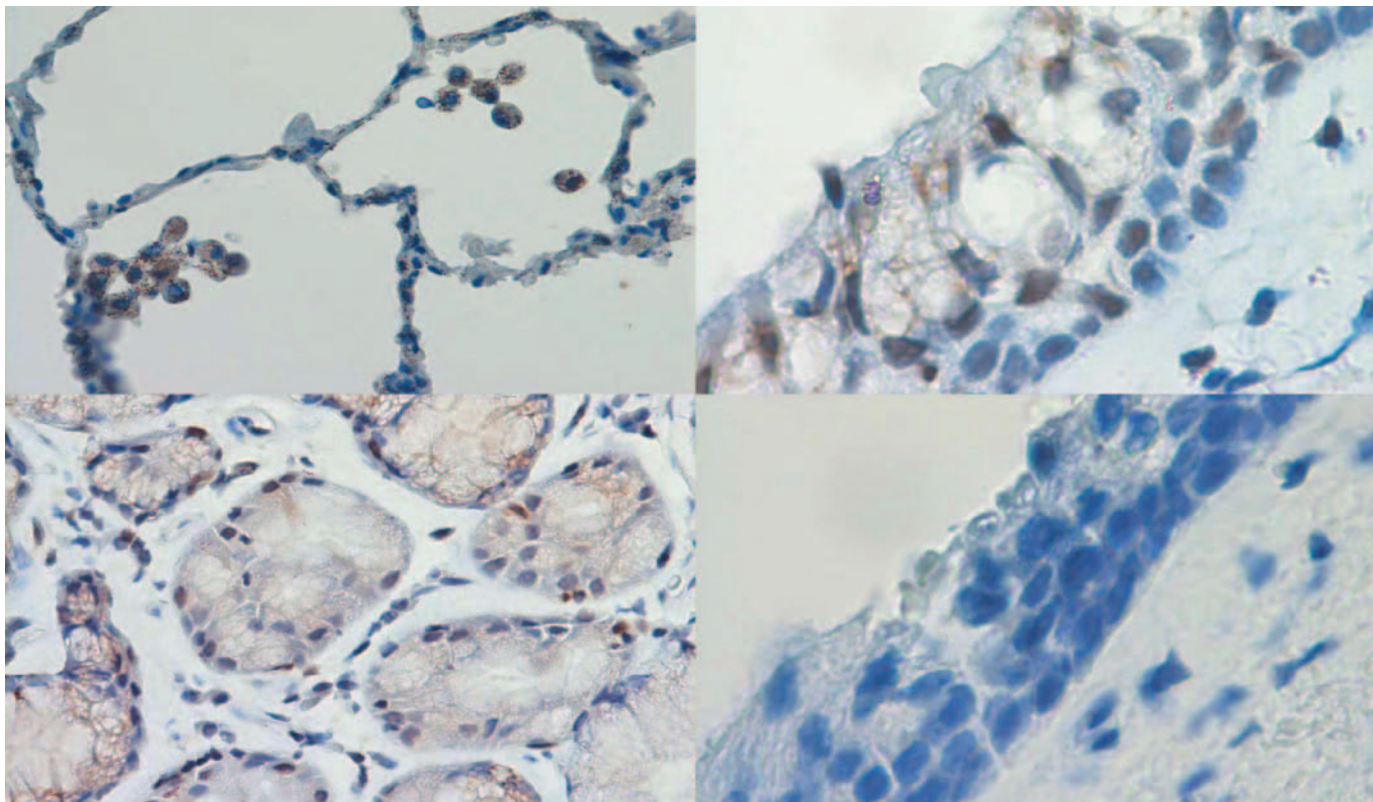
Smoking rates



COPD rates

Counties are elevated by COPD prevalence

Data for 'A disease on the rise' came from the American Lung Association. Data for the map came from the American Lung Association and the CDC's Behavioural Risk Factor Surveillance System. Map illustrated by Chris Wilson.



Immune cells taken from the lung seen expressing the protein Nrf2 (brown) which acts as a master switch for genes that encode protective antioxidants.

BIOCHEMISTRY

A radical treatment

Researchers are counting on drugs that activate a master switch for antioxidant genes to protect lung tissue of COPD patients from an onslaught of free radicals.

BY KEN GARBER

Smoking is the most common cause of chronic obstructive pulmonary disease (COPD), a progressive condition characterized by lung damage, a narrowing of the airways and difficulty breathing. No surprise given that each puff of cigarette smoke contains more than 10^{15} free radicals — atoms or molecules with unpaired electrons that can react violently with other molecules, setting off chain reactions that damage proteins, lipids, and DNA. “In excess, [free radicals] will cause injury, and will cause impairment in the repair process,” says biochemist Irfan Rahman of the University of Rochester in New York. “That’s what happens in lungs in response to tobacco smoke.”

COPD continues to progress long after a person quits smoking, and free radicals are partly to blame. COPD involves chronic inflammation, and inflammatory cells release abundant free radicals. As a result, the lungs of COPD patients exist in a constant state of oxidative stress — an imbalance of free radicals

and antioxidants. Antioxidant enzymes convert free radicals to less reactive molecules, and antioxidant free radical scavengers donate electrons to halt free radical chain reactions. In COPD, the shower of free radicals overwhelms these antioxidants, causing cell death and tissue damage.

But clinical trials of antioxidants have mostly failed to prove they work as a COPD treatment. That may be because each chemical antioxidant molecule can extinguish only one target molecule; it is therefore impossible to quench more than a fraction of the excess free radicals even using high doses of antioxidants. Such antioxidants behave in a “sacrificial” manner, says Paul Kirkham, a biochemist at Imperial College London. “Once it’s been used, it’s gone.” Another problem, says Kirkham, is that individual antioxidants may not reach the cellular compartment where they are needed most.

A new approach to COPD promises to solve these problems. Several drug companies are developing compounds that activate the DNA-binding protein Nrf2 (nuclear erythroid-related factor 2, also known as Nfe2l2), which

acts as a master switch of genes that encode antioxidants. Nrf2 emerged from obscurity in 1997, when biochemist Masayuki Yamamoto at the University of Tsukuba in Japan showed that it activates an entire class of detoxifying enzymes. Among these enzymes are many that generate critical antioxidants.

Drugs that activate Nrf2, in theory, would solve the problems of dose and compartmentalization that have so far derailed other antioxidant therapies. To begin with, Nrf2-activated enzymes aren’t spent each time they do their job. “They can effectively regenerate themselves — that’s the beauty of an enzyme,” says Kirkham. “So you need much less of it.” Together, these enzymes neutralize a variety of free radical molecules, not just one, and in all important cell compartments. Finally, Nrf2 induces the expression of proteins that can repair some of the damage inflicted by free radicals.

Researchers have been studying Nrf2 in animal models of COPD for more than a decade, and in human tissue. It now appears that Nrf2

activators may potentially benefit COPD patients beyond triggering antioxidant and detoxification enzymes. Following Yamamoto's discovery, researchers assumed that Nrf2 activators would need to be administered early in the disease — in particular, before the lung tissue destruction typical of emphysema, one of the two main manifestations of COPD. (The other is bronchitis, inflammation of the bronchi, the main airways that go into the lungs.) But work by toxicologist Shyam Biswal at the Johns Hopkins University School of Public Health in Baltimore, Maryland, and others suggests that Nrf2 activators might be effective not only in preventing COPD progression but in treating advanced cases. And, unlike bronchodilator drugs, says Biswal, Nrf2 activators might not just treat the disease's symptoms but also arrest its course.

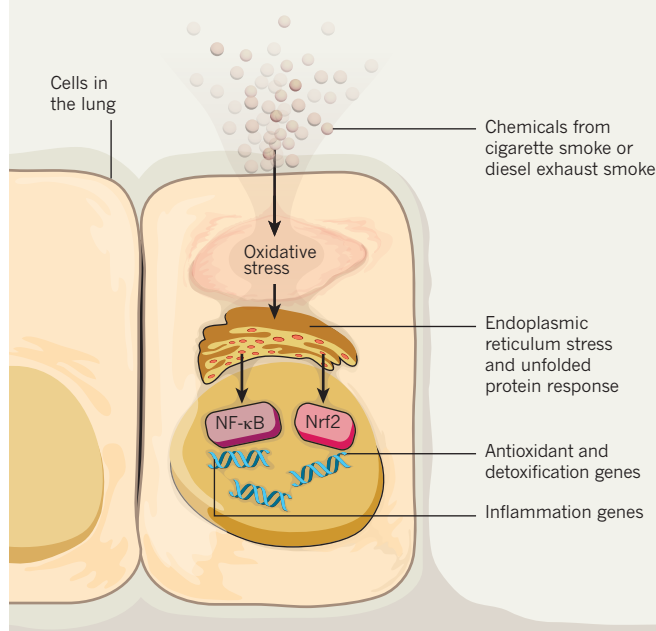
In 2004, Biswal's group found that mice genetically engineered to lack Nrf2 developed early-onset emphysema with more severe inflammation than did wild-type mice, and that this was a result of oxidative stress¹. Moreover, exposing the mice without Nrf2 to cigarette smoke over six months caused comparatively more lung damage. Four years later, three different research groups reported that Nrf2 activity declines as COPD progresses in humans — suggesting some protective role for Nrf2. Then Biswal's group found that lack of Nrf2 activity in human COPD lungs caused defective protein clearance, which led in turn to more oxidative stress and cell death. Adding an Nrf2 activator to cells prevented these effects. The overall picture emerging from these studies is that Nrf2 is a key stress-response factor whose absence worsens COPD.

Nrf2 may also help clear harmful bacteria from the lungs of COPD patients. Such bacteria can cause COPD exacerbations — acute and potentially fatal bouts of increased coughing, mucus production and shortness of breath. Biswal's group found that adding an Nrf2 activator to cultures of macrophages (crucial host defense cells) taken from the lungs of COPD patients restored the cells' ability to clear bacteria in culture and in mice². Biswal's group went on to show that Nrf2 in macrophages activates a scavenger receptor that recognizes pathogenic bacteria and enables the macrophages to clear infection — thus, in theory, limiting COPD exacerbations.

Finally, Nrf2 plays a crucial role in overcoming treatment resistance to corticosteroids, a mainstay in asthma therapy, which doctors often prescribe to COPD patients. Unfortunately these steroid hormones provide little

YIN AND YANG

Cigarette smoke and other toxins cause lung cells to activate transcription factors NF- κ B and Nrf2. In the nucleus, NF- κ B promotes inflammation whereas Nrf2 turns on antioxidant genes and dampens inflammation.



or no therapeutic benefit in COPD. In fact, says Biswal, “steroids cause more problems in COPD than they help,” mainly because steroid treatment can lead to pneumonia. An explanation for this corticosteroid resistance emerged in 2005, when pulmonologist Peter Barnes at Imperial College London reported that oxidants in cigarette smoke inactivated the enzyme histone deacetylase 2 (HDAC2), which normally blocks the expression of inflammatory genes. Corticosteroids reduce inflammation by signalling through a receptor that recruits HDAC2 and represses inflammatory gene expression.

“You’ve got to do the clinical trial and then see what happens.”

By reducing oxidative stress, Nrf2 activators can reverse corticosteroid resistance, at least in cell culture. Biswal and his Johns Hopkins colleague Robert Wise are planning a clinical trial of treating COPD patients with the steroid prednisone and the Nrf2 activator sulforaphane. “This would be a logical approach,” says Barnes. Sulforaphane is already in a phase II clinical trial for COPD, sponsored by the US National Institutes of Health. Cells extracted from the lungs of COPD patients will be tested to see if the drug raises levels of Nrf2.

But sulforaphane is not an ideal Nrf2 activator. It does activate Nrf2, but not always

very potently, and because it targets many other proteins it could potentially cause collateral damage. And although safe at low doses (it is derived from broccoli sprouts), sulforaphane can be toxic at high doses. Hence an intense search for more selective Nrf2 activators is underway.

Drug companies are already heavily involved. In December 2011, in one of the largest pre-clinical deals ever, Abbott Laboratories, headquartered in Abbott Park, Illinois, agreed to pay US\$400 million to Reata Pharmaceuticals, based in Irving, Texas, to license Reata's second-generation Nrf2 activators. Abbott executive vice president Thomas Freyman told investors in January 2012 that he expected the first of those compounds to enter clinical trials later in the year. Meanwhile, Cureveda, a Baltimore, Maryland, biotech firm cofounded in 2010 by Shyam Biswal, is screening compound libraries from the UK pharmaceutical company Glaxo-SmithKline for pro-Nrf2 activity.

Other companies are interested in targeting Nrf2, including Pfizer and Novartis, which are part of a consortium studying new therapeutic strategies for treating COPD, according to Kirkham.

Despite their great potential in COPD, Nrf2-activating drugs present possible safety issues. Nrf2 is usually inactive in cells, but is activated by spikes in oxidative stress. Using drugs to keep Nrf2 turned on could disrupt beneficial oxidative processes in cells. “The cell is actually maintained in a very fine redox [oxidation-reduction] balance, because it actually needs oxidative stress to do some of its signaling,” says Kirkham. Biswal concedes that continuous activation of Nrf2 could cause side effects. “You’ve got to do the clinical trial and then see what happens,” he says.

Then there is the evidence that Nrf2 might increase the risk of cancer. In 2008, a group at Japan's National Cancer Research Institute in Tokyo reported apparent Nrf2-activating mutations in human lung tumours and in head and neck tumours³. In their report, they contend that ongoing activation of Nrf2 might give cancer cells “undue protection from their inherently stressed microenvironment.” In 2011, two groups reported that in mouse models Nrf2 is indirectly activated by mutations that cause hereditary kidney cancer in humans. And a group from the Cambridge Research Institute, part of Cancer Research UK, found that three common cancer-causing genes activate Nrf2, which may promote tumorigenesis by reducing oxidative stress in

pre-cancerous cells⁴.

But, paradoxically, activated Nrf2 can also have anticancer effects. Several studies have found that Nrf2-activating compounds can prevent or suppress cancer in mouse models. And a recent study found that sulforaphane did not promote lung cancer in mice. Pharmacologists Mike Sporn and Karen Liby at Dartmouth College in Hanover, New Hampshire, explain that Nrf2 can either promote or suppress cancer depending on the cellular context⁵.

Safety concerns about Nrf2 activators in COPD have been lessened by trials of two Nrf2-activating drugs in other diseases. Weston, Massachusetts-based Biogen Idec recently completed phase III clinical trials of dimethyl fumarate (DMF) for multiple

sclerosis. Although DMF wasn't designed as an Nrf2 activator, the company claims it works at least partly that way. And Abbott and Reata are jointly developing bardoxolone methyl, another unintentional Nrf2 activator that's now in phase III trials for chronic kidney disease in type 2 diabetes. Side effects of bardoxolone methyl have been mild. Side effects reported for DMF include abdominal pain, diarrhea, flushing and headaches. On the other hand, it is too early to assess the risk of cancer — any cancers would likely take many years to appear.

Clinical trials should soon determine if Nrf2 can help resolve the many problems in COPD, from oxidative stress to inflammation. "COPD is a multifactorial disease — it's one of the

worst," says Biswal. Harnessing the power of Nrf2, that prolific protective protein, may eventually prove to be the solution. ■

Ken Garber is a freelance science writer based in Ann Arbor, Michigan.

1. Rangasamy, T. *et al. J. Clin. Invest.* **114**, 1248–1259 (2004).
2. Harvey, H. *et al. Sci. Transl. Med.* **3**, 78ra32 (2011).
3. Shibata, T. *et al. Proc. Natl. Acad. Sci.* **105**, 13568–13573 (2008).
4. DeNicola, G. M. *et al. Nature* **475**, 106–109 (2011).
5. Sporn, M. B. & Liby, K. T. *Nat. Rev. Cancer* **8**, 564–571 (2012).
6. Lee, S.H. *et al. Nature Med.* **13**, 567–569 (2007).
7. Shan, M. *et al. Sci. Transl. Med.* **1**(4):4ra10 (2009).
8. Chen, K. *et al. PLoS One* **6**, e2033 (2011).
9. Shan, M. *et al. Sci. Transl. Med.* **4**, 117ra9 (2012).

AUTOIMMUNITY

The T-cell connection

What exactly causes the destruction of lung tissue in emphysema? Free radicals definitely contribute, but for half a century, the prevailing hypothesis has been that emphysema, one of the two main aspects of COPD, develops when the activity of proteases — enzymes that digest proteins — falls out of balance with antiprotease activity. Proteases normally help maintain lung health by clearing roadblocks from the path of migrating immune cells hunting pathogenic viruses and bacteria. But cigarette smoke stimulates immune cells such as macrophages and neutrophils to release too many proteases, and wanton destruction of proteins ensues. Mysteriously and inexorably, this process continues in COPD patients even after they stop smoking, as emphysema slowly suffocates them.

That mystery is now beginning to be solved, as clues implicate autoimmunity. Th17 cells — a specialized class of CD4⁺ T cells, the cell type that orchestrates the adaptive immune response — appear to be central to the pathology. Therefore, therapies targeting these cells might be a promising strategy.

Early evidence for autoimmunity in COPD came in 2007, when Farrah Kheradmand, a pulmonologist and immunologist at Baylor College of Medicine in Houston, Texas, isolated CD4⁺ T cells from the blood of ex-smokers with COPD⁶. Elastin is an important structural protein in the lungs' connective tissue, and when Kheradmand added elastin fragments to these T-cell cultures, the T cells responded by releasing inflammatory cytokines as if the cells had encountered a microbial pathogen. "A large number of patients who have emphysema [who] stop smoking and continue to have the disease will have these

autoreactive T cells," says Kheradmand.

Why the body attacks its own lung tissue remains unknown. But by isolating the cells driving this autoimmunity, scientists can identify potential drug targets. Th17 cells, which secrete the inflammatory cytokine IL-17, are the main drivers of autoimmunity in rodent models of rheumatoid arthritis, psoriasis and multiple sclerosis. Th17 cells are also present in COPD. In 2009, Kheradmand's group found that culturing certain cells of emphysema patients with their own T cells drove those T cells to release IL-17, which in turn led to the production of destructive proteases⁷.

Evidence for IL-17 driving autoimmunity in COPD continues to be found. In 2011, University of Pittsburgh, Pennsylvania, pulmonologist Jay Kolls reported that mice genetically lacking the IL-17 receptor did not develop emphysema despite six months of exposure to cigarette smoke⁹. More recently, Kheradmand and collaborators at the MD Anderson Cancer Center in Houston, Texas, genetically engineered mice to overexpress one form of IL-17 — IL-17A — and then exposed these mice to cigarette smoke for four months⁸. The mice developed an especially severe form of emphysema along with producing more destructive proteases. Both studies fingered IL-17 as a culprit in COPD autoimmunity.

The picture emerging from these studies is that inhalation of cigarette smoke promotes the generation of T cells that express IL-17, which, in turn, causes the production of proteases that destroy lung tissue including elastin. Then, elastin fragments trigger an autoimmune response involving more IL-17-producing T cells, perpetuating a loop and more tissue destruction.

To disrupt this vicious cycle, pharmaceutical and biotech companies could test drugs they already have in hand that target these cells and the cytokines they produce. Antibodies specific for IL-17 and its receptor have been very effective in clinical trials for psoriasis. As for COPD, "I don't know if it is on the radar screen of these companies yet, but I think [IL-17] would be definitely an intriguing target," says Kolls. He is collaborating with an undisclosed company, testing whether anti-IL-17 receptor antibodies can treat COPD in mice.

Others are more ambivalent. "It would certainly be worth studying IL-17 or IL-17 receptor blockers," says Peter Barnes, a pulmonologist and COPD researcher at Imperial College London. He adds that such trials are planned. But he cautions that Th17 cells may not play the same role in human COPD as in the mouse version of the disease; indeed, he says, the evidence for increased Th17 cells in human COPD lungs is "not as striking" as it is in mice. "The evidence for Th17 cells playing an important role in COPD is not fully established," he adds.

Kheradmand disagrees. She says that IL-17 is "very much present" in lung tissue of human COPD patients. And Kheradmand points out that each case of emphysema is different, with not all manifesting autoimmunity. Her lab at Baylor College is developing an assay to identify COPD patients with an autoimmune form of the disease driven by Th17 cells, and hopes companies will eventually test their drugs in such patients. "Wouldn't it be wonderful," she asks, "if we can just identify this particular individual... who does have this autoimmune component, to then offer him these biologics?" — **K.G.**

PERSPECTIVE



How can genetics help?

Smoking and COPD have one of the strongest relationships in clinical epidemiology. But don't forget the genetics, says **Edwin K. Silverman**.

Many people who develop chronic obstructive pulmonary disease (COPD) blame themselves rather than the tobacco industry, which continues to promote cigarette smoking though the dangers are well-known. This disturbing 'blame and shame' attitude among patients is based on one of the most well-established associations in clinical epidemiology: the causal relationship between cigarette smoking and COPD. Exposure to cooking stove smoke from biomass fuels is also an important COPD risk factor in some parts of the world.

Although these environmental risk factors are strong, recent research suggests that genetics also plays a key role in COPD. Identifying genetic determinants and investigating their functions may lead to important progress in COPD pathobiology, diagnosis and treatment. It could also help patients understand that the disease is not their fault.

Genetics provided one of the first clues regarding COPD pathogenesis. A small percentage of patients inherit severe $\alpha 1$ -antitrypsin deficiency (A1ATD), a well-characterized, rare syndrome that often includes COPD. The discovery of A1ATD nearly 50 years ago led to the protease-antiprotease hypothesis for COPD, which postulates that lung destruction results from an excess of protein-degrading enzymes relative to their enzyme inhibitors. This hypothesis remains important in current COPD pathobiology.

Not all smokers are equally likely to develop COPD. An underlying susceptibility appears to run in families. Indeed, familial studies of severe, early-onset COPD patients without A1ATD suggest other genetic risk factors. Smokers who are first-degree relatives of these subjects are about three times more likely to develop COPD than are smokers in general. Non-smokers who are first-degree relatives of these subjects are not at increased risk¹, suggesting that genetic factors may interact with smoking.

As with other complex diseases — those influenced by multiple genetic and environmental factors — many studies of candidate genes have failed to replicate. Yet subsequent genome-wide association studies (GWAS) have found four genomic regions associated with COPD that meet the stringent standard for statistical significance in genome-wide studies^{2–5}.

Two of these genomic regions, near the *HHIP* and *FAM13A* genes — the former a member of the developmentally essential hedgehog pathway, the latter a gene of unknown function — are also associated with variations in lung function levels in samples taken from the general population^{5,6}. An association with lung function does not in and of itself prove susceptibility to COPD; genes that influence traits that vary among healthy people, such as height, are not always the same ones that influence pathological conditions, such as dwarfism. However, the associations of COPD to genomic regions near *HHIP* and *FAM13A* are convincing. They have been replicated in several studies, and a potential functional genetic variant that regulates *HHIP* gene expression has been found upstream from *HHIP*⁷. Further study of *HHIP* and *FAM13A* may identify new biological pathways involved in COPD.

The other two regions identified by GWAS, on chromosome 15 and chromosome 19, include many genes of interest, including several related to nicotine addiction. The chromosome 19q region has been associated with smoking behaviour; it is the location of the gene *CYP2A6*, involved

in nicotine metabolism. Similarly, the chromosome 15q25 region, which contains genes for several components of the nicotinic acetylcholine receptor, has been convincingly related to smoking behaviour. The same region also contains the gene *IREB2*, which encodes an iron binding protein that has been potentially linked to COPD susceptibility.

The overwhelming association between COPD and smoking provides a unique opportunity to understand the relationships between environmental and genetic influences on risk of disease. In most complex diseases, environmental factors are either unknown or difficult to measure. Cigarette smoking behaviour, on the other hand, can be accurately quantified. Of course, genes and the environment are intertwined; genetic determinants of nicotine addiction may influence exposure to COPD's key environmental risk factor. Furthermore, the risk from smoking suggests that epigenetic factors may also influence COPD pathogenesis⁸.

The next generation of genetic research on COPD will include studies of rare genetic variants assessed by sequencing or genotyping the variants in patients' exomes (the protein-coding portions of the genome) and ultimately by sequencing their entire genomes. Advances in computational biology and phenotype characterization based on imaging and clinical observation will also be needed in coordination with genetic studies to dissect the COPD syndrome into groups of patients with different subtypes — an initiative with both diagnostic and therapeutic implications. COPD is highly heterogeneous, with variable amounts of emphysema and airway disease. Integrating genetic studies with chest computed tomography (CT) scans has already identified the *BICD1* gene as a potential determinant of emphysema.

However, comprehensive understanding of the complex pathobiology of COPD will probably require the integration of multiple -omics data types (for example, proteomics, transcriptomics and metabolomics) with detailed phenotypic assessment, epigenetics, and genetic variants using systems biology and network science approaches.

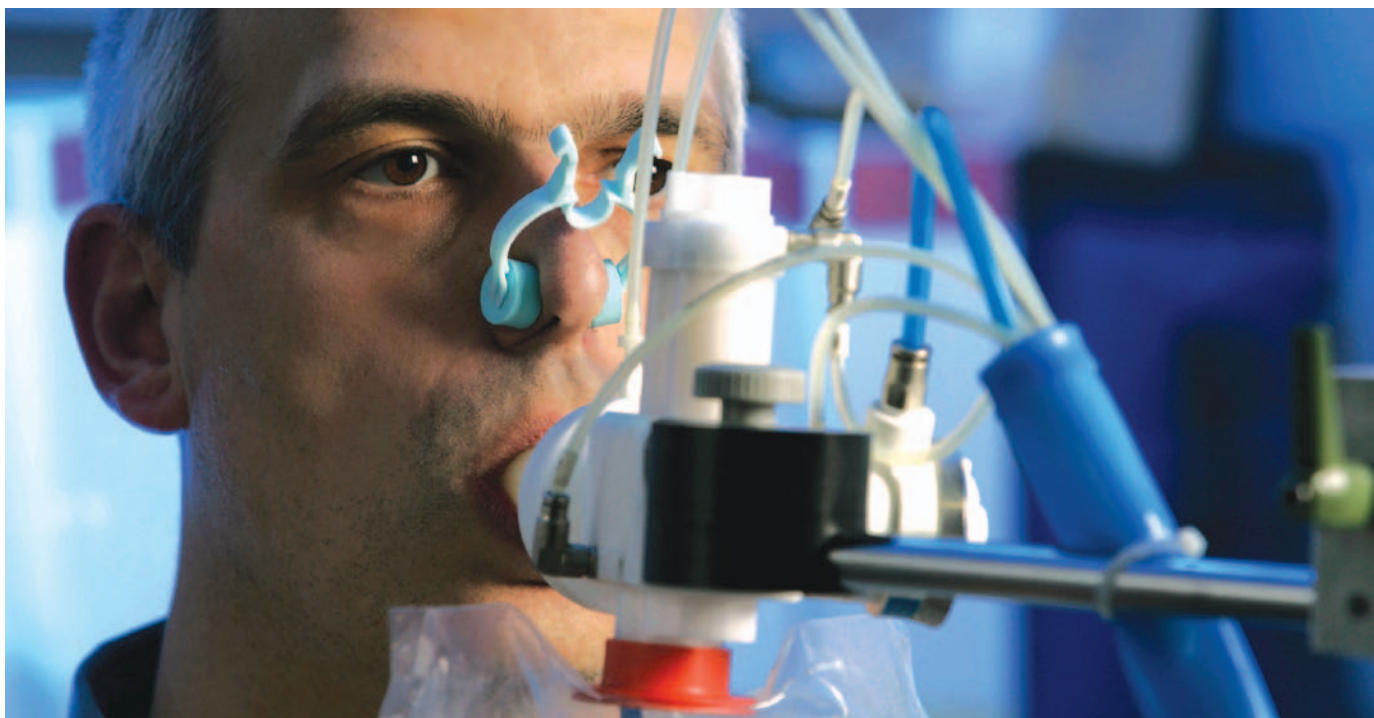
Avoiding tobacco smoke will always be an essential public health message. But for millions already suffering, advances in genetics, pathophysiology and phenotyping may lead to new opportunities for specific diagnosis and personalized treatment of COPD. ■

Edwin K. Silverman is chief of the Channing Division of Network Medicine at Brigham and Women's Hospital in Boston, Massachusetts, and associate professor of medicine at Harvard Medical School. email: ed.silverman@channing.harvard.edu

1. Pillai, S. G. *et al.* *PLoS Genet.* **5**(3), e1000421 (2009).
2. Wilk, J. B. *et al.* *PLoS Genet.* **5**(3), e1000429 (2009).
3. Cho, M. H. *et al.* *Nature Genet.* **42**, 200–202 (2010).
4. Cho, M. H. *et al.* *Hum. Mol. Genet.* **21**, 947–957 (2012).
5. Hancock, D. B. *et al.* *Nature Genet.* **42**, 45–52 (2010).
6. Repapi, E. *et al.* *Nature Genet.* **42**, 36–44 (2010).
7. Zhou, X. *et al.* *Hum. Mol. Genet.* **21**, 1325–1335 (2012).
8. Wan, E. S., *et al.* *Hum. Mol. Genet.* **21**, 3073–3082 (2012).

The author would like to acknowledge helpful discussions with Craig Hersh, Michael Cho, Dawn DeMeo, Scott Weiss and James Crapo. The author declares a conflict of interest go.nature.com/tah34c

GENETICS COULD HELP
PATIENTS REALIZE IT'S
NOT THEIR FAULT



ANTONIA REEVE/SCIENCE PHOTO LIBRARY

Impaired lung function, as measured by breathing apparatus, is a sign of COPD, but researchers are looking for easier and more reliable ways to diagnose disease.

DIAGNOSIS

To catch a killer

The first symptoms of COPD can be subtle, so the disease often goes undiagnosed. Researchers are searching for ways to detect the disease and to identify those most at risk.

BY CASSANDRA WILLYARD

In 1985, John Walsh began having trouble breathing. His doctor diagnosed him with asthma, but asthma medications didn't seem to help. John's non-identical twin brother, Fred, began having similar problems at about the same time. He too was told he had asthma, but asthma treatments didn't work for him either.

For years, the two men struggled to find a way to alleviate their symptoms. Then, in 1989, John got a phone call from his brother. "He said, 'I got good news and bad news,'" John Walsh recalls. The good news was that the brothers, who were 40 at the time, finally had a correct diagnosis. The bad news was that they had a genetic form of chronic obstructive pulmonary disease (COPD) — the same disorder that had killed their mother when they were 13 years old.

The Walsh brothers have a rare mutation in the gene *SERPINA1* (present in 5% of people with COPD) that causes them to produce an abnormal version of a protein called $\alpha 1$ -antitrypsin, which usually protects lung function. But the disease is common, killing millions of people each year, mainly as a result of exposure to tobacco smoke or airborne pollutants.

According to the World Health Organization, 65 million people worldwide have COPD, but the exact number is hard to pin down because many cases are not diagnosed. Data from the third National Health and Nutrition Examination Survey in 2000 showed that 24 million people in the United States had impaired lung function that might indicate COPD, but less than half had received a diagnosis of COPD.

Lack of awareness is part of the problem. COPD hasn't garnered the recognition that other chronic illnesses such as cardiovascular disease and cancer have, says Bartolome Celli, a doctor who specializes in lung diseases at Brigham and Women's Hospital in Boston, Massachusetts.

John Walsh — who is now president of the COPD Foundation, a non-profit organization based in Washington DC that advocates research and education — and health officials around the world are working to change that by launching massive awareness campaigns. Meanwhile, researchers are searching for new ways to identify individuals with COPD.

A SILENT EPIDEMIC

COPD comes on slowly, typically in individuals over the age of 50. The disease "sneaks up on

you", says James Kiley, director of the division of lung diseases at the National Heart, Lung, and Blood Institute (NHLBI) in Bethesda, Maryland. People often attribute their symptoms to normal ageing or to being out of shape, and thus they fail to seek medical care. For smokers, there may also be a sense of "I did it to myself", says Roger Goldstein, a doctor who specializes in respiratory medicine at the University of Toronto in Canada.

Because COPD symptoms resemble those of other conditions such as asthma, even patients who visit the doctor's office might be incorrectly diagnosed. In the early stages of the disease, people complain of "vague and minor symptoms that the doctor doesn't always associate with COPD", says Leonard Fromer, a family doctor who specializes in lung diseases at the University of California, Los Angeles. "It could be something like 'I can't play three sets of tennis anymore. I get tired too quickly.'" In some cultures, the doctor might not even ask about patients' smoking habits for fear that this might be "digging too much into people's private habits," says Anne Frølich, a doctor who studies chronic diseases at the University of Copenhagen.

Even a textbook case of the disease may be missed if the patient doesn't fit the stereotypical

COPD profile. Doctors have long been trained that COPD is a disease of elderly men who smoke, says Fromer. In 2001, for example, a team of researchers presented 192 general practitioners in the United States and Canada with a hypothetical case description that was indicative of COPD (Chapman, K. *et al. Chest* **119**, 1691–1695; 2001). When the researchers said that the patient was a man, 58% of the doctors gave COPD as the most probable diagnosis. That dropped to 42% when the researchers said the patient was a woman. Yet, in the United States at least, more women than men are being diagnosed now, and more women have died from COPD each year since 2000 — perhaps because women are biologically more susceptible to developing the disease than men or perhaps because, as a group, they started smoking later than men.

Among men and women, awareness of COPD is on the rise. In 2007, the NHLBI launched the Learn More Breathe Better campaign. And, in February 2010, an awareness campaign called DRIVE4COPD was launched by the German pharmaceutical company Boehringer Ingelheim, which markets the widely used COPD medication Spiriva (tiotropium bromide) together with pharmaceutical giant Pfizer. Boehringer Ingelheim selected stock-car racer Danica Patrick as its celebrity spokesperson, and the DRIVE4COPD campaign, now led by the COPD Foundation, has screened nearly 2.5 million people via an online questionnaire. Participants are encouraged to share the completed questionnaire with their doctor or other health-care professionals. These campaigns may be paying off. A 2011 web-based survey by the NHLBI found that 71% of US adults say that they're aware of the disease, up from 65% in 2008.

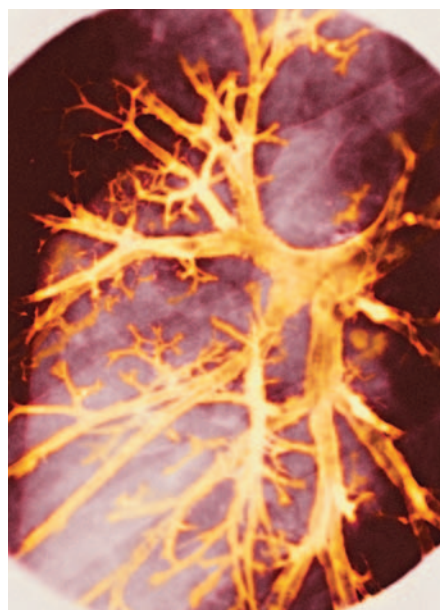
SEEKING THE SICK

In addition to lack of awareness, another factor that contributes to underdiagnosis is the diagnostic test itself. General practitioners and pulmonary specialists diagnose COPD based on a patient's medical history, symptoms and a lung function test called spirometry. The test requires the patient to blow into a tube as hard and fast as possible. A device then measures the total amount of air exhaled and the amount of air exhaled in 1 second.

Spirometry is simple, but it is not flawless. If the patient accidentally fails to blow hard enough, the results may mean little. "Thirty to forty per cent [of the test results are] pretty much uninterpretable," says David Mannino, an epidemiologist at the University of Kentucky in Lexington. Mannino is interested in devising alternative tests, such as one "where you see what happens to a person's blood oxygen as they hold their breath." But this research is still in the earliest stages: Mannino is currently putting together grant proposals. Other researchers are beginning to look for diagnostic biomarkers in the blood, urine and sputum. A peptide called *N*-acetyl-proline-glycine-proline, a by-product of the breakdown of collagen, has been found

in the sputum of COPD patients but not in the sputum of people without the disease. In addition, the protein fibrinogen, a marker of inflammation, appears to be elevated in the blood of people who have COPD, but it may be more useful for predicting future risk of exacerbations than as a diagnostic tool. One NHLBI initiative, the Subpopulations and Intermediate Outcome Measures in COPD Study (SPIROMICS), aims to identify molecular markers of disease progression. Such markers may enable doctors to "find [pulmonary] lesions extremely early," Kiley says.

Besides developing better tools for diagnosing COPD, researchers are also trying to find ways to target screening efforts. Mass spirometry screening doesn't seem to be a good option. In 2008, the US Preventive Services Task Force found that health workers would need to screen roughly 450 adults between the ages of 60 and 69 to pick out a single person who might later



Damaged bronchi lead to a build-up of mucus and swollen bronchioles (orange).

develop symptoms of COPD severe enough to require a trip to the emergency department.

Mannino and Fernando Martinez, a lung specialist at the University of Michigan in Ann Arbor, were recently awarded a multimillion dollar grant by the National Institutes of Health to develop a more targeted method of diagnosis that could be used for screening programmes. They plan to combine a series of five simple questions on COPD risk factors — for example smoking status, wheezing and a chronic cough — with an easy-to-use, hand-held device that costs about US\$30 and measures peak flow (the fastest speed at which an individual can breathe out). Spirometers, by comparison, generally cost several thousand dollars each, and health workers need special training to learn how to use them correctly. Both factors may have led to the underuse of spirometers in developing nations (see "Where there's smoke," page S18). Patients with a

normal peak flow are unlikely to have clinically significant COPD. Patients who fare poorly on peak-flow tests could undergo a more thorough assessment, including spirometry testing.

COPD occurs when the tiny sacs inside the lungs, called alveoli, become damaged or chronically inflamed. This damage or inflammation leads to breathing troubles. Spirometers and other airflow-sensing devices give doctors information about airway obstruction, but such tests cannot directly assess damage to lung tissue, says Jan-Willem Lammers, head of the respiratory medicine department at the University Medical Centre Utrecht in the Netherlands. This damage can be seen in computed tomography (CT) scans. In fact, research conducted as part of the COPDGene study, which aims to identify common genetic factors that may subtly predispose people to the disease, found that CT imaging can identify lung deterioration in an individual before considerable airway obstruction occurs. The guidelines don't recommend treating individuals who are asymptomatic, but Walsh and others hope that therapies might one day be able to prevent symptoms in those who are found to have early stages of COPD-like lung damage.

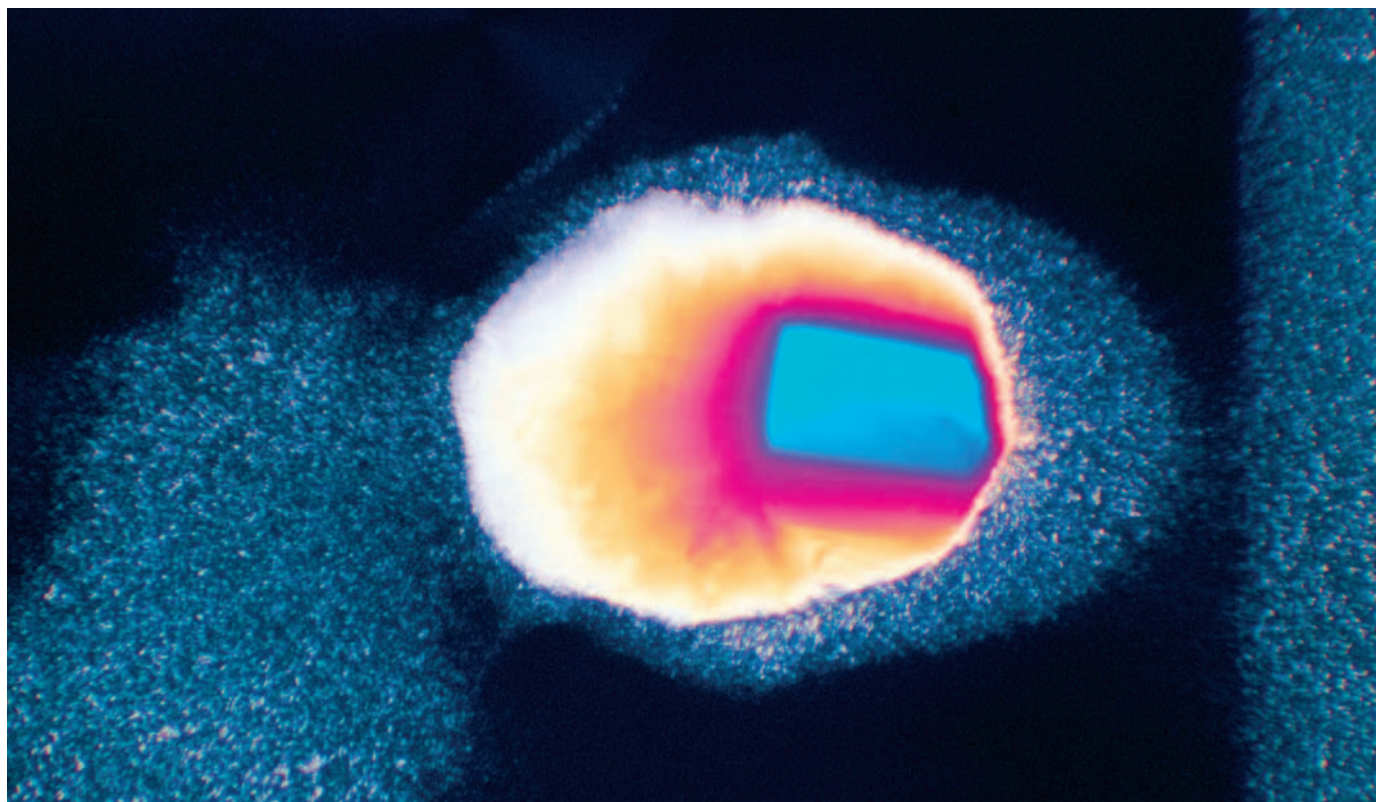
CT scans aren't likely to become a screening tool just for COPD though. "That's going to be way too expensive, and people are going to be worried about the exposure to radiation," Walsh says. However, joint guidelines issued in May 2012 by the American College of Chest Physicians and the American Society of Clinical Oncology recommend that former and current heavy smokers of 55 to 74 years of age have a CT scan each year to screen for lung cancer. Those same images could also reveal signs of COPD.

Clearly, a diagnosis isn't a cure. It is unclear whether detecting the disease early will actually benefit many patients. Will it help them live longer or improve the quality of their lives over the long term? Research addressing these questions is surprisingly scarce, says Mannino.

But an earlier diagnosis might have changed things for the Walsh brothers. Today, John Walsh is hooked up to an oxygen tank when he sleeps. His lung function is one-third of what it should be for a man his age. His brother Fred Walsh needs oxygen around the clock, and he is waiting for a lung transplant. John can't help but wonder how their lives might have been different had they been correctly diagnosed sooner. If the men had known that their mother died of COPD — which they didn't fully realize until they themselves were diagnosed — would Fred have taken up smoking? Did Fred's lifestyle choices make his disease more severe than that of his brother, who has never smoked?

The Walsh brothers can't change their own past. John, however, hopes that organizations such as the COPD Foundation can change the future for others, and soon, he says: "I'm an impatient patient." ■

Cassandra Willyard is a freelance writer based in New York.



DAVID PARKER/SCIENCE PHOTO LIBRARY

Vitamin D₂, shown in its crystalline form, can be used as a dietary supplement and is being studied for its therapeutic effects in patients.

NUTRITION

The vitamin D complex

Many COPD patients are deficient in vitamin D, a condition that can lead to bone problems as well as difficulty breathing. Can dietary supplements be of help?

BY THEA SINGER

My sister, Candice Singer, was a smoking fiend. Hooked since age 12, she was up to two packs a day by the time she started university, eventually rolling her own cigarettes to save money. In 2010, at age 50, she was diagnosed with chronic obstructive pulmonary disease (COPD) and needed to wear an oxygen mask at night to regulate her breathing while she slept.

When she finally quit smoking, seven months ago, her vitamin D level was an alarmingly low 8 nanograms of 25-hydroxyvitamin D (25-[OH]D) — the major circulating, though inactive, form of vitamin D and used to measure sufficiency — per milliliter of blood serum. The Institute of Medicine (IOM), a non-profit group affiliated the US National Academy of Sciences, defines vitamin D sufficiency at over twice Candice's level — 20 ng/mL. And The Endocrine Society, an international group of endocrinologists, set an even higher sufficient range of 40–60 ng/mL.

That's for good reason. Vitamin D deficiency can lead to osteoporosis and osteomalacia, a fragility and a softening of the bones. Candice came to know the symptoms, with pains in her feet and back. And new research suggests that patients like Candice have other things to worry about, as vitamin D deficiency may affect more than the skeleton — even the ability to breathe.

A COPD-VITAMIN D LINK?

COPD is primarily an inflammatory disease. The predominating hypothesis holds that cigarette smoke damages the lung's tissue, sparking an innate immune response. Immune cells, including macrophages and neutrophils, rush into the lungs to protect the cells lining the airways from the smoke, releasing reactive, oxygen-containing molecules along the way. Antimicrobial peptides, a group of molecules that damage and kill microorganisms, join the fray, as do pro-inflammatory T cells stimulating the production of antibodies of as yet unknown specificity.

In smokers, this proinflammatory response is relentless. In the emphysema form of COPD, holes appear in the alveoli — the tiny, balloon-like structures in the lungs where oxygen and carbon dioxide are exchanged. And in response to noxious stimuli, the smooth muscle beneath the epithelial and connective layers of tissue contracts and expresses adhesion molecules, cytokines, chemokines and growth factors¹. Over the years, this muscle thickens. “Think of it as weight lifting,” says Reynold Panettieri Jr, professor of medicine at the University of Pennsylvania in Philadelphia. “If you keep lifting weights, your muscle bulks up — it gets thicker. And the problem with thicker is that the [airway becomes narrower] simply by the increased mass of the muscle.” Hence the shortness of breath that characterizes COPD. Most of the inhalant corticosteroids and some other medications for COPD aim to relax that stiffened muscle.

This is where vitamin D comes in. Nearly every cell in the body has a surface-bound

receptor that directs vitamin D to the nucleus. In fact, about 3% of the human genome is regulated by the active form of vitamin D, 1,25-dihydroxyvitamin D⁵. Studies of human cells in culture, have shown that vitamin D stunts the growth of human airway smooth muscle cells⁶. This effect, says Panettieri, is even more pronounced than that induced by inhaled steroids. Moreover, during an infection — a common occurrence in COPD patients given their compromised lungs — vitamin D aggravates the misfiring immune response. Studies have also found a link between vitamin D deficiency and autoimmune diseases including multiple sclerosis and rheumatoid arthritis^{2,3,4}.

SEARCHING FOR PROOF

It is not known whether vitamin D deficiency can cause COPD, but there's evidence that it may be involved in its pathogenesis. One epidemiological study found vitamin D deficiency in more than 60% of patients with severe COPD, and the more severe the disease, the worse the deficiency⁵. Research presented in May 2012 at the American Thoracic Society's annual meeting found that a three-year decline in a crucial metric of breathing, forced expiratory volume (FEV1), was linked to vitamin D deficiency. The decline was so steep it is comparable to the effects of smoking⁶. And a 2011 study in mice found that vitamin D deficiency causes deficits in lung function⁷.

So if vitamin D levels correlate with the severity of COPD, could a dietary supplement of the vitamin — which the body synthesizes from the sun's ultraviolet-B (UVB) — help abate the debilitating condition? There are few studies that have given vitamin D to COPD patients.

A randomized, double-blind placebo-controlled study, the gold standard of clinical trials, led by pulmonologist Wim Janssens at University Hospitals Leuven, Belgium, had mixed results. Patients 50 years of age or older with moderate to very severe COPD were given large doses of vitamin D or a placebo at 4-week intervals for a year. The researchers then recorded the incidence of COPD exacerbations — a worsening of respiratory symptoms over 48 hours — and monitored blood serum levels of 25-[OH]D.

In the supplemented group, mean levels of 25-[OH]D increased (to 52 ng/mL) compared to the placebo group. But there was no improvement in the timing and frequency of exacerbations, FEV1, or rates of hospitalization and fatality⁸. “The main message of the paper is a null message,” says Janssens.

Despite discouraging results, Janssens remains convinced that vitamin D deficiency plays a role in COPD progression and that dietary supplements might slow the course of the disease. Janssens' team took another look at the

trial's data and found that those with the most severe deficiency — 30 patients with baseline serum 25-(OH)D levels below 10 ng/mL — had 43% fewer exacerbations over the year.

That analysis matters, says Panettieri, noting the treatment's potential efficacy in certain subgroups. He explains that vitamin D, in high enough doses, can act as an anti-inflammatory.

“If we used vitamin D in a more challenging approach maybe the study would have been positive.”

But, he says, the vitamin D levels induced in Janssens's study may not have been high enough to produce an anti-inflammatory effect. “They simply corrected the deficiency but didn't



Former smoker Candice Singer now lives with COPD.

use vitamin D as an anti-inflammatory,” he says. “We believe that if we used vitamin D in a more challenging approach to enhance the anti-inflammatory effects, maybe the study would have been positive, although more data is necessary to prove that.”

Diane R. Gold and JoAnn E. Manson, professors of medicine at Harvard Medical School in Boston, Massachusetts, addressed the issue of vitamin D dosing in an editorial accompanying publication of the clinical trial. They cited the benefits of daily versus intermittent dosing in other, non-COPD-related vitamin D trials⁹. They also suggest that differences in participants' physiology, immunology, and genetics may partly explain the null results in the general COPD population. COPD is not a monolithic disease: muscles thicken and tissues are destroyed to varying degrees, and molecular variants in the vitamin D binding protein — which transports vitamin D in the bloodstream — affect activation of immune cells including macrophages. In fact, Janssens had found that COPD patients with two copies of a particular

variant in the gene for vitamin D binding protein were more likely to be deficient in vitamin D deficiency⁵.

Unraveling whether vitamin D deficiency is a cause of COPD requires more clinical data. Gold and Manson are leading one of the most extensive of those efforts. Their National Institutes of Health-funded Vitamin D and Omega-3 Trial (VITAL) is just starting; it will follow 20,000 participants age 50 and older as they receive 2,000 international units (IU) of vitamin D daily for five years.

DEFICIENCY AS CAUSE?

At least one study in mice sheds some light on the relationship between COPD and vitamin D. A team led by Graeme Zosky, who heads the Lung Growth and Respiratory Environmental Health at the Telethon Institute for Child Health Research, in Subiaco, Australia, fed one group of female mice a vitamin D-deficient diet and another group a diet with sufficient levels. They studied the offspring of both, looking for differences in lung physiology. They measured lung volume and dissected the lungs to take a look inside.

The offspring of the vitamin D deficient mice — also deficient in vitamin D — had statistically significantly smaller lungs than normal: about 18% smaller in female offspring and 28% smaller in males⁷. “Our point was that vitamin D deficiency isn't causing gross structural changes in the lung, but it might be slowing down lung growth,” Zosky says. “What we don't know is what that means when you put disease on top of it. My suspicion is, if we introduced COPD pathology in these mice, the effect would be much larger.”

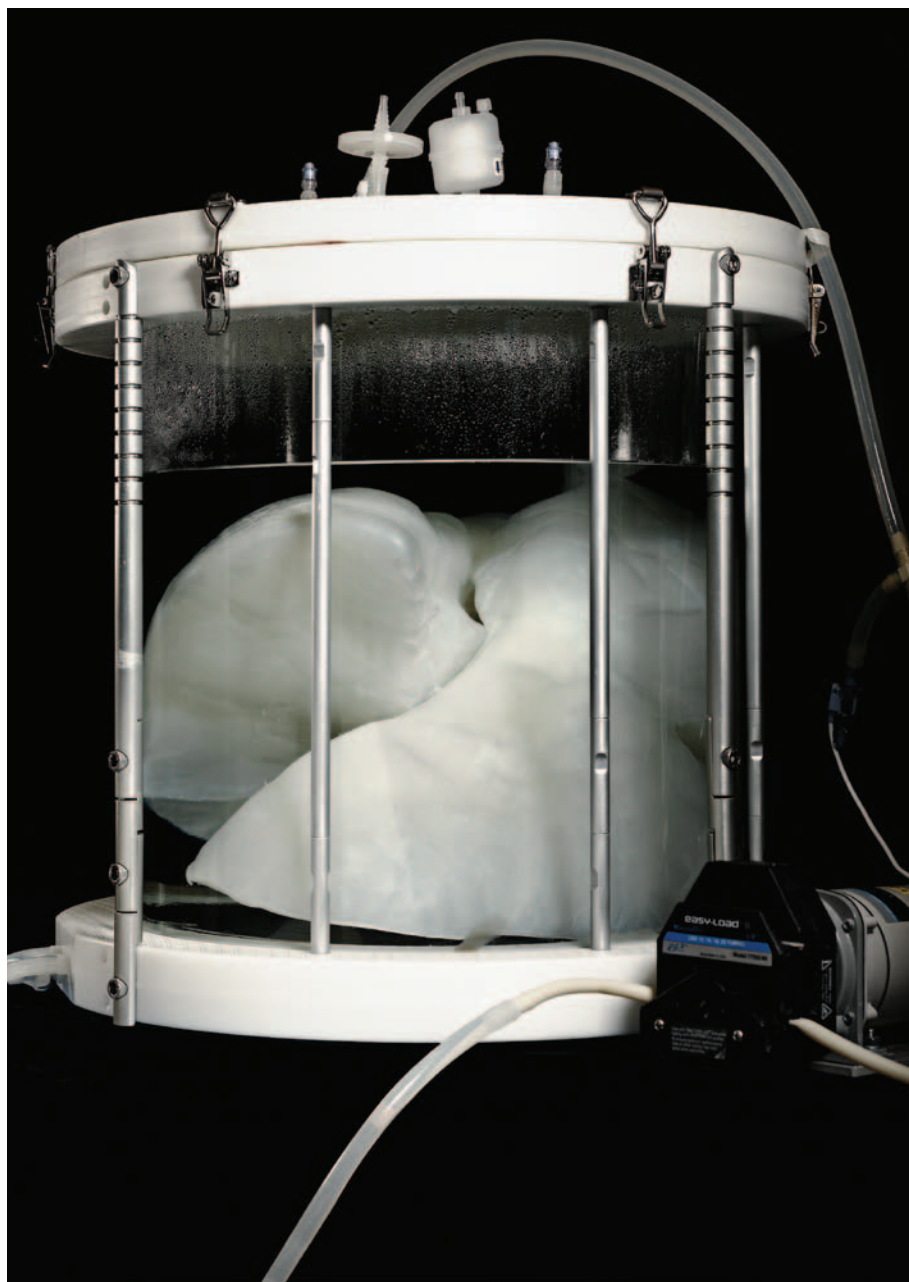
My sister Candice, for one, believes her lung capacity has increased since she started taking vitamin D as part of a smoking cessation program. She began with a daily dose of 10,000 IUs for four weeks, and continued with a daily dose of 5,000 IU (The IOM recommends just 600 IU a day for adults up to age 70 and 800 IU a day for those 71 and older). Candice can't separate out the benefits of supplementation from those of not smoking, but she attributes her improved health to both. She has little trouble carrying her four-year-old daughter up the stairs now — whereas before, she says, “I couldn't do that without losing my breath.”

Thea Singer is a freelance writer in Brookline, Massachusetts.

1. Banerjee, A. & Panettieri R. *Curr. Opin. Pharmacol.* **12**, 266–274 (2012).
2. Janssens, W. et al. *Vitamins and Hormones*, Vol. 86 (ed. Litwack, G.) Ch. 17, 379–393 (Elsevier, 2011).
3. Holick, M. F. *N. Engl. J. Med.* **357**, 266–281 (2007).
4. Merlino, L. A. et al. *Arthritis Rheum.* **50**, 72–77 (2004).
5. Janssens, W. et al. *Thorax* **65**, 215–220 (2010).
6. Persson, L. J. P. et al. *Am. J. Respir. Crit. Care Med.* **185**, A3889 (2012).
7. Zosky, G. R. et al. *Am. J. Respir. Crit. Care Med.* **183**, 1336–1343 (2011).
8. Lehouck, A. et al. *Ann. Intern. Med.* **156**, 105–114 (2012).
9. Gold, D. R. & Manson, J. E. *Ann. Intern. Med.* **156**, 156–157 (2012).

NATURE.COM

Nutritional advice—The vitamin D-lemma: go.nature.com/1jpppLb



Cadaveric or animal lungs might form the framework for new lungs made of a patient's own cells.

DEVICES

Artificial inspiration

The donor lungs of the future — built from collagen or silicone rubber or engineered from donor organs stripped of their original cells — might give a new lease of life to COPD patients.

BY ELIE DOLGIN

Sarah Gilpin is talking to a pair of opalescent human lungs. “You guys are so cool,” she says, peering into a keg-sized glass bioreactor at Massachusetts General Hospital (MGH) in Boston. The lungs float inside, puffing up as 40 litres of soapy fluid is pumped through their network of blood vessels. Less than a week earlier, these lungs belonged to a 47-year-old New Yorker, allowing him to take one last breath before dying of cardiac arrest. Now, his donated lungs have been stripped of their cells and genetic material. All that remains are two cone-shaped objects made of collagen and other structural proteins, dangling as though in suspended animation.

Gilpin, a postdoctoral fellow, is using such protein scaffolds to try to grow a set of bioartificial lungs in the laboratory. Together with Harald Ott, a cardiothoracic surgeon at MGH, Gilpin is devising a protocol to flush out the cells from donated lungs that are ineligible for direct transplantation. Eventually, they plan to seed the support structure with stem cells and to direct these cells to develop, or differentiate, into the various cell types in the lung, thereby rebuilding functioning tissue. Using the techniques the lab has developed so far, Ott has already engineered bioartificial rat lungs that can perform the appropriate gas-exchange functions when transplanted back into living rats¹. Now, he and Gilpin are scaling up to humans.

Success in their quest would bring good news to the estimated 65 million people worldwide who live with chronic obstructive pulmonary disease (COPD), a lung disorder mainly caused by exposure to tobacco smoke and airborne pollutants. Medication can often help treat the symptoms and complications of COPD, such as breathlessness and chronic coughing. But, for many people with severe forms of the disease, the only option is to replace a bad set of lungs with a good set. Relatively few lungs are donated, however, and most of these are damaged and therefore unsuitable for transplantation (see ‘Organ refit’). So, each year, around the world, only a few thousand patients with COPD receive a life-saving transplant. New sources of healthy lungs or devices that serve the same purpose are desperately needed.

Such technologies are lacking. “Count the number of devices you can use if your heart is failing, and you can make a nice long list. But if your lung is failing, you have very few options,” says Scott Merz, president and co-founder of Michigan Critical Care Consultants in Ann Arbor, a company that designs and develops ‘lung-support’ technologies.

Lab-grown lungs, reconstructed from damaged donor lungs and seeded with a patient's own cells, offer one attractive option. What's more, these bioartificial transplants could have a major advantage over their natural counterparts: by

➔ NATURE.COM
Artificial pancreas to make diabetes more manageable:
go.nature.com/spn6zs

JOSEPH FERRARO / MGH PHOTOGRAPHY SERVICES

incorporating a patient's own (autologous) cells, the lungs would be less prone to rejection by the immune system than lungs transplanted directly from a donor, and recipients wouldn't have to take lifelong cocktails of immunosuppressive agents. However, considering that Gilpin, on this particular July morning, was only part way through removing the cells from her second set of human lungs and that no other team has reported success with this approach on a similar scale, the research is still a long way from the clinic.

"We're a couple of decades away from having an autologous, tissue-engineered lung," says Laura Niklason, a biomedical engineer at Yale University in New Haven, Connecticut, who has independently created bioartificial rodent lungs². "There are technological hurdles, and there are stem-cell differentiation hurdles. But I don't think anything is insurmountable."



Surgeons strip lungs of their original cells.

In the meantime, many academic and industry researchers are turning to mechanical devices that can help the lungs to carry out their main function: gas exchange, specifically the removal of carbon dioxide from the bloodstream and the delivery of oxygen. The first such products are already on the market, and the next generation of 'artificial lungs' is not far behind.

OUTSIDE THE BOX

Novalung, a device manufacturer based in Talheim, Germany and spun off from Merz's company, is the market leader in lung-support technologies. The company's interventional lung assist (iLA) membrane ventilator takes blood from a patient's thigh and circulates it under ambient pressure from the femoral

artery through a rod lined with hundreds of tubes full of pure oxygen. Oxygenated blood then flows back into the femoral vein. This system, which was approved in Europe and a handful of other countries in the past ten years for providing respiratory support for up to 29 days, has mainly been used as a stopgap for people urgently awaiting lung transplants. But doctors are beginning to test whether this device, and similar technologies, can be used earlier in the treatment process to avoid the need for transplants altogether.

Long before needing a new set of lungs, a patient with COPD will be well acquainted with the hospital emergency department because of frequent episodes of severe breathing difficulty. These attacks — called acute exacerbations — occur, on average, two to three times a year in people with moderate-to-severe COPD. To give the lungs a break and help the patient breathe during one of these episodes, doctors usually attempt to deliver air through a face mask. Although these masks are easier to apply and less cumbersome for patients to wear than the iron lungs of the early twentieth century, mask-based ventilation doesn't work for everybody. For example, individuals who are not fully conscious and cooperative are not considered good candidates. So, if the mask approach fails, doctors turn to more invasive techniques, in which a breathing tube is inserted into the windpipe and a ventilating machine pushes air directly into the lungs. Such mechanical ventilation can save lives during a COPD attack. But it also significantly increases the risk of pneumonia, and forcing the air into the lungs can cause injury.

Lung support devices such as the iLA might obviate the need for invasive ventilation during exacerbations. For example, in a pilot study of the iLA system reported in June 2012 at the annual meeting of the German Society for Internal Intensive and Emergency Medicine in Cologne, doctors at the University Medical Center Hamburg-Eppendorf in Germany helped 13 of 14 patients with COPD avoid tracheal intubation.

"You have something that breathes outside the patient, allowing the lungs to recover and heal rather than being forced to perform by mechanical ventilation," says Georg Matheis, a managing director of Novalung, based in Heilbronn, Germany. "This might affect the long-term cause of COPD by mitigating or avoiding the damage inflicted by these exacerbations." In this way, patients who are protected against progressive damage by a system such as Novalung's might ultimately live longer or have an easier time breathing.

Novalung is now moving towards a new iLA design, with a pump that exchanges blood through the jugular veins, in the neck. This approach gives patients greater mobility, as well as lowers the risk of heart attack and other problems associated with an arterial puncture. But Novalung is not alone in pursuing this strategy: another company, ALung

ORGAN REFIT

All donations accepted

More than 80% of donated lungs worldwide are too damaged to transplant. These lungs can still be used to study tissue-engineering techniques, such as those used for generating bioartificial lungs in the laboratory of Harald Ott, a cardiothoracic surgeon at Massachusetts General Hospital in Boston. But, with many people dying while on the waiting list for a lung transplant, researchers are beginning to explore whether the unsuitable lungs might be of immediate benefit to patients, especially if some of the tissue damage can be repaired.

In a 2012 study, a British team of doctors assessed the survival of nearly 1,300 lung-transplant recipients, some 500 of whom had received lungs from donors who smoked⁵, which is permitted under UK policy. As might be expected, transplant recipients whose lung donors had not smoked survived longer. But recipients of smokers' lungs fared better than patients with COPD who remained on the waiting list. "It's better to get a lung with a smoking history than no lung at all," says Lorraine Ware, a doctor who studies lung transplantation at the Vanderbilt University School of Medicine in Nashville, Tennessee.

However, before doctors race to transplant suboptimal lungs from smokers, they might consider applying a recently developed technique called the Toronto XVIVO Lung Perfusion System. Developed by Shaf Keshavjee and his colleagues at the University Health Network in Toronto, Canada, the procedure involves pumping a protein and nutrient solution into the donor lungs and ventilating them with an oxygen gas mixture for several hours to repair damage caused by swelling or inflammation.

In a 2011 report, the Toronto team showed that only 15% of suboptimal lungs prepared in this way showed signs of acute organ injury three days after transplantation, in contrast to 30% of the supposedly healthy lungs that were transplanted without such preparation⁶. "The advantage isn't just that we can use more lungs but that we also make these transplants safer and more predictable," says Keshavjee, adding that around 20% of organs transplanted at the Toronto Lung Transplant Program undergo this perfusion treatment. (The Toronto program, like those in the UK, allows the use of smokers' lungs, which Keshavjee says make up 30–40% of lungs considered for transplant.)

"This is our first foray into partially engineering or repairing donor lungs," Keshavjee notes. If he succeeds more broadly, maybe bioartificial lungs won't be necessary after all. **E.D.**

Technologies based in Pittsburgh, Pennsylvania, is advancing a similar device as an alternative to mechanical ventilation.

In June 2012, at the 58th Annual Conference of the American Society of Artificial Internal Organs in San Francisco, California, ALung reported success with its Hemolung device, showing that patients with severe exacerbations of COPD experienced, on average, 28% reductions in their blood levels of carbon dioxide within 24 hours of the start of Hemolung treatment. “We’re bringing the technology down to a level of safety, simplicity and superior efficacy, all with a lower level of invasiveness,” says Scott Morley, a biomedical engineer who heads product management at ALung. The company plans to file for European approval of the Hemolung system later this year.

POOR EXCHANGE

Not everyone is convinced that lung-support devices offer any real advantage over mechanical ventilation for treating COPD. “Right now, the risk-benefit ratio of those two is very close, and it’s hard to tell how that’s going to play out,” says Joseph Zwischenberger, a cardiothoracic critical-care doctor at the University of Kentucky in Lexington, who has been working on artificial lungs for about 30 years. “There are those who think the technology has evolved to the point where the risk of the devices is less than the risk of being on a ventilator, and then there are a large majority who say, ‘Nope, it’s just not there yet.’”

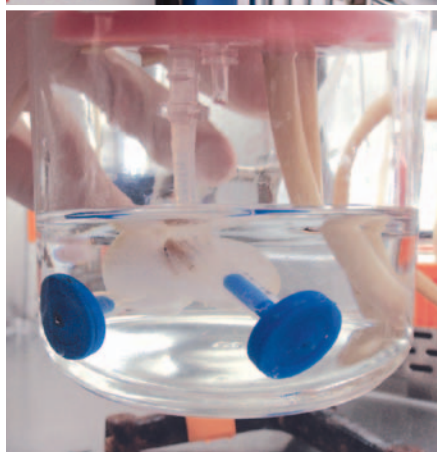
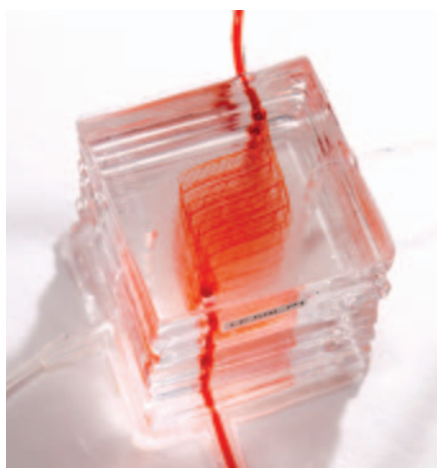
One of the biggest problems with the existing technologies is their tendency to clot: rapid blood cells encounter something akin to a traffic jam as they flow into and out of the devices. The devices are also bulky, and only limited gas exchange happens as the blood passes over the oxygen-filled fibres. Thus, many advocates of lung-support systems are looking to completely redesign the technology and are turning to the science of very small volumes — microfluidics.

Using microfluidics “enables you to get much more surface area for gas exchange per unit blood volume than the traditional devices,” says William Federspiel, a bioengineer at the University of Pittsburgh and a co-founder of ALung. “That could allow for a more compact device that is potentially efficient enough to run off room air,” unlike existing devices, which typically require a tank of pure oxygen.

Some success has been achieved already. Air delivered at near ambient pressures was able to oxygenate blood in a microfluidic

Only a pair of healthy human lungs can reverse the downward progression

device designed by Joseph Potkay and his colleagues at Case Western Reserve University in Cleveland, Ohio. In a proof-of-principle test published in 2011 (ref. 3),



A lung-on-a-chip (top), a lung-support machine (middle) and a bioreactor containing a rat lung removed of cells and ready for regeneration.

Potkay and his team created a credit-card-sized device with artificial capillaries that achieved gas-exchange rates far surpassing those of current devices, without the need for pure oxygen. “We’re pushing the size limits of this technology,” says Potkay, who is now at the Veterans Affairs Medical Center in Ann Arbor. But “through [such] microfabrication, we can get

devices on the same size scale as the structures in the natural lung.”

SIZE MATTERS

The device still has some kinks that need to be worked out. For one thing, it would take more than 1,000 of them on top of one another to provide just one-quarter of the body’s baseline gas-exchange support. And Potkay’s team designed the device to maximize gas exchange but didn’t optimize it to prevent clotting. By more closely mimicking natural blood-vessel architecture, however, a few research teams have designed microfluidic chips that circumvent the clotting problem, paving the way for long-term lung-support devices that could aid even mobile patients with COPD.

Joseph Vacanti, a transplant surgeon at MGH, is leading one such effort. Vacanti helped Ott to engineer bioartificial rat lungs, but he is now focused on developing a microfluidic device. Vacanti’s group has built a device with a bifurcating architecture that closely matches the branching of blood vessels in the body⁴. With an eye to miniaturization, his group is now working to make the system out of collagen instead of silicone, a material that introduces much dead space into the device. “We’ve got a lot of work to do on choosing the best material and making it in the thinnest possible way so the size of the thing is either wearable or implantable,” says Vacanti.

Across the river from MGH, Jeffrey Borenstein, director of the Biomedical Engineering Center at the Charles Stark Draper Laboratory in Cambridge, who has his own microfluidic lung prototype, is focused on optimizing another part of the design. To reduce the possibility of clotting, Borenstein and his colleagues are seeding the channels of their branching gas-exchange device with the cells that line blood vessels — endothelial cells — and, so far, they have seen no decline in the rates of gas transfer. “As we think about clinical implementation we really want to make this as natural a device as possible so we’re not always dealing with these blood interactions with synthetic surfaces,” Borenstein says.

Gilpin, the MGH postdoc, praises the efforts to develop lung-support devices and hopes they will soon provide some relief for people with COPD. But, ultimately, she says, only a pair of healthy human lungs can reverse the downward progression of this devastating condition. She leans her elbows on the lab bench, props her face in her hands, and gazes at the stripped set of lungs. “Seeing this makes me think we have the platform,” she says. “You’d never be able to create this. Only nature can create this.” ■

Elie Dolgin is a news editor at Nature Medicine.

- Ott, H. C. *et al. Nature Med.* **16**, 927–933 (2010).
- Petersen, T. H. *et al. Science* **329**, 538–541 (2010).
- Potkay, J. A. *et al. Lab Chip* **11**, 2901–2909 (2011).
- Hoganson, D. M. *et al. Lab Chip* **11**, 700–707 (2011).
- Bonser, R. F. *et al. Lancet* **380**, 747–755 (2012).
- Cypel, M. *et al. N. Engl. J. Med.* **364**, 1431–1440 (2011).

PERSPECTIVE



Clues, not conclusions

Scientists have some way to go before they can prove that COPD should be treated as an autoimmune disease, says **Steven R. Duncan**.

Chronic obstructive pulmonary disease (COPD) has many enigmatic traits. A progressive respiratory disorder that causes severe breathing difficulties, it can worsen even after patients stop smoking, may flare up unpredictably without apparent cause, and is often associated with other medical conditions such as atherosclerosis, osteoporosis, renal dysfunction and cancer. Many characteristics of COPD could be attributable to pathologic autoimmune processes¹. And there are increasing numbers of reports that autoantibodies against many different lung proteins are often present in COPD patients^{2,3}. If the underlying cause of COPD were indeed autoimmunity, new treatments might improve quality of life for patients.

Nonetheless, scepticism about the role of autoimmunity in COPD still abounds and is probably justified, albeit with several qualifications.

Some of the uncertainty may be explained by the nuanced and complex biology of autoimmunity⁴. Low-level reactivity to most (or maybe even all) of the body's own proteins is common, and is probably critical in preventing the immune system from mistakenly launching an injurious inflammatory response against our own cells and tissues. But in several studies, patients diagnosed with certain diseases, including COPD, have shown significantly higher levels of one or more antibodies that bind to the body's own proteins, compared to demographically matched healthy people. These findings are generally considered evidence of autoimmunity.

Several investigators have used variations of this approach to identify a "COPD autoimmune response." The increasing availability of high-throughput antigen array chips that can detect the presence of autoantibodies against thousands of proteins simultaneously, and the ease by which antigen-specific autoantibodies can be discovered, may soon spur a profusion of similar studies.

However, not all of these autoantibodies should be considered pathogenic, even if their presence is abnormal. The problem lies in understanding whether a particular one causes or contributes to disease.

Autoimmunity often develops as a consequence of chronic inflammation caused by distinct disease processes⁴. In all but a few cases, it is unknown how or why initial, narrowly targeted, and appropriate immune responses become misdirected to attack normal tissues and cause disease. One plausible explanation goes that in COPD patients, host defences triggered by microbial infection of the airways promote the development of autoimmune responses^{1,2}. The tobacco smoke that is the number-one risk factor for COPD in industrialized societies is a complex mix of highly reactive chemicals that can modify native proteins. These modified proteins may no longer be recognized as 'self' by the immune system, and can be targeted by an immune response³.

Most autoantibodies have no apparent pathogenicity. A few, however, are profoundly pathogenic and cause severe tissue damage⁴. The trick for researchers is to determine whether observed autoimmune responses are actually pathogenic, or simply abnormal and harmless. Many studies have found links between autoantibodies and the severity of COPD. That's a good start. But because underlying

inflammation could be proportionally driving harmless (epiphenomenal) autoimmune responses, it is a less than wholly compelling explanation. Some researchers maintain that particular COPD autoantibodies can be meaningful only if they are not associated with other diseases. In reality, however, fundamental immunologic processes are often shared among very different clinical syndromes. Hence, the presence of a superficially similar autoantibody in two or more clinical syndromes says little about the pathogenicity in any one of those diseases. Someday someone might discover the autoantibody that is the exclusive cause of COPD, and then the respective assay will be absolutely sensitive and specific for this disease. For now, though, this seems unlikely.

In the meantime, establishing the contribution of any given autoimmune response to COPD requires, at the least, a demonstration of pathogenicity. Autoantibodies can be isolated from patients and tested for their effects on human cell targets *in vitro*². If auto-immune responses are truly pathogenic, there should also be clear evidence of characteristic injuries within the target organ^{2,3}. T cells have exquisite specificity for antigens and considerable potential pathogenicity, and are inert to self-antigens in healthy patients. Accordingly, the presence of autoreactive T-cells is highly abnormal and is strong evidence for the presence of a pathogenic autoimmune process.

So far, however, few mechanistic studies show specific COPD autoimmune responses that cause injury. Proof that a particular autoimmune response contributes to COPD will probably require recreating the disease in an animal model through adoptive transfers of patient-derived pathogenic autoantibodies or lymphocytes — a task that may prove difficult because

of key differences between the immune systems of mice and humans.

When, as many of us working on COPD anticipate, autoimmune mechanisms are more convincingly demonstrated to be factors in COPD pathogenesis, clinical trials will have the potential to yield unprecedented medical advances. Currently available treatments for COPD primarily ameliorate symptoms. Some treatments do attack the underlying inflammation, but not very effectively, and they do not dramatically alter the overall progression of the disease. But modalities to remove autoantibodies or minimize their subsequent production are already available, and several more agents are now being developed that could also work⁵. We may soon have the rationale and tools to implement novel, and potentially better, therapies for this extremely morbid and otherwise unremitting syndrome. ■

Steven R. Duncan is a pulmonary and critical care medicine physician at the University of Pittsburgh in Pennsylvania.
email: duncsr@upmc.edu

1. Agusti, A. *et al.* *Thorax* **58**, 832–834 (2003).
2. Feghali-Bostwick, C. A. *et al.* *Am. J. Resp. Crit. Care Med.* **177**, 156–163 (2008).
3. Kirkham, P. A. *Am. J. Resp. Crit. Care Med.* **184**, 796–802 (2011).
4. Marrack, P. *et al.* *Nature Immunol.* **7**, 899–905 (2001).
5. Cancro, M. P. *et al.* *J. Clin. Invest.* **119**, 1066–1073 (2009).

NOT ALL OF THESE ANTIBODIES
SHOULD BE CONSIDERED
PATHOGENIC, EVEN IF THEIR
PRESENCE IS ABNORMAL



Drugs to treat COPD, such as Spiriva, aim to relax the smooth muscle of the airways.

THERAPEUTICS

Strength in numbers

Several new drugs for treating chronic obstructive pulmonary disease are about to hit the market, with more in the pipeline.

BY DUNCAN GRAHAM-ROWE

Shortness of breath, a tightening of the chest, wheezing and that desperate feeling that you can't get enough air into your lungs: these are all familiar to asthma sufferers. For people with chronic obstructive pulmonary disease (COPD), however, such symptoms are not fleeting. They are constant and aggravated by a steady build-up of sputum, shallow breathing and a persistent cough. The most that patients can hope for in terms of treatment is merely to manage their symptoms as they steadily worsen over time.

COPD, unlike asthma, is associated with tobacco smoking and long-term exposure to airborne toxicants, which irreparably damage the lungs, causing inflammation and airway

narrowing. But traditionally, COPD has been treated in much the same way as asthma. For relief, patients can inhale short-acting bronchodilators, which relax the airways: for example, salbutamol, which is marketed as Ventolin by the London-based drug giant GlaxoSmith-Kline (GSK). Inhaled corticosteroids also reduce inflammation in the lungs and therefore decrease the risk of acute episodes known as exacerbations, which can leave patients hospitalized for days. For managing symptoms over the longer term, there are bronchodilator-corticosteroid combinations such as salmeterol-fluticasone propionate (Advair; also marketed by GSK), which can ease symptoms for up to 12 hours. Another long-term option is tiotropium bromide (Spiriva), which acts by a different bronchodilation mechanism to provide 24-hour

relief, and is marketed by pharmaceutical companies Boehringer Ingelheim, based in Germany, and Pfizer, based in Groton, Connecticut.

Now, several new drugs for COPD treatment are on the verge of being approved by regulatory authorities (see 'Long-acting, daily medications'). The new candidates are not cures, but they may offer genuine hope that COPD sufferers can have a better quality of life.

FAST ACTION

On the surface, the offerings look like simple replacements for Spiriva and Advair. The closest to market is glycopyrronium bromide (NVA237; Seebri), which is awaiting approval in Europe and has been developed by the pharmaceutical giant Novartis, headquartered in Basel, Switzerland. Like Spiriva, this once-daily drug acts on a set of nerves in the smooth muscle around the airways. "Acetylcholine acts on muscarinic receptors found in the muscles surrounding the airways, causing the muscle in the airways to contract and the airways to narrow," explains Dave Morris, who heads global development for primary care at Novartis. In patients with COPD, the new drug competes with acetylcholine, blocking the receptors and preventing the airways from closing up. It is therefore classified, together with Spiriva, as a long-acting muscarinic antagonist (LAMA).

Novartis has carried out three large-scale phase III trials of Seebri. In May 2012, it reported the results of the second trial, GLOW2, at the American Thoracic Society International Conference in San Francisco, California. GLOW2 was conducted over one year and involved 1,066 individuals: Seebri not only improved lung function to the same extent as its analogue, Spiriva, but also took effect quicker. At both 5 minutes and 15 minutes after inhalation, it produced a doubling in FEV₁, the amount of air that can be exhaled in 1 second (as measured by blowing into a spirometer). It has also been clinically shown to produce greater bronchodilation in the first 4 hours of use than Spiriva.

GSK is taking a different tack. In July, together with Theravance, a biopharmaceutical company based in South San Francisco, California, it applied for regulatory approval in both Europe and the United States for a new drug combination: vilanterol-fluticasone furoate (previously known as Relovair but now called Relvar or Breo). Relvar is similar to Advair in that it consists of a long-acting β_2 -agonist (LABA) bronchodilator and an inhaled corticosteroid. Like Seebri (and Spiriva), Relvar works on the nerves in the smooth muscles, but it does so by stimulating β_2 -adrenergic receptors, which triggers a biochemical cascade that leads to the relaxation of the smooth muscle in the airways. In phase III trials, Relvar improved lung function compared with placebo or Advair when taken over a 12-week period, as measured by standard spirometry tests.

GSK has not yet published numbers showing the extent of the improvement. But, according

LONG-ACTING, DAILY MEDICATIONS

Do combination therapies really add value to COPD treatments? The pros and cons of long acting therapies in the pipeline.

Name	Main benefit	Type of drug	Active components	Delivery method	Doses per day	Adverse effects	Stage
Advair	Improves lung function for a period of time	Long-acting β_2 -agonist (LABA) and corticosteroid	Fluticasone/salmeterol	Dry powder inhaler	2	Increased risk of non-fatal pneumonia	Available
Spiriva	Improves lung function for a period of time	Long-acting muscarinic antagonist (LAMA)	Tiotropium bromide	Dry powder inhaler	1	Hives, rash, swelling and dry mouth	Available
PT003	Efficient delivery, improved lung function	LAMA + LABA (two molecules)	Glycopyrrolate and formoterol (LAMA + LABA)	Metered dose inhaler (MDI)	2	Headache, dry mouth and coughing	Phase II completed and Phase III to begin 2013
NVA237	Improves breathing in a matter of minutes	LAMA	Glycopyrronium bromide (LAMA)	Dry powder inhaler	1	Headache, dry mouth and coughing	Phase III completed and approval sought in Europe
Relvar	Once daily instead of twice	LABA + inhaled corticosteroid	Vilanterol and fluticasone furoate	Dry powder inhaler	1	Fatal pneumonia reported	Phase III completed and approval sought in USA and Europe
MABA	Dual action molecule improves lung function	LAMA + LABA	MABA	Most likely dry powder inhaler	Unknown	Unknown	Phase II

to a spokesperson, Relvar's effects last longer than those of Advair, so it need only be taken once a day rather than twice. A once-daily dose should significantly increase compliance. "Patients frequently don't take their second dose," says James Donohue, a pulmonary diseases specialist at the University of North Carolina at Chapel Hill, who has been involved in trials of Spiriva and has worked as a consultant to both GSK and Novartis.

DYNAMIC DUOS

Patient compliance concerns are also driving the development of combination therapies — the rationale being that patients find it easier to take a single medication. Combination therapies also have another advantage. Inhaled corticosteroids don't seem to have strong anti-inflammatory effects when they are used in isolation. When used in conjunction with separate bronchodilators, however, they've been shown to reduce the frequency of exacerbations. This synergistic effect probably arises because "the β -agonist facilitates the entry of the steroid into the [cell's] nucleus", Donohue says. So delivering them as part of a combination therapy has the potential to optimise this synergy.

Another effect with ramifications for treating COPD involves the simultaneous use of a LAMA and a LABA. The idea is to open the airways further by simultaneously switching off the nerves that tighten the passages while stimulating the ones that relax them, says Chris Cates, a population health researcher at St George's University of London who studies COPD.

Such LAMA-LABA combinations are being developed by a company called Pearl Therapeutics, based in Redwood City, California. Pearl has already carried out eight clinical trials on a combination therapy called PT003, and phase III trials are set to commence in the first half of 2013, says Colin Reisner, Pearl's chief medical officer.

PT003 is notable not so much for its chemistry

as for its novel method of delivery, says Donald Tashkin, medical director of the Pulmonary Function Laboratory at the David Geffen School of Medicine, University of California, Los Angeles, who has consulted for the company. Both the LAMA and LABA components — glycopyrrolate and formoterol fumarate, respectively — are established drugs. But PT003 delivers them together, bound to particles with a diameter of less than 5 micrometers. In this way, the drug molecules are suspended in solution and can be dispensed through a metered dose inhaler, a device that many patients find easier to operate than the commonly used dry powder inhalers. The molecular vehicle also provides an efficient means of delivery, ensuring that around half of the drug reaches its target, as opposed to as little as 5% with some delivery systems, says Tashkin.

Synergistic effects can occur in the lungs even when LABAs and LAMAs are inhaled separately, but one after the other. However there is preclinical evidence that the approach of administering

"The big question of drug combinations is whether the costs outweigh the benefits."

them simultaneously through a single device, as for PT003, may enhance their effect even further, says Darrell Baker, a senior vice president who oversees GSK's respiratory portfolio.

If this is the case, then another novel drug, being developed jointly by GSK and Theravance, could prove successful. The drug is a single molecule with both LAMA and LABA properties. Phase II clinical trials of this muscarinic antagonist- β_2 agonist (MABA) have been promising, says Baker, which when compared to salmeterol "improved bronchial dilation across a range of doses".

Even so, no trial data have been released so far, and the company's plans for this MABA are unclear. "We are keen to see how it works as a

bronchodilator by itself," says Baker. "However, we also see the opportunity for a triple-mechanism action with an inhaled corticosteroid."

Ultimately, this is where the greatest value may lie — not in the pharmacological precision of a single molecule with a dual mechanism of action, but rather in the ease with which it could pass through the drug regulatory system. "The beauty of this is when it is approved, MABA would count as one drug," says Baker.

In principle, companies hoping to develop a triple therapy by adding one drug to this MABA would therefore have a low regulatory bar, says Tashkin. Normally, triple combination therapy would require a six-way study — demonstrating improvement over not just the individual constituents but also their various combinations — but combining the MABA with an inhaled corticosteroid would require a simpler burden of proof.

The big question, says Cates, is whether the costs outweigh the benefits. For instance, adding corticosteroids may lower the risk of exacerbations but increase the risk of pneumonia. Indeed, there have been fatal cases of pneumonia associated with Relvar (although it is not the only drug to carry that potential risk). According to Baker, the company is likely to market the drug at lower doses than those given to trial subjects who developed pneumonia.

Although many of these new drug candidates hold promise and have short-term benefits, none of them has yet been shown to improve lung function year on year, says Cates. So until drug companies start to find ways to help repair damaged lungs and reverse the effects of COPD, there is only one long-term 'treatment' available to patients, he adds, and it does not involve taking drugs but abstaining from them: quitting smoking. ■

Duncan Graham-Rowe is a freelance science writer based in Brighton, UK.



GUY VANDERLST/GETTY IMAGES

The Pearl River runs through Guangzhou in China, where high levels of smog increase the incidence of COPD.

PUBLIC HEALTH

Where there's smoke

Air pollution and smoking have made COPD a major problem in China, now compounded by outdated diagnostics and treatments — and experts say it's bound to get worse.

BY VIRGINIA HUGHES

A visitor to China may well notice the country's smog problem as the plane descends. Smog levels in large cities such as Beijing and Shanghai frequently dwarf those of other metropolitan centres. Then there's the cigarette smoke. China, the world's most populous country, claims about one-third of the world's smokers — at least 300 million people — who collectively puff 1.7 trillion cigarettes a year. In rural areas, cigarette smoke permeates buses, shops and even doctors' offices.

Beyond cigarette smoke and outdoor air pollution, hundreds of millions of Chinese people breathe unclean air while working in factories and on industrial-scale farms or while cooking at wood-burning stoves inside their homes.

These airborne toxicants — many of which are by-products of China's economic boom — are risk factors for chronic obstructive pulmonary disease (COPD), an incurable respiratory disorder that can cause severe breathing

difficulties. And they have public-health officials worldwide worried about a coming epidemic. "We're just seeing the tip of the iceberg on COPD in China," says Don Sin, a respiratory medicine specialist at the University of British Columbia in Vancouver, Canada, who researches COPD. "In 30 years, [the number of cases] is going to explode."

A large-scale study in China put the prevalence of COPD in 2004 at roughly 8% in people who are 40 or older¹, in line with rates in the United Kingdom and the United States. But because China has seen soaring rates of industrialization and tobacco use over the past few decades, and because COPD symptoms aren't typically noticed until after age 50, public-health experts say the future is bleak. According to Sin, projections based on current trends and World Health Organization estimates show that by 2030, COPD will kill 3 million Chinese people a

year — a million more than die annually now.

SMOKE SIGNALS

Since the late 1970s, disposable income has been on the rise in China and so has the Chinese tobacco industry, which has ramped up production and advertising. (However, recent laws have banned cigarette advertisements on television, the radio and in newspapers.) Cigarettes are cheap: as little as 30 US cents per pack, says Sin.

Because of a strong cultural stigma, only about one in fifty Chinese women smoke. But more than half of all men, and about two-thirds of middle-aged men, do. Smoking is popular among men in the city and the country, among those of all educational levels. And a survey of doctors in six Chinese cities, published in 2007, found that 41% of male doctors smoke, and about 15% have smoked in front of their patients².

Smoking-cessation programmes exist, but their impact is minimal. Chunxue Bai, director of the Respiratory Research Institute at Fudan University, in Shanghai, says he has launched

NATURE.COM
Nature China
covers the best of
Chinese research:
go.nature.com/xuaofu

smoking-cessation clinics at 58 hospitals across China. But the clinic at his own hospital sees only about 300 people a year.

Despite the known link between smoking and COPD, most Chinese smokers do not fully appreciate the harm caused by smoking or are unconcerned. “They have some knowledge, but it doesn’t go deep enough to change their behaviour,” says Frank Hu, a nutrition specialist and epidemiologist at the Harvard School of Public Health in Boston, Massachusetts, who grew up in China.

China’s high smoking rates explain only part of its COPD problem though, because non-smokers are also at risk. For example, even though few women smoke, women still have high rates of COPD.

One explanation is that women — 82.5%, according to one study³ — are exposed to second-hand cigarette smoke. Two large studies in China have pointed to a link between this ‘passive smoking’ and COPD. The first of these studies, published in 2007, relied on the Guangzhou Biobank Cohort Study, a collection of blood samples and extensive medical data from more than 20,000 people over age 50 from Guangzhou, the largest city in southern China. In this group, the longer the duration of exposure to second-hand smoke, the higher the likelihood of COPD. The authors of this study also estimated that, of the 240 million people in China who were 50 years or older at the time of the study, 1.9 million non-smokers would die because of second-hand smoke⁴.

Similarly, the second study, published in May 2012 by Hu and his colleagues, followed 910 non-smoking Chinese women for 17 years. They found that women who were exposed to second-hand smoke were 2.3 times more likely to die from COPD than those who were not exposed, with cumulative exposure increasing the risk⁵.

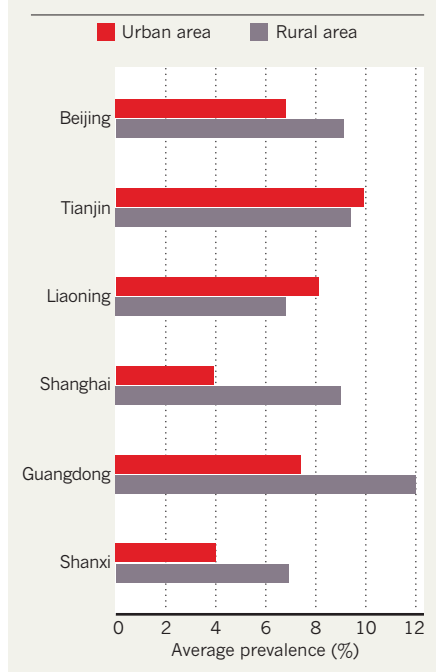
But these data are controversial. Studies of second-hand smoke in Western countries have shown a suggestive but not definitive link to COPD. Three other studies in China also did not find an association between second-hand smoke and COPD. And COPD rates are up to three times higher for non-smoking Chinese women who live in rural areas than for non-smoking Chinese women who live in cities, even though their levels of second-hand smoke exposure are similar.

“There’s no question that second-hand smoke is bad, but the [estimate] for how much COPD it causes in China is still not known,” says David Christiani, an environmental geneticist at the Harvard School of Public Health. “It’s much more than just a simple linear connection.”

Christiani became interested in the non-smoking causes of COPD in the late 1970s, when US health officials were pushing for regulations to limit workers’ exposure to cotton dust in textile factories. The process of turning fluffy cotton flowers into strong thread throws off particles of plant matter, pesticides and

COPD IN CHINA: WHERE IT’S WORST

In four of six provinces included in one study¹, the disease was more common in the countryside, which has its own risk factors — such as home cook stoves that throw off toxins and poor healthcare.



bacterial endotoxin, and textile workers had high levels of respiratory disease. But, at the time, the US cotton industry suggested that workers’ lung problems stemmed from cigarette smoking rather than conditions at the mills. “Most workers were smokers, so it was very hard to tease these things apart,” Christiani says.

Thanks to a serendipitous partnership with a university in Shanghai, Christiani realized that China offered a natural experiment to settle the debate. In Chinese factories, men and women work side by side; however, whereas most of the men smoke, hardly any of the women do.

For the past 30 years, Christiani has followed hundreds of people working at two cotton mills and one silk mill in Shanghai. His research has shown that even in non-smokers, breathing cotton dust causes significant airway blockage.

Although China has passed some labour laws to limit exposure to cotton dust, they’re often not enforced. And many other industries pose similar threats or worse ones. Coal mining, welding, construction, grain processing and animal breeding produce their own airborne toxicants — including silica crystals, asbestos and faecal matter — all of which can contribute to COPD.

The impact of these occupational hazards is evident even in the layout of Chinese hospitals, notes Peymané Adab, an epidemiologist at the University of Birmingham in the UK and an investigator on the Guangzhou Biobank Cohort Study. “There are specific wards for

people who have been exposed to certain dusts or people with lung disease related to a particular toxin,” she says.

Another key factor is indoor air pollution. More than 70% of all Chinese households, and 90% of rural ones, use stoves that run on wood, crop residues, coal or animal dung. Burning these fuels releases particulate matter, as well as fumes laced with carbon monoxide, formaldehyde and free radicals. In 2007, China’s Ministry of Environmental Protection set emissions standards for pollutants inside the home, but studies that measure air quality in rural homes have found levels exceeding the standards many times over. And exposure to biomass smoke increases COPD risk by 2.4 times, according to a 2010 meta-analysis of 15 studies⁶. “Women being the predominant cooks for families, they would be exposed to more of that,” says Sin. That might partly explain why the COPD rates in non-smoking Chinese women are higher in rural areas than in cities — the dangerous types of stove are more common in the countryside.

Sin points to a slew of other factors too. About 1.5 million people in China have tuberculosis, and many areas of China have high rates of childhood pneumonia and malnutrition. All three factors increase the risk of COPD later in life.

DEVICES WANTED

As recently as a decade ago, COPD research in China was scant. Although awareness has grown considerably in the past few years, scientists still have trouble gauging the full extent of the disease.

COPD prevalence ranges widely from region to region, from 5.5% in the province of Shanxi to 13.7% in the city of Chongqing, according to the large prevalence survey of 2004¹. Other studies have found even greater discrepancies (see ‘COPD in China: Where it’s worst’).

One reason for this variability is inconsistency in the methods of diagnosis. Spirometry, in which the patient blows as hard as possible for as long as possible into a machine that measures lung capacity, is the global gold standard. But spirometers are rarely used in China, especially outside the big cities. Even though these machines are relatively inexpensive for specialized medical equipment — several thousand dollars apiece — many doctors, especially in the countryside, do not use them. The large COPD prevalence study found that less than 7% of participants diagnosed with COPD had previously been tested by spirometry¹.

Instead, Chinese doctors tend to rely on subjective descriptions of symptoms to make the call, which can lead to misdiagnosis as asthma or a non-chronic form of bronchitis. “People go to see their doctor complaining of shortness of breath, and responses would be, ‘You’re getting old’ or ‘You have bronchitis, take some antibiotics,’” Sin says.

Even for individuals who receive a bona fide COPD diagnosis, medical care and drug treatments can be lacking. In Western countries,



One study found that fewer than 7% of COPD patients in China had been tested by spirometry.

common treatments for COPD include several kinds of inhalants, such as corticosteroids and β -agonists, that open up the airways in the lungs and provide immediate relief from symptoms. In the later stages of the disease, many patients use portable oxygen tanks. But these options are far too expensive for most Chinese patients.

In China, the most common COPD treatments are two inexpensive tablets. One, called carbocisteine, helps break up mucus and phlegm in the respiratory tract and has antioxidant properties that may slow the progression of COPD (see 'A radical treatment', page S4). The other, called theophylline, is a decades-old bronchodilator, or respiratory muscle relaxant, and anti-inflammatory. Theophylline is structurally similar to caffeine and is known for its erratic absorption and harsh side effects, including nausea, headache and life-threatening changes to heart rhythms.

Chinese researchers are focused on rigorously testing the effectiveness of their small drug arsenal. Studies of Western patients have found little benefit to adding carbocisteine or theophylline to other, reportedly more effective, treatments. But, in China, where most patients use nothing else, research has shown that the two drugs can help. For example, a 2008 report found that in Chinese patients with COPD, carbocisteine treatment for one year reduced the number of exacerbations, or sustained disease flare-ups, better than a placebo⁷. The same was found for theophylline given in a slow-release formulation at doses low enough to prevent severe side effects⁸.

Both drugs are much cheaper than inhalants. In 2008, the average annual cost of carbocisteine therapy in China was 650 renminbi (about US\$90 at the time) for each patient, compared with 4,320 renminbi (\$580) for treatment with the standard combination of

inhaled medications used in Western countries. Yet even the cheap drugs present an economic burden for most families, who shoulder the bulk of their healthcare costs without insurance or government assistance. One study found that the total cost for a patient with COPD in China was US\$1,732 a year — a tremendous amount, given that the average urban Chinese household pulled in only \$3,000 per capita in 2010, according to an analysis of government statistics by the China Market Research Group.

Beyond cost, the difference in quality of life is enormous. The inhalers used in Western countries slow down lung deterioration and give patients years of additional mobility. They are also better at preventing exacerbations, which cause intense anxiety and often take weeks to recover from. These flare-ups often mean time off from work, making treatment costs even harder to bear.

HAZY FUTURE

For now, inhalers are available only to wealthy Chinese citizens. But, as China's economy continues to grow, so too will its middle class — and its market for more expensive drugs.

Pharmaceutical giants have taken notice. A spokesperson for Novartis, headquartered in Basel, Switzerland, says the company recently approached a regulatory agency in China about one of its inhalers, a once-a-day bronchodilator. Jinping Zheng, deputy director of the Guangzhou Institute of Respiratory Disease, says that London-based AstraZeneca is investigating COPD in China. And he says that four years ago, GlaxoSmithKline (GSK), also headquartered in London, launched

COPD Academy, a programme that has reached more than 20,000 general practitioners across China. A third of the programme focuses on a COPD drug called Seretide, a combined anti-inflammatory and bronchodilator that is marketed by GSK. The other two-thirds — developed with the help of the top 18 respiratory experts in China, according to GSK — aims to deliver unbiased education on the basics of COPD diagnosis.

There has also been some regulatory movement on the antismoking front. In the past few years, major cities in China have banned smoking in hospitals, restaurants, public transport and other indoor public places, and a similar nationwide ban was instituted in 2011. These laws are difficult to enforce, however, and many smokers blatantly ignore them.

Smoking regulations promoted by prominent doctors and China's Ministry of Health have a powerful enemy in the Chinese tobacco companies, which are controlled by the government at the local and national levels. "The tobacco companies are much stronger [than the health department] because they have the money," says Tai Hing Lam, director of the School of Public Health at the University of Hong Kong. "That's why the progress has not been as good as we would like." Lam and other experts say that China's COPD problem will not be curbed until the public makes demands for more-sweeping political changes from its government.

There is a precedent. It happened in the summer of 2008, when the Olympic Games were held in Beijing, and China shut down dozens of nearby factories and ordered half of all private cars off the road. The Beijing government also passed smoking bans in schools, hospitals and government offices, and required non-smoking sections in hotels and restaurants. Air pollution dropped quickly.

But as soon as the festivities were over, business continued as usual, and many of the smoking bans were lifted.

All China needs is a wake-up call to realize the significant human and economic burden of COPD, according to Christiani. "Once China starts recognizing the problem as something that needs to be tackled, it can make some significant strides." But for millions of older Chinese people, any hope of avoiding COPD risks has gone up in smoke. ■

Virginia Hughes is a freelance science writer based in Brooklyn, New York.

1. Zhong, N. *et al.* *Am. J. Respir. Crit. Care Med.* **176**, 753–760 (2007).
2. Jiang, Y. *et al.* *Am. J. Prev. Med.* **33**, 15–22 (2007).
3. Han, J. X. *et al.* [in Chinese with English abstract] *Wei Sheng Yan Jiu* **35**, 609–611 (2006).
4. Yin, P. *et al.* *Lancet* **370**, 751–757 (2007).
5. He, Y. *et al.* *Chest* <http://dx.doi.org/10.1378/chest.11-2884> (23 May 2012).
6. Hu, G. *et al.* *Chest* **138**, 20–31 (2010).
7. Zheng, J. P. *et al.* *Lancet* **371**, 2013–2018 (2008).
8. Zhou, Y. *et al.* *Respirology* **11**, 603–610 (2006).